



UNIVERSITÉ PIERRE ET MARIE CURIE

ÉCOLE DOCTORALE D'ASTRONOMIE ET D'ASTROPHYSIQUE  
D'ÎLE-DE-FRANCE (ED127)

INSTITUT D'ASTROPHYSIQUE DE PARIS

# Bayesian large-scale structure inference and cosmic web analysis

THÈSE DE DOCTORAT

DISCIPLINE : COSMOLOGIE

présentée et soutenue publiquement le 24 septembre 2015

par

Florent LECLERCQ

devant un jury composé de :

Bertrand LAFORGE  
Benjamin WANDELT  
Oliver HAHN  
Alan HEAVENS  
Ofer LAHAV  
Will PERCIVAL  
Rien VAN DE WEYGAERT  
Matías ZALDARRIAGA

Professeur, Université Pierre et Marie Curie  
Professeur, Université Pierre et Marie Curie  
Professeur, Université Nice Sophia Antipolis  
Professeur, Imperial College London  
Professeur, University College London  
Professeur, University of Portsmouth  
Professeur, University of Groningen  
Professeur, Institute for Advanced Study, Princeton

*Président du jury*  
*Directeur de thèse*  
*Rapporteur*  
*Rapporteur*  
*Examineur*  
*Examineur*  
*Invité*  
*Invité*



Because all things balance – as on a wheel – and we cannot see nine-tenths of what is real,  
our claims of self-reliance are pieced together by unpanned gold.

— [Franklin D'Olier Reeve \(1995\)](#), *Coasting*

There's gold, and it's haunting and haunting;

It's luring me on as of old;

Yet it isn't the gold that I'm wanting

So much as just finding the gold.

It's the great, big, broad land 'way up yonder,

It's the forests where silence has lease;

It's the beauty that thrills me with wonder,

It's the stillness that fills me with peace.

— [Robert William Service \(1907\)](#), *The Spell of the Yukon*





---

# Preface

---

“But especially he loved to run in the dim twilight of the summer midnights, listening to the subdued and sleepy murmurs of the forest, reading signs and sounds as a man may read a book, and seeking for the mysterious something that called – called, waking or sleeping, at all times, for him to come.”

— [Jack London](#) (1903), *The Call of the Wild*

---

This PhD thesis is written as completion of my work at the Institut d’Astrophysique de Paris from 2012 to 2015. Three years ago, I started this project with heartfelt enthusiasm, but it turned out to be much more than expected – an incredibly rewarding journey. This thesis is the report of this long process. It expresses my vision – that I have had incredible trouble in organizing linearly – of the final scientific products.

Unfortunately, it cannot describe the thought process and the strange mechanism by which something out in there in the Universe, be it a galaxy cluster, a scientific tool, or a concept – something that a month ago was a stranger – becomes intimate. Neither does it capture my feelings during the long days – and nights – spent in front of a black board, a paper or a computer, alone or in the lab: the sadness and tiredness with failed endeavors, the bittersweet taste of learning I was wrong, the hope for good results, the joy for successes, and the wonder at the elegance of the cosmos.

As a consequence, this preface takes the occasion to describe how this thesis came into being.

## Stars and physical sciences

I have always thought that modern physics is fascinating. Not only does it manipulate extraordinary ideas and concepts (quantum mechanics, relativity), it also deals with important societal issues (energy, natural resources). In this respect, I am fascinated by how far the physical sciences, in just a few hundred years, have taken us in our understanding of nature. Given this incredible evolution, it is amazing to realize that looking at the sky – the amusement during the warm summers in ancient Greece – still gathers so much attention. This strange mixture of tradition and modernity may be the reason why, as far as I remember, I have always had a particular attraction for astrophysics.

For most of the history of humanity, cosmology was part of religion or metaphysics. Only recently did it become a science, its peculiarity being the uniqueness of its object of interest – the Universe as a whole. The idea that the entire Universe can be treated as a physical system was one of the most striking revelation of my life as a student. It is commonly predicted that early 21st century cosmology is on the verge of a revolution. In upcoming years, surprising or unexpected results may or may not be found, but I believe that cosmology will stay one of humanity’s greatest intellectual endeavors, and certainly the one that has produced the deepest description of the natural world as we find it.

## Models and beliefs

Contrary to my long-held passion for the Universe, my interest in probability theory came in a rather fortuitous manner. But faced with the immodest, enthralling questions of cosmology, one soon realizes that there is no absolute truth, only beliefs. Colleagues showed me that this viewpoint makes all the problems of modern cosmology appear in a very different light. Then, in a quick succession, reading about probability theory, which truly is the “logic of science”, in the words of [Jaynes](#) (2003), made me realize that in the much larger and permanent world of plausible reasoning, i.e. rational thinking in the presence of uncertainty, the current problems of physics appear only as details: what matters is the road, not the destination.

Few, if any, of our ordinary-life beliefs are certain to the degree that we cannot imagine them being overthrown by sufficient contradictory evidence. Similarly, typical commonsense inferences rely on applying rules that are general, but not universal. Therefore, deduction does not entirely characterize commonsense reasoning. This thesis exploits theories of inductive and abductive logic, to draw and assess the strength of conclusions from uncertain rules and partial evidence.

Probability theory, when seen as an extension of ordinary logic incorporates the description of randomness but also statistical inference and becomes a field of logical unity and simplicity. It allows us to solve problems of great complexity, and reproduces many aspects of human cognitive activity, often in disturbing detail. In doing so, it captures something about how our minds operate when we form inductive judgments, of which we may not be consciously aware. This aspect takes a very particular meaning when we deal with the Universe.

## Why bother about this thesis?

This thesis focuses on methodology for the analysis of the large-scale structure of the Universe. I should say from the beginning that the methods presented do not have the same degree of maturity as standard techniques for the analysis of galaxy surveys. So why should the reader bother?

1. I believe that new solutions to complex problems involving both data and uncertainty are needed to exploit the full potential of future, but also of existing surveys. However many data sets we record and analyze, if we use the same old models without questioning them, we will always miss the same crucially important feature that the experiment was competent to find, of which we may not be aware. If we want to detect any phenomenon, we must have a data model that at least allows the possibility that it may exist.
2. Innovative methods also allow the possibility to crosscheck the validity of cosmological analyses that are widely accepted. A false premise or a confirmation bias, when built into a model that is never questioned, cannot be removed by any amount of new data. Only a fresh look can get rid of that.

In the hope to make progress in the analysis of the cosmic large-scale structure, this thesis tries to develop a “healthy disrespect for tradition and authority, which have retarded progress throughout the 20th century” (Jaynes, 2003).

## How to read this thesis

The thesis is divided into four parts. Part I is a preparatory discussion on the analytical and numerical description of the large-scale structure. The heart of this thesis is part II on Bayesian large-scale structure inference and part IV on cosmic web analysis. The transitional part III focuses on the non-linear regime of structure formation.

It is my hope that at least some chapters are written in a sufficiently engaging textbook style for graduate students. This should be the case in particular for chapter 1 on structure formation, chapter 3 on Bayesian statistics and appendix B on numerical simulations. There, except in section 1.1, I have struggled to avoid the dreadful sentence “It can be shown that...” as much as possible. I have tried to give references to the original literature whenever it is possible, but I certainly did not attempt a true bibliography as can be found in excellent review papers on the large-scale structure and on probability theory. Chapter 4 describes the BORG algorithm, which is the basis this entire thesis. It gathers information scattered through published journal papers, and hence is also intended for reference use. The rest of the thesis directly draws from the research papers that have been published during my PhD work: chapter 2 from Leclercq *et al.* (2013) and its addendum, Leclercq, Jasche & Wandelt (2015b), chapter 5 from Jasche, Leclercq & Wandelt (2015), chapter 6 from Leclercq *et al.* (2013), chapter 7 from Leclercq *et al.* (2015) and Leclercq, Jasche & Wandelt (2015c), chapter 8 from Leclercq *et al.* (2015), chapter 9 from Leclercq, Jasche & Wandelt (2015c), and chapter 10 from Leclercq, Jasche & Wandelt (2015a). There, the style becomes more succinct and the aim is rather to describe specific projects, give a guide to the literature and report on the results obtained.

Considering that this thesis is a rare occasion to include whatever I want in a research work, I decided to tackle the difficult task of choosing epigraphs. The various quotes spread throughout the thesis may or may not have something to do with the main text. Some are inspirational, thought-provoking, some are openly provocative, some can just be considered as Easter eggs, and some are just there for free.

The online version of thesis will be revised to correct for any mistakes, typographical and otherwise, found after it goes to press and archiving. I will try to maintain a list of corrections on my website, currently hosted at <http://www2.iap.fr/users/leclercq/>. Please feel free to send me any comments at [florent.leclercq@polytechnique.org](mailto:florent.leclercq@polytechnique.org).

## Cosmology is a journey

---

“Bien lire l’Univers, c’est bien lire la vie.”

— Victor Hugo (1856), *Les Contemplations*

---

Though physical cosmology is celebrating its first century, it is no relic of the past. We live unique and very exciting times, when we expect to see a qualitative leap in our knowledge of the Universe within a lifetime. I consider myself incredibly fortunate to be part of this adventure.

In my experience, the loneliness felt by some researchers is easily overcome in our field by a simple thought: a cosmologist’s quest is the quest of all humanity. This is why, I believe, cosmology resonates with people all around the world well beyond professional scientists, in different places and cultures. It touches everybody intellectually, but also emotionally and spiritually, without prejudice. As probability theory says something about how our mind works, physical cosmology tells us how we can think of ourselves as a species.

Before moving to the traditionally must-read acknowledgement section, I would like to quote Paulo Coelho’s prologue to *The Alchemist* (1988). When Narcissus falls into the lake and dies, the lake weeps, and declares: “I weep for Narcissus, but I never noticed that Narcissus was beautiful. I weep because, each time he knelt beside my banks, I could see, in the depths of his eyes, my own beauty reflected.” When we look into the deep Universe, the Universe also may be looking deeply into us.

## Acknowledgments

---

“There are all kinds of love in this world, but never the same love twice.”

— Francis Scott Fitzgerald (1925), *The Great Gatsby*

---

What a long road this has been. It is difficult to believe that the end has finally arrived. That I could write this thesis, and much more importantly, that I became who I am to write it, is due in no small part to the support of a great many people. It is not a process that started three years ago, but way before that. Along the road, I met thousands of wonderful people. I wish I could mention by name anyone who has helped, in one way or another, but the list is very, very long. I hope that I have been as kind with you as you have been with me, and I apologize for not writing down your name.

I first wish to express my gratitude to my supervisor, Benjamin Wandelt, who was abundantly helpful and offered invaluable assistance, support and guidance. I cannot emphasize enough how delightful it has been to work with you, not only for your knowledge, dedication and modesty, but also for your interest in the human being that lies behind the scientist. Your expertise, understanding, and patience added considerably to my experience during the preparation of this thesis. Our meetings were always rich in ideas, jokes and laughs; I learned so much from you, not only scientifically, but also on how to be successful as a researcher. This is something very precious that I intend to keep forever.

I would like to address very special thanks to Jens Jasche for the opportunity to work within the larger effort surrounding Bayesian large-scale structure inference – such a stimulating endeavor – and for his assistance at all levels during this research project. I am very grateful for the time that you gave selflessly to provide me with direction and technical assistance, especially during my first two years. I greatly enjoyed our many scientific discussions and the way you influenced my scientific approaches. You have been a friendly, creative and supportive advisor.

I am also grateful to several researchers with whom I have had the chance to collaborate in the last three years: Jacopo Chevallard, Héctor Gil-Marín, Nico Hamaus, Guilhem Lavaux, Emilio Romano-Díaz, Paul Sutter, and Alice Pisani. I greatly benefited from the experience of each of you, and it has been a pleasure to work on common projects. To Nico, thanks for the organization of the weekly happy hour and for your unfailing contribution to the good atmosphere. To Paul, thanks for a very nice workshop in Ohio and for a memorable void barbecue at the occasion of the “Breaking of the Fellowship”. À Guilhem, merci de m’avoir fait partager ton expérience, tout en me rappelant qu’il ne faut pas trop parler de science comme si c’était un sujet sérieux ! À Alice, merci pour ton sourire, pour nos discussions et tout ce qu’on a partagé.

Two people, with whom I have not worked directly, deserve however a very special mention: Joseph Silk and Matías Zaldarriaga. Joe is one of the scientists I admire most, not only for his immense knowledge in astrophysics and cosmology, but also for his kindness and simplicity. Many thanks for sharing valuable insights into your vision of science and research. Matías followed my work at various stages during my PhD project. I am grateful for your invitations in Princeton, for your encouragements and for many useful discussions and suggestions. This year, applying for postdoctoral positions has been both stimulating and challenging – yet another experience of what it means to grow up. In this respect, I want to thank my recommendation letter writers, Ben Wandelt, Jens Jasche, Joe Silk and Matías Zaldarriaga, who very kindly accepted to support my applications. I am very obliged to Will Percival for his trust and for the perspective of thought-provoking exchanges, stimulating discussions and a fruitful collaboration.

I am indebted to my defense committee, Oliver Hahn, Alan Heavens, Bertrand Laforge, Ofer Lahav, Will Percival, Rien van de Weygaert and Matías Zaldarriaga for the honor to judge my work. I am extremely proud to be able to gather such a prestigious jury. Additional thanks go to the rapporteurs, Oliver Hahn and Alan Heavens, for having spent part of their summer reviewing the manuscript and for their positive judgment of my work. I am very obliged to Alan Heavens for the honor to feature one of the cosmic web maps presented in this thesis as the front cover of the proceedings of IAU Symposium 306 “Statistical challenges in 21st century cosmology”.

Participating in various international conferences and summer schools has always been a fruitful and enjoyable experience. I want to thank the organizers of the ICTP summer school on cosmology and workshop on large-scale structure (2012), the Varenna summer school (2013), the Les Houches summer school (2013), the Rencontres de Moriond (2014, Cosmology session), the IAU symposia 306 and 308 in Lisbon and Tallinn (2014), the CCAPP workshop on cosmic voids (2014), COSMO 2014 in Chicago, the MPA-EXC workshop on the dynamic Universe (2014, Garching), the ICTP workshop on cosmological structures (2015), the ESO-MPA-EXC large-scale structure conference (2014, Garching), and the Rencontres du Vietnam in Quy Nhon (2015, Cosmology session). Best greetings, in particular, to the Les Houches’ cosmologists group; thanks also to the organizers of the student conferences I attended: Elbereth 2012, 2013, 2014, and the SCGSC 2013. On various occasions, I have had the chance to have friendly and interesting discussions (even if sometimes short) within the cosmology community. In particular, my work benefited from interactions with Niayesh Afshordi, Raul Angulo, Stephen Bailey, Robert Cahn, Olivier Doré, Torsten Enßlin, Luigi Guzzo, Oliver Hahn, Jean-Christophe Hamilton, Alan Heavens, Shirley Ho, Mike Hudson, Eiichiro Komatsu, Ofer Lahav, Mark Neyrinck, Nelson Padilla, Bruce Partridge, Will Percival, David Schlegel, Uroš Seljak, Sergei Shandarin, Ravi Sheth, Svetlin Tassev, and Rien van de Weygaert (among many others). At this point, it also seems needed to acknowledge the decisive contribution of a familiar  $\sim 20$  Mpc/ $h$  void (at coordinates  $x \approx -100$ ,  $y \approx 200$  in the slice that I usually show), which very nicely makes my point during presentations.

Cette thèse n’aurait pas été la même si elle n’avait pas été préparée dans l’excellent environnement scientifique de l’IAP. Pour cette raison, je suis reconnaissant à tous ses chercheurs, et en particulier, pour d’intéressantes conversations, à Francis Bernardeau, Luc Blanchet, François Bouchet, Jean-François Cardoso, Stéphane Charlot, Yohan Dubois, Florence Durret, Silvia Galli, Valérie de Lapparent, Matt Lehnert, Gary Mamon, Henry McCracken, Jean-Philippe Uzan, Sébastien Peirani, Patrick Peter, Cyril Pitrou, et Sébastien Renaux-Petel. Merci à Valérie de Lapparent pour son aide, utile pour la rédaction de l’introduction de cette thèse, concernant l’historique des relevés de galaxies et plusieurs questions observationnelles. Thanks to Matt Lehnert for sharing his experience of the politics of research. Une pensée amicale aux étudiants en thèse que j’ai eu l’opportunité de côtoyer pendant trois ans: Sylvain et Guillaume (docteurs en 2013); Vincent, Vincent, Maxime, Jean, Hayley, Guillaume, Manuel et Flavien (docteurs en 2014); Nicolas, Hélène, Sandrine, Charlotte, Vivien et Clément (vous me devancez de quelques jours, félicitations !); et ceux pour qui ce n’est pas encore fini (bon courage !): Pierre, Thomas, Alba, Clotilde, Jean-Baptiste, Julia, Laura, Mélanie, Rebekka, Caterina, Erwan, Federico, Nicolas, Sébastien, Tilman. Amitiés également à quelques uns des labos voisins: Fabien, Julian, Benjamin, Julien, Mathilde, Tico, Anaïs, François, Linc, Agnès, Marta. Pour la gestion sans faille des serveurs Horizon, dont mon travail a beaucoup bénéficié, merci à Stéphane Rouberol et Christophe Pichon. Enfin, merci aux services informatique et administratif de l’IAP, en particulier à Isabelle Guillerme et Olivia Leroy pour la gestion de mes missions.

Je voudrais exprimer ma reconnaissance à l’École polytechnique pour une formation hors pair. Tout particulièrement, je dois à certains professeurs de m’avoir ouvert les yeux sur la relativité, l’astrophysique et la cosmologie, et d’avoir partagé avec moi leur vision de la recherche : Francis Bernardeau, David Langlois et Martin Lemoine. Merci à Fabio Iocco d’avoir guidé mes premiers pas dans le monde de la recherche, et à tous

les professeurs de la première promotion du M2 Physique des Hautes Énergies à l’X, en particulier aux directeurs Ignatios Antoniadis et Jean-Claude Brient, de m’avoir engagé sur la bonne voie pour commencer cette thèse. Pour leur suivi pendant ces trois ans, merci à l’ED 127 et à la commission des thèses de physique, en particulier, respectivement, à Florence Durret et Benoît Semelin.

Bisous à mes amis de longue date (je ne suis pas sûr que vous pensiez trouver votre nom ici !): les BIP Antoine (comment vont les caribous ?), Sébastien, Nico, Vincent, Arnaud et Nicopathe; Alex et Élise – plus un p’tit gars dont je ne connais pas encore le prénom au moment d’écrire ces lignes; Thomas et Agathe; Amandine, Arnaud et Aymeric; Anaëlle, Justin, Kéan et Aaron; Manuela, Thibaut, Marine, Clotilde, Benji, Julien, Samuel, Stéphane, et tous les autres. Merci pour les soirées, les vacances, les jeux, et pour me rappeler que s’évader n’est pas uniquement faire de la cosmologie.

« *Vivre d’orgies est ma seule espérance, le seul bonheur que j’aie pu conquérir. C’est sur les flots qu’j’ai passé mon enfance, c’est sur les flots qu’un forban doit mourir.* » Une pensée très particulière pour les corsaires de la Ciotat et les bretteurs de l’X: Cap’taine Daniel; mes différents partenaires Kornichon, Sasha, Seva, et Daniel le Savant; Emmanuel le Gaucher, Guillaume la Montagne, Charles Ventre-Sec, Dino l’Italien, Lauriane Joli-cœur, Céline Fleur d’épine, Benoît la Grenouille; et tous les corsaires ciotadens. Merci pour les combats, l’ambiance et les chants. May your swords stay sharp!

Enfin, il conviendrait sûrement d’exprimer ma reconnaissance à ma famille, mais ce que j’aurais à leur dire va bien au-delà de ce qu’il est possible d’écrire ici.

My final thanks go to you, the reader. If you are reading this thesis linearly, you have already read 9 pages and only have 228 to go. I hope the galaxies shine brightly over you through the rest of your life!

Florent Leclercq  
Paris, September 2015



---

# Contents

Introduction	1
<b>I Morphology and dynamics of the large-scale structure</b>	<b>5</b>
<b>1 Cosmological perturbations and structure formation</b>	<b>7</b>
1.1 The homogeneous Universe	8
1.2 Statistical description of cosmological fields	9
1.2.1 Average and ergodicity	9
1.2.2 Statistical homogeneity and isotropy	9
1.2.3 Gaussian and log-normal random fields in cosmostatistics	10
1.2.4 Correlation functions and power spectra	12
1.3 Dynamics of gravitational instability	15
1.3.1 The Vlasov-Poisson system	16
1.3.2 Fluid dynamics approach, evolution equations in phase space	17
1.3.3 The single-stream approximation	18
1.4 Eulerian perturbation theory	18
1.4.1 Eulerian linear perturbation theory	18
1.4.2 The growth of fluctuations in linear theory	19
1.4.3 Eulerian perturbation theory at higher order	21
1.5 Lagrangian perturbation theory	22
1.5.1 Lagrangian fluid approach for cold dark matter	22
1.5.2 The Zel'dovich approximation	23
1.5.3 Second-order Lagrangian perturbation theory	24
1.6 Non-linear approximations to gravitational instability	25
1.6.1 The Zel'dovich approximation as a non-linear approximation	25
1.6.2 Other velocity potential approximations	26
1.6.3 The adhesion approximation	26
<b>2 Numerical diagnostics of Lagrangian perturbation theory</b>	<b>29</b>
2.1 Correlation functions of the density field	30
2.1.1 One-point statistics	30
2.1.2 Two-point statistics	31
2.1.3 Three-point statistics	34
2.2 Statistics of the Lagrangian displacement field	37
2.2.1 Lagrangian $\psi$ versus Eulerian $\delta$ : one-point statistics	37
2.2.2 Perturbative and non-perturbative prescriptions for $\psi$	41
2.2.3 Non-linear evolution of $\psi$ and generation of a vector part	43
2.3 Comparison of structure types in LPT and $N$ -body dynamics	44
<b>II Bayesian large-scale structure inference</b>	<b>47</b>
<b>3 Bayesian cosmostatistics</b>	<b>49</b>
3.1 Introduction: plausible reasoning	49
3.1.1 On the definition of probability	50
3.1.2 On parameter determination	50
3.1.3 Probability theory as extended logic	50
3.2 Inverse problems and the mechanism of experimental learning	51
3.2.1 What is Bayesian analysis?	52
3.2.2 Prior choice	52
3.3 Bayesian data analysis problems	54

3.3.1	First level analysis: Bayesian parameter inference . . . . .	54
3.3.2	Exploration of the posterior . . . . .	54
3.3.3	Second level analysis: Bayesian model comparison . . . . .	56
3.4	Markov Chain Monte Carlo techniques for parameter inference . . . . .	58
3.4.1	Markov Chains . . . . .	58
3.4.2	The Metropolis-Hastings algorithm . . . . .	59
3.4.3	Hamiltonian Monte Carlo . . . . .	60
<b>4</b>	<b>Physical large-scale structure inference with the BORG algorithm</b>	<b>63</b>
4.1	The challenge: the curse of dimensionality . . . . .	64
4.1.1	Sparse sampling . . . . .	64
4.1.2	Shape of high-dimensional pdfs . . . . .	65
4.1.3	Algorithms in high dimensions . . . . .	65
4.2	The BORG data model . . . . .	66
4.2.1	The physical density prior . . . . .	67
4.2.2	The large-scale structure likelihood . . . . .	68
4.2.3	The posterior distribution . . . . .	71
4.2.4	The $\Gamma$ -distribution for noise sampling . . . . .	71
4.3	Sampling procedure and numerical implementation . . . . .	72
4.3.1	Calibration of the noise level . . . . .	72
4.3.2	Hamiltonian Monte Carlo and equations of motion for the LSS density . . . . .	72
4.3.3	The mass matrix . . . . .	73
4.3.4	The leapfrog scheme integrator . . . . .	73
4.4	Testing BORG . . . . .	74
4.4.1	Generating mock observations . . . . .	74
4.4.2	Convergence and correlations of the Markov Chain . . . . .	74
4.4.3	Large-scale structure inference . . . . .	75
4.5	Future extensions of BORG . . . . .	75
<b>5</b>	<b>Past and present cosmic structure in the Sloan Digital Sky Survey</b>	<b>79</b>
5.1	The SDSS galaxy sample . . . . .	80
5.2	The BORG SDSS analysis . . . . .	80
5.3	Inference results . . . . .	82
5.3.1	Inferred 3D density fields . . . . .	82
5.3.2	Inference of 3D velocity fields . . . . .	86
5.3.3	Inference of LSS formation histories . . . . .	86
5.4	Summary and conclusions . . . . .	89
<b>III</b>	<b>The non-linear regime of structure formation</b>	<b>93</b>
<b>6</b>	<b>Remapping Lagrangian perturbation theory</b>	<b>95</b>
6.1	Introduction . . . . .	95
6.2	Method . . . . .	97
6.2.1	Remapping procedure . . . . .	97
6.2.2	Comparison of structure types in LPT and in $N$ -body dynamics . . . . .	99
6.2.3	Improvement of the remapping procedure . . . . .	100
6.2.4	Remapping function and transfer function . . . . .	100
6.3	Statistics of remapped fields . . . . .	101
6.3.1	One-point statistics . . . . .	103
6.3.2	Two-point statistics . . . . .	105
6.3.3	Three-point statistics . . . . .	105
6.4	Discussion and conclusion . . . . .	106



<b>7</b>	<b>Non-linear filtering of large-scale structure samples</b>	<b>109</b>
7.1	Introduction . . . . .	109
7.1.1	Motivation for non-linear filtering of large-scale structure samples . . . . .	109
7.1.2	Filtering in the final conditions . . . . .	110
7.1.3	Filtering via constrained simulations . . . . .	110
7.2	Fully non-linear filtering with Gadget . . . . .	110
7.3	Fast non-linear filtering with COLA . . . . .	112
7.3.1	The COLA method . . . . .	112
7.3.2	Non-linear BORG-COLA realizations . . . . .	113
<b>IV</b>	<b>Cosmic web analysis</b>	<b>115</b>
<b>8</b>	<b>Dark matter voids in the SDSS galaxy survey</b>	<b>117</b>
8.1	Introduction . . . . .	117
8.2	Methodology . . . . .	120
8.2.1	Bayesian large-scale structure inference with the BORG algorithm . . . . .	120
8.2.2	Generation of data-constrained reconstructions . . . . .	121
8.2.3	Void finding and processing . . . . .	121
8.2.4	Blackwell-Rao estimators for dark matter void realizations . . . . .	122
8.2.5	Void catalogs for comparison of our results . . . . .	124
8.3	Properties of dark matter voids . . . . .	125
8.3.1	Number function . . . . .	125
8.3.2	Ellipticity distribution . . . . .	126
8.3.3	Radial density profiles . . . . .	127
8.4	Summary and conclusions . . . . .	128
<b>9</b>	<b>Bayesian analysis of the dynamic cosmic web in the SDSS galaxy survey</b>	<b>131</b>
9.1	Introduction . . . . .	132
9.2	Methods . . . . .	134
9.2.1	Bayesian large-scale structure inference with BORG . . . . .	134
9.2.2	Non-linear filtering of samples with COLA . . . . .	135
9.2.3	Classification of the cosmic web . . . . .	135
9.3	The late-time large-scale structure . . . . .	136
9.3.1	Tidal environment . . . . .	136
9.3.2	Probabilistic web-type cartography . . . . .	137
9.3.3	Volume and mass filling fractions . . . . .	140
9.4	The primordial large-scale structure . . . . .	141
9.4.1	Tidal environment . . . . .	142
9.4.2	Probabilistic web-type cartography . . . . .	142
9.4.3	Volume and mass filling fractions . . . . .	143
9.5	Evolution of the cosmic web . . . . .	143
9.5.1	Evolution of the probabilistic maps . . . . .	147
9.5.2	Volume filling fraction . . . . .	147
9.5.3	Mass filling fraction . . . . .	147
9.6	Summary and Conclusion . . . . .	148
<b>10</b>	<b>Cosmic-web type classification using decision theory</b>	<b>149</b>
10.1	Introduction . . . . .	149
10.2	Method . . . . .	150
10.3	Maps of structure types in the SDSS . . . . .	151
10.4	Conclusions . . . . .	154
	<b>Summary, Conclusion and Outlook</b>	<b>155</b>

<b>Appendices</b>	<b>161</b>
<b>A Complements on Gaussian random fields</b>	<b>161</b>
A.1 Characteristic function . . . . .	161
A.2 General definition of a Gaussian random vector . . . . .	162
A.3 Some well-known properties of Gaussian random vectors . . . . .	162
A.4 Marginal and conditionals of Gaussian random vectors . . . . .	163
<b>B Simulating collisionless dark matter fluids</b>	<b>165</b>
B.1 Model equations . . . . .	166
B.1.1 Model equations in the standard PM code . . . . .	166
B.1.2 Model equations with COLA . . . . .	166
B.2 Steps and data structures . . . . .	167
B.2.1 Main PM steps . . . . .	167
B.2.2 Definitions and data structures . . . . .	167
B.3 Mesh assignments and interpolations . . . . .	168
B.3.1 The mesh assignment function . . . . .	169
B.3.2 Low-pass filtering . . . . .	169
B.3.3 Common mesh assignment schemes . . . . .	170
B.3.4 Interpolation . . . . .	173
B.4 Poisson equation and accelerations . . . . .	173
B.4.1 Solving the Poisson equation . . . . .	173
B.4.2 Computation of the accelerations . . . . .	174
B.5 Update of positions and momenta . . . . .	175
B.5.1 Time integrators . . . . .	175
B.5.2 Kick and Drift operators . . . . .	176
B.6 Setting up initial conditions . . . . .	177
B.6.1 The initial Gaussian random field . . . . .	177
B.6.2 The high-redshift particle realization . . . . .	178
<b>C Cosmic structures identification and classification algorithms</b>	<b>179</b>
C.1 VIDE: the Void IDentification and Examination toolkit . . . . .	179
C.1.1 Voronoi Tessellation Density Estimation . . . . .	179
C.1.2 The watershed algorithm . . . . .	180
C.1.3 Processing and analysis of void catalogs . . . . .	180
C.1.4 Radial density profiles . . . . .	181
C.2 The T-web . . . . .	181
C.2.1 The tidal tensor . . . . .	181
C.2.2 Analogy with the Zel'dovich formalism . . . . .	182
C.2.3 The T-web: original procedure . . . . .	182
C.2.4 Extensions of the T-web . . . . .	183
C.2.5 Implementation . . . . .	184
C.2.6 Example . . . . .	185
<b>Bibliography</b>	<b>187</b>
<b>Index</b>	<b>222</b>

---

# Introduction

---

“Make your choice, adventurous Stranger,  
Strike the bell and bide the danger,  
Or wonder, till it drives you mad,  
What would have followed if you had.”

— [Clive Staples Lewis \(1955\)](#), *The Chronicles of Narnia, The Magician’s Nephew*

---

## Large-scale structure surveys during the age of precision cosmology

Understanding the structure of the Universe at the largest scales is one of the main goals of cosmology. The existence of such a structure has been suggested by early observational projects aimed at mapping the distribution of galaxies, which resulted in a number of discoveries of individual elements – filamentary bridges between superclusters, and large voids – on scales of tens of megaparsecs ([Gregory & Thompson, 1978](#); [Gregory, Thompson & Tifft, 1981](#); [Kirshner et al., 1981](#); [Zel’dovich, Einasto & Shandarin, 1982](#)). In 1986, the results of the Center for Astrophysics redshift survey marked a milestone, with the discovery of bubble-like structures separated by sheets on which galaxies tend to lie ([de Lapparent, Geller & Huchra, 1986](#)). These results renewed interest for large-scale structure cartography, leading to new galaxy catalogs up to a depth of  $\sim 400$  Mpc ([Geller & Huchra, 1989](#); [Shectman et al., 1996](#); [Vettolani et al., 1997](#); [Schuecker & Ott, 1991](#)). In spite of their incompleteness, these maps conclusively confirmed the existence of a large-scale organization of galaxies into a hierarchical structure, the *cosmic web*. At the turn of the century, massive surveys, aimed at obtaining the spectra of hundreds of thousands of galaxies (e.g. the 2dFGRS, [Colless et al., 2003](#); the SDSS, [Strauss et al., 2002](#); WiggleZ, [Drinkwater et al., 2010](#) or the 2MASS redshift survey, [Huchra et al., 2012](#)), mapped large volumes of the nearby Universe. They allowed to largely increase the completeness of observations and to obtain large enough samples for statistical analyses. Other observational programs (e.g. DEEP2, [Davis et al., 2003, 2007](#); VVDS, [Le Fèvre et al., 2005, 2013](#); zCOSMOS, [Lilly et al., 2007](#); GAMA, [Driver et al., 2009](#); VIPERS, [Guzzo et al., 2014](#)) focused on targeting galaxies in a smaller area on the sky, but at higher redshift.

In the coming decade, ongoing or planned cosmological programs will measure the distribution of galaxies at an unprecedented level. These include wide photometric surveys (DES, [Dark Energy Survey Collaboration, 2005](#); HSC, [Miyazaki et al., 2012](#); J-PAS, [Benítez et al., 2015](#); LSST, [LSST Science Collaboration, 2009, 2012](#)), deep spectroscopic surveys (eBOSS; HETDEX, [Hill et al., 2008](#); the Subaru Prime Focus Spectrograph, [Takada et al., 2014](#); DESI, [Schlegel et al., 2011](#); Abdalla et al., 2012; Levi et al., 2013), and the Euclid ([Laureijs et al., 2011](#); [Amendola et al., 2013](#)) and WFIRST ([Green et al., 2012](#); [Spergel et al., 2013](#)) satellites.

How do we compare this avalanche of data to cosmological models? The standard picture of LSS formation, developed over the last three decades, relies of the gravitational self-evolution of a set of initial density fluctuations, giving rise to the complex structures observed in galaxy surveys. Extracting the wealth of information that surveys contain thus requires a quantitative understanding of both the generation of the initial seed perturbations and of the dynamics of gravitational instability.

## Early Universe physics and generation of the initial conditions of the Universe

Inflation and the Hot Big Bang scenario provide an observationally well-supported physical model for the initial conditions. The inflationary paradigm (see e.g. [Baumann, 2011](#), for a review) is generally favored over other theories for the origin of seed perturbations, since it also provides explanations for some shortcomings of the standard Hot Big Bang picture, e.g. the statistical homogeneity and isotropy of the Universe, and the horizon problem ([Guth, 1981](#); [Linde, 1982](#); [Albrecht & Steinhardt, 1982](#)). According to this model, during the inflationary era, the equation of state of the Universe is governed by a potential-dominated quantum scalar field with negative pressure, the so-called *inflaton field*. This quantum field drives an exponential growth of the cosmic scale factor. What is remarkable with inflation is that the accelerated expansion in the very early Universe can magnify the vacuum quantum fluctuations of the inflaton into macroscopic cosmological perturbations.

This model naturally provides us with a statistically homogeneous and isotropic density field with small, very nearly Gaussian-distributed, and nearly scale-invariant density perturbations (Guth & Pi, 1982; Hawking, 1982; Starobinsky, 1982; Bardeen, Steinhardt & Turner, 1983).

Phenomena such as primordial nucleosynthesis (Alpher, Bethe & Gamow, 1948), decoupling and recombination, free-streaming of neutrinos, acoustic oscillations of the photon-baryon plasma, and transition from radiation to matter domination, come next. They are predicted by the Hot Big Bang model, which remains a cornerstone of our understanding of the past and present Universe (see e.g. Kolb & Turner, 1990; Peacock, 1999). They change the post-inflationary density field into what we call the “initial conditions” for gravitational evolution. Then, during the matter and dark-energy dominated eras, self-gravity and the expansion of the Universe modify these initial conditions into an evolved density field, at first through linear transfer and then through non-linear structure formation.

Due to their quantum origin, the process of generating seed perturbations is stochastic (see e.g. Baumann, 2011, section 2.3). Therefore, a probability distribution function is the most fundamental characterization of the large-scale structure of the Universe. As a consequence, it is now standard to describe in a probabilistic way the generation of the initial density fluctuations by the above-mentioned early Universe processes.

## Large-scale structure evolution and galaxy formation

According to the current picture of cosmic structure formation, all presently observed structures have their origins in primordial seed fluctuations. Zel’dovich & Novikov (1983) recognized the central role played by gravitational instability. Peebles (1982a, 1984) realized that baryonic models of structure formation are insufficient to explain observed galaxies morphology and distribution, and consequently proposed the introduction of cold dark matter. The ensuing controversy between the “top-down” (in which large structures form first, then fragment; as is the case when hot dark matter, such as neutrinos, dominates) and “bottom-up” (in which small structures such as galaxies form first, then aggregate; as is the case when cold dark matter dominates) structure formation scenarios was subsequently settled in favor of the latter (Bond, Szalay & Turner, 1982; Melott *et al.*, 1983; Blumenthal *et al.*, 1984). Therefore, it is currently believed that structure formation is mostly governed by the gravitational aggregation of a dark matter fluid. As proposed by Rees & Ostriker (1977); Silk (1977); White & Rees (1978), luminous objects such as galaxies form via condensation and cooling of baryonic matter in gravitational potential wells shaped by the dark matter structure.

## Physical processes and information content

The detailed appearance of the presently observed galaxy distribution contains a record of its origin and formation history. Large-scale structure formation therefore encodes information on a wide range of processes involving very different physics, ranging from quantum field theory and general relativity, to the dynamics of collisionless dark matter and the hydrodynamics and radiation transfer processes involved in galaxy formation. The next generation of galaxy surveys is therefore expected to provide insights into many fundamental physics questions: What is the Universe made of? What is the microphysics of dark matter? How does dark energy behave? What is the mass of neutrinos? Is general relativity complete or does it require modifications? What were the conditions in the early Universe?

All LSS observations are informative in some ways about these questions, but due to an incomplete understanding of the dark matter-galaxy connection (the “bias problem”: see in particular the “peak-background split model”, Bardeen *et al.*, 1986; Cole & Kaiser, 1989, and the “halo model”, Seljak, 2000; Peacock & Smith, 2000; Cooray & Sheth, 2002) and observational effects (the Alcock-Paczynski effect, Alcock & Paczynski, 1979; redshift-space distortions, Kaiser, 1987; Peacock *et al.*, 2001; Hawkins *et al.*, 2003; Guzzo *et al.*, 2008; non-trivial selection functions; see e.g. Percival, 2014, for a review), the message is encoded and sometimes hard to extricate. Hence, crucial to the aim of answering the above questions is identifying where is the information content and developing efficient tools to extract it.

The usual strategy is to look at the shape and length scales imprinted in the galaxy power spectrum, such as the baryon acoustic oscillation scale (Percival *et al.*, 2001; Cole *et al.*, 2005; Eisenstein *et al.*, 2005; Percival *et al.*, 2010). However, at small scales and at late times, non-linear dynamics shifts the information content away from the two-point function to the higher-order correlators. One of the main goals of this thesis is to access the untapped information in late-time, non-linear modes. The number of modes accessible for cosmological

analyses grows like  $k^3$ , where  $k$  is the largest usable wavenumber. In the case of BAOs, a technique known as “reconstruction” has been designed to correct for the effects of non-linearities, and has been shown to improve distance measurements (Eisenstein *et al.*, 2007; Padmanabhan *et al.*, 2012). Hence, our strategy is twofold: pushing down the smallest scale that can be both modeled and resolved; and inferring the initial conditions that give rise to the observed LSS. The reward for undertaking this project is a potentially vast gain of information for the determination of model parameters.

## The scientific method and the process of data assimilation

Generally, contact between theory and observations cannot be established directly. Historically, scientific progress relied on experimental assessment (the “first paradigm” of science) and theoretical modeling (the “second paradigm”). In the last few decades, with growing complexity of the real-world processes to be described, testable predictions of theories often had to be obtained through numerical simulations of phenomena. Additionally, even elaborate experiments do not allow for direct comparison to the results of simulations, due to the fact that there exists no ideal observation in reality, as they are subject to a variety of uncertainties. One has to model the response functions of devices and treat their outputs, a step we refer to as signal processing (for example, the representation of a real-world signal and the application of fast Fourier transforms require its computer representation to be discrete both in configuration and in frequency space). Numerical simulations and data processing constitute the “third paradigm” of science. Their outputs are compared to judge and evaluate current models. These results can be used to perform inferences, i.e. update our knowledge on theoretical parameters, test hypotheses and compare competing models. They can also be used to optimize the design of new experiments. These last two steps close loops that go from theory to data, and from data to theory, as illustrated in figure 1. Scientific progress in any of the physical sciences crucially depends on these steps.

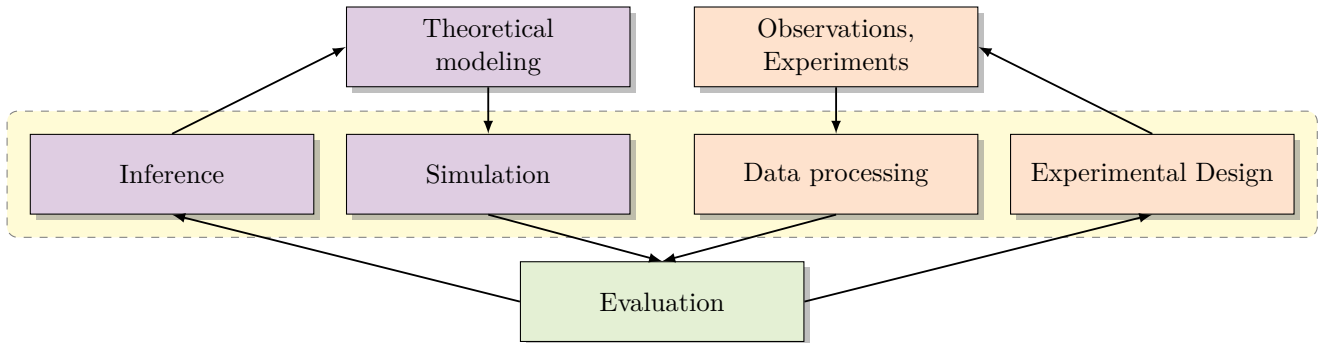


Figure 1: Diagram illustrating steps in the scientific method. Progress in physical sciences depends on each of these steps: experimental assessment (the first paradigm), theoretical modeling (the second paradigm), computational studies (simulation of phenomena and data processing – the third paradigm). The outputs of simulations and data processing are compared to judge and evaluate current models. These results are used to infer theoretical parameters and to design new experiments. The yellow rectangle shows the emergence of a fourth research paradigm: data-intensive scientific discovery, where extremely large data sets captured by instruments and generated by complex simulations are used.

Several authors are now describing the emergence of a so-called “fourth paradigm” of research: data-intensive scientific discovery (Microsoft Research, 2009; Szalay, 2014). Scientific insights are wrested from extremely vast data sets. This transition from hypothesis-driven to data-driven research is made possible by new technologies for gathering, processing, manipulating, analyzing, mining, and displaying data. For example, exascale computers, expected around 2018, will be of the order of processing power of the human brain at the neural level.

This thesis falls within the context of this emerging fourth paradigm. Its field is cosmostatistics, the discipline that uses stochastic quantities as seeds of structure to make the connection between cosmological models and observations. This area is at the interface between theory and observational data (see Leclercq, Pisani & Wandelt, 2014):

- It consists of predicting cosmological observables from stochastic quantities as seeds of structure in the Universe (*from theory to data*). Theoretical hypotheses are used to model, predict and anticipate results.

- It uses the departures from homogeneity and isotropy, observed in astronomical surveys, to distinguish between cosmological models (*from data to theory*). Data sets are used to infer parameters of the theoretical models and to compare their relative suitability.

More specifically, this work focuses on the process of *data assimilation* for the large-scale structure, i.e. the process by which observations are incorporated into a numerical model of a real system. Data assimilation is a field of statistics, widely understood and used outside of astrophysics (e.g. in meteorology, geophysics, oceanography and climate sciences). The general mechanism consists of iteratively correcting the state of a prediction based on a physical model, using successive observations. In this work, we borrow ideas from these sciences and apply them to large-scale structure data analysis. For all quantities of interest, we do not only provide a best-guess estimate, but fully account for all credible regions by a detailed quantification of the probability density.

## Goal and structure of this thesis

The ambition of this work is to describe progress towards enriching the standard for the analysis of galaxy surveys. The central ingredient is the recently proposed BORG (Bayesian Origin Reconstruction from Galaxies, [Jasche & Wandelt, 2013a](#); [Jasche, Leclercq & Wandelt, 2015](#)) algorithm. BORG is a Bayesian data assimilation code, which provides a fully probabilistic, physical model of the non-linearly evolved density field as probed by LSS surveys.

The goal of this thesis is to demonstrate that Bayesian large-scale structure inference with the BORG algorithm has moved beyond the proof-of-concept stage. In particular, it describes the first application to real cosmological data from the Sloan Digital Sky Survey, and shows how these results can be used for cosmic web classification and analysis.

This thesis is organized as follows. Part I focuses on the analytical and numerical description of the morphology and growth of the LSS. Chapter 1 is an introduction to the theory of structure formation, as relevant for this thesis. As Lagrangian perturbation theory is a key ingredient of the BORG algorithm, the reliability of its numerical predictions is investigated in chapter 2.

Part II introduces Bayesian large-scale structure inference. In chapter 3, we present the framework of Bayesian probability theory. Chapter 4 reviews the latest version of the BORG algorithm and its implementation. Chapter 5 presents the application of BORG to the Sloan Digital Sky Survey data. These results quantify the distribution of initial conditions as well as the possible formation history of the observed structures.

As LSS surveys contain a wealth of information that cannot be trivially extracted due to the non-linear dynamical evolution of the density field, part III discusses methods designed to improve upon standard techniques by including non-Gaussian and non-linear data models for the description of late-time structure formation. Chapter 6 presents a computationally fast and flexible model of mildly non-linear density fields via the technique of remapping LPT. In chapter 7, we introduce the concept of non-linear filtering, designed to improve LSS samples at non-linear scales.

Finally, part IV exploits the BORG SDSS analysis for different cosmographic projects aiming at characterizing and analyzing the cosmic web. Chapter 8 demonstrates that the inference of voids in the dark matter distribution is possible, and that, in addition, our method yields a drastic reduction of statistical uncertainty in void catalogs. In chapter 9, we describe a probabilistic classification of the dynamic cosmic web into four distinct components: voids, sheets, filaments, and clusters. Subsequently, chapter 10 introduces a new decision criterion for labeling different regions, on the basis of posterior probabilities and the strength of data constraints.

In the last chapter, we summarize our results and give our conclusions. Prospective applications and possible directions for future investigations are also mentioned.

The appendices provide complementary material: a mathematical exposition of Gaussian random fields (appendix A), a review of the particle-mesh technique for dark matter simulations (appendix B), and a description of the cosmic web analysis algorithms used in this thesis (appendix C).

## **Part I**

# **Morphology and dynamics of the large-scale structure**





# Cosmological perturbations and structure formation

---

## Contents

---

<b>1.1</b>	<b>The homogeneous Universe</b>	<b>8</b>
<b>1.2</b>	<b>Statistical description of cosmological fields</b>	<b>9</b>
1.2.1	Average and ergodicity	9
1.2.2	Statistical homogeneity and isotropy	9
1.2.3	Gaussian and log-normal random fields in cosmostatistics	10
1.2.4	Correlation functions and power spectra	12
<b>1.3</b>	<b>Dynamics of gravitational instability</b>	<b>15</b>
1.3.1	The Vlasov-Poisson system	16
1.3.2	Fluid dynamics approach, evolution equations in phase space	17
1.3.3	The single-stream approximation	18
<b>1.4</b>	<b>Eulerian perturbation theory</b>	<b>18</b>
1.4.1	Eulerian linear perturbation theory	18
1.4.2	The growth of fluctuations in linear theory	19
1.4.3	Eulerian perturbation theory at higher order	21
<b>1.5</b>	<b>Lagrangian perturbation theory</b>	<b>22</b>
1.5.1	Lagrangian fluid approach for cold dark matter	22
1.5.2	The Zel'dovich approximation	23
1.5.3	Second-order Lagrangian perturbation theory	24
<b>1.6</b>	<b>Non-linear approximations to gravitational instability</b>	<b>25</b>
1.6.1	The Zel'dovich approximation as a non-linear approximation	25
1.6.2	Other velocity potential approximations	26
1.6.3	The adhesion approximation	26

---



---

“For the mind wants to discover by reasoning what exists in the infinity of space that lies out there, beyond the ramparts of this world – that region into which the intellect longs to peer and into which the free projection of the mind does actually extend its flight.”  
— [Lucretius](#), *De Rerum Natura*

---

## Abstract

This chapter provides an overview of the current paradigm of cosmic structure formation, as relevant for this thesis. It also reviews standard tools for large-scale structure analysis.

This chapter is organized as follows. In section 1.1, key equations of general relativistic Friedmann-Lemaître cosmological models are briefly reviewed, followed by a discussion of the statistical description of cosmological fields in section 1.2 and of the dynamics of gravitational instability in section 1.3. In section 1.4 and 1.5 we describe cosmological perturbation theory in Eulerian and Lagrangian descriptions. Finally, section 1.6 deals with various non-linear approximations to gravitational instability.

## 1.1 The homogeneous Universe

This section provides an overview of the standard picture of cosmology, describing the homogeneous evolution of the Universe. In particular, we reproduce some very standard equations around which perturbation theory will be implemented in the following. A demonstration can be found in any introduction to cosmology, see for example Peebles (1980); Kolb & Turner (1990); Liddle & Lyth (2000); Bernardeau *et al.* (2002); Lesgourgues (2004); Trodden & Carroll (2004); Langlois (2005, 2010).

Let  $a$  be the cosmic scale factor, normalized to unity at the present time:  $a_0 = 1$ . We denote by  $t$  the cosmic time, by  $\tau$  the conformal time, defined by  $dt = a(\tau) d\tau$ , and by  $z$  the redshift, defined by  $a = 1/(1+z)$ . In the following, a dot denotes a differentiation with respect to  $t$  and a prime a differentiation with respect to  $\tau$ . Friedmann's equations, describing the dynamics of the Universe, are derived from Einstein's equations of general relativity. In conformal time, they read:

$$\mathcal{H}^2 = \frac{8\pi G}{3} a^2 \rho - k, \quad (1.1)$$

$$\text{and } \mathcal{H}' = -\frac{4\pi G}{3} a^2 (\rho + 3P), \quad (1.2)$$

where  $\mathcal{H} \equiv a'/a = aH$  is the conformal expansion rate,  $H \equiv \dot{a}/a$  is the Hubble parameter,  $\rho$  the total energy density and  $P$  the pressure.  $k$  is the reduced curvature parameter, taking one of the following values:  $-1$  for an open universe,  $0$  for a flat universe,  $1$  for a closed universe.  $G$  denotes the gravitational constant, and we adopt units such that  $c = 1$ .

As a direct consequence, Friedmann's equations immediately determine the evolution of the energy density, described as:

$$\rho' = -3\mathcal{H}(\rho + P). \quad (1.3)$$

Throughout this thesis, we will particularly focus on the eras of matter domination and dark-energy domination within the standard  $\Lambda$ CDM paradigm. Hence, we will consider that the content of the Universe is limited to two components: matter (mostly cold dark matter) and dark energy in the form of a cosmological constant  $\Lambda$ . We denote by  $\rho_m$  and  $\rho_\Lambda \equiv \Lambda/8\pi G$  their respective energy densities. Introducing their respective equations of state,  $w_i \equiv P_i/\rho_i$ , we have  $w \approx 0$  for cold dark matter and  $w = -1$  for the cosmological constant. For this cosmology, equation (1.2) reads

$$\mathcal{H}' = -\frac{4\pi G}{3} a^2 \rho_m + \frac{8\pi G}{3} a^2 \rho_\Lambda. \quad (1.4)$$

It is convenient to introduce the dimensionless cosmological parameters as the ratio of density to critical density,  $\rho_{\text{crit}}(t) \equiv 3H^2(t)/8\pi G$ , which corresponds to the total energy density in a flat universe:  $\Omega_m(t) \equiv 8\pi G \rho_m(t)/3H^2(t)$  and  $\Omega_\Lambda(t) \equiv 8\pi G \rho_\Lambda/3H^2(t) = \Lambda/3H^2(t)$ . Their expression in terms of conformal time is given by

$$\Omega_m(\tau) \mathcal{H}^2(\tau) = \frac{8\pi G}{3} \rho_m(\tau) a^2(\tau), \quad (1.5)$$

$$\Omega_\Lambda(\tau) \mathcal{H}^2(\tau) = \frac{8\pi G}{3} \rho_\Lambda a^2(\tau) \equiv \frac{\Lambda}{3} a^2(\tau). \quad (1.6)$$

Note that  $\Omega_m(\tau)$  and  $\Omega_\Lambda(\tau)$  are time-dependent. Inserting these two expressions in equation (1.4) yields the following form of the second Friedmann equation,

$$\mathcal{H}'(\tau) = \left( -\frac{\Omega_m(\tau)}{2} + \Omega_\Lambda(\tau) \right) \mathcal{H}^2(\tau), \quad (1.7)$$

and the first one reads

$$\mathcal{H}^2 = \frac{8\pi G}{3} a^2 \rho_m + \frac{8\pi G}{3} a^2 \rho_\Lambda - k = \Omega_m \mathcal{H}^2 + \Omega_\Lambda \mathcal{H}^2 - k, \quad (1.8)$$

which yields

$$k = (\Omega_{\text{tot}}(\tau) - 1) \mathcal{H}^2(\tau), \quad (1.9)$$

where  $\Omega_{\text{tot}}(\tau) \equiv \Omega_m(\tau) + \Omega_\Lambda(\tau)$ . In the following, we will note  $\Omega_m^{(0)} = \Omega_m(a=1)$  and  $\Omega_\Lambda^{(0)} = \Omega_\Lambda(a=1)$ .

## 1.2 Statistical description of cosmological fields

In this section, we consider some cosmic scalar field  $\lambda(\mathbf{x})$  whose statistical properties are to be described. It denotes either the cosmological density contrast,  $\delta(\mathbf{x})$ , the gravitational potential,  $\Phi(\mathbf{x})$  (see section 1.3), or any other field of interest derived from vectorial fields (e.g. the velocity divergence field), polarization fields, etc.

As discussed in the [introduction](#), values of  $\lambda(\mathbf{x})$  have to be treated as stochastic variables. For an arbitrary number  $n$  of spatial positions  $\mathbf{x}_i$ , one can define the *joint multivariate probability distribution function* to have  $\lambda(\mathbf{x}_1)$  between  $\lambda_1$  and  $\lambda_1 + d\lambda_1$ ,  $\lambda(\mathbf{x}_2)$  between  $\lambda_2$  and  $\lambda_2 + d\lambda_2$ , etc. This pdf is written

$$\mathcal{P}(\lambda_1, \lambda_2, \dots, \lambda_n) d\lambda_1 d\lambda_2 \dots d\lambda_n. \quad (1.10)$$

### 1.2.1 Average and ergodicity

**Average.** The word “average” (and in the following, the corresponding  $\langle \rangle$  symbols) may have two different meanings. First, one can average by taking many realizations drawn from the distribution, all of them produced in the same way (e.g. by  $N$ -body simulations). This is the *ensemble average*, defined to be for any quantity  $X(\lambda_1, \lambda_2, \dots, \lambda_n)$ :

$$\langle X \rangle \equiv \int X(\lambda_1, \lambda_2, \dots, \lambda_n) \mathcal{P}(\lambda_1, \lambda_2, \dots, \lambda_n) d\lambda_1 d\lambda_2 \dots d\lambda_n, \quad (1.11)$$

where  $\mathcal{P}(\lambda_1, \lambda_2, \dots, \lambda_n)$  is the joint multivariate pdf.

One can also average by considering the quantity of interest at different locations within the same realization of the distribution. This is the *sample average*. For some volume  $V$  in the Universe, the sample average over  $V$  of a quantity  $X$  is defined to be:

$$\bar{X} \equiv \frac{1}{V} \int_V X(\mathbf{x}) d^3\mathbf{x}. \quad (1.12)$$

**Ergodicity.** If the ensemble average of any quantity coincides with the sample average of the same quantity, the system is said to be *ergodic*. In cosmology, the hypothesis of ergodicity is often adopted, at least if the considered catalogue is large enough. For instance, if ergodicity holds, the mean density of the Universe is given by

$$\langle \rho(\mathbf{x}) \rangle = \bar{\rho} \equiv \frac{1}{V} \int_V \rho(\mathbf{x}) d^3\mathbf{x}, \quad (1.13)$$

in the limit where  $V \rightarrow \infty$ . The term of ergodicity historically refers to time processes, not to spatial ones. If the above property is fulfilled in cosmology, one says that the system is a *fair sample* of the Universe.<sup>1</sup>

### 1.2.2 Statistical homogeneity and isotropy

A random field is said to be *statistically homogeneous* if all joint multivariate pdfs  $\mathcal{P}(\lambda(\mathbf{x}_1), \lambda(\mathbf{x}_2), \dots, \lambda(\mathbf{x}_n))$  are invariant under translations of the coordinates  $\mathbf{x}_1, \mathbf{x}_2, \dots, \mathbf{x}_n$  in space. Thus probabilities depend only on relative positions, but not on locations. Note that statistical homogeneity is a weaker assumption than homogeneity, which would mean that  $\lambda(\mathbf{x})$  takes the same value everywhere in space.

Similarly, a random field is said to be *statistically isotropic* if all  $\mathcal{P}(\lambda(\mathbf{x}_1), \lambda(\mathbf{x}_2), \dots, \lambda(\mathbf{x}_n))$  are invariant under spatial rotations.

From now on, cosmic fields will be considered statistically homogeneous and isotropic, as a consequence of the cosmological principle that underlies most inflationary calculations (see [Guth, 1981](#); [Linde, 1982](#); [Albrecht & Steinhardt, 1982](#); [Linde, 1995](#)), and of standard gravitational evolution (e.g. [Peebles, 1980](#)). Of course, the validity of this assumption has to be checked against observational data. It is also important to note that a lot of the information from galaxy surveys comes from effects that distort the observed signal away from this ideal. In particular, observational effects such as the Alcock-Paczynski effect ([Alcock & Paczynski, 1979](#)) and redshift-space distortions ([Kaiser, 1987](#)) in galaxy surveys introduce significant deviations from statistical homogeneity and isotropy.

<sup>1</sup> In the case of the LSS, care should be taken with deep surveys. Indeed, as data lie on the surface of the relativistic lightcone, we cannot have access to a fair sample of the Universe at the present time. Rigorously, ergodicity is not verified.

### 1.2.3 Gaussian and log-normal random fields in cosmostatistics

This section draws from subsection 2.2 of [Leclercq, Pisani & Wandelt \(2014\)](#).

Gaussian random fields are ubiquitous in cosmostatistics (see [Lahav & Suto, 2004](#); [Wandelt, 2013](#); [Leclercq, Pisani & Wandelt, 2014](#), for reviews). Indeed, as mentioned in the [introduction](#), inflationary models predict the initial density perturbations to arise from a large number of independent quantum fluctuations, and therefore to be very nearly Gaussian-distributed. Even in models which are said to produce “large” non-Gaussianities, deviations from Gaussianity are strongly constrained by observational tests (see [Planck Collaboration, 2014b, 2015](#), for the latest results). Grfs are essential for the analysis of the cosmic microwave background, but the large scale distribution of galaxies can also be approximately modeled as a grf, at least on very large scales, where gravitational evolution is still well-described by linear perturbation theory (see sections 1.4 and 1.5). The log-normal distribution is convenient for modeling the statistical behavior of evolved density fields, partially accounting for non-linear gravitational effects at the level of the one-point distribution.

In the following, we summarize some results about finite-dimensional Gaussian and log-normal random fields. Without loss of generality, infinite-dimensional fields can be discretized. If the field is sufficiently regular and the discretization scale is small enough, no information will be lost. In practice, throughout this thesis, any field that we want to describe is already discretized on a grid of particles or voxels. Let us denote the values of the considered cosmic scalar field  $\lambda(\mathbf{x})$  at comoving positions  $\mathbf{x}_i$  as  $\lambda_i \equiv \lambda(\mathbf{x}_i)$  for  $i$  from 1 to any arbitrary integer  $n$ .

#### 1.2.3.1 Gaussian random fields

The  $n$ -dimensional vector  $\lambda = (\lambda_i)_{1 \leq i \leq n}$  is a Gaussian random field (we will often say “is Gaussian” in the following) with mean  $\mu \equiv (\mu_i)_{1 \leq i \leq n}$  and covariance matrix  $C \equiv (C_{ij})_{1 \leq i \leq n, 1 \leq j \leq n}$  if its joint multivariate pdf is a multivariate Gaussian:<sup>2</sup>

$$\mathcal{P}(\lambda|\mu, C) = \frac{1}{\sqrt{|2\pi C|}} \exp\left(-\frac{1}{2}(\lambda - \mu)^* C^{-1}(\lambda - \mu)\right) = \frac{1}{\sqrt{|2\pi C|}} \exp\left(-\frac{1}{2} \sum_{i=1}^n \sum_{j=1}^n (\lambda_i - \mu_i) C_{ij}^{-1} (\lambda_j - \mu_j)\right). \quad (1.14)$$

where  $z^*$  denotes the conjugate transpose of  $z$ , vertical bars indicate the determinant of the surrounded matrix and  $C$  is assumed to be a positive-definite Hermitian matrix (and therefore invertible). In practical cases,  $\mu$  is often taken to be zero. As can be seen from this definition, a grf is completely specified by its mean  $\mu$  and its covariance matrix  $C$ .

It is interesting to note that for the density contrast  $\delta(\mathbf{x})$ , the Gaussian assumption has to break down at later epochs of structure formation since it predicts density amplitudes to be symmetrically distributed among positive and negative values, but weak and strong energy conditions require  $\delta(\mathbf{x}) \geq -1$ . Even in the initial conditions, Gaussianity can not be exact due to the existence of this lower bound. The Gaussian assumption is therefore strictly speaking only valid in the limit of infinitesimally small density fluctuations,  $|\delta(\mathbf{x})| \ll 1$ .

#### 1.2.3.2 Moments of Gaussian random fields, Wick’s theorem

From equation (1.14) it is easy to check that the mean  $\langle \lambda \rangle$  is really  $\mu$  and the covariance matrix is really  $\langle (\lambda - \mu)^* (\lambda - \mu) \rangle = C$ , just by evaluating the Gaussian integrals:

$$\langle \lambda_i \rangle = \int \lambda_i \mathcal{P}(\lambda|\mu, C) d\lambda_i = \mu_i, \quad (1.15)$$

$$\langle (\lambda_i - \mu_i)^* (\lambda_j - \mu_j) \rangle = \int (\lambda_i - \mu_i)^* (\lambda_j - \mu_j) \mathcal{P}(\lambda|\mu, C) d\lambda_i d\lambda_j = C_{ij}. \quad (1.16)$$

We now want to compute higher-order moments of a grf. Let us focus on central moments, or equivalently, let us assume in the following that the mean is  $\mu = 0$ . Here we omit the star denoting conjugate transpose for simplicity. Any odd moments, e.g. the third  $\langle \lambda_i \lambda_j \lambda_k \rangle$ , the fifth  $\langle \lambda_i \lambda_j \lambda_k \lambda_l \lambda_m \rangle$ , etc. are found to be zero

<sup>2</sup> Here we use the common terminology in physics and refer to this pdf as a “multivariate Gaussian”. It is called a “multivariate normal” distribution in statistics. Note that it is possible to generalize this definition to the case where  $C$  is only a positive semi-definite Hermitian matrix, using the notion of characteristic function (see appendix A).

by symmetry of the Gaussian pdf. The higher-order even ones (e.g. the fourth, the sixth, etc.) can be evaluated through the application of Wick's theorem, an elegant method of reducing high-order statistics to a combinatorics problem.

Wick's theorem states that high-order even moments of a grf are computed by connecting up all possible pairs of the field (Wick contractions) and writing down the covariance matrix for each pair using equation (1.16). For instance,

$$\begin{aligned}\langle \lambda_i \lambda_j \lambda_k \lambda_l \rangle &= \langle \lambda_i \lambda_j \rangle \langle \lambda_k \lambda_l \rangle + \langle \lambda_i \lambda_k \rangle \langle \lambda_j \lambda_l \rangle + \langle \lambda_i \lambda_l \rangle \langle \lambda_j \lambda_k \rangle \\ &= C_{ij} C_{kl} + C_{ik} C_{jl} + C_{il} C_{jk}.\end{aligned}\quad (1.17)$$

The number of terms generated in this fashion for the  $n$ -th order moment is  $\prod_{i=1}^{n/2} (2i - 1)$ .

### 1.2.3.3 Marginals and conditionals of Gaussian random fields

Let us split the grf up into two parts  $x = \llbracket 1, m \rrbracket$  and  $y = \llbracket m + 1, n \rrbracket$  ( $m < n$ ), so that

$$\lambda = \begin{pmatrix} \lambda_x \\ \lambda_y \end{pmatrix}, \quad \mu = \begin{pmatrix} \mu_x \\ \mu_y \end{pmatrix} \quad \text{and} \quad C = \begin{pmatrix} C_{xx} & C_{xy} \\ C_{yx} & C_{yy} \end{pmatrix}. \quad (1.18)$$

$C_{xy} = (C_{yx})^*$  since  $C$  is Hermitian.

Easy computation of marginal and conditional pdfs is a very convenient property of grfs. First of all, marginal and conditional densities of grfs are multivariate Gaussians. Therefore, all we need to calculate are their means and covariances. For the marginal pdfs, the results are

$$\langle \lambda_x \rangle = \mu_x, \quad (1.19)$$

$$\langle (\lambda_x - \mu_x)^* (\lambda_x - \mu_x) \rangle = C_{xx}, \quad (1.20)$$

$$\langle \lambda_y \rangle = \mu_y, \quad (1.21)$$

$$\langle (\lambda_y - \mu_y)^* (\lambda_y - \mu_y) \rangle = C_{yy}. \quad (1.22)$$

These expressions simply mean that the marginal means and marginal covariances are just the corresponding parts of the joint mean and covariance, as defined by equation (1.18).

Less trivially, here are the parameters of the conditional densities:

$$\mu_{x|y} \equiv \langle \lambda_x | \lambda_y \rangle = \mu_x + C_{xy} C_{yy}^{-1} (\lambda_y - \mu_y), \quad (1.23)$$

$$C_{x|y} \equiv \langle (\lambda_x - \mu_x)^* (\lambda_x - \mu_x) | \lambda_y \rangle = C_{xx} - C_{xy} C_{yy}^{-1} C_{yx}, \quad (1.24)$$

$$\mu_{y|x} \equiv \langle \lambda_y | \lambda_x \rangle = \mu_y + C_{yx} C_{xx}^{-1} (\lambda_x - \mu_x), \quad (1.25)$$

$$C_{y|x} \equiv \langle (\lambda_y - \mu_y)^* (\lambda_y - \mu_y) | \lambda_x \rangle = C_{yy} - C_{yx} C_{xx}^{-1} C_{xy}. \quad (1.26)$$

A demonstration of these formulae can be found in appendix A. From these expressions, it is easy to see that for grfs, lack of covariance ( $C_{xy} = 0$ ) implies independence, i.e.  $\mathcal{P}(x, y) = \mathcal{P}(x)\mathcal{P}(y)$ . This is most certainly not the case for general random fields. Similarly, if  $\lambda_1, \dots, \lambda_n$  are jointly Gaussian, then each  $\lambda_i$  is Gaussian-distributed, but not conversely.

A particular case is the optimal de-noising of a data set  $d$ , modeled as the sum of some signal  $s$  and a stochastic noise contribution  $n$ :  $d = s + n$ . We model all three fields  $d, s, n$  as grfs. Assuming a vanishing signal mean, an unbiased measurement (i.e.  $\mu_d = \mu_s = \mu_n = 0$ ), and lack of covariance between signal and noise (i.e.  $C_{sn} = C_{ns} = 0$ , which implies  $C_{sd} = C_{ss}$  and  $C_{dd} = C_{ss} + C_{nn}$ ), equations (1.23) and (1.24) yield the famous Wiener filter equations:

$$\mu_{s|d} = C_{ss} (C_{ss} + C_{nn})^{-1} d, \quad (1.27)$$

$$C_{s|d} = C_{ss} - C_{ss} (C_{ss} + C_{nn})^{-1} C_{ss} = (C_{nn}^{-1} + C_{ss}^{-1})^{-1}. \quad (1.28)$$

### 1.2.3.4 Log-normal random fields

In the case where  $\delta(\mathbf{x})$  is the density contrast, gravitational evolution will yield very high positive density contrast amplitudes. In order to prevent negative mass ( $\delta(\mathbf{x}) < -1$ ) while preserving  $\langle \delta(\mathbf{x}) \rangle = 0$ , the resultant

pdf must be strongly skewed (e.g. [Peacock, 1999](#)). In the absence of an exact pdf for the density field in non-linear regimes, solution to dynamical equations, one can describe the statistical properties of the evolved matter distribution by phenomenological probability distributions. A common choice is the log-normal distribution, which approximates well the one-point behavior observed in galaxy observations and  $N$ -body simulations (e.g. [Hubble, 1934](#); [Peebles, 1980](#); [Coles & Jones, 1991](#); [Gaztañaga & Yokoyama, 1993](#); [Colombi, 1994](#); [Kayo, Taruya & Suto, 2001](#); [Neyrinck, Szapudi & Szalay, 2009](#)). This is the model adopted as a prior for the density field in the HADES algorithm ([Jasche & Kitaura, 2010](#); [Jasche & Wandelt, 2012](#), see also table 4.2). The assumption is that the log-density,  $\ln(1 + \delta)$ , instead of the density contrast  $\delta$ , obeys Gaussian statistics.

If  $\lambda$  is a  $n$ -dimensional vector having multivariate Gaussian distribution with mean  $\mu$  and covariance matrix  $C$ , then  $\xi$ , defined by its components  $\xi_i = \exp(\lambda_i)$ , has a multivariate log-normal distribution given by

$$\mathcal{P}(\xi|\mu, C) = \frac{1}{\sqrt{|2\pi C|}} \exp \left( -\frac{1}{2} \sum_{i=1}^n \sum_{j=1}^n (\ln(\xi_i) - \mu_i)^* C_{ij}^{-1} (\ln(\xi_j) - \mu_j) \right) \prod_k \frac{1}{\xi_k}. \quad (1.29)$$

The mean of  $\xi$  is  $\nu$  defined by

$$\nu_i \equiv \langle \xi_i \rangle = \exp \left( \mu_i + \frac{1}{2} C_{ii} \right), \quad (1.30)$$

and its covariance matrix is  $D$  defined by

$$D_{ij} \equiv \langle (\xi_i - \mu_i)^* (\xi_j - \mu_j) \rangle = \exp \left( \mu_i + \mu_j + \frac{1}{2} (C_{ii} + C_{jj}) \right) (\exp(C_{ij}) - 1). \quad (1.31)$$

In cosmology, we assume that  $\lambda = \ln(1 + \delta)$  is a grf with mean  $\mu$  and covariance matrix  $C$ . Then  $\delta = \exp(\lambda) - 1$  follows a log-normal distribution, given by

$$\mathcal{P}(\delta|\mu, C) = \frac{1}{\sqrt{|2\pi C|}} \exp \left( -\frac{1}{2} \sum_{i=1}^n \sum_{j=1}^n (\ln(1 + \delta_i) - \mu_i)^* C_{ij}^{-1} (\ln(1 + \delta_j) - \mu_j) \right) \prod_k \frac{1}{1 + \delta_k}. \quad (1.32)$$

To ensure that  $\langle \delta \rangle$  vanishes everywhere, i.e. that

$$\nu_i = \langle 1 + \delta_i \rangle = \exp \left( \mu_i + \frac{1}{2} C_{ii} \right) = 1, \quad (1.33)$$

one has to impose the following choice for  $\mu$ :

$$\mu_i = -\frac{1}{2} C_{ii} = -\frac{1}{2} C_{00} = \mu_0. \quad (1.34)$$

We have used that  $C_{ii} = C_{00}$ , since the correlation function depends only on distance (assuming statistical homogeneity and isotropy). Hence, the mean for the lognormal distribution is the same throughout the entire field.

For further discussion on the log-normal behavior of density fields, see chapters 2 and 6.

## 1.2.4 Correlation functions and power spectra

### 1.2.4.1 Two-point correlation function and power spectrum

**Definitions.** The two-point correlation function is defined in configuration space as the joint ensemble average of the field at two different locations:

$$\xi(r) = \langle \lambda^*(\mathbf{x}) \lambda(\mathbf{x} + \mathbf{r}) \rangle. \quad (1.35)$$

It depends only on the norm of  $\mathbf{r}$  if statistical isotropy and homogeneity hold.

The scalar field  $\lambda(\mathbf{x})$  is usually written in terms of its Fourier components,

$$\lambda(\mathbf{x}) = \frac{1}{(2\pi)^{3/2}} \int \lambda(\mathbf{k}) \exp(i\mathbf{k} \cdot \mathbf{x}) d^3\mathbf{k}, \quad (1.36)$$

or, equivalently,

$$\lambda(\mathbf{k}) = \frac{1}{(2\pi)^{3/2}} \int \lambda(\mathbf{x}) \exp(-i\mathbf{k} \cdot \mathbf{x}) d^3\mathbf{x}. \quad (1.37)$$

The quantities  $\lambda(\mathbf{k})$  are complex random variables. If  $\lambda(\mathbf{x})$  is real, one has  $\lambda(-\mathbf{k}) = \lambda^*(\mathbf{k})$  which means that half of the Fourier space contains redundant information.

The computation of the two-point correlator for  $\lambda(\mathbf{k})$  in Fourier space gives:

$$\langle \lambda^*(\mathbf{k}) \lambda(\mathbf{k}') \rangle = \frac{1}{(2\pi)^{3/2}} \frac{1}{(2\pi)^{3/2}} \iint \langle \lambda^*(\mathbf{x}) \lambda(\mathbf{x} + \mathbf{r}) \rangle \exp(i(\mathbf{k} - \mathbf{k}') \cdot \mathbf{x} - i\mathbf{k}' \cdot \mathbf{r}) d^3\mathbf{x} d^3\mathbf{r} \quad (1.38)$$

$$= \frac{1}{(2\pi)^3} \iint \xi(r) \exp(i(\mathbf{k} - \mathbf{k}') \cdot \mathbf{x} - i\mathbf{k}' \cdot \mathbf{r}) d^3\mathbf{x} d^3\mathbf{r} \quad (1.39)$$

$$= \frac{1}{(2\pi)^3} \delta_D(\mathbf{k} - \mathbf{k}') \int \xi(r) \exp(i\mathbf{k} \cdot \mathbf{r}) d^3\mathbf{r} \quad (1.40)$$

$$\equiv \frac{1}{(2\pi)^{3/2}} \delta_D(\mathbf{k} - \mathbf{k}') P(k), \quad (1.41)$$

where  $\delta_D$  is a Dirac delta distribution and

$$P(k) \equiv \frac{1}{(2\pi)^{3/2}} \int \xi(r) \exp(i\mathbf{k} \cdot \mathbf{r}) d^3\mathbf{r} \quad (1.42)$$

is defined to be the *power spectrum* of the field  $\lambda(\mathbf{x})$  (this relation is known as the Wiener-Khinchin theorem). Because of statistical homogeneity and isotropy, it depends only on the norm of  $\mathbf{k}$ . The inverse relation between the two-point correlation function,  $\xi(r)$ , and the power spectrum,  $P(k)$ , reads

$$\xi(r) = \frac{1}{(2\pi)^{3/2}} \int P(k) \exp(-i\mathbf{k} \cdot \mathbf{r}) d^3\mathbf{k}. \quad (1.43)$$

In spherical coordinates, using

$$\int_{\Omega} \exp(-ikr \cos \theta) d\Omega = \int_{\theta=0}^{\pi} \int_{\varphi=0}^{2\pi} \exp(-ikr \cos \theta) \sin \theta d\theta d\varphi = 4\pi \frac{\sin(kr)}{kr}, \quad (1.44)$$

we obtain the one-dimensional relations between  $\xi(r)$  and  $P(k)$ ,

$$P(k) = \frac{2}{\sqrt{\pi}} \int_0^{\infty} \xi(r) j_0(kr) r^2 dr, \quad (1.45)$$

$$\xi(r) = \frac{2}{\sqrt{\pi}} \int_0^{\infty} P(k) j_0(kr) k^2 dk, \quad (1.46)$$

where  $j_0$  is the zero-th order spherical Bessel function,

$$j_0(x) \equiv \frac{\sin(x)}{x}. \quad (1.47)$$

**Two-point probability function and two-point correlation function.** The following physical interpretation of the two-point correlation function establishes a link between the ensemble average and the sample average. Indeed, correlation functions are directly related to multivariate probability functions (in fact, they are sometimes defined from them). Here we exemplify this fact for the density contrast at position  $\mathbf{x}$ ,  $\delta(\mathbf{x}) \equiv \rho(\mathbf{x})/\bar{\rho} - 1$ .

Let us consider two infinitesimal volumes  $dV_1$  and  $dV_2$  inside the volume  $V$ . Let  $n_1$  and  $n_2$  be the particle densities at locations  $\mathbf{x}_1$  and  $\mathbf{x}_2$  and  $n \equiv N/V$  the average numerical density. Then the density contrasts are  $\delta(\mathbf{x}_1) = n_1/(n dV_1) - 1$  and  $\delta(\mathbf{x}_2) = n_2/(n dV_2) - 1$  and the two-point correlation function reads

$$\xi(x_{12}) = \langle \delta(\mathbf{x}_1) \delta(\mathbf{x}_2) \rangle = \frac{dN_{12}}{n^2 dV_1 dV_2} - 1, \quad (1.48)$$

where  $x_{12} \equiv |\mathbf{x}_2 - \mathbf{x}_1|$  and  $dN_{12} = \langle n_1 n_2 \rangle$  is the average number of *pairs* in the volumes  $dV_1$  and  $dV_2$  (i.e. the product of the number of particles in one volume times the number in the other volume). One can then rewrite

$$dN_{12} = \langle n_1 n_2 \rangle = n^2 (1 + \xi(x_{12})) dV_1 dV_2. \quad (1.49)$$

The physical interpretation of the two-point correlation function is that it measures the excess over uniform probability that two particles at volume elements  $dV_1$  and  $dV_2$  are separated by a distance  $x_{12}$ . If particle

positions are drawn from uniform distributions (i.e. if there is no clustering), then  $dN_{12}$  is independent of the separation. In this case, the average number of pairs is the product of the average number of particles in the two volumes,  $\langle n_1 n_2 \rangle = \langle n_1 \rangle \langle n_2 \rangle = n^2 dV_1 dV_2$  and the correlation  $\xi$  vanishes. Particles are said to be uncorrelated. Conversely, if  $\xi$  is non-zero, particle distributions are said to be correlated (if  $\xi > 0$ ) or anti-correlated (if  $\xi < 0$ ).

It is sometimes easier to derive the correlation function as the average density of particles at a distance  $r$  from another particle, i.e. by choosing the volume element  $dV_1$  such as  $n dV_1 = 1$ . Then the number of pairs is given by the number of particles in volume  $dV_2$ :

$$dN_2 = n(1 + \xi(r)) dV_2. \quad (1.50)$$

Hence, one can evaluate the correlation function as follows:

$$\xi(r) = \frac{dN(r)}{n dV} - 1 = \frac{\langle n(r) \rangle}{n} - 1, \quad (1.51)$$

i.e. as the average number of particles at distance  $r$  from any given particle, divided by the expected number of particles at the same distance in a uniform distribution, minus one. As  $dN_2$  is linked to the conditional probability that there is a particle in  $dV_2$  given that there is one in  $dV_1$ , the previous expression is sometimes referred to as the *conditional density contrast*.

**Two-point correlation function and power spectrum of Gaussian fields.** If  $\lambda(\mathbf{x})$  is a real grf of mean 0 and covariance matrix  $C$ , then equation (1.16) means that its two-point correlation function in configuration space is directly given by the covariance matrix:  $\langle \lambda(\mathbf{x}_i) \lambda(\mathbf{x}_j) \rangle = C_{ij}$ .

Additionally, if  $\lambda(\mathbf{x})$  is also statistically homogeneous, equation (1.41) implies that  $\lambda(\mathbf{k})$  has independent Fourier modes and that its covariance matrix in Fourier space is diagonal and contains the power spectrum coefficients  $P(k)/(2\pi)^{3/2}$ . Finally, according to Wick's theorem (section 1.2.3.2), one can write for any integer  $p$ :

$$\langle \lambda(\mathbf{k}_1) \dots \lambda(\mathbf{k}_{2p+1}) \rangle = 0, \quad (1.52)$$

$$\begin{aligned} \langle \lambda(\mathbf{k}_1) \dots \lambda(\mathbf{k}_{2p}) \rangle &= \sum_{\text{all pair associations}} \prod_{p \text{ pairs } (i,j)} \langle \lambda(\mathbf{k}_i) \lambda(\mathbf{k}_j) \rangle \\ &= \sum_{\text{all pair associations}} \prod_{p \text{ pairs } (i,j)} \delta_D(\mathbf{k}_i - \mathbf{k}_j) \frac{P(k_i)}{(2\pi)^{3/2}}. \end{aligned} \quad (1.53)$$

Hence, for grfs, all statistical properties are included in two-point correlations. More specifically, all statistical properties of random variables  $\lambda(\mathbf{k})$  are conclusively determined by the shape of the power spectrum  $P(k)$ .

#### 1.2.4.2 Higher-order correlation functions

**Higher-order correlation functions in configuration space.** It is possible to define higher-order correlation functions, as the *connected part* (denoted by a subscript c) of the joint ensemble average of the field  $\lambda(\mathbf{x})$  in an arbitrary number of locations. This can be formally written as

$$\begin{aligned} \xi_n(\mathbf{x}_1, \mathbf{x}_2, \dots, \mathbf{x}_n) &= \langle \lambda(\mathbf{x}_1) \lambda(\mathbf{x}_2) \dots \lambda(\mathbf{x}_n) \rangle_c \\ &\equiv \langle \lambda(\mathbf{x}_1) \lambda(\mathbf{x}_2) \dots \lambda(\mathbf{x}_n) \rangle - \sum_{\mathcal{S} \in \mathcal{P}(\{\mathbf{x}_1, \mathbf{x}_2, \dots, \mathbf{x}_n\})} \prod_{s_i \in \mathcal{S}} \xi_{\#s_i}(\mathbf{x}_{s_i(1)}, \mathbf{x}_{s_i(2)}, \dots, \mathbf{x}_{s_i(\#s_i)}), \end{aligned} \quad (1.54)$$

where the sum is made over the proper partitions (any partition except the set itself) of  $\{\mathbf{x}_1, \mathbf{x}_2, \dots, \mathbf{x}_n\}$  and  $s_i$  is a subset of  $\{\mathbf{x}_1, \mathbf{x}_2, \dots, \mathbf{x}_n\}$  contained in partition  $\mathcal{S}$ . When the average of  $\lambda(\mathbf{x})$  is zero, only partitions that contain no singlets contribute. The decomposition in connected and non-connected parts of the joint ensemble average of the field can be easily visualized in a diagrammatic way (see e.g. [Bernardeau et al., 2002](#)).

For grfs, as a consequence of Wick's theorem (section 1.2.3.2), all connected correlations functions are zero except  $\xi_2$ .



**Higher-order correlators in Fourier space.** This definition in configuration space can be extended to Fourier space. By statistical isotropy of the field, the  $n$ -th Fourier-space correlator does not depend on the direction of the  $\mathbf{k}$ -vectors. By statistical homogeneity, the  $\mathbf{k}$ -vectors have to sum up to zero. We can thus define  $P_n(\mathbf{k}_1, \mathbf{k}_2, \dots, \mathbf{k}_n)$  by

$$\langle \lambda(\mathbf{k}_1) \lambda(\mathbf{k}_2) \dots \lambda(\mathbf{k}_n) \rangle_c \equiv \delta_D(\mathbf{k}_1 + \mathbf{k}_2 + \dots + \mathbf{k}_n) P_n(\mathbf{k}_1, \mathbf{k}_2, \dots, \mathbf{k}_n). \quad (1.55)$$

The Dirac delta distribution  $\delta_D$  ensures that  $\mathbf{k}$ -vector configurations form closed polygons:  $\sum_i \mathbf{k}_i = \mathbf{0}$ .

Let us now examine the lowest-order connected moments.

**Bispectrum.** After the power spectrum, the second statistic of interest is the bispectrum  $B$ , for  $n = 3$ , defined by

$$\langle \lambda(\mathbf{k}_1) \lambda(\mathbf{k}_2) \lambda(\mathbf{k}_3) \rangle = \langle \lambda(\mathbf{k}_1) \lambda(\mathbf{k}_2) \lambda(\mathbf{k}_3) \rangle_c \equiv \delta_D(\mathbf{k}_1 + \mathbf{k}_2 + \mathbf{k}_3) B(\mathbf{k}_1, \mathbf{k}_2, \mathbf{k}_3). \quad (1.56)$$

**Reduced bispectrum.** It is convenient to define the reduced bispectrum  $Q(\mathbf{k}_1, \mathbf{k}_2, \mathbf{k}_3)$  as

$$Q(\mathbf{k}_1, \mathbf{k}_2, \mathbf{k}_3) \equiv \frac{B(\mathbf{k}_1, \mathbf{k}_2, \mathbf{k}_3)}{P(k_1)P(k_2) + P(k_1)P(k_3) + P(k_2)P(k_3)}, \quad (1.57)$$

which takes away most of the dependence on scale and cosmology. The reduced bispectrum is useful for comparing different models, because its weak dependence on cosmology is known to break degeneracies between cosmological parameters and to isolate the effects of gravity (see [Gil-Marín et al., 2011](#), for an example).

**Trispectrum.** The trispectrum is the following correlator, for  $n = 4$ . It is defined as

$$\langle \lambda(\mathbf{k}_1) \lambda(\mathbf{k}_2) \lambda(\mathbf{k}_3) \lambda(\mathbf{k}_4) \rangle_c \equiv \delta_D(\mathbf{k}_1 + \mathbf{k}_2 + \mathbf{k}_3 + \mathbf{k}_4) T(\mathbf{k}_1, \mathbf{k}_2, \mathbf{k}_3, \mathbf{k}_4). \quad (1.58)$$

## 1.3 Dynamics of gravitational instability

The standard picture for the formation of the LSS as seen in galaxy surveys is the gravitational amplification of primordial density fluctuations. The dynamics of this process is mostly governed by gravitational interactions of collisionless (or at least, weakly-interacting) dark matter particles in an expanding universe.

For scales much smaller than the Hubble radius, relativistic effects (such as the curvature of the Universe or the apparent distance-redshift relation) are believed to be subdominant or negligible (e.g. [Kolb & Turner, 1990](#), and references therein) and as we will show, the expansion of the background can be factored out by a redefinition of variables. Although the microscopic nature of dark matter particles remains unknown, candidates have to pass several tests in order to be viable ([Taoso, Bertone & Masiero, 2008](#)). In particular, particles which are relativistic at the time of structure formation lead to a large damping of small-scale fluctuations ([Silk, 1968](#); [Bond & Szalay, 1983](#)), incompatible with observed structures. The standard theory thus requires dark matter particles to be cold during structure formation, i.e. non-relativistic well before the matter-dominated era ([Peebles, 1982b](#); [Blumenthal et al., 1984](#); [Davis et al., 1985](#)). For these two reasons, at scales much smaller than the Hubble radius the equations of motion can be well approximated by Newtonian gravity.

In addition, all dark matter particle candidates are extremely light compared to the mass of typical astrophysical objects such as stars or galaxies, with an expected number density of at least  $10^{50}$  particles per  $\text{Mpc}^3$ . Therefore, discreteness effects are negligible and collisionless dark matter can be well described in the fluid limit approximation.

In this section, we present the dynamics of gravitational instability in the framework of Newtonian gravity within a flat, expanding background and in the fluid limit approximation. It is of course possible to do a detailed relativistic treatment of structure formation dynamics and cosmological perturbation theory ([Bardeen, 1980](#); [Mukhanov, Feldman & Brandenberger, 1992](#)) and to derive the Newtonian limit from general relativity (see e.g. [Peebles, 1980](#)).

### 1.3.1 The Vlasov-Poisson system

**The cosmological Poisson equation.** Let us consider a large number of particles that interact only gravitationally in an expanding universe. For a particle of velocity  $\mathbf{v}$  at position  $\mathbf{r}$ , the action of all other particles can be treated as a smooth gravitational potential induced by the local mass density  $\rho(\mathbf{r})$ ,

$$\phi(\mathbf{r}) = G \int \frac{\rho(\mathbf{r}' - \mathbf{r})}{|\mathbf{r}' - \mathbf{r}|} d^3\mathbf{r}', \quad (1.59)$$

and the equation of motion reads

$$\frac{d\mathbf{v}}{dt} = -\nabla_{\mathbf{r}}\phi = G \int \frac{\rho(\mathbf{r}' - \mathbf{r})(\mathbf{r}' - \mathbf{r})}{|\mathbf{r}' - \mathbf{r}|^3} d^3\mathbf{r}'. \quad (1.60)$$

Examining gravitational instabilities in the context of an expanding universe requires to consider the departure from the homogeneous Hubble flow. It is natural to describe the positions of particles in terms of their comoving coordinates  $\mathbf{x}$  such that the physical coordinates are  $\mathbf{r} = a\mathbf{x}$  and of the conformal time  $\tau$ , defined by  $dt = a(\tau) d\tau$ . Hereafter, when there is no ambiguity, we will denote  $\nabla \equiv \nabla_{\mathbf{x}}$  and  $\Delta \equiv \Delta_{\mathbf{x}}$ . The Jacobian of the spatial coordinate transformation is  $|J| = a^3$  so that the right-hand side of the previous equation becomes

$$G \int \frac{\rho(\mathbf{r}' - \mathbf{r})(\mathbf{r}' - \mathbf{r})}{|\mathbf{r}' - \mathbf{r}|^3} d^3\mathbf{r}' = G \int \frac{\rho(\mathbf{x}' - \mathbf{x}) a(\mathbf{x}' - \mathbf{x})}{a^3 |\mathbf{x}' - \mathbf{x}|^3} a^3 d^3\mathbf{x}' \quad (1.61)$$

$$= Ga\bar{\rho} \int \frac{(\mathbf{x}' - \mathbf{x})}{|\mathbf{x}' - \mathbf{x}|^3} d^3\mathbf{x}' + Ga\bar{\rho} \int \delta(\mathbf{x}' - \mathbf{x}) \frac{(\mathbf{x}' - \mathbf{x})}{|\mathbf{x}' - \mathbf{x}|^3} d^3\mathbf{x}', \quad (1.62)$$

where we have introduced the density contrast  $\delta(\mathbf{x})$ , defined as

$$\rho(\mathbf{x}, t) \equiv \bar{\rho}(t) [1 + \delta(\mathbf{x}, t)], \quad (1.63)$$

where  $\bar{\rho}(t) \propto 1/a^3$  (consequence of equation (1.3) with  $w = 0$ ).

Velocities of particles are  $\mathbf{v} = \dot{a}\mathbf{x} + a d\mathbf{x}/dt$ , permitting us to define peculiar velocities as the difference between total velocities and the Hubble flow:

$$\mathbf{u} \equiv a \frac{d\mathbf{x}}{dt} = \mathbf{v} - \dot{a}\mathbf{x}. \quad (1.64)$$

$d\mathbf{v}/dt$  is written in terms of  $\mathbf{u}$  as

$$\frac{d\mathbf{v}}{dt} = \frac{d\mathbf{u}}{dt} + \ddot{a}\mathbf{x} + \dot{a} \frac{d\mathbf{x}}{dt} \quad (1.65)$$

$$= \frac{d\mathbf{u}}{dt} + \ddot{a}\mathbf{x} + \frac{\dot{a}}{a} \mathbf{u}. \quad (1.66)$$

By the use of the second Friedmann equation for the homogeneous background (equation (1.2)),

$$\ddot{a} = -\frac{4\pi G}{3} a \bar{\rho}, \quad (1.67)$$

and Gauss's theorem,

$$\frac{4\pi}{3} \mathbf{x} = - \int \frac{(\mathbf{x}' - \mathbf{x})}{|\mathbf{x}' - \mathbf{x}|^3} d^3\mathbf{x}', \quad (1.68)$$

the term  $\ddot{a}\mathbf{x}$  is equal to

$$Ga\bar{\rho} \int \frac{(\mathbf{x}' - \mathbf{x})}{|\mathbf{x}' - \mathbf{x}|^3} d^3\mathbf{x}' \equiv -\frac{1}{a} \nabla_{\mathbf{x}}\phi, \quad (1.69)$$

which leaves for the peculiar velocity the following equation of motion (see equations (1.60), (1.62) and (1.66)):

$$\frac{d\mathbf{u}}{dt} + \frac{\dot{a}}{a} \mathbf{u} = Ga\bar{\rho} \int \delta(\mathbf{x}' - \mathbf{x}) \frac{(\mathbf{x}' - \mathbf{x})}{|\mathbf{x}' - \mathbf{x}|^3} d^3\mathbf{x}' \equiv -\frac{1}{a} \nabla_{\mathbf{x}}\Phi. \quad (1.70)$$

Here we have defined the cosmological gravitational potential  $\Phi$  such that  $\phi \equiv \phi + \Phi$  with, for the background,

$$\phi(\mathbf{x}) = \frac{4\pi G}{3} a^2 \bar{\rho} \left( \frac{1}{2} |\mathbf{x}|^2 \right) = -\mathcal{H}' \left( \frac{1}{2} |\mathbf{x}|^2 \right), \quad \text{satisfying} \quad \Delta\phi = 4\pi G a^2 \bar{\rho}. \quad (1.71)$$

Using the overall Poisson equation,  $\Delta_{\mathbf{r}}\phi = \Delta\phi/a^2 = 4\pi G\bar{\rho}(1+\delta)$ , we find that  $\Phi$  follows a cosmological Poisson equation sourced only by density fluctuations, as expected:

$$\Delta\Phi = 4\pi G a^2 \bar{\rho} \delta = \frac{3}{2} \Omega_m(\tau) \mathcal{H}^2(\tau) \delta. \quad (1.72)$$

The second equality comes from the first Friedmann equation in a flat universe (equation (1.1) with  $k = 0$ ).

**The Vlasov equation.** Looking at equation (1.70), the momentum of a single particle of mass  $m$  is identified as:

$$\mathbf{p} = ma\mathbf{u}, \quad (1.73)$$

and the equation of motion reads:

$$\frac{d\mathbf{p}}{dt} = -m\nabla_{\mathbf{x}}\Phi = -ma\nabla_{\mathbf{r}}\Phi \quad \text{or} \quad \frac{d\mathbf{p}}{d\tau} = -ma\nabla_{\mathbf{x}}\Phi. \quad (1.74)$$

Let us now define the particle number density in phase space by  $f(\mathbf{x}, \mathbf{p}, \tau)$ . Phase-space conservation and Liouville's theorem imply the Vlasov equation (collisionless version of the Boltzmann equation):

$$\frac{df}{d\tau} = \frac{\partial f}{\partial \tau} + \frac{\mathbf{p}}{ma} \cdot \nabla f - ma\nabla\Phi \cdot \frac{\partial f}{\partial \mathbf{p}} = 0. \quad (1.75)$$

Given equations (1.72) and (1.75), the Vlasov-Poisson system is closed.

### 1.3.2 Fluid dynamics approach, evolution equations in phase space

The Vlasov equation is very difficult to solve, since it is a partial differential equation involving seven variables, with non-linearity induced by the dependence of the potential  $\Phi$  on the density through the Poisson equation. Its complicated structure prevents the analytic analysis of dark matter dynamics. In practice, we are usually not interested in solving the full phase-space dynamics, but only the evolution of the spatial distribution. It is therefore convenient to take momentum moments of the distribution function. This yields a fluid dynamics approach for the motion of collisionless dark matter. The zeroth-order momentum, by construction, relates the phase-space density to the density field,

$$\int f(\mathbf{x}, \mathbf{p}, \tau) d^3\mathbf{p} \equiv \rho(\mathbf{x}, \tau). \quad (1.76)$$

The next order moments,

$$\int \frac{\mathbf{p}}{ma} f(\mathbf{x}, \mathbf{p}, \tau) d^3\mathbf{p} \equiv \rho(\mathbf{x}, \tau) \mathbf{u}(\mathbf{x}, \tau), \quad (1.77)$$

$$\int \frac{\mathbf{p}_i \mathbf{p}_j}{m^2 a^2} f(\mathbf{x}, \mathbf{p}, \tau) d^3\mathbf{p} \equiv \rho(\mathbf{x}, \tau) \mathbf{u}_i(\mathbf{x}, \tau) \mathbf{u}_j(\mathbf{x}, \tau) + \sigma_{ij}(\mathbf{x}, \tau), \quad (1.78)$$

define the *peculiar velocity flow*  $\mathbf{u}(\mathbf{x}, \tau)$  (average local velocity of particles in a region of space; for simplification, we use the same notation as the peculiar velocity of a single particle) and the *stress tensor*  $\sigma_{ij}(\mathbf{x}, \tau)$  which can be related to the *velocity dispersion tensor*,  $v_{ij}(\mathbf{x}, \tau)$ , by  $\sigma_{ij}(\mathbf{x}, \tau) \equiv \rho(\mathbf{x}, \tau) v_{ij}(\mathbf{x}, \tau)$ .

By taking successive momentum moments of the Vlasov equation and integrating out phase-space information, a hierarchy of equations that couple successive moments of the distribution function can be constructed. The zeroth moment of the Vlasov equation gives the continuity equation,

$$\frac{\partial \delta(\mathbf{x}, \tau)}{\partial \tau} + \nabla \cdot \{[1 + \delta(\mathbf{x}, \tau)] \mathbf{u}(\mathbf{x}, \tau)\} = 0, \quad (1.79)$$

which describes the conservation of mass. Taking the first moment and subtracting  $\bar{\rho} \mathbf{u}(\mathbf{x}, \tau)$  times the continuity equation yields the Euler equation,

$$\frac{\partial \mathbf{u}_i(\mathbf{x}, \tau)}{\partial \tau} + \mathcal{H}(\tau) \mathbf{u}_i(\mathbf{x}, \tau) + \mathbf{u}_j(\mathbf{x}, \tau) \cdot \nabla_j \mathbf{u}_i(\mathbf{x}, \tau) = -\nabla_i \Phi(\mathbf{x}, \tau) - \frac{1}{\rho(\mathbf{x}, \tau)} \nabla_j (\sigma_{ij}(\mathbf{x}, \tau)), \quad (1.80)$$

which describes the conservation of momentum. This equation is very similar to that of hydrodynamics, apart from an additional term which accounts for the expansion of the Universe and the fact that, contrary to perfect fluids, auto-gravitating systems may have an anisotropic stress tensor.

The infinite sequence of momentum moments of the Vlasov equation is usually truncated at this point and completed by fluid dynamics assumptions to close the system. Specifically, one postulates an Ansatz for the stress tensor, namely the equation of state of the cosmological fluid. For example, if the fluid is locally thermalized, the velocity dispersion becomes isotropic and proportional to the pressure (e.g. [Bernardeau et al., 2002](#)):

$$\sigma_{ij} = -P\delta_K^{ij}, \quad (1.81)$$

where  $\delta_K^{ab}$  is a Kronecker symbol. Standard fluid dynamics also prescribes, with the addition of a viscous stress tensor, the following equation (e.g. [Bernardeau et al., 2002](#)):

$$\sigma_{ij} = -P\delta_K^{ij} + \zeta(\nabla \cdot \mathbf{u})\delta_K^{ij} + \mu \left[ \nabla_i \mathbf{u}_j + \nabla_j \mathbf{u}_i - \frac{2}{3}(\nabla \cdot \mathbf{u})\delta_K^{ij} \right], \quad (1.82)$$

where  $\zeta$  is the coefficient of bulk viscosity and  $\mu$  is the coefficient of shear viscosity.

### 1.3.3 The single-stream approximation

At the early stages of cosmological gravitational instability, it is possible to further simplify and to rely on a different hypothesis, namely the *single-stream approximation*. At sufficiently large scales, gravity-induced cosmic flows will dominate over the velocity dispersion due to peculiar motions. The single-stream approximation consists in assuming that for CDM, velocity dispersion and pressure are negligible, i.e.  $\sigma_{ij} = 0$ , and that all particles have identical peculiar velocities. Hence, the density in phase space can be written

$$f(\mathbf{x}, \mathbf{p}, \tau) = \rho(\mathbf{x}, \tau) \delta_D[\mathbf{p} - m\mathbf{a}\mathbf{u}(\mathbf{x})]. \quad (1.83)$$

Note, that from its definition, equation (1.78), the stress tensor characterizes the deviation of particle motions from a single coherent flow.

The single-stream approximation only works at the beginning of gravitational structure formation, when structures had no time to collapse and virialize. Because of non-linearity in the Vlasov-Poisson system, later stages will involve the superposition of three or more streams in phase space, indicating the break down of the approximation at increasingly larger scales. The breakdown of  $\sigma_{ij} \approx 0$ , describing the generation of velocity dispersion or anisotropic stress due to the multiple-stream regime, is generically known as *shell-crossing*. Beyond that point, the density in phase space exhibits no simple form, generally preventing further analytic analysis. This issue will be discussed further in chapters 2 and 6.

The single-stream approximation yields the following system of equations:

$$\frac{\partial \delta(\mathbf{x}, \tau)}{\partial \tau} + \nabla \cdot \{ [1 + \delta(\mathbf{x}, \tau)] \mathbf{u}(\mathbf{x}, \tau) \} = 0, \quad (1.84)$$

$$\frac{\partial \mathbf{u}_i(\mathbf{x}, \tau)}{\partial \tau} + \mathcal{H}(\tau) \mathbf{u}_i(\mathbf{x}, \tau) + \mathbf{u}_j(\mathbf{x}, \tau) \cdot \nabla_j \mathbf{u}_i(\mathbf{x}, \tau) = -\nabla_i \Phi(\mathbf{x}, \tau), \quad (1.85)$$

$$\Delta \Phi(\mathbf{x}, \tau) = 4\pi G a^2(\tau) \bar{\rho}(\tau) \delta(\mathbf{x}, \tau). \quad (1.86)$$

It is a non-linear, closed system of equations involving the local density contrast, the local velocity field and the local gravitational potential.

There exists no general analytic solution to the fluid dynamics of collisionless self-gravitating CDM, even in the single-stream regime. However, literature provides several different analytic perturbative expansion techniques to yield approximate solutions for the dark matter dynamics, which we briefly review below (sections 1.4 and 1.5).

## 1.4 Eulerian perturbation theory

### 1.4.1 Eulerian linear perturbation theory

As mentioned above, at large scales and during the early stages of gravitational evolution, we expect the matter distribution to be smooth and to follow a single velocity stream. In this regime, it is therefore possible to linearize equation (1.84) and (1.85), assuming that fluctuations of density are small compared to the

homogeneous contribution and that gradients of velocity fields are small compared to the Hubble parameter,

$$|\delta(\mathbf{x}, \tau)| \ll 1, \quad (1.87)$$

$$|\nabla_j \mathbf{u}_i(\mathbf{x}, \tau)| \ll \mathcal{H}(\tau). \quad (1.88)$$

We obtain the equation of motion in the *linear regime*,

$$\frac{\partial \delta(\mathbf{x}, \tau)}{\partial \tau} + \theta(\mathbf{x}, \tau) = 0, \quad (1.89)$$

$$\frac{\partial \mathbf{u}(\mathbf{x}, \tau)}{\partial \tau} + \mathcal{H}(\tau) \mathbf{u}(\mathbf{x}, \tau) = -\nabla \Phi(\mathbf{x}, \tau), \quad (1.90)$$

where  $\theta(\mathbf{x}, \tau) \equiv \nabla \cdot \mathbf{u}(\mathbf{x}, \tau)$  is the divergence of the velocity field. The velocity field, as any vector field, is completely described by its divergence  $\theta(\mathbf{x}, \tau)$  and its curl, referred to as the vorticity,  $\mathbf{w}(\mathbf{x}, \tau) \equiv \nabla \times \mathbf{u}(\mathbf{x}, \tau)$ , whose equations of motion follow from taking the divergence and the curl of equation (1.85) and using the Poisson equation:

$$\frac{\partial \theta(\mathbf{x}, \tau)}{\partial \tau} + \mathcal{H}(\tau) \theta(\mathbf{x}, \tau) + 4\pi G a^2(\tau) \bar{\rho}(\tau) \delta(\mathbf{x}, \tau) = 0, \quad (1.91)$$

$$\frac{\partial \mathbf{w}(\mathbf{x}, \tau)}{\partial \tau} + \mathcal{H}(\tau) \mathbf{w}(\mathbf{x}, \tau) = 0. \quad (1.92)$$

Since vorticity is not sourced in the linear regime, any initial vorticity rapidly decays due to the expansion of the Universe. Indeed, its evolution immediately follows from equation (1.92):  $\mathbf{w}(\tau) \propto 1/a(\tau)$ . In the non-linear regime, the emergence of anisotropic stress in the right-hand side of Euler's equation can lead to vorticity generation (Pichon & Bernardeau, 1999).

The density contrast evolution follows by replacing equation (1.89) and its time derivative in equation (1.91):

$$\frac{\partial^2 \delta(\mathbf{x}, \tau)}{\partial \tau^2} + \mathcal{H}(\tau) \frac{\partial \delta(\mathbf{x}, \tau)}{\partial \tau} = 4\pi G a^2(\tau) \bar{\rho}(\tau) \delta(\mathbf{x}, \tau) = \frac{3}{2} \Omega_m(\tau) \mathcal{H}^2(\tau) \delta(\mathbf{x}, \tau). \quad (1.93)$$

### 1.4.2 The growth of fluctuations in linear theory

This linear equation allows us to look for different fluctuation modes, decoupling spatial and time contributions by writing  $\delta(\mathbf{x}, \tau) = D_1(\tau) \delta(\mathbf{x}, 0)$ , where some “initial” reference time is labeled as 0 and where  $D_1(\tau)$  is called the *linear growth factor*. The time dependence of the fluctuation growth rate satisfies

$$\frac{d^2 D_1(\tau)}{d\tau^2} + \mathcal{H}(\tau) \frac{dD_1(\tau)}{d\tau} = \frac{3}{2} \Omega_m(\tau) \mathcal{H}^2(\tau) D_1(\tau), \quad (1.94)$$

regardless of  $\mathbf{x}$  (or of the Fourier mode  $\mathbf{k}$ ): in the linear regime, the growth of fluctuations is scale-independent. This equation, together with Friedmann's equations, equations (1.7) and (1.9), determines the growth of density perturbations in the linear regime as a function of cosmological parameters. There are two independent solutions, the fastest growing mode  $D_1^{(+)}(\tau)$  and the slowest growing mode  $D_1^{(-)}(\tau)$ . The evolution of the density contrast is then given by:

$$\delta(\mathbf{x}, \tau) = D_1^{(+)}(\tau) \delta_+(\mathbf{x}) + D_1^{(-)}(\tau) \delta_-(\mathbf{x}), \quad (1.95)$$

where  $\delta_+(\mathbf{x})$  and  $\delta_-(\mathbf{x})$  are two functions of position only describing the initial density field configuration.

In terms of the scale factor and using Friedmann's equations, equation (1.94) can be rewritten as

$$a^2 \frac{d^2 D_1}{da^2} + \left( \Omega_\Lambda(a) - \frac{\Omega_m(a)}{2} + 2 \right) a \frac{dD_1}{da} = \frac{3}{2} \Omega_m(a) D_1, \quad (1.96)$$

where the cosmological parameters  $\Omega_\Lambda(a)$  and  $\Omega_m(a)$  now depend on the scale factor (for more details on this derivation and a generalization to time-varying dark energy models, see Percival, 2005b).

Using the linearized continuity equation, equation (1.89), the velocity divergence is given by

$$\theta(\mathbf{x}, \tau) = -\mathcal{H}(\tau) [f(\Omega_i) \delta_+(\mathbf{x}, \tau) + g(\Omega_i) \delta_-(\mathbf{x}, \tau)]. \quad (1.97)$$

It does not depend directly on the linear growth factor of each mode, but on its logarithmic derivative, the exponent in the momentary power law relating  $D$  to  $a$ ,

$$f(\Omega_i) \equiv \frac{1}{\mathcal{H}(\tau)} \frac{d \ln D_1^{(+)} }{d\tau} = \frac{d \ln D_1^{(+)} }{d \ln a}, \quad g(\Omega_i) \equiv \frac{1}{\mathcal{H}(\tau)} \frac{d \ln D_1^{(-)} }{d\tau} = \frac{d \ln D_1^{(-)} }{d \ln a}, \quad (1.98)$$

with  $\delta_{\pm}(\mathbf{x}, \tau) \equiv D_1^{(\pm)}(\tau) \delta_{\pm}(\mathbf{x})$ .

We now review some cosmological models for which analytic expressions exist.

1. For a standard cold dark matter (SCDM) model, i.e. a particular case of an Einstein-de Sitter universe (Einstein & de Sitter, 1932) where dark matter is cold, the cosmological parameters are time-independent:  $\Omega_m(a) = 1$  and  $\Omega_\Lambda(a) = 0$ . Using equation (1.96), the evolution of the linear growth factor satisfies

$$a^2 \frac{d^2 D_1}{da^2} + \frac{3}{2} a \frac{d D_1}{da} = \frac{3}{2} D_1. \quad (1.99)$$

Two independent solutions are

$$D_1^{(+)} \propto a, \quad f(\Omega_m = 1, \Omega_\Lambda = 0) = 1, \quad D_1^{(-)} \propto a^{-3/2}, \quad g(\Omega_m = 1, \Omega_\Lambda = 0) = -\frac{3}{2}, \quad (1.100)$$

thus density fluctuations grow as the scale factor,  $\delta \propto a$ , once the decaying mode has vanished.

2. For an open cold dark matter (OCDM) model, the cosmological parameters are  $\Omega_m(a) < 1$  and  $\Omega_\Lambda(a) = 0$ . The solutions of equation (1.96) are (Groth & Peebles, 1975), with  $x \equiv a(\tau)(1/\Omega_m^{(0)} - 1)$ ,

$$D_1^{(+)} = 1 + \frac{3}{x} + 3 \frac{(1+x)^{1/2}}{x^{3/2}} \ln \left[ (1+x)^{1/2} - x^{1/2} \right], \quad D_1^{(-)} = \frac{(1+x)^{1/2}}{x^{3/2}}. \quad (1.101)$$

The dimensionless parameter  $g$  is calculated to be

$$g(\Omega_m, \Omega_\Lambda = 0) = -\frac{\Omega_m}{2} - 1, \quad (1.102)$$

and the dimensionless parameter  $f$  can be approximated by (Peebles, 1976, 1980)

$$f(\Omega_m, \Omega_\Lambda = 0) \approx \Omega_m^{3/5}. \quad (1.103)$$

As  $\Omega_m \rightarrow 0$  ( $a \rightarrow \infty$  and  $x \rightarrow \infty$ ),  $D_1^{(+)} \rightarrow 1$  and  $D_1^{(-)} \sim x^{-1}$ : perturbations cease to grow.

3. For a universe with cold dark matter and a cosmological constant,  $\Omega_m(a) < 1$  and  $0 < \Omega_\Lambda(a) \leq 1$  ( $\Lambda$ CDM model), allowing the possibility of a curvature term ( $\Omega_{\text{tot}}(a) = \Omega_m(a) + \Omega_\Lambda(a) \neq 1$ ), the first Friedmann equation, equation (1.1), allows to write the Hubble parameter as

$$H(a) = H_0 \sqrt{\Omega_\Lambda^{(0)} + (1 - \Omega_\Lambda^{(0)} - \Omega_m^{(0)})a^{-2} + \Omega_m^{(0)}a^{-3}}. \quad (1.104)$$

It can be checked that this expression is a solution of equation (1.96). The decaying mode is then

$$D_1^{(-)} \propto H(a) = \frac{\mathcal{H}(a)}{a}. \quad (1.105)$$

Using this particular solution and the variation of parameters method, the other solution is found to be (Heath, 1977; Carroll, Press & Turner, 1992; Bernardeau *et al.*, 2002)

$$D_1^{(+)} \propto a^3 H^3(a) \int_0^a \frac{d\tilde{a}}{\tilde{a}^3 H^3(\tilde{a})}. \quad (1.106)$$

Due to equations (1.7) and (1.105), one finds for arbitrary  $\Omega_m$  and  $\Omega_\Lambda$ ,

$$g(\Omega_m, \Omega_\Lambda) = \Omega_\Lambda - \frac{\Omega_m}{2} - 1, \quad (1.107)$$

and  $f$  can be approximated by (Lahav *et al.*, 1991)

$$f(\Omega_m, \Omega_\Lambda) \approx \left[ \frac{\Omega_m^{(0)} a^{-3}}{\Omega_m^{(0)} a^{-3} + (1 - \Omega_\Lambda^{(0)} - \Omega_m^{(0)}) a^{-2} + \Omega_\Lambda^{(0)}} \right]^{3/5} \quad (1.108)$$

or (Lightman & Schechter, 1990; Carroll, Press & Turner, 1992)

$$f(\Omega_m, \Omega_\Lambda) \approx \left[ \frac{\Omega_m^{(0)} a^{-3}}{\Omega_m^{(0)} a^{-3} + (1 - \Omega_\Lambda^{(0)} - \Omega_m^{(0)}) a^{-2} + \Omega_\Lambda^{(0)}} \right]^{4/7}. \quad (1.109)$$

For flat Universe,  $\Omega_m + \Omega_\Lambda = 1$ , we have (Bouchet *et al.*, 1995; Bernardeau *et al.*, 2002)

$$f(\Omega_m, \Omega_\Lambda = 1 - \Omega_m) \approx \Omega_m^{5/9}. \quad (1.110)$$

In the case of the Einstein-de Sitter universe, an interpretation of the growing and decaying modes can be easily given. Referring to the solution for the growth factor, equation (1.100), the initial density field (equation (1.95)) and the initial velocity field (equation (1.97)) are written

$$\delta_{\text{init}}(\mathbf{x}) \equiv \delta(\mathbf{x}, 0) = \delta_+(\mathbf{x}) + \delta_-(\mathbf{x}), \quad (1.111)$$

$$\theta_{\text{init}}(\mathbf{x}) \equiv \theta(\mathbf{x}, 0) = -\mathcal{H}(0) \left[ \delta_+(\mathbf{x}) - \frac{3}{2} \delta_-(\mathbf{x}) \right], \quad (1.112)$$

if we assume that  $D_+$  and  $D_-$  are normalized to unity at the initial time. These relations can be inverted to give

$$\delta_+(\mathbf{x}) = \frac{3}{5} \left( \delta_{\text{init}}(\mathbf{x}) - \frac{2}{3} \frac{\theta_{\text{init}}(\mathbf{x})}{\mathcal{H}(0)} \right), \quad (1.113)$$

$$\delta_-(\mathbf{x}) = \frac{2}{5} \left( \delta_{\text{init}}(\mathbf{x}) + \frac{\theta_{\text{init}}(\mathbf{x})}{\mathcal{H}(0)} \right). \quad (1.114)$$

From these expressions, the interpretation of the modes become clear. The sign is significant: recall that for a growing mode alone we would expect  $\theta_{\text{init}} = -\mathcal{H}(0)\delta_{\text{init}}$  and for a decaying mode alone,  $\theta_{\text{init}} = 3/2 \mathcal{H}(0)\delta_{\text{init}}$ . A pure growing mode corresponds to the case where the density and velocity fields are initially “in phase”, in the sense that the velocity field converges towards the potential wells defined by the density field. A pure decaying mode corresponds to the case where the density and velocity fields are initially “opposite in phase”, the velocity field being such that particles escape potential wells.

### 1.4.3 Eulerian perturbation theory at higher order

At higher order, Eulerian perturbation theory can be implemented by expanding the density and velocity fields,

$$\delta(\mathbf{x}, \tau) = \sum_{n=1}^{\infty} \delta^{(n)}(\mathbf{x}, \tau) = \delta^{(1)}(\mathbf{x}, \tau) + \delta^{(2)}(\mathbf{x}, \tau) + \dots, \quad (1.115)$$

$$\theta(\mathbf{x}, \tau) = \sum_{n=1}^{\infty} \theta^{(n)}(\mathbf{x}, \tau) = \theta^{(1)}(\mathbf{x}, \tau) + \theta^{(2)}(\mathbf{x}, \tau) + \dots, \quad (1.116)$$

where  $\delta^{(1)}(\mathbf{x}, \tau)$  and  $\theta^{(1)}(\mathbf{x}, \tau)$  are the linear order solution studied in the previous section. Focusing only on the growing mode, the first-order density field reads,

$$\delta^{(1)}(\mathbf{x}, \tau) = D_1(\tau) \delta_{\text{init}}(\mathbf{x}), \quad (1.117)$$

with  $D_1(\tau) \equiv D_1^{(+)}(\tau)$  and  $\delta_{\text{init}}(\mathbf{x}) = \delta_+(\mathbf{x})$ .  $\delta^{(2)}(\mathbf{x}, \tau)$  describes to leading order the non-local evolution of the density field due to gravitational interactions. It is found to be proportional to the *second-order growth factor*,  $D_2(\tau)$ , which satisfies the differential equation (equation 43 in Bouchet *et al.*, 1995)

$$a^2 \frac{d^2 D_2}{da^2} + \left( \Omega_\Lambda(a) - \frac{\Omega_m(a)}{2} + 2 \right) a \frac{dD_2}{da} = \frac{3}{2} \Omega_m(a) \left[ D_2 - (D_1^{(+)})^2 \right]. \quad (1.118)$$

In the codes implemented for this thesis, we use the fitting function

$$D_2(\tau) \approx -\frac{3}{7}D_1^2(\tau)\Omega_m^{-1/143}, \quad (1.119)$$

valid for a flat  $\Lambda$ CDM model (Bouchet *et al.*, 1995). Depending on the cosmological parameters, different expressions can be found in the literature (see e.g. Bernardeau *et al.*, 2002), but  $D_2(\tau)$  always stays of the order of  $D_1^2(\tau)$  as expected in perturbation theory.

A detailed presentation of non-linear Eulerian perturbation theory involves new types of objects (kernels, propagators, vertices) and is beyond the scope of this thesis. For an existing review, see e.g. Bernardeau *et al.* (2002).

## 1.5 Lagrangian perturbation theory

### 1.5.1 Lagrangian fluid approach for cold dark matter

As we have seen (section 1.3.2), our approach is based on the assumption that CDM is well described by a fluid. A way of looking at fluid motion is to focus on specific locations in space through which the fluid flows as time passes. It is then possible to study dynamics of density and velocity fields in this context, which constitutes the Eulerian point of view. We have developed Eulerian perturbation theory in section 1.4.

Alternatively, in fluid dynamics, one can choose to describe the field by following the trajectories of particles or fluid elements. This is the so-called Lagrangian description. The goal of this paragraph is to apply this description to the cosmological fluid and to build *Lagrangian perturbation theory* in this framework.

**Mapping from Lagrangian to Eulerian coordinates.** In Lagrangian description, the object of interest is not the position of particles but the *displacement field*  $\Psi(\mathbf{q})$  which maps the initial comoving particle position  $\mathbf{q}$  into its final comoving Eulerian position  $\mathbf{x}$ , (e.g. Buchert, 1989; Bouchet *et al.*, 1995; Bernardeau *et al.*, 2002):

$$\mathbf{x}(\mathbf{q}, \tau) \equiv \mathbf{q} + \Psi(\mathbf{q}, \tau). \quad (1.120)$$

Let  $J(\mathbf{q}, \tau)$  be the Jacobian of the transformation between Lagrangian and Eulerian coordinates,

$$J(\mathbf{q}, \tau) \equiv \left| \frac{\partial \mathbf{x}}{\partial \mathbf{q}} \right| = |\det \mathcal{D}| = |\det(\mathcal{I} + \mathcal{R})|, \quad (1.121)$$

where the deformation tensor  $\mathcal{D}$  can be written as the identity tensor  $\mathcal{I}$  plus the shear of the displacement,<sup>3</sup>  $\mathcal{R} \equiv \partial \Psi / \partial \mathbf{q}$ . The Jacobian can be obtained by requiring that the Lagrangian mass element be conserved in the relationship between density contrast and trajectories:

$$\rho(\mathbf{x}, \tau) d^3\mathbf{x} = \rho(\mathbf{q}) d^3\mathbf{q} \quad \Rightarrow \quad \bar{\rho}(\tau) [1 + \delta(\mathbf{x}, \tau)] d^3\mathbf{x} = \bar{\rho}(\tau) d^3\mathbf{q}. \quad (1.122)$$

Hence,

$$J(\mathbf{q}, \tau) = \frac{1}{1 + \delta(\mathbf{x}, \tau)} \quad \text{or} \quad \delta(\mathbf{x}, \tau) = J^{-1}(\mathbf{q}, \tau) - 1. \quad (1.123)$$

Note that this result (without the absolute value for  $J$ ) is valid as long as no shell-crossing occurs. At the first crossing of trajectories, fluid elements with different initial positions  $\mathbf{q}$  end up at the same Eulerian position  $\mathbf{x}$  through the mapping in equation (1.120). The Jacobian vanishes and one expects a singularity, namely a collapse to infinite density. At this point, the description of dynamics in terms of a mapping does not hold anymore, the correct description involves a summation over all possible streams.

**Equation of motion in Lagrangian coordinates.** The equation of motion for a fluid element, equation (1.70), reads in conformal time,

$$\frac{\partial \mathbf{u}}{\partial \tau} + \mathcal{H}(\tau)\mathbf{u} = -\nabla_{\mathbf{x}}\Phi, \quad (1.124)$$

<sup>3</sup>  $\mathcal{R}$  is mathematically a tensor. It is sometimes referred to as the tidal tensor and noted  $\mathcal{T}$ . We will avoid this nomenclature and notation here, so as not to introduce confusion with the Hessian of the gravitational potential  $\mathcal{T} \equiv \partial^2 \Phi / \partial \mathbf{x}^2$  (see section C.2).



where  $\Phi$  is the cosmological gravitational potential and  $\nabla_{\mathbf{x}}$  is the gradient operator in Eulerian comoving coordinates  $\mathbf{x}$ . Taking the divergence of this equation, noting that  $\mathbf{u} = d\mathbf{x}/d\tau = \partial\mathbf{\Psi}/\partial\tau$ , using equation (1.123) and the Poisson equation, equation (1.72), and multiplying by the Jacobian, we obtain

$$J(\mathbf{q}, \tau) \nabla_{\mathbf{x}} \cdot \left[ \frac{\partial^2 \mathbf{\Psi}}{\partial \tau^2} + \mathcal{H}(\tau) \frac{\partial \mathbf{\Psi}}{\partial \tau} \right] = \frac{3}{2} \Omega_m(\tau) \mathcal{H}^2(\tau) [J(\mathbf{q}, \tau) - 1]. \quad (1.125)$$

This equation shows the principal difficulty of the Lagrangian approach: the gradient operator has to be taken with reference to the Eulerian variable  $\mathbf{x}$ , which depends on  $\mathbf{q}$  according to equation (1.120). Equation (1.125) can be rewritten in terms of Lagrangian coordinates only by using  $(\nabla_{\mathbf{x}})_i = \left[ \delta_K^{ij} + \Psi_{i,j} \right]^{-1} (\nabla_{\mathbf{q}})_j$ , where  $\Psi_{i,j} \equiv \partial \Psi_i / \partial q_j = \mathcal{R}_{ij}$  are the shears of the displacement. The resulting non-linear differential equation for  $\Psi(\mathbf{q}, \tau)$  is then solved perturbatively, expanding about its linear solution.

### 1.5.2 The Zel'dovich approximation

**Displacement field in the Zel'dovich approximation.** In Lagrangian approach, non-linearities of the dynamics are encoded in the relation between  $\mathbf{q}$  and  $\mathbf{x}$  (equation (1.120)) and in the relation between the displacement field and the local density (equation (1.123)). The Zel'dovich approximation (Zel'dovich, 1970; Shandarin & Zel'dovich, 1989, hereafter ZA) is first order Lagrangian perturbation theory. It consists of taking the linear solution of equation (1.125) for the displacement field while keeping the general equation with the Jacobian, equation (1.123), to reconstruct the density field. At linear order in the displacement field, the relation between the gradients in Eulerian and Lagrangian coordinates is  $J(\mathbf{q}, \tau) \nabla_{\mathbf{x}} \approx \nabla_{\mathbf{q}}$ , and the first-order Jacobian is  $J(\mathbf{q}, \tau) \approx 1 + \nabla_{\mathbf{q}} \cdot \mathbf{\Psi}$ . The equation to solve becomes

$$\nabla_{\mathbf{q}} \cdot \left[ \frac{\partial^2 \mathbf{\Psi}}{\partial \tau^2} + \mathcal{H}(\tau) \frac{\partial \mathbf{\Psi}}{\partial \tau} \right] = \frac{3}{2} \Omega_m(\tau) \mathcal{H}^2(\tau) (\nabla_{\mathbf{q}} \cdot \mathbf{\Psi}). \quad (1.126)$$

The addition of any divergence-free displacement field to a solution of the previous equation will also be a solution. In the following, we remove this indeterminacy by assuming that the movement is potential, i.e.  $\nabla_{\mathbf{q}} \times \mathbf{\Psi} = 0$ . Introducing the divergence of the Lagrangian displacement field,  $\psi \equiv \nabla_{\mathbf{q}} \cdot \mathbf{\Psi}$ , one has to solve,

$$\psi'' + \mathcal{H}(\tau) \psi' = \frac{3}{2} \Omega_m(\tau) \mathcal{H}^2(\tau) \psi. \quad (1.127)$$

Therefore, the linear solution of equation (1.125) is separable into a product of a temporal and a spatial contribution. It can be written as  $\mathbf{\Psi}^{(1)}(\mathbf{q}, \tau)$  such that

$$\psi^{(1)}(\mathbf{q}, \tau) \equiv \nabla_{\mathbf{q}} \cdot \mathbf{\Psi}^{(1)}(\mathbf{q}, \tau) = -D_1(\tau) \delta(\mathbf{q}), \quad (1.128)$$

where  $D_1(\tau)$  denotes the linear growth factor studied in section 1.4.1 and  $\delta(\mathbf{q})$  describes the growing mode of the initial density contrast field in Lagrangian coordinates. This can be checked in equation (1.127) using the differential equation satisfied by the growth factor, equation (1.94). The above choice for the spatial contribution permits to recover the linear Eulerian behaviour, since initially  $\delta(\mathbf{x}) \approx D_1(\tau) \delta(\mathbf{q}) \approx (1 + \psi)^{-1} - 1 \approx -\psi$ .

Note that the evolution of fluid elements at linear order is *local evolution*, i.e. it does not depend on the behavior of the rest of fluid elements. We have assumed that at linear order, the displacement field is entirely determined by its divergence, i.e. that vorticity vanishes. As we have already noted from equation (1.92), in the linear regime, any initial vorticity decays away due to the expansion of the Universe. Thus, one might consider that the solutions will apply anyway, even if vorticity is initially present, because at later times it will have negligible effect. Similarly, we have neglected the effect of the decaying mode in equation (1.95).

**Shell-crossing in the Zel'dovich approximation.** Since the displacement field in the ZA is curl-free, it is convenient to introduce the potential from which it derives,  $\phi^{(1)}(\mathbf{q})$ , such that  $\mathbf{\Psi}^{(1)}(\mathbf{q}, \tau) = -D_1(\tau) \nabla_{\mathbf{q}} \phi^{(1)}(\mathbf{q})$ . At linear order in the displacement field, its shear  $\mathcal{R} \equiv \partial \mathbf{\Psi}^{(1)} / \partial \mathbf{q}$  is equal to  $-D_1(\tau) \mathcal{H}(\phi^{(1)}(\mathbf{q}))$ . Let  $\lambda_1(\mathbf{q}) \leq \lambda_2(\mathbf{q}) \leq \lambda_3(\mathbf{q})$  be the local eigenvalues of the Hessian of the Zel'dovich potential  $\phi^{(1)}(\mathbf{q})$ . At conformal time  $\tau$ , these values have grown of a factor  $-D_1(\tau)$  to give the eigenvalues of the shear of the displacement  $\mathcal{R}$ . Using equation (1.123), the density contrast may then be written as (e.g. Bouchet *et al.*, 1995; Bernardeau *et al.*, 2002)

$$1 + \delta(\mathbf{x}, \tau) = \frac{1}{[1 - \lambda_1(\mathbf{q}) D_1(\tau)] [1 - \lambda_2(\mathbf{q}) D_1(\tau)] [1 - \lambda_3(\mathbf{q}) D_1(\tau)]}. \quad (1.129)$$

This equation allows an interpretation of what happens at shell-crossing in the ZA. If all eigenvalues  $\lambda_i$  are negative, this is a developing underdense region, eventually reaching  $\delta = -1$ . If  $\lambda_3$  only is positive, when  $\lambda_3 D_1(\tau) \rightarrow 1$ , the ZA leads to a planar collapse to infinite density along the axis of  $\lambda_3$  and the formation of a two-dimensional “cosmic pancake”. In the case when two eigenvalues are positive,  $\lambda_2, \lambda_3 > 0$ , there is collapse to a filament. The case  $\lambda_1, \lambda_2, \lambda_3 > 0$  leads to gravitational collapse along all directions (spherical collapse if  $\lambda_1 \approx \lambda_2 \approx \lambda_3$ ). This picture of gravitational structure formation leads to a cosmic web classification algorithm, which labels different regions either as voids, sheets, filaments, or halos (see [Hahn \*et al.\*, 2007a](#); [Lavaux & Wandelt, 2010](#), an section C.2).

### 1.5.3 Second-order Lagrangian perturbation theory

**Displacement field in second-order Lagrangian perturbation theory.** The Zel’dovich approximation being local, it fails at sufficiently non-linear stages when particles are forming gravitationally bound structures instead of following straight lines. Already second-order Lagrangian perturbation theory (hereafter 2LPT) provides a remarkable improvement over the ZA in describing the global properties of density and velocity fields ([Melott, Buchert & Weiß, 1995](#)). The solution of equation (1.125) up to second order takes into account the fact that gravitational instability is *non-local*, i.e. it includes the correction to the ZA displacement due to gravitational tidal effects. It reads

$$\mathbf{x}(\tau) = \mathbf{q} + \mathbf{\Psi}(\mathbf{q}, \tau) = \mathbf{q} + \mathbf{\Psi}^{(1)}(\mathbf{q}, \tau) + \mathbf{\Psi}^{(2)}(\mathbf{q}, \tau), \quad \text{or} \quad \mathbf{\Psi}(\mathbf{q}, \tau) = \mathbf{\Psi}^{(1)}(\mathbf{q}, \tau) + \mathbf{\Psi}^{(2)}(\mathbf{q}, \tau), \quad (1.130)$$

where the divergence of the first order solution is the same as in the ZA (equation (1.128)),

$$\psi^{(1)}(\mathbf{q}, \tau) = \nabla_{\mathbf{q}} \cdot \mathbf{\Psi}^{(1)}(\mathbf{q}, \tau) = -D_1(\tau) \delta(\mathbf{q}), \quad (1.131)$$

and the divergence of the second order solution describes the tidal effects,

$$\psi^{(2)}(\mathbf{q}, \tau) = \nabla_{\mathbf{q}} \cdot \mathbf{\Psi}^{(2)}(\mathbf{q}, \tau) = \frac{1}{2} \frac{D_2(\tau)}{D_1^2(\tau)} \sum_{i \neq j} \left[ \Psi_{i,i}^{(1)} \Psi_{j,j}^{(1)} - \Psi_{i,j}^{(1)} \Psi_{j,i}^{(1)} \right], \quad (1.132)$$

where  $\mathbf{\Psi}_{k,l}^{(1)} \equiv \partial \mathbf{\Psi}_k^{(1)} / \partial \mathbf{q}_l$  and  $D_2(\tau)$  denotes the second-order growth factor, defined in section 1.4.3.

**Lagrangian potentials.** Since Lagrangian solutions up to second order are irrotational ([Melott, Buchert & Weiß, 1995](#); [Buchert, Melott & Weiß, 1994](#); [Bernardeau \*et al.\*, 2002](#); this is assuming that initial conditions are only in the growing mode, in the same spirit as neglecting completely the decaying vorticity), it is convenient to define the Lagrangian potentials  $\phi^{(1)}$  and  $\phi^{(2)}$  from which  $\mathbf{\Psi}^{(1)}$  and  $\mathbf{\Psi}^{(2)}$  derive, so that in 2LPT,

$$\mathbf{\Psi}^{(1)}(\mathbf{q}, \tau) = -D_1(\tau) \nabla_{\mathbf{q}} \phi^{(1)}(\mathbf{q}) \quad \text{and} \quad \mathbf{\Psi}^{(2)}(\mathbf{q}, \tau) = D_2(\tau) \nabla_{\mathbf{q}} \phi^{(2)}(\mathbf{q}). \quad (1.133)$$

Since  $\mathbf{\Psi}^{(1)}$  is of order  $D_1(\tau)$  (equation (1.131)) and  $\mathbf{\Psi}^{(2)}$  is of order  $D_2(\tau)$  (equation (1.132)), the above potentials are time-independent. They satisfy Poisson-like equations ([Buchert, Melott & Weiß, 1994](#)),

$$\Delta_{\mathbf{q}} \phi^{(1)}(\mathbf{q}) = \delta(\mathbf{q}), \quad (1.134)$$

$$\Delta_{\mathbf{q}} \phi^{(2)}(\mathbf{q}) = \sum_{i > j} \left[ \phi_{,ii}^{(1)}(\mathbf{q}) \phi_{,jj}^{(1)}(\mathbf{q}) - (\phi_{,ij}^{(1)}(\mathbf{q}))^2 \right]. \quad (1.135)$$

The mapping from Eulerian to Lagrangian, equation (1.130), thus reads

$$\mathbf{x}(\tau) = \mathbf{q} - D_1(\tau) \nabla_{\mathbf{q}} \phi^{(1)}(\mathbf{q}) + D_2(\tau) \nabla_{\mathbf{q}} \phi^{(2)}(\mathbf{q}). \quad (1.136)$$

**Velocity field in second-order Lagrangian perturbation theory.** Taking the derivative of the previous equation yields for the velocity field,

$$\mathbf{u} = -f_1(\tau) D_1(\tau) \mathcal{H}(\tau) \nabla_{\mathbf{q}} \phi^{(1)}(\mathbf{q}) + f_2(\tau) D_2(\tau) \mathcal{H}(\tau) \nabla_{\mathbf{q}} \phi^{(2)}(\mathbf{q}). \quad (1.137)$$

which involves the logarithmic derivatives of the growth factors,  $f_i \equiv d \ln D_i / d \ln a$ , well approximated in a flat  $\Lambda$ CDM model by ([Bouchet \*et al.\*, 1995](#))

$$f_1 \approx \Omega_m^{5/9} \quad \text{and} \quad f_2 \approx 2 \Omega_m^{6/11} \approx 2 f_1^{54/55}. \quad (1.138)$$

Other expressions for different cosmologies can be found in [Bouchet \*et al.\* \(1995\)](#); [Bernardeau \*et al.\* \(2002\)](#).

## 1.6 Non-linear approximations to gravitational instability

When fluctuations become strongly non-linear in the density field, Eulerian perturbation theory breaks down. Lagrangian perturbation theory is often more successful, since the Lagrangian picture is intrinsically non-linear in the density field (see e.g. equation (1.125)). A small perturbation in the Lagrangian displacement field carries a considerable amount of non-linear information about the corresponding Eulerian density and velocity fields. However, at some point, computers are required to study gravitational instability (in particular through  $N$ -body simulations), the important drawback being that the treatment becomes numerical instead of analytical. We will adopt this approach in this thesis. However, several non-linear approximations to the equations of motion have been suggested in the literature to allow the extrapolation of analytical calculations in the non-linear regime. We now briefly review some of them.

Non-linear approximations consist of replacing one of the equations of the dynamics (Poisson – equation (1.72) –, continuity – equation (1.79) – or Euler – equation (1.80)) by a different assumption.<sup>4</sup> In general, the Poisson equation is replaced (Munshi & Starobinsky, 1994). These modified dynamics are often local, in the sense described above for the ZA, in order to provide a simpler way of calculating the evolution of fluctuations than the full non-local dynamics.

### 1.6.1 The Zel'dovich approximation as a non-linear approximation

As we have seen in section 1.3, in Eulerian dynamics, non-linearity is encoded in the Poisson equation, equation (1.72),  $\Delta\Phi = 4\pi G a^2 \bar{\rho} \delta$ . The goal of this paragraph is to see what replaces the Poisson equation in the Eulerian description of the ZA. From this point of view, the ZA is the original non-linear Eulerian approximation, and it remains one of the most famous.

If we restrict our attention to potential movements, the peculiar velocity field  $\mathbf{u}$  is irrotational. It can be written as the gradient of a velocity potential,

$$\mathbf{u} = -\frac{\nabla_{\mathbf{x}} V}{a}. \quad (1.139)$$

As discussed before, the main reason to restrict to this case is the decay of vortical perturbations.

It is then possible to postulate various forms for the velocity potential  $V$ . The ZA corresponds to the Ansatz (Munshi & Starobinsky, 1994; Hui & Bertschinger, 1996; appendix B in Scoccimarro, 1997)

$$V = \frac{2fa}{3\Omega_m \mathcal{H}} \Phi, \quad (1.140)$$

where  $\Phi$  is the cosmological gravitational potential and  $f$  is the logarithmic derivative of the linear growth factor. The Zel'dovich approximation is therefore equivalent to the replacement of the Poisson equation by

$$\mathbf{u} = -\frac{2f}{3\Omega_m \mathcal{H}} \nabla \Phi. \quad (1.141)$$

This can be explicitly checked as follows. Combining equations (1.124) and (1.141), one gets

$$\frac{\partial \mathbf{u}}{\partial \tau} + \mathcal{H} \mathbf{u} = \frac{3\Omega_m \mathcal{H}}{2f} \mathbf{u}. \quad (1.142)$$

Then, noting that  $\nabla_{\mathbf{q}} \cdot \mathbf{u} = \psi'$ , the differential equation for  $\psi$  is

$$\psi'' + \mathcal{H} \psi' = \frac{3\Omega_m \mathcal{H}}{2f} \psi', \quad (1.143)$$

Using the time evolution of  $D_1$  (equation (1.94)) and the identity  $D'_1 = \mathcal{H} f D_1$ , one can check that the Zel'dovich solution,  $\psi = -D_1 \delta(\mathbf{q})$  indeed verifies the above equation.

Equation (1.141) means that at linear order, particles just go straight (in comoving coordinates) in the direction set by their initial velocity. In the Zel'dovich approximation, the proportionality between velocity field and gravitational field always holds (not just to first order in  $\Psi$ ).

<sup>4</sup> In this section, we have come back to a Eulerian description of the cosmological fluid.

Note that during the matter era,  $a \propto t^{2/3}$  and thus  $\mathcal{H} \equiv \dot{a} = 2a/(3t)$ , which means that an equivalent form for the ZA Ansatz is

$$V = \frac{f}{\Omega_m} \Phi t \approx \Phi t. \quad (1.144)$$

The ZA is a local approximation that represents exactly the true dynamics in one-dimensional collapse (Buchert, 1989; Yoshisato *et al.*, 2006). It is also possible to formulate local approximations that besides describing correctly planar collapse like the ZA, are suited for cylindrical or spherical collapse (leading to the formation of cosmic filaments and halos, in addition to cosmic pancakes). These approximations, namely the “non-magnetic” approximation (NMA, Bertschinger & Jain, 1994) and the “local tidal” approximation (LTA, Hui & Bertschinger, 1996), are not straightforward to implement for the calculation of statistical properties of density and velocity fields.

### 1.6.2 Other velocity potential approximations

Some other possibilities for the velocity potential can be found in literature (Coles, Melott & Shandarin, 1993; Munshi & Starobinsky, 1994). The frozen flow (FF) approximation postulates

$$V = \Phi^{(1)} t, \quad (1.145)$$

where  $\Phi^{(1)}$  is the first-order solution (the linear approximation) for the gravitational potential. It satisfies the Poisson equation in the linear regime,

$$\Delta \Phi^{(1)} = \frac{3}{2} \Omega_m(\tau) \mathcal{H}^2(\tau) \delta_1(\mathbf{x}, \tau), \quad (1.146)$$

where  $\delta_1(\mathbf{x}, \tau) = D_1(\tau) \delta_1(\mathbf{x})$  is the linearly extrapolated density field. In FF, the Poisson equation is replaced by the analog of equation (1.141), substituting equation (1.145),

$$\mathbf{u} = -\frac{2f}{3\Omega_m \mathcal{H}} \nabla \Phi^{(1)}, \quad (1.147)$$

or, by taking the divergence and using equation (1.146),

$$\theta(\mathbf{x}, \tau) = -\mathcal{H}(\tau) f \delta_1(\mathbf{x}, \tau). \quad (1.148)$$

The physical meaning of this approximation is that the velocity field is assumed to remain linear while the density field is allowed to explore the non-linear regime.

In the linear potential (LP) approximation, the gravitational potential is instead assumed to remain the same as in the linear regime; therefore, the Poisson equation is replaced by

$$\Phi = \Phi^{(1)}, \quad \Delta \Phi = \frac{3}{2} \Omega_m(\tau) \mathcal{H}^2(\tau) \delta_1(\mathbf{x}, \tau). \quad (1.149)$$

The idea is that since  $\Phi \propto \delta/k^2$  in Fourier space, the gravitational potential is dominated by the long-wavelength modes more than the density field, and therefore it ought to obey linear perturbation theory to a better approximation.

### 1.6.3 The adhesion approximation

All the above approximations (ZA, NMA, LTA, FF, LP) are local, which means that we neglect the self-gravity of inhomogeneities. A significant problem of the ZA, and of subsequent variations, is the fact that after shell-crossing, matter continues to flow throughout the newly-formed structure, which should instead be gravitationally bound. This phenomenon washes out cosmic structures on small scales.

A possible phenomenological solution is to add a viscosity term to the single-stream Euler equation, equation (1.85), which then becomes Burgers’ equation,

$$\frac{\partial \mathbf{u}_i(\mathbf{x}, \tau)}{\partial \tau} + \mathcal{H}(\tau) \mathbf{u}_i(\mathbf{x}, \tau) + \mathbf{u}_j(\mathbf{x}, \tau) \cdot \nabla_j \mathbf{u}_i(\mathbf{x}, \tau) = -\nabla_i \Phi(\mathbf{x}, \tau) + v \Delta \mathbf{u}_i(\mathbf{x}, \tau). \quad (1.150)$$

This is the so-called *adhesion approximation* (Kofman & Shandarin, 1988; Gurbatov, Saichev & Shandarin, 1989; Kofman *et al.*, 1992; Valageas & Bernardeau, 2011; Hidding *et al.*, 2012). For a potential flow, it can be

reduced to a linear diffusion equation, and therefore solved exactly. Surprisingly, in the adhesion approximation, the dynamical equations describing the evolution of the self-gravitating cosmological fluid can be written in the form of a Schrödinger equation coupled to a Poisson equation describing Newtonian gravity (Short & Coles, 2006b). The dynamics can therefore be studied with the tools of wave mechanics. An alternative to the adhesion model is the free-particle approximation (FPA), in which the artificial viscosity term in Burgers' equation is replaced by a non-linear term known as the *quantum pressure*. This also leads to a free-particle Schrödinger equation (Short & Coles, 2006b,a).

Comparisons of the adhesion approximation to full-gravitational numerical simulations show an improvement over the ZA at small scales, even if the fragmentation of structures into dense clumps is still underestimated (Weinberg & Gunn, 1990). At weakly non-linear scales, the adhesion approximation is essentially equal to the ZA.



# Numerical diagnostics of Lagrangian perturbation theory

## Contents

<b>2.1</b>	<b>Correlation functions of the density field</b>	<b>30</b>
2.1.1	One-point statistics	30
2.1.2	Two-point statistics	31
2.1.3	Three-point statistics	34
<b>2.2</b>	<b>Statistics of the Lagrangian displacement field</b>	<b>37</b>
2.2.1	Lagrangian $\psi$ versus Eulerian $\delta$ : one-point statistics	37
2.2.2	Perturbative and non-perturbative prescriptions for $\psi$	41
2.2.3	Non-linear evolution of $\psi$ and generation of a vector part	43
<b>2.3</b>	<b>Comparison of structure types in LPT and <math>N</math>-body dynamics</b>	<b>44</b>

---

“**Hector Barbossa**: The world used to be a bigger place.

**Jack Sparrow**: The world’s still the same. There’s just... less in it.”

— [Pirates of the Caribbean: At World’s End](#) (2007)

---

## Abstract

This chapter is intended as a guide on the approximation error in using Lagrangian perturbation theory instead of fully non-linear gravity in large-scale structure analysis. We compare various properties of particle realizations produced by LPT and by  $N$ -body simulations. In doing so, we characterize differences and similarities, as a function of scale, resolution and redshift.

The goal of this chapter is to characterize the accuracy of Lagrangian perturbation theory in terms of a set of numerical diagnostics. It is organized as follows. In section 2.1, we look at the correlations functions of the density field, which usually are the final observable in cosmological surveys. As the displacement field plays a central role in LPT, we study its statistics in section 2.2. In particular, we illustrate that in some regimes, when the perturbative parameter is large, 2LPT performs worse than the ZA. We examine the decomposition of the displacement field in a scalar and rotational part and review various approximations based on its divergence. Finally, in section 2.3, we compare cosmic web elements (voids, sheets, filaments, and clusters) as predicted by LPT and by non-linear simulations of the LSS.<sup>1</sup>

Corresponding LPT and  $N$ -body simulations used in this chapter have been run from the same initial conditions, generated at redshift  $z = 63$  using second-order Lagrangian perturbation theory. The  $N$ -body simulations have been run with the GADGET-2 cosmological code (Springel, Yoshida & White, 2001; Springel, 2005). Evolutions of the Zel’dovich approximation were performed with N-GENIC (Springel, 2005), and of second-order Lagrangian perturbation theory with 2LPTIC (Crocce, Pueblas & Scoccimarro, 2006a). To ensure sufficient statistical significance, we used eight realizations of the same cosmology, changing the seed used to generate respective initial conditions. All computations are done after binning the dark matter particles with a Cloud-in-Cell (CiC) method (see section B.3). The simulations contain  $512^3$  particles in a  $1024 \text{ Mpc}/h$  cubic box with periodic boundary conditions. We checked that with this setup, the power spectrum agrees with

---

<sup>1</sup> In the following, we will often write “full gravity”, even if, strictly speaking,  $N$ -body simulations also involve some degree of approximation.

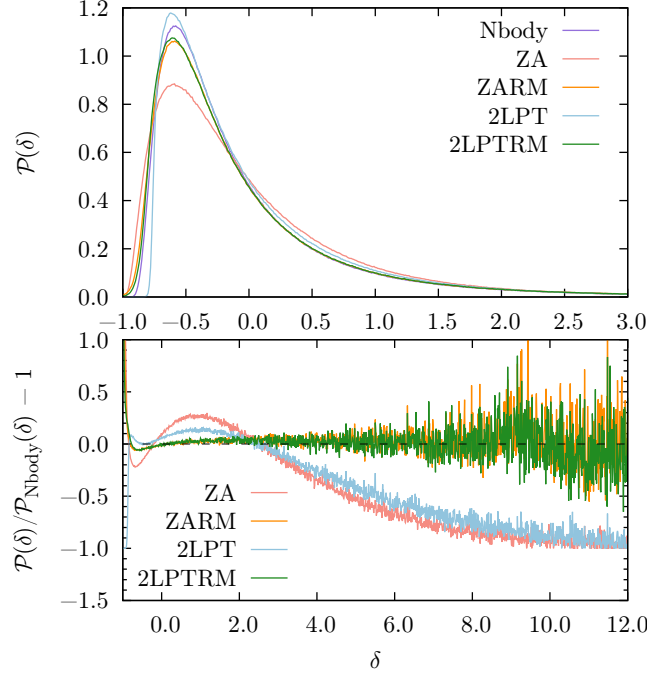


Figure 2.1: *Upper panel.* Redshift-zero probability distribution function for the density contrast  $\delta$ , computed from eight 1024 Mpc/ $h$ -box simulations of  $512^3$  particles. The particle distribution is determined using: a full  $N$ -body simulation (purple curve), the Zel’dovich approximation, alone (ZA, light red curve) and after remapping (ZARM, orange curve), second-order Lagrangian perturbation theory, alone (2LPT, light blue curve) and after remapping (2LPTRM, green curve). *Lower panel.* Relative deviations of the same pdfs with reference to  $N$ -body simulation results. Note that, contrary to standard LPT approaches, remapped fields follow the one-point distribution of full  $N$ -body dynamics in an unbiased way, especially in the high density regime.

the non-linear power spectrum of simulations run with higher mass resolution, provided by COSMIC EMULATOR tools (Heitmann *et al.*, 2009, 2010; Lawrence *et al.*, 2010) (deviations are at most sub-percent level for  $k \lesssim 1$  (Mpc/ $h$ ) $^{-1}$ ). Therefore, at the scales of interest of this work,  $k \leq 0.4$  (Mpc/ $h$ ) $^{-1}$  (corresponding to the linear and mildly non-linear regime at redshift zero), the clustering of dark matter is correctly reproduced by our set of simulations.

The cosmological parameters used are WMAP-7 fiducial values (Komatsu *et al.*, 2011),

$$\Omega_\Lambda = 0.728, \Omega_m = 0.2715, \Omega_b = 0.0455, \sigma_8 = 0.810, h = 0.704, n_s = 0.967. \quad (2.1)$$

Thus, each particle carries a mass of  $6.03 \times 10^{11} M_\odot/h$ .

## 2.1 Correlation functions of the density field

This section draws from section III in Leclercq *et al.* (2013).

In this section, we analyze the correlation functions of the density contrast field,  $\delta$ , in LPT and  $N$ -body fields.

*Note.* All plots presented in this section contain lines labeled as “ZARM” and “2LPTRM” which correspond to remapped fields based on the ZA and on 2LPT, respectively. They are ignored in this chapter, which focuses on diagnostics of LPT. For a description of the remapping procedure and for comments on these approximations in comparison to the ZA, 2LPT and  $N$ -body dynamics, the reader is referred to chapter 6.

### 2.1.1 One-point statistics

Figure 2.1 shows the pdf for the density contrast,  $\mathcal{P}_\delta$ , at redshift zero, for  $N$ -body simulations, and for ZA and 2LPT density fields. All pdfs are non-Gaussian with a substantial skewness, are tied down to 0 at  $\delta = -1$



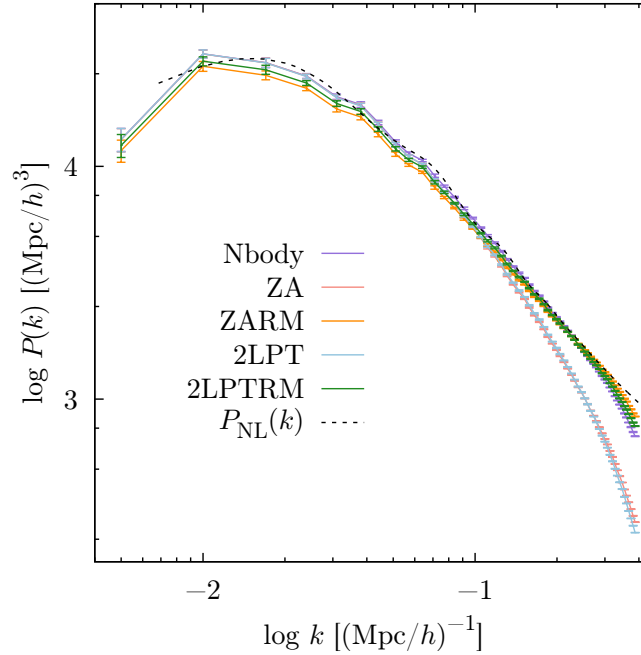


Figure 2.2: Redshift-zero dark matter power spectra in a 1024 Mpc/h simulation, with density fields computed with a mesh size of 8 Mpc/h. The particle distribution is determined using: a full  $N$ -body simulation (purple curve), the Zel’dovich approximation, alone (ZA, light red curve) and after remapping (ZARM, orange curve), second-order Lagrangian perturbation theory, alone (2LPT, light blue curve) and after remapping (2LPTRM, green curve). The dashed black curve represents  $P_{\text{NL}}(k)$ , the theoretical power spectrum expected at  $z = 0$ . Both ZARM and 2LPTRM show increased power in the mildly non-linear regime compared to ZA and 2LPT (at scales corresponding to  $k \gtrsim 0.1 \text{ (Mpc/h)}^{-1}$  for this redshift), indicating an improvement of two-point statistics with the remapping procedure.

with a large tail in the high-density values. As discussed in section 1.2.3.4, the late-time pdf for density fields is approximately log-normal. However, already at the level of one-point statistics, the detailed behaviors of LPT and  $N$ -body simulations disagree: the peak of the pdf is shifted and the tails differ. In particular, LPT largely underpredicts the number of voxels in the high-density regime. This effect is more severe for the ZA than for 2LPT. This comes from the fact that 2LPT captures some of non-local effects involved in the formation of the densest halos.

The one-point pdf of the density is further analyzed in section 2.2.1, in comparison to the one-point pdf of the Lagrangian displacement field.

## 2.1.2 Two-point statistics

### 2.1.2.1 Power spectrum

We measured the power spectrum of dark matter density fields, as defined by equation (1.41). Dark matter particles have been displaced according to each prescription and assigned to cells with a CiC scheme, for different mesh sizes. Power spectra were measured from these meshes, with a correction for aliasing effects (Jing, 2005). Redshift-zero results computed on a 8 Mpc/h mesh are presented in figure 2.2. There, the dashed line corresponds to the theoretical, non-linear power spectrum expected, computed with COSMIC EMULATOR tools (Heitmann *et al.*, 2009, 2010; Lawrence *et al.*, 2010). A deviation of full  $N$ -body simulations from this theoretical prediction can be observed at small scales. This discrepancy is a gridding artifact, completely due to the finite mesh size used for the analysis. As a rule of thumb, a maximum threshold in  $k$  for trusting the simulation data is set by a quarter of the Nyquist wavenumber, defined by  $k_{\text{N}} \equiv 2\pi/L \times N_{\text{p}}^{1/3}/2$ , where  $L$  is the size of the box and  $N_{\text{p}}$  is the number of cells in the Lagrangian grid on which particles are placed in the initial conditions; which makes for our analysis ( $L = 1024 \text{ Mpc/h}$ ,  $N_{\text{p}} = 512^3$ ),  $k_{\text{N}}/4 \approx 0.39 \text{ (Mpc/h)}^{-1}$ . At this scale, it has been observed that the power spectrum starts to deviate at the percent-level with respect to higher resolution simulations (Heitmann *et al.*, 2010). The relative deviations of various power spectra with reference

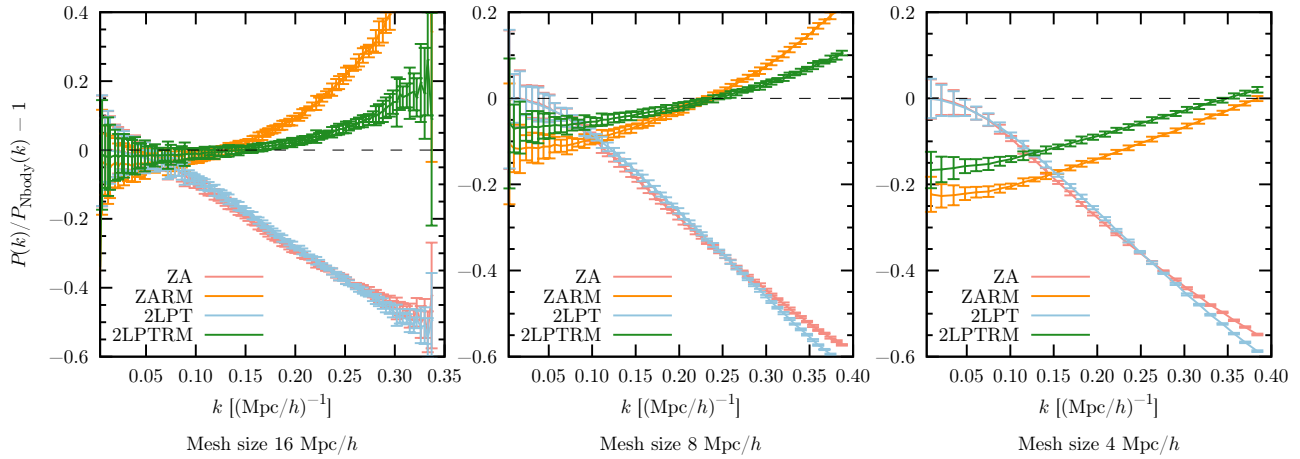


Figure 2.3: *Power spectrum: mesh size-dependence.* Relative deviations for the power spectra of various particle distributions, with reference to the density field computed with a full  $N$ -body simulation. The particle distribution is determined using: the Zel’dovich approximation, alone (ZA, light red curve) and after remapping (ZARM, orange curve), second-order Lagrangian perturbation theory, alone (2LPT, light blue curve) and after remapping (2LPTRM, green curve). The computation is done on different meshes: 16 Mpc/h ( $64^3$ -voxel grid, left panel), 8 Mpc/h ( $128^3$ -voxel grid, central panel) and 4 Mpc/h ( $256^3$ -voxel grid, right panel). All results are shown at redshift  $z = 0$ . LPT fields exhibit more small-scale correlations after remapping and their power spectra get closer to the shape of the full non-linear power spectrum.

to full gravity are presented in figures 2.3 and 2.4. In all the plots, the error bars represent the dispersion of the mean among eight independent realizations.

Generally, LPT correctly predicts the largest scales, when  $k \rightarrow 0$  (the smallest wavelength mode accessible here is set by the box size:  $k_{\min} = 2\pi/L$  with  $L = 1024$  Mpc/h, giving  $k_{\min} \approx 0.006$  (Mpc/h) $^{-1}$ ), as these are in the linear regime. These are affected by cosmic variance, but the effect is not visible in our plots, as corresponding LPT and  $N$ -body fields start from the same initial conditions. Differences arise in the mildly non-linear and non-linear regime, where LPT predicts too little power. Indeed, as LPT only captures part of the non-linearity of the Vlasov-Poisson system, presented in section 1.3.1, the clustering of dark matter particles is underestimated.

The discrepancy between LPT and  $N$ -body power spectra depends both on the target resolution (see figure 2.3) and on the desired redshift (see figure 2.4). For example, at a resolution of 8 Mpc/h and at a comoving wavelength of  $k = 0.40$  (Mpc/h) $^{-1}$ , 2LPT only lacks 5% power at  $z = 3$  but more than 50% at  $z = 0$ . At fixed redshift, the lack of small scale power in LPT weakly depends on the mesh size.

### 2.1.2.2 Fourier-space cross-correlation coefficient

The Fourier space cross-correlation coefficient between two density fields  $\delta$  and  $\delta'$  is defined as the cross-power spectrum of  $\delta$  and  $\delta'$ , normalized by the auto-power spectra of the same fields:

$$R(k) \equiv \frac{P_{\delta \times \delta'}(k)}{\sqrt{P_{\delta}(k)P_{\delta'}(k)}} \equiv \frac{\langle \delta^*(\mathbf{k})\delta'(\mathbf{k}) \rangle}{\sqrt{\langle \delta^*(\mathbf{k})\delta(\mathbf{k}) \rangle \langle \delta'^*(\mathbf{k})\delta'(\mathbf{k}) \rangle}}. \quad (2.2)$$

It is a dimensionless coefficient, in modulus between 0 and 1, representing the agreement, at the level of two-point statistics, between the *phases* of  $\delta$  and  $\delta'$  (as the overall power has been divided out). Here we choose as a reference the density field predicted by  $N$ -body simulations,  $\delta' = \delta_{\text{Nbody}}$ , and compare with approximate density fields generated from the same initial conditions with LPT. In this fashion, we characterize the phase accuracy of the ZA and 2LPT.

In figure 2.5 we present the Fourier-space cross-correlation coefficient between the redshift-zero density field in the  $N$ -body simulation and other density fields. At this point, it is useful to recall that an approximation well-correlated with the non-linear density field can be used in a variety of cosmological applications, such as the reconstruction of the non-linear power spectrum (Tassev & Zaldarriaga, 2012c). As pointed out by Neyrinck (2013), the cross-correlation between 2LPT and full gravitational dynamics is higher at small  $k$  than the cross-

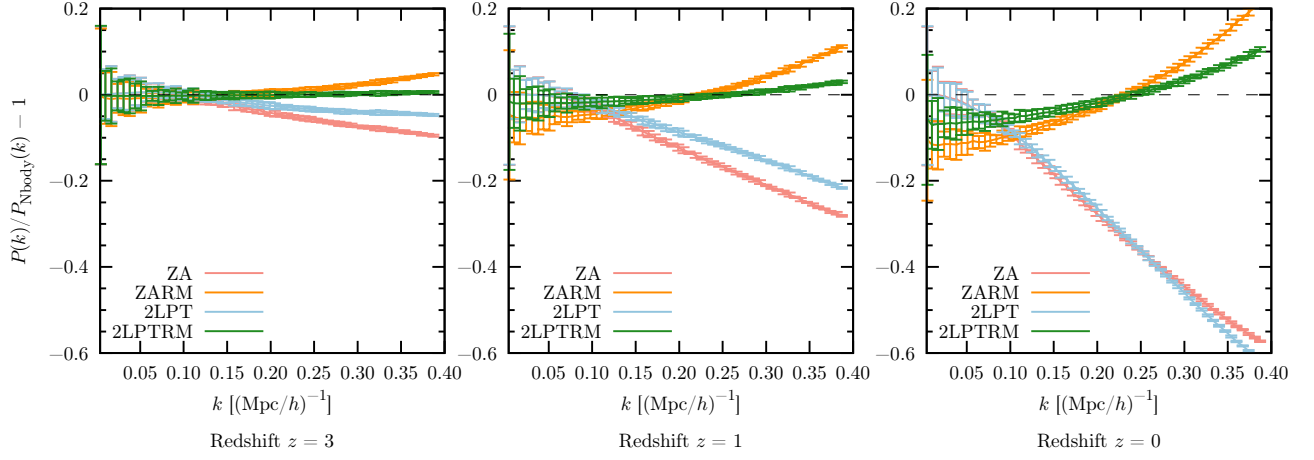


Figure 2.4: *Power spectrum: redshift-dependence.* Relative deviations for the power spectra of various particle distributions (see the caption of figure 2.3), with reference to the density field computed with a full  $N$ -body simulation. The computation is done on a 8 Mpc/ $h$  mesh ( $128^3$ -voxel grid). Results at different redshifts are shown:  $z = 3$  (right panel),  $z = 1$  (central panel) and  $z = 0$  (left panel). The remapping procedure is increasingly successful with increasing redshift.

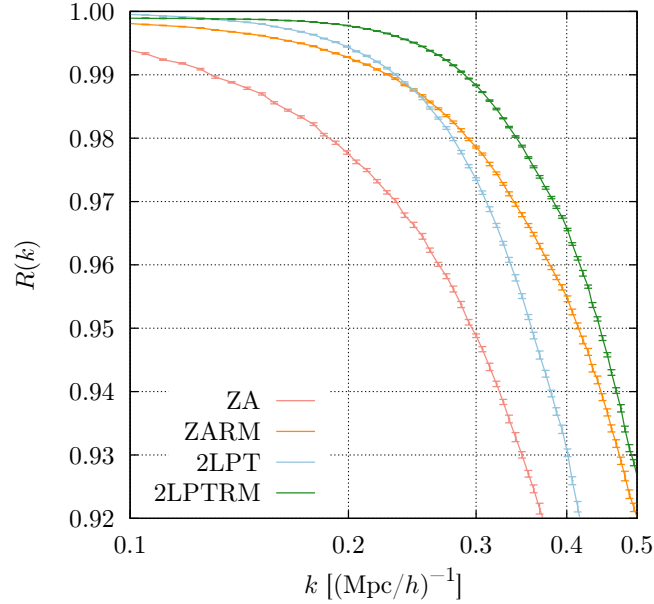


Figure 2.5: Fourier-space cross-correlation coefficient between various approximately-evolved density fields and the particle distribution as evolved with full  $N$ -body dynamics, all at redshift zero. The binning of density fields is done on a 8 Mpc/ $h$  mesh ( $128^3$ -voxel grid). At small scales,  $k \geq 0.2$  (Mpc/ $h$ ) $^{-1}$ , the cross-correlations with respect to the  $N$ -body-evolved field are notably better after remapping than with LPT alone.

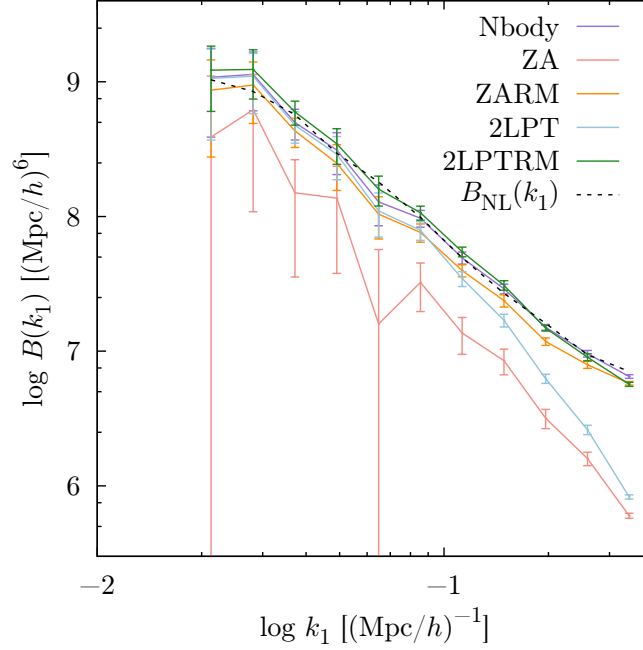


Figure 2.6: Redshift-zero dark matter bispectra for equilateral triangle shape, in 1024 Mpc/h simulations, with density fields computed on mesh of 8 Mpc/h size. The particle distribution is determined using: a full  $N$ -body simulation (purple curve), the Zel’dovich approximation, alone (ZA, light red curve) and after remapping (ZARM, orange curve), second-order Lagrangian perturbation theory, alone (2LPT, light blue curve) and after remapping (2LPTRM, green curve). The dashed line,  $B_{\text{NL}}(k)$ , corresponds to theoretical predictions for the bispectrum, found using the fitting formula of (Gil-Marín *et al.*, 2012). Note that both ZARM and 2LPTRM show increased bispectrum in the mildly non-linear regime compared to ZA and 2LPT, indicating an improvement of three-point statistics with the remapping procedure.

correlation between the ZA and the full dynamics, meaning that the position of structures is more correct when additional physics (non-local tidal effects) is taken into account.

### 2.1.3 Three-point statistics

In this section, we analyze the accuracy of LPT beyond second-order statistics, by studying the three-point correlation function of the density field in Fourier space, i.e. the bispectrum, defined by equation (1.56). The importance of three-point statistics relies in their ability to test the shape of structures. Some of the natural applications are to test gravity (Shirata *et al.*, 2007; Gil-Marín *et al.*, 2011), to break degeneracies due to the galaxy bias (Matarrese, Verde & Heavens, 1997; Verde *et al.*, 1998; Scoccimarro *et al.*, 2001; Verde *et al.*, 2002) or to test the existence of primordial non-Gaussianities in the initial matter density field (Sefusatti & Komatsu, 2007; Jeong & Komatsu, 2009).

As for the power spectrum, we construct the dark matter density contrast field, by assigning particles to the grid using a CiC scheme. We then deconvolve the CiC kernel to correct for corresponding smoothing effects. The algorithm used to compute the bispectrum  $B(\mathbf{k}_1, \mathbf{k}_2, \mathbf{k}_3)$  from this  $\delta(\mathbf{k})$  field consists of randomly drawing  $k$ -vectors from a specified bin, namely  $\Delta k$ , and randomly orientating the  $(\mathbf{k}_1, \mathbf{k}_2, \mathbf{k}_3)$  triangle in space. We chose the number of random triangles to depend on the number of fundamental triangle per bin, that scales as  $k_1 k_2 k_3 \Delta k^3$  (Scoccimarro, 1997), where  $\Delta k$  is the chosen  $k$ -binning: given  $k_i$  we allow triangles whose  $i$ -side lies between  $k_i - \Delta k/2$  and  $k_i + \Delta k/2$ . In this paper we always set  $\Delta k = k_{\text{min}} = 2\pi/L$ , where  $L$  is the size of the box. For the equilateral case, at scales of  $k \approx 0.1 \text{ (Mpc/h)}^{-1}$  we generate  $\sim 1.7 \times 10^6$  random triangles. We have verified that increasing the number of triangles beyond this value does not have any effect on the measurement. The rule of thumb presented in section 2.1.2.1 for the smallest scale to trust applies for the bispectrum as well. Also, as a lower limit in  $k$ , we have observed that for scales larger than  $\sim 3 k_{\text{min}}$ , effects of cosmic variance start to be important and considerable deviations with respect to linear theory can be observed. For this reason, we limit the largest scale for our bispectrum analysis to  $3 k_{\text{min}} \approx 1.8 \times 10^{-2} \text{ (Mpc/h)}^{-1}$ .

Error bars in bispectrum plots represent the dispersion of the mean among eight independent realizations, all

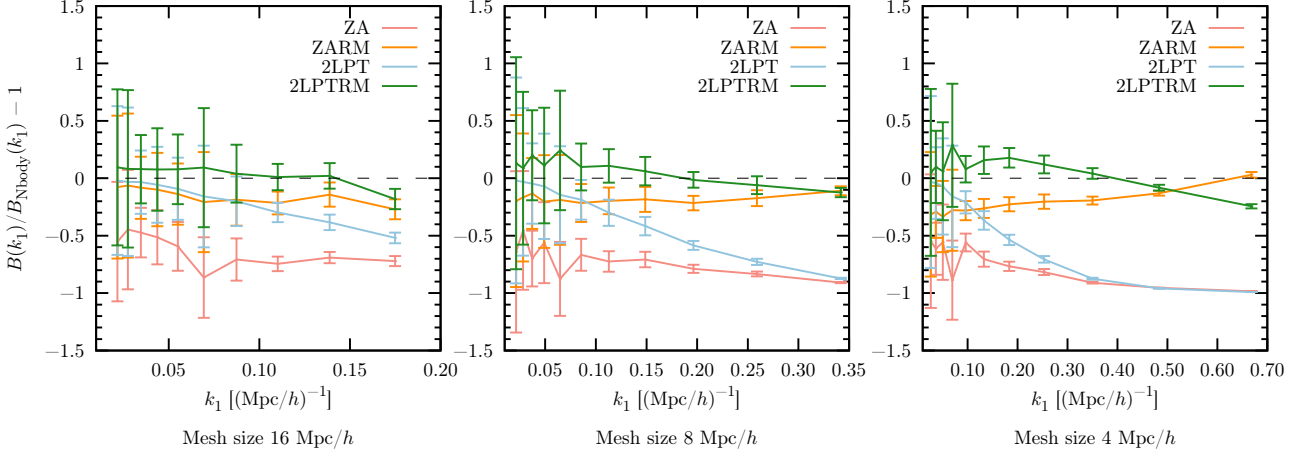


Figure 2.7: *Bispectrum: mesh size-dependence.* Relative deviations for the bispectra  $B(k_1)$  of various particle distributions, with reference to the prediction from a full  $N$ -body simulation,  $B_{N\text{body}}(k_1)$ . The particle distribution is determined using: the Zel'dovich approximation, alone (ZA, light red curve) and after remapping (ZARM, orange curve), second-order Lagrangian perturbation theory, alone (2LPT, light blue curve) and after remapping (2LPTRM, green curve). The computation of bispectra is done for equilateral triangles and on different meshes: 16 Mpc/h ( $64^3$ -voxel grid, left panel), 8 Mpc/h ( $128^3$ -voxel grid, central panel) and 4 Mpc/h ( $256^3$ -voxel grid, right panel). All results are shown at redshift  $z = 0$ . LPT fields exhibit more small-scale three-point correlations after remapping and their bispectra get closer to the shape of the full non-linear bispectrum.

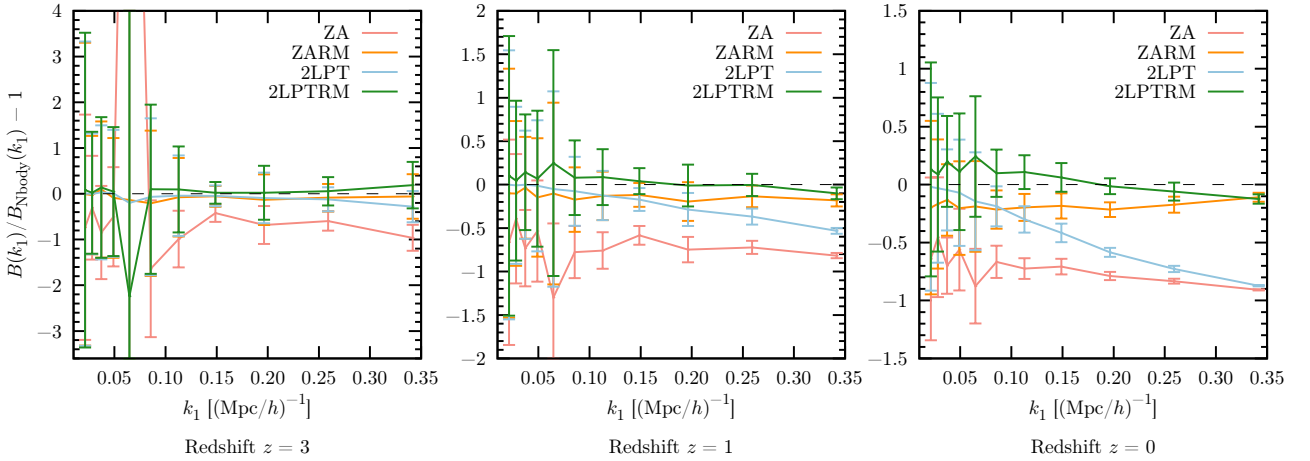


Figure 2.8: *Bispectrum: redshift-dependence.* Relative deviations for the bispectra  $B(k_1)$  of various particle distributions (see the caption of figure 2.7), with reference to a full  $N$ -body simulation,  $B_{N\text{body}}(k_1)$ . The computation of bispectra is done on a 8 Mpc/h mesh ( $128^3$ -voxel grid) and for equilateral triangles. Results at different redshifts are shown:  $z = 3$  (right panel),  $z = 1$  (central panel) and  $z = 0$  (left panel).

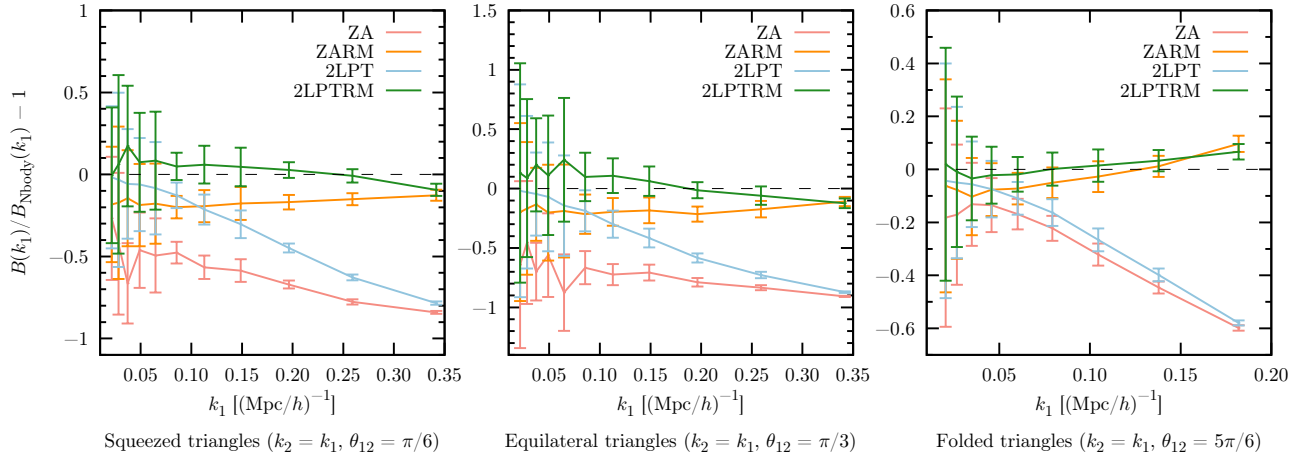


Figure 2.9: *Bispectrum: scale-dependence for different triangle shapes.* Relative deviations for the bispectra  $B(k_1)$  of various particle distributions (see the caption of figure 2.7), with reference to a full  $N$ -body simulation,  $B_{\text{Nbody}}(k_1)$ . The computation is done on a 8 Mpc/h mesh ( $128^3$ -voxel grid) and results are shown at redshift  $z = 0$  for various triangle shapes as defined above.

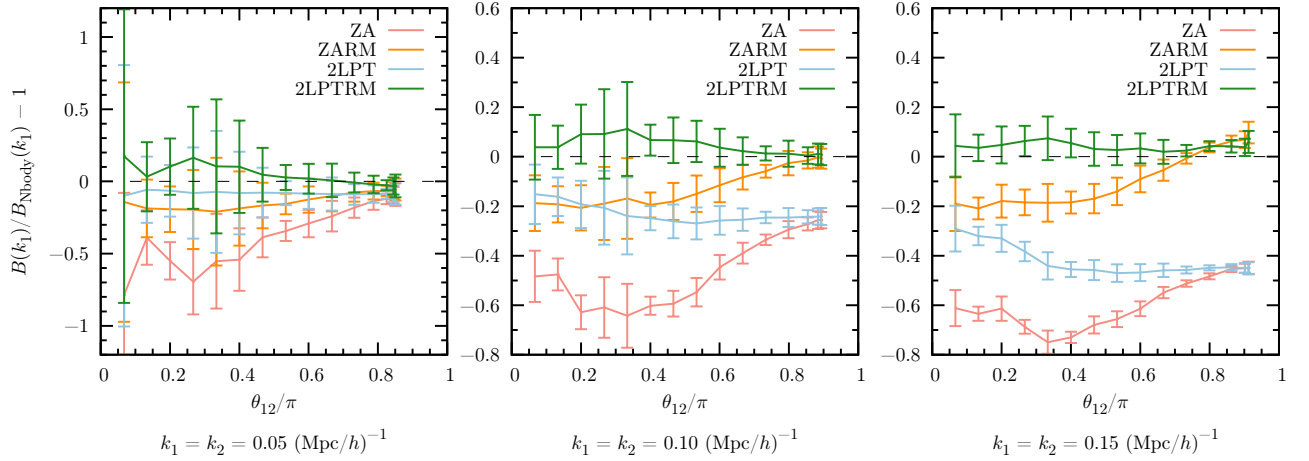


Figure 2.10: *Bispectrum: triangle shape-dependence.* Relative deviations for the bispectra  $B(k_1)$  of various particle distributions (see the caption of figure 2.7), with reference to a full  $N$ -body simulation,  $B_{\text{Nbody}}(k_1)$ . The computation is done on a 8 Mpc/h mesh ( $128^3$ -voxel grid) and results are shown at redshift  $z = 0$ . The dependence on the angle of the triangle  $\theta_{12} = (\mathbf{k}_1, \mathbf{k}_2)$  is shown for different scales:  $k_1 = k_2 = 0.05 (\text{Mpc}/h)^{-1}$  (corresponding to 125 Mpc/h),  $k_1 = k_2 = 0.10 (\text{Mpc}/h)^{-1}$  (corresponding to 63 Mpc/h),  $k_1 = k_2 = 0.15 (\text{Mpc}/h)^{-1}$  (corresponding to 42 Mpc/h).

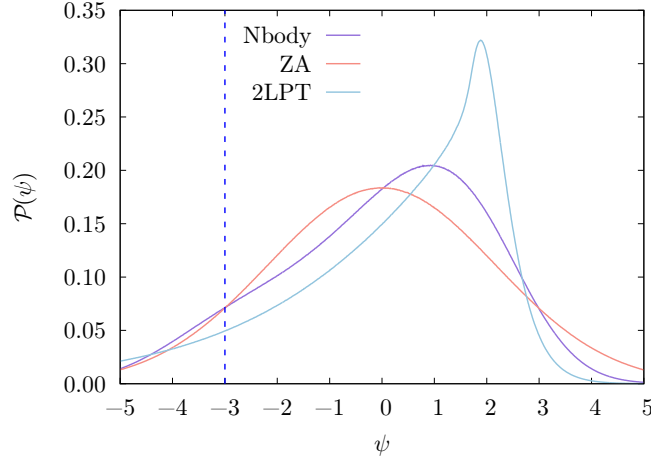


Figure 2.11: Redshift-zero probability distribution function for the divergence of the displacement field  $\psi$ , computed from eight 1024 Mpc/h-box simulations of  $512^3$  particles. A quantitative analysis of the deviation from Gaussianity of these pdfs is given in table 2.1. The particle distribution is determined using: a full  $N$ -body simulation (purple curve), the Zel’dovich approximation (ZA, light red curve) and second-order Lagrangian perturbation theory (2LPT, light blue curve). The vertical line at  $\psi = -3$  represents the collapse barrier about which  $\psi$  values bob around after gravitational collapse. A bump at this value is visible with full gravity, but LPT is unable to reproduce this feature. This regime corresponds to virialized, overdense clusters.

of them with the same cosmological parameters. It has been tested (Gil-Marín *et al.*, 2012), that this estimator for the error is in good agreement with theoretical predictions based on the Gaussianity of initial conditions (Scoccimarro, 1998).

The subtracted shot noise is always assumed to be Poissonian:

$$B_{\text{SN}}(\mathbf{k}_1, \mathbf{k}_2, \mathbf{k}_3) = \frac{1}{\bar{n}} [P(k_1) + P(k_2) + P(k_3)] + \frac{1}{\bar{n}^2}, \quad (2.3)$$

(see e.g. Peebles, 1980, and references therein), where  $\bar{n}$  is the number density of particles in the box.

A triangle shape is defined by the relative length of vectors  $\mathbf{k}_1$  and  $\mathbf{k}_2$  and the inner angle  $\theta_{12}$ , in such a way that  $\mathbf{k}_1 + \mathbf{k}_2 + \mathbf{k}_3 = 0$  and  $\mathbf{k}_1 \cdot \mathbf{k}_2 = k_1 k_2 \cos(\pi - \theta_{12})$ . In figure 2.6, we plot the redshift-zero bispectrum, computed on a 8 Mpc/h mesh, of the different density fields for equilateral triangles ( $\theta_{12} = \pi/3$  and  $k_2/k_1 = 1$ ). There, the dashed line corresponds to theoretical predictions for the non-linear bispectrum, found using the fitting formula of Gil-Marín *et al.* (2012). The relative deviations of various bispectra with reference to full  $N$ -body simulations are shown in figures 2.7, 2.8, 2.9 and 2.10.

The main result is that LPT predicts less three-point correlation than full gravity. This is true even at large scales for the ZA: as it is local, it generally fails to predict the shape of structures. 2LPT agrees with  $N$ -body simulations at large scales, with differences starting to appear only in the mildly non-linear regime,  $k \gtrsim 0.1$  (Mpc/h) $^{-1}$  at  $z = 0$ .

## 2.2 Statistics of the Lagrangian displacement field

### 2.2.1 Lagrangian $\psi$ versus Eulerian $\delta$ : one-point statistics

This section draws from Leclercq, Jasche & Wandelt (2015b), addendum to Leclercq *et al.* (2013).

As noted by previous authors (see in particular Neyrinck, 2013), in the Lagrangian representation of the LSS, it is natural to use the divergence of the displacement field  $\psi$  instead of the Eulerian density contrast  $\delta$ . This section comments the one-point statistics of  $\psi$  in LPT and full gravity and comparatively analyzes key features of  $\psi$  and  $\delta$ .

As seen in section 1.5, in the Lagrangian frame, the quantity of interest is not the position, but the displacement field  $\Psi(\mathbf{q})$  which maps the initial comoving particle position  $\mathbf{q}$  to its final comoving Eulerian position  $\mathbf{x}$



Model	$\mathcal{P}_\delta$	$\mathcal{P}_\psi$
Skewness $\gamma_1$		
ZA	$2.36 \pm 0.01$	$-0.0067 \pm 0.0001$
2LPT	$2.83 \pm 0.01$	$-1.5750 \pm 0.0002$
<i>N</i> -body	$5.14 \pm 0.05$	$-0.4274 \pm 0.0001$
Excess kurtosis $\gamma_2$		
ZA	$9.95 \pm 0.09$	$-2.2154 \times 10^{-6} \pm 0.0003$
2LPT	$13.91 \pm 0.15$	$3.544 \pm 0.0011$
<i>N</i> -body	$62.60 \pm 2.75$	$-0.2778 \pm 0.0004$

Table 2.1: Non-Gaussianity parameters (the skewness  $\gamma_1$  and the excess kurtosis  $\gamma_2$ ) of the redshift-zero probability distribution functions  $\mathcal{P}_\delta$  and  $\mathcal{P}_\psi$  of the density contrast  $\delta$  and the divergence of the displacement field  $\psi$ , respectively. The confidence intervals given correspond to the 1- $\sigma$  standard deviations among eight realizations. In all cases,  $\gamma_1$  and  $\gamma_2$  are reduced when measured from  $\psi$  instead of  $\delta$ .

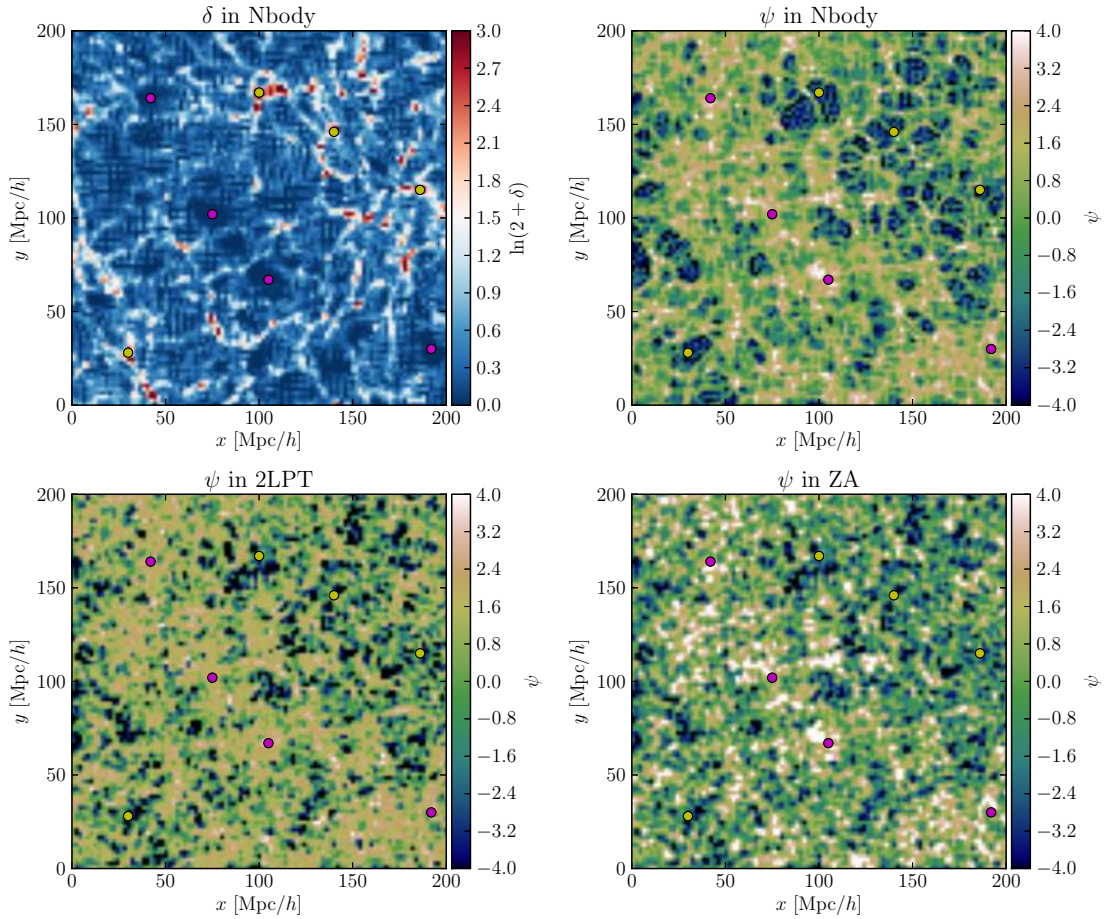


Figure 2.12: Slices of the divergence of the displacement field,  $\psi$ , on a Lagrangian sheet of  $512^2$  particles from a  $512^3$ -particle simulation of box size  $1024 \text{ Mpc}/h$ , run to redshift zero. For clarity we show only a  $200 \text{ Mpc}/h$  region. Each pixel corresponds to a particle. The particle distribution is determined using respectively a full *N*-body simulation, the Zel’dovich approximation (ZA) and second-order Lagrangian perturbation theory (2LPT). In the upper left panel, the density contrast  $\delta$  in the *N*-body simulation is shown, after binning on a  $512^3$ -voxel grid. To guide the eye, some clusters and voids are identified by yellow and purple dots, respectively. The “lakes”, Lagrangian regions that have collapsed to form halos, are only visible in the *N*-body simulation, while the “mountains”, Lagrangian regions corresponding to cosmic voids, are well reproduced by LPT.



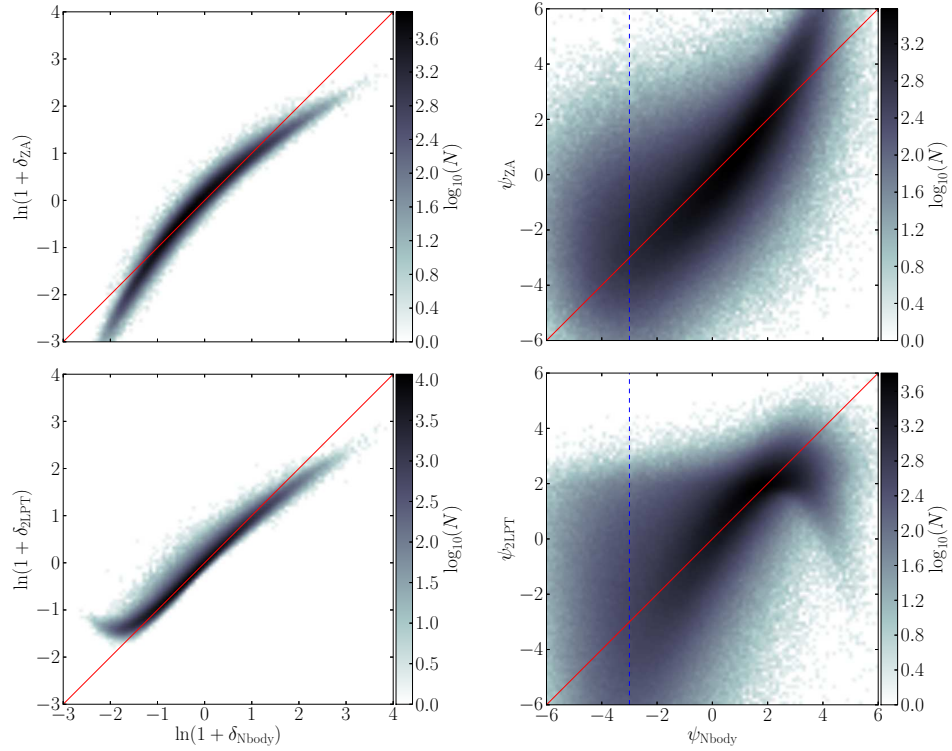


Figure 2.13: *Left panel.* Two-dimensional histograms comparing particle densities evolved with full  $N$ -body dynamics (the  $x$ -axis) to densities in the LPT-evolved particle distributions (the  $y$ -axis). The red lines show the ideal  $y = x$  locus. A turn-up at low densities is visible with 2LPT, meaning that some overdense regions are predicted where there should be deep voids. *Right panel.* Same plot for the divergence of the displacement field  $\psi$ . Negative  $\psi$  corresponds to overdensities and positive  $\psi$  correspond to underdensities. The dotted blue line shows the collapse barrier at  $\psi = -3$  where particle get clustered in full gravity. The scatter is bigger with  $\psi$  than with  $\delta$ , in particular in overdensities, since with LPT, particles do not cluster. The turn-up at low densities with 2LPT, observed with the density contrast, is also visible with the divergence of the displacement field.

(see e.g. [Bouchet et al., 1995](#) or [Bernardeau et al., 2002](#) for overviews),

$$\mathbf{x} \equiv \mathbf{q} + \Psi(\mathbf{q}). \quad (2.4)$$

It is important to note that, though  $\Psi(\mathbf{q})$  is *a priori* a full three-dimensional vector field, it is curl-free up to second order in LPT (appendix D in [Bernardeau, 1994](#) or [Bernardeau et al., 2002](#) for a review). In this thesis, we do not consider perturbative contributions beyond 2LPT.

Let  $\psi(\mathbf{q}) \equiv \nabla_{\mathbf{q}} \cdot \Psi(\mathbf{q})$  denote the divergence of the displacement field, where  $\nabla_{\mathbf{q}}$  is the divergence operator in Lagrangian coordinates.  $\psi$  quantifies the angle-averaged spatial-stretching of the Lagrangian dark matter “sheet” in comoving coordinates ([Neyrinck, 2013](#)). Let  $\mathcal{P}_{\psi, \text{LPT}}$  and  $\mathcal{P}_{\psi, \text{Nbody}}$  be the one-point probability distribution functions for the divergence of the displacement field in LPT and in full  $N$ -body fields, respectively. We denote by  $\mathcal{P}_{\delta}$  the corresponding pdfs for the Eulerian density contrast.

In figure 2.11, we show the pdfs of  $\psi$  for the ZA, 2LPT and full  $N$ -body gravity. The most important feature of  $\psi$  is that, whatever the model for structure formation, the pdf exhibits reduced non-Gaussianity compared to the pdf for the density contrast  $\delta$  (see the upper panel of figure 2.1 for comparison). The main reason is that  $\mathcal{P}_{\delta}$ , unlike  $\mathcal{P}_{\psi}$ , is tied down to zero at  $\delta = -1$ . It is highly non-Gaussian in the final conditions, both in  $N$ -body simulations and in approximations to the true dynamics. For a quantitative analysis, we looked at the first and second-order non-Gaussianity statistics: the skewness  $\gamma_1$  and the excess kurtosis  $\gamma_2$ ,

$$\gamma_1 \equiv \frac{\mu_3}{\sigma^3} \quad \text{and} \quad \gamma_2 \equiv \frac{\mu_4}{\sigma^4} - 3, \quad (2.5)$$

where  $\mu_n$  is the  $n$ -th moment about the mean and  $\sigma$  is the standard deviation. We estimated  $\gamma_1$  and  $\gamma_2$  at redshift zero in our simulations, in the one-point statistics of the density contrast  $\delta$  and of the divergence of the displacement field  $\psi$ . The results are shown in table 2.1. In all cases, we found that both  $\gamma_1$  and  $\gamma_2$  are much smaller when measured from  $\mathcal{P}_{\psi}$  instead of  $\mathcal{P}_{\delta}$ .

At linear order in Lagrangian perturbation theory (the Zel’dovich approximation), the divergence of the displacement field is proportional to the density contrast in the initial conditions,  $\delta(\mathbf{q})$ , scaling with the negative growth factor,  $-D_1(\tau)$ :

$$\psi^{(1)}(\mathbf{q}, \tau) = \nabla_{\mathbf{q}} \cdot \Psi^{(1)}(\mathbf{q}, \tau) = -D_1(\tau) \delta(\mathbf{q}). \quad (2.6)$$

Since we take Gaussian initial conditions, the pdf for  $\psi$  is Gaussian at any time with the ZA. In full gravity, non-linear evolution slightly breaks Gaussianity.  $\mathcal{P}_{\psi, \text{Nbody}}$  is slightly skewed towards negative values while its mode gets shifted around  $\psi \approx 1$ . Taking into account non-local effects, 2LPT tries to get closer to the shape observed in  $N$ -body simulations, but the correct skewness is overshoot and the pdf is exceedingly peaked.

Figure 2.12 shows a slice of the divergence of the displacement field, measured at redshift zero for particles occupying a flat 512<sup>2</sup>-pixel Lagrangian sheet from one of our simulations. For comparison, see also the figures in [Mohayaee et al. \(2006\)](#); [Pueblas & Scoccimarro \(2009\)](#) and [Neyrinck \(2013\)](#). We used the color scheme of the latter paper, suggesting a topographical analogy when working in Lagrangian coordinates. As structures take shape,  $\psi$  departs from its initial value; it takes positive values in underdensities and negative values in overdensities. The shape of voids (the “mountains”) is found to be reasonably similar in LPT and in the  $N$ -body simulation. For this reason, the influence of late-time non-linear effects in voids is milder as compared to overdense structures, which makes them easier to relate to the initial conditions. However, in overdense regions where  $\psi$  decreases, it is not allowed to take arbitrary values: where gravitational collapse occurs, “lakes” form and  $\psi$  gets stuck around a collapse barrier,  $\psi \approx -3$ . As expected, these “lakes”, corresponding to virialized clusters, can only be found in  $N$ -body simulations, since LPT fails to accurately describe the highly non-linear physics involved. A small bump at  $\psi = -3$  is visible in  $\mathcal{P}_{\psi, \text{Nbody}}$  (see figure 2.11). We checked that this bump gets more visible in higher mass-resolution simulations (200 Mpc/ $h$  box for 256<sup>3</sup> particles), where matter is more clustered. This means that part of the information about gravitational clustering can be found in the one-point statistics of  $\psi$ . Of course, the complete description of halos requires to precisely account for the shape of the “lakes”, which can only be done via higher-order correlation functions. More generally, it is possible to use Lagrangian information in order to classify structures of the cosmic web. In particular, DIVA ([Lavaux & Wandelt, 2010](#)) uses the shear of the displacement field and ORIGAMI ([Falck, Neyrinck & Szalay, 2012](#)) the number of phase-space folds. While these techniques cannot be straightforwardly used for the analysis of galaxy surveys, where we lack Lagrangian information, recently proposed techniques for physical inference of the initial conditions (chapters 4 and 5 [Jasche & Wandelt, 2013a](#); [Jasche, Leclercq & Wandelt, 2015](#)) should allow their use with observational data.

Figure 2.13 shows two-dimensional histograms comparing  $N$ -body simulations to the LPT realizations for the density contrast  $\delta$  and the divergence of the displacement field  $\psi$ . At this point, it is useful to note that a good mapping exists in the case where the relation shown is monotonic and the scatter is narrow. As pointed out by Sahni & Shandarin (1996) and Neyrinck (2013), matter in the substructure of 2LPT-voids has incorrect statistical properties: there are overdense particles in the low density region of the 2LPT  $\delta$ -scatter plot. This degeneracy is also visible in the  $\psi > 0$  region of the 2LPT  $\psi$ -scatter plot. On average, the scatter is bigger with  $\psi$  than with  $\delta$ , in particular in overdensities ( $\psi < 0$ ), since with LPT, particles do not cluster:  $\psi$  takes any value between 2 and  $-3$  where it should remain around  $-3$ .

Summing up our discussions in this paragraph, we analyzed the relative merits of the Lagrangian divergence of the displacement field  $\psi$ , and the Eulerian density contrast  $\delta$  at the level of one-point statistics. The important differences are the following:

1.  $\Psi$  being irrotational up to order two, its divergence  $\psi$  contains nearly all information on the displacement field in one dimension, instead of three. The collapse barrier at  $\psi = -3$  is visible in  $\mathcal{P}_\psi$  for  $N$ -body simulations but not for LPT. A part of the information about non-linear gravitational clustering is therefore encoded in the one-point statistics of  $\psi$ .
2.  $\psi$  exhibits much fewer gravitationally-induced non-Gaussian features than  $\delta$  in the final conditions (figure 2.11 and table 2.1).
3. However, the values of  $\psi$  are more scattered than the values of  $\delta$  with respect to the true dynamics (figure 2.13), meaning that an unambiguous mapping is more difficult.

### 2.2.2 Perturbative and non-perturbative prescriptions for $\psi$

Even if  $\psi$  does not contain all the information about the vector displacement field  $\Psi$ , knowledge of its evolution allows for methods to produce approximate particle realizations at the desired redshift, for the variety of cosmological applications described in the introduction of this thesis. These methods include, but are not limited to, the ZA and 2LPT. On the contrary, 3LPT involves a non-zero rotational component and comes at the expense of significantly greater complexity, for an agreement with full gravity that does not improve substantially (Buchert, Melott & Weiß, 1994; Bouchet *et al.*, 1995; Sahni & Shandarin, 1996). Since we have adopted the approximation that the displacement field is potential, we stop our analysis of LPT at second order. However, we will describe various non-perturbative schemes.

Importantly,  $\psi$ -based methods are essentially as fast as producing initial conditions for  $N$ -body simulations. Their implementation can be decomposed in several steps:

1. Generation of a voxel-wise initial-density field  $\delta$ . It is typically a grf, given a prescription for the linear power spectrum (see section B.6), but it can also include primordial non-Gaussianities.
2. Estimation of  $\psi$  from  $\delta$  at the desired redshift.
3. Generation of the final vector displacement field  $\Psi$  from  $\psi$  with an inverse-divergence operator.
4. Application of  $\Psi$  to the particles of a regular Lagrangian lattice to get their final positions.

In practice, steps 1 and 3 are performed in Fourier space, using fast Fourier transforms to translate between configuration space and Fourier space when necessary. In the remainder of this paragraph, we review various prescriptions that have been proposed in the literature to estimate  $\psi(\mathbf{q}, \tau)$  from  $\delta(\mathbf{q})$  (step 2).

**The Zel'dovich approximation.** The first scheme, already studied in section 1.5.2, is the ZA (equation (1.128)),

$$\psi_{\text{ZA}}(\mathbf{q}, \tau) = -D_1(\tau) \delta(\mathbf{q}) \equiv -\delta_{\text{L}}(\mathbf{q}, \tau). \quad (2.7)$$

The ZA allows to separate prescriptions for  $\psi$  into two classes: *local* Lagrangian approximations, where  $\psi$  depends only on its linear value,  $\psi_{\text{L}}(\mathbf{q}, \tau) \equiv -\delta_{\text{L}}(\mathbf{q}, \tau)$  and *non-local* ones (e.g. higher-order LPT) where  $\psi$  depends on derivatives of  $\psi_{\text{L}}$  as well (which means that the behavior of a Lagrangian particle depends on its neighbours).

**Second-order Lagrangian perturbation theory.** In 2LPT, the non-local prescription for  $\psi$  is (see equation (1.133))

$$\psi_{2\text{LPT}}(\mathbf{q}, \tau) = -D_1(\tau)\Delta_{\mathbf{q}}\phi^{(1)}(\mathbf{q}) + D_2(\tau)\Delta_{\mathbf{q}}\phi^{(2)}(\mathbf{q}), \quad (2.8)$$

where the Lagrangian potentials follow the Poisson-like equations (1.134) and (1.135). As pointed out by Neyrinck (2013), since 2LPT is a second-order scheme,  $\psi_{2\text{LPT}}$  is roughly parabolic in the local  $\delta_L$ , which yields, using  $D_2(\tau) \approx -\frac{3}{7}D_1^2(\tau)$  (Bouchet *et al.*, 1995),

$$\psi_{2\text{LPT}}(\mathbf{q}, \tau) \approx \psi_{2\text{LPT,parab}}(\mathbf{q}, \tau) \equiv -\delta_L(\mathbf{q}, \tau) + \frac{1}{7}(\delta_L(\mathbf{q}, \tau))^2. \quad (2.9)$$

**The spherical collapse approximation.** Bernardeau (1994) provides a simple formula for the time-evolution (collapse or expansion) of a spherical Lagrangian volume element, independent of cosmological parameters:

$$V(\mathbf{q}, \tau) = V(\mathbf{q}) \left(1 - \frac{2}{3}\delta_L(\mathbf{q}, \tau)\right)^{3/2}. \quad (2.10)$$

Building upon this result, Mohayaee *et al.* (2006); Lavaux (2008) and Neyrinck (2013) derived a prescription for the divergence of the displacement field. Considering the isotropic stretch of a Lagrangian mass element that occupies a cube of side length  $1 + \psi/3$  (giving  $\nabla_{\mathbf{q}} \cdot \mathbf{\Psi} = \psi$ ), mass conservation imposes

$$\frac{V(\mathbf{q}, \tau)}{V(\mathbf{q})} = \frac{1}{1 + \delta} = \left(1 + \frac{\psi}{3}\right)^3. \quad (2.11)$$

Equations (2.10) and (2.11) yield

$$\psi = 3 \left( \sqrt{1 - \frac{2}{3}\delta_L} - 1 \right). \quad (2.12)$$

However, there exists no solution for  $\delta_L > 3/2$ . Neyrinck (2013) proposes to fix  $\psi = -3$  in such volume elements. This corresponds to the ideal case of a Lagrangian patch contracting to a single point ( $\nabla_{\mathbf{q}} \cdot \mathbf{x} = 0$ ). The final prescription for the spherical collapse (SC) approximation is then

$$\psi_{\text{SC}}(\mathbf{q}, \tau) = \begin{cases} 3 \left( \sqrt{1 - \frac{2}{3}\delta_L(\mathbf{q}, \tau)} - 1 \right) & \text{if } \delta_L < 3/2, \\ -3 & \text{if } \delta_L \geq 3/2. \end{cases} \quad (2.13)$$

One possible concern with this formula is that, in full gravity, there are roughly as many particles with  $\psi > -3$  as with  $\psi < -3$  (see e.g. trajectories in  $\psi$  as a function of the scale factor  $a$ , figure 7 in Neyrinck, 2013). Yet, this remains more correct than what happens with LPT, where  $\psi$  can take any negative value, indicating severe unphysical over-crossing of particles in collapsed structures.

Compared to LPT, the SC approximation gives reduced stream-crossing, better small-scale flows and one-point pdf correspondence to the results of full gravity. However, a significant drawback is its incorrect treatment of large-scale flows, leading to a negative offset in the large-scale power spectrum (figure 14 in Neyrinck, 2013).<sup>2</sup> LPT realizations, on the other hand, give more accurate large-scale power spectra, as well as improved cross-correlation to the density field evolved with full gravity.

**Local Lagrangian approximations.** The SC approximation belongs to a more general family of “local Lagrangian” approximations investigated by Protogeros & Scherrer (1997), parameterized by  $1 \leq \alpha \leq 3$ , the effective number of axes along which the considered volume element undergoes gravitational collapse. The corresponding density is given by

$$\delta_{\alpha}(\psi) = \left(1 + \frac{\psi}{\alpha}\right)^{-\alpha} - 1. \quad (2.14)$$

<sup>2</sup> An empirical correction may be added to the SC formula to fix this issue: multiplying  $\delta_L$  in equation (2.13) by a factor such that the large-scale power spectrum of SC realizations agrees with that of LPT realizations (Neyrinck, 2013). See also the paragraph on MUSCLE.

Here,  $\psi$  is the actual non-linear displacement-divergence of a volume element, not necessarily related to the linearly evolved  $\psi_L$ . From equations (2.10) and (2.11), we get

$$\delta = \left(1 - \frac{2}{3}\delta_L\right)^{-3/2} - 1 = \left(1 + \frac{2}{3}\psi_L\right)^{-3/2} - 1, \quad (2.15)$$

therefore the spherical collapse approximation corresponds to the case  $\alpha = 3/2$  for  $\psi = \psi_L$ . The cubic mass-element approximation that would follow directly from using equation (2.11) without equation (2.10) corresponds to the case  $\alpha = 3$  for the full  $\psi$ . Neyrinck (2013) shows that the  $\delta$ - $\psi$  relation closely follows  $\delta_3(\psi)$  for  $\psi < 0$ , whereas for  $\psi > 0$  the result is between  $\delta_3(\psi)$  and  $\delta_{3/2}(\psi)$ , when accounting for the anisotropy of gravitational expansion.

**Augmented Lagrangian Perturbation Theory.** As discussed before, LPT correctly describes large scales and SC more accurately captures small, collapsed structures. Kitaura & Heß (2013) proposed a recipe to interpolate between the LPT displacement on large scales and the SC displacement on small scales, calling it Augmented Lagrangian Perturbation Theory (ALPT). It reads

$$\psi_{\text{ALPT}}(\mathbf{q}, \tau) = (K_{R_s} * \psi_{2\text{LPT}})(\mathbf{q}, \tau) + [(1 - K_{R_s}) * \psi_{\text{SC}}](\mathbf{q}, \tau), \quad (2.16)$$

or, in Lagrangian Fourier space,<sup>3</sup>

$$\psi_{\text{ALPT}}(\mathbf{\kappa}, \tau) = K_{R_s}(\kappa) \psi_{2\text{LPT}}(\mathbf{\kappa}, \tau) + [1 - K_{R_s}(\kappa)] \psi_{\text{SC}}(\mathbf{\kappa}, \tau). \quad (2.17)$$

This method introduces a free parameter,  $R_s$ , the width of the Gaussian kernel used in the above equations to filter between large and small displacements,  $K_{R_s}(k) \propto \exp(-k^2/2 \times (R_s/2\pi)^2)$ . In numerical experiments, Kitaura & Heß (2013) empirically found that the range  $R_s = 4-5$  Mpc/ $h$  yields the best density cross-correlation to full gravity.

**Multi-scale spherical collapse evolution.** Neyrinck (2015a) argued that the major deficiency in the SC approximation is its treatment of the void-in-cloud process (in the terminology originally introduced by Sheth & van de Weygaert, 2004), i.e. of small underdensities in larger-scale overdensities. Such regions should eventually collapse, which is not accounted for in SC. To overcome this problem, he proposes to use the SC prescription as a function of the initial density contrast on multiple Gaussian-smoothed scales, thus including the void-in-cloud process. The resulting parameter-free scheme, MUSCLE (MULTIscale Spherical-CoLLapse Evolution), mathematically reads

$$\psi_{\text{MUSCLE}}(\mathbf{q}, \tau) = \begin{cases} 3 \left( \sqrt{1 - \frac{2}{3}\delta_L(\mathbf{q}, \tau)} - 1 \right) & \text{if } \delta_L < 3/2 \text{ and } \forall R_s \geq R_i, K_{R_s} * \delta_L < 3/2, \\ -3 & \text{otherwise,} \end{cases} \quad (2.18)$$

where  $R_i$  is the resolution of the initial density field  $\delta(\mathbf{q})$ , and  $K_{R_s} * \delta_L$  is the linearly extrapolated initial density field, smoothed using a Gaussian kernel of width  $R_s$ . In practice, a finite number of scales  $r > R_i$  have to be tried (for example  $r = 2^n R_i$  for integers  $0 \leq n \leq n_{\text{max}}$  such that  $2^{n_{\text{max}}} R_i \leq L$  and  $2^{n_{\text{max}}+1} R_i > L$ ).

Neyrinck (2015a) checked that MUSCLE corrects the problems of SC at large scales and outperforms the ZA and 2LPT in terms of the density cross-correlation to full gravity.

### 2.2.3 Non-linear evolution of $\psi$ and generation of a vector part

Beyond the approximations presented in the previous section, Chan (2014) analyzed the non-linear evolution of  $\Psi$  in full gravity, splitting it into its scalar and vector parts (the so-called ‘‘Helmholtz decomposition’’):

$$\Psi(\mathbf{q}) = \nabla_{\mathbf{q}} \phi(\mathbf{q}) + \nabla_{\mathbf{q}} \times \mathbf{A}(\mathbf{q}), \quad (2.19)$$

with

$$\Delta_{\mathbf{q}} \phi = \nabla_{\mathbf{q}} \cdot \Psi(\mathbf{q}), \quad (2.20)$$

$$\Delta_{\mathbf{q}} \mathbf{A}(\mathbf{q}) = -\nabla_{\mathbf{q}} \times \Psi(\mathbf{q}). \quad (2.21)$$

<sup>3</sup> We denote by  $\mathbf{\kappa}$  a Fourier mode on the Lagrangian grid,  $\kappa$  its norm.

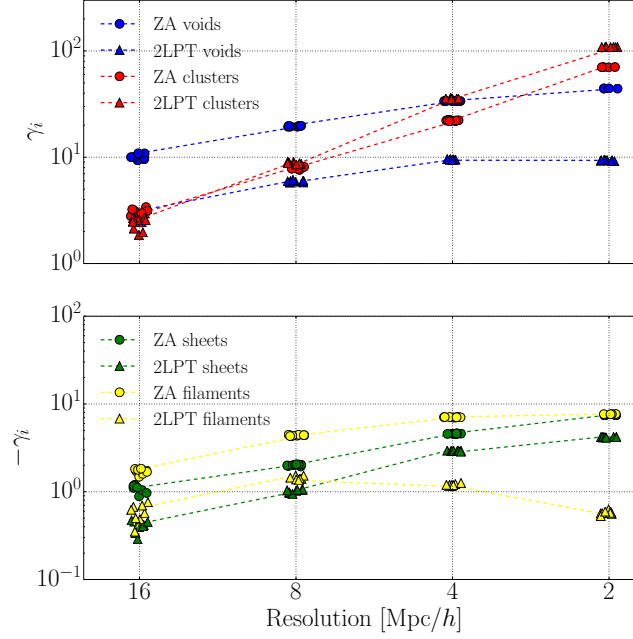


Figure 2.14: Relative volume fraction of voids, sheets, filaments and clusters predicted by LPT, compared to  $N$ -body simulations, as a function of the resolution used for the definition of the density fields. The points are slightly randomized on the  $x$ -axis for clarity. The estimators  $\gamma_i$  are defined by eq (2.22). Eight realizations of the ZA (circles) and 2LPT (triangles) are compared to the corresponding  $N$ -body realization, for various resolutions. The volume fraction of incorrectly predicted structures in LPT generally increases with increasing resolution.

Looking at two-point statistics of  $\Psi$ , he found that shell-crossing leads to a suppression of small-scale power in the scalar part, and, subdominantly, to the generation of a vector contribution. Even at late-time and non-linear scales, the scalar part of the displacement field remains the dominant contribution. The rotational component is much smaller and does not have a coherent large-scale component. Therefore, the potential approximation is still good even when shell-crossing is non-negligible.

However, as pointed out by Neyrinck (2015a), even if we neglect the rotational component, there is still a long way to go before we can perfectly predict  $\psi$ . Variants of LPT, such as ALPT (primarily motivated by the agreement in the scatter plot of final versus initial  $\psi$  – see figure 6 in Neyrinck, 2013 and figure 10 in Chan, 2014) or the inclusion of a suppression factor in the LPT displacement potential (Chan, 2014 – designed for fitting the non-linear power spectrum of  $\Psi$ ) extract information from simulations by taking the average of some statistics. Since shell-crossing is a highly non-linear process, it may not be surprising that such approaches yield limited success compared to standard LPT for some other statistics (such as the density power spectrum or phase accuracy). This suggests that a more detailed understanding and modeling of the small-scale physics beyond the simple phenomenological approach is required for improvement in  $\psi$ -based schemes, which would substantially increase the accuracy of particle realizations.

## 2.3 Comparison of structure types in LPT and $N$ -body dynamics

This section draws from section II.B. in Leclercq *et al.* (2013).

In this section, we perform a study of differences in structure types in density fields predicted by LPT and  $N$ -body simulations. We employ the web-type classification algorithm proposed by Hahn *et al.* (2007a), which relies on estimating the eigenvalues of the Hessian of the gravitational potential (see section C.2). This algorithm dissects the voxels into four different web types (voids, sheets, filaments and clusters). Due to the different representations of the non-linear regime of structure formation, we expect differences in structure types in LPT and  $N$ -body simulations. In particular, overdense clusters are objects in the strongly non-linear regime, far beyond shell-crossing, where predictions of LPT fail, while underdense voids are believed to be better apprehended (e.g. Bernardeau *et al.*, 2002).

As an indicator of the mismatch between the volume occupied by different structure types in LPT and  $N$ -body dynamics, we use the quantities  $\gamma_i$  defined by

$$\gamma_i \equiv \frac{N_i^{\text{LPT}} - N_i^{\text{Nbody}}}{N_i^{\text{Nbody}}}, \quad (2.22)$$

where  $i$  indexes one of the four structure types ( $T_0$  = void,  $T_1$  = sheet,  $T_2$  = filament,  $T_3$  = cluster), and  $N_i^{\text{LPT}}$  and  $N_i^{\text{Nbody}}$  are the numbers of voxels flagged as belonging to a structure of type  $T_i$ , in corresponding LPT and in  $N$ -body realizations, respectively. At fixed resolution, corresponding realizations have the same total number of voxels  $N_{\text{tot}}$ , so we also have

$$\gamma_i = \frac{\text{VFF}_i^{\text{LPT}}}{\text{VFF}_i^{\text{Nbody}}} - 1, \quad (2.23)$$

where the volume filling fraction of structure type  $T_i$  is defined by  $\text{VFF}_i \equiv N_i/N_{\text{tot}}$ .

In figure 2.14, we plot  $\gamma_i$  as a function of the voxel size used to define the density fields.  $\gamma_i$  is positive for clusters and voids, and negative for sheets and filaments, meaning that too large cluster and void regions are predicted in LPT, at the detriment of sheets and filaments. More specifically, LPT predicts fuzzier halos than  $N$ -body dynamics, and incorrectly predicts the surroundings of voids as part of them. This result indicates that even though LPT and  $N$ -body fields look visually similar, there are crucial differences in the representation of structure types. As demonstrated by figure 2.14, this mismatch increases with increasing resolution. This effect is of general interest when employing LPT in LSS data analysis.





## **Part II**

# **Bayesian large-scale structure inference**



# Bayesian cosmostatistics

## Contents

<b>3.1 Introduction: plausible reasoning</b>	<b>49</b>
3.1.1 On the definition of probability	50
3.1.2 On parameter determination	50
3.1.3 Probability theory as extended logic	50
<b>3.2 Inverse problems and the mechanism of experimental learning</b>	<b>51</b>
3.2.1 What is Bayesian analysis?	52
3.2.2 Prior choice	52
<b>3.3 Bayesian data analysis problems</b>	<b>54</b>
3.3.1 First level analysis: Bayesian parameter inference	54
3.3.2 Exploration of the posterior	54
3.3.3 Second level analysis: Bayesian model comparison	56
<b>3.4 Markov Chain Monte Carlo techniques for parameter inference</b>	<b>58</b>
3.4.1 Markov Chains	58
3.4.2 The Metropolis-Hastings algorithm	59
3.4.3 Hamiltonian Monte Carlo	60

---

“A previous acquaintance with probability and statistics is not necessary; indeed, a certain amount of innocence in this area may be desirable, because there will be less to unlearn.”

— [Edwin Thompson Jaynes \(2003\)](#), *Probability Theory: The Logic of Science*

---

## Abstract

In this chapter, essential concepts of Bayesian statistics in the context of cosmological data analysis are presented. We discuss motivations for seeing probabilistic calculations as an extension of ordinary logic and justify the use of a prior in an experimental learning process by referring to the “no-free lunch theorem”. This chapter also reviews parameter inference, model comparison, and contains a brief introduction to the subject of Markov Chain Monte Carlo methods.

This chapter aims at introducing the necessary background in Bayesian probability theory for presenting the BORG algorithm in chapter 4 and applications in the following chapters. A much more complete picture can be found in the reference book of [Gelman \*et al.\* \(2013\)](#). For introductions to Bayesian statistics in a cosmological context, see [Hobson \(2010\)](#) and the reviews or lecture notes by [Trotta \(2008\)](#); [Heavens \(2009\)](#); [Verde \(2010\)](#); [Leclercq, Pisani & Wandelt \(2014\)](#).

This chapter is organized as follows. Section 3.1 is a general introduction on plausible reasoning. Basic concepts and definitions used in Bayesian statistics are presented in section 3.2. In section 3.3, we discuss standard statistical inference problems. Finally, section 3.4 summarizes the basics of Markov Chain Monte Carlo methods.

## 3.1 Introduction: plausible reasoning

When discussing statistical data analysis, two different points of view are traditionally reviewed and opposed: the frequentist (see e.g. [Kendall & Stuart, 1968](#)) and the Bayesian approaches. In this author’s experience,

arguments for or against each of them are generally on the level of a philosophical or ideological position, at least among cosmologists in 2015. Before criticizing this controversy, somewhat dated to the 20th century, and stating that more recent scientific work suppresses the need to appeal to such arguments, we report the most common statements encountered.

### 3.1.1 On the definition of probability

Frequentist and Bayesian statistics differ in the epistemological interpretation of probability and their consequences for testing hypotheses and comparing models. First and foremost, the methods differ on the understanding of the concept of the probability  $\mathcal{P}(A)$  of an event  $A$ . In frequentist statistics, one defines the probability  $\mathcal{P}(A)$  as the relative frequency with which the event  $A$  occurs in repeated experiments, i.e. the number of times the event occurs over the total number of trials, in the limit of a infinite series of equiprobable repetitions. As forcefully argued for example by Trotta (2008), this probability (definition) has several shortcomings. Besides being useless in real life (as it assumes an infinite repetition of experiments with nominally identical test conditions, requirement that is never met in most practical cases), it cannot handle unrepeatable situations, which have a particular importance in cosmology, as we have exactly one sample of the Universe. More importantly, this definition is surprisingly circular, in the sense that it assumes that repeated trials are equiprobable, whereas it is the very notion of probability that is being defined in the first place.

On the other hand, in Bayesian statistics, the probability  $\mathcal{P}(A)$  represents the degree of belief that any reasonable person (or machine) shall attribute to the occurrence of event  $A$  under consideration of all available information. This definition implies that in Bayesian theory, probabilities are used to quantify uncertainties independently of their origin, and therefore applies to any event. In other words, probabilities represent a state of knowledge in presence of partial information. This is the intuitive concept of probability as introduced by Laplace, Bayes, Bernoulli, Gauß, Metropolis, Jeffreys, etc. (see Jaynes, 2003).

### 3.1.2 On parameter determination

Translated to the measurement of a parameter in an experiment, the definitions of probabilities given in the previous section yield differences in the questions addressed by frequentist and Bayesian statistical analyses.

In the frequentist point of view, statements are of the form: “the measured value  $x$  occurs with probability  $\mathcal{P}(x)$  if the measurand  $X$  has the true value  $\mathcal{X}$ ”. This means that the only questions that can be answered are of the form: “given the true value  $\mathcal{X}$  of the measurand  $X$ , what is the probability distribution of the measured values  $x$ ?”. It also implies that statistical analyses are about building *estimators*,  $\hat{X}$ , of the truth,  $\mathcal{X}$ .

In contrast, Bayesian statistics allows statements of the form: “given the measured value  $x$ , the measurand  $X$  has the true value  $\mathcal{X}$  with probability  $Q$ ”. Therefore, one can also answer the question: “given the observed measured value  $x$ , what is the probability that the true value of  $X$  is  $\mathcal{X}$ ?”, which arguably is the only natural thing to demand from data analysis. For this reason, Bayesian statistics offers a principled approach to the question underlying every measurement problem, of how to *infer* the true value of the measurand given all available information, including observations.

In summary, in the context of parameter determination, the fundamental difference between the two approaches is that frequentist statistics assumes the measurement to be uncertain and the measurand known, while Bayesian statistics assumes the observation to be known and the measurand uncertain. Similar considerations can be formulated regarding the problems of hypothesis testing and model comparison.

### 3.1.3 Probability theory as extended logic

As outlined in the seminal work of Cox (1946), popularized and generalized by Jaynes (in particular in his inspirational posthumous book, Jaynes, 2003),<sup>1</sup> neither the Bayesian nor the frequentist approach is universally applicable. It is possible to adopt a more general viewpoint that can simply be referred to as “probability theory”, which encompasses both approaches. This framework automatically includes all Bayesian and frequentist calculations, but also contains concepts that do not fit into either category (for example, the principle of maximum entropy, which can be applied in the absence of a particular model, when very little is known beyond the raw data).

<sup>1</sup> At this point, the influence of Shannon (1948) and Pólya (1954a,b) should also be emphasized.

In the author's view, this approach is a breakthrough that remains shockingly unknown in astrophysics. As we believe that a conceptual understanding of these concepts are of interest for the purpose of this thesis, we now qualitatively describe the salient features of this way of thinking.

The Cox-Jaynes theorem (1946) states that there is only a single set of rules for doing plausible reasoning which is consistent with a set of axioms that is in qualitative correspondence with common sense. These axioms, or desiderata, are (Jaynes, 2003, section 1.7):

1. *Degrees of plausibility are represented by real numbers.* We denote by  $w(A|B)$  the real number assigned to the plausibility of some proposition  $A$ , given some other proposition  $B$ .
2. *Plausible reasoning qualitatively agrees with human common sense with respect to the “direction” in which reasoning is to go.* Formally, we introduce a continuity assumption:  $w(A)$  changes only infinitesimally if  $A$  changes infinitesimally. In addition, if some old information  $C$  gets updated to  $C'$  in such a way that the plausibility of  $A$  is increased, but the plausibility of  $A$  given  $B$  is unchanged, i.e.  $w(A|C') > w(A|C)$  and  $w(B|AC') = w(B|AC)$ , we demand that the plausibility that  $A$  is false decrease, i.e.  $w(\bar{A}|C') < w(\bar{A}|C)$ , and that the plausibility of  $A$  and  $B$  can only increase, i.e.  $w(AB|C') \geq w(AB|C)$ .
3. *Plausible reasoning is performed consistently.* This is requiring the three common colloquial meanings of the word “consistent”:
  - (a) *If a conclusion can be reached in more than one way, then every possible way must lead to the same result.*
  - (b) *Consistent plausible reasoning always takes into account all of the evidence it has relevant to a question. It does not arbitrarily ignore some of the available information, basing its conclusion on what remains. In other words, it is completely non-ideological.*
  - (c) *Equivalent states of knowledge (up to the labeling of propositions) are represented by equal plausibility assignments.*

The Cox-Jaynes theorem demonstrates that the only consistent system to manipulate numerical “plausibilities” that respect these rules is isomorphic to probability theory,<sup>2</sup> and shows that this system consistently extends the two-valued Boolean algebra  $\{0, 1\}$  to the continuum  $[0, 1]$ . This paradigm therefore introduces a “logical” interpretation of probabilities that can be deduced without any reference to frequencies.

In this perspective, statistical techniques that use Bayes' theorem or the maximum-entropy inference rule are fully as valid as any based on the frequentist interpretation of probability. In fact, they are the *unique* consistent generalization of logical deduction in the presence of uncertainty. As demonstrated by Jaynes, their introduction enables to broaden the scope of probability theory so that it includes various seemingly unrelated fields, such as communication theory of the maximum-entropy interpretation of thermodynamics. They also provides a rational basis to the mechanism of logical induction and therefore to machine learning.

## 3.2 Inverse problems and the mechanism of experimental learning

This section draws from section 3 in Leclercq, Pisani & Wandelt (2014).

The “plausible reasoning” framework described in section 3.1 can be formulated mathematically by introducing the concept of conditional probability  $\mathcal{P}(A|B)$ , which describes the probability that event  $A$  will occur given whatever information  $B$  is given on the right side of the vertical conditioning bar. To conditional probabilities applies the following famous identity, which allows to go from forward modeling to the inverse problem, by noting that if one knows how  $x$  arises from  $y$ , then one can use  $x$  to constrain  $y$ :

$$\mathcal{P}(y|x)\mathcal{P}(x) = \mathcal{P}(x|y)\mathcal{P}(y) = \mathcal{P}(x, y). \quad (3.1)$$

This observation forms the basis of Bayesian statistics.

<sup>2</sup> Formally, the theorem states that there exists an isomorphism  $f$  such that for any two propositions  $A, B$ , we have  $f \circ w(A|B) = \mathcal{P}(A|B)$ .

### 3.2.1 What is Bayesian analysis?

Bayesian analysis is a general method for updating the probability estimate for a theory in light of new data. It is based on Bayes' theorem,

$$\mathcal{P}(\theta|d) = \frac{\mathcal{P}(d|\theta)\mathcal{P}(\theta)}{\mathcal{P}(d)}. \quad (3.2)$$

In the previous formula,  $\theta$  represents the set of model parameters for a particular theory and  $d$  the data (before it is known), written as a vector. Therefore,

- $\mathcal{P}(d|\theta)$  is the probability of the data *before it is known*, given the theory. It is called the *likelihood*;
- $\mathcal{P}(\theta)$  is the probability of the theory in the absence of data. It is called the prior probability distribution function or simply the *prior*;
- $\mathcal{P}(\theta|d)$  is the probability of the theory after the data is known. It is called the posterior probability distribution function or simply the *posterior*;
- $\mathcal{P}(d)$  is the probability of the data *before it is known*, without any assumption about the theory. It is called the *evidence*.

A simple way to summarize Bayesian analysis can be formulated by the following:

*Whatever is uncertain gets a pdf.*

This statement can be a little disturbing at first (e.g. the value of  $\Omega_m$  is a constant of nature, certainly not a random number of an experiment). What it means is that in Bayesian statistics, pdfs are used to quantify uncertainty of all kinds, not just what is usually referred to as “randomness” in the outcome of an experiment. In other words, the pdf for an uncertain parameter can be thought as a “belief distribution function”, quantifying the degree of truth that one attributes to the possible values for some parameter (see the discussion in section 3.1.1). Certainty can be represented by a Dirac distribution, e.g. if the data determine the parameters completely.

The inputs of a Bayesian analysis are of two sorts:

- the *prior*: it includes modeling assumptions, both theoretical and experimental. Specifying a prior is a systematic way of quantifying what one assumes true about a theory before looking at the data.
- the *data*: in cosmology, these can include the temperature in pixels of a CMB map, galaxy redshifts, photometric redshifts pdfs, etc. Details of the survey specifications have also to be accounted for at this point: noise, mask, survey geometry, selection effects, biases, etc.

A key point is that the output of a Bayesian analysis is a pdf, the *posterior density*. Therefore, contrary to frequentist statistics, the output of the analysis is not an estimator for the parameters. The word “estimator” has a precise meaning in frequentist statistics: it is a function of the data which returns a number that is meant to be close to the parameter it is designed to estimate; or the left and right ends of a confidence interval, etc. The outcome of a Bayesian analysis is the posterior pdf, a pdf whose values give a quantitative measure of the relative degree of rational belief in different parameter values given the combination of prior information and the data.

### 3.2.2 Prior choice

The prior choice is a key ingredient of Bayesian statistics. It is sometimes considered problematic, since there is no unique prescription for selecting the prior. Here we argue that prior specification is not a limitation of Bayesian statistics and does not undermine objectivity as sometimes misstated.

The guiding principle is that there can be no inference without assumptions, that there does not exist an “external truth”, but that science is building predictive models in certain axiomatic frameworks. In this regard, stating a prior in Bayesian probability theory becomes a systematic way to quantify one's assumptions and state of knowledge about the problem in question before the data is examined. While it is true that such probability assignment does not describe something that could be measured in a physical experiment, it is completely objective in the sense that it is independent of the “personal feelings” of the user. Anyone who has

the same information, but comes to a different conclusion, is necessarily violating one of Cox’s desiderata (see the discussion in section 3.1.3).

Bayes’ theorem gives an unequivocal procedure to update even different degrees of beliefs. As long as the prior has a support that is non-zero in regions where the likelihood is large (Cromwell’s rule), the repeated application of the theorem will converge to a unique posterior distribution (Bernstein-von Mises theorem). Generally, objectivity is assured in Bayesian statistics by the fact that, if the likelihood is more informative than the prior, the posterior converges to a common function.

Specifying priors exposes assumptions to falsification and scientific criticism. This is a positive feature of Bayesian probability theory, because frequentists also have to make assumptions that may be more difficult to find within the analysis. An important theorem (Wolpert & Macready, 1997) states that there is “no-free lunch” for optimization problems: when searching for the local extremum of a target function (the likelihood in our case) in a finite space, the average performance of algorithms (that do not resample points) across all possible problems is identical. An important implication is that no universally good algorithm exists (Ho & Pepyne, 2002); prior information should always be used to match procedures to problems.

In many situations, domain knowledge is highly relevant and should be included in the analysis. For example, when trying to estimate a mass  $m$  from some data, one should certainly enforce it to be a positive quantity by setting a prior such that  $\mathcal{P}(m) = 0$  for  $m < 0$ . Frequentist techniques based on the likelihood can give estimates and confidence intervals that include negative values. Taken at face value, this result is meaningless, unless special care is taken (e.g. the so-called “constrained likelihood” methods). The use of Bayes’ theorem ensures that meaningless results are excluded from the beginning and that one knows how to place bets on values of the parameter given the actual data set at hand.

As discussed in the introduction, in cosmology, the current state-of-the-art is that previous data (COBE, WMAP, Planck, SDSS etc.) allowed to establish an extremely solid theoretical footing: the so-called  $\Lambda$ CDM model. Even when trying to detect deviations from this model in the most recent data, it is absolutely well-founded to use it as prior knowledge about the physical behaviour of the Universe. Therefore, using less informative priors would be refusing to “climb on the shoulder of giants”.

It can happen that the data are not informative enough to override the prior (e.g. for sparsely sampled data or very high-dimensional parameter space), in which case care must be given in assessing how much of the final (first level, see section 3.3.1) inference depends on the prior choice. A good way to perform such a check is to simulate data using the posterior and see if it agrees with the observed data. This can be thought of as “calculating doubt” (Starkman, Trotta & Vaudrevange, 2008; March *et al.*, 2011) to quantify the degree of belief in a model given observational data in the absence of explicit alternative models. Note that even in the case where the inference strongly depends on prior knowledge, information has been gained on the constraining power (or lack thereof) of the data.

For model selection questions (second level analysis, see section 3.3.3), the impact of the prior choice is much stronger, since it is precisely the available prior volume that matters in determining the penalty that more complex models should incur. Hence, care should be taken in assessing how much the outcome would change for physically reasonable changes in the prior.

There exists a vast literature about quantitative prescriptions for prior choice that we cannot summarize here. An important topic concerns the determination of “ignorance priors” or “Jeffreys’ priors”: a systematic way to quantify a maximum level of uncertainty and to reflect a state of indifference with respect to symmetries of the problem considered. While the ignorance prior is unphysical (nothing is ever completely uncertain) it can be viewed as a convenient approximation to the problem of carefully constructing an accurate representation of weak prior information, which can be very challenging – especially in high dimensional parameter spaces.

For example, it can be shown that, if one is wholly uncertain about the position of the pdf, a “flat prior” should be chosen. In this case, the prior is taken to be constant (within some minimum and maximum value of the parameters so as to be proper, i.e. normalizable to unity). In this fashion, equal probability is assigned to equal states of knowledge. However, note that a flat prior on a parameter  $\theta$  does not necessarily correspond to a flat prior on a non-linear function of that parameter,  $\varphi(\theta)$ . Since  $\mathcal{P}(\varphi) = \mathcal{P}(\theta) \times |d\theta/d\varphi|$ , a non-informative (flat) prior on  $\theta$  can be strongly informative about  $\varphi$ . Analogously, if one is entirely uncertain about the width of the pdf, i.e. about the scale of the inferred quantity  $\theta$ , it can be shown that the appropriate prior is  $\mathcal{P}(\theta) \propto 1/\theta$ , which gives the same probability in logarithmic bins, i.e. the same weight to all orders of magnitude.

### 3.3 Bayesian data analysis problems

This section draws from section 3 in [Leclercq, Pisani & Wandelt \(2014\)](#).

Bayesian data analysis problems can be typically classified as: parameter inference, model comparison, hypothesis testing. For example, cosmological questions of these three types, related to the large-scale structure, would be respectively

- What is the value of  $w$ , the equation of state of dark energy?
- Is structure formation driven by general relativity or by massive gravity?
- Are large-scale structure observations consistent with the hypothesis of a spatially flat universe?

In this section; we describe the methodology for questions of the first two types. Hypothesis testing, i.e. inference within an uncertain model, in the absence of an explicit alternative, can be treated in a similar manner.

#### 3.3.1 First level analysis: Bayesian parameter inference

The general problem of Bayesian parameter inference can be stated as follows. Given a physical model  $\mathcal{M}$ ,<sup>3</sup> a set of hypotheses is specified in the form of a vector of parameters,  $\theta$ . Together with the model, priors for each parameter must be specified:  $\mathcal{P}(\theta|\mathcal{M})$ . The next step is to construct the likelihood function for the measurement, with a probabilistic, generative model of the data:  $\mathcal{P}(d|\theta, \mathcal{M})$ . The likelihood reflects how the data are obtained: for example, a measurement with Gaussian noise will be represented by a normal distribution.

Once the prior is specified and the data is incorporated in the likelihood function, one immediately obtains the posterior distribution for the model parameters, integrating all the information known to date, by using Bayes' theorem (equation (3.2)):

$$\mathcal{P}(\theta|d, \mathcal{M}) \propto \mathcal{P}(d|\theta, \mathcal{M})\mathcal{P}(\theta|\mathcal{M}). \quad (3.3)$$

Note that the normalizing constant  $\mathcal{P}(d|\mathcal{M})$  (the Bayesian evidence) is irrelevant for parameter inference (but fundamental for model comparison, see section 3.3.3).

Usually, the set of parameters  $\theta$  can be divided in some physically interesting quantities  $\varphi$  and a set of nuisance parameters  $\psi$ . The posterior obtained by equation (3.3) is the joint posterior for  $\theta = (\varphi, \psi)$ . The marginal posterior for the parameters of interest is written as (marginalizing over the nuisance parameters)

$$\mathcal{P}(\varphi|d, \mathcal{M}) \propto \int \mathcal{P}(d|\varphi, \psi, \mathcal{M})\mathcal{P}(\varphi, \psi|\mathcal{M}) d\psi. \quad (3.4)$$

This pdf is the final inference on  $\varphi$  from the joint posterior. The following step, to apprehend and exploit this information, is to explore the posterior. It is the subject of the next section.

#### 3.3.2 Exploration of the posterior

The result of parameter inference is contained in the posterior pdf, which is the actual output of the statistical analysis. Since this pdf cannot always be easily represented, convenient communication of the posterior information can take different forms:

- a direct visualization, which is only possible if the parameter space has sufficiently small dimension (see figure 3.1).
- the computation of statistical summaries of the posterior, e.g. the mean, the median, or the mode of the distribution of each parameter, marginalizing over all others, its standard deviation; the means and covariance matrices of some groups of parameters, etc. It is also common to present the inference by plotting two-dimensional subsets of parameters, with the other components marginalized over (this is especially useful when the posterior is multi-modal or with heavy tails).

<sup>3</sup> In this section, we make explicit the choice of a model  $\mathcal{M}$  by writing it on the right-hand side of the conditioning symbol of all pdfs.



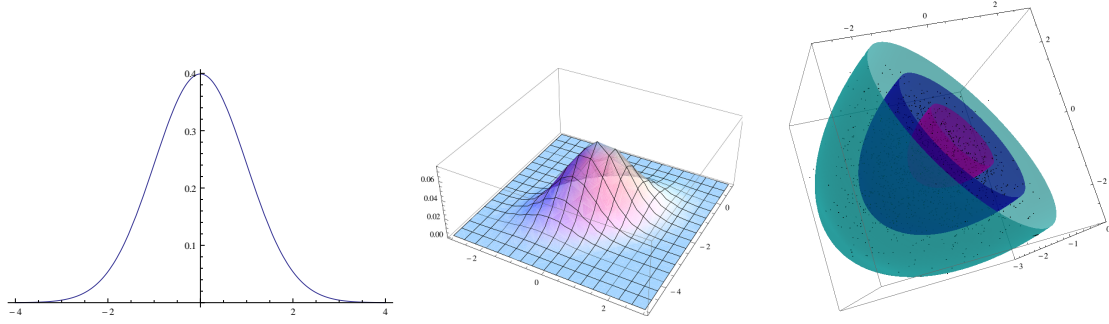


Figure 3.1: Example visualizations of posterior densities in low-dimensional parameter spaces (from left to right: one, two and three).

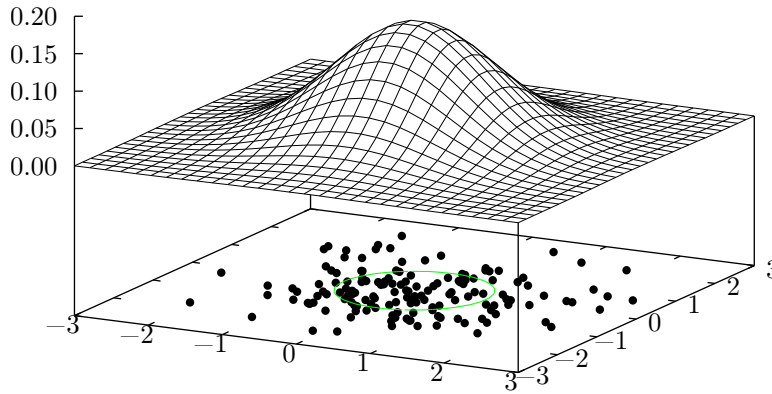


Figure 3.2: Example of a sampled representation of a posterior distribution in two dimensions. A set of samples is constructed in such a way that at any point, the posterior probability is proportional to the local density of samples in parameter space.

For typical problems in cosmology, the exploration of a posterior density meets practical challenges, depending on the dimension  $D$  of the parameter space. Due to the computational time requirements, direct integration and mapping of the posterior density is almost never a smart idea, except for  $D < 4$ . Besides, computing statistical summaries by marginalization means integrating out the other parameters. This is rarely possible analytically (Gaussian random fields being one notable exception), and even numerical direct integration is basically hopeless for  $D > 5$ .

In this thesis, we will be looking at cases where  $D$  is of the order of  $10^7$ : the density in each voxel of the map to infer is a parameter of the analysis. This means that direct evaluation of the posterior is impossible and one has to rely on a numerical approximation: sampling the posterior distribution.

The idea is to approximate the posterior by a set of samples drawn from the real posterior distribution. In this fashion, one replaces the real posterior distribution,  $\mathcal{P}(\theta|d)$ , by the sum of  $N$  Dirac delta distributions,  $\mathcal{P}_N(\theta|d)$ :

$$\mathcal{P}(\theta|d) \approx \mathcal{P}_N(\theta|d) = \frac{1}{N} \sum_{i=1}^N \delta_D(\theta - \theta_i). \quad (3.5)$$

A sampled representation of the posterior is constructed in such a way that at any point, the posterior probability is proportional to the local density of samples in parameter space (see figure 3.2).

An intuitive way to think about these samples is to consider each of them as a “possible version of the truth”. The variation between different samples quantifies the uncertainty. At this point, it is worth stressing again that an advantage of Bayesian approach is that it deals with uncertainty independently of its origin, i.e. there is no fundamental distinction between “statistical uncertainty” coming from the stochastic nature of the experiment and “systematic uncertainty”, deriving from deterministic effects that are only partially known.

The advantage of a sampling approach is that marginalization over some parameters becomes trivial: one just has to histogram. Specifically, it is sufficient to count the number of samples falling within different bins of some subset of parameters, simply ignoring the values of the others parameters. Integration to get means and variances is also much simpler, since the problem is limited to the computation of discrete sums. More generally, the expectation value of any function of the parameters,  $f(\theta)$  is

$$\langle f(\theta) \rangle = \int f(\theta) \mathcal{P}(\theta) d\theta \approx \frac{1}{N} \sum_{i=1}^N f(\theta_i). \quad (3.6)$$

We make an extensive use of this last property in part IV of this thesis, when exploiting the BORG SDSS analysis for cosmic web classification.

How can one get a sampled representation of the posterior? The ideal case would be to have an infinitely powerful computer. Then, a naïve but straightforward sampling algorithm would be the following: simulate data from the generative model (draw  $\theta$  from the prior, then data from the likelihood knowing  $\theta$ ) and check that the real data agree with the simulated data. If it is the case, keep  $\theta$  as one sample, otherwise try again. This is correct in principle, but hugely inefficient, particularly in high dimensions where it can become prohibitively expensive to evaluate the posterior pdf. Fortunately, a battery of powerful methods exists for approximating and sampling from probability distributions. Interestingly, sampling algorithms exist that do not evaluate the posterior pdf (except perhaps occasionally, to maintain high numerical precision).

One class of approaches is Approximate Bayesian Computation (ABC) sometimes also known as “likelihood-free” methods (see [Marin \*et al.\*, 2011](#) for an overview, or [Cameron & Pettitt, 2012](#); [Weyant, Schafer & Wood-Vasey, 2013](#); [Lin & Kilbinger, 2015](#) for applications to astrophysics). The general principle is similar to the naïve approach described above, but ABC makes it practical by using an approximate forward model, the outcomes  $\tilde{d}$  of which are compared with the observed data  $d$ . The candidate sample  $\tilde{d}$  is accepted with tolerance  $\varepsilon > 0$  if  $\rho(\tilde{d}, d) \leq \varepsilon$ , where the distance measure  $\rho$  determines the allowed level of discrepancy between  $\tilde{d}$  and  $d$  based on a given metric.

Another important class of standard techniques to sample the posterior is to use Markov Chain Monte Carlo, which is the subject of section 3.4.

### 3.3.3 Second level analysis: Bayesian model comparison

In the case where there are several competing theoretical models, second level inference (or Bayesian model comparison) provides a systematic way of evaluating their relative probability in light of the data and any prior information available. It does not replace parameter inference, but rather extends the assessment of hypotheses to the space of theoretical models.

This allows quantitatively to address everyday questions in cosmology – Is the Universe flat or should one allow a non-zero curvature parameter? Are the primordial perturbations Gaussian or non-Gaussian? Are there isocurvature modes? Are the perturbations strictly scale-invariant ( $n_s = 1$ ) or should the spectrum be allowed to deviate from scale-invariance? Is there evidence for a deviation from general relativity? Is the equation of state of dark energy equal to  $-1$ ?

In many of the situations above, Bayesian model comparison offers a way of balancing complexity and goodness of fit: it is obvious that a model with more free parameters will always fit the data better, but it should also be “penalized” for being more complex and hence, less predictive. The notion of predictiveness really is central to Bayesian model comparison in a very specific way: the evidence is actually the prior predictive pdf, the pdf over all data sets predicted for the experiment before data are taken. Since predictiveness is a criterion for good science everyone can agree on, it is only natural to compare models based on how well they predicted the data set before it was obtained. This criterion arises automatically in the Bayesian framework.

The guiding scientific principle is known as Occam’s razor: the simplest model compatible with the available information ought to be preferred. We now understand this principle as a consequence of using predictiveness as the criterion. A model that is so vague (e.g. has so many parameters) that it can predict a large range of possible outcomes will predict any data set with smaller probability than a model that is highly specific and therefore has to commit to predicting only a small range of possible data sets. It is clear that the specific model should be preferred if the data falls within the narrow range of its prediction. Conversely we default to the broader more general model only if the data are incompatible with the specific model. Therefore, Bayesian model comparison offers formal statistical grounds for selecting models based on an evaluation whether the data truly favor the extra complexity of one model compared to another.

Contrary to frequentists goodness-of-fit tests, second level inference always requires an alternative explanation for comparison (finding that the data are unlikely within a theory does not mean that the theory itself is improbable, unless compared with an alternative). The prior specification is crucial for model selection issues: since it is the range of values that parameters can take that controls the sharpness of Occam's razor, the prior should exactly reflect the available parameter space under the model before obtaining the data.

The evaluation of model  $\mathcal{M}$ 's performance given the data is quantified by  $\mathcal{P}(\mathcal{M}|d)$ . Using Bayes' theorem to invert the order of conditioning, we see that it is proportional to the product of the prior probability for the model itself,  $\mathcal{P}(\mathcal{M})$ , and of the Bayesian evidence already encountered in first level inference,  $\mathcal{P}(d|\mathcal{M})$ :

$$\mathcal{P}(\mathcal{M}|d) \propto \mathcal{P}(\mathcal{M}) \mathcal{P}(d|\mathcal{M}). \quad (3.7)$$

Usually, prior probabilities for the models are taken as all equal to  $1/N_m$  if one considers  $N_m$  different models (this choice is said to be *non-committal*). When comparing two competing models denoted by  $\mathcal{M}_1$  and  $\mathcal{M}_2$ , one is interested in the ratio of the posterior probabilities, or *posterior odds*, given by

$$\mathcal{P}_{12} \equiv \frac{\mathcal{P}(\mathcal{M}_1|d)}{\mathcal{P}(\mathcal{M}_2|d)} = \frac{\mathcal{P}(\mathcal{M}_1)}{\mathcal{P}(\mathcal{M}_2)} \frac{\mathcal{P}(d|\mathcal{M}_1)}{\mathcal{P}(d|\mathcal{M}_2)}. \quad (3.8)$$

With non-committal priors on the models,  $\mathcal{P}(\mathcal{M}_1) = \mathcal{P}(\mathcal{M}_2)$ , the ratio simplifies to the ratio of evidences, called the *Bayes factor*,

$$\mathcal{B}_{12} \equiv \frac{\mathcal{P}(d|\mathcal{M}_1)}{\mathcal{P}(d|\mathcal{M}_2)}. \quad (3.9)$$

The Bayes factor is the relevant quantity to update our state of belief in two competing models in light of the data, regardless of the relative prior probabilities we assign to them: a value of  $\mathcal{B}_{12}$  greater than one means that the data support model  $\mathcal{M}_1$  over model  $\mathcal{M}_2$ . Note that, generally, the Bayes factor is very different from the ratio of likelihoods: a more complicated model will always yield higher likelihood values, whereas the evidence will favor a simpler model if the fit is nearly as good, through the smaller prior volume.

Posterior odds (or directly the Bayes factor in case of non-committal priors) are usually interpreted against the Jeffreys' scale for the strength of evidence. For two competing models  $\mathcal{M}_1$  and  $\mathcal{M}_2$  with non-committal priors ( $\mathcal{P}(\mathcal{M}_1) = \mathcal{P}(\mathcal{M}_2) = 1/2$ ) and exhausting the model space ( $\mathcal{P}(\mathcal{M}_1|d) + \mathcal{P}(\mathcal{M}_2|d) = 1$ ), the relevant quantity is the logarithm or the Bayes factor,  $\ln \mathcal{B}_{12}$  for which thresholds at values of 1.0, 2.5 and 5.0 are set (corresponding to odds of about 3:1, 12:1 and 150:1, representing weak, moderate and strong evidence, respectively). The use of a logarithm in this empirical scale quantifies the principle that the evidence for a model only accumulates slowly with new informative data: rising up one level in the evidence strength requires about one order of magnitude more support.

The computation of the Bayesian evidence is generally technically challenging. For this reason, simplifying assumptions often have to be introduced (see [Heavens, Kitching & Verde, 2007](#), for the Gaussian likelihood approximation within a model selection context). Another important particular situation is when  $\mathcal{M}_2$  is a simpler model, described by fewer ( $n' < n$ ) parameters than  $\mathcal{M}_1$ .  $\mathcal{M}_2$  is said to be *nested* in model  $\mathcal{M}_1$  if the  $n'$  parameters of  $\mathcal{M}_2$  are also parameters of  $\mathcal{M}_1$ .  $\mathcal{M}_1$  has  $p \equiv n - n'$  extra parameters that are fixed to fiducial values in  $\mathcal{M}_2$ . For simplicity, let us assume that there is only one extra parameter  $\zeta$  in model  $\mathcal{M}_1$ , fixed to 0 in  $\mathcal{M}_2$  ( $\zeta$  describes the continuous deformation from one model to the other). Let us denote the set of other parameters by  $\theta$ . Under these hypotheses, the evidence for  $\mathcal{M}_1$  is  $\mathcal{P}(d|\mathcal{M}_1) \equiv \mathcal{P}(d|\mathcal{M}_{\theta,\zeta})$  and the evidence for  $\mathcal{M}_2$  is  $\mathcal{P}(d|\mathcal{M}_2) \equiv \mathcal{P}(d|\mathcal{M}_{\theta,\zeta=0}) = \mathcal{P}(d|\zeta=0, \mathcal{M}_{\theta,\zeta})$ . We also assume non-committal priors for  $\mathcal{M}_1$  and  $\mathcal{M}_2$ .

If the prior for the additional parameter  $\zeta$  is independent of the other parameters (which makes the joint prior separable:  $\mathcal{P}(\zeta, \theta|\mathcal{M}_{\theta,\zeta}) = \mathcal{P}(\zeta|\mathcal{M}_{\theta,\zeta})\mathcal{P}(\theta|\mathcal{M}_{\theta,\zeta=0})$ ), it can be shown that the Bayes factor takes a simple form, the Savage-Dickey ratio ([Dickey, 1971](#); [Verdinelli & Wasserman, 1995](#))

$$\mathcal{B}_{12} = \frac{\mathcal{P}(d|\mathcal{M}_{\theta,\zeta})}{\mathcal{P}(d|\mathcal{M}_{\theta,\zeta=0})} = \frac{\mathcal{P}(\zeta=0|\mathcal{M}_{\theta,\zeta})}{\mathcal{P}(\zeta=0|d, \mathcal{M}_{\theta,\zeta})}, \quad (3.10)$$

that is, the ratio of the marginal prior and the marginal posterior of the larger model  $\mathcal{M}_1$ , where the additional parameter  $\zeta$  is held at its fiducial value. The Bayes factor favors the "larger" model only if the data decreases the posterior pdf at the fiducial value compared to the prior. Operationally, if  $n - n'$  is small, one can easily compute the Savage-Dickey ratio given samples from the posterior and prior of  $\mathcal{M}_1$  by simply estimating the marginal densities at the fiducial value.

## 3.4 Markov Chain Monte Carlo techniques for parameter inference

This section draws from section 3 in [Leclercq, Pisani & Wandelt \(2014\)](#).

### 3.4.1 Markov Chains

The purpose of Markov Chain Monte Carlo (MCMC) sampling is to construct a sequence of points in parameter space (a so-called “chain”), whose density is proportional to the pdf that we want to sample.

A sequence  $\{\theta_0, \theta_1, \theta_2, \dots, \theta_n, \dots\}$  of random elements of some set (the “state space”) is called a *Markov Chain* if the conditional distribution of  $\theta_{n+1}$  given all the previous elements  $\theta_1, \dots, \theta_n$  depends only on  $\theta_n$  (the *Markov property*). It is said to have *stationary transition probability* if, additionally, this distribution does not depend on  $n$ . This is the main kind of Markov chains of interest for MCMC.

Such stationary chains are completely characterized by the marginal distribution for the first element  $\theta_0$  (the *initial distribution*) and the conditional distribution of  $\theta_{n+1}$  given  $\theta_n$ , called the *transition probability distribution*.

Let us denote by  $\mathcal{P}(\theta)$  the target pdf and by  $\mathcal{T}(\theta'|\theta)$  the transition pdf. When designing a MCMC method, we want to construct a chain with the following properties.

1. The desired distribution  $\mathcal{P}(\theta)$  should be an *invariant distribution* of the chain, namely the probability of the next state being  $\theta$  must satisfy the general balance property,

$$\mathcal{P}(\theta) = \int \mathcal{T}(\theta|\theta') \mathcal{P}(\theta') d\theta'. \quad (3.11)$$

Formally, an invariant distribution is a fixed point of the transition probability operator, i.e. an eigenvector with eigenvalue 1.

2. The chain should be *ergodic* (or *irreducible*) which means that it is possible to go from every state to every state (not necessarily in one move).

Property 1 ensures the existence of an invariant distribution, and property 2 its uniqueness: it is the target pdf  $\mathcal{P}(\theta)$ . Therefore, the crucial property of such Markov chains is that, after some steps depending on the initial position (the so-called “burn-in” phase), they reach a state where successive elements of the chain are drawn from the high-density regions of the target distribution, in our case the posterior of a Bayesian parameter inference: the probability to draw  $\theta$  as the  $n$ -th element of the chain,  $\mathcal{P}^{(n)}(\theta)$ , satisfies

$$\mathcal{P}^{(n)}(\theta) \rightarrow \mathcal{P}(\theta) \text{ as } n \rightarrow \infty, \text{ for any } \theta_0. \quad (3.12)$$

Exploiting this property, MCMC algorithms use Markovian processes to move from one state to another in parameter space; then, given a set of random samples, they reconstruct the probability heuristically. Several MCMC algorithms exist and the relevant choice is highly dependent on the problem addressed and on the posterior distribution to be explored (see the discussion of the “no-free lunch” theorem in section 3.2.2), but the basic principle is always similar to that of the popular COSMOMC code ([Lewis & Bridle, 2002](#)): perform a random walk in parameter space, constrained by the posterior probability distribution.

Many useful transition probabilities satisfy the detailed balance property,

$$\mathcal{T}(\theta|\theta') \mathcal{P}(\theta') = \mathcal{T}(\theta'|\theta) \mathcal{P}(\theta). \quad (3.13)$$

While general balance expresses the “balance of flow” into and out of any state  $\theta$ , detailed balance expresses the “balance of flow” between every pair of states: the flow from  $\theta$  to  $\theta'$  is the flow from  $\theta'$  to  $\theta$ . Markov chains that satisfy detailed balance are also called *reversible Markov chains*. The reason why the detailed balance property is of interest is that it is a sufficient (but not necessary) condition for the invariance of the distribution  $\mathcal{P}$  under the transition pdf  $\mathcal{T}$  (equation (3.11)), which can be easily checked:

$$\int \mathcal{T}(\theta|\theta') \mathcal{P}(\theta') d\theta' = \int \mathcal{T}(\theta'|\theta) \mathcal{P}(\theta) d\theta' = \mathcal{P}(\theta) \int \mathcal{T}(\theta'|\theta) d\theta' = \mathcal{P}(\theta). \quad (3.14)$$

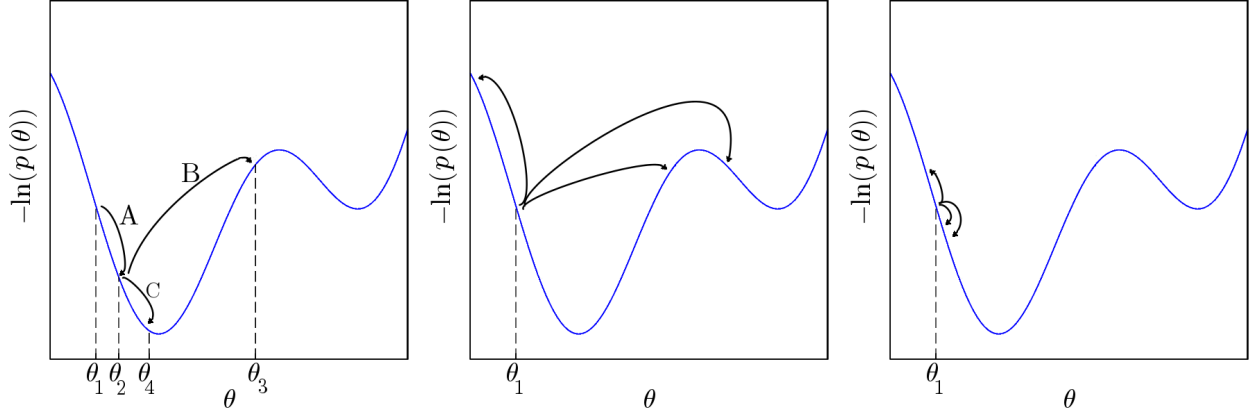


Figure 3.3: *Left panel.* An example of Markov chain constructed by the Metropolis-Hastings algorithm: starting at  $\theta_1$ ,  $\theta_2$  is proposed and accepted (step A),  $\theta_3$  is proposed and refused (step B),  $\theta_4$  is proposed and accepted (step C). The resulting chain is  $\{\theta_1, \theta_2, \theta_2, \theta_4, \dots\}$ . *Central panel.* An example of what happens with too broad a jump size: the chain lacks mobility because all the proposals are unlikely. *Right panel.* An example of what happens with too narrow a jump size: the chain samples the parameter space very slowly.

### 3.4.2 The Metropolis-Hastings algorithm

A popular version of MCMC is called the Metropolis-Hastings (MH) algorithm, which works as follows. Initially, one chooses an arbitrary point  $\theta_0$  to be the first sample, and specifies a distribution  $Q(\theta'|\theta)$  which proposes a candidate  $\theta'$  for the next sample value, given the previous sample value  $\theta$  ( $Q$  is called the proposal density or jumping distribution). At each step, one draws a realization  $\theta'$  from  $Q(\theta'|\theta)$  and calculates the *Hastings ratio*:

$$r(\theta, \theta') \equiv \frac{\mathcal{P}(\theta') Q(\theta|\theta')}{\mathcal{P}(\theta) Q(\theta'|\theta)}. \quad (3.15)$$

The proposed move to  $\theta'$  is accepted with probability  $a(\theta, \theta') \equiv \min[1; r(\theta, \theta')] = \mathcal{T}(\theta'|\theta)$ . In case it is accepted,  $\theta'$  becomes the new state of the chain, otherwise the chain stays at  $\theta$ . A graphical illustration of the MH algorithm is shown in figure 3.3. Note that each step only depends on the previous one and is also independent of the number of previous steps, therefore the ensemble of samples of the target distribution, constructed by the algorithm, is a stationary Markov chain.

The probability that the next state is  $\theta'$  is the sum of the probability that the current state is  $\theta'$  and the update leads to rejection – which happens with a probability that we note  $\mathcal{R}(\theta')$  – and of the probability that the current state is some  $\theta$  and a move from  $\theta$  to  $\theta'$  is proposed and accepted. This is formally written

$$\mathcal{P}(\theta') = \int \mathcal{P}(\theta) \mathcal{T}(\theta'|\theta) d\theta = \mathcal{P}(\theta') \mathcal{R}(\theta') + \int \mathcal{P}(\theta) Q(\theta'|\theta) d\theta. \quad (3.16)$$

The probability to depart from  $\theta'$  to any  $\theta$  is  $\int Q(\theta|\theta') d\theta = 1 - \mathcal{R}(\theta')$ .

The special case of a symmetric proposal distribution, i.e.  $Q(\theta|\theta') = Q(\theta'|\theta)$  for all  $\theta$  and  $\theta'$  is called the *Metropolis update*. Then the Hastings ratio simplifies to

$$r(\theta, \theta') = \frac{\mathcal{P}(\theta')}{\mathcal{P}(\theta)} \quad (3.17)$$

and is called the *Metropolis ratio*. Given this result, the detailed balance condition, equation (3.13) reads

$$\mathcal{P}(\theta') \min \left[ 1; \frac{\mathcal{P}(\theta)}{\mathcal{P}(\theta')} \right] = \mathcal{P}(\theta) \min \left[ 1; \frac{\mathcal{P}(\theta')}{\mathcal{P}(\theta)} \right], \quad (3.18)$$

which is easily seen to be true.

In many cases, the MH algorithm will be inefficient if the proposal distribution is sub-optimal. It is often hard to find good proposal distributions if the parameter space has high dimension (e.g. larger than 10). Typically, the chain moves very slowly, either due to a tiny step size, either because only a tiny fraction of proposals are

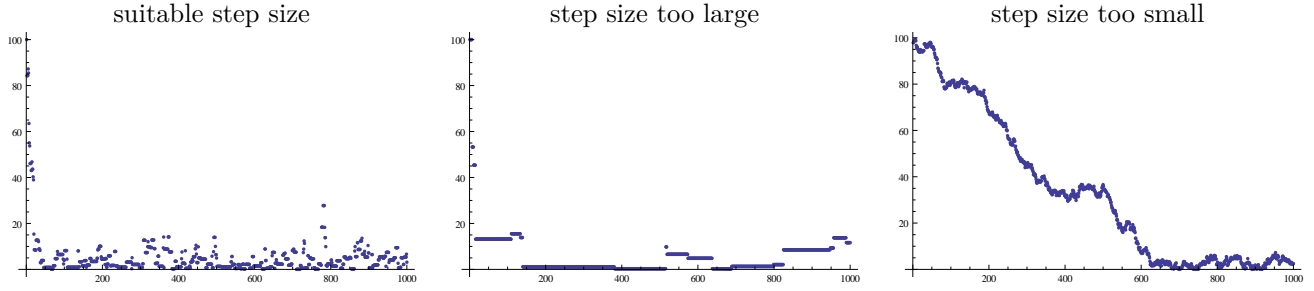


Figure 3.4: Example of Markov chains constructed by the Metropolis-Hastings algorithm, sampling the same target distribution but with varying proposal distribution (step size). The plots show the value of the sampled parameter as a function of the position in the chain. The ideal behavior with a suitable step size is shown in the left panel. On the central panel, the step size is too large: the maximum likelihood region is not well sampled. On the right panel, the step size is too small: the burn-in phase is very long and the sampling is slow. Note that this phenomena are easily diagnosed using the auto-correlation function of the chain, equation (3.19).

accepted. The initial burn-in phase can be very long, i.e. the chain takes some time to reach high likelihood regions, where the initial position chosen has no influence on the statistics of the chain. Even in the stationary state, sufficient sampling of the likelihood surface can take a very large number of steps. In the central and left panels of figure 3.3, we illustrate what happens with too broad a jump size (the chain lacks mobility and all proposals are unlikely) or too narrow (the chain moves slowly to sample all the parameter space). Note that the step-size issues can be diagnosed using the lagged auto-correlation function of the chain,

$$\xi(\Delta) = \int \theta(t)\theta(t + \Delta) dt. \quad (3.19)$$

A convergence criterion using different chains or sections of chains is proposed in Gelman & Rubin (1992). Possible solutions to the issues mentioned involve an adaptive step size or refinements of the standard Metropolis-Hastings procedure.

In some particular cases, the proposal density itself satisfies the detailed balance property,

$$Q(\theta|\theta') \mathcal{P}(\theta') = Q(\theta'|\theta) \mathcal{P}(\theta), \quad (3.20)$$

which implies that the Hastings ratio is always unity, i.e. that proposed states are always accepted ( $Q$  is  $\mathcal{T}$  and  $\mathcal{R}$  is zero). For example, Gibbs sampling is a particular case of a generalized MH algorithm, alternating between different proposals (see e.g. Wandelt, Larson & Lakshminarayanan, 2004 for a cosmological example). It is particularly helpful when the joint probability distribution is difficult to sample directly, but the conditional distribution of some parameters given the others is known. It uses a block scheme of individual *Gibbs updates* to sample an instance from the distribution of each variable in turn, conditional on the current values of the other variables. Formally, the proposal for a single Gibbs update is from a conditional distribution of the target pdf:  $Q(\theta'|\theta) \equiv \mathcal{P}(\theta'|f(\theta))$  where  $f(\theta)$  is  $\theta$  with some components omitted.  $\theta'$  is an update of these missing components, keeping the others at the values they had in  $\theta$ . Therefore,  $f(\theta') = f(\theta)$ , and we have

$$Q(\theta'|\theta) \equiv \mathcal{P}(\theta'|f(\theta)) = \mathcal{P}(\theta'|f(\theta')) = \mathcal{P}(\theta'), \quad (3.21)$$

which trivially implies the detailed balance property (equation (3.20)) and ensures an acceptance rate of unity.

### 3.4.3 Hamiltonian Monte Carlo

A very efficient MCMC algorithm for high-dimensional problems such as those encountered in cosmology is Hamiltonian Monte Carlo (HMC, originally introduced under the name of hybrid Monte Carlo, Duane *et al.*, 1987). A detailed overview is provided by Neal (2011).

The general idea of HMC is to use concepts borrowed from classical mechanics to solve statistical problems. As it is a core ingredient in the BORG code, we now discuss the most important features of HMC. We start by reviewing physical properties of Hamiltonian dynamics. The system is described by the Hamiltonian  $H(\boldsymbol{\theta}, \mathbf{p})$ ,



a function of the  $D$ -dimensional position vector  $\boldsymbol{\theta}$  and of the  $D$ -dimensional momentum vector  $\mathbf{p}$ .<sup>4</sup> Its time evolution is described by Hamilton's equations,

$$\frac{d\boldsymbol{\theta}}{dt} = \frac{\partial H}{\partial \mathbf{p}}, \quad (3.22)$$

$$\frac{d\mathbf{p}}{dt} = -\frac{\partial H}{\partial \boldsymbol{\theta}}. \quad (3.23)$$

For any time interval of duration  $s$ , these equations define a mapping  $T_s$  from the state at any time  $t$  to the state at time  $t + s$ . The first important property of Hamiltonian dynamics is time reversibility, which means for any  $s$ , that the mapping  $T_s$  has an inverse. It is easy to check that this inverse is  $T_{-s}$ .

A second property of the dynamics is that it conserves the Hamiltonian during the evolution, which can be checked explicitly:

$$\frac{dH}{dt} = \frac{\partial H}{\partial \boldsymbol{\theta}} \frac{d\boldsymbol{\theta}}{dt} + \frac{\partial H}{\partial \mathbf{p}} \frac{d\mathbf{p}}{dt} = \frac{\partial H}{\partial \boldsymbol{\theta}} \frac{\partial H}{\partial \mathbf{p}} - \frac{\partial H}{\partial \mathbf{p}} \frac{\partial H}{\partial \boldsymbol{\theta}} = 0. \quad (3.24)$$

In  $2D$  dimensions, using  $\mathbf{z} = (\boldsymbol{\theta}, \mathbf{p})$  and the matrix

$$\mathbf{J} = \begin{pmatrix} \mathbf{0}_D & \mathbf{I}_D \\ -\mathbf{I}_D & \mathbf{0} \end{pmatrix}, \quad (3.25)$$

one can rewrite Hamilton's equations as

$$\frac{d\mathbf{z}}{dt} = \mathbf{J} \cdot \nabla H. \quad (3.26)$$

The third important property is that Hamiltonian dynamics is *symplectic*, which means that the Jacobian matrix  $\mathbf{B}_s$  of the mapping  $T_s$  satisfies

$$\mathbf{B}_s^\top \mathbf{J}^{-1} \mathbf{B}_s = \mathbf{J}^{-1}. \quad (3.27)$$

This property implies volume conservation in  $(\boldsymbol{\theta}, \mathbf{p})$  phase space (a result also known as Liouville's theorem), since  $\det(\mathbf{B}_s)^2$  must be one.

Crucially, reversibility and symplecticity are properties that can be maintained exactly, even when Hamiltonian dynamics is approximated by numerical integrators (see section 4.3.4).

The link between probabilities and Hamiltonian dynamics is established via the concept of *canonical distribution* from statistical mechanics. Given the energy distribution  $E(\mathbf{x})$  for possible states  $\mathbf{x}$  of the physical system, the canonical distribution over states  $\mathbf{x}$  has pdf

$$\mathcal{P}(\mathbf{x}) = \frac{1}{Z} \exp\left(\frac{-E(\mathbf{x})}{k_B T}\right) \quad (3.28)$$

where  $k_B$  is the Boltzmann constant,  $T$  the temperature of the system, and the *partition function*  $Z$  is the normalization constant needed to ensure  $\int \mathcal{P}(\mathbf{x}) d\mathbf{x} = 1$ . In Hamiltonian dynamics,  $H$  is an energy function for the joint state of positions  $\boldsymbol{\theta}$  and momenta  $\mathbf{p}$ , and hence defines a joint pdf as

$$\mathcal{P}(\boldsymbol{\theta}, \mathbf{p}) = \frac{1}{Z} \exp\left(\frac{-H(\boldsymbol{\theta}, \mathbf{p})}{k_B T}\right) \quad (3.29)$$

Viewing this the opposite way, if we are interested in some joint distribution with probability  $\mathcal{P}(\boldsymbol{\theta}, \mathbf{p})$ , we can obtain it as a canonical distribution with temperature  $k_B T = 1$ , by setting  $H(\boldsymbol{\theta}, \mathbf{p}) = -\ln \mathcal{P}(\boldsymbol{\theta}, \mathbf{p}) - \ln Z$ , where  $Z$  is any convenient positive constant (we choose  $Z = 1$  in the following for simplicity).

We are now ready to discuss the Hamiltonian Monte Carlo algorithm. HMC interprets the negative logarithm of the pdf to sample as a physical potential,  $\psi(\boldsymbol{\theta}) = -\ln \mathcal{P}(\boldsymbol{\theta})$  and introduces auxiliary variables: “conjugate momenta”  $p_i$  for all the different parameters. Using these new variables as nuisance parameters, one can formulate a Hamiltonian describing the dynamics in the multi-dimensional phase space. Such a Hamiltonian is given as:

$$H(\boldsymbol{\theta}, \mathbf{p}) = \frac{1}{2} \mathbf{p}^\top \mathbf{M}^{-1} \mathbf{p} + \psi(\boldsymbol{\theta}) = -\ln \mathcal{P}(\boldsymbol{\theta}, \mathbf{p}), \quad (3.30)$$

where the kinetic term,  $K(\mathbf{p}) \equiv \frac{1}{2} \mathbf{p}^\top \mathbf{M}^{-1} \mathbf{p}$  involves  $\mathbf{M}$ , a symmetric positive definite “mass matrix” whose choice can strongly impact the performance of the sampler. Masses characterize the inertia of parameters when

<sup>4</sup> In this section we use boldface notations for all vectors, to strengthen the link between physics and statistics.

moving through the parameter space. Consequently, too large masses will result in slow exploration efficiency, while too light masses will result in large rejection rates (see also figure 3.4).

Each iteration of the HMC algorithm works as follows. One draws a realization of the momenta from the distribution defined by the kinetic energy term, i.e. a multi-dimensional Gaussian with a covariance matrix  $\mathbf{M}$ , then moves the positions  $\boldsymbol{\theta}$  using a Hamiltonian integrator in parameter space, respecting symplectic symmetry. In other words, we first “kick the system” then follow its deterministic dynamical evolution in phase space according to Hamilton’s equations, which read

$$\frac{d\boldsymbol{\theta}}{dt} = \mathbf{M}^{-1} \mathbf{p}, \quad (3.31)$$

$$\frac{d\mathbf{p}}{dt} = -\frac{\partial\psi(\boldsymbol{\theta})}{\partial\boldsymbol{\theta}}. \quad (3.32)$$

If the integrator is reversible, then the proposal is symmetric, and the acceptance probability for the new point  $(\boldsymbol{\theta}', \mathbf{p}')$  follows the Metropolis rule (see equation (3.17)):

$$a(\boldsymbol{\theta}', \mathbf{p}', \boldsymbol{\theta}, \mathbf{p}) = \min \left[ 1; \frac{\mathcal{P}(\boldsymbol{\theta}', \mathbf{p}')}{\mathcal{P}(\boldsymbol{\theta}, \mathbf{p})} \right] = \min [1; \exp(-H(\boldsymbol{\theta}', \mathbf{p}') + H(\boldsymbol{\theta}, \mathbf{p}))]. \quad (3.33)$$

Using the results of sections 3.4.1 and 3.4.2, this proves that detailed balance is verified and that HMC leaves the canonical distribution invariant.

In exact Hamiltonian dynamics, the energy is conserved, and therefore, ideally, this procedure always provides an acceptance rate of unity. In practice, numerical errors can lead to a somewhat lower acceptance rate but HMC remains computationally much cheaper than standard MH techniques in which proposals are often refused. In the end, we discard the momenta and yield the target parameters by marginalization:

$$\mathcal{P}(\boldsymbol{\theta}) = \int \mathcal{P}(\boldsymbol{\theta}, \mathbf{p}) d\mathbf{p}. \quad (3.34)$$

Applications of HMC in cosmology include: the determination of cosmological parameters (Hajian, 2007; in combination with PICO, Fendt & Wandelt, 2007), CMB power spectrum inference (Taylor, Ashdown & Hobson, 2008) and Bayesian approach to non-Gaussianity analysis (Elsner & Wandelt, 2010), log-normal density reconstruction (Jasche & Kitaura, 2010; including from photometric redshift surveys, Jasche & Wandelt, 2012), dynamical, non-linear reconstruction of the initial conditions from galaxy surveys (Jasche & Wandelt, 2013a), joint power spectrum and bias model inference (Jasche & Wandelt, 2013b), inference of CMB lensing (Anderes, Wandelt & Lavaux, 2015).



# Physical large-scale structure inference with the BORG algorithm

---

## Contents

---

<b>4.1</b>	<b>The challenge: the curse of dimensionality</b>	<b>64</b>
4.1.1	Sparse sampling	64
4.1.2	Shape of high-dimensional pdfs	65
4.1.3	Algorithms in high dimensions	65
<b>4.2</b>	<b>The BORG data model</b>	<b>66</b>
4.2.1	The physical density prior	67
4.2.2	The large-scale structure likelihood	68
4.2.3	The posterior distribution	71
4.2.4	The $\Gamma$ -distribution for noise sampling	71
<b>4.3</b>	<b>Sampling procedure and numerical implementation</b>	<b>72</b>
4.3.1	Calibration of the noise level	72
4.3.2	Hamiltonian Monte Carlo and equations of motion for the LSS density	72
4.3.3	The mass matrix	73
4.3.4	The leapfrog scheme integrator	73
<b>4.4</b>	<b>Testing BORG</b>	<b>74</b>
4.4.1	Generating mock observations	74
4.4.2	Convergence and correlations of the Markov Chain	74
4.4.3	Large-scale structure inference	75
<b>4.5</b>	<b>Future extensions of BORG</b>	<b>75</b>

---



---

“We are the Borg. Lower your shields and surrender your ships. We will add your biological and technological distinctiveness to our own. Your culture will adapt to service us. Resistance is futile.”  
— [Star Trek: First Contact \(1996\)](#)

---

## Abstract

This chapter describes the development and implementation of the BORG algorithm, which aims at physical large-scale structure inference in the linear and mildly non-linear regime. It describes the data model, which jointly accounts for the shape of three-dimensional matter field and its formation history. Based on an efficient implementation of the Hamiltonian Monte Carlo algorithm, BORG samples the joint posterior of the several millions parameters involved, which allows for thorough uncertainty quantification.

This chapter presents BORG (Bayesian Origin Reconstruction from Galaxies), a data assimilation method for probabilistic, physical large-scale structure inference. In section 4.1, the main challenge faced, namely the curse of dimensionality, is discussed. In section 4.2, we describe the latest formulation of BORG data model, initially introduced by [Jasche & Wandelt \(2013a\)](#) and updated by [Jasche, Leclercq & Wandelt \(2015\)](#). Section 4.3 gives considerations about the sampling procedure and the numerical implementation of the algorithm. Finally, in section 4.4, we report on a test of the BORG algorithm using a synthetic catalog of tracers.

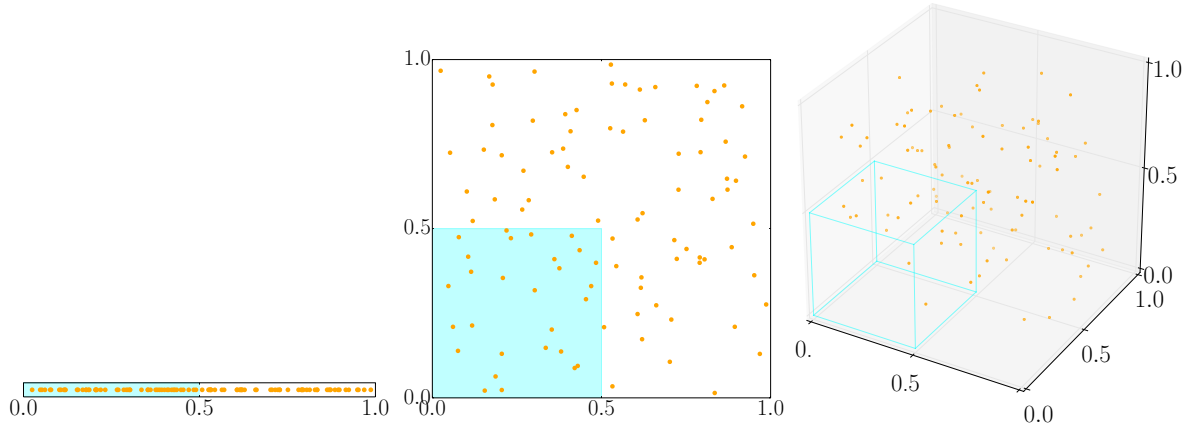


Figure 4.1: Illustration of the curse of dimensionality in one, two and three dimensions. We draw an original sample of 100 random points uniformly distributed in  $[0; 1]$ , then progressively add a second and third coordinate, also uniformly drawn in  $[0; 1]$ . The sparsity of the data (here illustrated by the number of samples in the  $[0; \frac{1}{2}]$  hypercube, in cyan) increases exponentially with the number of dimensions.

Dimension $D$	$\mathcal{P}_D = 2^{-D}$	Numerical representation
1	$2^{-1}$	0.5
10	$2^{-10}$	$9.77 \times 10^{-4}$
100	$2^{-100}$	$7.89 \times 10^{-31}$
1000	$2^{-1000}$	$9.33 \times 10^{-302}$
10000	$2^{-10000}$	0.

Table 4.1: Probability for a sample uniformly drawn in  $[0; 1]^D$  to be in  $[0; \frac{1}{2}]^D$ , as a function of the dimension  $D$ . The mathematical result,  $2^{-D}$  (second column) is compared to its double-precision computer representation (third column). For  $D \geq 1075$ ,  $\mathcal{P}_D$  is below the minimum positive subnormal double representable.

## 4.1 The challenge: the curse of dimensionality

Statistical analyses of large-scale structure surveys require to go from the few parameters describing the homogeneous Universe to a point-by-point characterization of the inhomogeneous Universe. The latter description typically involves tens of millions of parameters: the density in each voxel of the discretized survey volume.

“Curse of dimensionality” phenomena (Bellman, 1961) are the significant obstacle in this high-dimensional data analysis problem. They refer to the difficulties caused by the exponential increase in volume associated with adding extra dimensions to a mathematical space. In the following, we discuss the basic aspects of the high-dimensional situation. In particular, we outline three aspects of the curse of dimensionality phenomena.

### 4.1.1 Sparse sampling

The first and most obvious aspect is the exponential increase of sparsity given a fixed amount of sampling points. Reciprocally, the number of points drawn from a uniform distribution, needed for sampling at a constant density a region in parameter space, increases exponentially with its dimension.

We illustrate this phenomenon in figure 4.1 with 100 points randomly drawn in  $[0; 1]^D$  for  $D = 1, 2, 3$ . The number of samples that fall in some fixed region in parameter space exponentially decreases with the dimensionality of the problem. For example, the probability  $\mathcal{P}_D$  for a random point to be in the  $[0; \frac{1}{2}]^D$  hyperquadrant (shown in cyan in figure 4.1) is  $2^{-D}$ . Difficulties to represent such probabilities numerically (table 4.1) arise well before  $D = 10^7$ , as we now discuss.

In standard double-precision binary floating-point format (the IEEE 754 “binary64” norm), numbers are represented in base  $b = 2$ . The bits are laid out as follows (figure 4.2): 1 sign bit, 11 bits for the exponent width, and  $p = 52$  bits for the significand precision. The real value assigned by the machine to a set of **binary64** digits

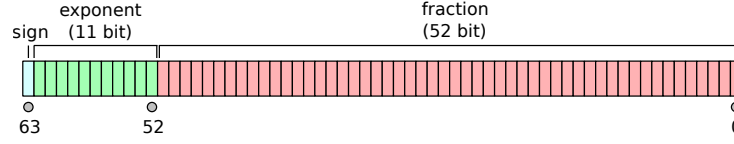


Figure 4.2: Computer representation of double-precision binary floating-point numbers. One bit is used to store the sign, 11 to store the exponent, and 52 bits to store the fractional part. This representation on a finite number of bits implies the existence of both a minimal and a maximal positive representable number.

is

$$(-1)^{\text{sign}} \left( 1 + \sum_{i=1}^{52} b_{52-i} 2^{-i} \right) \times 2^{e-1023}, \quad (4.1)$$

where  $1 \leq e \leq 2046$  is the “biased exponent” encoded in the 11 exponent bits and  $b_i$  are the values of the significand bits.

This representation implies that the maximum relative rounding error when rounding a number to the nearest representable one (the “machine epsilon”) is  $b^{-(p-1)} = 2^{-52}$ . Therefore, the maximum positive double is  $\text{max\_double} \equiv (1 + (1 - 2^{-52})) \times 2^{1023} \approx 1.798 \times 10^{308}$  and the minimum positive double is  $\text{min\_normal\_double} \equiv 2^{-1022} \approx 2.225 \times 10^{-308}$ .

In a normal floating-point value, there are no leading zeros in the significand; instead leading zeros are moved to the exponent. By using leading zeros in the significand, it is possible to represent “subnormal numbers”, i.e. numbers where this representation would result in an exponent that is too small for the allowed number of bits. The smallest subnormal number representable with the `binary64` norm is  $\text{min\_subnormal\_double} \equiv 2^{-52} \times 2^{-1022} \approx 4.941 \times 10^{-324}$ .

Coming back to the representation of  $\mathcal{P}_D$  is a large number of dimensions, the discussion above implies that  $\mathcal{P}_D$  is exactly zero, at computer precision, for  $D \geq 1075$ . More generally, typical probabilities are often below  $\text{min\_subnormal\_double}$  for  $D \gtrsim 1000$ , which means that their computer representations as doubles is impossible. Representing such numbers requires more than 64 bits. This number of dimensions is well below that of the problem that we want to tackle,  $D \approx 10^7$ .

### 4.1.2 Shape of high-dimensional pdfs

Generally, high-dimensional functions can have more complex features than low-dimensional functions (there is more “space” for that), and hence can be harder to characterize.

Since it is not possible to store arbitrarily small positive numbers, numerical representations of high-dimensional pdfs will tend to have narrow support and very peaked features. This can also cause difficulties, as pdfs have to be normalized to unity: if the support is sufficiently small, the value of the pdf at its peaks can easily be above the maximum double  $\text{max\_double}$ , which will cause computer crashes.

### 4.1.3 Algorithms in high dimensions

It is important to note that curse of dimensionality phenomena are generally not an intrinsic problem of high-dimensional problems, but a joint problem of the data set and the algorithm used. In particular, a dramatic increase of computational time (both to get one sample and to reach the required number of samples) is common. The curse of dimensionality often means that the number of samples available is small compared to the dimension of the space, which can lead to issues such as overfitting the data or getting poor classification or clustering when searching for specific patterns (Verleysen & François, 2005).

For most MCMC algorithms, the slow convergence, due a high rejection rate, is the most significant obstacle. In particular, for many interesting problems (typically non-linear and where components are not independently distributed), traditional sampling techniques that perform a random walk in parameter space, like the Metropolis-Hastings algorithm (see section 3.4.2) will unequivocally fail in  $D \approx 10^7$ .<sup>1</sup> However, gradients

<sup>1</sup> At least, unless the proposal distribution approximates extremely well the target distribution – which would imply to have already solved the problem!

Code	Density field model	Response operator	Multi-survey	$P(k)$	Photo- $z$	Galaxy bias model	$b$	$\tilde{N}$	RSD
ARES	Gaussian (J+10b)	(J+10b)	(JW13b)	(J+10b)		linear (J+10b); $M$ -dep., linear (JW13b)	sampled (JW13b)	(JW13b)	(J+in prep.)
HADES	Log-normal (JK10)	(JK10)	(J+in prep.)	(J+in prep.)	(JW12)	linear (JK10)		(J+in prep.)	
BORG	2LPT (JW13a)	(JW13a)	(JLW15)			linear (JW13a); $M$ -dep., power-law (JLW15)	calibrated with ARES (LJ16); sampled (J+in prep.)	(JLW15)	

Table 4.2: Current status of Bayesian large-scale structure analysis codes ARES, HADES and BORG. Green cells correspond to features implemented in the data model and tested, as reported in the corresponding papers. Blue cells correspond to features which will be described in upcoming publications. The column correspond respectively to: the model used to describe the prior density field; treatment of the survey response operator (survey mask and selection effects); treatment of multiple, independent surveys (or sub-samples of the same survey); power spectrum sampling; photometric redshifts sampling; galaxy bias model ( $M$ -dep. stands for luminosity-dependent bias); treatment of bias parameters; sampling of noise levels; treatment of peculiar velocities and redshift-space distortions. The references are J+10b = Jasche *et al.* (2010a); JK10 = Jasche & Kitaura (2010); JW12 = Jasche & Wandelt (2012); JW13a = Jasche & Wandelt (2013a); JW13b = Jasche & Wandelt (2013b); JLW15 = Jasche, Leclercq & Wandelt (2015); LJ16 = Lavaux & Jasche (2016).

of pdfs carry capital information, as they indicate the direction to high-density regions, permitting fast travel through a large volume in parameter space.

One way forward is to reduce the dimensionality of the problem, which is actually an entire research field. For example, principal component analysis converts a set of correlated variables to a set of linearly uncorrelated “principal components”. Unfortunately, due to the highly non-linear and complex physics involved in structure formation (see chapter 1), no obvious reduction of the problem size exists in our case. Under the assumption of an initial grf with independent density amplitudes in Fourier space, we cannot make any further dimension reduction, and we have to deal with all  $D \approx 10^7$  dimensions. Dimensionality can only be reduced by coarsening the resolution and discarding information.

As we will demonstrate in the rest of this chapter, Hamiltonian Monte Carlo (see section 3.4.3) beats the curse of dimensionality for the problem of physical large-scale structure inference. In particular, the approximate conservation of the Hamiltonian enables us to keep a high acceptance rate, and the use of gradients of the posterior pdf  $(\partial\psi(\boldsymbol{\theta})/\partial\boldsymbol{\theta})$  in Hamilton’s equations) allows efficient search for high density of probability regions.

## 4.2 The BORG data model

In this section, we discuss the BORG data model, i.e. the set of assumptions concerning the generation of observed large-scale structure data. In other words, we write down a probabilistic data-generating process.

This model was initially introduced by Jasche & Wandelt (2013a). In Jasche, Leclercq & Wandelt (2015), we updated the data model and modified to the original formulation of the BORG sampling scheme to introduce the improvements presented in Jasche & Wandelt (2013b). These improvements permit to account for luminosity-dependent galaxy bias and to perform automatic noise level calibration.

BORG is the successor of ARES (Algorithm for REconstruction and Sampling, Jasche *et al.*, 2010a; Jasche & Wandelt, 2013b) and HADES (HAMiltonian Density Estimation and Sampling Jasche & Kitaura, 2010; Jasche & Wandelt, 2012). In table 4.2, we summarize the different aspects covered by the ARES, HADES, and BORG data models. Contrary to ARES and HADES, which use phenomenological models to describe the density field, BORG involves a physical structure formation model (see table 4.2). LSS observations are merged with actual dynamics. Therefore, even if it is the least advanced algorithm in terms of the aspects covered by the data

model, its physical modeling is the most sophisticated.

In the following,  $x$  labels one of the  $D$  voxels of the discretized domain,  $\delta^i$  and  $\delta^f$  are realizations of the initial (at  $a = 10^{-3}$ ) and final (at  $a = 1$ ) density contrast, respectively, expressed as  $D$ -dimensional vectors. For improved clarity, we use colors in equations to distinguish the different quantities that are involved in the data model.

### 4.2.1 The physical density prior

In contrast to earlier algorithms (see table 4.2) BORG includes a physical density prior i.e. involves a model for structure formation. This makes the prior (expressed in terms of the final density contrast) highly non-Gaussian and non-linear. Writing down this prior is the subject of the present section.

#### 4.2.1.1 The initial Gaussian prior

As discussed in the [introduction](#) and in chapter 1, it is commonly admitted that the density contrast early in the matter era obeys Gaussian statistics. Consistently with the discussion of section 3.2.2, this is the prior that we adopt.

Explicitly, in Fourier space, the prior for the initial density contrast is a multivariate Gaussian process with zero mean and diagonal covariance matrix  $\hat{S}$  (see equation (1.14)):

$$\mathcal{P}(\hat{\delta}^i | \hat{S}) = \frac{1}{\sqrt{|2\pi\hat{S}|}} \exp \left( -\frac{1}{2} \sum_{k,k'} \hat{\delta}_k^i \hat{S}_{kk'}^{-1} \hat{\delta}_{k'}^i \right). \quad (4.2)$$

where we explicitly noted by a hat the Fourier-space quantities.

The elements in matrix  $\hat{S}$  are fixed parameters in BORG. They characterize the variance of the initial density field and therefore contain a cosmological dependence. We further assume that the covariance matrix  $\hat{S}$  is diagonal in Fourier space (this is assuming statistical homogeneity of the initial density contrast, as seen in section 1.2.4.1). The diagonal coefficients are  $\sqrt{P(k)/(2\pi)^3}$ , where  $P(k)$  are the initial power spectra coefficients for the adopted fiducial cosmological parameters. They are chosen to follow the prescription of [Eisenstein & Hu \(1998, 1999\)](#), including baryonic wiggles.

Alternatively, using the configuration space representation yields

$$\mathcal{P}(\delta^i | S) = \frac{1}{\sqrt{|2\pi S|}} \exp \left( -\frac{1}{2} \sum_{x,x'} \delta_x^i S_{xx'}^{-1} \delta_{x'}^i \right). \quad (4.3)$$

#### 4.2.1.2 Translating to the final density field

Following [Jasche & Wandelt \(2013a\)](#), we now show that the problem of physical inference of final density fields can be recast into the problem of inferring the corresponding initial conditions, given the structure formation model.

As seen before, it is straightforward to express a prior in the initial conditions,  $\mathcal{P}(\delta^i)$ . Given this, we can obtain a prior distribution for the final density contrast at scale factor  $a$  by using the standard formula for conditional probabilities:

$$\mathcal{P}(\delta^f) = \int \mathcal{P}(\delta^f, \delta^i) d\delta^i \quad (4.4)$$

$$= \int \mathcal{P}(\delta^f | \delta^i) \mathcal{P}(\delta^i) d\delta^i. \quad (4.5)$$

For a deterministic model of structure formation  $\delta^i \mapsto \mathcal{G}(\delta^i, a)$ , the conditional probability is given by Dirac delta distributions:

$$\mathcal{P}(\delta^f | \delta^i) = \prod_x \delta_D(\delta_x^f - [\mathcal{G}(\delta^i, a)]_x). \quad (4.6)$$

Therefore, given a model  $\mathcal{G}$  for structure formation, a prior distribution for the late-time density field can be obtained by a two-step sampling process:

1. drawing an initial condition realization from the prior  $\mathcal{P}(\delta^i)$ ;
2. propagating the initial state forward in time with  $\mathcal{G}$  (this step is entirely deterministic).

This process amounts to drawing samples from the joint prior distribution of initial and final conditions:

$$\mathcal{P}(\delta^f, \delta^i) = \mathcal{P}(\delta^i) \prod_x \delta_D(\delta_x^f - [\mathcal{G}(\delta^i, a)]_x). \quad (4.7)$$

Marginalization over initial density realizations then yields samples of the non-Gaussian prior for final density fields. In practice, as initial conditions are also interesting for a variety of cosmological applications, we do not discard them and we always store them, whenever we draw a sample from the prior.

#### 4.2.1.3 The structure formation model

Ideally, the structure formation model should be fully non-linear gravity. For reasons of computational feasibility, in BORG,  $\mathcal{G}$  is obtained from second-order Lagrangian perturbation theory and the cloud-in-cell scheme. More specifically, the initial density field is populated by dark matter particles that are evolved according to the equations for 2LPT displacements given in section 1.5.3. In the final state, these particles are assigned to the grid using a CiC scheme, yielding the final density contrast  $\delta^f$ . The reader is referred to appendix B for details on the numerical implementation of 2LPT and CiC.

Using equations (4.3) and (4.7), the joint physical prior for initial and late-time density fields is found to be

$$\mathcal{P}(\delta^f, \delta^i | \mathbf{S}) = \frac{1}{\sqrt{|2\pi\mathbf{S}|}} \exp\left(-\frac{1}{2} \sum_{x, x'} \delta_x^i \mathbf{S}_{xx'}^{-1} \delta_{x'}^i\right) \prod_x \delta_D(\delta_x^f - [\mathcal{G}(\delta^i, a)]_x). \quad (4.8)$$

Note that the first part (corresponding to the initial conditions) is more easily handled in Fourier space, while the second part (corresponding to the propagation from initial to final conditions) involves density fields in configuration space.

### 4.2.2 The large-scale structure likelihood

This section discusses the BORG likelihood,  $\mathcal{P}(d|\delta^i)$ . The data  $d$  used by BORG are galaxy (or matter tracer) number counts in each voxel of the discretized domain. To compute it, the position of galaxies is translated from spherical to Cartesian coordinates using the following coordinate transform:

$$x = d_{\text{com}}(z) \cos(\lambda) \cos(\eta), \quad (4.9)$$

$$y = d_{\text{com}}(z) \cos(\lambda) \sin(\eta), \quad (4.10)$$

$$z = d_{\text{com}}(z) \sin(\lambda), \quad (4.11)$$

with  $\lambda$  being the declination,  $\eta$  the right ascension and  $d_{\text{com}}(z)$  the radial comoving distance to redshift  $z$  for the fiducial cosmology. Galaxies are then binned using the Nearest Grid Point (NGP) assignment scheme to get voxel-wise galaxy number counts.

#### 4.2.2.1 Splitting the galaxy distribution

In order to account for the luminosity-dependence of selection effects and galaxy biases, we split the data into several bins of absolute magnitude. In the following,  $\ell$  labels one of these bins, and  $N^\ell$  is the data set containing the number counts of galaxies in the luminosity bin  $\ell$  and in voxel  $x$ ,  $N_x^\ell$ .

BORG treats different magnitude bins as independent data sets. Each of them is assigned a likelihood function,  $\mathcal{P}(N^\ell|\delta^i)$ . Since it is fair to assume that galaxies in different luminosity bins are independent and identically distributed, once the density field is given, the final likelihood of the total data set  $d = \{N^\ell\}$  is obtained by multiplying these likelihood functions,

$$\mathcal{P}(d|\delta^i) = \prod_\ell \mathcal{P}(N^\ell|\delta^i). \quad (4.12)$$

#### 4.2.2.2 The galaxy distribution as an inhomogeneous Poisson process

Galaxies are tracers of the mass distribution. The statistical uncertainty due to the discrete nature of their distribution is often modeled as a Poisson process (Layzer, 1956; Peebles, 1980; Martínez & Saar, 2002). Before BORG, Poissonian likelihoods have been successfully applied to perform reconstructions of the matter density by Kitaura, Jasche & Metcalf (2010); Jasche & Kitaura (2010); Jasche *et al.* (2010a). Adopting this picture, we write

$$\mathcal{P}(N^\ell | \lambda(\delta^i)) = \prod_x \frac{\exp(-\lambda_x^\ell(\delta^i)) (\lambda_x^\ell(\delta^i))^{N_x^\ell}}{N_x^\ell!}. \quad (4.13)$$

The Poisson intensity field,  $\lambda^\ell(\delta^i)$ , characterizes the expected number of galaxies in voxel  $x$  given the initial density contrast  $\delta^i$ . As it depends on the position, it is an *inhomogeneous* Poisson process.

Real galaxy samples can have a sub- or super-Poissonian behavior (i.e. be under- or over-dispersed), depending on local and non-local properties (Mo & White, 1996; Somerville *et al.*, 2001; Casas-Miranda *et al.*, 2002). These effects are neglected here, but in the context of large-scale structure reconstructions, deviations from Poissonity have been introduced in the likelihood by Kitaura (2012); Ata, Kitaura & Müller (2015).

#### 4.2.2.3 The Poisson intensity field

The expected number of galaxies in a voxel depends – of course – on the underlying large-scale structure, but also on galaxy bias, redshift-space distortions, dynamical processes along the observer’s backwards lightcone, selection effects, and instrumental noise. All these effects should in principle be taken into account in the Poisson intensity field. In the following, we detail, step by step, how to go from  $\delta^i$  to  $\lambda(\delta^i)$  in the BORG likelihood.

1. **Structure formation.** The first step is to translate initial to evolved dark matter overdensity:

$$\delta^i \mapsto \mathcal{G}(\delta^i, a). \quad (4.14)$$

As discussed before, for this step BORG relies on 2LPT instead of fully non-linear gravitational dynamics, meaning that there exists some degree of approximation in the inference process. Accurate quantification this level of approximation is unfortunately not currently possible, as it would require the fully non-linear inference process for reference, which so far is not computationally tractable.

2. **Lightcone effects.** Along with step 1, we could account for lightcone effects so that the distant structures are less evolved than the closest ones. This is exploiting the dependence of  $\mathcal{G}$  on  $a$  to build the dark matter density on the lightcone. For simplicity, this is not currently implemented in BORG; rather, we run 2LPT up to  $a = 1$  everywhere. In the following we simplify the notations and we write  $\delta^f \equiv \mathcal{G}(\delta^i) \equiv \mathcal{G}(\delta^i, a = 1)$ .
3. **Redshift-space distortions.** At this point, the data model could also include a treatment of redshift-space distortions (see Heavens & Taylor, 1995; Tadros *et al.*, 1999; Percival, Verde & Peacock, 2004; Percival, 2005a; Percival & White, 2009). Though not explicitly included in the present BORG data model, we find empirically that redshift-space distortions are mitigated by the prior preference for homogeneity and isotropy (see chapter 5): BORG interprets deviations from isotropy as noise, and fits an isotropic distribution to the data.
4. **Galaxy bias.** The following step is to get the galaxy density  $\rho_g$  given the dark matter density  $\rho$ . This is making assumptions for physical biasing in galaxy formation. Various LSS inference algorithms assume a linear bias model. In order to be well defined, a Poisson likelihood requires intensities of the inhomogeneous Poisson process to be strictly positive. Since a linear bias model does not guarantee a positive density field and corresponding Poisson intensity, it is not applicable to the present case. For this reason, we assume a phenomenological power-law to account for galaxy biasing:

$$\rho_g \propto \beta \rho^\alpha. \quad (4.15)$$

In luminosity bin  $\ell$  and in terms of the dark matter overdensity, this is step written

$$\delta^f \mapsto \beta^\ell (1 + \delta^f)^{\alpha^\ell} \propto \rho_g^\ell. \quad (4.16)$$



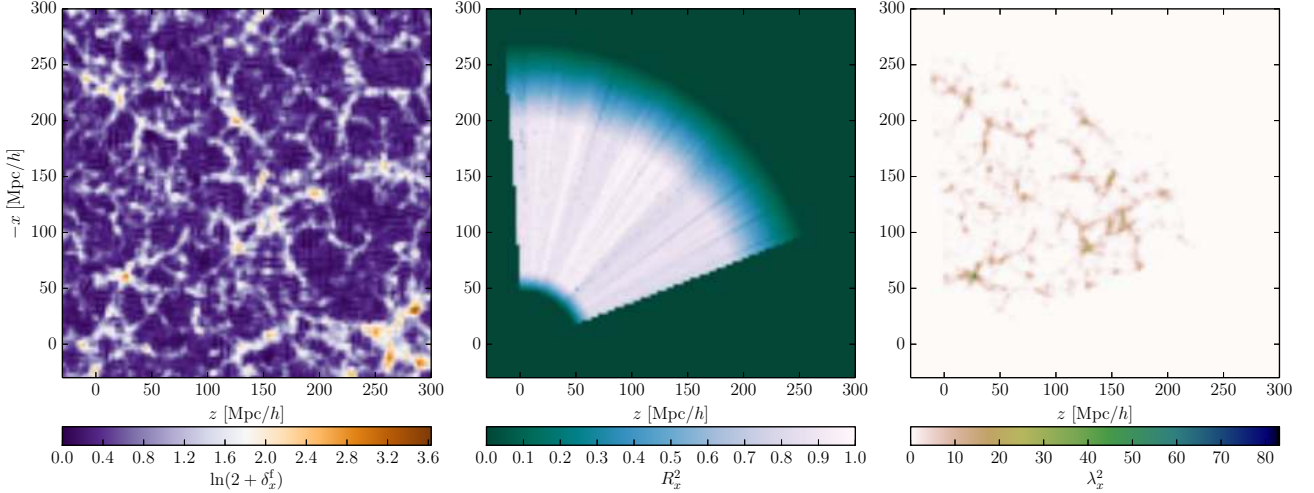


Figure 4.3: Slices through the box used in the BORG SDSS analysis (see chapter 5). *Left panel.* Density in one sample (for clarity, the quantity shown is  $\ln(2 + \delta_x^f)$ ). *Middle panel.* Survey response operator  $R_x^2$  in the  $\ell = 2$  luminosity bin, corresponding to absolute  $r$ -band magnitudes in the range  $-19.67 < M_{0.1r}^2 < -19.00$ . *Right panel.* Poisson intensity field  $\lambda_x^2$  for this sample and luminosity bin, computed with equation (4.20). The bias and noise parameters are respectively  $\alpha^2 = 1.30822$  and  $\tilde{N}^2 = 1.39989$  (see table 5.1).

Note that coefficients  $\alpha^\ell$  and  $\beta^\ell$  depend on  $\ell$ , which means that the data model accounts for *luminosity-dependent* galaxy biases. Parameters  $\beta^\ell$  are automatically calibrated during the generation of the Markov Chain (see section 4.3.1). For simplicity, parameters  $\alpha^\ell$  are kept at fixed, fiducial values. In the BORG analysis of the SDSS (chapter 5), these values are determined using a standard model for luminosity-dependent galaxy bias. In their analysis of the 2M++ catalog (Lavaux & Hudson, 2011), Lavaux & Jasche (2016) show that it is possible to calibrate these values with a preliminary ARES inference, for subsequent use in BORG.

5. **Mean number of galaxies.** To get the expected number of galaxies from the unnormalized galaxy density, the quantity  $\beta^\ell(1 + \delta_x^f)\alpha^\ell$  has to be multiplied by the mean number of galaxies in bin  $\ell$ ,  $\tilde{N}^\ell$ . This step is therefore simply:

$$\beta^\ell(1 + \delta_x^f)\alpha^\ell \mapsto \tilde{N}^\ell \beta^\ell(1 + \delta_x^f)\alpha^\ell. \quad (4.17)$$

6. **Observational effects.** The last step is to put in the luminosity-dependent selection effects and the survey mask. For this, we multiply with the linear survey response operator  $R_x^\ell$ , a voxel-wise three-dimensional function that incorporates survey geometries and selection effects:

$$\tilde{N}^\ell \beta^\ell(1 + \delta_x^f)\alpha^\ell \mapsto R_x^\ell \tilde{N}^\ell \beta^\ell(1 + \delta_x^f)\alpha^\ell. \quad (4.18)$$

Eventually, the Poisson intensity field is given by

$$\lambda_x^\ell(\delta^i) = R_x^\ell \tilde{N}^\ell \beta^\ell (1 + [\mathcal{G}(\delta^i)]_x) \alpha^\ell. \quad (4.19)$$

We note that  $\tilde{N}^\ell$  and  $\beta^\ell$  are degenerate, in the sense that only the product  $\tilde{N}^\ell \beta^\ell$  matters. We define  $\tilde{N}^\ell \equiv \tilde{N}^\ell \beta^\ell$ , so that

$$\lambda_x^\ell(\delta^i) = R_x^\ell \tilde{N}^\ell (1 + [\mathcal{G}(\delta^i)]_x) \alpha^\ell. \quad (4.20)$$

$\tilde{N}^\ell$  represents the overall noise level in bin  $\ell$ . With the improved BORG data model (Jasche, Leclercq & Wandelt, 2015), we automatically calibrate this parameter (see section 4.3.1). In figure 4.3, we illustrate the construction of the Poisson intensity field for the  $\ell = 2$  bin of the SDSS analysis. We show the dark matter density,  $\delta_x^f$ , the survey response operator  $R_x^2$  and the Poisson intensity  $\lambda_x^2$ .



#### 4.2.2.4 The comprehensive large-scale structure likelihood

Noting  $\mathbf{d} \equiv \{N^\ell\}$  the total data set, i.e. all available galaxy number counts, and  $\tilde{N} \equiv \{\tilde{N}^\ell\}$  the set of noise parameters in each bin, we obtain the final expression for the LSS likelihood using equations (4.12), (4.13) and (4.20). It reads

$$\mathcal{P}(\mathbf{d}|\delta^i, \tilde{N}) = \prod_{x,\ell} \frac{\exp\left(-R_x^\ell \tilde{N}^\ell (1 + [\mathcal{G}(\delta^i)]_x)^{\alpha^\ell}\right) \left(R_x^\ell \tilde{N}^\ell (1 + [\mathcal{G}(\delta^i)]_x)^{\alpha^\ell}\right)^{N_x^\ell}}{N_x^\ell!} \quad (4.21)$$

In this equation, we omitted on the right side of the conditioning bar the sets  $\{R_x^\ell\}$  and  $\{\alpha^\ell\}$  (one can consider that all probabilities inferred by BORG are conditional on these). However, we now write explicitly  $\tilde{N}$ , as this will be of importance later.

### 4.2.3 The posterior distribution

As usual in Bayesian statistics, the posterior distribution is obtained, up to a normalization constant, by the use of Bayes' formula,

$$\mathcal{P}(\delta^i|\mathbf{d}, \mathbf{S}, \tilde{N}) \propto \mathcal{P}(\delta^i|\mathbf{S}, \tilde{N}) \mathcal{P}(\mathbf{d}|\delta^i, \mathbf{S}, \tilde{N}) = \mathcal{P}(\delta^i|\mathbf{S}) \mathcal{P}(\mathbf{d}|\delta^i, \tilde{N}). \quad (4.22)$$

Substituting equations (4.3) and (4.21) allows to write down the full problem solved by BORG for the density distribution:

$$\mathcal{P}(\delta^i|\mathbf{d}, \mathbf{S}, \tilde{N}) \propto \frac{1}{\sqrt{|2\pi\mathbf{S}|}} \exp\left(-\frac{1}{2} \sum_{x,x'} \delta_x^i \mathbf{S}_{xx'}^{-1} \delta_{x'}^i\right) \prod_{x,\ell} \frac{\exp\left(-R_x^\ell \tilde{N}^\ell (1 + [\mathcal{G}(\delta^i)]_x)^{\alpha^\ell}\right) \left(R_x^\ell \tilde{N}^\ell (1 + [\mathcal{G}(\delta^i)]_x)^{\alpha^\ell}\right)^{N_x^\ell}}{N_x^\ell!}. \quad (4.23)$$

It is simpler to express the BORG posterior in terms of the initial conditions, but recall that one gets the final conditions (and in fact the entire LSS history, as demonstrated in chapter 5) automatically and entirely deterministically via the structure formation model  $\mathcal{G}$  (see section 4.2.1.2):

$$\mathcal{P}(\delta^f, \delta^i|\mathbf{d}, \mathbf{S}, \tilde{N}) = \mathcal{P}(\delta^i|\mathbf{d}, \mathbf{S}, \tilde{N}) \prod_x \delta_D(\delta_x^f - [\mathcal{G}(\delta^i)]_x). \quad (4.24)$$

### 4.2.4 The $\Gamma$ -distribution for noise sampling

This section draws from appendix A of [Jasche, Leclercq & Wandelt \(2015\)](#).

We aim at automatically calibrating, during the sampling procedure, the noise level of each luminosity bin, given the data and the current density sample. This requires to write down the conditional probability  $\mathcal{P}(\tilde{N}^\ell|N^\ell, \delta^f)$ , which we do in this section.

According to Bayes' formula, we can write

$$\mathcal{P}(\tilde{N}^\ell|N^\ell, \delta^f) \propto \mathcal{P}(\tilde{N}^\ell) \mathcal{P}(N^\ell|\tilde{N}^\ell, \delta^f), \quad (4.25)$$

where we have assumed the conditional independence  $\mathcal{P}(\tilde{N}^\ell|\delta^f) = \mathcal{P}(\tilde{N}^\ell)$ . In the absence of any further information on the parameter  $\tilde{N}^\ell$ , we follow the maximum agnostic approach pursued by [Jasche & Wandelt \(2013b\)](#) by setting the prior distribution  $\tilde{N}^\ell$  constant. By using the Poisson likelihood for  $\mathcal{P}(N^\ell|\tilde{N}^\ell, \delta^f)$  (equations (4.13) and (4.20)) into equation (4.25), we obtain the conditional posterior for the noise parameter  $\tilde{N}^\ell$  as:

$$\mathcal{P}(\tilde{N}^\ell|N^\ell, \delta^f) \propto \exp\left(-\tilde{N}^\ell A_\ell\right) \times \left(\tilde{N}^\ell\right)^{B_\ell}, \quad (4.26)$$

where  $A_\ell \equiv \sum_x R_x^\ell (1 + \delta_x^f)^{\alpha^\ell}$  and  $B_\ell \equiv \sum_x N_x^\ell$ . By choosing  $k_\ell \equiv B_\ell + 1$  and  $\theta_\ell \equiv 1/A_\ell$ , we yield a properly normalized  $\Gamma$ -distribution for the noise parameter  $\tilde{N}^\ell$ , given as:

$$\mathcal{P}(\tilde{N}^\ell|N^\ell, \delta^f) = \Gamma[k_\ell, \theta_\ell] \left(\tilde{N}^\ell\right) = \frac{\left(\tilde{N}^\ell\right)^{k_\ell-1} \exp\left(-\frac{\tilde{N}^\ell}{\theta_\ell}\right)}{\theta_\ell^{k_\ell} \Gamma(k_\ell)}. \quad (4.27)$$

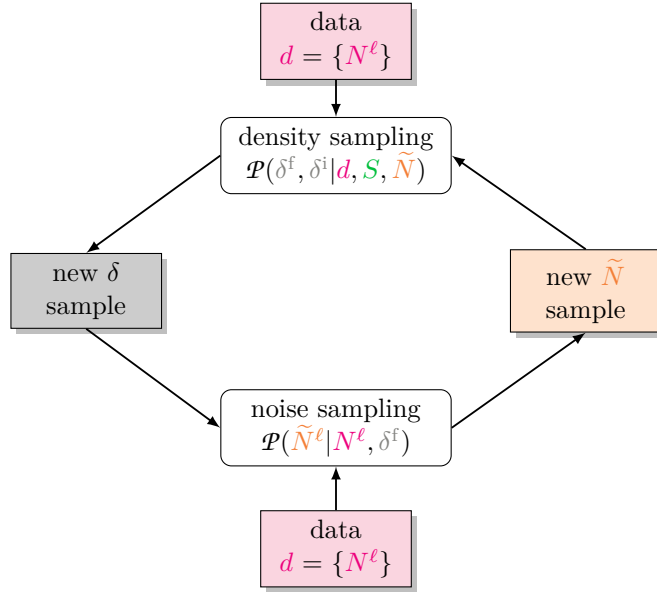


Figure 4.4: Flow chart depicting the multi-step iterative block sampling procedure. In the first step, BORG generates random realizations of the initial and final density fields conditional on the galaxy samples  $d$  and on the noise levels  $\{\tilde{N}^\ell\}$ . In a subsequent step, the noise parameters  $\tilde{N}^\ell$  are sampled conditional on the previous density realizations.

with shape parameter

$$k_\ell \equiv 1 + \sum_x N_x^\ell, \quad (4.28)$$

and scale parameter

$$\theta_\ell \equiv \frac{1}{\sum_x R_x^\ell (1 + \delta_x^f)^{\alpha^\ell}}. \quad (4.29)$$

## 4.3 Sampling procedure and numerical implementation

### 4.3.1 Calibration of the noise level

This section draws from section 3.2. in [Jasche, Leclercq & Wandelt \(2015\)](#).

Following the approach described in [Jasche & Wandelt \(2013b\)](#), density fields and noise level parameters can be jointly inferred by introducing an additional sampling block to the original implementation of the BORG algorithm. The additional sampling block is designed to provide random samples of the noise parameters  $\tilde{N}^\ell$  given the galaxy data set  $N^\ell$  and the current final density sample  $\delta^f$ .

As indicated by figure 4.4, in a first step, the algorithm infers density fields, then conditionally samples the noise parameters. Iteration of this procedure yields Markovian samples from the joint target distribution.

As demonstrated in section 4.2.4, the posterior distributions of noise parameters  $\tilde{N}^\ell$  are  $\Gamma$ -distributions. In the new sampling block, random variates of the  $\Gamma$ -distribution are generated by standard routines provided by the GNU scientific library ([Galassi et al., 2003](#)).

### 4.3.2 Hamiltonian Monte Carlo and equations of motion for the LSS density

Sampling of the posterior distribution for density fields is achieved via Hamiltonian Monte Carlo. As described in section 3.4.3, HMC permits to explore the non-linear posterior by following Hamiltonian dynamics in the high-dimensional parameter space. Omitting normalization constants, the Hamiltonian potential  $\psi(\delta^i)$  can be written as:

$$\psi(\delta^i) = -\ln \mathcal{P}(\delta^i | d, S, \tilde{N}) - \ln Z \quad (4.30)$$

$$= \psi_{\text{prior}}(\delta^i) + \psi_{\text{likelihood}}(\delta^i), \quad (4.31)$$

with the “prior potential”  $\psi_{\text{prior}}(\delta^i)$  given as

$$\psi_{\text{prior}}(\delta^i) = \frac{1}{2} \sum_{x,x'} \delta_x^i \mathbf{S}_{xx'}^{-1} \delta_{x'}^i, \quad (4.32)$$

and the “likelihood potential”  $\psi_{\text{likelihood}}(\delta^i)$  given as

$$\psi_{\text{likelihood}}(\delta^i) = \sum_{x,\ell} R_x^\ell \tilde{N}^\ell (1 + [\mathcal{G}(\delta^i)]_x)^{\alpha^\ell} - N_x^\ell \ln \left( R_x^\ell \tilde{N}^\ell (1 + [\mathcal{G}(\delta^i)]_x)^{\alpha^\ell} \right). \quad (4.33)$$

Given the above definitions of the potential  $\psi(\delta^i)$ , one can obtain the required Hamiltonian force (see equation (3.32)) by differentiating with respect to  $\delta_x^i$ :

$$\frac{\partial \psi(\delta^i)}{\partial \delta_x^i} = \frac{\partial \psi_{\text{prior}}(\delta^i)}{\partial \delta_x^i} + \frac{\partial \psi_{\text{likelihood}}(\delta^i)}{\partial \delta_x^i}. \quad (4.34)$$

The prior term is given by

$$\frac{\partial \psi_{\text{prior}}(\delta^i)}{\partial \delta_x^i} = \sum_{x'} \mathbf{S}_{xx'}^{-1} \delta_{x'}^i \quad (4.35)$$

The likelihood term cannot be obtained trivially. However, the choice of 2LPT and a CiC kernel to model  $\mathcal{G}(\delta^i)$  makes possible to derive this term analytically. This is of crucial importance, because a numerical estimation of gradients is very expensive. A detailed computation can be found in appendix D of [Jasche & Wandelt \(2013a\)](#). The result is

$$\frac{\partial \psi_{\text{likelihood}}(\delta^i)}{\partial \delta_x^i} = -D_1 J_x + D_2 \sum_{a>b} (\tau_x^{aabb} + \tau_x^{bbaa} - 2\tau_x^{abab}), \quad (4.36)$$

where  $D_1$  and  $D_2$  are the first and second-order growth factors at the desired time ( $a = 1$ ), and  $J_x$  and  $\tau_x^{abcd}$  are a vector and a tensor that depend on  $R_x^\ell$ ,  $\tilde{N}^\ell$ ,  $\alpha^\ell$ ,  $N_x^\ell$ .

Finally, the equations of motion for the Hamiltonian system can be written as

$$\frac{d\delta_x^i}{dt} = \sum_{x'} M_{xx'}^{-1} p_{x'}, \quad (4.37)$$

$$\frac{dp_x}{dt} = - \sum_{x'} \mathbf{S}_{xx'}^{-1} \delta_{x'}^i + D_1 J_x(\delta^i) - D_2 \sum_{a>b} (\tau_x^{aabb}(\delta^i) + \tau_x^{bbaa}(\delta^i) - 2\tau_x^{abab}(\delta^i)) \quad (4.38)$$

### 4.3.3 The mass matrix

As mentioned in section 3.4.3, the HMC algorithm possesses a large number of tunable parameters contained in the mass matrix  $M$ , whose choice can strongly impact the efficiency of the sampler. As shown in [Jasche & Wandelt \(2013a\)](#), section 5.2 and appendix F), a good approach to obtain suitable masses is to perform a stability analysis of the numerical leapfrog scheme (see section 4.3.4) implemented as integrator. This results in the following prescription:

$$M_{xx'} \equiv \mathbf{S}_{xx'}^{-1} - \delta_K^{xx'} D_1 \frac{\partial J_x(\delta^i)}{\partial \delta_x^i}(\xi_x), \quad (4.39)$$

where  $\delta_K$  is a Kronecker delta symbol and  $\xi_x$  is assumed to be the mean initial density contrast in high probability regions, i.e. once the sampler has moved beyond the burn-in phase.

Due to the high-dimensionality of the problem, inverting  $M$  and storing  $M^{-1}$  is computationally impractical. Therefore, a diagonal mass matrix is constructed from equation (4.39).

### 4.3.4 The leapfrog scheme integrator

For computer implementation, Hamilton’s equations, (4.37) and (4.38), must be approximated by discretizing time, using some small stepsize,  $\varepsilon$ . Several choices of integrator, such as the popular Euler’s method, are possible (see section B.5.1).

As discussed in section 3.4.3, it is essential that the adopted scheme respect reversibility and symplecticity, to ensure incompressibility in phase space. Additionally, achieving high acceptance rates require the numerical integration scheme to be very accurate in order to conserve the Hamiltonian. For these reasons, the integrator adopted for implementing BORG is the leapfrog scheme (e.g. [Birdsall & Langdon, 1985](#)), which relies on a sequence of “kick–drift–kick” operations that work as follows (see also figure B.3):

$$p_x\left(t + \frac{\varepsilon}{2}\right) = p_x(t) - \frac{\varepsilon}{2} \frac{\partial \psi(\delta^i)}{\partial \delta_x^i}(\delta_x^i(t)), \quad (4.40)$$

$$\delta_x^i(t + \varepsilon) = \delta_x^i(t) + \varepsilon \frac{p_x\left(t + \frac{\varepsilon}{2}\right)}{m_x}, \quad (4.41)$$

$$p_x(t + \varepsilon) = p_x\left(t + \frac{\varepsilon}{2}\right) - \frac{\varepsilon}{2} \frac{\partial \psi(\delta^i)}{\partial \delta_x^i}(\delta_x^i(t + \varepsilon)), \quad (4.42)$$

where  $m_x$  is the element of the diagonal mass matrix at position  $x$ .

The equations of motion are integrated by making  $n$  such steps with a finite step size  $\varepsilon$ . In order to prevent resonant trajectories, time steps are slightly randomized ( $\varepsilon$  is randomly drawn from a uniform distribution).

## 4.4 Testing BORG

Demonstrating of the performance of the BORG algorithm is the subject of sections 6 and 7 in [Jasche & Wandelt \(2013a\)](#). As these results are relevant to set the BORG SDSS analysis on firm statistical grounds, in the following, we briefly report on the original test using mock observations.

### 4.4.1 Generating mock observations

The first step is to generate an initial Gaussian random field (see section B.3). This was done on a three-dimensional Cartesian grid of  $128^3$  voxels covering a comoving cubic box of length 750 Mpc/ $h$  with periodic boundary conditions. The Fourier-space covariance matrix includes an [Eisenstein & Hu \(1998, 1999\)](#) cosmological power spectrum with baryonic wiggles. The cosmological parameters are fixed at fiducial values,

$$\Omega_\Lambda = 0.78, \Omega_m = 0.22, \Omega_b = 0.04, \sigma_8 = 0.807, h = 0.702, n_s = 0.961. \quad (4.43)$$

The Gaussian initial conditions are populated by a Lagrangian lattice of  $256^3$  particles, that are propagated forward in time using the same implementation of second-order Lagrangian perturbation theory as used in BORG. The final density field is constructed from the resultant particle distribution using the cloud-in-cell scheme. Note that it is crucial to use the 2LPT model for structure formation at this point, instead of, for example, a full  $N$ -body simulation, in order to demonstrate that BORG correctly infers the input field. Only in this fashion can we demonstrate that the BORG complicated statistical machinery works, and compare the input and output without differences due to additional physics.

An artificial tracer catalog is then generated by simulating an inhomogeneous Poisson process characterized by equations (4.13) and (4.20) (see also figure 4.3 for an illustration). For the purpose of the test run, the problem is simplified to only one luminosity bin ( $\ell = 0$ ), the mean number of galaxies  $\bar{N}^0$  is fixed, and the tracers are supposed to be unbiased (which amounts to fixing  $\alpha^0 = 1$ ,  $\beta^0 = 1$ ). However, the survey response operator  $R_x^0$  involves a highly-structured survey mask (mimicking the geometry of the Sloan Digital Sky Survey data release 7) and realistic selection functions (based on standard Schechter luminosity functions), in order to demonstrate the possibility of doing large-scale structure inference from real data sets.

### 4.4.2 Convergence and correlations of the Markov Chain

As mentioned in section 3.4.3, HMC is designed to have the target distribution as its stationary distribution. Therefore, the sampling process provides samples of the posterior distribution (equation (4.23)) after an initial burn-in phase. [Jasche & Wandelt \(2013a\)](#) showed that during this phase, of the order of 600 samples, the power spectrum converges at all scales towards the true power in the initial density field. The absence of any power excess or deficiency demonstrates the correct treatment of the response operator. The analysis also showed that burn-in also manifests itself in the acceptance rate, which has a dip around after 100 samples, then increases and asymptotes at a constant value of around 84%.

Generally, successive samples of the chain will be correlated to previous samples. The correlation length of the chain determines the amount of independent samples that can be drawn from the total chain. [Jasche & Wandelt \(2013a\)](#) estimated the correlation length to about 200 samples and obtained a total of 15,000 samples; which amounts to around 72 independent samples after burn-in.

These statistical tests demonstrate that exploring the large-scale structure posterior is numerically feasible despite the high dimensionality of the problem.

### 4.4.3 Large-scale structure inference

This section discusses the large-scale structure inferred via the application of BORG to the synthetic data set. Figure 4.5 shows slices through various three-dimensional quantities: the true initial density field, one sample of initial conditions, the posterior mean for the initial density field; the same quantities for final density fields; the posterior standard deviation in the initial and final conditions; and the mock data set.

Comparison of initial and final density fields permits to check the correspondence between structures with growing statistical complexity. Furthermore, comparison of final density fields to the data demonstrates the accuracy of the inference of the underlying dark matter density field. In particular, one can see that the algorithm extrapolates unobserved filaments between clusters, based on the physical picture of structure formation provided by 2LPT. At high redshift or near the survey boundaries, complex structures appear continuous, which proves that the algorithm augments unobserved or poorly constrained regions with statistically correct information, consistently with the structure formation model. Therefore, each individual sample is a physical dark matter realization, to the level of accuracy of 2LPT.

The variation between samples quantifies joint and correlated uncertainties. This is illustrated in figure 4.5 by unobserved regions in the posterior means, where the values in different samples average to cosmic mean density, and by the posterior standard deviations. Therefore, contrary to other reconstruction approaches found in the literature, BORG possesses a demonstrated capability of quantifying uncertainty of inferred maps, locally and globally. These uncertainties can then be propagated to any derived quantity, as we demonstrate for example with cosmic web types in chapter 9.

Finally, [Jasche & Wandelt \(2013a\)](#) demonstrated that the inferred initial density contrast follows Gaussian one-point statistics, that inferred density fields cross-correlate with the true solution as expected (i.e.  $R(k) \equiv P_{\delta_{\text{inferred}} \times \delta_{\text{true}}} / \sqrt{P_{\delta_{\text{inferred}}} P_{\delta_{\text{true}}}} \rightarrow 1$  as  $k \rightarrow 0$ ), and that BORG also infers the underlying velocity field in detail.

## 4.5 Future extensions of BORG

The method described in this chapter forms the basis of a sophisticated, but also extensible, physical large-scale structure inference framework. In particular, natural extensions of the BORG algorithm would enable automatic calibration of bias parameters (the exponents  $\alpha^\ell$  in previous sections) and of the covariance matrix of initial fluctuations (the matrix  $S$ ). This would allow precise inference of the early-time matter power spectrum from biased catalogs of tracers. As noted in the [introduction](#), this endeavor could yield a vast gain of information for the determination of cosmological parameters, in comparison to state-of-the-art techniques.

Let us consider a set of comoving wavenumbers  $\{k_n\}$  and let us denote by  $P \equiv \{P(k_n)\}$  the set of corresponding power spectrum coefficients. Since direct sampling from  $\mathcal{P}(P|d)$  is impossible, or at least difficult, [Jasche et al. \(2010a\)](#) proposed to explore the full multi-dimensional joint posterior of power spectra coefficients and density fluctuations,  $\mathcal{P}(\delta^f, P|d)$ . They employ a two-steps Gibbs sampling scheme, a method previously applied to CMB data analysis ([Wandelt, Larson & Lakshminarayanan, 2004](#); [Eriksen et al., 2004](#); [Jewell, Levin & Anderson, 2004](#)):

$$\delta^f \curvearrowright \mathcal{P}(\delta^f|P, d), \quad (4.44)$$

$$P \curvearrowright \mathcal{P}(P|\delta^f, d), \quad (4.45)$$

where the arrow denotes a random draw from the pdf on its right. The ARES code is an implementation of this scheme. It assumes the conditional independence  $\mathcal{P}(P|\delta^f, d) = \mathcal{P}(P|\delta^f)$ , which yields an inverse-Gamma distribution for power spectrum coefficients, and a Gaussian prior for  $\delta^f$  (i.e. a Wiener posterior for  $\mathcal{P}(\delta^f|P, d)$ ; see [Jasche et al., 2010a](#)). In [Jasche & Wandelt \(2013b\)](#), updates and improvements of ARES are introduced, in order to account for uncertainties arising from galaxy biases and normalizations of the galaxy density (i.e. noise levels).



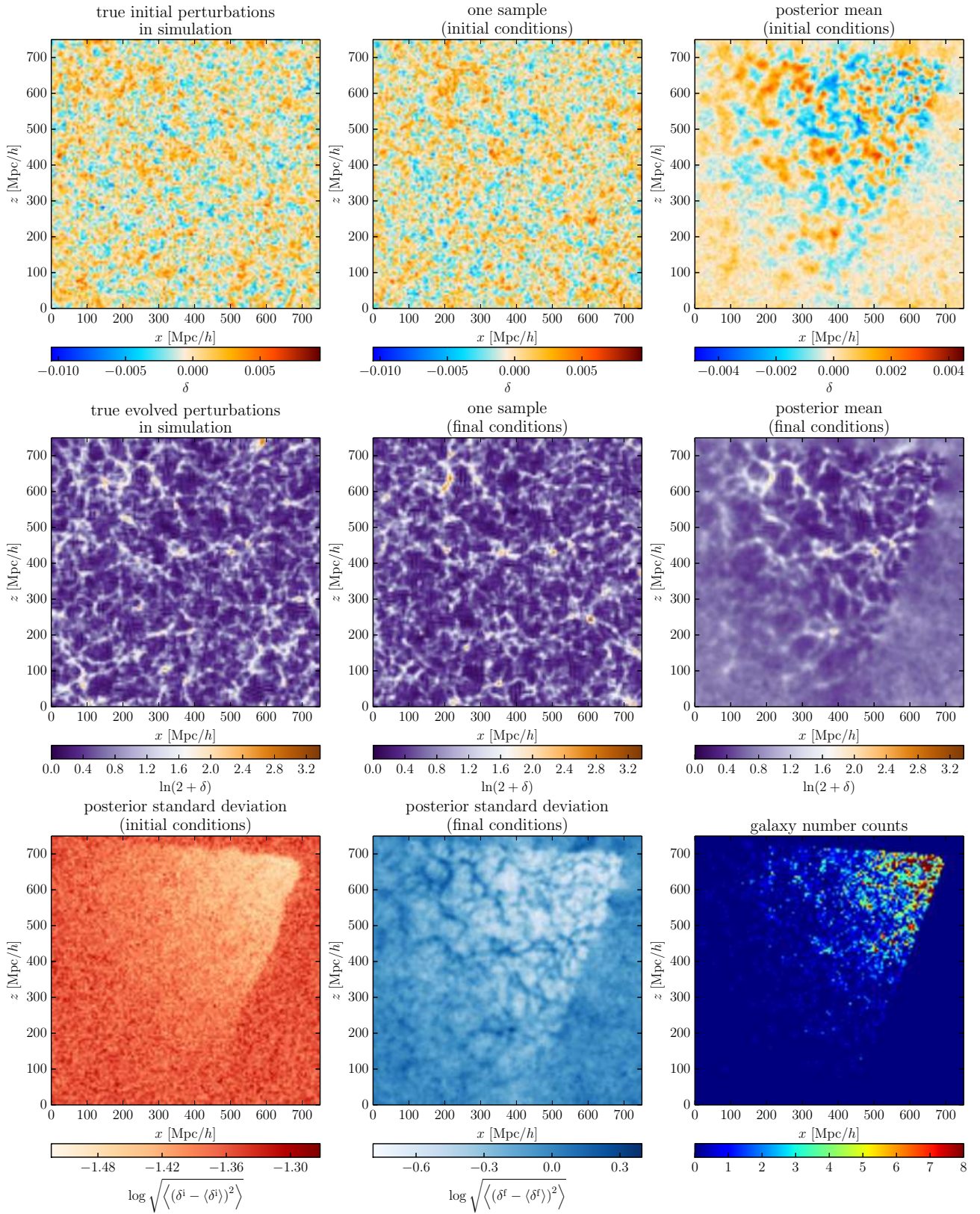


Figure 4.5: Slices through the box used for testing BORG on a synthetic data set. Various quantities (indicated above the panels) are shown. The comparison between panels illustrates the performance of BORG at inferring density fields and demonstrates its capability of quantifying uncertainties. This figure shows results originally obtained by [Jasche & Wandelt \(2013a\)](#), courtesy of Jens Jasche.

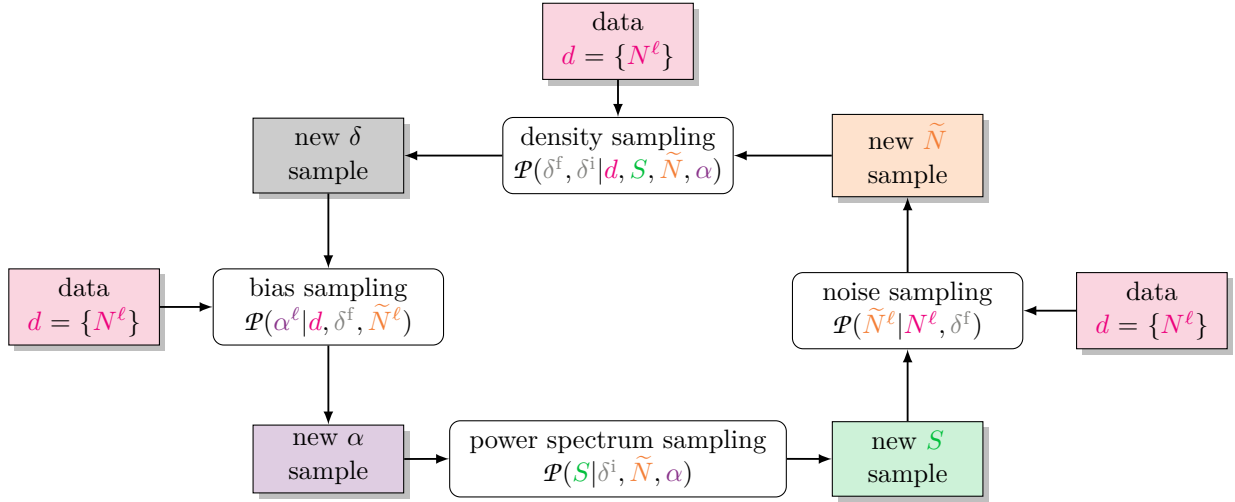


Figure 4.6: Flow chart depicting the multi-step iterative block sampling procedure for a natural extension of the BORG algorithm. In the first step, BORG generates random realizations of initial and final density fields conditional on the galaxy samples  $d$ , on the covariance matrix of initial fluctuations,  $S$ , on the noise levels  $\{\tilde{N}^\ell\}$  and on the bias parameters  $\{\alpha^\ell\}$ . In subsequent steps, the bias parameters, the covariance matrix and the noise parameters are sampled conditional on respective previous samples and on the data when necessary. Iterations of this procedure yield samples from the full joint posterior distribution,  $\mathcal{P}(\delta^f, \delta^i, S, \tilde{N}, \alpha | d)$ .

Following these ideas, an extended BORG algorithm should perform iterative block sampling according to the scheme given in figure 4.6 (for reference, see also figure 4.4 for the current BORG algorithm, and figure 1 in Jasche & Wandelt, 2013b, for the ARES algorithm). In comparison to the conditional posterior expressions written down by Jasche *et al.* (2010a) and Jasche & Wandelt (2013b), this procedure would involve the expression of  $\mathcal{P}(\alpha^\ell | d, \delta^f, \tilde{N}^\ell)$  in terms of the BORG power-law bias model (instead of the linear bias model of ARES) and of  $\mathcal{P}(S | \delta^i, \tilde{N}, \alpha)$  in terms of initial (instead of final) density fields.<sup>2</sup> In ARES, density sampling is by far the most expensive step. It can be done by constructing the Wiener-filtered map (which requires inversions of large matrices, see equations (1.27) and (1.28)) and augmenting missing fluctuations from the prior (Jasche *et al.*, 2010a), by means of HMC (Jasche & Wandelt, 2013b), or by using an auxiliary messenger field, which removes the need for matrix inversion (Jasche & Lavaux, 2015; see also Elsner & Wandelt, 2013). For the BORG data model, involving a structure formation model instead of a Gaussian prior for the galaxy density, HMC is the state-of-the-art technique.

An upcoming improvement of BORG will involve the joint sampling of density  $\delta^i$ , noise levels  $\tilde{N}^\ell$  and bias parameters  $\alpha^\ell$ . Unfortunately, computational time issues mean that joint, physical inference of density and power spectra is still out of reach. Correlation lengths are of the order of 200 samples for BORG density fields (Jasche & Wandelt, 2013a) and 100 samples for ARES power spectrum coefficients (Jasche & Wandelt, 2013b).<sup>3</sup> Preliminary tests indicate that the correlation length for the joint inference process is of the order of a few hundred samples. However, even with a correlation length of 100 samples, accurate characterization of power spectra and corresponding uncertainties require, at least, about 40,000 samples. With the current performance of the BORG sampler (discussed in sections 4.4.2 and 5.2), such a run would take several years on a typical computer. For this reason, this thesis focuses on sampling the matter density field for a fixed power spectrum of primordial fluctuations, rather than sampling this as well. Algorithmic and methodological innovations that would render such a run possible are currently being discussed but will require a considerable additional implementation effort and are outside the scope of this thesis.

<sup>2</sup> As noted in section 4.2.1.1, the Fourier-space representation of  $S$  is a diagonal matrix containing the coefficients  $\sqrt{P(k)/(2\pi)^{3/2}}$ .

<sup>3</sup> See Jasche & Wandelt, 2013b; Jewell *et al.*, 2009, for the discussion of a method designed to reduce the otherwise prohibitively long correlation length of ARES chains.





# Past and present cosmic structure in the Sloan Digital Sky Survey

## Contents

<b>5.1</b>	<b>The SDSS galaxy sample</b>	<b>80</b>
<b>5.2</b>	<b>The BORG SDSS analysis</b>	<b>80</b>
<b>5.3</b>	<b>Inference results</b>	<b>82</b>
5.3.1	Inferred 3D density fields	82
5.3.2	Inference of 3D velocity fields	86
5.3.3	Inference of LSS formation histories	86
<b>5.4</b>	<b>Summary and conclusions</b>	<b>89</b>

“Map-making had never been a precise art on the Discworld. People tended to start off with good intentions and then get so carried away with the spouting whales, monsters, waves, and other twiddly bits of cartographic furniture that they often forgot to put the boring mountains and rivers in at all.”

— Terry Pratchett (1990), *Moving Pictures*

## Abstract

We present a chrono-cosmography project, aiming at the inference of the four dimensional formation history of the observed large-scale structure from its origin to the present epoch. To do so, we perform a full-scale Bayesian analysis of the northern galactic cap of the Sloan Digital Sky Survey (SDSS) Data Release 7 main galaxy sample, relying on a fully probabilistic, physical model of the non-linearly evolved density field. Besides inferring initial conditions from observations, our methodology naturally and accurately reconstructs non-linear features at the present epoch, such as walls and filaments, corresponding to high-order correlation functions generated by late-time structure formation. Our inference framework self-consistently accounts for typical observational systematic and statistical uncertainties such as noise, survey geometry and selection effects. We further account for luminosity dependent galaxy biases and automatic noise calibration within a fully Bayesian approach. As a result, this analysis provides highly-detailed and accurate reconstructions of the present density field on scales larger than  $\sim 3$  Mpc/ $h$ , constrained by SDSS observations. This approach also leads to the first quantitative inference of plausible formation histories of the dynamic large scale structure underlying the observed galaxy distribution. The results described in this chapter constitute the first full Bayesian non-linear analysis of the cosmic large scale structure with the demonstrated capability of uncertainty quantification. Some of these results have been made publicly available along with the corresponding paper. The level of detail of inferred results and the high degree of control on observational uncertainties pave the path towards high precision chrono-cosmography, the subject of simultaneously studying the dynamics and the morphology of the inhomogeneous Universe.

This chapter is adapted from its corresponding publication, [Jasche, Leclercq & Wandelt \(2015\)](#).

This chapter describes the BORG analysis of the Sloan Digital Sky Survey Data Release 7 main galaxy sample. It is structured as follows. In section 5.1, we give a brief overview about the SDSS data set used in the analysis. In section 5.2, we demonstrate the application of the BORG inference algorithm to observations and discuss

the general performance of the Hamiltonian Monte Carlo sampler. Section 5.3 describes the inference results obtained in the course of this work. In particular, we present results on inferred 3D initial and final density as well as velocity fields and show the ability of our method to provide accurate uncertainty quantification for any finally inferred quantity. Further, we also demonstrate the ability of our methodology to perform chronocosmography, by accurately inferring plausible 4D formation histories for the observed LSS from its origins to the present epoch. In section 5.4, we conclude by summarizing and discussing the results obtained in the course of this project.

## 5.1 The SDSS galaxy sample

In this work, we follow a similar procedure as described in Jasche *et al.* (2010b), by applying the BORG algorithm to the SDSS main galaxy sample. Specifically, we employ the `Sample dr72` of the New York University Value Added Catalogue<sup>1</sup> (NYU-VAGC). This is an updated version of the catalogue originally constructed by Blanton *et al.* (2005) and is based on the final data release (DR7; Abazajian *et al.*, 2009) of the Sloan Digital Sky Survey (SDSS; York *et al.*, 2000). Based on `Sample dr72`, we construct a flux-limited galaxy sample with spectroscopically measured redshifts in the range  $0.001 < z < 0.4$ ,  $r$ -band Petrosian apparent magnitude  $r \leq 17.6$  after correction for Galactic extinction, and  $r$ -band absolute magnitude  $-21 < M_{0.1r} < -17$ . Absolute  $r$ -band magnitudes are corrected to their  $z = 0.1$  values using the  $K$ -correction code of Blanton *et al.* (2003a); Blanton & Roweis (2007) and the luminosity evolution model described in Blanton *et al.* (2003b). We also restrict our analysis to the main contiguous region of the SDSS in the northern Galactic cap, excluding the three survey strips in the southern cap (about 10 per cent of the full survey area). The NYU-VAGC provides required information on the incompleteness in our spectroscopic sample. This includes a mask, indicating which areas of the sky have been targeted and which not. The mask defines the effective area of the survey on the sky, which is  $6437 \text{ deg}^2$  for the sample we use here. This survey area is divided into a large number of smaller subareas, called *polygons*, for each of which the NYU-VAGC lists a spectroscopic completeness, defined as the fraction of photometrically identified target galaxies in the polygon for which usable spectra were obtained. Throughout our sample the average completeness is 0.92. To account for radial selection functions, defined as the fraction of galaxies in the absolute magnitude range considered here, that are within the apparent magnitude range of the sample at a given redshift, we use a standard luminosity function proposed by Schechter (1976) with  $r$ -band parameters  $\alpha = -1.05$ ,  $M_* - 5 \log_{10}(h) = -20.44$  (Blanton *et al.*, 2003c).

Our analysis accounts for luminosity dependent galaxy biases, by following the approach described in section 4.2. In order to do so, we subdivide our galaxy sample into six equidistant bins in absolute  $r$ -band magnitude in the range  $-21 < M_{0.1r} < -17$ , resulting in a total of 372,198 main sample galaxies to be used in the analysis. As described in section 4.2, splitting the galaxy sample permits us to treat each of these sub-samples as an individual data set, with its respective selection effects, biases and noise levels.

## 5.2 The BORG SDSS analysis

We performed the analysis of the SDSS main galaxy sample on a cubic Cartesian domain with a side length of  $750 \text{ Mpc}/h$  consisting of  $256^3$  equidistant grid nodes, resulting in  $\sim 1.6 \times 10^7$  inference parameters. Thus, the inference procedure provides data-constrained realizations for initial and final density fields at a grid resolution of about  $\sim 3 \text{ Mpc}/h$ . For the analysis, we assume a standard  $\Lambda\text{CDM}$  cosmology with the set of cosmological parameters

$$\Omega_\Lambda = 0.728, \Omega_m = 0.272, \Omega_b = 0.045, \sigma_8 = 0.807, h = 0.702, n_s = 0.961. \quad (5.1)$$

The cosmological power spectrum for initial density fields is calculated according to the prescription provided by Eisenstein & Hu (1998, 1999). In order to sufficiently resolve the final density field, the 2LPT model is evaluated with  $512^3$  particles, by oversampling initial conditions by a factor of eight.

We adjusted the parameters  $\alpha^\ell$  of the assumed power-law bias model during the initial 1000 sampling steps, but kept them fixed afterwards. For the purpose of this work, the power-law indices  $\alpha^\ell$  of the bias relations are determined by requiring them to resemble the linear luminosity dependent bias when expanded in a Taylor series to linear order as:

$$(1 + \delta^f)^{\alpha^\ell} = 1 + \alpha^\ell \delta^f + \mathcal{O}\left((\delta^f)^2\right). \quad (5.2)$$

<sup>1</sup> <http://sdss.physics.nyu.edu/vagc/>

$M_{0.1r}^\ell$	$\alpha^\ell$	$\tilde{N}^\ell$
$-21.00 < M_{0.1r}^0 < -20.33$	1.58029	$4.67438 \times 10^{-2} \pm 3.51298 \times 10^{-4}$
$-20.33 < M_{0.1r}^1 < -19.67$	1.41519	$9.54428 \times 10^{-2} \pm 5.77786 \times 10^{-4}$
$-19.67 < M_{0.1r}^2 < -19.00$	1.30822	$1.39989 \times 10^{-1} \pm 1.21087 \times 10^{-3}$
$-19.00 < M_{0.1r}^3 < -18.33$	1.23272	$1.74284 \times 10^{-1} \pm 1.89168 \times 10^{-3}$
$-18.33 < M_{0.1r}^4 < -17.67$	1.17424	$2.19634 \times 10^{-1} \pm 3.42586 \times 10^{-3}$
$-17.67 < M_{0.1r}^5 < -17.00$	1.12497	$2.86236 \times 10^{-1} \pm 5.57014 \times 10^{-3}$

Table 5.1: Bias and noise parameters, as described in the text, for six galaxy sub-samples, subdivided by their absolute  $r$ -band magnitudes.

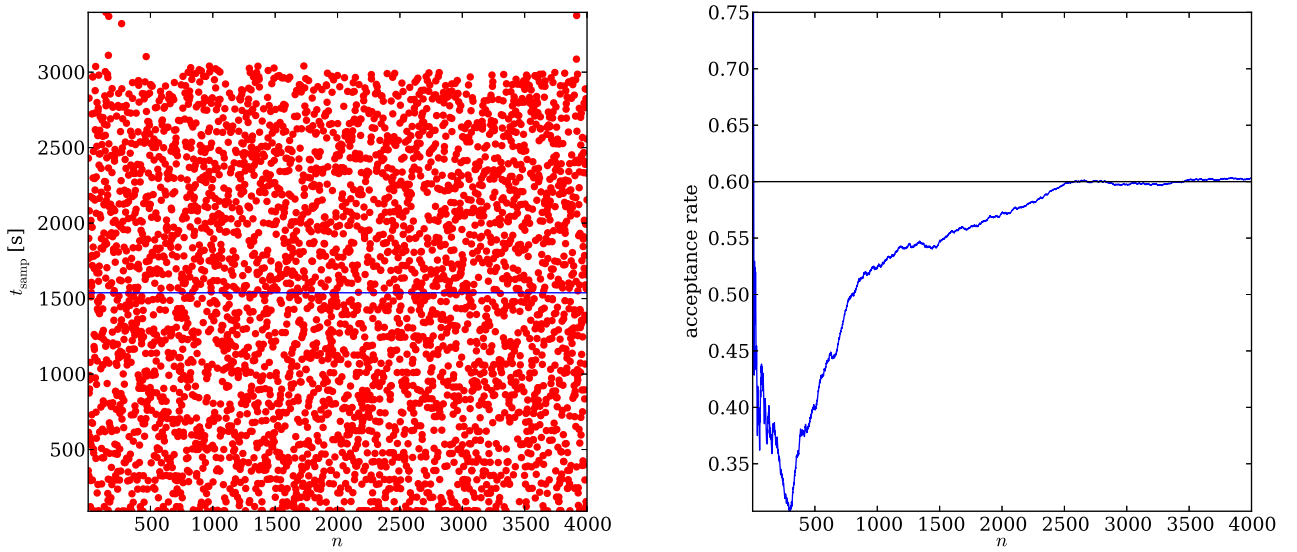


Figure 5.1: Diagnostics of the Markov chain: scatter plot of sample generation times (left panel) and Markov acceptance rates during the initial burn-in phase (right panel). As shown by the left panel, times to generate individual samples range from zero to about 3000 seconds. The average execution time per sample generation is about 1500 seconds on 16 cores. Initially, acceptance rates drop during burn-in but rise again to reach an asymptotic value of about 60 percent.

In particular, we assume the functional shape of the luminosity dependent bias parameter  $\alpha^\ell$  to follow a standard model for the linear luminosity dependent bias in terms of absolute  $r$ -band magnitudes  $M_{0.1r}$ , as given by:

$$\alpha^\ell = b(M_{0.1r}^\ell) = b_* \left( a + b \times 10^{0.4(M_* - M_{0.1r}^\ell)} + c \times (M_{0.1r}^\ell - M_*) \right), \quad (5.3)$$

with the fitting parameters  $a = 0.895$ ,  $b = 0.150$ ,  $c = -0.040$  and  $M_* = -20.40$  (see e.g. [Norberg et al., 2001](#); [Tegmark et al., 2004](#), for details). The parameter  $b_*$  was adjusted during the initial burn-in phase and was finally set to a fixed value of  $b_* = 1.44$ , such that the sampler recovers the correct shape of the assumed initial power spectrum.

As described in sections 4.2.4 and 4.3.1, contrary to bias exponents, corresponding noise parameters  $\tilde{N}^\ell$  are sampled and explored throughout the entire Markov chain. Inferred ensemble means and standard deviations for the  $\tilde{N}^\ell$  along with chosen power-law parameters  $\alpha^\ell$  are provided in table 5.1.

The entire analysis yielded 12,000 realizations for initial and final density fields. The generation of a single Markov sample requires an operation count equivalent to about  $\sim 200$  2LPT model evaluations. Typical generation times for data-constrained realizations are shown in the left panel of figure 5.1. On average the sampler requires about 1500 seconds to generate a single density field realization on 16 cores. The total analysis consumed several months of computing time and produced on the order of  $\sim 3$  TB of information represented by the set of Markov samples.

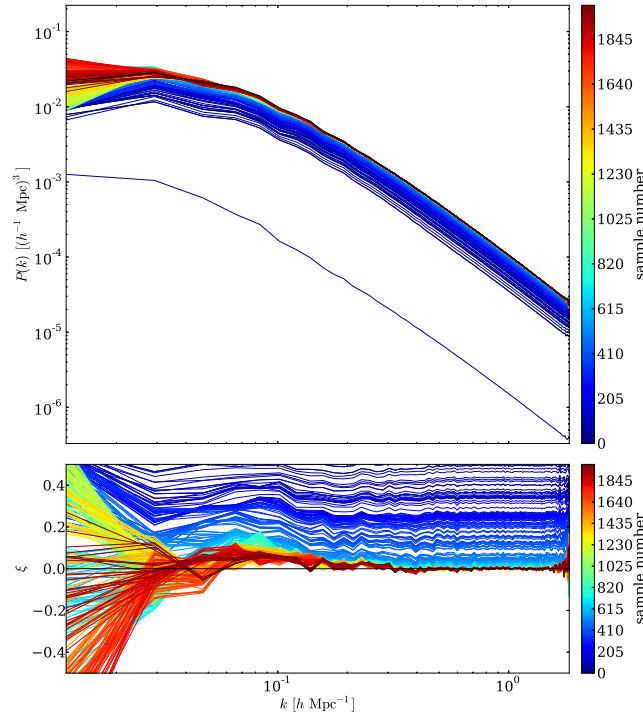


Figure 5.2: Burn-in power spectra measured from the first 2000 samples of the Markov chain colored corresponding to their sample number as indicated by the colorbar. The black line represents a fiducial reference power spectrum for the cosmology assumed in this work. Subsequent power spectra approach the fiducial cosmological power spectrum homogeneously throughout all scales in Fourier space.

The numerical efficiency of any Markov Chain Monte Carlo algorithm, particularly in high dimensions, is crucially determined by the average acceptance rate. As demonstrated by the right panel of figure 5.1, after an initial burn-in period, the acceptance rate asymptotes at a value of about 60 percent, rendering our analysis numerically feasible. As a simple consistency check, we follow a standard procedure to determine the initial burn-in behavior of the sampler via a simple experiment (see e.g. Eriksen *et al.*, 2004; Jasche & Kitaura, 2010; Jasche & Wandelt, 2013a, for more details). The sampler is initialized with an overdispersed state, far remote from the target region in parameter space, by scaling normal random amplitudes of the initial density field at a cosmic scale factor of  $a = 10^{-3}$  by a constant factor of 0.01. In the course of the initial burn-in phase, the Markov chain should then drift towards preferred regions in parameter space. As demonstrated by figure 5.2, this drift is manifested by a sequence of posterior power spectra measured from subsequent initial density field realizations. It can be clearly seen that the chain approaches the target region within the first 2000 sampling steps. The sequence of power spectra shows a homogeneous drift of all modes with no indication of any particular hysteresis or bias across different scales in Fourier space. As improper treatment of survey systematics, uncertainties and galaxy bias typically result in obvious erroneous features in power spectra, figure 5.2 clearly demonstrates that these effects have been accurately accounted for by the algorithm.

## 5.3 Inference results

This section describes inference results obtained by our Bayesian analysis of the SDSS main galaxy sample.

### 5.3.1 Inferred 3D density fields

A major goal of this work is to provide inferred 3D initial and final density fields along with corresponding uncertainty quantification in a  $\sim 1.6 \times 10^7$  dimensional parameter space. To do this, the BORG algorithm provides a sampled LSS posterior distribution in terms of an ensemble of data-constrained samples, via an efficient implementation of a Markov Chain Monte Carlo algorithm. It should be remarked that, past the initial

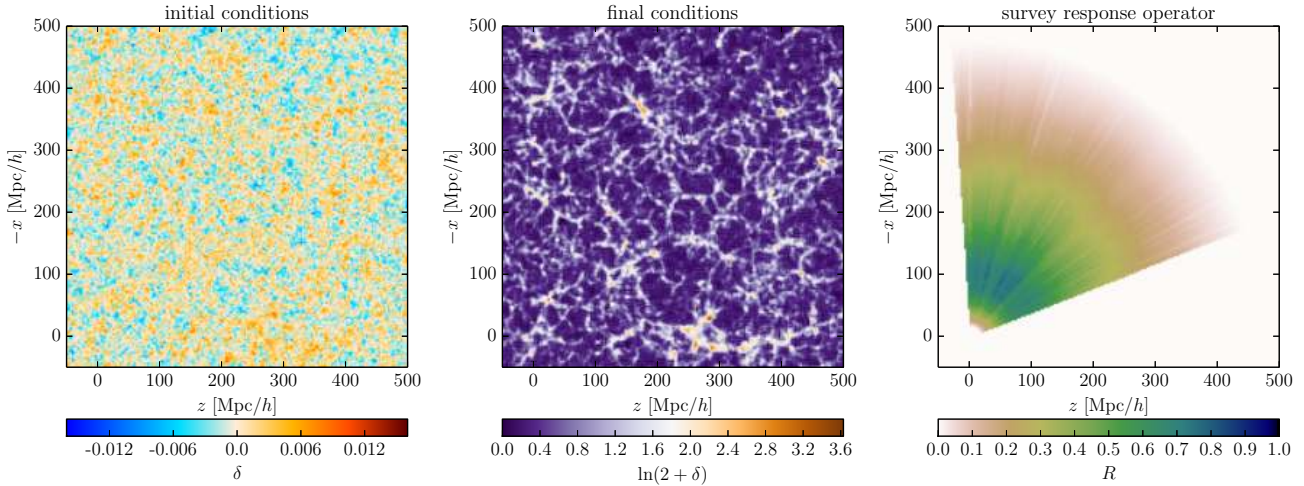


Figure 5.3: Slices through the initial (left panel) and corresponding final (middle panel) density fields of the 5000th sample. The right panel shows a corresponding slice through the combined survey response operator  $R$  for the six absolute magnitude bins considered in this work. As can be seen, unobserved and observed regions in the inferred initial and final density fields do not appear visually distinct, demonstrating the fact that individual data-constrained realizations constitute physically meaningful density fields. It also shows that the sampler naturally extends observed large scale structures beyond the survey boundaries in a physically and statistically fully consistent fashion.

burn-in phase, all individual samples reflect physically meaningful density fields, limited only by the validity of the employed 2LPT model. In particular, the present analysis correctly accounts for selection effects, survey geometries, luminosity dependent galaxy biases and automatically calibrates the noise levels of the six luminosity bins as described above. As can be seen in figure 5.2, past the initial burn-in phase, individual samples possess physically correct power throughout all ranges in Fourier space, and do not show any sign of attenuation due to survey characteristics such as survey geometry, selection effects or galaxy biases.

To further illustrate that individual samples qualify for physically meaningful density fields, in figure 5.3 we show slices through data-constrained realizations of the initial and final density fields of the 5000th sample as well as the corresponding slice through the combined survey response operator  $R$ , averaged over the six luminosity bins. It can be seen that the algorithm correctly augments unobserved regions with statistically correct information. Note that unobserved and observed regions in the inferred final density fields do not appear visually distinct, a consequence of the excellent approximation of 2LPT not just to the first but also higher-order moments (Moutarde *et al.*, 1991; Buchert, Melott & Weiß, 1994; Bouchet *et al.*, 1995; Scoccimarro, 2000; Scoccimarro & Sheth, 2002). Figure 5.3 therefore clearly reflects the fact that our sampler naturally extends observed large scale structures beyond the survey boundaries in a physically and statistically fully consistent fashion. This is a great advantage over previous methods relying on Gaussian or log-normal models specifying the statistics of the density field correctly only to two-point statistics by assuming a cosmological power spectrum. The interested reader may want to qualitatively compare with figure 2 in Jasche *et al.* (2010b), where a log-normal model, unable to represent filamentary structures, was employed.

The ensemble of the 12,000 inferred data-constrained initial and final density fields permits us to provide any desired statistical summary, such as mean and variance, for full 3D fields. In figure 5.4, we show slices through the ensemble mean initial and final density fields, to be used in subsequent analyses. The plot shows the correct anticipated behavior for inferred posterior mean final density fields, since observed regions represent data constraints, while unobserved regions approach cosmic mean density. This behavior is also present in corresponding initial density fields. In particular, the ensemble mean final density field shows a highly detailed LSS in regions where data constraints are available, and approaches cosmic mean density in regions where data are uninformative on average (see also Jasche *et al.*, 2010b, for comparison). Analogously, these results translate to the ensemble mean initial density field. Comparing the ensemble mean final density field to the galaxy number densities, depicted in the lower panels of figure 5.4, demonstrates the performance of the method in regions only poorly sampled by galaxies. In particular, comparing the right middle and right lower panel of figure 5.4 reveals the capability of our algorithm to recover highly detailed structures even in noise dominated regions (for a discussion see chapter 4 and Jasche & Wandelt, 2013a). By comparing ensemble mean initial and



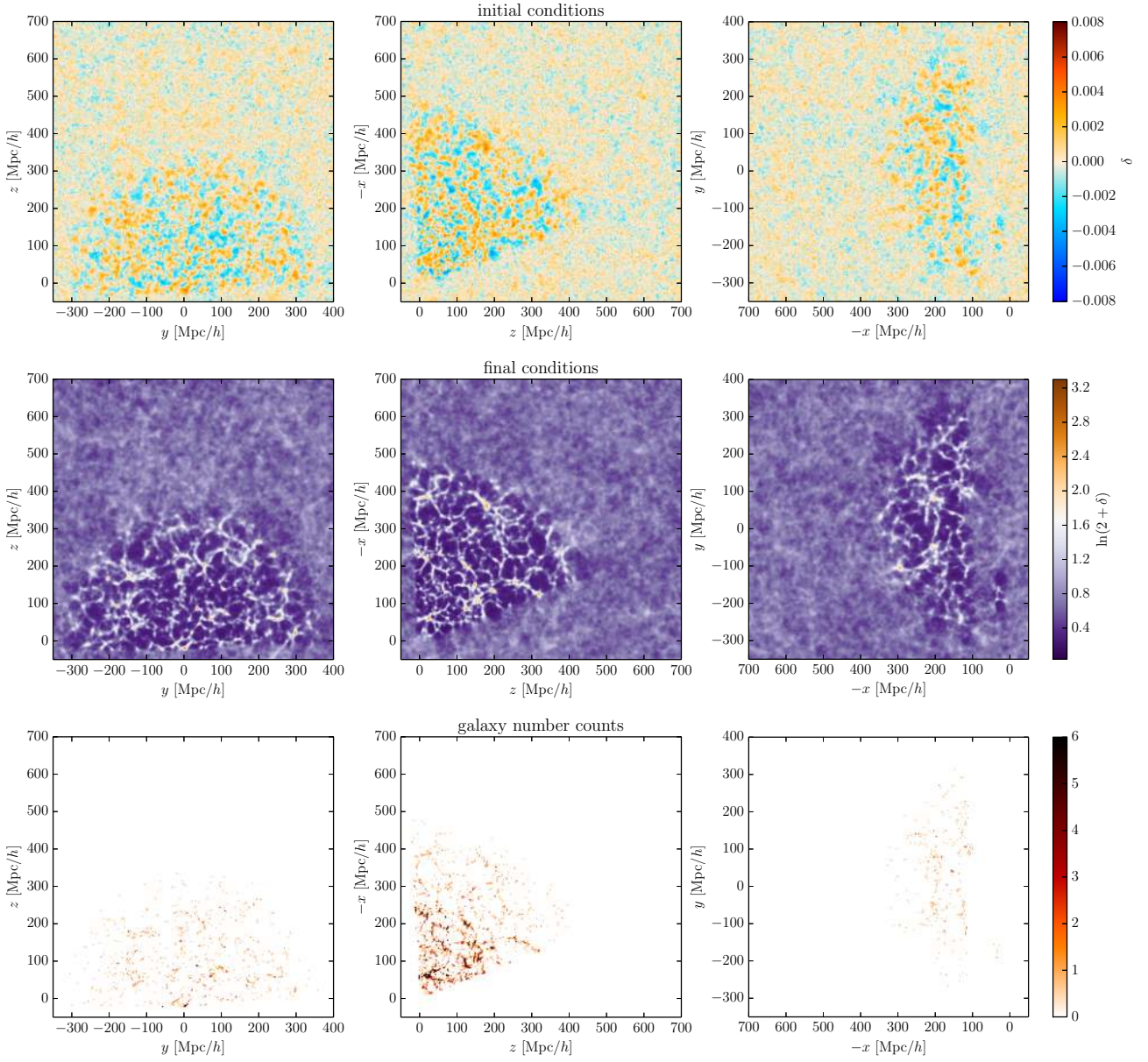


Figure 5.4: Three slices from different directions through the three dimensional ensemble posterior means for the initial (upper panels) and final density fields (middle panels) estimated from 12,000 samples. The lower panels depict corresponding slices through the galaxy number counts field of the SDSS main sample.

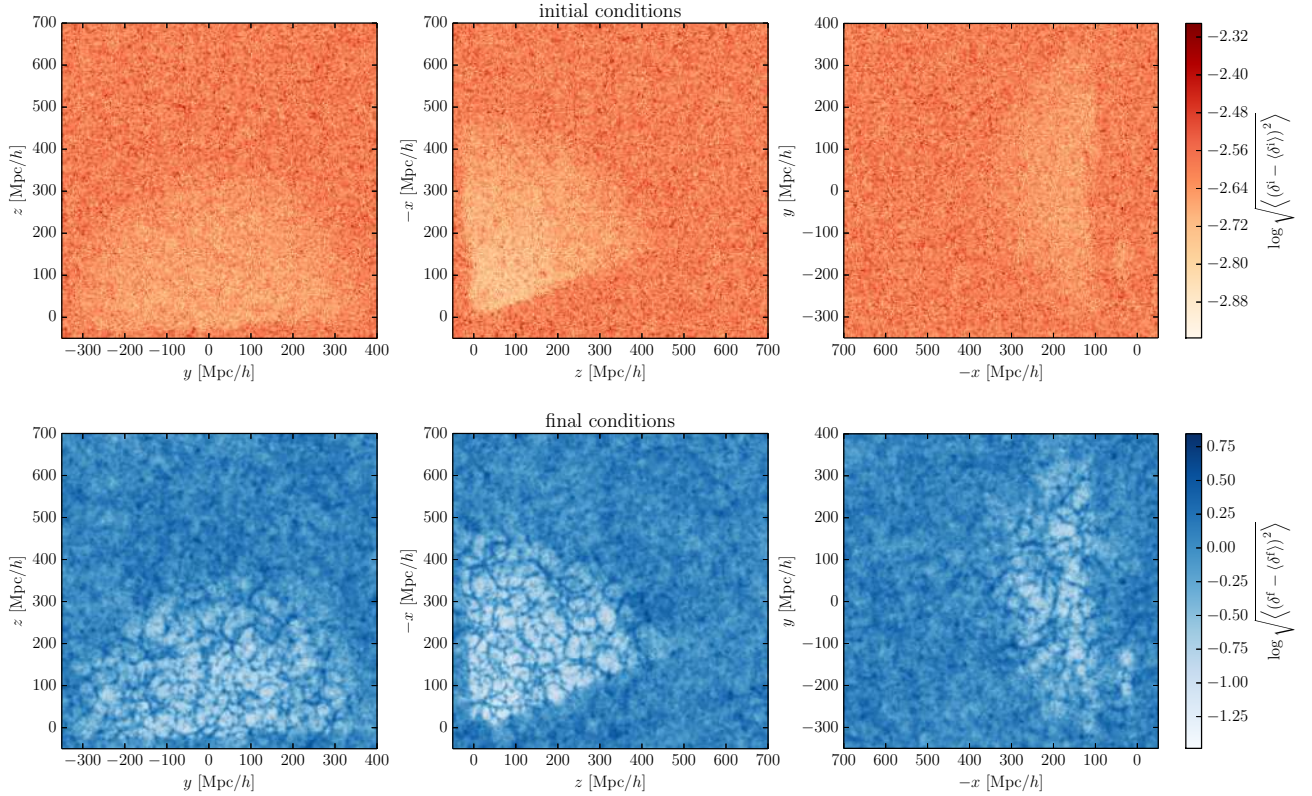


Figure 5.5: Three slices from different directions through the three dimensional voxel-wise posterior standard deviation for the initial (upper panels) and final density fields (lower panels) estimated from 12,000 samples. It can be seen that regions covered by observations show on average lower variance than unobserved regions. Also note, that voxel-wise standard deviations for the final density fields are highly structured, reflecting the signal-dependence of the inhomogeneous shot noise of the galaxy distribution. In contrast, voxel-wise standard deviations in the initial conditions are more homogeneously distributed, manifesting the flow of information between data and initial conditions as discussed in the text.

final density fields, upper and middle panels in figure 5.4, one can also see correspondences between structures in the present Universe and their origins at a scale factor of  $a = 10^{-3}$ .

The ensemble of data-constrained realizations also permits to provide corresponding uncertainty quantification. In figure 5.5 we plot voxel-wise standard deviations for initial and final density fields estimated from 12,000 samples. It can be seen that regions covered by data exhibit on average lower variances than unobserved regions, as expected. Note that for non-linear inference problems, signal and noise are typically correlated. This is particularly true for inhomogeneous point processes, such as discrete galaxy distributions tracing an underlying density field. In figure 5.5, the correlation between signal and noise is clearly visible for standard deviation estimates of final density fields. In particular high density regions also correspond to high variance regions, as is expected for Poissonian likelihoods since signal-to-noise ratios scale as the square root of the number of observed galaxies (also see Jasche *et al.*, 2010b, for a similar discussion). Also note that voxel-wise standard deviations for final density fields are highly structured, while standard deviations of initial conditions appear to be more homogeneous. This is related to the fact that our algorithm naturally and correctly translates information of the observations non-locally to the initial conditions via Lagrangian transport, as discussed below in section 5.3.3.

As mentioned in the introduction, results for the ensemble mean final density field and corresponding voxel-wise standard deviations have been published as supplementary material to the article (Jasche, Leclercq & Wandelt, 2015).<sup>2</sup>

<sup>2</sup> These data can be accessed at <http://iopscience.iop.org/1475-7516/2015/01/036>.

### 5.3.2 Inference of 3D velocity fields

In addition to initial and final density fields, the analysis further provides information on the dynamics of the large scale structure as mediated by the employed 2LPT model. Indeed, the BORG algorithm shows excellent performance in recovering large scale modes, typically poorly constrained by masked galaxy observations (Jasche & Wandelt, 2013a).

This is a crucial feature when deriving 3D velocity fields, which are predominantly governed by the largest scales. In this fashion, we can derive 3D velocity fields from our inference results. Note that these velocity fields are derived *a posteriori* and are only predictions of the 2LPT model given inferred initial density fields, since currently the algorithm does not exploit velocity information contained in the data. However, since inferred 2LPT displacement vectors are constrained by observations, and since 2LPT displacement vectors and velocities differ only by constant prefactors given a fixed cosmology, inferred velocities are considered to be accurate. For this reason, exploitation of velocity information contained in the data itself, being the subject of a future publication, is not expected to crucially change present results. To demonstrate the capability of recovering 3D velocity fields, in figure 5.6 we show the three components of the velocity field for the 5000th sample in spherical coordinates. More precisely, figure 5.6 shows the corresponding 2LPT particle distribution evolved to redshift  $z = 0$  in a 4 Mpc/h slice around the celestial equator. Particles are colored by their radial (upper panel), polar (middle panel) and azimuthal (lower panel) velocity components. To translate between Cartesian and spherical coordinates we used the standard coordinate transform,

$$x = d_{\text{com}} \cos(\lambda) \cos(\eta) \quad (5.4)$$

$$y = d_{\text{com}} \cos(\lambda) \sin(\eta) \quad (5.5)$$

$$z = d_{\text{com}} \sin(\lambda), \quad (5.6)$$

where  $\lambda$  is the declination,  $\eta$  is the right ascension and  $d_{\text{com}}$  is the radial comoving distance.

### 5.3.3 Inference of LSS formation histories

As described in chapter 4, the BORG algorithm employs a 2LPT model to connect initial conditions to present SDSS observations in a fully probabilistic approach. Besides inferred 3D initial and final density fields, our algorithm therefore also provides full four dimensional formation histories for the observed LSS as mediated by the 2LPT model. As an example, in figure 5.7 we depict the LSS formation history for the 5000th Markov sample ranging from a scale factor of  $a = 0.02$  to the present epoch at  $a = 1.00$ . Initially, the density field seems to obey close to Gaussian statistics and corresponding amplitudes are low. In the course of cosmic history, amplitudes grow and higher-order statistics such as three-point statistics are generated, as indicated by the appearance of filamentary structures. The final panel of figure 5.7, at a cosmic scale factor of  $a = 1.00$ , shows the inferred final density field overplotted by SDSS galaxies for the six bins in absolute magnitude, as described previously. Observed galaxies nicely trace the underlying density field. This clearly demonstrates that our algorithm infers plausible formation histories for large scale structures observed by the SDSS survey. By exploring the corresponding LSS posterior distribution, the BORG algorithm naturally generates an ensemble of such data-constrained LSS formation histories, permitting to accurately quantify the 4D dynamical state of our Universe and corresponding observational uncertainties inherent to galaxy surveys. Detailed and quantitative analysis of these cosmic formation histories will be the subject of forthcoming publications (see also chapter 9).

The BORG algorithm also provides a statistically valid framework for propagating observational systematics and uncertainties from observations to any finally inferred result. This is of particular importance, since detailed treatment of survey geometries and selection effects is a crucial issue if inferred results are to be used for thorough scientific analyses. These effects generally vary greatly across the observed domain and will result in erroneous artifacts if not accounted for properly. Since large scale structure formation is a non-local process, exact information propagation is complex, as it requires to translate uncertainties and systematics from observations to the inferred initial conditions. Consequently, the information content of observed data has to be distributed differently in initial and final density fields, even though the total amount of information is conserved. Following 2LPT particles from high density regions, and corresponding high signal-to-noise regions in the data, backward in time, demonstrates that the same amount of information contained in the data will be distributed over a larger region in the initial conditions. Analogously, for underdense regions, such as voids, the information content of the data will amass in a smaller volume at the initial state. This means that the signal-to-noise ratio for a given comoving Eulerian volume is a function of time along inferred cosmic histories (Jasche & Wandelt,



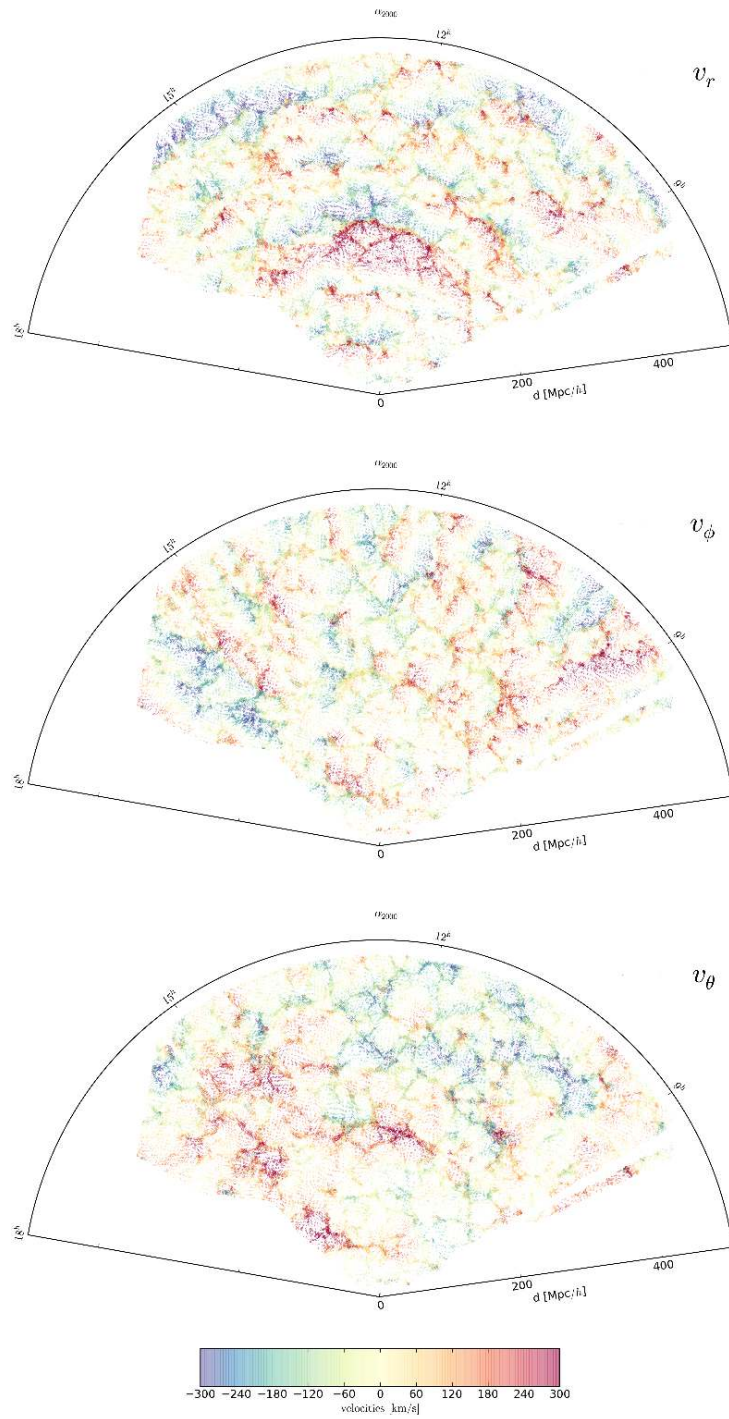


Figure 5.6: Slices through the 3D velocity fields, derived from the 5000th sample, for the radial (upper panel), polar (middle panel) and the azimuthal (lower panel) velocity components. The plot shows 2LPT particles in a  $4 \text{ Mpc}/h$  thick slice around the celestial equator for the observed domain, colored by their respective velocity components.

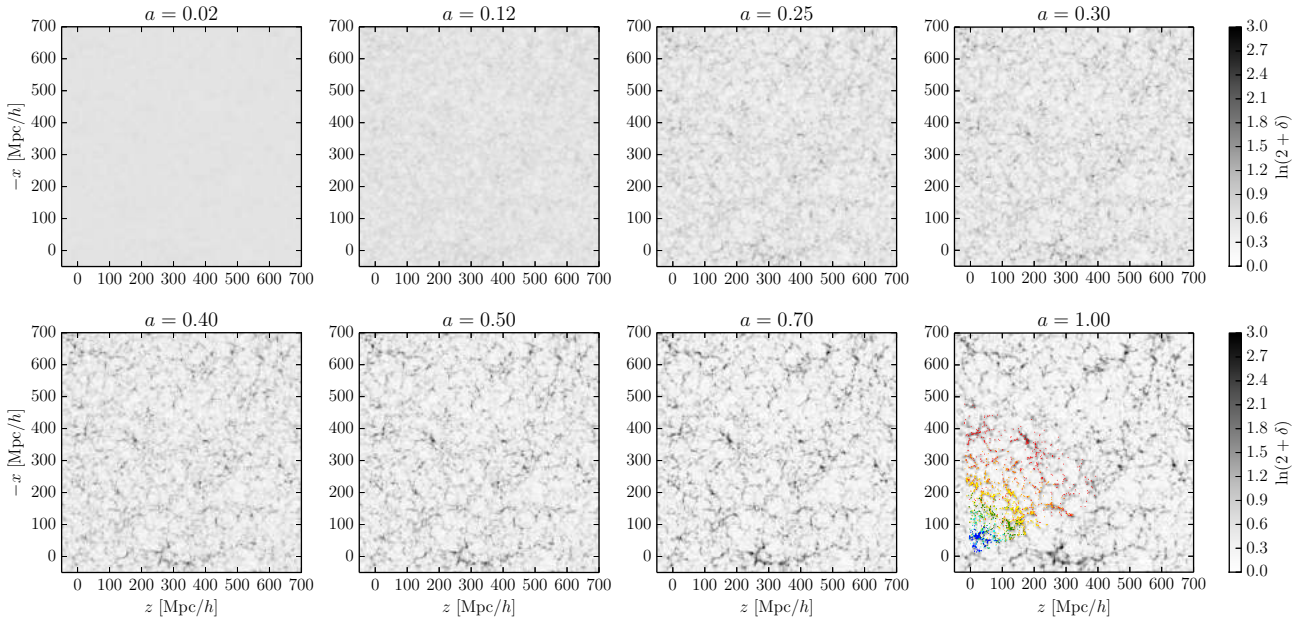


Figure 5.7: Slices through the inferred three dimensional density field of the 5000th sample at different stages of its evolution, as indicated by the cosmic scale factor in the respective panels. The plot describes a possible formation scenario for the LSS in the observed domain starting at a scale factor of  $a = 0.02$  to the present epoch  $a = 1.0$ . In the lower right panel, we overplotted the inferred present density field with the observed galaxies in the respective six absolute magnitude ranges  $-21.00 < M_{0.1r} < -20.33$  (red dots),  $-20.33 < M_{0.1r} < -19.67$  (orange dots),  $-19.67 < M_{0.1r} < -19.00$  (yellow dots),  $-19.00 < M_{0.1r} < -18.33$  (green dots),  $-18.33 < M_{0.1r} < -17.67$  (cyan dots) and  $-17.67 < M_{0.1r} < -17.00$  (blue dots). As can be clearly seen, observed galaxies trace the recovered three dimensional density field. Besides measurements of three dimensional initial and final density fields, this plot demonstrates that our algorithm also provides plausible four dimensional formation histories, describing the evolution of the presently observed LSS.

2013a). This fact manifests itself in the different behaviour of voxel-wise standard deviations for final and initial conditions, as presented in figure 5.5. While the signal-to-noise ratio is highly clustered in final conditions, the same amount of observational information is distributed more evenly over the entire volume in corresponding initial conditions.

Non-local propagation of observational information across survey boundaries, together with cosmological correlations in the initial density field, is also the reason why our method is able to extrapolate the cosmic LSS beyond survey boundaries, as discussed in section 5.3.1 above and demonstrated by figure 5.4. To further demonstrate this fact, in figure 5.8, we show the density field of the 5000th sample traced by particles from inside and outside the observed domain at the present epoch. At the present epoch, the set of particles can be sub-divided into two sets for particles inside and outside the observed domain. The boundary between these two sets of particles is the sharp outline of the SDSS survey geometry. When tracing these particles back to an earlier epoch at a scale factor of  $a = 0.02$ , it can clearly be seen that this sharp boundary starts to frazzle. Particles within the observed domain at the final state may originate from regions outside the corresponding Eulerian volume at the initial state, and vice versa. Information from within the observed domain non-locally influences the large scale structure outside the observed domain, thus increasing the region influenced by data beyond the survey boundaries. Figure 5.8 therefore demonstrates the ability of our algorithm to correctly account for information propagation via Lagrangian transport within a fully probabilistic approach. The ability to provide 4D dynamic formation histories for SDSS data together with accurate uncertainty quantification paves the path towards high precision chrono-cosmography, permitting us to study the inhomogeneous evolution of our Universe. Detailed and quantitative analysis of the various aspects of the results obtained in this chapter are discussed in part IV of this thesis and will be the subject of future publications.

## 5.4 Summary and conclusions

This chapter discusses a fully Bayesian chrono-cosmographic analysis of the 3D cosmological large scale structure underlying the SDSS main galaxy sample (Abazajian *et al.*, 2009). We presented a data application of the recently proposed BORG algorithm (see chapter 4 and Jasche & Wandelt, 2013a), which permits to simultaneously infer initial and present non-linear 3D density fields from galaxy observations within a fully probabilistic approach. As discussed in chapter 4, the algorithm incorporates a second-order Lagrangian perturbation model to connect observations to initial conditions and to perform dynamical large-scale structure inference from galaxy redshift surveys.

Besides correctly accounting for usual statistical and systematic uncertainties, such as noise, survey geometries and selection effects, this methodology also physically treats gravitational structure formation in the linear and mildly non-linear regime and captures higher-order statistics present in non-linear density fields (see e.g. Moutarde *et al.*, 1991; Buchert, Melott & Weiß, 1994; Bouchet *et al.*, 1995; Scoccimarro, 2000; Scoccimarro & Sheth, 2002). The BORG algorithm explores a high-dimensional posterior distribution via an efficient implementation of a Hamiltonian Monte Carlo sampler and therefore provides naturally and fully self-consistently accurate uncertainty quantification for any finally inferred quantity.

In the paper corresponding to this work (Jasche, Leclercq & Wandelt, 2015), we upgraded the original sampling procedure described in Jasche & Wandelt (2013a) to account for automatic noise calibration and luminosity dependent galaxy biases (see sections 4.2.4 and 4.3.1). To do so, we followed the philosophy described in Jasche & Wandelt (2013b) and splitted the main galaxy sample into six absolute magnitude bins in the range  $-21 < M_{0.1r} < -17$ . The Bayesian analysis treats each of this six galaxy sub-samples as an individual data set with its individual statistical and systematic uncertainties. As described in sections 4.2.4 and 4.3.1, the original algorithm described in Jasche & Wandelt (2013a) has been augmented by a power-law bias model and an additional sampling procedure to jointly infer corresponding noise levels for the respective galaxy samples.

As discussed in section 5.2, we applied this modified version of the BORG algorithm to the SDSS DR7 main galaxy samples and generated about 12,000 full three dimensional data-constrained initial conditions in the course of this work. The initial density field, at a scale factor of  $a = 10^{-3}$ , has been inferred on a comoving Cartesian equidistant grid, of side length 750 Mpc/ $h$  and  $256^3$  grid nodes. This amounts to a target resolution of about  $\sim 3$  Mpc/ $h$  for respective volume elements. Density amplitudes at these Lagrangian grid nodes correspond to about  $\sim 10^7$  parameters to be constrained by our inference procedure. Typically, the generation of individual data-constrained realizations involves an equivalent of  $\sim 200$  2LPT evaluations and requires on the order of 1500 seconds on 16 cores. Despite the complexity of the problem, we demonstrated that our sampler

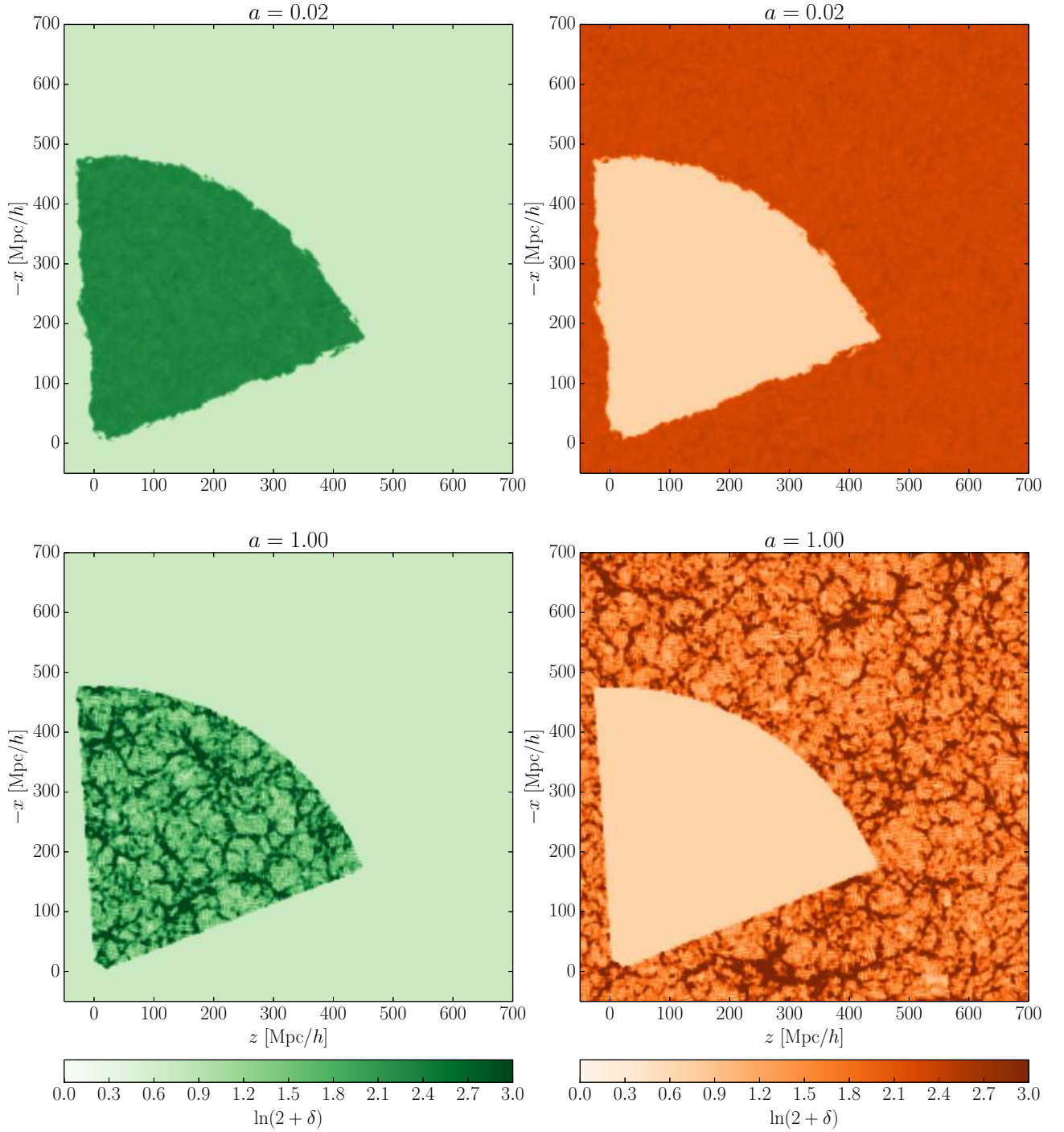


Figure 5.8: Slices through the distribution of particles in the 5000th sample, which are located inside (left panels) and outside (right panels) the observed domain at the time of observation, at two time snapshots as indicated above the panels. It can be seen that particles located within the observed region at the present time may originate from regions outside the corresponding comoving Eulerian volume at an earlier epoch and vice versa. As discussed in the text, this plot demonstrates the non-local transport of information, which provides accurate inference of the cosmic large scale structure beyond survey boundaries within a rigorous probabilistic approach.



can explore multi-million dimensional parameter spaces via efficient Markov Chain Monte Carlo algorithms with an asymptotic acceptance rate of about 60 percent, rendering our numerical inference framework numerically feasible.

To test the performance of the sampler, we followed a standard approach for testing the initial burn-in behavior via experiments (see e.g. Eriksen *et al.*, 2004; Jasche & Kitaura, 2010; Jasche & Wandelt, 2013a). We initialized the sampler with a Gaussian random field scaled by a factor of 0.01, to start from an over-dispersed state. During an initial burn-in period the sampler performed a systematic drift towards the target region in parameter space. We examined the initial burn-in behavior by following the sequence of *a posteriori* power spectra, measured from the first 2500 samples, and showed that subsequent samples homogeneously approach the target spectrum throughout all regions in Fourier space without any sign of hysteresis. This indicates the efficiency of the sampler to rapidly explore all scales of the inference problem. The absence of any particular bias or erroneous power throughout all scales in Fourier space, further demonstrates the fact that survey geometry, selection effects, galaxy biasing and observational noise have been accurately accounted for in this analysis. These *a posteriori* power spectra also indicate that individual data-constrained realizations possess the correct physical power in all regions in Fourier space, and can therefore be considered as physically meaningful density fields. This fact has been further demonstrated in section 5.3.1 by showing slices through an arbitrary data-constrained realization. These results clearly demonstrate the power of our Bayesian methodology to correctly treat the ill-posed inverse problem of inferring signals from incomplete observations, by augmenting unobserved regions with statistically and physically meaningful information. In particular, constrained and unconstrained regions in the samples are visually indistinguishable, demonstrating a major improvement over previous approaches, typically relying on Gaussian or log-normal statistics, incapable of representing the filamentary structure of the cosmic web (see e.g. Jasche & Kitaura, 2010). It should be remarked that this fact not only demonstrates the ability to access high-order statistics in finally inferred quantities such as 3D density maps, but also reflects the control of high-order statistics in uncertainty quantification far beyond standard normal statistics.

The ensemble of 12,000 full 3D data-constrained samples permits us to estimate any desired statistical summary. In particular, in section 5.3.1, we showed ensemble mean density fields for final and initial conditions. A particularly interesting aspect is the fact that the algorithm manages to infer highly-detailed large scale structures even in regimes only poorly covered by observations (for further comments see chapter 4 and Jasche & Wandelt, 2013a). To demonstrate the possibility of uncertainty quantification, we also calculated the ensemble voxel-wise posterior standard deviation, which reflects the degree of statistical uncertainty at every volume element in the inference domain. As discussed in section 5.3.1, these results clearly reflect the signal-dependence of noise for any inhomogeneous point processes, such as discrete Poissonian galaxy distribution. As expected, high signal regions correspond to high variance regions. These results further demonstrate the ability to accurately translate uncertainties in the final conditions to initial density fields, as demonstrated by the plots of voxel-wise standard deviations for corresponding initial density fields. However, note that voxel-wise standard deviations are just an approximation to the full joint and correlated uncertainty that otherwise can be correctly quantified by considering the entire set of data-constrained realizations. Besides 3D initial and final density fields, the methodology also provides information on cosmic dynamics, as mediated by the 2LPT model. In section 5.3.2, we showed a velocity field realization in one sample. In particular, we showed the radial, polar and azimuthal velocity components in a 4 Mpc/h thick slice around the celestial equator for the observed domain. These velocities are not primarily constrained by observations, but are derived from the 2LPT model. However, since 2LPT displacement vectors are data-constrained, and since displacement vectors and velocities differ only by constant factors independent of the inference process, derived velocities are considered to be accurate.

As pointed out frequently, the BORG algorithm employs 2LPT as a dynamical model to connect initial conditions to present observations of SDSS galaxies. As a consequence, the algorithm not only provides 3D density and velocity fields but also infers plausible 4D formation histories for the observed LSS. In section 5.3.3, we illustrated this feature with an individual sample. We followed its cosmic evolution from a initial scale factor of  $a = 0.02$  to the present epoch at  $a = 1.00$ . As could be seen, the initial density field appears homogeneous and obeys Gaussian statistics. In the course of structure formation clusters, filaments and voids are formed. To demonstrate that this formation history correctly recovers the observed large scale structure, we plotted the observed galaxies, for the six luminosity bins, on top of the final density field. These results clearly demonstrate the ability of our algorithm to infer plausible large scale structure formation histories compatible with observations. Additionally, since the BORG algorithm is a full Bayesian inference framework, it not only provides a single 4D history, but an ensemble of such data-constrained formation histories and thus accurate means to quantify corresponding observational uncertainties. In particular, our methodology correctly accounts

for the non-local transport of observational information between present observations and corresponding inferred initial conditions. As discussed in section 5.3.3, the information content in initial and final conditions has to be conserved but can be distributed differently. High-density regions in the final conditions, typically coinciding with high signal-to-noise regions in the data, form by clustering of matter which was originally distributed over a larger Eulerian volume in the initial conditions. For this reason, the observational information associated to a cluster in the final density field will be distributed over a larger volume in the corresponding initial density field. Conversely, the information content of voids in the final conditions will be confined to a smaller volume in the initial conditions. This fact is also reflected by the analysis of voxel-wise standard deviations presented in section 5.3.1. While the signal-to-noise ratio is highly clustered in the final conditions, the same amount of observational information is distributed more homogeneously over the entire volume in corresponding initial conditions. As discussed in section 5.3.3, particles within the observed domain at the final state may originate from regions outside the corresponding comoving Eulerian volume in the initial conditions and vice versa (also see chapter 4 and Jasche & Wandelt, 2013a). This non-local translation of information along Lagrangian trajectories is also the reason for the ability of our methodology to extrapolate beyond the survey boundaries of the SDSS and infer the LSS there within a fully probabilistic and rigorous approach. In particular, the high degree of control on statistical uncertainties permit us to perform accurate inferences on the nature of initial conditions and formation histories for the observed LSS in these regions. For these reasons we believe that inferred final ensemble mean fields and corresponding voxel-wise standard deviations as a means of uncertainty quantification, may be of interest to the scientific community. These data products have been published as supplementary material along with the article, and are accessible at <http://iopscience.iop.org/1475-7516/2015/01/036>.

In summary, this chapter describes an application of the previously proposed BORG algorithm to the SDSS DR7 main galaxy sample. As demonstrated, our methodology produces a rich variety of scientific results, various aspects of which are objects of detailed and quantitative analyses in subsequent chapters of this thesis and forthcoming publications. Besides pure three dimensional reconstructions of the present density field, the algorithm provides detailed information on corresponding initial conditions, large scale dynamics and formation histories for the observed LSS. Together with a thorough quantification of joint and correlated observational uncertainties, these results mark the first steps towards high precision chrono-cosmography, the subject of analyzing the four dimensional state of our Universe.

## **Part III**

# **The non-linear regime of structure formation**





# Remapping Lagrangian perturbation theory

## Contents

<b>6.1</b>	<b>Introduction</b>	<b>95</b>
<b>6.2</b>	<b>Method</b>	<b>97</b>
6.2.1	Remapping procedure	97
6.2.2	Comparison of structure types in LPT and in $N$ -body dynamics	99
6.2.3	Improvement of the remapping procedure	100
6.2.4	Remapping function and transfer function	100
<b>6.3</b>	<b>Statistics of remapped fields</b>	<b>101</b>
6.3.1	One-point statistics	103
6.3.2	Two-point statistics	105
6.3.3	Three-point statistics	105
<b>6.4</b>	<b>Discussion and conclusion</b>	<b>106</b>

---

“Everyone thinks of changing the world, but no one thinks of changing himself.”

— Leo Tolstoy

Quoted in [Bryan, Cameron & Allen \(1999\)](#), *The Artist’s Way at Work: Riding the Dragon*

---

## Abstract

On the smallest scales, three-dimensional large-scale structure surveys contain a wealth of cosmological information which cannot be trivially extracted due to the non-linear dynamical evolution of the density field. Lagrangian perturbation theory is widely applied to the generation of mock halo catalogs and data analysis. In this chapter, we propose a method designed to improve the correspondence between these density fields, in the mildly non-linear regime. We develop a computationally fast and flexible tool for a variety of cosmological applications. Our method is based on a remapping of the approximately-evolved density field, using information extracted from  $N$ -body simulations. The remapping procedure consists of replacing the one-point distribution of the density contrast by one which better accounts for the full gravitational dynamics. As a result, we obtain a physically more pertinent density field on a point-by-point basis, while also improving higher-order statistics predicted by LPT. We quantify the approximation error in the power spectrum and in the bispectrum as a function of scale and redshift. Our remapping procedures improves one-, two- and three-point statistics at scales down to 8 Mpc/ $h$ .

This chapter is adapted from its corresponding publication, [Leclercq et al. \(2013\)](#).

## 6.1 Introduction

At present, observations of the three-dimensional LSS are major sources of information on the origin and evolution of the Universe. According to the current paradigm of cosmological structure formation, the presently observed structures formed via gravitational clustering of cold dark matter particles and condensation of baryonic matter in gravitational potential wells. Consequently, the large-scale matter distribution retains a memory of

its formation history, enabling us to study the homogeneous as well as the inhomogeneous evolution of our Universe.

Due to non-linearities involved in the formation process, at present there exists just limited analytic understanding of structure formation in terms of perturbative expansions in Eulerian or Lagrangian representations. Both of these approaches rely on a truncated sequence of momentum moments of the Vlasov-Poisson system, completed by fluid dynamic assumptions (see chapter 1 or e.g. [Bernardeau et al., 2002](#), and references therein). For this reason, the validity of these approaches ceases, once the evolution of the LSS enters the multi-stream regime (see e.g. [Pueblas & Scoccimarro, 2009](#)).

Nevertheless, Eulerian and Lagrangian approximations have been successfully applied to the analysis of three-dimensional density fields in regimes where they are still applicable, either at large scales or in the early Universe. Particularly, LPT captures significant mode-coupling information that is encoded beyond linear theory, such as large-scale flows and free-streaming, yielding three-dimensional matter distributions approximating those of full scale numerical simulations with reasonable accuracy ([Moutarde et al., 1991](#); [Buchert, Melott & Weiß, 1994](#); [Bouchet et al., 1995](#); [Scoccimarro, 1998, 2000](#); [Scoccimarro & Sheth, 2002](#); [Yoshisato et al., 2006](#)). Especially, second-order Lagrangian perturbation theory has been widely applied in data analysis and for fast generation of galaxy mock catalogs (e.g. PTHALOS: [Scoccimarro & Sheth, 2002](#); [Manera et al., 2013](#); PINOCHIO: [Monaco et al., 2002](#); [Monaco, Theuns & Taffoni, 2002](#); [Taffoni, Monaco & Theuns, 2002](#); [Heisenberg, Schäfer & Bartelmann, 2011](#); [Monaco et al., 2013](#)) that can be useful to estimate error bounds when analyzing observations.

Modern cosmological data analysis has an increasing demand for analytic and computationally inexpensive models providing accurate representations of the mildly non-linear regime of structure formation. Over the years, various non-linear approximations and attempts to extend the validity of LPT have been proposed (see section 1.6). These include the spherical collapse model ([Gunn & Gott, 1972](#); [Bernardeau, 1994](#)), the truncated Zel'dovich approximation ([Melott, Pellman & Shandarin, 1994](#)) and models with various forms for the velocity potential ([Coles, Melott & Shandarin, 1993](#); [Munshi & Starobinsky, 1994](#)) or the addition of a viscosity term in the Euler equation (the adhesion model, [Gurbatov, Saichev & Shandarin, 1989](#)). Analytical techniques to improve the convergence and behavior of standard perturbation theory, successfully employed in quantum field theory and statistical physics, have also been applied in the context of gravitational clustering. These include renormalized perturbation theory ([Crocce & Scoccimarro, 2006](#)), the path integral formalism ([Valageas, 2007](#)), and the renormalization group flow ([Matarrese, Verde & Heavens, 1997](#)). More recently, [Tassev & Zaldarriaga \(2012a,c\)](#) constructed a physical picture of the matter distribution in the mildly non-linear regime, and developed a method yielding improvements over LPT ([Tassev, Zaldarriaga & Eisenstein, 2013](#)), in particular at the scales relevant for baryon acoustic peak reconstruction ([Tassev & Zaldarriaga, 2012b](#)).

In this chapter, we propose a numerically efficient method designed to improve the correspondence between approximate models and full numerical simulations of gravitational large-scale structure formation. Generally, it can be applied to any approximate model of gravitational instability, but it is especially targeted to improving Lagrangian methods. We illustrate both these methods on fields evolved with LPT: at order one, the Zel'dovich approximation ([Zel'dovich, 1970](#); [Shandarin & Zel'dovich, 1989](#)) and second-order Lagrangian perturbation theory.

LPT and  $N$ -body density fields are visually similar, which suggests that the properties of LPT could be improved by one-to-one mapping in voxel space, following a similar line of thoughts as the “Gaussianization” idea originally proposed by [Weinberg \(1992\)](#) and inspired existing techniques, widely used in cosmology ([Melott, 1993](#); [Croft et al., 1998](#); [Narayanan & Weinberg, 1998](#); [Croft et al., 1999](#); [Feng & Fang, 2000](#); [Neyrinck, Szapudi & Szalay, 2011](#); [Yu et al., 2011, 2012](#); [Neyrinck & Yang, 2013](#)). The method described in this chapter is based on a *remapping* of the approximately evolved particle distribution using information extracted from  $N$ -body simulations. It basically consists of replacing the one-point distribution of the approximately evolved distribution by one which better accounts for the full gravitational system. In this fashion, we adjust the one-point distribution to construct a physically more reasonable representation of the three-dimensional matter distribution, while retaining or improving higher order statistics, described already reasonably well by the ZA ([Zel'dovich, 1970](#); [Doroshkevich, 1970a](#); [Shandarin & Zel'dovich, 1989](#); [Buchert, 1989](#); [Moutarde et al., 1991](#); [Yoshisato et al., 2006](#)) and by 2LPT ([Moutarde et al., 1991](#); [Buchert, Melott & Weiß, 1994](#); [Bouchet et al., 1995](#); [Scoccimarro, 1998, 2000](#); [Scoccimarro & Sheth, 2002](#)).

Major problems with naive approaches to remapping LPT density fields arise from minor deviations in structure types represented by LPT models and full gravity. For this reason, in chapter 2, we discussed the different representations of clusters, voids, sheets, and filaments, predicted by LPT and  $N$ -body simulations.

Besides being of general interest for LSS data analysis, the insights gained from this comparison will allow us to improve the remapping procedure.

Implementing and testing the accuracy and the regime of validity of our method is essential, and is subject of the present chapter. Our study quantifies the approximation error as a function of scale in terms of a set of statistical diagnostics. From cosmographic measurements,  $\sigma_8$  is known to be of order unity, which means that gravity becomes highly non-linear at some scale around 8 Mpc/h. Our method is expected to break down due to shell-crossing in LPT, at some scale larger than 8 Mpc/h. Achieving a resolution of 16 Mpc/h would already constitute substantial improvement with respect to existing methods, since non-linearities begin to affect even large-scale cosmographic measurements such as the determination of the baryon acoustic oscillations scale from galaxy surveys (about 125 Mpc/h, e.g. [Eisenstein et al., 2005](#)). However, we explore the validity of the improvement at 8 Mpc/h down to 4 Mpc/h, to see to what extent we can push the limit for possible data analysis applications into the non-linear regime. Recall that in three-dimensional LSS surveys, the number of modes usable for cosmological exploitation scales as the cube of the largest wavenumber,  $k^3$ , meaning that even minor improvements in the mildly non-linear regime would give access to much more cosmological information from existing and upcoming observations.

As will be demonstrated, this method can be used to generate realizations of density fields much faster than  $N$ -body simulations. Even though approximate, these fast realizations of mock density fields may be sufficient to model the salient features of the non-linear density field for certain applications.

This chapter is structured as follows. In section 6.2, we describe the remapping procedure for the density contrast of present-day density fields, analyze the obstacles to straightforward application and present an improved method. In section 6.3, we apply the procedure to cosmological models using data from numerical simulations, we study the statistics of remapped fields and quantify the approximation error. We discuss our results and give our conclusions in section 6.4.

The setup of LPT and  $N$ -body simulations used in this chapter are described at the beginning of chapter 2.

## 6.2 Method

In this section, we discuss the remapping procedure and apply it to cosmological density fields evolved with LPT. Naively following the approach of [Weinberg \(1992\)](#) for present-day density fields yields the procedure described in section 6.2.1. This approach is not entirely satisfactory and we analyze the reasons for its shortcomings in section 6.2.2. In consequence, we propose a improvement of the remapping procedure in section 6.2.3. The properties of the remapping function are examined in section 6.2.4.

### 6.2.1 Remapping procedure

In this section, we describe the remapping algorithm used to go from a low-redshift realization of a density field evolved with LPT to one evolved with full  $N$ -body gravitational dynamics. Note that both fields obey the same initial conditions but are evolved by different physical models.

Density fields are defined on Cartesian grids of cubic voxels. Linear gravitational evolution exactly maintains the relative amplitude of fluctuations in different voxels. Due to mode coupling, positive and negative fluctuations grow at different rates in the non-linear regime, but even non-linear evolution tends to preserve the *rank order* of the voxels, sorted by density.

The one-point probability distribution functions and the cumulative distribution functions (cdf) of the final density fields, evolved with either LPT or full  $N$ -body gravitational dynamics, exhibit similar, but not identical shapes. This result suggests a way to improve the approximation with information extracted from the  $N$ -body simulation: maintain the rank order of the voxels, but reassign densities so that the two cdfs match. The method therefore resembles the ‘‘Gaussianization’’ procedure proposed by [Weinberg \(1992\)](#), an attempt to reconstruct the initial conditions of a density field from its final cdf.

Let  $\mathcal{P}_{\text{LPT}}$  and  $\mathcal{P}_{\text{Nbody}}$  denote the probability distribution functions for the density contrast in the LPT and in the full  $N$ -body density fields, respectively. Let  $\mathcal{C}_{\text{LPT}}$  and  $\mathcal{C}_{\text{Nbody}}$  be their integrals, the cumulative distribution functions.  $\mathcal{C}_{\text{LPT}}(\delta_{\text{LPT}})$  is the *fractional rank* for  $\delta_{\text{LPT}}$  i.e. the probability that the density contrast at a given voxel is smaller than  $\delta_{\text{LPT}}$ ,  $\mathcal{P}_{\text{LPT}}(\delta \leq \delta_{\text{LPT}})$ , and the analogous for the  $N$ -body field. The remapping procedure works as follows. A voxel with rank order  $\delta_{\text{LPT}}$  is assigned a new density  $\delta_{\text{Nbody}}$  such that

$$\mathcal{C}_{\text{LPT}}(\delta_{\text{LPT}}) = \mathcal{C}_{\text{Nbody}}(\delta_{\text{Nbody}}) \quad (6.1)$$

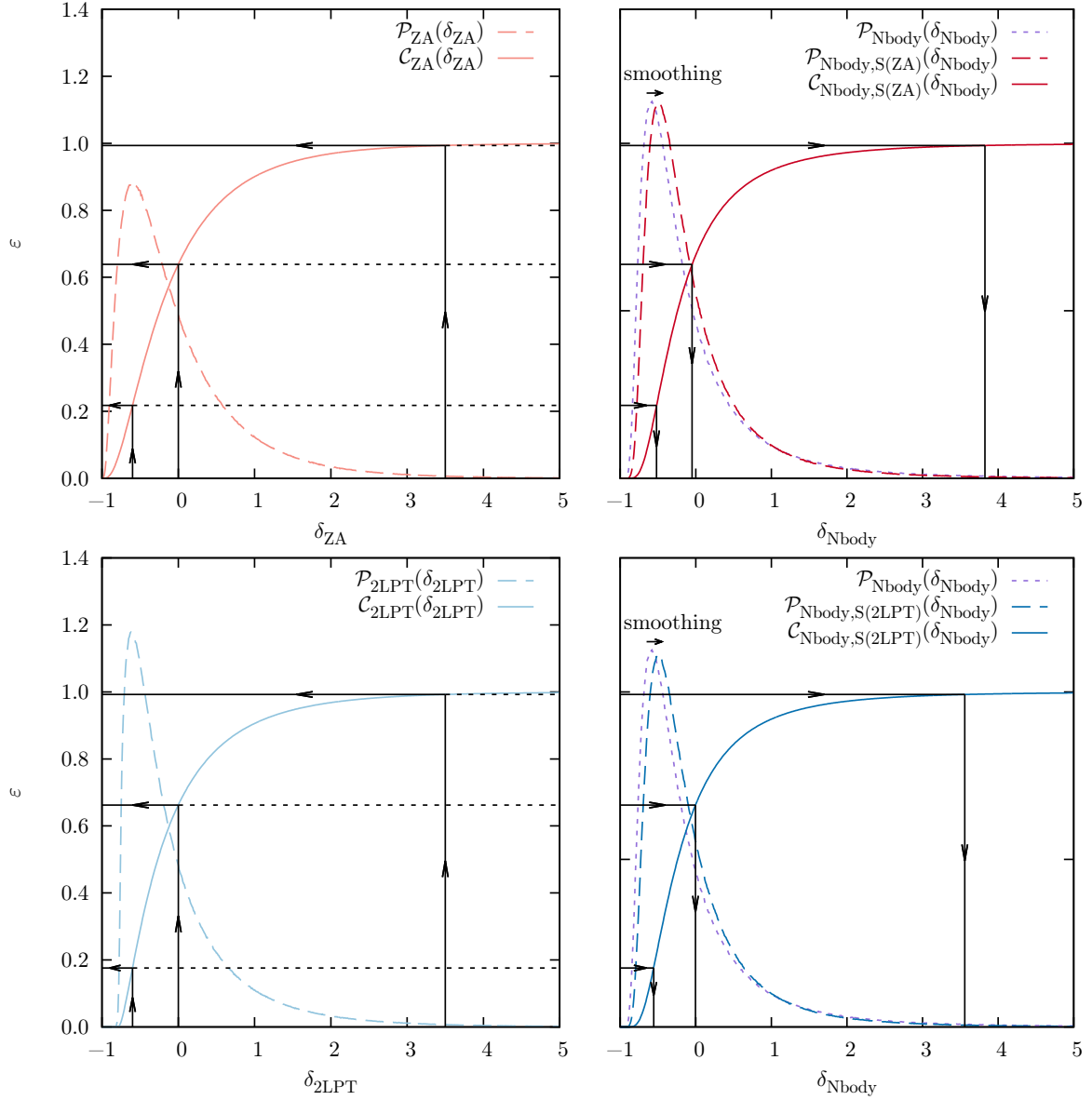


Figure 6.1: A graphical illustration of the improved remapping procedure at redshift zero, for the ZA (upper panel) and 2LPT (lower panel). On the right panels, the dotted purple curves are the probability distribution function for the density contrast in full  $N$ -body dynamics. The first step of the procedure is to smooth the  $N$ -body density field using the transfer function given by equation (6.2), which yields slightly different pdfs (dashed dark red and dark blue curves on the right panels). On the left panels, the dashed curves are the pdfs for the density contrast in the final density field, evolved from the same initial conditions with LPT (ZA: red line and 2LPT: blue line). The pdfs are computed on a  $8 \text{ Mpc}/h$  mesh ( $128^3$ -voxel grid) using the full statistics from eight realizations of  $512^3$ -particles in a  $1024 \text{ Mpc}/h$  box with periodic boundary conditions. The solid curves are their respective integrals, the cumulative distribution functions. The second step is remapping, which assigns a voxel with density contrast  $\delta_{\text{LPT}}$  and fractional rank  $\varepsilon$  the value of  $\delta_{\text{Nbody}}$  that would have the same fractional rank in the smoothed  $N$ -body distribution (equation (6.3)). This remapping is illustrated for 2LPT with three sample points:  $\delta_{2\text{LPT}} = -0.60$  maps to  $\delta_{\text{Nbody}} = -0.56$ ,  $\delta_{2\text{LPT}} = 0.00$  maps to  $\delta_{\text{Nbody}} = -0.01$ , and  $\delta_{2\text{LPT}} = 3.50$  maps to  $\delta_{\text{Nbody}} = 3.56$ . The remapping procedure imposes the one-point distribution of the smoothed  $N$ -body field while maintaining the rank order of the LPT-evolved density fields. The last step is an increase of small-scale power in the remapped distribution using the reciprocal transfer function, equation (6.4).

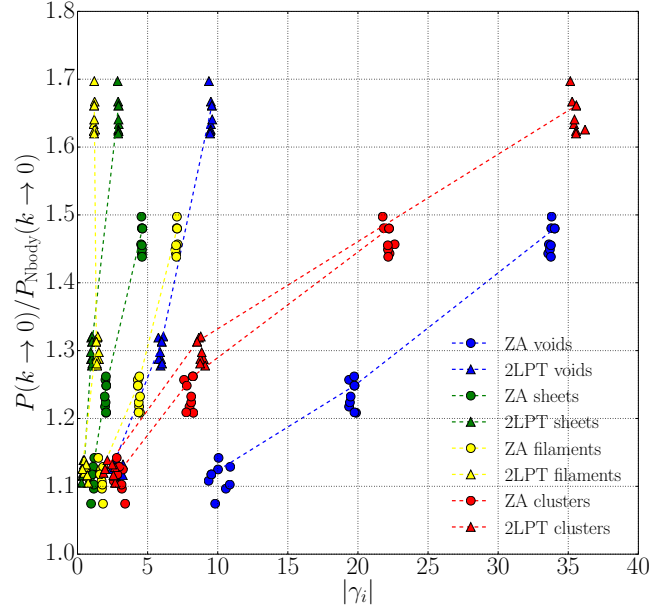


Figure 6.2: The large-scale bias in the power spectrum of density fields, remapped with the procedure described in section 6.2.1, as a function of the mismatch between structure types. The estimators  $\gamma_i$  are defined by equation (2.22). Eight realizations of the ZA (circles) and 2LPT (triangles) are compared to the corresponding  $N$ -body realization, for various resolutions (from bottom to top: 16 Mpc/h, 8 Mpc/h, 4 Mpc/h). The large-scale bias in the power spectra of remapped fields is strongly correlated to the volume fraction of structures incorrectly predicted by LPT.

(also see figure 6.1 for a schematic outline of this method). The left panels of figure 6.1 show  $\mathcal{P}_{\text{LPT}}$  (dashed curves) and the corresponding cumulative distributions,  $\mathcal{C}_{\text{LPT}}$  (solid curves). On the right panels, the dotted curves represent the pdf of the corresponding  $N$ -body realization,  $\mathcal{P}_{\text{Nbody}}$ . Remapping assigns to a voxel with density contrast  $\delta_{\text{LPT}}$  and fractional rank  $\varepsilon = \mathcal{C}_{\text{LPT}}(\delta_{\text{LPT}})$  the value of  $\delta_{\text{Nbody}}$  that would have the same fractional rank in the  $N$ -body distribution.

Since  $\mathcal{C}_{\text{Nbody}}$  contains exactly the same information as  $\mathcal{P}_{\text{Nbody}}$ , the remapping procedure imposes the one-point distribution taken from the  $N$ -body-evolved density field while maintaining the rank order of the LPT-evolved density field. In other words, only the weight of underdensities and overdensities is modified, while their locations remain unchanged. In this fashion, we seek to adjust the density field while maintaining higher-order statistics provided by LPT with reasonable accuracy. We checked numerically that mass is always conserved in this procedure.

### 6.2.2 Comparison of structure types in LPT and in $N$ -body dynamics

We implemented the remapping procedure described in the previous section and checked that we are able to modify LPT density fields so as to correctly reproduce the one-point distribution of a full  $N$ -body simulation. However, we experience a large-scale bias in the power spectrum, namely the amplitude of the spectrum of the remapped fields is slightly too high. Generally, a non-linear transformation in voxel space can change the variance of a field. This is consistent with the findings of Weinberg (1992), who found a similar effect in his reconstructions of the initial conditions, and who addressed the issue by rescaling the density field in Fourier space. However, such an approach will generally destroy the remapped one-point distribution, and may even further lead to Gibbs ringing effects which will make the remapped field unphysical.

The bias indicates a stronger clustering in the remapped density field. Since remapping is a local operation in voxel space, this large-scale bias means that erroneous remapping of small-scale structures affects the clustering at larger scales. To identify the cause of this bias, we performed a study of differences in structure types (voids, sheets, filaments, and clusters) in density fields predicted by LPT and  $N$ -body simulations. With this analysis, we wanted to understand the effect of remapping in different density and dynamical regimes of the LSS. The results are presented in section 2.3. We identified, in particular, a mismatch between the volume occupied by different structure types in LPT and  $N$ -body dynamics, quantified by the parameters  $\gamma_i$  defined by equation

(2.22).

In figure 6.2, we plot the large-scale bias observed in remapped fields obtained with the procedure of section 6.2.1 as a function of  $\gamma_i$ , for various resolutions. A strong correlation is observed between the bias and the mismatch in the volume occupied by different structure types. The difference in the prediction of the volume of extended objects is the cause of the bias: in clusters and in voids, remapping enhances a larger volume than should be enhanced, which yields on average a stronger clustering in the box.

### 6.2.3 Improvement of the remapping procedure

In the previous section, we noted that because too much volume of LPT density fields is mapped to the tails of the  $N$ -body one-point distribution (dense clusters and deep voids), the average two-point correlations are larger after remapping. Given this result, minor modifications of the procedure described in section 6.2.1 can solve the problem. We now propose to improve the remapping procedure of Weinberg (1992) for present-day density fields, in a similar fashion as in Narayanan & Weinberg (1998), combining it with transfer function techniques to deal with the mildly non-linear modes as in Tassev & Zaldarriaga (2012a,c). Our method works as follows.

1. We degrade the  $N$ -body density field to the same degree of smoothness as the LPT density field, by multiplying the Fourier modes of the density field by the transfer function

$$T(k) \equiv \sqrt{\frac{P_{\text{LPT}}(k)}{P_{\text{Nbody}}(k)}}. \quad (6.2)$$

This step yields a new density field, noted  $\text{Nbody,S(LPT)}$ , whose power spectrum matches that of the LPT density field.

2. We remap the LPT density field in the fashion described in section 6.2.1, but using as a reference the cdf of the smoothed density field,  $C_{\text{Nbody,S(LPT)}}$ , instead of the full  $N$ -body density field (see figure 6.1). The remapping condition, equation (6.1), now reads

$$C_{\text{LPT}}(\delta_{\text{LPT}}) = C_{\text{Nbody,S(LPT)}}(\delta_{\text{Nbody}}). \quad (6.3)$$

3. We increase the power of small scales modes in the remapped distribution to the same value as in a full  $N$ -body simulation, using the reciprocal of the transfer function (6.2), namely

$$T^{-1}(k) = \sqrt{\frac{P_{\text{Nbody}}(k)}{P_{\text{LPT}}(k)}}. \quad (6.4)$$

This procedure cures the large-scale bias issue experienced with the simple implementation of the remapping described in section 6.2.1, without requiring any prior knowledge on the corresponding  $N$ -body simulation. As we will demonstrate in section 6.3, it yields improvement of one-, two- and three-point statistics of LPT.

### 6.2.4 Remapping function and transfer function

Since  $C_{\text{LPT}}$  and  $C_{\text{Nbody,S(LPT)}}$  are monotonically increasing functions, there is no ambiguity in the choice of  $\delta_{\text{Nbody}}$ , and this procedure defines a *remapping function*  $f$  such that

$$\delta_{\text{LPT}} \mapsto \delta_{\text{Nbody}} = C_{\text{Nbody,S(LPT)}}^{-1}(C_{\text{LPT}}(\delta_{\text{LPT}})) \equiv f(\delta_{\text{LPT}}). \quad (6.5)$$

Establishing a remapping function  $f$  requires knowledge of both LPT and  $N$ -body density field statistics. Ideally, several realizations with different initial conditions should be combined in order to compute a precise remapping function. Indeed, a limited amount of available  $N$ -body simulations results in a lack of statistics and hence uncertainties for the remapping procedure in the high density regime. However, this effect is irrelevant from a practical point of view, since these high density events are very unlikely and affect only a negligible number of voxels. As a consequence this uncertainty will only affect to sub-percent level the usual statistical summaries of the density field. Note that in any case, if desired, the accuracy of the remapping function in the high density regime can be trivially enhanced by enlarging the size or number of  $N$ -body simulations used for



its construction. For the analysis presented in this chapter, the remapping functions have been computed using the full statistics from eight realizations of  $512^3$  particles in a  $1024 \text{ Mpc}/h$  box.

Note that once the relationship between the statistical behavior of the LPT fields and the full non-linear field is known, this procedure can be used on LPT realizations without the need of evolving corresponding  $N$ -body simulations. More specifically, the remapping function  $f$  (equation (6.5)) and the transfer function  $T$  (equation (6.2)) can be tabulated and stored, then used for the fast construction of a large number of large-scale structure density fields. Since producing LPT realizations is computationally faster than running full gravitational simulations by a factor of several hundreds, our method can be used to produce a large set of  $N$ -body-like realizations in a short time.

Some remapping functions are presented in figure 6.3. In each panel, the solid curves represent the remapping function  $f_z$  at redshift  $z$ , computed with the LPT and  $N$ -body simulations. The dashed black line shows the identity function. We checked that the remapping function converges to the identity function with increasing redshift, as expected. Critical values where the remapping function crosses the identity function are identified. Between these critical values, remapping either increases or decreases the local density.

The pdfs for the density contrast are evaluated on a grid after a CiC assignment of particles. This means that the remapping function *a priori* depends on the size of voxels. The problem of choosing a voxel size for the computation of the remapping function is linked to the more general problem of choosing a mesh for the CiC evaluation of density. Choosing too coarse a binning will result in an underestimation of the clustering of particles, whereas choosing too fine a binning will also result in artifacts in overdensities (some voxels may be empty due to their too small size). The right choice of voxel size for the evaluation of the remapping function is the one giving the best evaluation of the density contrast. This choice has to be made depending on the desired application of the remapped data.

The remapping function describes how the pdf for the density contrast is affected by non-linear structure formation. For this reason, it depends on the nature of the gravitational interaction, as described by LPT and by full  $N$ -body dynamics, but weakly depends on the detail of the cosmological parameters. We checked the cosmology-dependence of the remapping function in simulations with the dark matter and baryon density in the Universe,  $\Omega_m$  and  $\Omega_b$ , varying the WMAP-7 fiducial values (equation (2.1)) by  $\pm 3\sigma$  (still assuming a flat Universe):

$$\Omega_\Lambda = 0.750, \Omega_m = 0.2494, \Omega_b = 0.0428, \sigma_8 = 0.810, h = 0.704, n_s = 0.967; \quad (6.6)$$

$$\Omega_\Lambda = 0.700, \Omega_m = 0.2992, \Omega_b = 0.0488, \sigma_8 = 0.810, h = 0.704, n_s = 0.967. \quad (6.7)$$

Even for these models notably far from the fiducial values, we found that the remapping function almost perfectly overlaps that of our main analysis, for the density range  $\delta \in [-1; 5]$ , containing typically 98 to 99% of the voxels. We found a difference of less than 5% for  $\delta = 5$  (see the left panel of figure 6.4).

The transfer function used in steps 1 and 3 of the improved procedure also exhibits very weak redshift-dependence, with deviations limited to a few percents at the smallest scales of interest of this work ( $k \approx 0.4 \text{ (Mpc}/h)^{-1}$ , see the right panel of figure 6.4).

## 6.3 Statistics of remapped fields

In this section, we discuss the validity of the improved remapping procedure described in section 6.2.3, by studying the correlators of the remapped field in comparison to the input LPT and  $N$ -body fields. The remapping procedure based on the Eulerian density contrast essentially replaces the LPT one-point function by that of the smoothed  $N$ -body-evolved field. Since the position and shape of structures is left unchanged, we expect the higher-order correlators of the density field to be respected by the remapping procedure. Of particular interest is to check how remapping affects higher-order statistics and if possible improvements could be exploited in data analysis or artificial galaxy survey applications.

We implemented a numerical algorithm that computes and analyzes a remapped density field. The procedure can be divided in three steps:

1. We take as input two cosmological density fields, evolved from the same initial conditions with LPT (ZA or 2LPT) and with full  $N$ -body dynamics, and estimate the one-point statistics (pdf and cdf for  $\delta$ ) and the transfer function for this particular realization. We repeat this step for the eight realizations used in our analysis.

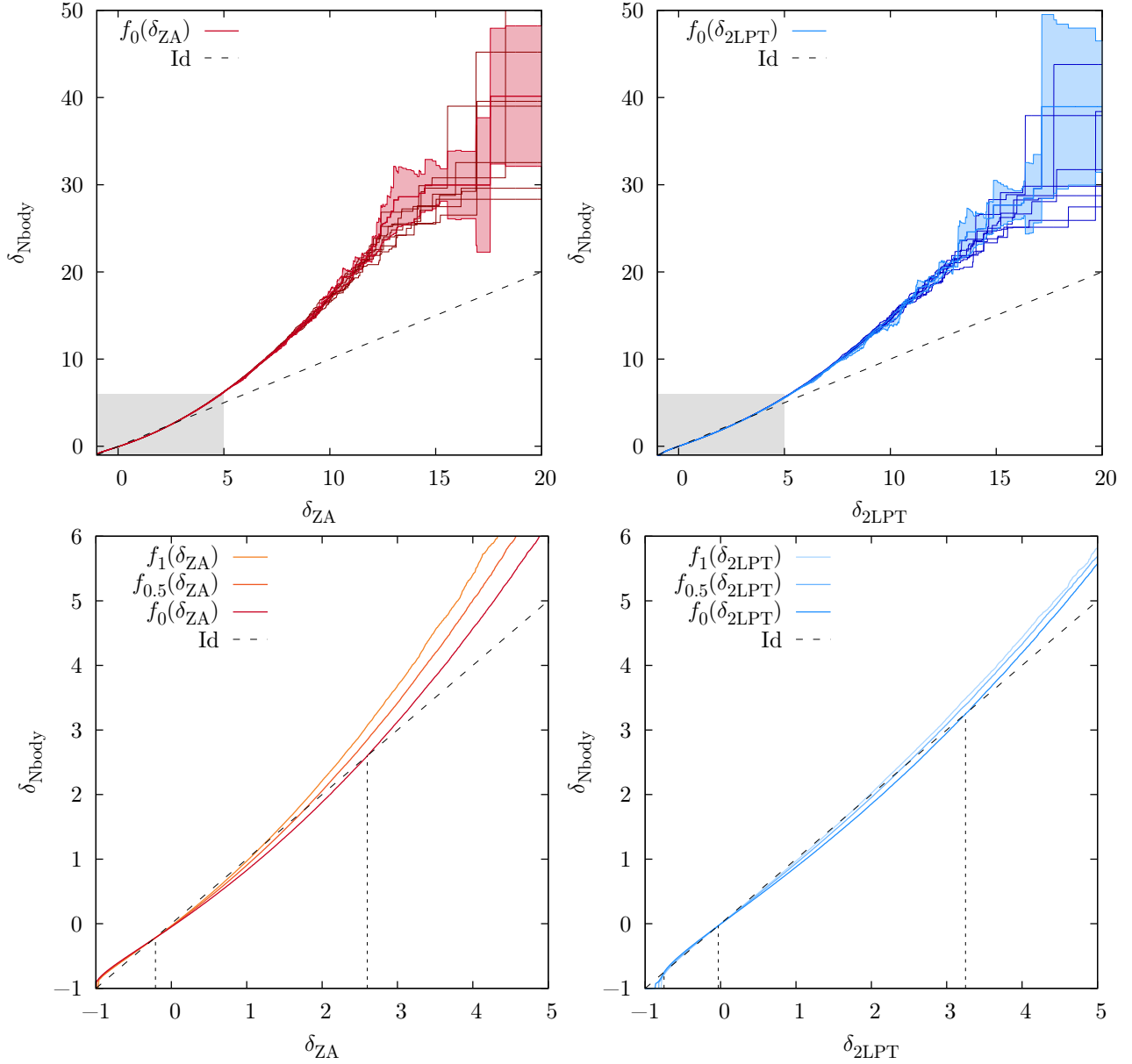


Figure 6.3: The remapping functions from LPT to smoothed  $N$ -body density fields, for the ZA (left panel) and 2LPT (right panel), all computed on a  $8 \text{ Mpc}/h$  mesh. The precise redshift-zero remapping functions  $f_0$  (red and blue solid curves) have been computed using the full statistics from eight realizations (darker red and blue solid curves). The error bars shown are the  $1\text{-}\sigma$  dispersion among the eight runs with reference to the full remapping function. The lower plots show the detail of the shaded area, in a density range containing most of the voxels. The redshift-dependence of the remapping function  $f_z$  is shown for  $z = 1$ ,  $z = 0.5$  and  $z = 0$ . The dashed line shows the identity function. Critical values of  $\delta_{\text{LPT}}$  for which remapping does not change the local density are identified.



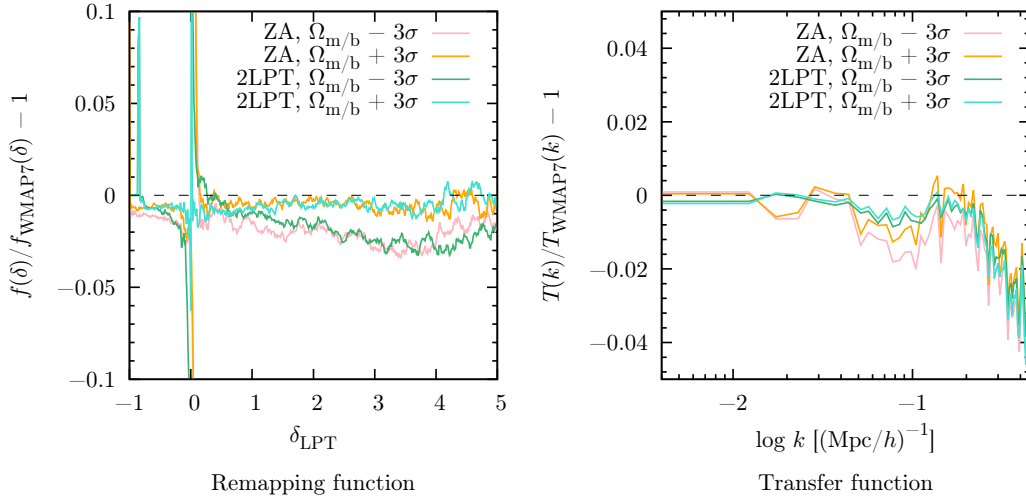


Figure 6.4: Relative deviations of the remapping function (left panel) and of the transfer function (right panel) for varying cosmological parameters (equations (6.6) and (6.7)), with respect to their behaviour in a fiducial cosmology (equation (2.1)).

2. We take as input all the one-point statistics computed with individual realizations, and we compute a precise remapping function using the full statistics of all available realizations, as described in section 6.2.1. The transfer function used as a reference is the mean of all available realizations. At this point, the remapping function and the transfer function can be tabulated and stored for later use, and  $N$ -body simulations are no longer required.
3. For each realization, we remap the density field using the improved three-step procedure described in section 6.2.3 and we analyze its correlation functions.

Our algorithm provides the one-point (section 6.3.1) and two-point (section 6.3.2) statistics. We used the code described in Gil-Marín *et al.* (2011, 2012) to study the three-point statistics (section 6.3.3). The results are presented below.

### 6.3.1 One-point statistics

The remapping procedure, described in section 6.2, is essentially a replacement of the cumulative distribution function of the density contrast  $\delta$  of the input LPT-evolved field,  $C_{\text{LPT}}$ , by that of the reference  $N$ -body-evolved field after smoothing,  $C_{\text{Nbody},S(\text{LPT})}$ . After having applied the remapping procedure, we recomputed the pdf of the remapped field and verified that it matches that of the fiducial field as a sanity check.

Remapping and rescaling the density modes alters local density values but positions of structures remain unchanged. It is therefore important to check that remapping visually alters the LPT-evolved distribution in such a way that structures resemble more their  $N$ -body evolved counterparts. Figure 6.5 shows a slice of the density contrast  $\delta$ , measured at redshift zero, on a  $128^2$ -pixel sheet of a  $512^3$ -particles realization in a  $1024 \text{ Mpc}/h$  box. The corresponding mesh size is  $8 \text{ Mpc}/h$ . Visually, remapped fields (ZARM and 2LPTRM) are closer to the full  $N$ -body result than their originals (ZA and 2LPT), with plausible particle distribution.

Since the improved remapping procedure involves a rescaling of the density modes in Fourier space (step 3), the pdf for the density contrast of the remapped fields is not guaranteed to be correct by construction, as would be the case with a naive remapping (section 6.2.1). Therefore, the one-point distribution has to be carefully checked at this point. In figure 2.1, we plot the pdf for the density contrast at redshift zero for  $N$ -body simulations and the approximately evolved fields: with the ZA and 2LPT alone, and after remapping (ZARM and 2LPTRM). It can be observed that the peaks of the pdfs get closer to the reference set by  $N$ -body dynamics and that the pdf of remapped fields accurately follows that of full gravitational dynamics for  $\delta > 0$ . The procedure being successful on average for one-point statistics and accurate for the most common events in overdensities, we expect the number count of objects such as clusters predicted by LPT to be made more robust by our procedure.

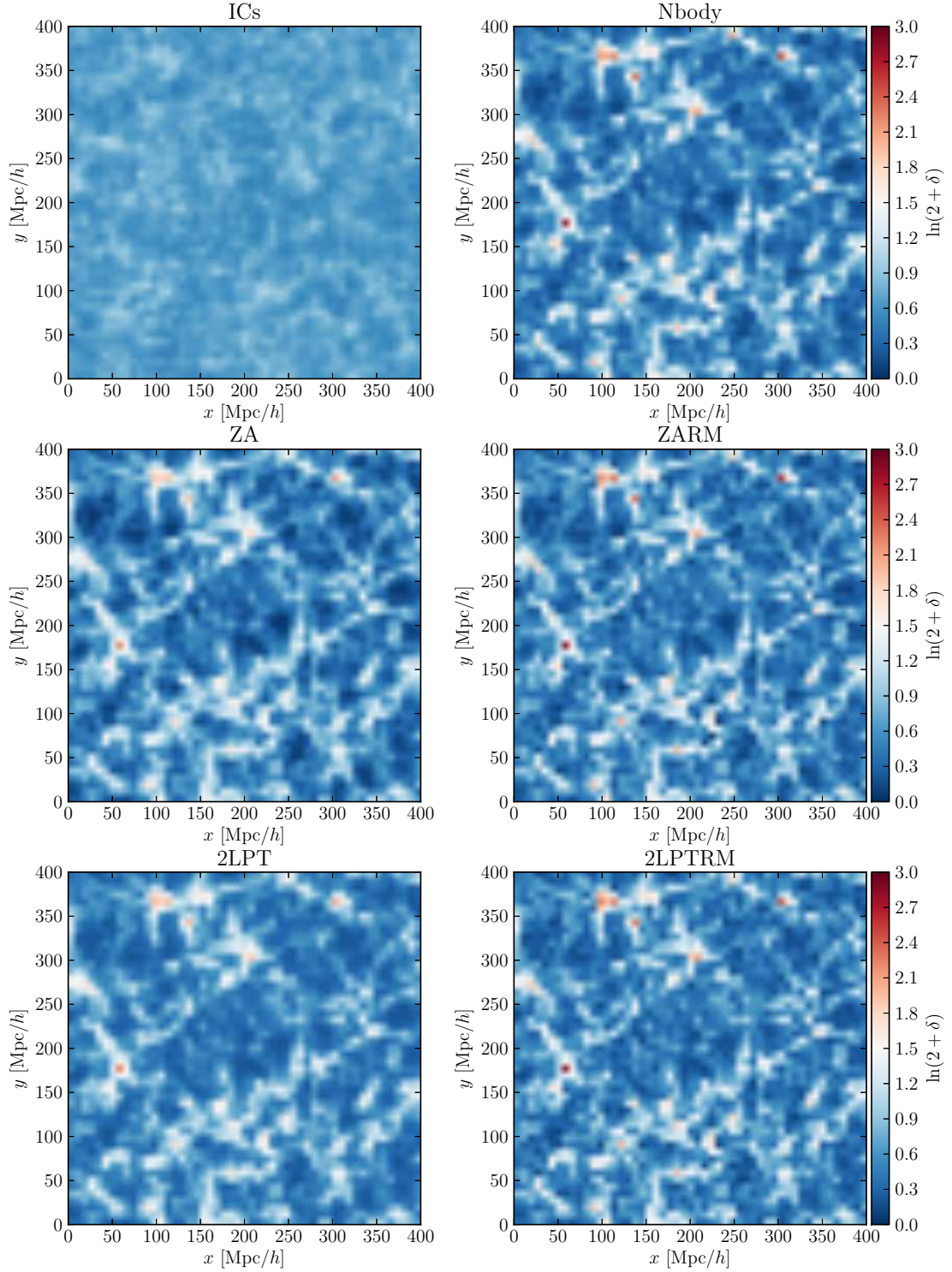


Figure 6.5: Redshift-zero density contrast on a  $128^2$ -pixel slice of a  $512^3$ -particles realization in a  $1024 \text{ Mpc}/h$  box with periodic boundary conditions. For clarity, the slice is limited to a square of  $400 \text{ Mpc}/h$  side, and the quantity shown is the log-density field,  $\ln(2+\delta)$ . For comparison with the initial conditions, the density field at high redshift ( $z=5$ ) is shown in the top left corner. The redshift-zero density fields are determined using, from top to bottom and from left to right: a full  $N$ -body simulation, the Zel'dovich approximation, alone (ZA) and after remapping (ZARM), second-order Lagrangian perturbation theory, alone (2LPT) and after remapping (2LPTRM). The remapping and the transfer function operations are performed on a  $128^3$ -voxel grid, corresponding to a mesh size of  $8 \text{ Mpc}/h$ .

### 6.3.2 Two-point statistics

#### 6.3.2.1 Power spectrum

In figure 2.2, we plot the redshift-zero power spectrum of the different density fields.<sup>1</sup> The relative deviations of power spectra with reference to the density field computed with a full  $N$ -body simulation are presented in figures 2.3 and 2.4.

At high redshift ( $z > 1$ ), we found no notable difference between the power spectrum of matter evolved with full  $N$ -body dynamics and that of LPT-remapped distributions. This indicates that our remapping procedure is increasingly successful as we go backwards in time towards the initial conditions, where LPT gives accurate results.

At low redshift, the power spectrum shape of remapped LPT fields is closer to the shape of the full non-linear power spectrum, turning down at smaller scales than the LPT power spectra. In particular, LPT fields exhibit more small-scale correlations after remapping, illustrating the success of our procedure in the mildly non-linear regime of large-scale structure formation.

Contrary to the density fields obtained via a naive remapping approach, whose power spectra exhibit a positive artificial offset at large scales as discussed in section 6.2.2, the fields obtained with the improved procedure have correct two-point statistics at all scales for coarse grids (down to 8 Mpc/ $h$ ). For finer grids, a negative large-scale bias appears in the power spectrum, meaning that we have suppressed too much small-scale power in the  $N$ -body field in the first step of our procedure, which propagates to large scales with remapping. Comparing the panels of figures 2.3 and 2.4, it can be observed that this effect is suppressed at higher redshift and for coarser binning. We found that a voxel size of 8 Mpc/ $h$  is the best compromise, with a large-scale power spectrum compatible with the error bars and clear improvement at small scales, as can be seen in figure 2.2. This mesh size corresponds to the target resolution for analyses in the mildly non-linear regime, as discussed in the introduction of this chapter.

#### 6.3.2.2 Fourier-space cross-correlation coefficient

In figure 2.5, we present the Fourier-space cross-correlation coefficient  $R \equiv P_{\delta \times \delta'} / \sqrt{P_{\delta} P_{\delta'}}$  between the redshift-zero density field in the  $N$ -body simulation and several other density fields. At redshift zero and at small scales, the agreement is better with remapped LPT fields than with LPT alone, confirming the success of the remapping procedure to explore the mildly non-linear regime. In particular, the remapping of 2LPT predicts more than 96% level accuracy at  $k = 0.4$  (Mpc/ $h$ )<sup>-1</sup> (corresponding to scales of 16 Mpc/ $h$ ), where 2LPT gives only 93%. The cross-correlation coefficient indicates better agreements for the remapping of 2LPT than for the remapping of the ZA, which is consistent with the better performance of 2LPT in predicting the phases of the full  $N$ -body field (see section 2.1.2.2).

### 6.3.3 Three-point statistics

We analyzed the accuracy of our method beyond second-order statistics by studying the bispectrum, using the code described in Gil-Marín *et al.* (2011, 2012).<sup>2</sup> Figure 2.6 shows the redshift-zero bispectrum for equilateral triangles. The overall result is a clear improvement of the bispectrum of LPT-evolved fields with the remapping procedure, especially on the small scales shown, probing the mildly non-linear regime,  $k \gtrsim 0.1$  (Mpc/ $h$ )<sup>-1</sup> corresponding to scales  $\lesssim 62$  Mpc/ $h$ , where LPT predicts less three-point correlation than full gravity. At large scales, the approximation error remains  $\lesssim 1\sigma$  of the estimated statistical uncertainty, even for a resolution of 8 Mpc/ $h$  and at late times ( $z = 0$ ).

The relative deviations of approximate bispectra with reference to full  $N$ -body simulations are shown in figures 2.7, 2.8, 2.9 and 2.10. As expected, the success of our remapping procedure in exploring small scales ( $k \gtrsim 0.1$  (Mpc/ $h$ )<sup>-1</sup>) is increased for more coarsely-binned density fields (see figure 2.7) and at higher redshift (see figure 2.8). In figure 2.9 we examine the scale-dependence of the bispectrum for various triangle shapes. The precise dependence on the triangle shape at different scales is shown in figure 2.10.

<sup>1</sup> The reader is referred to section 2.1.2.1 for practical details on the computation of these power spectra.

<sup>2</sup> Technical considerations concerning the computation of bispectra are presented in section 2.1.3.

## 6.4 Discussion and conclusion

The main subject of this chapter is the development of a method designed to improve the correspondence between approximate models for gravitational dynamics and full numerical simulation of large-scale structure formation. Our methodology relies on a remapping of the one-point distribution of the density contrast of the approximately evolved particle distribution using information extracted from  $N$ -body simulations.

Due to the differences in the precise structure of the density fields in Lagrangian perturbation theory and in full gravity, the naive implementation of this procedure, inspired by [Weinberg \(1992\)](#), gives a large-scale bias in the power spectrum. This is not solved by a simple rescaling of Fourier modes, which leads to Gibbs ringing artifacts and an overall unphysical representation of the density fields. Smoothing LPT and  $N$ -body density fields with the same kernel is also unsuccessful, as smoothed  $N$ -body fields will always keep a sharper structure than smoothed LPT fields.

We figured out that the cause of this large-scale bias is not the different density predicted locally by LPT and  $N$ -body dynamics on a point-by-point basis, but a problem of mismatch between the volume of extended objects. Our findings question the reliability of LPT for LSS data analysis and generation of mock catalogs at low redshift and high mass resolution. They are also a likely explanation for the discrepancy between the power spectrum of initial conditions reconstructed via Gaussianization and linear theory expectations, encountered by [Weinberg \(1992\)](#).

Considering these results, we improved [Weinberg's](#) remapping procedure for present-day density fields by the use of a transfer function. In this fashion, we obtain a physically more accurate representation of the three-dimensional matter distribution in the mildly non-linear regime, while improving higher-order statistics. Since LPT captures well the cosmological dependence and remapping operates on small-scale aspects of the density field, we found that our procedure that is nearly independent of cosmological parameters.

The aim of this method is to develop a fast, flexible and efficient way to generate realizations of LSS density fields, accurately representing the mildly non-linear regime. Our procedure, therefore, responds to the increasing demand for numerically inexpensive models of three-dimensional LSS, for applications to modern cosmological data analysis. At the level of statistical error in our numerical experiments, the approach provides a good method for producing mock halo catalogs and low-redshift initial conditions for simulations, if desired. The resulting information can also be used in a variety of cosmological analyses of present and upcoming observations.

We showed that our approach allows fast generation of cosmological density fields that correlate with  $N$ -body simulations at better than 96% down to scales of  $k \approx 0.4 \text{ (Mpc/h)}^{-1}$  at redshift zero and are substantially better than standard LPT results at higher redshifts on the same comoving scales. Remapping improves the fast LPT bispectrum predictions on small scales while the large scale bispectrum remains accurate to within about  $1\sigma$  of the measurement in our  $N$ -body simulations. Since real observations will have larger statistical errors for the foreseeable future, our method provides an adequate fast model of the non-linear density field on scales down to  $\sim 8 \text{ Mpc/h}$ . These results constitute a substantial improvement with respect to existing techniques, since non-linearities begin to affect even large-scale measurements in galaxy surveys. Since the number of modes usable for cosmological exploitation scale as  $k^3$ , even minor improvements in the smallest scale  $k$  allow access to much more knowledge from existing and upcoming observations. This work is a step further in the non-linear regime, which contains a wealth of yet unexploited cosmological information. For possible applications, we provided a cosmographic and statistical characterization of approximation errors.

Our remapping procedure predicts the two-point correlation function at around 95% level accuracy and three-point correlation function at around 80% level accuracy at redshift 3, for  $k$  between 0.1 and  $0.4 \text{ (Mpc/h)}^{-1}$ , illustrating the increasing success of our methods as we go backwards in time towards the initial conditions, when LPT is an accurate description of early structure formation. This is of particular interest in several areas of high-redshift cosmology, such as forecasting 21 cm surveys ([Lidz et al., 2007](#)), analyzing the properties of the intergalactic medium via the Lyman- $\alpha$  forest ([Kitaura, Gallerani & Ferrara, 2012](#)) or probing the reionization epoch ([Mesinger & Furlanetto, 2007](#)). This work might also add to methods of data analysis for the ongoing and upcoming high-redshift galaxy surveys mentioned in the [introduction](#).

However, the realization of density fields with these procedures stays approximate, since the full non-linear gravitational physics involves information contained in the shape of structures, which cannot be captured from a one-point modification of LPT, especially after shell-crossing. We studied the performance of one-point remapping of LPT and presented a statistical characterization of the errors, but additional refinements, such as a non-linear, density-dependent smoothing of the  $N$ -body field, could further improve on these approximations, for an increased computational cost. This is, however, beyond the scope and intent of this work. Generally,

the complications at large scales that we encounter when applying a local remapping seem difficult to solve in a Eulerian density field approach and would favor a Lagrangian, particle-based perspective.

As mentioned in section 6.1, fast and accurate methods to model the non-linearly evolved mass distribution in the Universe have the potential of profound influence on modern cosmological data analysis. Full Bayesian large-scale structure inference methods such as the BORG algorithm, which extract information on the matter distribution in the Universe from galaxy redshift surveys, rely on LPT (see chapter 4). The technique proposed in this chapter can be envisioned as a numerically efficient and flexible extension of these methods, permitting us to push dynamic analyses of the large scale structure further into the non-linear regime.





# Non-linear filtering of large-scale structure samples

---

## Contents

---

<b>7.1</b>	<b>Introduction</b>	<b>109</b>
7.1.1	Motivation for non-linear filtering of large-scale structure samples	109
7.1.2	Filtering in the final conditions	110
7.1.3	Filtering via constrained simulations	110
<b>7.2</b>	<b>Fully non-linear filtering with Gadget</b>	<b>110</b>
<b>7.3</b>	<b>Fast non-linear filtering with COLA</b>	<b>112</b>
7.3.1	The COLA method	112
7.3.2	Non-linear BORG-COLA realizations	113

---



---

“While o’er him fast, through sail and shroud,  
The wreathing fires made way.  
They wrapt the ship in splendour wild,  
They caught the flag on high,  
And streamed above the gallant child,  
Like banners in the sky.”  
— Felicia Hemans (1826), *Casabianca*

---

## Abstract

Due to the approximate 2LPT model implemented in the BORG algorithm, inferred large-scale structure samples are only correct in the linear and mildly non-linear regime of structure formation. This chapter describes subsequent improvement of such samples at non-linear scales, via an operation that we refer to as “non-linear filtering”. This process does not replace fully non-linear large-scale structure inference, but rather fills small scales with physically reasonable information. Several approaches to non-linear filtering are considered and discussed.

This chapter discusses the generation of non-linear, constrained realizations of the late-time large-scale structure via an operation that we call “filtering” of BORG samples. It is structured as follows. We give motivation for non-linear filtering and describe two different approaches (direct improvement of final conditions, and constrained simulations) in section 7.1. For later use in chapter 8, we describe a set of samples optimally filtered with GADGET in section 7.2. In section 7.3, we describe the efficient COLA scheme for fast production of non-linear large-scale structure realizations, and apply it to generate a large ensemble of samples, used in chapter 9.

## 7.1 Introduction

### 7.1.1 Motivation for non-linear filtering of large-scale structure samples

As noted in section 4.2.1.2, the likelihood for Bayesian large-scale structure inference involves a structure formation model to translate from the initial to the final density field:

$$\delta^i \mapsto \delta^f = \mathcal{G}(\delta^i, a). \quad (7.1)$$

Ideally, this step should involve a numerical model that fully accounts for the non-linearities of the Vlasov-Poisson system, which describes structure formation (see chapter 1). Unfortunately, this is not currently computationally tractable. For this reason, BORG uses 2LPT as a proxy for gravitational dynamics.<sup>1</sup>

Nevertheless, the description of particular patterns of the cosmic web (as presented in part IV of this thesis) requires description of the LSS not only correct at the scales correctly described by 2LPT ( $k \lesssim 0.1 \text{ Mpc}/h$ , see chapter 2), but also physically reasonable at smaller scales, up to  $k \sim 1 \text{ Mpc}/h$ . At this point, it is also useful to recall that the number of Fourier modes usable for cosmology scales as the cube of the smallest accessible mode,  $k^3$ .

For these reasons, data-constrained, non-linear realizations of the LSS have a large variety of applications. As noted before, constraining small, non-linear scales within the inference framework is not yet possible; therefore, such realizations will rely on fusing data-constrained large scales and unconstrained small scales that only reflect our theoretical understanding of structure formation. Throughout this thesis, we refer to the production of data-constrained, non-linear realizations, on the basis of BORG large-scale structure samples, as *non-linear filtering*.

### 7.1.2 Filtering in the final conditions

One possible way to perform non-linear filtering is to directly improve the final conditions produced as BORG outputs. The technique of remapping Lagrangian perturbation theory can be useful in this context: as demonstrated in chapter 6, it cheaply yields improvements of density fields in the mildly non-linear regime. A particular advantage of remapping is its very low computational cost, which allows to process a large number of samples.<sup>2</sup> As seen in chapters 4 and 5, this is crucial for adequate uncertainty quantification.

### 7.1.3 Filtering via constrained simulations

Another idea is to capitalize on the inference of the initial conditions by BORG. Starting from inferred density fields, which contain the data constraints (see in particular section 5.3.3 for a discussion of information transport), it is possible to go forward in time using an alternative structure formation model, noted  $\mathcal{G}_{\text{NL}}$ , that improves upon  $\mathcal{G}$  for the description of small scales structures:

$$\delta^i \mapsto \delta_{\text{NL}}^f = \mathcal{G}_{\text{NL}}(\delta^i, a). \quad (7.2)$$

This process is known in the literature as running *constrained simulations*. Final density fields  $\delta_{\text{NL}}^f$  constructed in this way agree with corresponding BORG final conditions  $\delta^f$  at large scales, but are also physically reasonable at smaller scales, up to the validity limit of  $\mathcal{G}_{\text{NL}}$ .

In this picture, interesting questions are the determination of the smallest scale influenced by the data and the characterization of the reliability of structures extrapolated in unobserved regions, at high redshift or near survey boundaries. An upcoming publication will investigate the validity of constrained simulations, in particular the strength of data constraints in domains or at scales that have not been considered in the inference scheme.

In the following, we examine two particular cases for  $\mathcal{G}_{\text{NL}}$ , corresponding to the GADGET-2 cosmological code (section 7.2) and to the fast COLA scheme (section 7.3).

## 7.2 Fully non-linear filtering with Gadget

This section draws from section II.B. in [Leclercq et al. \(2015\)](#).

Optimal non-linear filtering of BORG results is achieved when  $\mathcal{G}_{\text{NL}}$  fully accounts for non-linear gravitational dynamics. This is the case when a cosmological simulation code is used. For the purpose of this thesis, we consider that non-linear filtering of BORG results with the GADGET-2 cosmological code ([Springel, Yoshida & White, 2001](#); [Springel, 2005](#)) is optimal.

For a variety of later uses, in particular for inference of dark matter voids in the Sloan volume (chapter 8), we generate a set of such optimally filtered, data-constrained realizations of the present large-scale structure.

<sup>1</sup> For the record, a BORG run, using 2LPT, takes of the order of a year (wall-clock time).

<sup>2</sup> The computational cost for remapping all the outputs of a BORG run, about 10,000 samples, would be comparable to a few full-gravity dark matter simulations using GADGET-2.



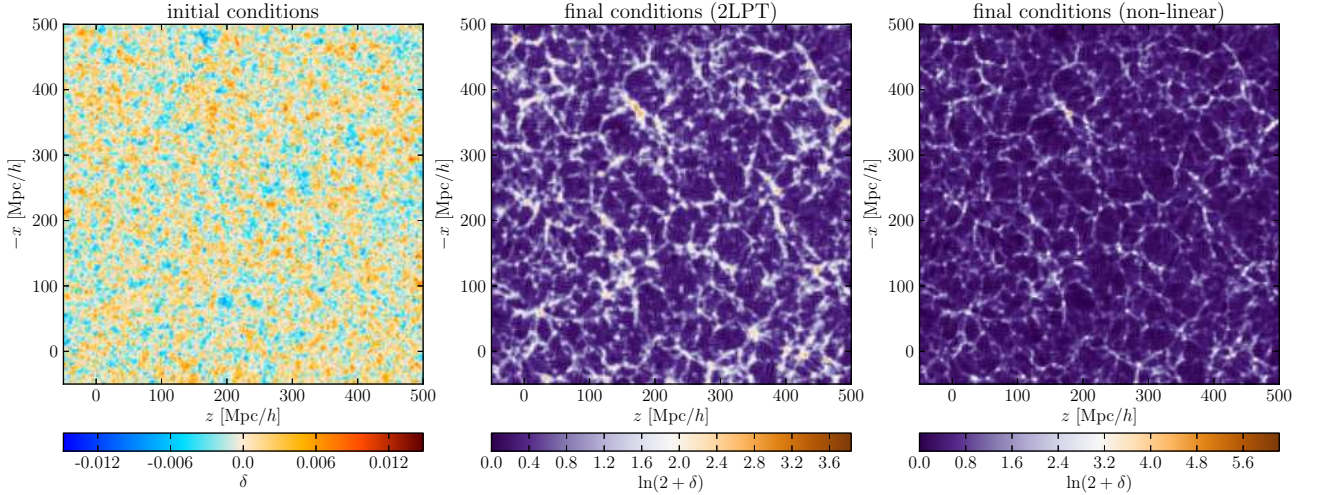


Figure 7.1: Non-linear filtering of BORG results. Slices through one sample of initial (left panel) and final density fields (middle panel) inferred by BORG. The final density field (middle panel) is a prediction of the 2LPT model used by BORG. On the right panel, a slice through the data-constrained realization obtained with the same sample via non-linear filtering (fully non-linear gravitational structure formation starting from the same initial conditions) is shown.

To do so, we rely on a subset of statistically independent initial conditions realizations, provided by [Jasche, Leclercq & Wandelt \(2015\)](#) (see chapter 5). The initial density field, defined on a cubic equidistant grid with side length of 750 Mpc/h and  $256^3$  voxels, is populated by  $512^3$  dark matter particles placed on a regular Lagrangian grid. The particles are evolved with 2LPT to the redshift of  $z = 69$ , followed by a propagation with GADGET-2 from  $z = 69$  to  $z = 0$ . In this fashion, we generate fully non-linear, data-constrained reconstructions of the present-day large-scale dark matter distribution.

As discussed in section 7.1, final conditions inferred by BORG are accurate only at linear and mildly non-linear scales. Application of fully non-linear dynamics to the corresponding initial conditions acts as an additional filtering step, extrapolating predictions to unconstrained non-linear regimes. In a Bayesian approach, this new information can then be tested with complementary observations in the actual sky for updating our knowledge on the Universe.

An illustration of the non-linear filtering procedure is presented in figure 7.1.<sup>3</sup> By comparing initial and final density fields, one can see correspondences between structures in the present Universe and their origins. Comparing final density fields before and after filtering (middle and left panels), one can check the conformity of the linear and mildly non-linear structures at large and intermediate scales, correctly predicted by 2LPT. Small-scale structures, corresponding to the deeply non-linear regime, are much better represented after non-linear filtering (resulting particularly in sharper filaments and clusters).  $N$ -body dynamics also resolves much more finely the substructure of voids – known to suffer from spurious artifacts in 2LPT, namely the presence of peaky, overdense spots where there should be deep voids ([Sahni & Shandarin, 1996](#); [Neyrinck, 2013](#); [Leclercq et al., 2013](#); see also chapter 2) – which is of particular relevance for the purpose of inferring dark matter voids (see chapter 8).

The improvement introduced by non-linear filtering at the level of two-point statistics is presented in figure 7.2, where we plot the power spectra of dark matter density fields at  $z = 0$ . The agreement between unconstrained and constrained realizations at all scales can be checked. The plot also shows that our set of constrained reconstructions contains the additional power expected in the non-linear regime<sup>4</sup>, up to  $k \approx 0.4$  (Mpc/h)<sup>-1</sup>.

<sup>3</sup> In figure 7.1 and in all slice plots of the rest of this thesis, we keep the coordinate system of [Jasche, Leclercq & Wandelt \(2015\)](#), also used in chapter 5.

<sup>4</sup> Note that the lack of small scale power in GADGET and COLA with respect to theoretical predictions, for  $k \gtrsim 0.5$  (Mpc/h)<sup>-1</sup>, is a gridding artifact due to the finite mesh size used for the analysis. This value corresponds to around one quarter of the Nyquist wavenumber.

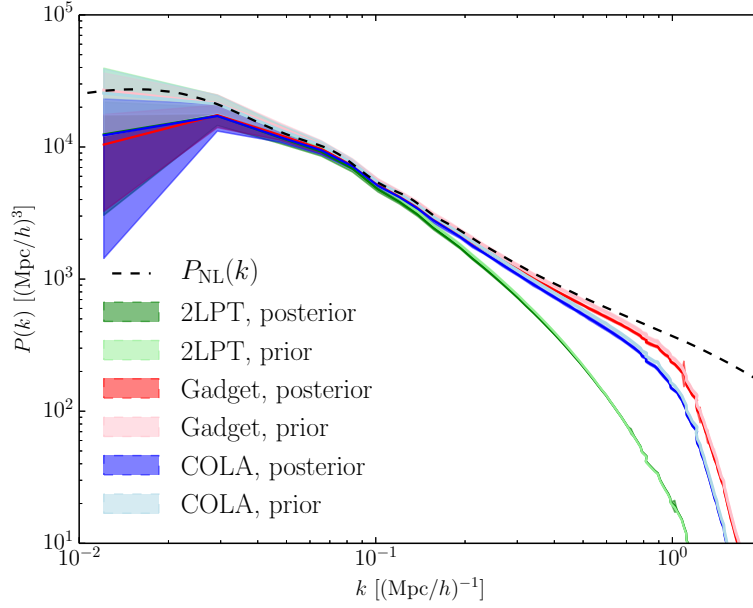


Figure 7.2: Power spectra of dark matter density fields at redshift zero, computed with a mesh size of 3 Mpc/h. The particle distributions are determined using: 1,000 unconstrained 2LPT realizations (“2LPT, prior”), 4,473 constrained 2LPT samples inferred by BORG (“2LPT, posterior”), 11 unconstrained GADGET-2 realizations (“Gadget, prior”), 11 constrained samples inferred by BORG and filtered with GADGET-2 (“Gadget, posterior”), 1,000 unconstrained COLA realizations (“COLA, prior”), 1,097 constrained samples inferred by BORG and filtered with COLA (“COLA, posterior”). The solid lines correspond to the mean among all realizations used in this work, and the shaded regions correspond to the  $2\text{-}\sigma$  credible interval estimated from the standard error of the mean. The dashed black curve represents  $P_{\text{NL}}(k)$ , the theoretical power spectrum expected at  $z = 0$  from high-resolution  $N$ -body simulations.

## 7.3 Fast non-linear filtering with COLA

For means of uncertainty quantification within large-scale structure inference, it is necessary to process a large number of samples. Unfortunately, optimal non-linear filtering with GADGET-2 is too expensive for the  $\sim 10,000$  samples of a single BORG run. However, an approximate model for non-linear structure formation, correct up to scales of a few Mpc/h, is enough for our purposes, as long as the approximation error is controlled and quantified.

### 7.3.1 The COLA method

The COLA (COmoving Lagrangian Acceleration, [Tassev, Zaldarriaga & Eisenstein, 2013](#); [Tassev et al., 2015](#)) technique offers a cheap way to perform non-linear filtering of a large number of BORG samples. A particular advantage (in opposition to standard particle-mesh codes) is its flexibility in trading accuracy at small scales for computational speed, without sacrificing accuracy at the largest scales.

The general idea of COLA is to use our analytic understanding of structure formation at large scales via LPT, and to solve numerically only for a subdominant contribution describing small scales. Specifically, [Tassev & Zaldarriaga \(2012c\)](#) propose to expand the Lagrangian displacement of particles as

$$\Psi(\mathbf{x}, \tau) = \Psi_{\text{LPT}}(\mathbf{x}, \tau) + \Psi_{\text{MC}}(\mathbf{x}, \tau) \quad (7.3)$$

where  $\Psi_{\text{LPT}}(\mathbf{x}, \tau)$  is the analytic displacement prescribed by LPT<sup>5</sup> (the ZA or 2LPT, see chapter 2) and  $\Psi_{\text{MC}}(\mathbf{x}, \tau) \equiv \Psi(\mathbf{x}, \tau) - \Psi_{\text{LPT}}(\mathbf{x}, \tau)$  is the “mode-coupling residual”. Using this Ansatz, the Eulerian position is  $\mathbf{x} = \mathbf{q} + \Psi_{\text{LPT}} + \Psi_{\text{MC}}$ , and the equation of motion, which reads schematically (omitting constants and Hubble expansion; see equation (1.74))

$$\frac{d^2 \mathbf{x}}{d\tau^2} = -\nabla_{\mathbf{x}} \Phi, \quad (7.4)$$

<sup>5</sup> Following [Tassev & Zaldarriaga \(2012c\)](#), this first term can be written more generally in Fourier space as  $\Psi_{\star}(\mathbf{k}, \tau) = R_{\text{LPT}}(k, \tau) \Psi_{\text{LPT}}(\mathbf{k}, \tau)$ , where  $R_{\text{LPT}}(k, \tau)$  is a transfer function that we ignore here for simplicity.

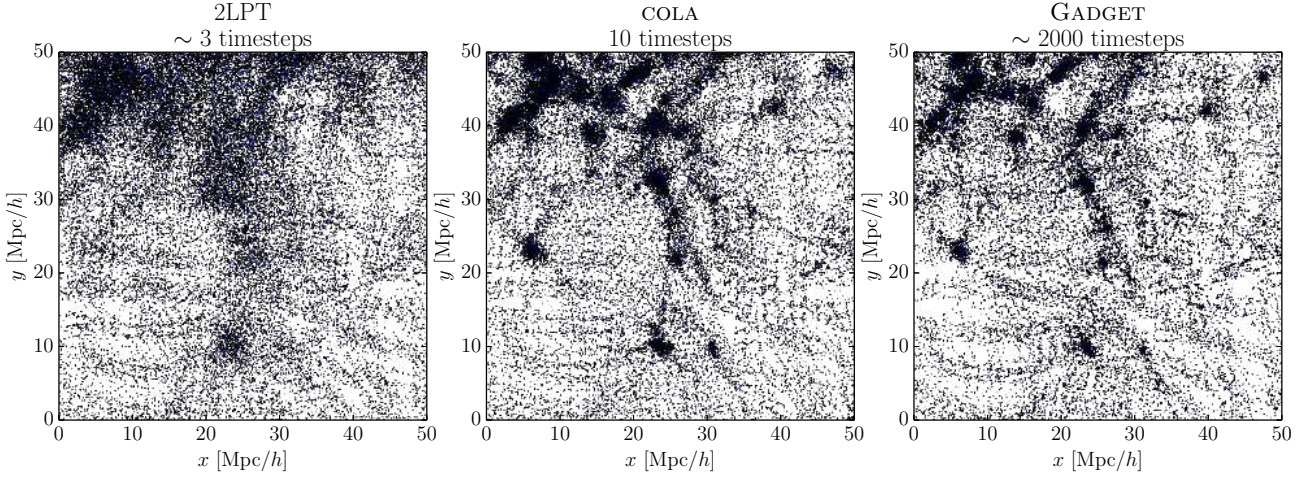


Figure 7.3: Slices through three particle realizations evolved from the same initial conditions up to  $z = 0$ . The particles are shown as black points. Each slice is 20 Mpc/h thick and 50 Mpc/h on the side. The left panel shows the 2LPT approximation, of computational cost roughly equivalent to 3 timesteps of a  $N$ -body code. The right panel shows the reference result obtained from GADGET-2 after  $\sim 2000$  timesteps, starting from 2LPT initial conditions at  $z = 69$ . The middle panel shows the result obtained with COLA with 10 timesteps, starting from 2LPT initial conditions at  $z = 9$ .

can be rewritten in a frame comoving with “LPT observers”, whose trajectories are given by  $\Psi_{\text{LPT}}$ , as

$$\frac{d^2\Psi_{\text{MC}}}{d\tau^2} = -\nabla_{\mathbf{x}}\Phi - \frac{d^2\Psi_{\text{LPT}}}{d\tau^2}. \quad (7.5)$$

In analogy with classical mechanics,  $d^2\Psi_{\text{LPT}}/d\tau^2$  can be thought of as a fictitious force acting on particles, coming from the fact that we are working in a non-inertial frame of reference.

The standard approach in PM codes (see appendix B) is to discretize the second-derivative time operator in equation (7.4). At large scales, this is nothing more than solving for the linear growth factor. Therefore, if few timesteps are used in PM codes, the large-scale structure will be miscalculated only because of a faulty estimation of the growth factor, the exact value of which being well-known.

In contrast, the COLA method uses a numerical discretization of the operator  $d^2/d\tau^2$  only on the left-hand side of equation (7.5) and exploits the exact analytic expression for the fictitious force,  $d^2\Psi_{\text{LPT}}/d\tau^2$ . The equation solved by COLA, equation (7.5), is obviously equivalent to (7.4). However, as demonstrated by Tassev, Zaldarriaga & Eisenstein (2013), using this framework requires a smaller number of timesteps to recover accurate particle realizations. In particular, they show that as few as 10 timesteps from  $z = 9$  to  $z = 0$  are sufficient to obtain an accurate description of halo statistics up to halos of mass  $10^{11} M_{\odot}/h$ , without resolving the internal dynamics of halos. Concerning the description of the large-scale matter density field, 10 COLA timesteps achieve better than 95% cross-correlation with the true result up to  $k \sim 2 \text{ Mpc}/h$ .

As an illustration of the performance of COLA, we show slices through corresponding 2LPT, COLA and GADGET particle realizations in figure 7.3. The simulations contain  $512^3$  particles in a  $750 \text{ Mpc}/h$  cubic box with periodic boundary conditions. Forces are calculated on a PM grid of  $512^3$  cells. The initial conditions are generated with 2LPT at a redshift of  $z = 69$  for GADGET and  $z = 9$  for COLA.

### 7.3.2 Non-linear BORG-COLA realizations

This section draws from section II.B. in Leclercq, Jasche & Wandelt (2015c).

In chapter 9, we use an ensemble of 1,097 large-scale structure realizations produced via non-linear filtering of BORG samples with COLA. The initial density field, defined on a cubic equidistant grid with side length of  $750 \text{ Mpc}/h$  and  $256^3$  voxels, is populated by  $512^3$  particles placed on a regular Lagrangian lattice. The particles are evolved with 2LPT to the redshift of  $z = 69$  and with COLA from  $z = 69$  to  $z = 0$ . The final density field is constructed by binning the particles with a CiC method on a  $256^3$ -voxel grid. This choice corresponds to a resolution of around  $3 \text{ Mpc}/h$  for all the maps described in chapter 9. In this fashion, we generate a

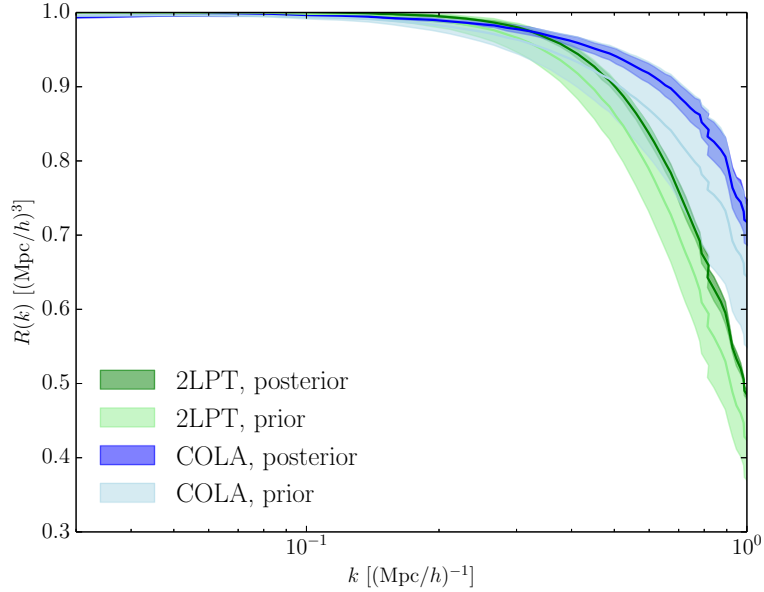


Figure 7.4: Cross-correlations between density fields at redshift zero, computed with a mesh size of 3 Mpc/h. The reference fields are the result of GADGET-2. The lines correspond to the cross-correlation between unconstrained 2LPT realizations and corresponding simulations (“2LPT, prior”), constrained 2LPT samples inferred by BORG and corresponding optimal filtering (“2LPT, posterior”), unconstrained COLA realizations and corresponding simulations (“COLA, prior”), constrained BORG-COLA samples and corresponding optimal filtering (“COLA, posterior”). In each case, we use 11 constrained or unconstrained realizations. The solid lines correspond to the mean among all realizations used in this work, and the shaded regions correspond to the  $2\text{-}\sigma$  credible interval estimated from the standard error of the mean.

large set of data-constrained reconstructions of the present-day dark matter distribution (see also Lavaux, 2010; Kitaura, 2013; Heß, Kitaura & Gottlöber, 2013; Nuza *et al.*, 2014). To ensure sufficient accuracy, 30 timesteps logarithmically-spaced in the scale factor are used for the evolution with COLA.

COLA enables us to cheaply generate non-linear density fields at the required accuracy, as we now show. The power spectrum of non-linear BORG-COLA realizations is shown in figure 7.2 in comparison to that of unconstrained realizations and to samples optimally filtered with GADGET-2. In figure 7.4, we plot the cross-correlation between approximate density fields (predicted by 2LPT or by COLA) and the result of GADGET-2, for both unconstrained and constrained realizations. On these plots, it can be checked that our constrained samples, inferred by BORG and filtered with COLA, contain the additional power expected in the non-linear regime and cross-correlate at better than 95% accuracy with the corresponding fully non-linear realizations, up to  $k \approx 0.4 \text{ Mpc}/h$ . Therefore, as for unconstrained simulations, our setup yields vanishing difference between the representation of constrained density fields with COLA and with GADGET-2, at the scales of interest of this work.

## **Part IV**

# **Cosmic web analysis**





# Dark matter voids in the SDSS galaxy survey

## Contents

<b>8.1</b>	<b>Introduction</b>	<b>117</b>
<b>8.2</b>	<b>Methodology</b>	<b>120</b>
8.2.1	Bayesian large-scale structure inference with the BORG algorithm	120
8.2.2	Generation of data-constrained reconstructions	121
8.2.3	Void finding and processing	121
8.2.4	Blackwell-Rao estimators for dark matter void realizations	122
8.2.5	Void catalogs for comparison of our results	124
<b>8.3</b>	<b>Properties of dark matter voids</b>	<b>125</b>
8.3.1	Number function	125
8.3.2	Ellipticity distribution	126
8.3.3	Radial density profiles	127
<b>8.4</b>	<b>Summary and conclusions</b>	<b>128</b>

---

“Lost and forgotten be, darker than the darkness,  
Where gates stand for ever shut, till the world is mended.”  
— [John Ronald Reuel Tolkien \(1954\)](#), *The Fellowship of the Ring*

---

## Abstract

What do we know about voids in the dark matter distribution given the Sloan Digital Sky Survey and assuming the  $\Lambda$ CDM model? In chapter 5, application of the Bayesian inference algorithm BORG to the SDSS Data Release 7 main galaxy sample has generated detailed Eulerian and Lagrangian representations of the large-scale structure as well as the possibility to accurately quantify corresponding uncertainties. Building upon these results, we present constrained catalogs of voids in the Sloan volume, aiming at a physical representation of dark matter underdensities and at the alleviation of the problems due to sparsity and biasing on galaxy void catalogs. To do so, we generate data-constrained reconstructions of the presently observed large-scale structure using a fully non-linear gravitational model. We then find and analyze void candidates using the VIDE toolkit. Our methodology therefore predicts the properties of voids based on fusing prior information from simulations and data constraints. For usual void statistics (number function, ellipticity distribution and radial density profile), all the results obtained are in agreement with dark matter simulations. Our dark matter void candidates probe a deeper void hierarchy than voids directly based on the observed galaxies alone. The use of our catalogs therefore opens the way to high-precision void cosmology at the level of the dark matter field. We have made the void catalogs used in this work available at <http://www.cosmicvoids.net>.

This chapter is adapted from its corresponding publication, [Leclercq et al. \(2015\)](#).

## 8.1 Introduction

Observations of the cosmic large-scale structure have revealed that galaxies tend to lie in thin wall-like structures surrounding large underdense regions known as voids, which constitute most of the volume of the Universe. Although the discovery of cosmic voids dates back to some of the first galaxy redshift surveys



(Gregory & Thompson, 1978; Kirshner *et al.*, 1981; de Lapparent, Geller & Huchra, 1986) and their significance was assessed in some early studies (Martel & Wasserman, 1990; van de Weygaert & van Kampen, 1993; Goldberg & Vogeley, 2004), the systematic analysis of void properties has only been considered seriously as a source of cosmological information in the last decade (e.g. Sheth & van de Weygaert, 2004; Colberg *et al.*, 2005; Viel, Colberg & Kim, 2008; Betancort-Rijo *et al.*, 2009; Lavaux & Wandelt, 2010; Biswas, Alizadeh & Wandelt, 2010; van de Weygaert & Platen, 2011; Lavaux & Wandelt, 2012, and references therein). Like overdense tracers of the density field such as clusters, voids can be studied by statistical methods in order to learn about their distribution and properties compared to theoretical predictions.

Generally, direct sensitivity of void statistics to cosmology is only guaranteed for the underdense regions of the overall matter density field, which includes a large fraction of dark matter. These are the physical voids in the LSS, for which theoretical modeling is established. However, absent direct measurements of dark matter underdensities, current void catalogs are defined using the locations of galaxies in large redshift surveys (Pan *et al.*, 2012; Sutter *et al.*, 2012b, 2014d; Nadathur & Hotchkiss, 2014). Since galaxies trace the underlying mass distribution only sparsely, void catalogs are subject to uncertainty and noise. Additionally, numerical simulations show that there exists a population of particles in cosmic voids. This is an indication of physical biasing in galaxy formation: there is primordial dark and baryonic matter in voids, but due to the low density, little galaxy formation takes place there. Additionally, due to complex baryonic physics effects during their formation and evolution, galaxies are biased tracers of the underlying density field, which gives rise to qualitatively different void properties.

The sensitivity of void properties to the sampling density and biasing of the tracers has only been recently analyzed in depth on simulations, by using synthetic models to mimic realistic surveys. Little & Weinberg (1994); Benson *et al.* (2003); Tinker & Conroy (2009); Sutter *et al.* (2014c) found that the statistical properties of voids in galaxy surveys are not the same as those in dark matter distributions. At lower tracer density, small voids disappear and the remaining voids are larger and more spherical. Their density profiles get slightly steeper, with a considerable increase of their compensation scale, which potentially may serve as a static ruler to probe the expansion history of the Universe (Hamaus *et al.*, 2014b). Hamaus, Sutter & Wandelt (2014) recently proposed a universal formula for the density profiles of voids, describing in particular dark matter voids in simulations (see also Colberg *et al.*, 2005; Paz *et al.*, 2013; Ricciardelli, Quilis & Varela, 2014; Nadathur *et al.*, 2014). The connection between galaxy voids and dark matter voids on a one-by-one basis is difficult due to the complex internal hierarchical structure of voids (Dubinski *et al.*, 1993; van de Weygaert & van Kampen, 1993; Sahni, Sathyaprakash & Shandarin, 1994; Sheth & van de Weygaert, 2004; Aragon-Calvo & Szalay, 2013; Sutter *et al.*, 2014d,b). However, the nature of this relationship determines the link between a survey, with its particular tracer density, and the portion of the cosmic web that it represents. Understanding this connection is of particular importance in light of recent results that probe the LSS via its effect on photons geodesics. These results include Melchior *et al.* (2014); Clampitt & Jain (2014), which probe the dark matter distribution via weak gravitational lensing; Ilić, Langer & Douspis (2013); Planck Collaboration (2014a) for the detection of the integrated Sachs-Wolfe effect in the cosmic microwave background, sensitive to the properties of dark energy. As a response to this demand, Sutter *et al.* (2014b) found that voids in galaxy surveys always correspond to underdensities in the dark matter, but that their centers may be offset and their size can differ, in particular in sparsely sampled surveys where void edges suffer fragmentation.

While previous authors offer broad prescriptions to assess the effects of sparsity and biasing of the tracers on voids, the connection between galaxy voids of a particular survey and dark matter underdensities remains complex. In particular, disentangling these effects from cosmological signals in presence of the uncertainty inherent to any cosmological observation (selection effects, survey mask, noise, cosmic variance) remains an open question. In this work, we propose a method designed to circumvent the issues due to the conjugate and intricate effects of sparsity and biasing on galaxy void catalogs. In doing so, we will show that voids in the dark matter distribution can be constrained by the *ab initio* analysis of surveys of tracers, such as galaxies. We will demonstrate the feasibility of our method and obtain catalogs of dark matter voids candidates in the Sloan Digital Sky Survey Data Release 7.

Our method is based on the identification of voids in the dark matter distribution inferred from large-scale structure surveys. The constitution of such maps from galaxy positions, also known as “reconstruction”, is a field in which Bayesian methods have led to enormous progress over the last few years. Initial approaches typically relied on approximations such as a multivariate Gaussian or log-normal distribution for density fields, with a prescription for the power spectrum to account for the correct two-point statistics (Lahav *et al.*, 1994; Zaroubi, 2002; Erdođdu *et al.*, 2004; Kitaura & Enßlin, 2008; Kitaura *et al.*, 2009; Kitaura, Jasche & Metcalf,

2010; Jasche & Kitaura, 2010; Jasche *et al.*, 2010b,a). However, due to their potentially complex shapes, proper identification of structures such as voids requires reconstructions correct not only at the level of the power spectrum, but also higher-order correlators. Inferences of this kind from observational data have only been made possible very recently by the introduction of physical models of structure formation in the likelihood. This naturally moves the problem to the inference of the initial conditions from which the large-scale structure originates (Jasche & Wandelt, 2013a; Kitaura, 2013; Wang *et al.*, 2013).

This work exploits the recent application of the BORG (Bayesian Origin Reconstruction from Galaxies, Jasche & Wandelt (2013a), see chapter 4) algorithm to the Sloan Digital Sky Survey galaxies (Jasche, Leclercq & Wandelt, 2015, see chapter 5), and on the subsequent generation of constrained non-linear realizations of the present large-scale distribution of dark matter. BORG is a full-scale Bayesian framework, permitting the four-dimensional physical inference of density fields in the linear and mildly non-linear regime, evolving gravitationally from the initial conditions to the presently observed large-scale structure. By exploring a highly non-linear and non-Gaussian LSS posterior distribution via efficient Markov Chain Monte Carlo methods, it also provides naturally and fully self-consistently accurate uncertainty quantification for all derived quantities. A straightforward use of reconstructed initial conditions is to resimulate the considered volume (Lavaux, 2010; Kitaura, 2013; Heß, Kitaura & Gottlöber, 2013). In the same spirit, building upon the inference of the initial conditions by BORG, one can generate a set of data-constrained realizations of the present large-scale structure via full  $N$ -body dynamics. As we will show, we make use of initial conditions reconstructed by BORG without any further post-processing, which demonstrates the high quality of inference results.

Due to the limited number of phase-space foldings, the influence of non-linearity in cosmic voids is expected to be milder as compared to galaxies and dark matter halos (Neyrinck, 2012; Neyrinck & Yang, 2013; Leclercq *et al.*, 2013, see also Abel, Hahn & Kaehler, 2012; Falck, Neyrinck & Szalay, 2012; Shandarin, Habib & Heitmann, 2012). For this reason, voids are more closely related to the initial conditions of the Universe, which makes them the ideal laboratories for physical application of Bayesian inference with BORG. In this work, we apply the void finder algorithm VIDE (Sutter *et al.*, 2015b), based on ZOBOV (Neyrinck, 2008), to data-constrained, non-linear reconstructions of the LSS. Each of them is a full physical realization of densely-sampled particles tracing the dark matter density field. In this fashion, we construct catalogs of dark matter voids in the SDSS volume robust to sparsity and biasing of galaxies. As we will show, this procedure drastically reduces statistical uncertainty in void catalogs. Additionally, the use of data-constrained reconstructions allows us to extrapolate the void identification in existing data (e.g. at very small or at the largest scales, at high redshift or near the survey boundary).

As described in chapters 4 and 5, (see Jasche & Wandelt, 2013a; Jasche, Leclercq & Wandelt, 2015), the BORG inference framework possesses a high degree of control on observational systematic and statistical uncertainties such as noise, survey geometry and selection effects. Uncertainty quantification is provided via efficient sampling of the corresponding LSS posterior distribution. The resultant set of initial and final density field realizations yields a numerical representation of the full posterior distribution, capturing all data constraints and observational uncertainties. Building upon these results, in this work, we will extend our Bayesian reasoning to void catalogs. Specifically, we apply full non-linear  $N$ -body dynamics to a set of data-constrained initial conditions to arrive at a set of non-linear dark matter density fields at the present epoch. As a result, we obtain a probabilistic description of non-linear density fields constrained by SDSS observations. Applying the VIDE void finder to this set of reconstructions yields  $N$  data-constrained realizations of the catalog, representing the posterior probability distribution for dark matter voids given observations. In this fashion, we have fully Bayesian access to uncertainty quantification via the variation between different realizations. In particular, we are now able to devise improved estimators for any void statistics by the use of Blackwell-Rao estimators. To assess the robustness of this technique for cosmological application, we focus on three key void observables: number functions, ellipticity distributions and radial density profiles. These are especially sensitive probes of non-standard cosmologies (Bos *et al.*, 2012) and are well understood in both data and simulations (e.g Sutter *et al.*, 2014d).

As a general matter, we stress that these data-constrained realizations of dark matter void catalogs were obtained assuming a  $\Lambda$ CDM prior. Using our products for model testing therefore requires care: in the absence of data constraints, one will simply be dealing with realizations of the  $\Lambda$ CDM prior. Consequently, any departure from unconstrained  $\Lambda$ CDM predictions are driven by the data. Conversely, for model tests where the data are not strongly informative, agreement with  $\Lambda$ CDM is the default answer.

This chapter is organized as follows. In section 8.2, we describe our methodology: Bayesian inference with the BORG algorithm, non-linear filtering of the results, void identification technique and Blackwell-Rao estimators

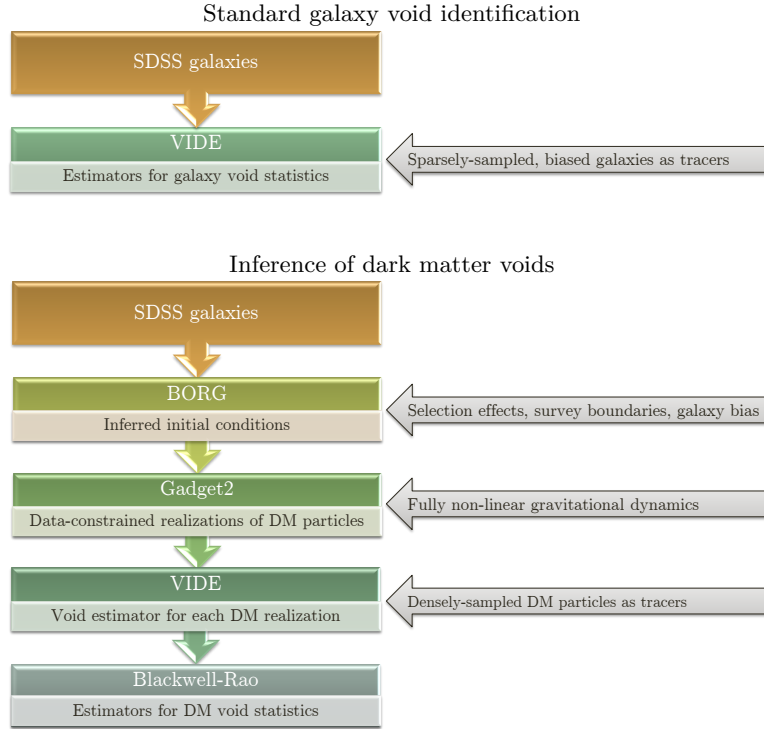


Figure 8.1: Schematic representation of our methodology for the inference of dark matter voids (lower panel) in comparison to the standard approach for the identification of galaxy voids (upper panel).

for void statistics. In section 8.3, we examine the properties of the dark matter voids in our catalogs. Finally, in section 8.4 we summarize our results, discuss perspectives for existing and upcoming galaxy surveys and offer concluding comments.

## 8.2 Methodology

In this section, we describe our methodology step by step:

1. inference of the initial conditions with BORG (section 8.2.1),
2. generation of data-constrained realizations of the SDSS volume (section 8.2.2),
3. void finding and processing (section 8.2.3),
4. combination of different void catalogs with Blackwell-Rao estimators (section 8.2.4).

In section 8.2.5, we describe the void catalogs used as references for comparison with our results. These are galaxy void catalogs directly based on SDSS galaxies without use of our methodology, and catalogs of voids in dark matter simulations.

A schematic representation of our procedure is represented in figure 8.1, in comparison to the standard approach of finding voids using galaxies as tracers.

### 8.2.1 Bayesian large-scale structure inference with the BORG algorithm

This work builds upon previous results, obtained by the application of BORG (Bayesian Origin Reconstruction from Galaxies, Jasche & Wandelt, 2013a) to SDSS main galaxy data (Jasche, Leclercq & Wandelt, 2015). In the rest of this section, we summarize its most stringent features; the reader is referred to chapters 4 and 5 for all details.

The BORG algorithm is a fully probabilistic inference machinery aiming at the analysis of linear and mildly-non-linear density and velocity fields in galaxy observations. It incorporates a physical model of cosmological

structure formation, which translates the traditional task of reconstructing the non-linear three-dimensional density field into the task of inferring corresponding initial conditions from present cosmological observations. This approach yields a highly non-trivial Bayesian inference, requiring to explore very high-dimensional and non-linear spaces of possible solutions to the initial conditions problem from incomplete observations. Typically, these parameter spaces comprise on the order of  $10^6$  to  $10^7$  parameters, corresponding to the elements of the discretized observational domain.

Specifically, the BORG algorithm explores a posterior distribution consisting of a Gaussian prior, describing the statistical behavior of the initial density field at a cosmic scale factor of  $a = 10^{-3}$ , linked via second-order Lagrangian perturbation theory to a Poissonian model of galaxy formation at the present epoch (for details see [Jasche & Wandelt, 2013a](#) and [Jasche, Leclercq & Wandelt, 2015](#)). As pointed out by previous authors (see e.g. [Moutarde \*et al.\*, 1991](#); [Buchert, Melott & Weiß, 1994](#); [Bouchet \*et al.\*, 1995](#); [Scoccimarro, 2000](#); [Bernardeau \*et al.\*, 2002](#); [Scoccimarro & Sheth, 2002](#), and chapter 2), 2LPT describes the one-, two- and three-point statistics correctly and represents higher-order statistics very well. Consequently, the BORG algorithm naturally accounts for features of the cosmic web, such as filaments, that are typically associated to high-order statistics induced by non-linear gravitational structure formation processes.

Besides physical structure formation, the posterior distribution also accounts for survey geometry, selection effects and noise, inherent to any cosmological observation (see section 4.2). Corresponding full Bayesian uncertainty quantification is provided by exploring this highly non-Gaussian and non-linear posterior distribution via an efficient Hamiltonian Markov Chain Monte Carlo sampling algorithm (see [Jasche & Wandelt, 2013a](#), and sections 3.4.3, 4.3.2, for details). In order to account for luminosity dependent galaxy bias ([Jasche & Wandelt, 2013b](#)) and to make use of automatic noise calibration, we further use modifications introduced to the original BORG algorithm by [Jasche, Leclercq & Wandelt \(2015\)](#) (see section 4.3.1).

In this work, we make use of the 12,000 samples of the posterior distribution generated by [Jasche, Leclercq & Wandelt \(2015\)](#), described in chapter 5, which constitute highly-detailed and accurate reconstructions of the initial and present-day density fields constrained by SDSS observations.

## 8.2.2 Generation of data-constrained reconstructions

Starting from 11 statistically independent initial conditions realizations from the BORG SDSS analysis, we generated a set of fully non-linear, constrained reconstructions of the LSS. This step is achieved via optimal filtering of BORG results with the GADGET-2 ([Springel, Yoshida & White, 2001](#); [Springel, 2005](#)) cosmological code. For details on the non-linear filtering procedure, see chapter 7, in particular section 7.2 for the description of the set of realizations used in this chapter.

## 8.2.3 Void finding and processing

### 8.2.3.1 Void finding

We identify and post-process voids with the VIDE (Void IDentification and Examination) toolkit<sup>1</sup> ([Sutter \*et al.\*, 2015b](#), also described in section C.1 of appendix C), which uses a highly modified version of ZOBOV ([Neyrinck, 2008](#); [Lavaux & Wandelt, 2012](#); [Sutter \*et al.\*, 2012b](#)) to create a Voronoi tessellation of the tracer particle population and the watershed transform to group Voronoi cells into zones and voids ([Platen, van de Weygaert & Jones, 2007](#)). The watershed transform identifies catchment basins as the cores of voids, and ridgelines, which separate the flow of water, as the boundaries of voids. It naturally builds a nested hierarchy of voids ([Lavaux & Wandelt, 2012](#); [Bos \*et al.\*, 2012](#)). For the purposes of this work, we examine all voids regardless of their position in the hierarchy. The pipeline imposes a density-based threshold within the void finding operation: voids only include as additional members Voronoi zones if the minimum ridge density between that zone and the void is less than 0.2 times the mean particle density ([Platen, van de Weygaert & Jones, 2007](#); see [Blumenthal \*et al.\*, 1992](#); [Sheth & van de Weygaert, 2004](#) for the role of the corresponding  $\delta = -0.8$  underdensity). If a void consists of only a single zone (as they often do in sparse populations) then this restriction does not apply.

VIDE provides several useful definitions used in this work, such as the effective radius,

$$R_v \equiv \left( \frac{3}{4\pi} V \right)^{1/3}, \quad (8.1)$$

<sup>1</sup> <http://www.cosmicvoids.net>

where  $V$  is the total volume of the Voronoi cells that contribute to the void. We use this radius definition to ignore voids with  $R_v$  below the mean particle spacing  $\bar{n}^{-1/3}$  of the tracer population, as these are increasingly affected by Poisson fluctuations. VIDE also reports the volume-weighted center, or macrocenter, as

$$\mathbf{x}_v \equiv \frac{1}{\sum_i V_i} \sum_i \mathbf{x}_i V_i, \quad (8.2)$$

where  $\mathbf{x}_i$  and  $V_i$  are the positions and Voronoi volumes of each tracer particle  $i$ , respectively.

In each tracer population, the VIDE pipeline provides void estimators ; in particular, the three statistics we will focus on in section 8.3: number count, ellipticity distribution and radial density profile.

In figure 8.2, we show slices through different data-constrained realizations. The density of dark matter particles identified by VIDE as being part of a void is represented in gray scale. Note that, since ZOBOV essentially performs a division of space in different void regions with vanishingly-thin ridges, almost all particles initially present in the dark matter field are conserved. For clarity of the visualization, the quantity represented is  $\ln(2 + \delta)$  where  $\delta$  is the density contrast of particles in voids. The SDSS galaxies used for the BORG analysis are overplotted as red dots. The core of dark matter voids (using a density threshold  $\delta < -0.3$ ) is shown in color. As can be observed, dark matter voids also correspond to underdensities in the field traced by galaxies, which is in agreement with the results obtained by Sutter *et al.* (2014b) in simulations.

### 8.2.3.2 Selection of voids

The VIDE pipeline identifies all dark matter voids in the non-linear data-constrained realizations described in section 8.2.2. These live in boxes of 750 Mpc/ $h$  side length with periodic boundary conditions. In order to select physically meaningful dark matter void candidates, we have to select a subsample of voids which intersect the volume of the box actually constrained by SDSS galaxies.

As described in chapter 5, unobserved and observed regions in the inferred final density fields do not appear visually distinct, a consequence of the excellent performance of the 2LPT model implemented in BORG as a physical description of structure formation. In addition, due to the non-local transport of observational information between initial and final conditions, the region influenced by data extends beyond the survey boundaries and the large-scale structure appears continuous there. The fact that data constraints can radiate out of the survey volume has been known since the first constrained reconstructions of the mass distribution (Bertschinger, 1987; Hoffman & Ribak, 1991; van de Weygaert & Bertschinger, 1996), where a power spectrum prior was assumed to sample constrained Gaussian random fields. Here, as detailed in chapters 4 and 5, constraints are propagated by the structure formation model assumed in the inference process (2LPT), which accounts not only for two-point statistics, but for the full hierarchy of correlators, in its regime of validity. Therefore, dark matter voids candidates intersecting the survey boundaries can be considered as physical if a significant fraction of their volume is influenced by the data.

The survey response operator  $R$  is a voxel-wise function representing simultaneously the survey geometry (observed and unobserved regions) and the selection effects in galaxy catalogs. Here, we kept for  $R$  the average over the six luminosity bins used in the BORG SDSS run (for details see chapter 5). For the purpose of this work, we keep all void candidates whose center is in a region where  $R$  is strictly positive. This region represents  $7.9 \times 10^7$  cubic Mpc/ $h$ , around 18.7% of the full box. In each of the 11 realizations used in this work, we kept around 166,000 data-constrained voids out of 886,000 voids in the entire box.

In figure 8.2, the survey response operator is shown in color from purple (totally unobserved region) to blue (region fully constrained by the data). One can see the correct propagation of information operated by BORG, as voids appear continuous at the survey boundaries.

### 8.2.4 Blackwell-Rao estimators for dark matter void realizations

A particular advantage of our Bayesian methodology is the ability to provide accurate uncertainty quantification for derived dark matter void properties. In particular, the Markovian samples described in chapter 5 permit us to employ a Blackwell-Rao estimator to describe the posterior distribution for inferred dark matter voids. Specifically, we are interested in deriving the posterior distribution  $\mathcal{P}(x|d)$  of a dark matter void property  $x$  given observations  $d$ . Using the realizations of the initial conditions  $\delta^i$  and the dark matter void realizations  $V$  generated by the approach described in sections 8.2.2 and 8.2.3, we obtain



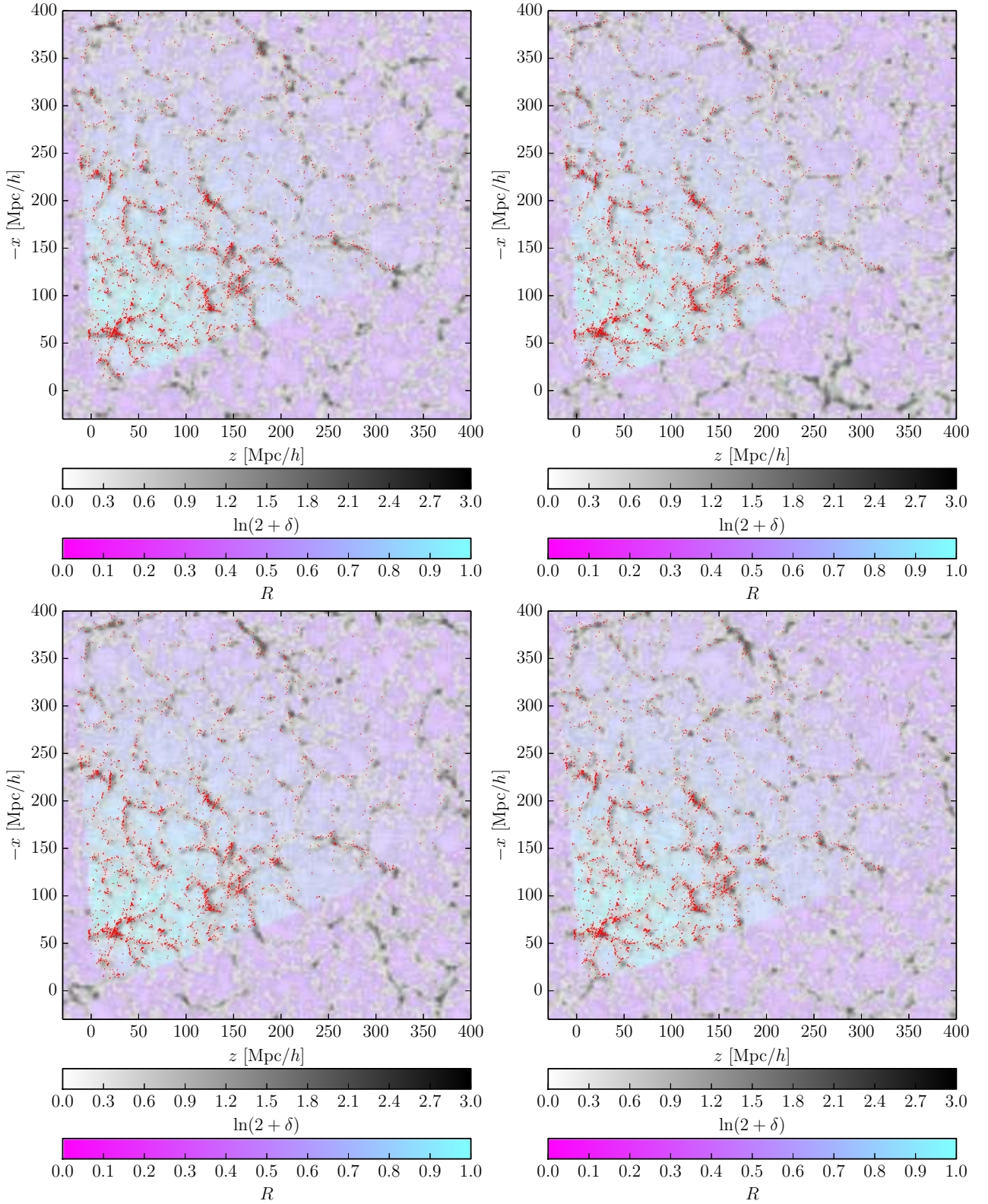


Figure 8.2: Slices through different data-constrained realizations used to build samples of the dark matter void catalog. The SDSS galaxies used for the inference with BORG are represented as red dots. The density of dark matter particles identified by VIDE as being part of a void is shown in gray scale. In color, we show the particles that live in the core of dark matter voids (in a density environment smaller than  $-0.3$  times the average density). The survey response operator  $R$  shows how well the results are constrained by the data (see text for details). In the observed region, the data are strongly informative about the cosmic web in general and voids in particular; the reconstructions are not prior-dominated.

$$\begin{aligned}
\mathcal{P}(x|d) &= \int \mathcal{P}(x|V) \mathcal{P}(V, \delta^i|d) dV d\delta^i \\
&= \int \mathcal{P}(x|V) \mathcal{P}(V|\delta^i, d) \mathcal{P}(\delta^i|d) dV d\delta^i \\
&= \int \mathcal{P}(x|V) \delta_D(V - \tilde{V}(\delta^i)) \mathcal{P}(\delta^i|d) dV d\delta^i \\
&= \int \mathcal{P}(x|\tilde{V}(\delta^i)) \mathcal{P}(\delta^i|d) d\delta^i \\
&\approx \frac{1}{N} \sum_k \mathcal{P}(x|\tilde{V}(\delta_k^i)) \\
&= \frac{1}{N} \sum_k \mathcal{P}(x|V_k),
\end{aligned} \tag{8.3}$$

where we assumed the dark matter void templates  $V$  to be conditionally independent of the data  $d$  given the initial conditions  $\delta^i$ , and to derive uniquely from the initial density field via the procedure described in sections 8.2.2 and 8.2.3, yielding  $\mathcal{P}(V|\delta^i, d) = \mathcal{P}(V|\delta^i) = \delta_D(V - \tilde{V}(\delta^i))$ . We also exploited the fact that we have a sampled representation of the initial conditions posterior distribution  $\mathcal{P}(\delta^i|d) \approx 1/N \sum_k \delta_D(\delta^i - \delta_k^i)$ , where  $k$  labels one of the  $N$  samples. The last line of equation (8.3) represents the Blackwell-Rao estimator for void property  $x$  to be inferred from our dark matter void catalogs  $V_k$ , providing thorough Bayesian means to quantify uncertainties. It consists of a mixture distribution over different realizations of dark matter void templates.

The VIDE pipeline provides estimated means and variances for derived quantities  $x$ , allowing us to model the distributions  $\mathcal{P}(x|V_k)$  as Gaussians with mean  $x_k$  and variance  $\sigma_k^2$ , for respective dark matter void templates. The final expression for the posterior distribution of  $x$  given the data is therefore

$$\mathcal{P}(x|d) \approx \frac{1}{N} \sum_k \frac{1}{\sqrt{2\pi\sigma_k^2}} \exp\left(-\frac{1}{2} \frac{(x - x_k)^2}{\sigma_k^2}\right). \tag{8.4}$$

Even though we have access to non-Gaussian uncertainty quantification via the posterior distribution given in equation (8.4), for the presentation in this chapter we will be content with estimating means and variances. The mean for  $x$  given  $d$  is

$$\langle x|d \rangle \approx \frac{1}{N} \sum_k x_k, \tag{8.5}$$

and the variance is

$$\langle (x - \langle x \rangle)^2 | d \rangle \approx \frac{1}{N} \sum_k (x_k^2 + \sigma_k^2) - \langle x|d \rangle^2. \tag{8.6}$$

As described in section 8.2.3.2, we select voids in the data-constrained regions of reconstructions of the dark matter density field. Since these regions are the same in different reconstructions, the different void catalogs describe the same region of the actual Universe. For this reason, while estimating uncertainties, it is not possible to simply use all the voids in our catalogs as if they were independent.<sup>2</sup> However, using an increasing number of reconstructions, we shall still see a decrease of statistical uncertainty. Indeed, from (8.5) and (8.6) it follows that

$$\langle (x - \langle x \rangle)^2 | d \rangle \leq \frac{1}{N} \sum_k \sigma_k^2, \tag{8.7}$$

which means that the combination of different realizations will generally yield an improved estimator for any original statistics.

Note that this procedure is completely general and applies to any estimator provided by the VIDE pipeline.

### 8.2.5 Void catalogs for comparison of our results

In section 8.3, we will compare our results for dark matter voids to state-of-the-art results for galaxy voids. To do so, we use the catalogs of [Sutter et al. \(2012b\)](#) based on the SDSS DR7 galaxies, publicly available at

<sup>2</sup> We generally recommend special care for proper statistical treatment while working with the data-constrained realizations of our dark matter void catalog, especially if one wants to use frequentist estimators of void properties.



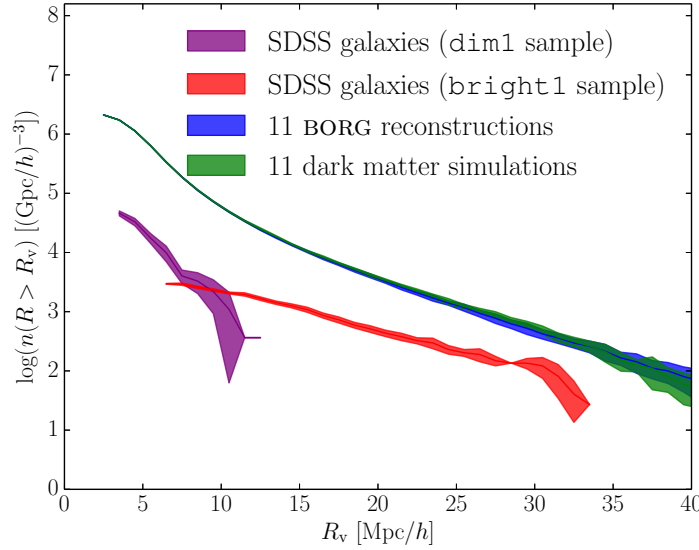


Figure 8.3: Cumulative void number functions. The results from 11 BORG reconstructions (blue) are compared to a dark matter  $N$ -body simulation (green) and to the galaxy voids directly found in two volume-limited sub-samples of the SDSS DR7 (**dim1**, purple and **bright1**, red). The solid lines are the measured or predicted number functions and the shaded regions are the  $2\text{-}\sigma$  Poisson uncertainties. Fewer voids are found in observations than in dark matter simulations, due to the sparsity and bias of tracers, as well as observational uncertainty coming from the survey geometry and selection effects. Number functions from BORG reconstructions agree with simulations at all scales.

<http://www.cosmicvoids.net>. In particular, we compare to the voids found in the **bright1** and **dim1** volume-limited galaxy catalogs, for which the mean galaxy separations are 8 and 3 Mpc/ $h$ , respectively (for details, see Sutter *et al.*, 2012b).

Assessment of our results for dark matter voids in SDSS data also require systematic comparison to dark matter voids found in cosmological simulations. We ran 11 such unconstrained simulations with the same setup as described in section 8.2.2 for the generation of data-constrained realizations. We started from Gaussian random fields with an Eisenstein & Hu (1998, 1999) power spectrum using the fiducial cosmological parameters of the BORG analysis ( $\Omega_m = 0.272$ ,  $\Omega_\Lambda = 0.728$ ,  $\Omega_b = 0.045$ ,  $h = 0.702$ ,  $\sigma_8 = 0.807$ ,  $n_s = 0.961$ , see chapter 5). These initial density fields, defined in a 750 Mpc/ $h$  cubic box of  $256^3$  voxels, are occupied by a Lagrangian lattice of  $512^3$  dark matter particles. These are evolved to  $z = 69$  with 2LPT and from  $z = 69$  to  $z = 0$  with GADGET-2. As for constrained realizations, in our simulations we selected the voids located inside the observed SDSS volume (see section 8.2.3.2) and combined properties using Blackwell-Rao estimators (see section 8.2.4).

## 8.3 Properties of dark matter voids

In this section, we describe the statistical properties of the dark matter voids found in the data-constrained parts of our reconstructions of the SDSS volume. We focus on three key statistical summaries abundantly described in the literature: number count, ellipticity distribution and radial density profiles.

### 8.3.1 Number function

The number function of voids provides a simple, easily accessible, and surprisingly sensitive cosmological probe. For example, the number function has been shown to respond to coupled dark matter-dark energy (Li & Zhao, 2009; Sutter *et al.*, 2015a), modified gravity (Li, Zhao & Koyama, 2012; Clampitt, Cai & Li, 2013), and variations in fundamental cosmological parameters (Pisani *et al.*, 2015). While most studies of the number function take place in  $N$ -body simulations, there has also been significant theoretical and analytical work, beginning with the excursion set formulation of Sheth & van de Weygaert (2004) and continuing through further enhancements to account for the complex nature of void shapes (Jennings, Li & Hu, 2013). As previous authors (Müller *et al.*, 2000; Sutter *et al.*, 2012b, 2014d; Nadathur & Hotchkiss, 2014; Nadathur *et al.*, 2014)

have noted, there tend to be fewer voids in observations than in numerical simulations, especially for small voids. This is due to the conjugate effects of sparsity and biasing of tracers, which can modify the number function in complex ways (Furlanetto & Piran, 2006; Sutter *et al.*, 2014c,d), as well as survey geometries and selection effects, which can non-trivially diminish the void population. However, recently Sutter *et al.* (2014d) showed a correspondence between observed and theoretical number functions once these factors are taken into account.

Figure 8.3 shows the cumulative void number function in BORG reconstructions (blue) compared to dark matter simulations using the same setup (green) and to galaxy voids in the SDSS DR7 (red and purple). The confidence regions are  $2\text{-}\sigma$  Poisson uncertainties and the blue and green lines use Blackwell-Rao estimators to combine the results in 11 realizations.

We can immediately note the excellent agreement between simulations and dark matter voids candidates in the SDSS as found by our methodology. The two void populations are almost indistinguishable at all scales, which demonstrates that the data-constrained number function predicted by our methodology is exactly that of dark matter voids in numerical simulations. In particular, this proves that our framework correctly permits to circumvent the effects of sparsity and biasing of SDSS galaxies on void number count. Indeed, dark matter voids in our reconstructions are densely-sampled with the same number density as in simulations,  $\bar{n} = 0.318 \text{ (Mpc/h)}^{-3}$  ( $512^3$  particles in  $(750 \text{ Mpc/h})^3$ ) compared to  $\bar{n} \approx 10^{-3} \text{ (Mpc/h)}^{-3}$  for SDSS galaxies (Sutter *et al.*, 2012b). Furthermore, any incorrect treatment of galaxy bias by the BORG algorithm would result in a residual bias in our reconstructions that would yield an erroneous void number function as compared to simulations (Sutter *et al.*, 2014c). The absence of any such feature confirms that galaxy bias is correctly accounted for in our analysis and further validates the framework described in chapter 5 (Jasche, Leclercq & Wandelt, 2015).

Additionally, due to the high density of tracer particles, we find at least around one order of magnitude more voids at all scales than the voids directly traced by the SDSS galaxies, which sample the underlying mass distribution only sparsely. This results in a drastic reduction of statistical uncertainty in void catalogs, as we demonstrate in sections 8.3.2 and 8.3.3.

### 8.3.2 Ellipticity distribution

The shape distribution of voids is complementary to overdense probes of the dark matter density field such as galaxy clusters. Indeed, as matter collapses to form galaxies, voids expand and can do so aspherically. While Icke (1984) argued that voids are expected to become more spherical as they expand, Platen, van de Weygaert & Jones (2008) found that the shape distribution of voids remains complex at late times and showed that the aspherical expansion of voids is strongly linked to the external tidal influence.<sup>3</sup> Therefore, the shapes of empty regions generally change during cosmic evolution and retain information on their formation history. In particular, the void shape distribution potentially serves as a powerful tracer of the equation of state of dark energy (Lee & Park, 2006; Park & Lee, 2007; Biswas, Alizadeh & Wandelt, 2010; Lavaux & Wandelt, 2012; Bos *et al.*, 2012). In addition, the mean stretch of voids along the line of sight may be used for an application of the Alcock-Paczynski test (Alcock & Paczynski, 1979; Ryden, 1995; Lavaux & Wandelt, 2012; Sutter *et al.*, 2012a, 2014a; Hamaus *et al.*, 2014a).

For these applications, it is of crucial importance for the void catalog to be unaffected by systematics due to baryonic physics. Furthermore, as pointed out by Bos *et al.* (2012), in sparse populations such as galaxies it is very difficult to statistically separate  $\Lambda$ CDM from alternative cosmologies using void shapes. As we now show, our framework allows to access void shapes at the level of the dark matter distribution, deeper than with the galaxies, and to reduce the statistical uncertainty due to their sparsity. Note that all the phase information and spatial organization of the LSS is unaffected by our prior assumptions, which generally affect the density amplitudes via the cosmological power spectrum. The geometry of voids discussed here is therefore strongly constrained by the observations.

We simplify the discussion by focusing on the ellipticity, computed by the VIDE toolkit using the eigenvalues of the inertia tensor (for details, see section C.1.3.2 and Sutter *et al.*, 2015b). Figure 8.4 shows the mean ellipticity and the standard error on the mean (i.e.  $\sigma/\sqrt{N_v}$ , where  $\sigma$  is the standard deviation and  $N_v$  is the number of voids) as a function of void effective radius. The red line represents the galaxy voids directly found in the SDSS data, the blue line the dark matter voids of our data-constrained catalogs, and the green line the voids

<sup>3</sup> Tidal effects are taken into account in our analysis since BORG models gravitational evolution up to second order in Lagrangian perturbation theory.

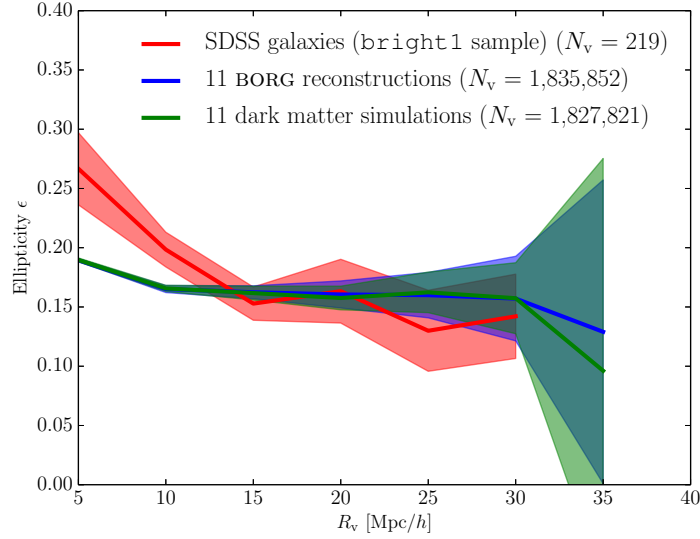


Figure 8.4: Distribution of ellipticities  $\epsilon$  versus effective radii of voids. The solid line shows the mean, and the shaded region is the  $2\text{-}\sigma$  confidence region estimated from the standard error on the mean in each radial bin. Small galaxy voids are found more elliptical than dark matter voids because of important Poisson fluctuations below the mean galaxy separation (8 Mpc/h). Ellipticities of dark matter voids in BORG reconstructions and simulations agree at all scales, and the statistical uncertainty in their determination is drastically reduced in comparison to galaxy void catalogs.

found in dark matter simulations prepared with the same setup. The blue and green lines use Blackwell-Rao estimators to combine the results of 11 realizations. For the interpretation of the ellipticity of small galaxy voids, it is useful to recall that the mean galaxy separation in the `bright1` sample is 8 Mpc/h, meaning that Poisson fluctuations will be of importance for voids whose effective radius is below this scale.

The comparison between dark matter voids of BORG reconstructions and of simulations shows that the predicted ellipticities fully agree with the expectations at all scales. This further demonstrates that our candidates qualify as dark matter voids as defined by numerical simulations, in particular alleviating the galaxy bias problem. Furthermore, as already noted, our inference framework produces many more voids than sparse galaxy catalogs, especially at small scales. This results in a radical reduction of statistical uncertainty in the ellipticity prediction for small dark matter voids as compared to galaxy voids, as can be observed in figure 8.4.

### 8.3.3 Radial density profiles

The radial density profile of voids, reconstructed in real space using techniques such as those described in [Pisani \*et al.\* \(2014\)](#), can be used to test general relativity and constrain dynamical dark energy models ([Shoji & Lee, 2012](#); [Spolyar, Sahlén & Silk, 2013](#)). More generally, it shows a self-similar structure ([Colberg \*et al.\*, 2005](#); [Ricciardelli, Quilis & Varela, 2014](#); [Hamaus, Sutter & Wandelt, 2014](#); [Nadathur \*et al.\*, 2014](#)), and characterizes the LSS in a fundamental way ([van de Weygaert & van Kampen, 1993](#)). All results presented in this section assume that dark matter particles in BORG reconstructions and in simulations live in physical space. The BORG algorithm automatically mitigates redshift-space distortions by treating anisotropic features in the data as noise ([Jasche, Leclercq & Wandelt, 2015](#)). Furthermore, as pointed out by [Padilla, Ceccarelli & Lambas \(2005\)](#), redshift-space distortions have very mild effects on void density profiles. We therefore expect our results to be robust under the transformation from real to redshift space.

Using VIDE, we construct the one-dimensional radial density profiles of stacked voids for various void sizes. Note that we do not apply any rescaling to the void sizes as we stack. Figure 8.5 shows two such profiles, for voids of effective radius in the range 6-8 Mpc/h (left panel) and 20-25 Mpc/h (right panel). The solid lines show the mean and the shaded regions are the  $2\text{-}\sigma$  confidence regions estimated from the standard error on the mean, using Blackwell-Rao estimators for BORG reconstructions and dark matter simulations. At the level of statistical error in our results, our reconstructions show radial density profiles in agreement with simulations at all radii and for all void sizes. Note that, if small voids essentially reflect the prior information used for the BORG analysis and  $N$ -body filtering, bigger voids are strongly constrained by the data. The profile shapes agree

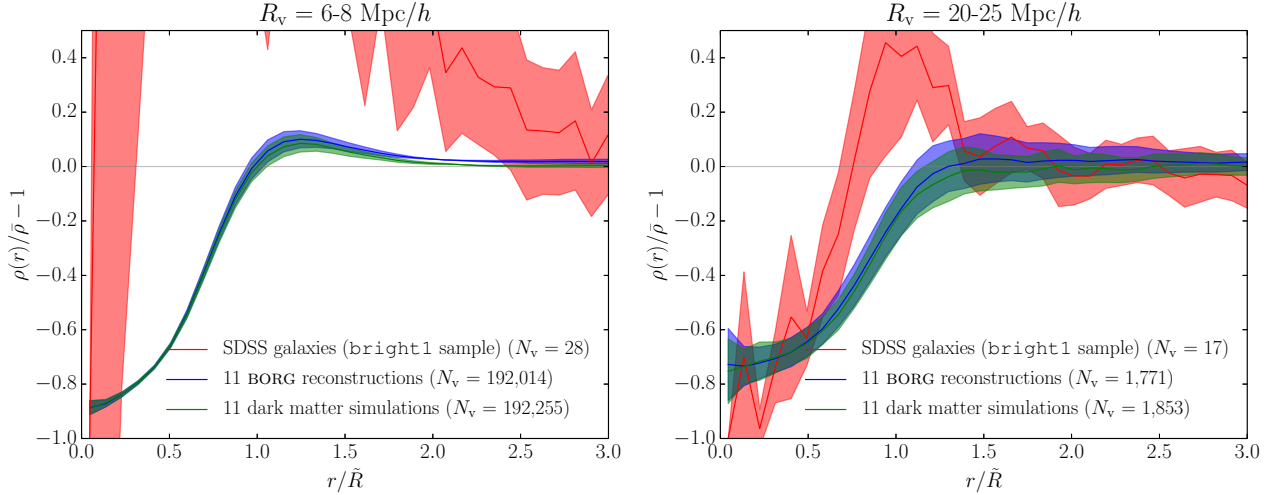


Figure 8.5: One-dimensional radial density profiles of stacked voids, for voids of effective radius in the range 6-8 Mpc/h (left) and 20-25 Mpc/h (right).  $\tilde{R}$  corresponds to the median void size in the stack. The solid line shows the mean, and the shaded region is the  $2\text{-}\sigma$  confidence region estimated from the standard error on the mean in each radial bin. Galaxy void profiles are strongly noise-dominated, contrary to dark matter voids. The heights of compensation ridges are different because dark matter voids are identified in a higher density of tracers, which induces a deeper void hierarchy.

nicely with the results of Sutter *et al.* (2014c); Hamaus, Sutter & Wandelt (2014) from dark matter simulations: higher ridges and lower central densities in smaller voids. Specifically, our reconstructions exhibit the same behaviour as simulations, with a transition scale between small overcompensated to large undercompensated voids (Ceccarelli *et al.*, 2013; Paz *et al.*, 2013; Cai *et al.*, 2014; Hamaus *et al.*, 2014b).

In contrast, galaxy void profiles at the same scales are strongly noise-dominated. This is due to the sparsity and biasing of galaxies, which are alleviated with the present approach. In particular, our methodology performs a meaningful compromise between data and prior information, which predicts corrected shapes and smaller variance for the profiles of dark matter voids as compared to galaxy voids. Note that at the same physical scales (e.g. 20 Mpc/h), galaxy voids and dark matter voids have different ridge heights. This is because a deeper void hierarchy emerges in higher tracer sampling densities, affecting the compensation of voids at a given size (Sutter *et al.*, 2014c).

In addition to the location of all dark matter particles, our inference framework also provides their individual velocity vectors, which are predicted from gravitational clustering. While the direct measurement of individual galaxy velocities is very difficult in most observations, our reconstruction technique readily allows to infer the velocity profile of voids. This allows to make a connection between a static (based on the density profiles) and a dynamic (based on the velocity profiles) characterization of voids. In particular, as mentioned before, our results agree with the existence of a transition scale between two regimes: undercompensated, inflowing voids and overcompensated, outflowing voids, respectively known as void-in-cloud and void-in-void in the terminology originally introduced by Sheth & van de Weygaert (2004).

## 8.4 Summary and conclusions

This chapter is an example of the rich variety of scientific results that have been produced by the recent application (Jasche, Leclercq & Wandelt, 2015) of the Bayesian inference framework BORG (Jasche & Wandelt, 2013a) to the Sloan Digital Sky Survey main sample galaxies. We proposed a method designed to find dark matter void candidates in the Sloan volume. In doing so, we proved that physical voids in the dark matter distribution can be correctly identified by the *ab initio* analysis of galaxy surveys.

Our method relies on the physical inference of the initial conditions for the entire LSS (Jasche & Wandelt, 2013a; Jasche, Leclercq & Wandelt, 2015). Starting from these, we generated realizations of the LSS using a fully non-linear cosmological code. In this fashion, as described in section 8.2.2, we obtained a set of data-constrained reconstructions of the present-day dark matter distribution. The use of fully non-linear dynamics as a filter allowed us to extrapolate the predictions of BORG to the unconstrained non-linear regimes and to obtain an

accurate description of structures. As described in section 8.2.3, we identified the voids in these reconstructions using the void finder of the VIDE pipeline (Sutter *et al.*, 2015b) and applied an additional selection criterion to limit the final catalogs of dark matter voids candidates to regions covered by observations. To check that these candidates qualify for physical voids, we analyzed our catalogs in terms of a set of statistical diagnostics. We focused on three key void statistics, well understood both in data and in simulations, provided by the VIDE toolkit: number function, ellipticity distribution and radial density profile. As mentioned in section 8.2.5, for comparison of our results, we used the void catalog of Sutter *et al.* (2012b), directly based on SDSS main sample galaxies, and unconstrained dark matter simulations produced with the same setup as our reconstructions.

For quantifying the uncertainty, we adopted the same Bayesian philosophy as in the LSS inference framework: several void catalogs are produced, based on different samples of the BORG posterior probability distribution function. Each of them represents a realization of the actual dark matter voids in the Sloan volume, and the variation between these catalogs quantifies the remaining uncertainties of various sources (in particular, survey geometry and selection effects, see chapter 5 for a complete discussion). In order to produce a statistically meaningful combination of our different dark matter void catalogs, in section 8.2.4, we introduced Blackwell-Rao estimators. We showed that the combination of different realizations generally yields an improved estimator for any original void statistic.

For all usual void statistics (number function in section 8.3.1, ellipticity distribution in section 8.3.2 and radial density profiles in section 8.3.3), we found remarkably good agreement between predictions for dark matter voids in our reconstructions and expectations from numerical simulations. This validates our inference framework and qualifies the candidates to physically reasonable dark matter voids, probing a level deeper in the mass distribution hierarchy than galaxies. Further, since sparsity and biasing of tracers modify these statistics (Sutter *et al.*, 2014c), it means that these effects have been correctly accounted for in our analysis. Indeed, in chapter 5 we showed that BORG accurately accounts for luminosity-dependent galaxy bias and performs automatic calibration of the noise level within a fully Bayesian approach. Building on the detailed representation of initial density fields, our reconstructions possess a high density of tracers,  $\bar{n} = 0.318 \text{ (Mpc/h)}^{-3}$ , contrary to galaxies, which sample the underlying mass distribution only sparsely ( $\bar{n} \approx 10^{-3} \text{ (Mpc/h)}^{-3}$ ).

Another important aspect of our methodology is that the use of full-scale physical density fields instead of a scarce population of galaxies allows to adjust the density of tracers to reduce shot noise at the desired level. In our analysis, we found at least one order of magnitude more voids at all scales. This yields a radical reduction of statistical uncertainty in noise-dominated void catalogs, as we have shown for ellipticity distributions and density profiles.

In summary, our methodology permits to alleviate the issues due to the conjugate and intricate effects of sparsity and biasing on galaxy void catalogs, to drastically reduce statistical uncertainty in void statistics, and yields new catalogs of dark matter voids for a variety of cosmological applications. For example, these enhanced data sets can be used for cross-correlation with other cosmological probes such as the cosmic microwave background, to study the integrated Sachs-Wolfe effect, or gravitational lensing shear maps. Along with the ensemble mean density field and corresponding standard deviations inferred by BORG, published as supplementary material with Jasche, Leclercq & Wandelt (2015), we believe that the catalogs of our dark matter voids candidates in the Sloan volume can be of interest to the scientific community. For this reason, all the void catalogs used to produce the results described in this chapter have been made publicly available at <http://www.cosmicvoids.net>, along with the paper corresponding to this chapter (Leclercq *et al.*, 2015).

Our Bayesian methodology, based on inference with BORG and subsequent non-linear filtering of the results, assumes some prior information, namely the standard  $\Lambda$ CDM cosmological framework and initially Gaussian density fluctuations. We want to emphasize that any analysis using our constrained catalogs will be biased toward the confirmation of these assumptions. Therefore, this method will be only applicable if the data contain sufficient support for the presence of non-standard cosmology to overrule the preference for  $\Lambda$ CDM and Gaussianity in our prior. However, any significant departure from standard cosmology means that the prior has been overridden by the likelihood and that such deviations really are supported by the data.

While the recommendations of Sutter *et al.* (2014c) for quantifying and disentangling the effects of sparsity and biasing depend on specific survey details, our inference framework is extremely general. It allows to translate void statistics from current and future galaxy surveys to theory-like, high-resolution dark matter predictions. In this fashion, it is straightforward to decide if any particular void statistic can be directly informative about cosmology. These results indicate a new promising path towards effective and precise void cosmology at the level of the dark matter field.



# Bayesian analysis of the dynamic cosmic web in the SDSS galaxy survey

---



---

“I just wonder how things were put together.”  
— [Claude Shannon](#)

---

## Contents

<b>9.1</b>	<b>Introduction</b>	<b>132</b>
<b>9.2</b>	<b>Methods</b>	<b>134</b>
9.2.1	Bayesian large-scale structure inference with BORG	134
9.2.2	Non-linear filtering of samples with COLA	135
9.2.3	Classification of the cosmic web	135
<b>9.3</b>	<b>The late-time large-scale structure</b>	<b>136</b>
9.3.1	Tidal environment	136
9.3.2	Probabilistic web-type cartography	137
9.3.3	Volume and mass filling fractions	140
<b>9.4</b>	<b>The primordial large-scale structure</b>	<b>141</b>
9.4.1	Tidal environment	142
9.4.2	Probabilistic web-type cartography	142
9.4.3	Volume and mass filling fractions	143
<b>9.5</b>	<b>Evolution of the cosmic web</b>	<b>143</b>
9.5.1	Evolution of the probabilistic maps	147
9.5.2	Volume filling fraction	147
9.5.3	Mass filling fraction	147
<b>9.6</b>	<b>Summary and Conclusion</b>	<b>148</b>

---

## Abstract

Recent application of the Bayesian algorithm BORG to the Sloan Digital Sky Survey main sample galaxies resulted in the physical inference of the formation history of the observed large-scale structure from its origin to the present epoch. In this work, we use these inferences as inputs for a detailed probabilistic cosmic web-type analysis. To do so, we generate a large set of data-constrained realizations of the large-scale structure using a fast, fully non-linear gravitational model. We then perform a dynamic classification of the cosmic web into four distinct components (voids, sheets, filaments, and clusters) on the basis of the tidal field. Our inference framework automatically and self-consistently propagates typical observational uncertainties to web-type classification. As a result, this study produces accurate cosmographic classification of large-scale structure elements in the SDSS volume. By also providing the history of these structure maps, the approach allows an analysis of the origin and growth of the early traces of the cosmic web present in the initial density field and of the evolution of global quantities such as the volume and mass filling fractions of different structures. For the problem of web-type classification, the results described in this chapter constitute the first connection between theory and observations at non-linear scales including a physical model of structure formation and the demonstrated capability of uncertainty quantification. A connection between cosmology and information theory using real data also naturally emerges from our probabilistic approach. Our results constitute quantitative chrono-cosmography of the complex web-like patterns underlying the observed galaxy distribution.

This chapter is adapted from its corresponding publication, [Leclercq, Jasche & Wandelt \(2015c\)](#).



## 9.1 Introduction

The large-scale distribution of matter in the Universe is known to form intricate, complex patterns traced by galaxies. The existence of this large-scale structure, also known as the *cosmic web* (Bond, Kofman & Pogosyan, 1996), has been suggested by early observational projects aiming at mapping the Universe (Gregory & Thompson, 1978; Kirshner *et al.*, 1981; de Lapparent, Geller & Huchra, 1986; Geller & Huchra, 1989; Shectman *et al.*, 1996), and has been extensively analyzed since then by massive surveys such as the 2dFGRS (Colless *et al.*, 2003), the SDSS (e.g. Gott *et al.*, 2005) or the 2MASS redshift survey (Huchra *et al.*, 2012). The cosmic web is usually segmented into different elements: voids, sheets, filaments, and clusters. At late times, low-density regions (voids) occupy most of the volume of the Universe. They are surrounded by walls (or sheets) from which departs a network of denser filaments. At the intersection of filaments lie the densest clumps of matter (clusters). Dynamically, matter tends to flow out of the voids to their compensation walls, transits through filaments and finally accretes in the densest halos.

Describing the cosmic web morphology is an involved task due to the intrinsic complexity of individual structures, but also to their connectivity and the hierarchical nature of their global organization. First approaches (e.g. Barrow, Bhavsar & Sonoda, 1985; Gott, Dickinson & Melott, 1986; Babul & Starkman, 1992; Mecke, Buchert & Wagner, 1994; Sahni, Sathyaprakash & Shandarin, 1998) often characterized the LSS with a set of global and statistical diagnostics, without providing a way to locally identify cosmic web elements. In the last decade, a variety of methods has been developed for segmenting the LSS into its components and applied to numerical simulations and observations. Among them, some focus on investigating one component at a time, in particular filaments (e.g. the Candy model – Stoica *et al.*, 2005; Stoica, Martínez & Saar, 2007, 2010, the skeleton analysis – Novikov, Colombi & Doré, 2006; Sousbie *et al.*, 2008, and DisPerSE – Sousbie, 2011; Sousbie, Pichon & Kawahara, 2011) or voids (e.g. Plionis & Basilakos, 2002; Colberg *et al.*, 2005; Shandarin *et al.*, 2006; Platen, van de Weygaert & Jones, 2007; Neyrinck, 2008; Sutter *et al.*, 2015b; Elyiv *et al.*, 2015, see also Colberg *et al.*, 2008 for a void finder comparison project). Unfortunately, this approach does not allow an analysis of the connections between cosmic web components, identified in the same framework. Another important class of web classifiers dissects clusters, filaments, walls, and voids at the same time. In particular, several recent studies deserve special attention due to their methodological richness. The “T-web” and “V-web” (Hahn *et al.*, 2007a; Forero-Romero *et al.*, 2009; Hoffman *et al.*, 2012) characterize the cosmic web based on the tidal and velocity shear fields. DIVA (Lavaux & Wandelt, 2010) rather uses the shear of the Lagrangian displacement field. ORIGAMI (Falck, Neyrinck & Szalay, 2012) identifies single and multi-stream regions in the full six-dimensional phase-space information (Abel, Hahn & Kaehler, 2012; Neyrinck, 2012; Shandarin, Habib & Heitmann, 2012). The Multiscale Morphology Filter (Aragón-Calvo *et al.*, 2007) and later refinements NEXUS/NEXUS+ (Cautun, van de Weygaert & Jones, 2013) follow a multiscale approach which probes the hierarchical nature of the cosmic web.

In the standard theoretical picture, the cosmic web arises from the anisotropic nature of gravitational collapse, which drives the formation of structure in the Universe from primordial fluctuations (Peebles, 1980). The capital importance of the large-scale tidal field in the formation and evolution of the cosmic web was first pointed out in the seminal work of Zel’dovich (1970). In the Zel’dovich approximation, the late-time morphology of structures is linked to the eigenvalues of the tidal tensor in the initial conditions. Gravitational collapse amplifies any anisotropy present in the primordial density field to give rise to highly asymmetrical structures. This picture explains the segmented nature of the LSS, but not its connectivity. The cosmic web theory of Bond, Kofman & Pogosyan (1996) asserted the deep connection between the tidal field around rare density peaks in the initial fluctuations and the final web pattern, in particular the filamentary cluster-cluster bridges. More generally, the shaping of the cosmic web through gravitational clustering is essentially a deterministic process described by Einstein’s equations and the main source of stochasticity in the problem enters in the generation of initial conditions, which are known, from inflationary theory, to resemble a Gaussian random field to very high accuracy (Guth & Pi, 1982; Hawking, 1982; Bardeen, Steinhardt & Turner, 1983). For these reasons, considerable effort has been devoted to a theoretical understanding of the LSS in terms of perturbation theory in the Eulerian and Lagrangian frames (for a review, see Bernardeau *et al.*, 2002). While this approach offers important analytical insights, it only permits to describe structure formation in the linear and mildly non-linear regimes and it is usually limited to the first few correlation functions of the density field. The complete description of the connection between primordial fluctuations and the late-time LSS, including a full phase-space treatment and the entire hierarchy of correlators, has to rely on a numerical treatment through  $N$ -body simulations. The characterization of cosmic web environments in the non-linear regime and

the description of their time evolution has only been treated recently, following the application of web classifiers to state-of-the-art simulations. In particular, [Hahn \*et al.\* \(2007a\)](#); [Aragón-Calvo, van de Weygaert & Jones \(2010\)](#) presented a local description of structure types in high-resolution cosmological simulations. [Hahn \*et al.\* \(2007b\)](#); [Bond, Strauss & Cen \(2010\)](#); [Cautun \*et al.\* \(2014\)](#) analyzed the time evolution of the cosmic web in terms of the mass and volume content of web-type components, their density distribution, and a set of new analysis tools especially designed for particular elements.

To the best of our knowledge, neither the classification of cosmic environments at non-linear scales in physical realizations of the LSS nor the investigation of their genesis and growth, using real data and with demonstrated capability of uncertainty quantification, have been treated in the existing literature. In this work, we propose the first probabilistic web-type analysis conducted with observational data in the deeply non-linear regime of LSS formation. We build accurate maps of dynamic cosmic web components with a resolution of around 3 Mpc/ $h$ , constrained by observations. In addition, our approach leads to the first quantitative inference of the formation history of these environments and allows the construction of maps of the embryonic traces in the initial perturbations of the late-time morphological features of the cosmic web.

Cosmographic descriptions of the LSS in terms of three-dimensional maps, and in particular a dynamic structure type cartography carry potential for a rich variety of applications. Such maps characterize the anisotropic nature of gravitational structure formation, the clustering behavior of galaxies as a function of their tidal environment and permit to describe the traces of the cosmic web already imprinted in the initial conditions. So far, most investigations focused on understanding the physical properties of dark halos and galaxies in relation to the LSS. [Hahn \*et al.\* \(2007a,b, 2009\)](#); [Hahn, Angulo & Abel \(2014\)](#); [Aragón-Calvo, van de Weygaert & Jones \(2010\)](#) found a systematic dependence of halo properties such as morphological type, color, luminosity and spin parameter on their cosmic environment (local density, velocity and tidal field). In addition, a correlation between halo shapes and spins and the orientations of nearby filaments and sheets, predicted in simulations ([Altay, Colberg & Croft, 2006](#); [Hahn \*et al.\*, 2007a,b, 2009](#); [Paz, Stasyszyn & Padilla, 2008](#); [Zhang \*et al.\*, 2009](#); [Codis \*et al.\*, 2012](#); [Libeskind \*et al.\*, 2013](#); [Welker \*et al.\*, 2014](#); [Aragon-Calvo & Yang, 2014](#); [Laigle \*et al.\*, 2015](#)), has been confirmed by observational galaxy data ([Paz, Stasyszyn & Padilla, 2008](#); [Jones, van de Weygaert & Aragón-Calvo, 2010](#); [Tempel, Stoica & Saar, 2013](#); [Zhang \*et al.\*, 2013](#)). Cartographic descriptions of the cosmic web also permit to study the environmental dependence of galaxy properties (see e.g. [Lee & Lee, 2008](#); [Lee & Li, 2008](#); [Park, Kim & Park, 2010](#); [Yan, Fan & White, 2012](#); [Kovač \*et al.\*, 2014](#)) and to make the connection between the sophisticated predictions for galaxy properties in hydrodynamic simulations (e.g. [Vogelsberger \*et al.\*, 2014](#); [Dubois \*et al.\*, 2014](#); [Codis \*et al.\*, 2015](#)) and observations. Another wide range of applications of structure type reconstructions is to probe the effect of the inhomogeneous large-scale structure on photon properties and geodesics. For example, it is possible to interpret the weak gravitational lensing effects of voids ([Melchior \*et al.\*, 2014](#); [Clampitt & Jain, 2014](#)). Dynamic information can also be used to produce prediction templates for secondary effects expected in the cosmic microwave background such as the kinetic Sunyaev-Zel'dovich effect ([Li \*et al.\*, 2014](#)), the integrated Sachs-Wolfe and Rees-Sciama effects (e.g. [Cai \*et al.\*, 2010](#); [Ilić, Langer & Douspis, 2013](#); [Planck Collaboration, 2014a](#)). Lastly, as the cosmic web morphology arises from gravitational instability, it can be used to test general relativity ([Falck, Koyama & Zhao, 2015](#)).

Building such refined cosmographic descriptions of the Universe requires high-dimensional, non-linear inferences. In chapter 5 ([Jasche, Leclercq & Wandelt, 2015](#)), we presented a chrono-cosmography project, aiming at reconstructing simultaneously the density distribution, the velocity field and the formation history of the LSS from galaxies. To do so, we used an advanced Bayesian inference algorithm to assimilate the Sloan Digital Sky Survey DR7 data into the forecasts of a physical model of structure formation (second order Lagrangian perturbation theory). Besides inferring the four-dimensional history of the matter distribution, these results permit us an analysis of the genesis and growth of the complex web-like patterns that have been observed in our Universe. Therefore, this work constitutes a new chrono-cosmography project, aiming at the analysis of the evolving cosmic web.

Our investigations rely on the inference of the initial conditions in the SDSS volume (see chapter 5). Starting from these, we generate a large set of constrained realizations of the Universe using the COLA method ([Tassev, Zaldarriaga & Eisenstein, 2013](#), see also section 7.3.1). This physical model allows us to perform the first description of the cosmic web in the non-linear regime, using real data, and to follow the time evolution of its constituting elements. Throughout this chapter, we adopt the [Hahn \*et al.\* \(2007a\)](#) dynamic “T-web” classifier, which segments the LSS into voids, sheets, filaments, and clusters. This choice is motivated by the close relation between the equations that dictate the dynamics of the growth of structures in the Zel'dovich formalism and the Lagrangian description of the LSS which naturally emerges with BORG. As this procedure

relies on the estimation of the eigenvalues of the tidal tensor in Fourier space, it constitutes a non-linear and non-local estimator of structure types, requiring adequate means to propagate observational uncertainties to finally inferred products (web-type maps and all derived quantities), in order not to misinterpret results. The BORG algorithm naturally addresses this problem by providing a set of density realizations constrained by the data. The variation between these samples constitute a thorough quantification of uncertainty coming from all observational effects (in particular the incompleteness of the data because of the survey mask and the radial selection functions, as well as luminosity-dependent galaxy biases, see chapter 5 for details), not only with a point estimation but with a detailed treatment of the likelihood. Hence, for all problems addressed in this work, we get a fully probabilistic answer in terms of a prior and a posterior distribution. Building upon the robustness of our uncertainty quantification procedure, we are able to make the first observationally-supported link between cosmology and information theory (see Neyrinck, 2015b, for theoretical considerations related to this question) by looking at the entropy and Kullback-Leibler divergence of probability distribution functions.

This chapter is organized as follows. In section 9.2, we describe our methodology: Bayesian large-scale structure inference with the BORG algorithm, non-linear filtering of samples with COLA and web-type classification using the T-web procedure. In sections 9.3 and 9.4, we describe the cosmic web at present and primordial times, respectively. In section 9.5, we follow the time evolution of web-types as structures form in the Universe. Finally, we summarize our results and offer concluding comments in section 9.6.

## 9.2 Methods

In this section, we describe our methodology step by step:

1. inference of the initial conditions with BORG (section 9.2.1),
2. generation of data-constrained realizations of the SDSS volume via non-linear filtering of BORG samples with COLA (section 9.2.2),
3. classification of the cosmic web in voids, sheets, filaments, and clusters, using the T-web algorithm (section 9.2.3).

### 9.2.1 Bayesian large-scale structure inference with BORG

This work builds upon results previously obtained by application of the BORG (Bayesian Origin Reconstruction from Galaxies, Jasche & Wandelt, 2013a) algorithm to the Sloan Digital Sky Survey data release 7 (Jasche, Leclercq & Wandelt, 2015). BORG is a full-scale Bayesian inference code which permits to simultaneously analyze morphology and formation history of the cosmic web (see chapters 4 and 5 for a complete description).

As discussed in Jasche & Wandelt (2013a), accurate and detailed cosmographic inferences from observations require modeling the mildly non-linear and non-linear regime of the presently observed matter distribution. The exact statistical behavior of the LSS in terms of a full probability distribution function for non-linearly evolved density fields is not known. For this reason, the first full-scale reconstructions relied on phenomenological approximations, such as multivariate Gaussian or log-normal distributions, incorporating a cosmological power spectrum to accurately represent correct two-point statistics of density fields (see e.g. Lahav *et al.*, 1994; Zaroubi, 2002; Erdoğdu *et al.*, 2004; Kitaura & Enßlin, 2008; Kitaura *et al.*, 2009; Kitaura, Jasche & Metcalf, 2010; Jasche & Kitaura, 2010; Jasche *et al.*, 2010b,a). However, these prescriptions only model the one and two-point statistics of the matter distribution. Additional statistical complexity of the evolved density field arises from the fact that gravitational structure formation introduces mode coupling and phase correlations. This manifests itself not only in a sheer amplitude difference of density and velocity fields at different redshifts, but also in a modification of their statistical behavior by the generation of higher-order correlation functions. An accurate modeling of these high-order correlators is of crucial importance for a precise description of the connectivity and hierarchical nature of the cosmic web, which is the aim of this chapter.

While the statistical nature of the late-time density field is poorly understood, the initial conditions from which it formed are known to obey Gaussian statistics to very great accuracy (Planck Collaboration, 2015). Therefore, it is reasonable to account for the increasing statistical complexity of the evolving matter distribution by a dynamical model of structure formation linking initial and final conditions. This naturally turns the problem of LSS analysis to the task of inferring the initial conditions from present cosmological observations (Jasche & Wandelt, 2013a; Kitaura, 2013; Wang *et al.*, 2013). This approach yields a very high-dimensional

and non-linear inference problem. Typically, the parameter space to explore comprises on the order of  $10^6$  to  $10^7$  elements, corresponding to the voxels of the map to be inferred. For reasons linked to computational cost, the BORG algorithm employs 2LPT as an approximation for the actual gravitational dynamics linking initial three-dimensional Gaussian density fields to present, non-Gaussian density fields. As known from perturbation theory (see e.g. [Bernardeau \*et al.\*, 2002](#)), in the linear and mildly non-linear regime, 2LPT correctly describes the one-, two- and three-point statistics of the matter distribution and also approximates very well higher-order correlators. It accounts in particular for tidal effects in its regime of validity. Consequently, the BORG algorithm correctly transports the observational information corresponding to complex web-like features from the final density field to the corresponding initial conditions. Note that such an explicit Bayesian forward-modeling approach is always more powerful than constraining (part of) the sequence of correlation functions, as it accounts for the entire dark matter dynamics (in particular for the infinite hierarchy of correlators), in its regime of validity. This is of particular importance, since the hierarchy of correlation functions has been shown to be an insufficient description of density fields in the non-linear regime ([Carron, 2012](#); [Carron & Neyrinck, 2012](#)).

As discussed in chapter 5 ([Jasche, Leclercq & Wandelt, 2015](#)), our analysis comprehensively accounts for observational effects such as selection functions, survey geometry, luminosity-dependent galaxy biases and noise. Corresponding uncertainty quantification is provided by sampling from the high-dimensional posterior distribution via an efficient implementation of the Hamiltonian Markov Chain Monte Carlo method (see chapter 4 and [Jasche & Wandelt, 2013a](#), for details). In particular, luminosity-dependent galaxy biases are explicitly part of the BORG likelihood and the bias amplitudes are inferred self-consistently during the run. Though not explicitly modeled, redshift-space distortions are automatically mitigated: due to the prior preference for homogeneity and isotropy, such anisotropic features are treated as noise in the data.

In the following, we make use of the 12,000 samples of the posterior distribution for primordial density fields, obtained in chapter 5. These reconstructions, constrained by SDSS observations, act as initial conditions for the generation of constrained large-scale structure realizations. It is important to note that we directly make use of BORG outputs without any further post-processing, which demonstrates the remarkable quality of our inference results.

### 9.2.2 Non-linear filtering of samples with COLA

In section 2.3 ([Leclercq \*et al.\*, 2013](#), section 2.A), we performed a study of differences in the representation of structure types in density fields predicted by LPT and  $N$ -body simulations. To do so, we used the same web-type classification procedure as in this work (see sections 9.2.3 and C.2). In spite of the visual similarity of LPT and  $N$ -body density fields at large and intermediate scales (above a few  $\text{Mpc}/h$ ), we found crucial differences in the representation of structures. Specifically, LPT predicts fuzzier halos than full gravity, and incorrectly assigns the surroundings of voids as part of them. This manifests itself in an overprediction of the volume occupied by clusters and voids at the detriment of sheets and filaments. The substructure of voids is also known to be incorrectly represented in 2LPT ([Sahni & Shandarin, 1996](#); [Neyrinck, 2013](#); [Leclercq \*et al.\*, 2013](#)).

For these reasons, in this chapter we cannot directly make use of the final BORG density samples, which are a prediction of the 2LPT model. Instead, we rely on the inferred initial conditions, which contain the data constraints (as described in chapter 5) and on a non-linear filtering step (see chapter 7) similar to the one described in chapter 8 ([Leclercq \*et al.\*, 2015](#)). Due to the large number of samples to be processed for this work, we do not use a fully non-linear simulation code as in chapter 8, but the COLA method ([Tassev, Zaldarriaga & Eisenstein, 2013](#), see also section 7.3.1).

The generation of the set of non-linear BORG-COLA samples, used in this chapter, is described in section 7.3.2.

### 9.2.3 Classification of the cosmic web

The BORG filtered reconstructions permit a variety of scientific analyses of the large scale structure in the observed Universe. In this work, we focus specifically on the possibility to characterize the cosmic web by distinct structure types. Generally, any of the methods cited in the introduction (section 9.1) can be employed for analysis of our density samples, however for the purpose of this chapter, we follow the “T-web” classification procedure as proposed by [Hahn \*et al.\* \(2007a\)](#), described in section C.2.

The basic idea of this dynamical classification approach is that the eigenvalues  $\mu_1 \leq \mu_2 \leq \mu_3$  of the tidal tensor  $\mathcal{T}_{ij} \equiv H(\tilde{\Phi})_{ij}$  (Hessian of the rescaled gravitational potential) characterize the geometrical properties of each point in space. With these definitions, the three eigenvalues of the tidal tensor form a decomposition of the density contrast field, in the sense that the trace of  $\mathcal{T}$  is  $\mu_1 + \mu_2 + \mu_3 = \delta$ . Each spatial point can then be classified as a specific web type by considering the signs of  $\mu_1, \mu_2, \mu_3$ , according to the rules given in table C.1.

Several extensions of this classification procedure exist, that permit different classification up to sub-megaparsec scales (see section C.2.4). In this work, we will probe scales down to  $\sim 3$  Mpc/h (the voxel size in our reconstructions). Therefore, we will be content with the original classification procedure as proposed by Hahn *et al.* (2007a).

It is important to note that the tidal tensor and the rescaled gravitational potential are both physical quantities, and hence their calculation requires the availability of a full physical density field in contrast to a smoothed mean reconstruction of the density field. As described in chapter 5, density samples obtained by the BORG algorithm provide such required full physical density fields. The tidal tensor can therefore easily be calculated in each density sample from the Fourier space representations of equations (C.6) and (C.7) (see section C.2.5 and Hahn *et al.*, 2007a; Forero-Romero *et al.*, 2009, for details on the technical implementation).

The web classifier provides four voxel-wise scalar fields that characterize the large scale structure. In a specific realization, the answer is unique, meaning that these fields obey the following conditions at each voxel position  $\vec{x}_k$ :

$$T_i(\vec{x}_k) \in \{0, 1\} \text{ for } i \in \llbracket 0, 3 \rrbracket \quad \text{and} \quad \sum_{i=0}^3 T_i(\vec{x}_k) = 1 \quad (9.1)$$

where  $T_0$  = void,  $T_1$  = sheet,  $T_2$  = filament,  $T_3$  = cluster. In this work, we follow the Bayesian approach of Jasche, Leclercq & Wandelt (2015) and quantify the degree of belief in structure type classification. Specifically, our web classification is given in terms of four voxel-wise scalar fields that obey the following conditions at each voxel position  $\vec{x}_k$ :

$$\mathcal{T}_i(\vec{x}_k) \in [0, 1] \text{ for } i \in \llbracket 0, 3 \rrbracket \quad \text{and} \quad \sum_{i=0}^3 \mathcal{T}_i(\vec{x}_k) = 1. \quad (9.2)$$

Here,  $\mathcal{T}_i(\vec{x}_k) \equiv \langle T_i(\vec{x}_k) \rangle_{\mathcal{P}(T_i(\vec{x}_k)|d)} = \mathcal{P}(T_i(\vec{x}_k)|d)$  are the posterior probabilities indicating the possibility to encounter specific structure types at a given position in the observed volume, conditional on the data. These are estimated by applying the web classification to all density samples and counting the relative frequencies at each individual spatial coordinate within the set of samples (see section 5 in Jasche *et al.*, 2010b). With this definition, the cosmic web-type posterior mean is given by

$$\langle \mathcal{P}(T_i(\vec{x}_k)|d) \rangle = \frac{1}{N} \sum_{n=1}^N \sum_{j=0}^3 \delta_K^{T_i(\vec{x}_k) T_j^n(\vec{x}_k)}, \quad (9.3)$$

where  $n$  labels one of the  $N$  samples,  $T_j^n(\vec{x}_k)$  is the result of the web classifier on the  $n$ -th sample (i.e. a unit four-vector at each voxel position  $\vec{x}_k$  containing zeros except for one component, which indicates the structure type), and  $\delta_K^{ab}$  is a Kronecker symbol.

## 9.3 The late-time large-scale structure

In this section, we discuss the results of our analysis of the final density field, at  $a = 1$ . For reasons of computational time with COLA filtering (see section 9.2.2), we kept around 10% of the original set of samples obtained in chapter 5. In order to mitigate as much as possible the effects of correlation among samples, we maximally separated the samples kept for the present analysis, keeping one out of ten consecutive samples of the original Markov Chain. Hence, for all results discussed in this section, we used a total of 1,097 samples inferred by BORG and filtered with COLA.

### 9.3.1 Tidal environment

As a natural byproduct, the application of the T-web classifier to density samples yields samples of the pdfs for the three eigenvalues of the tidal field tensor. These pdfs account for the assumed physical model of structure formation and the data constraints, and quantify uncertainty coming in particular from selection



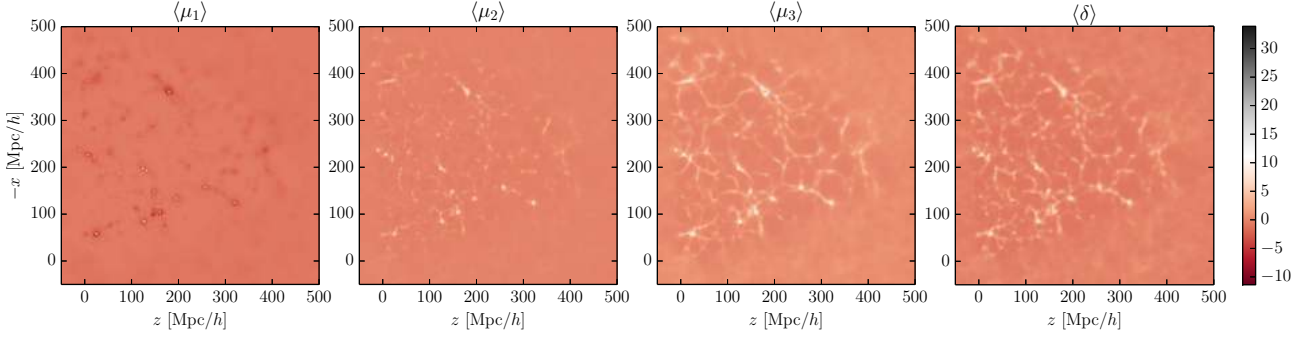


Figure 9.1: Slices through the three-dimensional ensemble posterior mean for the eigenvalues  $\mu_1 \leq \mu_2 \leq \mu_3$  of the tidal field tensor in the final conditions, estimated from 1,097 samples. The rightmost panel shows the corresponding slice through the posterior mean for the final density contrast  $\delta = \mu_1 + \mu_2 + \mu_3$ , obtained in section 5.3.1.

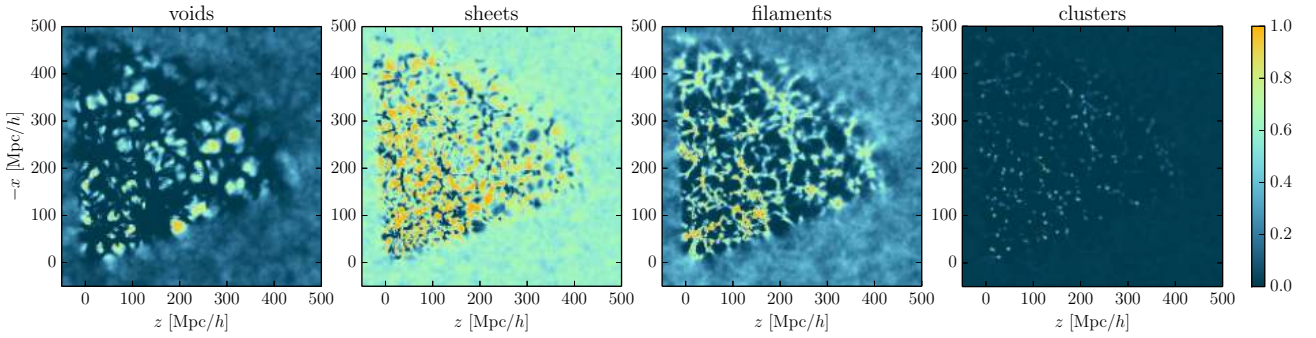


Figure 9.2: Slices through the posterior mean for different structure types (from left to right: void, sheet, filament, and cluster) in the late-time large-scale structure in the Sloan volume ( $a = 1$ ). These four three-dimensional voxel-wise pdfs sum up to one on a voxel basis.

effects, surveys geometries and galaxy biases. In a similar fashion as described in section 5.3, the ensemble of samples permits us to provide any desired statistical summary such as mean and variance.

In figure 9.1, we show slices through the ensemble mean fields  $\mu_1$ ,  $\mu_2$  and  $\mu_3$ . For visual comparison, the rightmost panel of figure 9.1 shows the corresponding slice through the posterior mean of the final density contrast,  $\delta = \mu_1 + \mu_2 + \mu_3$ , obtained in section 5.3.1. Different morphologies can be observed in the data-constrained parts of these slices:  $\mu_1$ ,  $\mu_2$  and  $\mu_3$  respectively trace well the clusters, filaments and sheets, as we now argue. The  $\mu_1$  field is rather homogeneous, apart for small spots where all eigenvalues are largely positive, i.e. undergoing dramatic gravitational collapse along three axes. These correspond to the dynamic clusters. Note that there exists a form of “tidal compensation”: these clusters are surrounded by regions where  $\mu_1$  is smaller than its cosmic mean. More patterns can be observed in the  $\mu_2$  field: it also exhibits filaments (appearing as dots when piercing the slice). Finally, the  $\mu_3$  field is highly-structured, as it also traces sheets (which appear filamentary when sliced). Dynamic voids can also be easily distinguished in this field, wherever  $\mu_3$  is negative.

### 9.3.2 Probabilistic web-type cartography

Building upon previous results and using the procedure described in section 9.2.3, we obtain probabilistic maps of structures. More precisely, we obtain four probability distributions at each spatial position,  $\mathcal{P}(T_i(x_k)|d)$ , indicating the possibility to encounter a specific structure type (cluster, filament, sheet, void) at that position. As noted in section 9.2.3, these pdfs take their values in the range  $[0, 1]$  and sum up to one on a voxel-basis. Figure 9.2 shows slices through their means (see equation (9.3)). The plot shows the anticipated behavior, with a high degree of structure and values close to certainty (i.e. zero or one) in regions covered by data, while the unobserved regions approach a uniform value corresponding to the prior. At this point, it is worth noting that the T-web classifier has a prior preference for some structure types. Using unconstrained large-scale structure

Structure type	$\mu_{\mathcal{P}(\mathbf{T}_i)}$	$\sigma_{\mathcal{P}(\mathbf{T}_i)}$
Late-time large-scale structure ( $a = 1$ )		
Void	0.14261	$6.1681 \times 10^{-4}$
Sheet	0.59561	$6.3275 \times 10^{-4}$
Filament	0.24980	$5.5637 \times 10^{-4}$
Cluster	0.01198	$5.8793 \times 10^{-5}$

Table 9.1: Prior probabilities assigned by the T-web classifier to the different structures types, in the late-time large-scale structure ( $a = 1$ ).

realizations produced with the same setup,<sup>1</sup> we measured that these prior probabilities,  $\mathcal{P}(\mathbf{T}_i)$ , can be well described by Gaussians whose mean and standard deviation are given in table 9.1.

In addition to their ensemble mean, the set of samples permits to propagate uncertainty quantification to web-type classification. In particular, it allows us to locally assess the strength of data constraints. In information theory, a convenient way to characterize the uncertainty content of a random source  $\mathcal{S}$  is the Shannon entropy (Shannon, 1948), defined by

$$H[\mathcal{S}] \equiv - \sum_i p_i \log_2(p_i), \quad (9.4)$$

where the  $p_i$  are the probabilities of possible events. This definition yields expected properties and accounts for the intuition that the more likely an event is, the less information it provides when it occurs (i.e. the more it contributes to the source entropy). We follow this prescription and write the voxel-wise entropy of the web-type posterior,  $\mathcal{P}(\mathbf{T}(\vec{x}_k)|d)$ , as

$$H[\mathcal{P}(\mathbf{T}(\vec{x}_k)|d)] \equiv - \sum_{i=0}^3 \mathcal{P}(\mathbf{T}_i(\vec{x}_k)|d) \log_2(\mathcal{P}(\mathbf{T}_i(\vec{x}_k)|d)). \quad (9.5)$$

It is a number in the range  $[0, 2]$  and its natural unit is the shannon (Sh).  $H = 0$  Sh in the case of perfect certainty, i.e. when the data constraints entirely determine the underlying structure type:  $\mathcal{P}(\mathbf{T}_{i_0}(\vec{x}_k)|d)$  is 1 for one  $i_0$  and 0 for  $i \neq i_0$ .  $H$  reaches its maximum value of 2 Sh when all  $\mathcal{P}(\mathbf{T}_i(\vec{x}_k)|d)$  are equal to  $1/4$ . This is the case of maximal randomness: all the events being equally likely, no information is gained when one occurs.

A slice through the voxel-wise entropy of the web-type posterior is shown in the left panel of figure 9.3. Generally, the entropy map reflects the information content of the posterior pdf, which comes from augmenting the information content of the prior pdf with the data constraints, in the Bayesian way.

The entropy takes low values and shows a high degree of structure in the regions where data constraints exist, and even reaches zero in some spots where the data are perfectly informative. Comparing with figures 9.1 and 9.2, one can note that this structure is highly non-trivial and does not follow any of the previously described patterns. This is due to the facts that in a Poisson process, the signal (here the density, inferred in section 5.3.1) is correlated with the uncertainty and that structure types classification further is a non-linear function of the density field. In the unobserved regions, the entropy fluctuates around a constant value of about 1.4 Sh, which characterizes the information content of the prior. This value is consistent with the expectation, which can be computed using equation (9.5) (unconditional on the data) and the numbers given in table 9.1.

The information-theoretic quantity that measures the information gain (in shannons) due to the data is the relative entropy or Kullback-Leibler divergence (Kullback & Leibler, 1951) of the posterior from the prior,

$$\begin{aligned} D_{\text{KL}}[\mathcal{P}(\mathbf{T}(\vec{x}_k)|d) \parallel \mathcal{P}(\mathbf{T})] &\equiv \sum_{i=0}^3 \mathcal{P}(\mathbf{T}_i(\vec{x}_k)|d) \log_2 \left( \frac{\mathcal{P}(\mathbf{T}_i(\vec{x}_k)|d)}{\mathcal{P}(\mathbf{T}_i)} \right) \\ &= -H[\mathcal{P}(\mathbf{T}(\vec{x}_k)|d)] - \sum_{i=0}^3 \mathcal{P}(\mathbf{T}_i(\vec{x}_k)|d) \log_2(\mathcal{P}(\mathbf{T}_i)). \end{aligned} \quad (9.6)$$

<sup>1</sup> By this, we specifically mean realizations obtained from initial randomly-generated Gaussian density fields with an Eisenstein & Hu (1998, 1999) power spectrum using the fiducial cosmological parameters of the BORG analysis ( $\Omega_m = 0.272$ ,  $\Omega_\mu = 0.728$ ,  $\Omega_b = 0.045$ ,  $h = 0.702$ ,  $\sigma_8 = 0.807$ ,  $n_s = 0.961$ , see equation (5.1)). The density field is defined on a  $750 \text{ Mpc}/h$  cubic grid of  $256^3$ -voxels and populated by  $512^3$  dark matter particles, which are evolved to  $z = 69$  with 2LPT and from  $z = 69$  to  $z = 0$  with COLA, using 30 timesteps logarithmically-spaced in the scale factor. The particles are binned on a  $256^3$ -voxel grid with the CiC scheme to get the final density field.



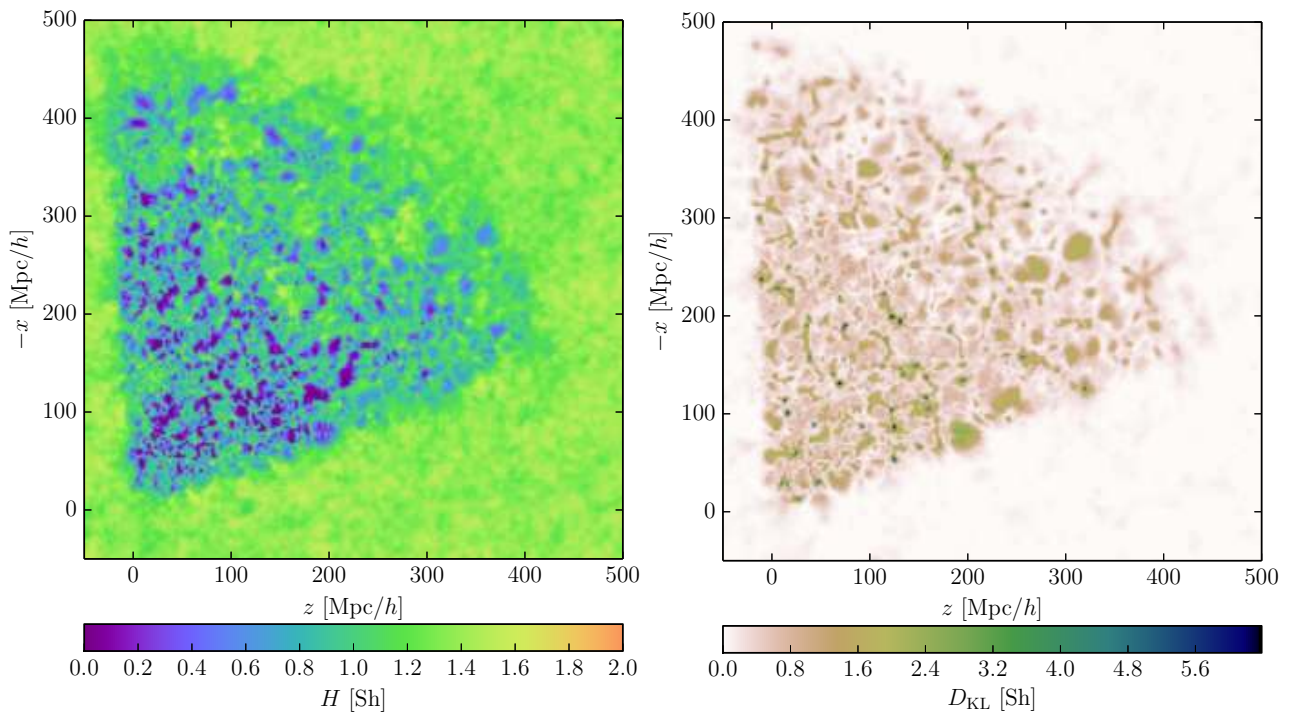


Figure 9.3: Slices through the entropy of the structure types posterior (left panel) and the Kullback-Leibler divergence of the posterior from the prior (right panel), in the final conditions. The entropy  $H$ , defined by equation (9.5), quantifies the information content of the posterior pdf represented in figure 9.2, which results from fusing the information content of the prior and the data constraints. The Kullback-Leibler divergence  $D_{\text{KL}}$ , defined by equation (9.6), represents the information gained in moving from the prior to the posterior. It quantifies the information that has been learned on structure types by looking at SDSS galaxies.

It is a non-symmetric measure of the difference between the two probability distributions.

A slice through the voxel-wise Kullback-Leibler divergence of the web-type posterior from the prior is shown in the right panel of figure 9.3. As expected, the information gain is zero out of the survey boundaries. In the observed regions, SDSS galaxies are informative on underlying structure types at the level of at least  $\sim 1$  Sh. This number can go to  $\sim 3$  Sh in the interior of deep voids and up to  $\sim 6$  Sh in the densest clusters. This map permits to visualize the regions where additional data would be needed to improve structure type classification, e.g. in some high-redshift regions where uncertainty remains due to selection effects.

### 9.3.3 Volume and mass filling fractions

A characterization of large scale environments commonly found in literature involves evaluating global quantities such as the volume and mass content of these structures. In a particular realization, the volume filling fraction (VFF) for structure type  $T_i$  is the number of voxels of type  $T_i$  divided by the total number of voxels in the considered volume,

$$\text{VFF}(T_i) \equiv \frac{\sum_{\vec{x}_k} \sum_{j=0}^3 \delta_K^{T_i(\vec{x}_k) T_j^n(\vec{x}_k)}}{N_{\text{vox}}}. \quad (9.7)$$

The mass filling fraction (MFF) can be obtained in a similar manner by weighting the same sum by the local density  $\rho(\vec{x}_k) = \bar{\rho}(1 + \delta(\vec{x}_k))$ ,

$$\text{MFF}(T_i) \equiv \frac{\sum_{\vec{x}_k} \sum_{j=0}^3 (1 + \delta(\vec{x}_k)) \delta_K^{T_i(\vec{x}_k) T_j^n(\vec{x}_k)}}{\sum_{\vec{x}_k} (1 + \delta(\vec{x}_k))}. \quad (9.8)$$

To ensure that results are not prior-dominated, we measured the VFFs and MFFs in the data-constrained parts of our realizations. More precisely, we limited ourselves to the voxels where the survey response operator (representing simultaneously the survey geometry and the selection effects, see sections 4.2 and 5.1) is strictly positive. This amounts to  $N_{\text{vox}} = 3,148,504$  out of  $256^3 = 16,777,216$  voxels, around 18.7% of the full box (see also section 8.2.3.2 and figure 8.2). In equations (9.7) and (9.8),  $\vec{x}_k$  labels one of these voxels.

By measuring the VFF and MFF of different structure types in each constrained realization of our ensemble, we obtained the posterior pdfs,  $\mathcal{P}(\text{VFF}(T_i)|d)$  and  $\mathcal{P}(\text{MFF}(T_i)|d)$ , conditional on the data. Similarly, we computed the prior pdfs,  $\mathcal{P}(\text{VFF}(T_i))$  and  $\mathcal{P}(\text{MFF}(T_i))$ , using unconstrained realizations produced with the same setup. We found that all these pdfs can be well described by Gaussians, the mean and variance of which are given in tables 9.2 and 9.3.

Previous studies on this topic (e.g. Doroshkevich, 1970b; Shen *et al.*, 2006; Hahn *et al.*, 2007a; Forero-Romero *et al.*, 2009; Jasche *et al.*, 2010b; Aragón-Calvo, van de Weygaert & Jones, 2010; Shandarin, Habib & Heitmann, 2012; Cautun *et al.*, 2014) have found a wide range of values for the VFF and MFF of structures (see e.g. table 3 in Cautun *et al.*, 2014). For example, existing studies found that clusters occupy at most a few percent of the volume of the Universe but contribute significantly to the mass content, with a MFF ranging from  $\sim 10\%$  (Hahn *et al.*, 2007a; Cautun *et al.*, 2014) to  $\sim 40\%$  (Shandarin, Habib & Heitmann, 2012). The void volume fraction can vary from  $\sim 10\%$  (Hahn *et al.*, 2007a) to  $\sim 80\%$  (Aragón-Calvo, van de Weygaert & Jones, 2010; Shandarin, Habib & Heitmann, 2012; Cautun *et al.*, 2014); in the Forero-Romero *et al.* (2009) formalism (see section C.2.4), it is a very sensitive function of the threshold  $\mu_{\text{th}}$  (figure 9 in Jasche *et al.*, 2010b). These large disparities in the literature arise because different algorithms use various information and criteria for classifying the cosmic web. For this reason, we believe that it is only relevant to make relative statements for the same setup, i.e. to compare our results to the corresponding prior quantities, as done in tables 9.2 and 9.3. In this purpose, the large number of samples used allowed a precise characterization of the pdfs so that all digits quoted in the tables are significant. Note that all our analyses are repeatable for different setups, which allows in principle a comparison with any previous work.

As expected for a Bayesian update of the degree of belief, the posterior quantities generally have smaller variance and a mean value displaced from the prior mean. For the MFF, the posterior means are always within two standard deviations of the corresponding prior means. The analysis shows that in the SDSS, a larger mass fraction is occupied by clusters, sheets, and voids, at the detriment of filaments, in comparison to the prior expectation. The data also favor a smaller filling of the Sloan volume by filaments and sheets and larger filling by voids and clusters. For the cluster VFF, the posterior mean,  $\mu_{\text{VFF}(T_3)|d} = 0.01499$  is at about 15 standard deviations ( $\sigma_{\text{VFF}(T_3)} = 1.9194 \times 10^{-4}$ ) of the prior mean,  $\mu_{\text{VFF}(T_3)} = 0.01198$ . Given other results on the VFF and MFF, we believe that the data truly favor a higher volume content in clusters as compared to the

Structure type	$\mu_{\text{VFF}}$	$\sigma_{\text{VFF}}$	$\mu_{\text{VFF}}$	$\sigma_{\text{VFF}}$
Late-time large-scale structure ( $a = 1$ )				
	Posterior		Prior	
Void	0.14897	$1.8256 \times 10^{-3}$	0.14254	$6.2930 \times 10^{-3}$
Sheet	0.58914	$1.3021 \times 10^{-3}$	0.59562	$2.2375 \times 10^{-3}$
Filament	0.24689	$1.1295 \times 10^{-3}$	0.24986	$4.4440 \times 10^{-3}$
Cluster	0.01499	$8.7274 \times 10^{-5}$	0.01198	$1.9194 \times 10^{-4}$

Table 9.2: Mean and standard deviation of the prior and posterior pdfs for the volume filling fraction of different structure types in the late-time large-scale structure ( $a = 1$ ).

Structure type	$\mu_{\text{MFF}}$	$\sigma_{\text{MFF}}$	$\mu_{\text{MFF}}$	$\sigma_{\text{MFF}}$
Late-time large-scale structure ( $a = 1$ )				
	Posterior		Prior	
Void	0.04050	$8.3531 \times 10^{-4}$	0.03876	$2.3352 \times 10^{-3}$
Sheet	0.35605	$1.2723 \times 10^{-3}$	0.35286	$3.6854 \times 10^{-3}$
Filament	0.47356	$1.5661 \times 10^{-3}$	0.48170	$4.2215 \times 10^{-3}$
Cluster	0.12990	$6.4966 \times 10^{-4}$	0.12666	$1.8284 \times 10^{-3}$

Table 9.3: Mean and standard deviation of the prior and posterior pdfs for the mass filling fraction of different structure types in the late-time large-scale structure ( $a = 1$ ).

structure formation model used as prior. However, this surprising result should be treated with care; part of the discrepancy is likely due to the original BORG analysis, which optimizes the initial conditions for evolution with 2LPT (instead of the non-linear evolution with COLA used for the present work). LPT predicts fuzzier halos than  $N$ -body dynamics, which results in the incorrect prediction of a high cluster VFF (see section 2.3; [Leclercq et al., 2013](#)).

## 9.4 The primordial large-scale structure

In this section, we discuss the results of our analysis of the initial density field, at  $a = 10^{-3}$ . Since the analysis of the primordial large-scale structure does not involve an additional filtering step, we have been able to keep a larger number of samples of the posterior pdf for initial conditions, obtained in chapter 5. Hence, for all results described in this section, we used a total of 4,473 samples.

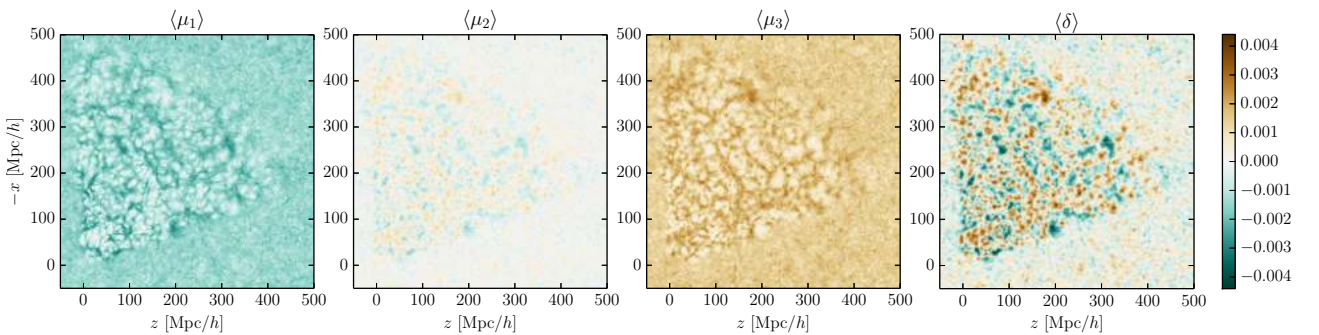


Figure 9.4: Slices through the three-dimensional ensemble posterior mean for the eigenvalues  $\mu_1 \leq \mu_2 \leq \mu_3$  of the tidal field tensor in the initial conditions, estimated from 4,473 samples. The rightmost panel shows the corresponding slice through the posterior mean for the initial density contrast  $\delta = \mu_1 + \mu_2 + \mu_3$ , obtained in section 5.3.1.

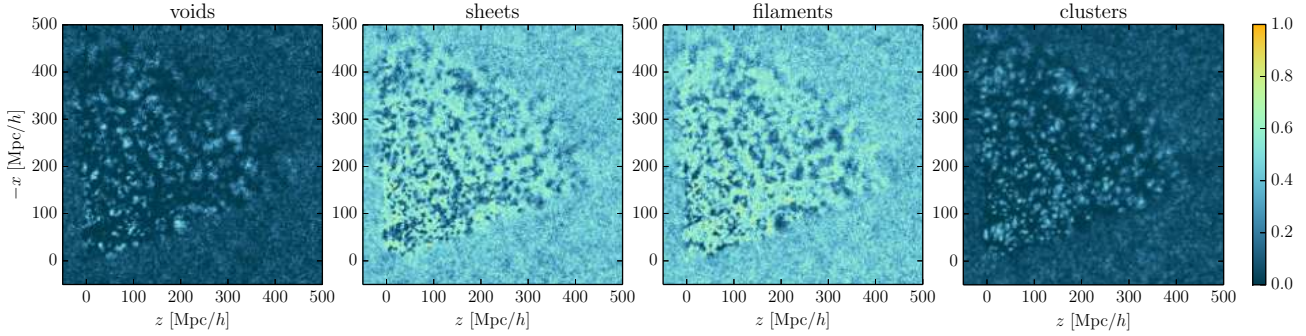


Figure 9.5: Slices through the posterior mean for different structure types (from left to right: void, sheet, filament, and cluster) in the primordial large-scale structure in the Sloan volume ( $a = 10^{-3}$ ). These four three-dimensional voxel-wise pdfs sum up to one on a voxel basis.

### 9.4.1 Tidal environment

In a similar fashion as in section 9.3.1, the application of the T-web classifier to initial density samples yields the posterior pdf for the three eigenvalues,  $\mu_1$ ,  $\mu_2$  and  $\mu_3$ , of the initial tidal field tensor. Figure 9.4 shows slices through their means. For visual comparison, the rightmost panel shows the corresponding slice through the posterior mean of the initial density contrast,  $\delta = \mu_1 + \mu_2 + \mu_3$ , obtained in section 5.3.1.

In a Gaussian random field,  $\mu_1$  is generally negative,  $\mu_3$  is generally positive and  $\mu_2$  close to zero (see the unobserved parts of the slices in figure 9.4). In addition,  $\mu_2$  closely resembles the total density contrast  $\delta$  up to a global scaling. In the constrained regions, the eigenvalues of the initial tidal tensor follow this behavior. The structure observed in their maps is visually consistent with the decomposition of Gaussian density fluctuations as shown by the right panel.

### 9.4.2 Probabilistic web-type cartography

Looking at the sign of the eigenvalues of the initial tidal tensor and following the procedure described in section 9.2.3, we obtain a probabilistic cartography of the primordial large-scale structure. As before, we obtain four voxel-wise pdfs  $\mathcal{P}(T_i(\vec{x}_k)|d)$ , taking their values in the range  $[0, 1]$  and summing up to one. Figure 9.5 shows slices through their means, defined by equation (9.3). As in the final conditions, the maps exhibit structure in the data-constrained regions and approach uniform values in the unobserved parts, corresponding to the respective priors. Using unconstrained realizations of Gaussian random fields produced with the same setup,<sup>2</sup> we measured these prior probabilities. Their means and standard deviations are given in table 9.4.

At this point, it is worth mentioning that there exists an additional symmetry for Gaussian random fields. Since the definition of the tidal tensor is linear in the density contrast (see equations (C.6) and (C.7)) and since positive and negative density contrasts are equally likely, a positive and negative value for a given  $\mu_i$  have the same probabilities. Because of this sign symmetry, the pdfs for voids and clusters (0 or 3 positive/negative eigenvalues) and the pdfs for sheets and filaments (1 or 2 positive/negative eigenvalues) are equal. This can be checked both in table 9.4 and in the unconstrained regions of the maps in figure 9.5. In the constrained regions, a qualitative complementarity between pdfs for voids and clusters and for sheets and filaments can be observed. This can be explained by the following. As  $\sum_i \mathcal{P}(T_i(\vec{x}_k)|d) = 1$  and assuming that  $\mathcal{P}(T_i(\vec{x}_k)|d) \approx \mathcal{P}(T_{3-i}(\vec{x}_k)|d)$  for unlikely events, consistently with the previous remark, we get  $\mathcal{P}(T_0(\vec{x}_k)|d) \approx 1 - \mathcal{P}(T_3(\vec{x}_k)|d)$  wherever  $\mathcal{P}(T_1(\vec{x}_k)|d) \approx \mathcal{P}(T_2(\vec{x}_k)|d)$  is sufficiently small; and  $\mathcal{P}(T_1(\vec{x}_k)|d) \approx 1 - \mathcal{P}(T_2(\vec{x}_k)|d)$  wherever  $\mathcal{P}(T_0(\vec{x}_k)|d) \approx \mathcal{P}(T_3(\vec{x}_k)|d)$  is sufficiently small. These results are therefore consistent with expectations based on Gaussianity for the primordial large-scale structure in the Sloan volume.

In a similar fashion as in section 9.3.2, the ensemble of samples permits us to propagate uncertainties to structure type classification and to characterize the strength of data constraints. In the left panel of figure 9.6, we show a slice through the voxel-wise entropy of the web-type posterior pdf in the initial conditions, defined by equation (9.5). This function quantifies the information content of the posterior, which comes from both the prior and the data constraints. As in the final conditions, the entropy takes lower values inside the survey

<sup>2</sup> We used the initial conditions of our set of unconstrained simulations (see footnote 1).

Structure type	$\mu_{\mathcal{P}(\mathbf{T}_i)}$	$\sigma_{\mathcal{P}(\mathbf{T}_i)}$
Primordial large-scale structure ( $a = 10^{-3}$ )		
Void	0.07979	$5.4875 \times 10^{-5}$
Sheet	0.42022	$1.0240 \times 10^{-4}$
Filament	0.42022	$1.0412 \times 10^{-4}$
Cluster	0.07978	$5.6337 \times 10^{-5}$

Table 9.4: Prior probabilities assigned by the T-web classifier to the different structures types, in the primordial large-scale structure ( $a = 10^{-3}$ ).

Structure type	$\mu_{\text{VFF}}$	$\sigma_{\text{VFF}}$	$\mu_{\text{VFF}}$	$\sigma_{\text{VFF}}$
Primordial large-scale structure ( $a = 10^{-3}$ )				
	Posterior		Prior	
Void	0.07994	$4.0221 \times 10^{-4}$	0.07977	$1.0200 \times 10^{-3}$
Sheet	0.41994	$6.1770 \times 10^{-4}$	0.42019	$1.7885 \times 10^{-3}$
Filament	0.42048	$6.3589 \times 10^{-4}$	0.42024	$1.7820 \times 10^{-3}$
Cluster	0.07964	$3.8043 \times 10^{-4}$	0.07980	$1.0260 \times 10^{-3}$

Table 9.5: Mean and standard deviation of the prior and posterior pdfs for the volume filling fraction of different structure types in the primordial large-scale structure ( $a = 10^{-3}$ ).

region. In the unobserved parts, the entropy fluctuates around 1.6 Sh, value which characterizes the information content of the prior. Using equation (9.5) (unconditional on the data) and the numbers given in table 9.4, one can check that this number is consistent with the expectation. In the right panel of figure 9.6, we show a map of the Kullback-Leibler divergence of the posterior from the prior, which represents the information gain due to the data.

### 9.4.3 Volume and mass filling fractions

We computed the volume and mass filling fractions (defined by equations (9.7) and (9.8)) of different structure types in the primordial large-scale structure in the Sloan volume. As for the final conditions, we kept only the regions where the survey response operator is strictly positive. Consequently, we obtained the posterior pdfs  $\mathcal{P}(\text{VFF}(\mathbf{T}_i)|d)$  and  $\mathcal{P}(\text{MFF}(\mathbf{T}_i)|d)$ . Using a set of unconstrained Gaussian random fields, we also measured  $\mathcal{P}(\text{VFF}(\mathbf{T}_i))$  and  $\mathcal{P}(\text{MFF}(\mathbf{T}_i))$  and found that all these pdfs are well described by Gaussians, the means and standard deviations of which are given in table 9.5 and 9.6.

All posterior quantities obtained are within two standard deviations of the corresponding prior means, and show smaller variance, as expected. Hence, all results obtained are consistent with Gaussian initial conditions.

## 9.5 Evolution of the cosmic web

In addition to the inference of initial and final density fields, BORG allows to simultaneously analyze the formation history and morphology of the observed large-scale structure, a subject that we refer to as chrono-

Structure type	$\mu_{\text{MFF}}$	$\sigma_{\text{MFF}}$	$\mu_{\text{MFF}}$	$\sigma_{\text{MFF}}$
Primordial large-scale structure ( $a = 10^{-3}$ )				
	Posterior		Prior	
Void	0.07958	$4.0122 \times 10^{-4}$	0.07941	$1.0163 \times 10^{-3}$
Sheet	0.41933	$6.1907 \times 10^{-4}$	0.41957	$1.7912 \times 10^{-3}$
Filament	0.42110	$6.3543 \times 10^{-4}$	0.42087	$1.7785 \times 10^{-3}$
Cluster	0.07999	$3.8206 \times 10^{-4}$	0.08015	$1.0293 \times 10^{-3}$

Table 9.6: Mean and standard deviation of the prior and posterior pdfs for the mass filling fraction of different structure types in the primordial large-scale structure ( $a = 10^{-3}$ ).



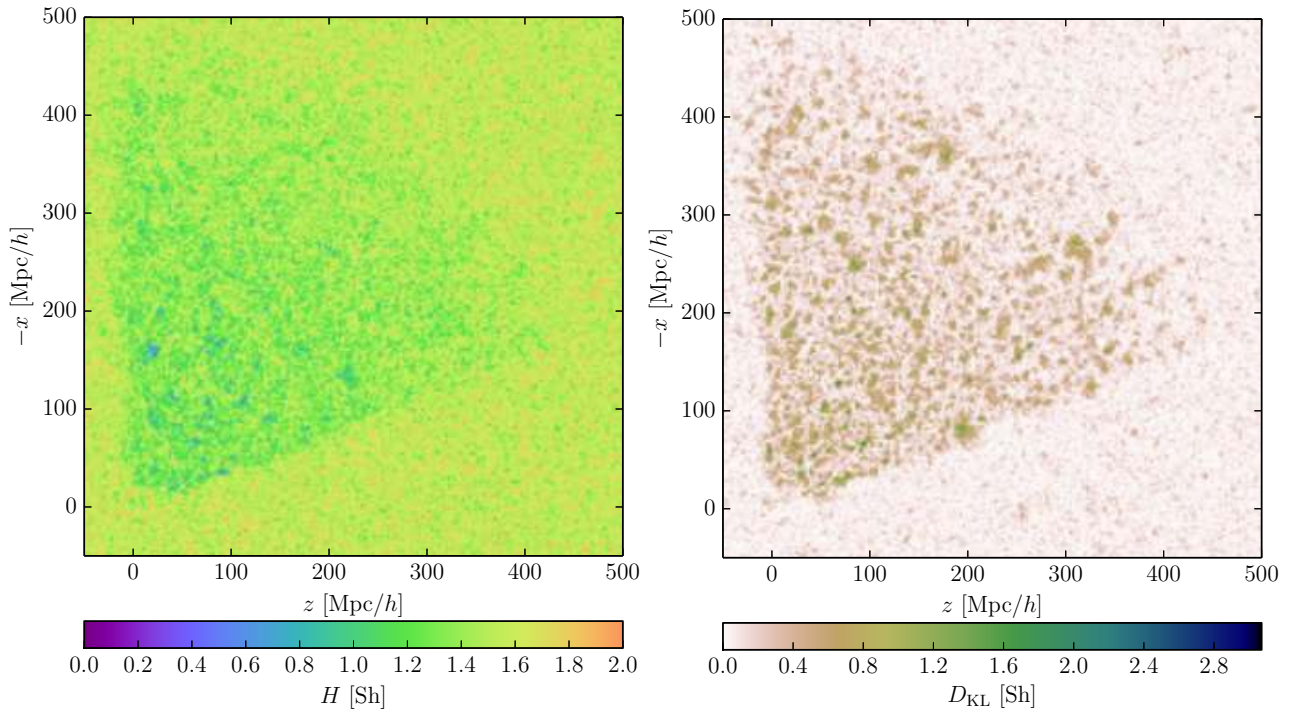


Figure 9.6: Slices through the entropy of the structure types posterior (left panel) and the Kullback-Leibler divergence of the posterior from the prior (right panel), in the initial conditions. The entropy  $H$ , defined by equation (9.5), quantifies the information content of the posterior pdf represented in figure 9.5, which results from fusing the information content of the prior and the data constraints. The Kullback-Leibler divergence  $D_{\text{KL}}$ , defined by equation (9.6), represents the information gained in moving from the prior to the posterior. It quantifies the information that has been learned on structure types by looking at SDSS galaxies.

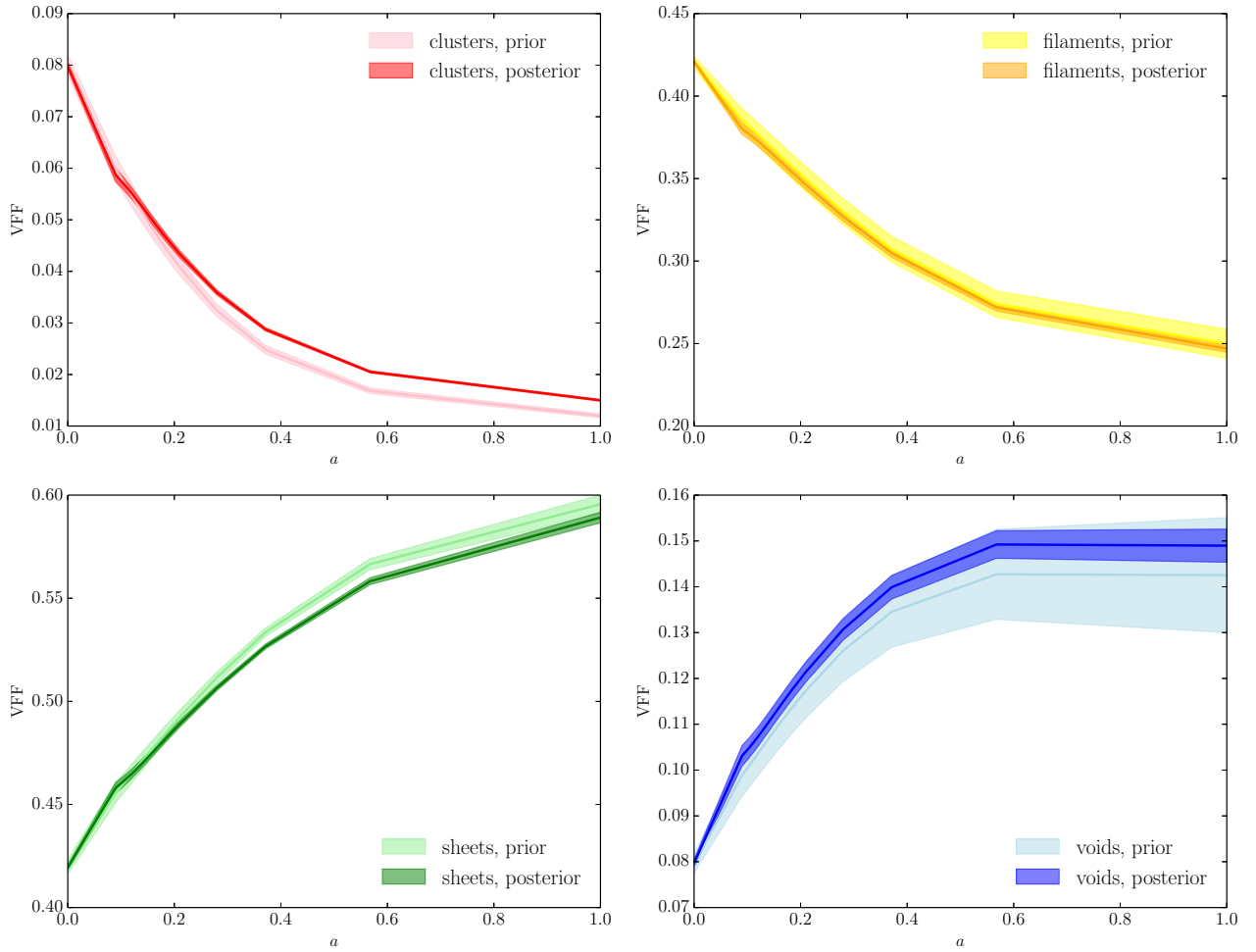


Figure 9.7: Time evolution of the volume filling fractions of different structure types (from left to right and top to bottom: clusters, filaments, sheets, voids). The solid lines show the pdf means and the shaded regions are the  $2\sigma$  credible intervals. Light colors are used for the priors and dark colors for the posteriors.



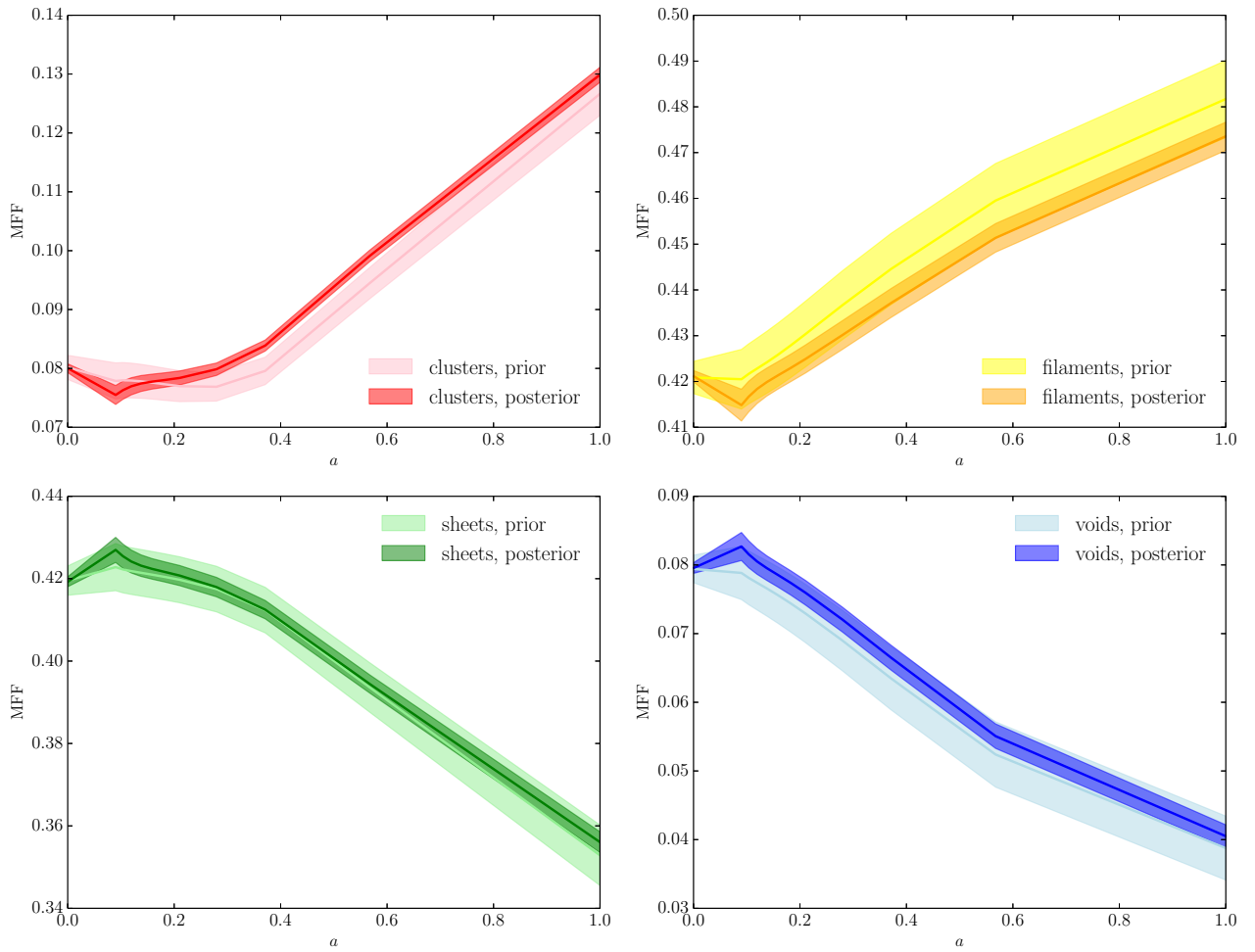


Figure 9.8: Same as figure 9.7 but for the mass filling fractions.

cosmography. In this section, we discuss the evolution of the cosmic web from its origin ( $a = 10^{-3}$ , analyzed in section 9.4) to the present epoch ( $a = 1$ , analyzed in section 9.3). To do so, we use 11 snapshots saved during the COLA filtering of our results (see section 9.2.2). These are linearly separated in redshift from  $z = 10$  to  $z = 0$ . We perform this analysis in the 1,097 samples filtered with COLA considered in section 9.3. For each of these samples and for each redshift, we follow the procedure described in sections 9.2.2 and 9.2.3 to compute the density field and to classify the structure types.

### 9.5.1 Evolution of the probabilistic maps

We followed the time evolution of the probabilistic web-type maps from the primordial (figure 9.5) to the late-time large-scale structure (figure 9.2). In unconstrained regions, these maps show the evolution of the prior preference for specific structure types (see tables 9.1 and 9.4), in particular the breaking of the initial symmetry between voids and clusters and between sheets and filaments, discussed in section 9.4.2.

In data-constrained regions, the time evolution of web-type maps permits to visually check the expansion history of individual regions where the posterior probability of one specific structure is high. In particular, it is easy to see that, as expected from their dynamical definition, voids expand and clusters shrink in comoving coordinates, from  $a = 10^{-3}$  to  $a = 1$  (the reader is invited to compare the leftmost and rightmost panels of figures 9.2 and 9.5). Similarly, regions corresponding with high probability to sheets and filaments expand along two and one axis, respectively, and shrink along the others. This phenomenon is more difficult to see in slices, however, as the slicing plane intersects randomly the eigendirections of the tidal tensor.

The time evolution of maps of the web-type posterior entropy (absolute and relative to the prior) also exhibit some interesting features. There, it is possible to simultaneously check the increase of the information content of the prior (from  $H \approx 1.6$  Sh to  $H \approx 1.4$  Sh) and the displacement of observational information operated by the physical model. As the large-scale structure forms in the Sloan volume, data constraints are propagated and the complex structure of the final entropy map (figure 9.3), discussed in section 9.3.2, takes shape.

### 9.5.2 Volume filling fraction

Our ensemble of snapshots allows us to check the time evolution of global characterizations of the large-scale structure such as the volume and mass filling fractions of different structures. As in sections 9.3.3 and 9.4.3, we computed these quantities using only the volume where the survey response operator is non-zero. In figure 9.7, we plot these VFF as a function of the scale factor. There, the solid lines correspond to the pdf means and the shaded regions to the  $2\text{-}\sigma$  credible intervals, with light colors for the priors and dark colors for the posteriors.

The time variation of the VFF in figure 9.7 is consistent with the expected dynamical behavior of structures. As voids and sheets expand along three and two axes, respectively, their volume fraction increases. Here, the posterior probabilities are mild updates of this prediction. Conversely, as clusters and filaments shrink along three and two axes, respectively, their volume fraction decreases. An explanation for the substantial displacement of the posterior from the prior, observed for clusters, can be found in section 9.3.3.

As already noted, the VFF is a very sensitive function of the precise definition of structures, grid size, density assignment scheme, smoothing scale, etc. For this reason, even for prior probabilities, our results can be in qualitative disagreement with previous authors (e.g. figure 23 in Cautun *et al.*, 2014), due to their very different definitions of structures. Therefore, we only found relevant to compare our posterior results with the prior predictions based on unconstrained realizations. The same remark applies to the MFF in the following section.

### 9.5.3 Mass filling fraction

In figure 9.8, we show the time evolution of the mass filling fractions using the same plotting conventions. Results are consistent with an interpretation based on large scale flows of matter. According to this picture, voids always loose mass while clusters always become more massive. The behavior of sheets and filaments can in principle be more complex, since these regions have both inflows and outflows of matter depending on the detail of their expansion profiles. In our setup, we found that the number of axes along which there is expansion dominates in the determination of the balance of inflow versus outflow, for global quantities such as the MFF. Therefore, filaments always gain mass and sheets always loose mass. Summing up our prior predictions, as they expand along at least two axes, matter flows out of voids and sheets and streams towards filaments and clusters.

The posterior probabilities slightly update this picture. Observations support smaller outflowing of matter from voids. For structures globally gaining matter, the priors are displaced towards less massive filaments and more massive clusters. All posterior predictions fall within the  $\sim 2\text{-}\sigma$  credible interval from corresponding prior means.

## 9.6 Summary and Conclusion

Along with chapter 8 (Leclercq *et al.*, 2015), this work exploits the high quality of inference results produced by the application of the Bayesian code BORG (chapter 4; Jasche & Wandelt, 2013a) to the Sloan Digital Sky Survey main galaxy sample (chapter 5; Jasche, Leclercq & Wandelt, 2015). We presented a Bayesian cosmic web analysis of the nearby Universe probed by the northern cap of the SDSS and its surrounding. In doing so, we produced the first probabilistic, four-dimensional maps of dynamic structure types in real observations.

As described in section 9.2.1, our method relies on the physical inference of the initial density field in the LSS (Jasche & Wandelt, 2013a; Jasche, Leclercq & Wandelt, 2015). Starting from these, we generated a large set of data-constrained realizations using the fast COLA method (section 9.2.2). The use of 2LPT as a physical model in the inference process and of the fully non-linear gravitational dynamics, provided by COLA, as a filter allowed us to describe structures at the required statistical accuracy, by very well representing the full hierarchy of correlation functions. Even though initial conditions were inferred with the approximate 2LPT model, we checked that the clustering statistics of constrained non-linear model evaluations agree with theoretical expectations up to scales considered in this work. As described in section 9.2.3, we used the dynamic web-type classification algorithm proposed by Hahn *et al.* (2007a) to dissect the cosmic web into voids, sheets, filaments, and clusters.

In sections 9.3 and 9.4, we presented the resulting maps of structures in the final and initial conditions, respectively, and studied the distribution of global quantities such as volume fraction and mass filling fractions. In section 9.5, we further analyzed the time evolution of our results, in a rigorous chrono-cosmographic framework.

For all results presented in this chapter, we demonstrated a thorough capability of uncertainty quantification. Specifically, for all inferred maps and derived quantities, we got a probabilistic answer in terms of a prior and a posterior distribution. The variation between samples of the posterior distribution quantifies the remaining uncertainties of various origins (in particular noise, selection effects, survey geometry and galaxy bias, see chapters 4 and 5 for a detailed discussion). Building upon our accurate probabilistic treatment, we looked at the entropy of the structure type posterior and at the relative entropy between posterior and prior. In doing so, we quantified the information gain due to SDSS galaxy data with respect to the underlying dynamic cosmic web and analyzed how this information is propagated during cosmic history. This study constitutes the first link between cosmology and information theory using real data.

In summary, our methodology yields an accurate cosmographic description of web types in the non-linear regime of structure formation, permits to analyze their time evolution and allows a precise uncertainty quantification in a full-scale Bayesian framework. These inference results can be used for a rich variety of applications, ranging from studying galaxies inside their environment to cross-correlating with other cosmological probes. They count among the first steps towards accurate chrono-cosmography, the subject of simultaneously analyzing the morphology and formation history of the inhomogeneous Universe.

*Note added:* As we were finalizing the paper corresponding to this chapter (Leclercq, Jasche & Wandelt, 2015c) for submission, the works by Zhao *et al.* (2015) and Shi, Wang & Mo (2015) appeared where the relationship between halos and the cosmic web environment defined by the tidal tensor is being studied.

# Cosmic-web type classification using decision theory

## Contents

10.1 Introduction . . . . .	149
10.2 Method . . . . .	150
10.3 Maps of structure types in the SDSS . . . . .	151
10.4 Conclusions . . . . .	154

---

“If no mistake have you made, yet losing you are... a different game you should play.”

Master Yoda, in recollections of Mace Windu,

— [Matthew Stover \(2003\)](#), *Star Wars: Shatterpoint*

---

## Abstract

We propose a decision criterion for segmenting the cosmic web into different structure types (voids, sheets, filaments, and clusters) on the basis of their respective probabilities and the strength of data constraints. Our approach is inspired by an analysis of games of chance where the gambler only plays if a positive expected net gain can be achieved based on some degree of privileged information. The result is a general solution for classification problems in the face of uncertainty, including the option of not committing to a class for a candidate object. As an illustration, we produce high-resolution maps of web-type constituents in the nearby Universe as probed by the Sloan Digital Sky Survey main galaxy sample. Other possible applications include the selection and labeling of objects in catalogs derived from astronomical survey data.

This chapter is adapted from its corresponding publication, [Leclercq, Jasche & Wandelt \(2015a\)](#).

Credit: Leclercq *et al.* 2015, A&A, 576, L17. Reproduced with permission © ESO.

## 10.1 Introduction

Building accurate maps of the cosmic web from galaxy surveys is one of the most challenging tasks in modern cosmology. Rapid progress in this field took place in the last few years with the introduction of inference techniques based on Bayesian probability theory ([Kitaura \*et al.\*, 2009](#); [Jasche \*et al.\*, 2010b](#); [Nuza \*et al.\*, 2014](#); [Jasche, Leclercq & Wandelt, 2015](#)). This facilitates the connection between the properties of the cosmic web, thoroughly analyzed in simulations (e.g. [Hahn \*et al.\*, 2007a](#); [Aragón-Calvo, van de Weygaert & Jones, 2010](#); [Cautun \*et al.\*, 2014](#)), and observations (see chapter 3 and [Leclercq, Pisani & Wandelt, 2014](#), for a review on the interface between theory and data in cosmology).

In chapter 9 ([Leclercq, Jasche & Wandelt, 2015c](#)), we conducted a fully probabilistic analysis of structure types in the cosmic web as probed by the Sloan Digital Sky Survey main galaxy sample. This study capitalized on the large-scale structure inference performed by [Jasche, Leclercq & Wandelt \(2015, chapter 5\)](#) using the BORG (Bayesian Origin Reconstruction from Galaxies, [Jasche & Wandelt, 2013a](#), chapter 4) algorithm. As the full gravitational model of structure formation COLA (COmoving Lagrangian Acceleration, [Tassev, Zaldarriaga & Eisenstein, 2013](#); see also section 7.3.1) was used, our approach resulted in the first probabilistic and time-dependent classification of cosmic environments at non-linear scales in physical realizations of the large-scale

structure conducted with real data. Using the [Hahn \*et al.\* \(2007a\)](#) definition (appendix C.2, see also its extensions, [Forero-Romero \*et al.\*, 2009](#); [Hoffman \*et al.\*, 2012](#)), we obtained three-dimensional, time-dependent maps of the posterior probability for each voxel to belong to a void, sheet, filament or cluster.

These posterior probabilities represent all the available structure type information in the observational data assuming the framework of  $\Lambda$ CDM cosmology. Since the large-scale structure cannot be uniquely determined from observations, uncertainty remains about how to assign each voxel to a particular structure type. The question we address in this chapter is how to proceed from the posterior probabilities to a particular choice of assigning a structure type to each voxel. Decision theory (see, for example, [Berger, 1985](#)) offers a way forward, since it addresses the general problem of how to choose between different actions under uncertainty. A key ingredient beyond the posterior is the utility function that assigns a quantitative profit to different actions for all possible outcomes of the uncertain quantity. The optimal decision is that which maximizes the expected utility.

After setting up the problem using our example and briefly recalling the relevant notions of Bayesian decision theory, we will discuss different utility functions and explore the results based on a particular choice.

## 10.2 Method

The decision problem for structure-type classification can be stated as follows. We have four different web-types that constitute the “space of input features:”  $\{T_0 = \text{void}, T_1 = \text{sheet}, T_2 = \text{filament}, T_3 = \text{cluster}\}$ . We want to either choose one of them, or remain undecided if the data constraints are not sufficient. Therefore our “space of actions” consists of five different elements:  $\{a_0 = \text{“decide void,” } a_1 = \text{“decide sheet,” } a_2 = \text{“decide filament,” } a_3 = \text{“decide cluster,” and } a_{-1} = \text{“do not decide.”}\}$  The goal is to write down a decision rule prescribing which action to take based on the posterior information.

Bayesian decision theory states that the action  $a_j$  that should be taken is that which maximizes the expected utility function (conditional on the data  $d$ ), given in this example by

$$U(a_j(\vec{x}_k)|d) = \sum_{i=0}^3 G(a_j|T_i) \mathcal{P}(T_i(\vec{x}_k)|d), \quad (10.1)$$

where  $\vec{x}_k$  labels one voxel of the considered domain,  $\mathcal{P}(T_i(\vec{x}_k)|d)$  are the posterior probabilities of the different structure types given the data, and  $G(a_j|T_i)$  are the gain functions that state the profitability of each action, given the “true” underlying structure. Formally,  $G$  is a mapping from the space of input features to the space of actions. For our particular problem, it can be thought of as a  $5 \times 4$  matrix  $\mathbf{G}$  such that  $\mathbf{G}_{ij} \equiv G(a_j|T_i)$ , in which case eq. (10.1) can be rewritten as a linear algebra equation,  $\mathbf{U} = \mathbf{G} \cdot \mathbf{P}$  where the 5-vector  $\mathbf{U}$  and the 4-vector  $\mathbf{P}$  contain the elements  $\mathbf{U}_j \equiv U(a_j(\vec{x}_k)|d)$  and  $\mathbf{P}_i \equiv \mathcal{P}(T_i(\vec{x}_k)|d)$ , respectively.

Let us consider the choice of gain functions. Several choices are possible. For example, the 0/1-gain functions reward a correct decision with 1 for each voxel, while an incorrect decision yields 0. This leads to choosing the structure type with the highest posterior probability. While this seems like a reasonable choice, we need to consider that a decision is made in each voxel, whereas we are interested in identifying structures as objects that are made of many voxels. For instance, since clusters are far smaller than voids, the *a priori* probability for a voxel to belong to a cluster is much smaller than for the same voxel to belong to a void. To treat different structures on an equal footing, it makes sense to reward the correct choice of structure type  $T_i$  by an amount inversely proportional to the average volume  $V_i$  of one such structure. In the following, we use the prior probability as a proxy for the volume fractions,

$$\mathcal{P}(T_i) \approx \frac{V_i}{V_0 + V_1 + V_2 + V_3}. \quad (10.2)$$

We further introduce an overall cost for choosing a structure with respect to remaining undecided, leading to the following specification of the utility,

$$G(a_j|T_i) = \begin{cases} \frac{1}{\mathcal{P}(T_i)} - \alpha & \text{if } j \in \llbracket 0, 3 \rrbracket \text{ and } i = j, \\ -\alpha & \text{if } j \in \llbracket 0, 3 \rrbracket \text{ and } i \neq j, \\ 0 & \text{if } j = -1. \end{cases} \quad (10.3)$$

This choice limits 20 free functions to only one free parameter,  $\alpha$ . With this set of gain functions, making (or not) a decision between structure types can be thought of as choosing to play or not to play a gambling game costing  $\alpha$ . Not playing the game, i.e. remaining undecided ( $j = -1$ ), is always free ( $G(a_{-1}|\mathbf{T}_i) = 0$  for all  $i$ ). If the gambler decides to play the game, i.e. to make a decision ( $j \in \llbracket 0, 3 \rrbracket$ ), they pay  $\alpha$  but may win a reward,  $\frac{1}{\mathcal{P}(\mathbf{T}_i)}$ , by betting on the correct underlying structure ( $i = j$ ).

In the absence of data, the posterior probabilities in equation (10.1) are the prior probabilities  $\mathcal{P}(\mathbf{T}_i)$ , which are independent of the position  $\vec{x}_k$ , and the utility functions are, for  $j \in \llbracket 0, 3 \rrbracket$ ,

$$\begin{aligned} U(a_j) &= \sum_{i=0}^3 G(a_j|\mathbf{T}_i) \mathcal{P}(\mathbf{T}_i) \\ &= \left( \frac{1}{\mathcal{P}(\mathbf{T}_j)} - \alpha \right) \mathcal{P}(\mathbf{T}_j) - \sum_{\substack{i=0 \\ i \neq j}}^3 \alpha \mathcal{P}(\mathbf{T}_i) \\ &= 1 - \alpha \left( \mathcal{P}(\mathbf{T}_j) + \sum_{\substack{i=0 \\ i \neq j}}^3 \mathcal{P}(\mathbf{T}_i) \right) \\ &= 1 - \alpha, \end{aligned} \tag{10.4}$$

$$\text{and } U(a_{-1}) = 0. \tag{10.5}$$

Equations (10.4) and (10.5) mean that, in the absence of data, this reduces to the roulette game utility function, where, if correctly guessed, *a priori* unlikely outcomes receive a higher reward, inversely proportional to the fraction of the probability space they occupy. Betting on outcomes according to the prior probability while paying  $\alpha = 1$  leads to a *fair game* with zero expected net gain. The gambler will always choose to play if the cost per game is  $\alpha \leq 1$  and will never play if  $\alpha > 1$ .

The posterior probabilities update the prior information in light of the data, providing an advantage to the gambler through privileged information about the outcome. In the presence of informative data, betting on outcomes based on the posterior probabilities will therefore ensure a positive expected net gain and the gambler will choose to play even if  $\alpha > 1$ . Increasing the parameter  $\alpha$  therefore represents a growing *aversion for risk* and limits the probability of losing. Indeed, for high  $\alpha$ , the gambler will only play in cases where the posterior probabilities give sufficient confidence that the game will be won, i.e. that the decision will be correct.

### 10.3 Maps of structure types in the SDSS

We applied the above decision rule to the web-type posterior probabilities presented in chapter 9 (Leclercq, Jasche & Wandelt, 2015c), for different values of  $\alpha \geq 1$  as defined by equation (10.3). In doing so, we produced various maps of the volume of interest, consisting of the northern Galactic cap of the SDSS main galaxy sample and its surroundings. Slices through these three-dimensional maps are shown in figure 10.1 for the late-time large-scale structure (at  $a = 1$ ) and in figure 10.2 for the primordial large-scale structure (at  $a = 10^{-3}$ ).

When the game is fair (namely when  $\alpha = 1$ ), it is always played, i.e. a decision between one of the four structure types is always made. This results in the *speculative map* of structure types (top left panel of figures 10.1 and 10.2). There, a decision is made even in regions that are not constrained by the data (at high redshift or outside of the survey boundaries), based on prior betting odds.

By increasing the value of  $\alpha > 1$ , we demand higher confidence in making the correct decision. This yields increasingly *conservative maps* of the Sloan volume (see figures 10.1 and 10.2). In particular, at high values of  $\alpha$ , the algorithm makes decisions in the regions where data constraints are strong (see figures 9.3 and 9.6), but often stays undecided in the unobserved regions. It can be observed that even at very high values,  $\alpha \gtrsim 3$ , a decision for one structure is made in some unconstrained voxels (typically in favor of the structure for which the reward is the highest: clusters in the final conditions, and clusters or voids in the initial conditions). This effect is caused by the limited number of samples used in our analysis. Indeed, because of the finite length of the Markov Chain, the sampled representation of the posterior has not yet fully converged to the true posterior. For this reason, the numerical representation of the posterior can be artificially displaced too much from the prior, which results in an incorrect web-type decision. This effect could be mitigated by obtaining more samples in the original BORG analysis (for an increased computational cost); or can be avoided by further increasing  $\alpha$ ,



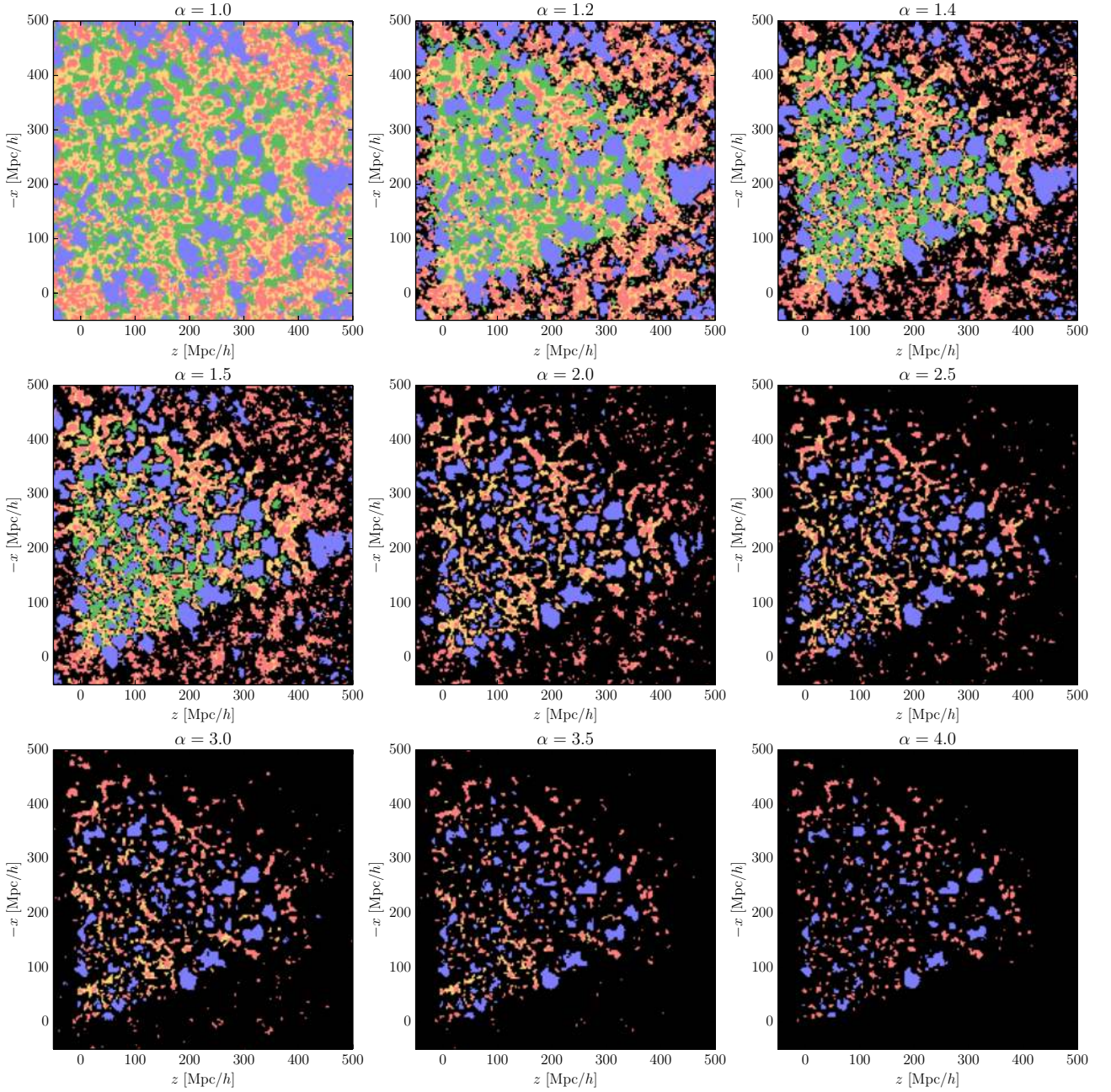


Figure 10.1: Slices through maps of structure types in the late-time large-scale structure, at  $a = 1$ . The color coding is blue for voids, green for sheets, yellow for filaments, and red for clusters. Black corresponds to regions where data constraints are insufficient to make a decision. The parameter  $\alpha$ , defined by equation (10.3), quantifies the risk aversion in the map:  $\alpha = 1.0$  corresponds to the most speculative map of the large-scale structure, and maps with  $\alpha \geq 1$  are increasingly conservative. These maps are based on the posterior probabilities inferred in chapter 9 and on the Bayesian decision rule subject of the present chapter.



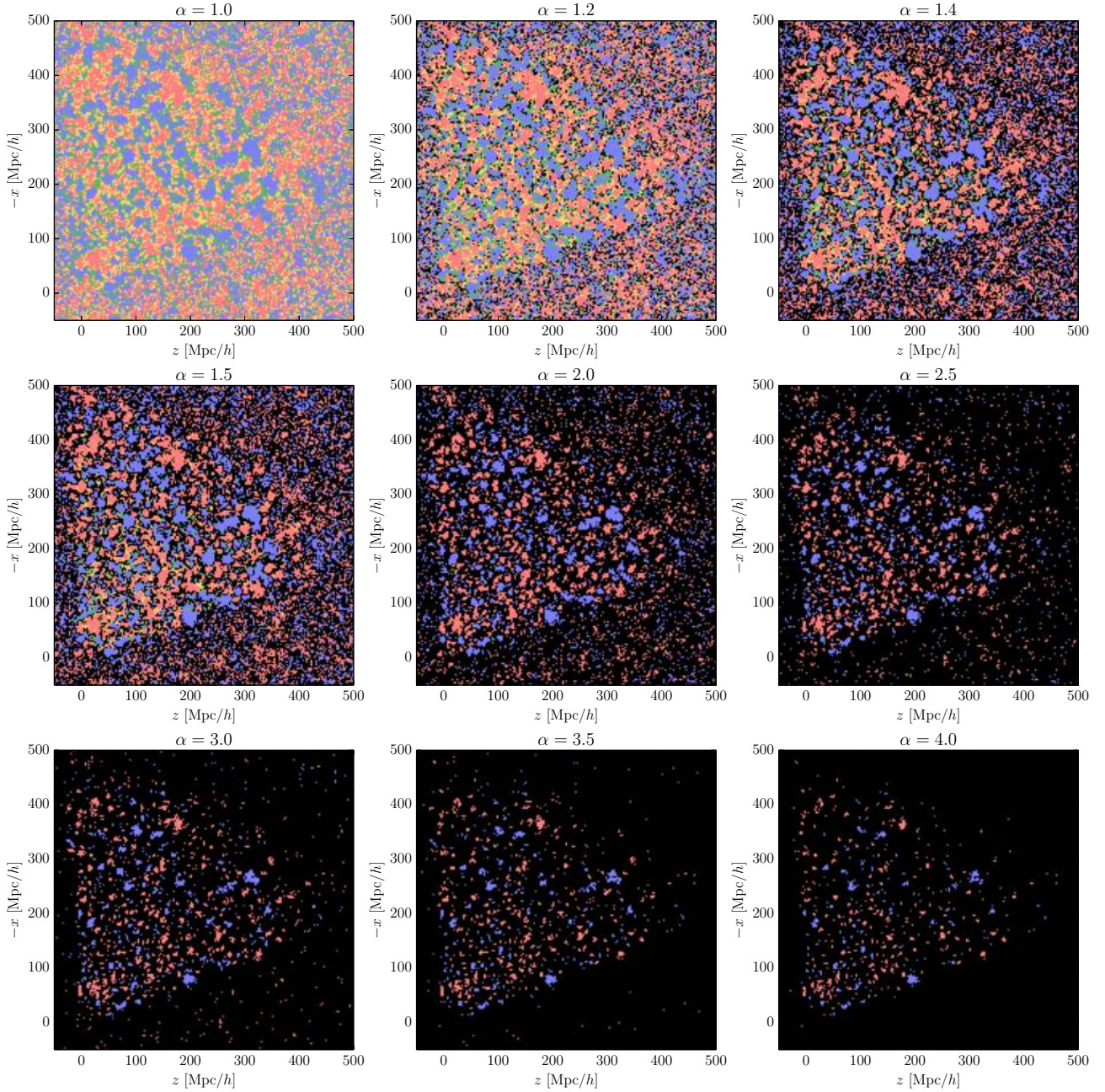


Figure 10.2: Same as figure 10.1 for the primordial large-scale structure, at  $a = 10^{-3}$ .

at the expense of also degrading the map in the observed regions. We found the value of  $\alpha = 4$  (bottom right panel of figures 10.1 and 10.2) to be the best compromise between reducing the number of unobserved voxels in which a decision is made to a tiny fraction and keeping information in the volume covered by the data.

As expected, structures for which the prior probabilities are the highest disappear first from the map when one increases  $\alpha$ : betting on these structures being poorly rewarded, this choice is avoided in case of high risk aversion. In the final conditions (figure 10.1), we found that sheets completely disappear for  $\alpha \approx 1.68$  and filaments for  $\alpha \approx 4.01$ . In the initial conditions (figure 10.2), the critical value is around  $\alpha \approx 2.36$  for both sheets and filaments. In the most conservative maps displayed in figures 10.1 and 10.2 ( $\alpha = 4.0$ ), the SDSS data provide extremely high evidence for the voids and clusters shown. In constrained parts, extended regions belonging to a given structure type may not have the expected shape. This is true in particular for filamentary regions. Several factors can explain this: first, slicing through filaments make them appear as dots; second, with the dynamic T-web definition, filament regions often extend out into sheets and voids, and their static skeleton geometry is not the most prominent at the voxel scale (3 Mpc/ $h$  in this work).

As detailed in chapters 4 and 5, data constraints are propagated by the structure formation model assumed in the inference process (second-order Lagrangian perturbation theory) and therefore radiate out of the SDSS boundaries. For this reason, for moderate values of  $\alpha$ , web-type classification can be extended beyond the survey boundaries to regions influenced by data. This can be observed in figures 10.1 and 10.2, where one can see, for instance, that the shape of voids that intersect the mask is correctly recovered. Similarly, the classification of high-redshift structures confirms that the treatment of selection effects by BORG is correctly propagated to web-type analysis.

We finally comment on the required computational resources for the complete chain for running BORG, computing the web-type posterior, and making a decision. Inference with BORG is the most expensive part: on average, one sample is generated in 1500 seconds on 16 cores (chapter 5; Jasche, Leclercq & Wandelt, 2015). Then, in each sample, tidal shear analysis (chapter 9; Leclercq, Jasche & Wandelt, 2015c) is a matter of a few seconds. Once the web-type posterior is known, making a decision, which is the subject of the present chapter, is almost instantaneous. Therefore, once the density field has been inferred, which is useful for a much larger variety of applications, our method is substantially cheaper than several state-of-the-art techniques for cosmic web analysis (e.g. the method of Tempel, Stoica & Saar, 2013; Tempel *et al.*, 2014, for detecting filaments).

## 10.4 Conclusions

In this chapter, we proposed a rule for optimal decision making in the context of cosmic web classification. We described the problem set-up in Bayesian decision theory and proposed a set of gain functions that permit an interpretation of the problem in the context of game theory. This framework enables the dissection of the cosmic web into different elements (voids, sheets, filaments, and clusters) given their prior and posterior probabilities and naturally accounts for the strength of data constraints.

As an illustration, we produced three-dimensional templates of structure types with various risk aversion, describing a volume covered by the SDSS main galaxy sample and its surrounding. These maps constitute an efficient statistical summary of the inference results presented in chapter 9 (Leclercq, Jasche & Wandelt, 2015c) for cross-use with other astrophysical and cosmological data sets.

Beyond this specific application, our approach is more generally relevant to the solution of classification problems in the face of uncertainty. For example, the construction of catalogs from astronomical surveys is directly analogous to the problem we describe here: it simultaneously involves a decision about whether or not to include a candidate object and which class label (e.g. star or galaxy) to assign to it.

---

# Summary, Conclusion and Outlook

---

“Je crois qu’on obtiendra des résultats étonnants. C’est justement pour cela que je ne puis rien vous en dire; car si je les prévoyais, que leur resterait-il d’étonnant?”

— [Henri Poincaré \(1900\)](#)

---

## Summary

The main subject of this thesis is the process of data assimilation for the analysis of the cosmological large-scale structure. It aims at finding the best realizations of a physical model of structure formation in light of the data, while fully accounting for all uncertainties inherent to the inference problem. To this end, the BORG (Bayesian Origin Reconstruction from Galaxies) algorithm derives the initial conditions and produces physical large-scale structure reconstructions, by assimilating survey data into a cosmological model. It is an inference engine that allows the simultaneous analysis of the morphology and the formation history of the cosmic web, a subject introduced in this work that we refer to as chrono-cosmography. The present thesis contributed to the establishment of physical large-scale structure inference as a functional and effective tool for the analysis of real survey data.

We started by a review of the standard picture of LSS formation, discussing the gravitational self-evolution of the dark matter fluid and introducing cosmological perturbation theory (chapter 1). We then examined the accuracy of Lagrangian perturbation theory, a tool widely applied in LSS data analysis and also a key ingredient of the BORG algorithm (chapter 2). We characterized the approximation error in particle realizations produced by LPT at first or second order instead of fully non-linear gravity. In particular, we analyzed the one-, two- and three-point statistics of the density field, examined the displacement field and compared the volume of different cosmic web elements. In spite of visual similarities, we found that LSS realizations produced by LPT and by  $N$ -body simulations can drastically differ in some regimes, an effect of general interest for data analysis.

Since unique recovery of signals from data subject to observational effects (incomplete sky coverage, selection effects, biases and noise) is not possible, BORG uses a Bayesian approach to quantify uncertainties. We discussed the fundamental concepts, mathematical framework and computer implementation of Bayesian probability theory (chapter 3). Building upon these notions, we introduced physical large-scale structure inference with the BORG algorithm (chapter 4). We exposed the data model and described the numerical sampler, based on the Hamiltonian Monte Carlo technique. Our approach allows the exploration of the posterior distribution, which lives in an extremely high-dimensional parameter space (usually of the order of 10 million free parameters), in computationally reasonable times. As a result, it provides a sampled representation of the large-scale structure inferred from the data, in the form of four-dimensional cosmographic maps of the matter distribution. We applied the BORG algorithm to the Sloan Digital Sky Survey main galaxy sample data and presented our analysis (chapter 5). Our results constitute accurate three-dimensional reconstructions of the present density and velocity fields, but also of the initial conditions and of the formation history of the large-scale structures in the observed domain.

The full data-assimilation problem is deeply non-linear, implying that probability distributions for observed cosmic fields are far from a multivariate Gaussian. We discussed the challenges associated with a fully non-linear description of late-time structure formation. We proposed a fast method to improve the correspondence between density fields in approximate models and in full numerical simulations (chapter 6). The technique relies on remapping the one-point distribution of approximate fields using information extracted from simulations, and allows to extend the validity of LPT beyond shell-crossing, in the mildly non-linear regime. We introduced the concept of non-linear filtering of BORG samples (chapter 7). This procedure improves constrained realizations by augmenting them with physically plausible information at small scales. We checked the accuracy of the fast COLA scheme as a non-linear filter versus GADGET-2, and used it to produce a large ensemble of non-linear BORG-COLA samples for subsequent use.

We finally made use of our results for cosmic web analysis. With the VIDE toolkit, we produced and analyzed constrained catalogs of cosmic voids in the Sloan volume. In doing so, we showed that the inference of voids at the level of the dark matter field, deeper than with the galaxies, is achievable, and that suitable inference technology is capable of tapping a mine of information even in existing surveys. In particular, we found at least



one order of magnitude more voids at all scales considered, between 5 and 40 Mpc/h. As a consequence, our method yields a drastic reduction of statistical uncertainty for the determination of void properties and carries a vast potential for their use as cosmological probes. We presented a probabilistic analysis of the dynamic cosmic web, dissected into voids, sheets, filaments, and clusters, on the basis of the tidal field (chapter 9). We examined the history and characterized the information content of our web-type maps. This study demonstrated that our inference framework allows self-consistent propagation of observational uncertainties to cosmic web analysis, and counts among the pioneering steps toward a data-supported connection between cosmology and information theory. Eventually, we introduced a new framework for optimal decision-making based on the web-type posterior probabilities and the strength of data constraints (chapter 10). We obtained efficient statistical summaries of our inference results and outlined more general applications to classification problems in the face of uncertainty.

## Conclusion and Outlook

### What does chrono-cosmography predict about the Universe?

The aim of physical large-scale structure inference is to provide a cosmographic description of a subvolume of the observable Universe, as well as a probabilistic characterization of uncertainties. In this fashion, we have access to a wealth of information on the present and past of this region. This material can be used in a variety of subsequent astrophysical and cosmological analyses, many of which can be already conducted based on the results obtained during this PhD project.

A first class of possible projects build upon the inference of the initial conditions, in which gravitational non-Gaussianity is largely suppressed.

**Genesis and growth of the cosmic web.** As we have shown, Bayesian large-scale structure inference paves the path toward a high-fidelity description of the complex web-like patterns in cosmic structure. A natural follow-up project is to exploit the richness of the information inferred by BORG, including quantities so far only accessible in simulations, to build and compare classifications of the cosmic web. These will use, for example: the Lagrangian displacement field (DIVA, [Lavaux & Wandelt, 2010](#)) or the stretchings and foldings of the dark matter phase-space sheet (ORIGAMI, [Falck, Neyrinck & Szalay, 2012](#)).

**Primordial non-Gaussianity and inflation.** The BORG algorithm has the potential to accurately characterize the statistics of primordial seeds. In particular, estimators of bispectra ([Schmittfull, Baldauf & Seljak, 2015](#)) or based on the phases of inferred fields ([Obreschkow \*et al.\*, 2013](#); [Wolstenhulme, Bonvin & Obreschkow, 2014](#)) – for which no prior information is assumed – may detect signatures of primordial non-Gaussianity or constrain models of inflation. While it will be extremely challenging for LSS measurements to improve upon CMB constraints on inflation, the theoretically interesting threshold for many models involving deviations from Gaussian initial conditions has not yet been reached. Hence, it is crucial to develop new methods that will extract this information from the LSS.

**Galaxies within the large-scale structure.** Physical properties of galaxies (luminosity, color, spin, morphological type, etc.) are known to be correlated with their large-scale environment (see e.g. [Lee & Lee, 2008](#); [Park, Kim & Park, 2010](#); [Eardley \*et al.\*, 2015](#)). Cosmic web analyses enabled by BORG straightforwardly allow to test models of galaxy formation and evolution within their time-varying environment. The resulting information could then be used in future large-scale structure inference procedures, to obtain more refined information on the matter density field traced by these galaxies.

BORG provides a complete description of the gravitational dynamics of the volume of interest. A second class of projects is to use this information and see what it implies for other cosmological observables. In this regard, we use BORG as a forecast-generating machine, whose predictions can be tested with complementary observations in the actual sky.

**Effects of the inhomogeneous large-scale structure on photons.** Inferred information permits to produce various prediction templates for cross-correlations with other cosmological data sets. In particular, it is possible to predict the effects of inhomogeneities in the LSS on photon properties and geodesics, given galaxy observations:

deviations in redshift (in the radial direction) and weak gravitational lensing effects (in the angular directions). In a similar fashion, dynamic information such as velocity fields and evolution of the gravitational potential can be used to enhance the detectability of secondary effects expected in the cosmic microwave background, such as the kinetic Sunyaev-Zel'dovich effect, the integrated Sachs-Wolfe effect, and the non-linear Rees-Sciama effect.

**Cosmological parameters, baryon acoustic oscillations and dynamic dark energy.** The incorporation of a physical model in the likelihood provides a natural way to infer cosmological parameters from observations. The work presented in this thesis is also expected to provide an alternative way to reconstruct the baryon acoustic oscillation signal (Padmanabhan *et al.*, 2012) and to infer the equation of state of a possible dark energy component. This approach will yield a more precise picture of the expansion history of the Universe and help to understand the origin of cosmic acceleration.

## How do we include more aspects in the data model?

Contrary to traditional approaches, which apply various cosmological tests to data separately and combine constraints in a suboptimal fashion, the approach presented in this thesis automatically and fully self-consistently performs a joint analysis of all aspects. It models their interdependence and accounts for the ways in which different observables can mutually enhance one another. The joint analysis of all phenomena can be used to perform consistency tests of the standard cosmological model and has the potential to rule out some of its possible extensions.

However, many relevant aspects are still absent of the current BORG data model: a fully non-linear treatment of gravitational structure formation, redshift-space distortions, lightcone effects, photometric redshifts uncertainty, density-dependent selection effects, scale-dependent and stochastic galaxy bias or predictions of non-standard cosmologies. The joint analysis of other probes of the LSS (CMB lensing, weak lensing shear maps, etc.) should also be addressed in our framework, via a joint likelihood or sequential data assimilation. The inclusion of these aspects in the LSS data model involves conceptual, but also technical challenges. Bayesian large-scale structure inference is highly computationally expensive, to the degree that it touches the border of what is currently possible.

In the author's opinion, future progress will not only depend on adequate approximations, but also on the development of new methodological ways to implement sampling. In comparison to the state-of-the-art Hamiltonian Monte Carlo algorithm, efficient, advanced non-linear data assimilation techniques will have to allow a much cheaper statistical inference (presumably by several orders of magnitude), which will open the way for the inclusion of more physical effects.

## What can ultimately be learned from the large-scale structure?

How deterministic is the formation of structure in the Universe? In other words, at what scale does one-to-one mapping from initial to final conditions (valid at large, linear and weakly non-linear scales) break down? Since state-of-the-art simulations are still very far from resolving all relevant physical processes, the issue of the scale at which structure formation is non-deterministic is not yet considered crucial for numerical modeling. However, a theoretical understanding of this question would be of central interest in the context of an Effective Field Theory of the LSS (Baumann *et al.*, 2012; Carrasco, Hertzberg & Senatore, 2012; Senatore & Zaldarriaga, 2014). A quantification of the information content of primordial patches that collapse to form structures (such as the Milky Way) characterizes the LSS in a fundamental way and contains a wealth of information on the properties of matter at the highest energies, far beyond the reach of particle colliders.

High amount of primordial information contained in small-scale structures would for example disfavor warm dark matter or any mechanism suppressing small-scale density fluctuations, and could even require further initial degrees of freedom such as isocurvature perturbations. Issues related to the information content of primordial patches have been recently speculatively examined by Neyrinck (2015b), who proposed, as a thought experiment, a test about the scale at which structure formation is deterministic. Unfortunately, simulations do not provide much insight into the questions of where the information content is, and how to optimally extract it from the data.

Building upon the inference of initial conditions from which the LSS originates, the first steps toward a practical implementation of a scale-dependent test of determinism in structure formation can be taken. This task will involve the careful definition of a measure of complexity in Lagrangian patches inferred by BORG and of

a means to compare initial and final information. It will also require careful analysis of information propagation via Lagrangian transport within a fully probabilistic approach (see sections 5.3.3 and 9.5.1; figures 5.8, 9.3 and 9.6 for a preparatory discussion). Further investigation will have to consider information sinks such as baryonic processes and black hole formation, and information sources that broadcast non-primordial randomness at large scales, such as supernovae, active galactic nuclei and unstable astrophysical phenomena. The link between astrophysical, thermodynamic entropy, as well as statistical, information-theoretic entropy will also have to be clarified.

In the last few years, ESA's *Planck* mission confirmed our picture of the evolution of the homogeneous Universe to spectacular accuracy and provided the highest precision probe to date of the physical origin of cosmic structure. Challenges for accurate cosmology now arise from studying the inhomogeneous cosmic structure. This research will provide an exceptionally detailed characterization of the cosmic web underlying the observed galaxy distribution, extract information about the nature of dark energy, and furnish unprecedentedly accurate information on the initial conditions from which structure appeared in the Universe. Progress will not only depend on our ability to handle ever larger data sets: crucial to the longer-term aims is developing efficient tools for assimilating data into the forecasts of a physical model and quantifying the information content uniquely encoded in the primordial large-scale structure. Only through such a quantitative statistical approach can we expand our understanding of the dynamic Universe and make significant progress on the age-old puzzles of cosmic beginning and ultimate fate of the Universe. I am confident that the methods and results described in this thesis, counting among the first steps towards precision chrono-cosmography, will contribute to this endeavor.



# **Appendices**



# Complements on Gaussian random fields

## Contents

A.1	Characteristic function . . . . .	161
A.2	General definition of a Gaussian random vector . . . . .	162
A.3	Some well-known properties of Gaussian random vectors . . . . .	162
A.4	Marginal and conditionals of Gaussian random vectors . . . . .	163

“I have had my results for a long time: but I do not yet know how I am to arrive at them.”

— Carl Friedrich Gauß

Quoted in [Arber \(1954\)](#), *The Mind and the Eye*

## Abstract

This appendix provides complements on Gaussian random fields. It offers a mathematical exposition of their definition and demonstrates well-known properties, used in particular in chapter 1 and for the generation of initial conditions for cosmological simulations (section B.6).

## A.1 Characteristic function

**Definition A.1.** For a random scalar vector  $\lambda \in \mathbb{C}^n$  whose pdf is  $\mathcal{P}(\lambda)$ , the characteristic function  $\varphi_\lambda$  is defined as the inverse Fourier transform of  $\mathcal{P}(\lambda)$ . In other words, it is the expectation value of  $e^{it^*\lambda}$ , where  $t \in \mathbb{C}^n$  is the argument of the characteristic function (e.g. [Manolakis, Ingle & Kogon, 2000](#)):

$$\varphi_\lambda(t) \equiv \langle e^{it^*\lambda} \rangle = \int_{\mathbb{C}} e^{it^*\lambda} \mathcal{P}(\lambda) d\lambda. \quad (\text{A.1})$$

Characteristic functions have well-known properties. In particular, an important theorem is the following.

**Theorem A.2. (Kac’s theorem).** Let  $\lambda_1, \lambda_2 \in \mathbb{C}^n$  be random vectors. The following statements are equivalent:

1.  $\lambda_1$  and  $\lambda_2$  are independent (we note  $\lambda_1 \perp\!\!\!\perp \lambda_2$ ),
2. the characteristic function of the joint random vector  $(\lambda_1, \lambda_2)$  is the product of the characteristic functions of  $\lambda_1$  and  $\lambda_2$  i.e.  $\varphi_{(\lambda_1, \lambda_2)} = \varphi_{\lambda_1} \varphi_{\lambda_2}$ .

*Proof.* 1.  $\Rightarrow$  2. is straightforward using  $\langle f(\lambda_1)g(\lambda_2) \rangle = \langle f(\lambda_1) \rangle \langle g(\lambda_2) \rangle$ .

2.  $\Rightarrow$  1. Let  $\widetilde{\lambda}_1$  and  $\widetilde{\lambda}_2$  be random vectors such that  $\widetilde{\lambda}_1$  and  $\lambda_1$  have the same pdf,  $\widetilde{\lambda}_2$  and  $\lambda_2$  have the same pdf and  $\widetilde{\lambda}_1 \perp\!\!\!\perp \widetilde{\lambda}_2$ . Then

$$\begin{aligned} \varphi_{(\lambda_1, \lambda_2)} &= \varphi_{\lambda_1} \varphi_{\lambda_2} && \text{using 2.} \\ &= \varphi_{\widetilde{\lambda}_1} \varphi_{\widetilde{\lambda}_2} && \text{using the pdfs} \\ &= \varphi_{(\widetilde{\lambda}_1, \widetilde{\lambda}_2)} && \text{using 1. } \Rightarrow 2. \end{aligned}$$

i.e. the characteristic functions of  $(\lambda_1, \lambda_2)$  and  $(\widetilde{\lambda}_1, \widetilde{\lambda}_2)$  coincide. From the uniqueness of the inverse Fourier transform we conclude that  $(\lambda_1, \lambda_2)$  and  $(\widetilde{\lambda}_1, \widetilde{\lambda}_2)$  are drawn from the same distribution, hence  $\lambda_1 \perp\!\!\!\perp \lambda_2$ .  $\square$

## A.2 General definition of a Gaussian random vector

**Definition A.3.** A multivariate random scalar vector  $\lambda \in \mathbb{C}^n$  is a Gaussian random vector if and only if there exists a vector  $\mu \in \mathbb{C}^n$  and a Hermitian, positive semi-definite matrix  $C \in \mathcal{M}_n(\mathbb{C})$  such that the characteristic function of  $\lambda$  is

$$\varphi_\lambda(t) = \exp \left( it^* \mu - \frac{1}{2} t^* C t \right). \quad (\text{A.2})$$

In this case,  $\mu$  and  $C$  are called the mean and covariance matrix of  $\lambda$ , respectively, and we note  $\lambda \sim \mathcal{N}_n[\mu, C]$ . Here, the covariance matrix is allowed to be singular. This definition generalizes the one given in section 1.2.3.1, as we see from the following theorem.

**Theorem A.4.** When  $C$  is positive-definite (and therefore invertible), the distribution of  $\lambda$  has a multivariate normal density

$$\mathcal{P}(\lambda|\mu, C) = \frac{1}{\sqrt{|2\pi C|}} \exp \left( -\frac{1}{2} (\lambda - \mu)^* C^{-1} (\lambda - \mu) \right). \quad (\text{A.3})$$

*Proof.* By explicitly computing the inverse Fourier transform of the multivariate normal distribution above (i.e. calculating the Gaussian integral), we can check that the characteristic function of this distribution coincides with the value of equation (A.2). From the uniqueness of the inverse Fourier transform, we conclude that  $\lambda$  is drawn from the distribution whose pdf is given above.  $\square$

When this condition is fulfilled, we say that  $\lambda$  is *non-degenerate*.

## A.3 Some well-known properties of Gaussian random vectors

**Proposition A.5.** Linear transformations preserve Gaussianity, i.e. for all  $A \in \mathcal{M}_{m \times n}(\mathbb{C})$  and  $b \in \mathbb{C}^m$ , if  $\lambda \sim \mathcal{N}_n[\mu, C]$ , then  $A\lambda + b \sim \mathcal{N}_m[A\mu + b, ACA^*]$ .

*Proof.* The characteristic function of  $A\lambda + b$  is, for all  $s \in \mathbb{C}^m$ ,

$$\begin{aligned} \varphi_{A\lambda+b}(s) &= \left\langle e^{is^*(A\lambda+b)} \right\rangle \\ &= \left\langle e^{i(A^*s)^*\lambda} \right\rangle e^{is^*b} \\ &= \varphi_\lambda(A^*s) e^{is^*b} \\ &= \exp \left( i(A^*s)^*\mu - \frac{1}{2} (A^*s)^* C A^* s \right) \exp(i s^* b) \\ &= \exp \left( is^*(A\mu + b) - \frac{1}{2} s^* (ACA^*) s \right). \end{aligned}$$

$\square$

**Proposition A.6.** Adding two independent Gaussians yields a Gaussian, i.e. if  $\lambda_1 \sim \mathcal{N}_n[\mu_1, C_1]$ ,  $\lambda_2 \sim \mathcal{N}_n[\mu_2, C_2]$  and  $\lambda_1 \perp \lambda_2$ , then  $\lambda_1 + \lambda_2 \sim \mathcal{N}_n[\mu_1 + \mu_2, C_1 + C_2]$ .

*Proof.* The independence of  $\lambda_1$  and  $\lambda_2$  implies the independence of  $e^{it^*\lambda_1}$  and  $e^{it^*\lambda_2}$ . Therefore,

$$\varphi_{\lambda_1+\lambda_2}(t) = \left\langle e^{it^*(\lambda_1+\lambda_2)} \right\rangle = \left\langle e^{it^*\lambda_1} e^{it^*\lambda_2} \right\rangle = \left\langle e^{it^*\lambda_1} \right\rangle \left\langle e^{it^*\lambda_2} \right\rangle = \varphi_{\lambda_1}(t) \varphi_{\lambda_2}(t).$$

Using the characteristic functions of  $\lambda_1$  and  $\lambda_2$  yields

$$\varphi_{\lambda_1+\lambda_2}(t) = \exp \left( it^* \mu_1 - \frac{1}{2} t^* C_1 t \right) \exp \left( it^* \mu_2 - \frac{1}{2} t^* C_2 t \right) = \exp \left( it^* (\mu_1 + \mu_2) - \frac{1}{2} t^* (C_1 + C_2) t \right).$$

$\square$

## A.4 Marginal and conditionals of Gaussian random vectors

To study the partition of Gaussian random vectors, let us define

$$\lambda = \begin{pmatrix} \lambda_x \\ \lambda_y \end{pmatrix}, \quad \mu = \begin{pmatrix} \mu_x \\ \mu_y \end{pmatrix} \quad \text{and} \quad C = \begin{pmatrix} C_{xx} & C_{xy} \\ C_{yx} & C_{yy} \end{pmatrix}, \quad (\text{A.4})$$

where  $\lambda_x, \mu_x \in \mathbb{C}^m$ ,  $C_{xx} \in \mathcal{M}_m(\mathbb{C})$ ,  $\lambda_y, \mu_y \in \mathbb{C}^{n-m}$ ,  $C_{yy} \in \mathcal{M}_{n-m}(\mathbb{C})$ ,  $C_{xy} \in \mathcal{M}_{m \times (n-m)}(\mathbb{C})$  and  $C_{yx} = (C_{xy})^* \in \mathcal{M}_{(n-m) \times m}(\mathbb{C})$ . We assume that  $m < n$  and we want to prove that the marginal and conditional distributions of  $\lambda_x$  and  $\lambda_y$  are Gaussians with parameters given by equations (1.19)–(1.22) and (1.23)–(1.26). By symmetry, we limit the discussion to  $\lambda_x$  and  $\lambda_x|\lambda_y$ .

**Proposition A.7.** The marginal distribution of  $\lambda_x$  is that of a Gaussian random vector with mean  $\mu_x$  and variance  $C_{xx}$ .

*Proof.* Consider  $A = \begin{pmatrix} 1_{xx} & 0_{xy} \\ 0_{yx} & 0_{yy} \end{pmatrix}$ . Proposition A.5. yields  $A\lambda = \lambda_x \sim \mathcal{N}_m[A\mu, ACA^*] = \mathcal{N}_m[\mu_x, C_{xx}]$ .  $\square$

Let us now consider the conditionals.

**Lemma A.8.**  $\lambda_x$  and  $\lambda_y$  are independently distributed if and only if  $C_{xy} = 0_{xy}$ .

*Proof.* This proposition follows by considering the characteristic function of  $\lambda$ :

$$\begin{aligned} \varphi_\lambda(t) &= \varphi_{(\lambda_x, \lambda_y)}(t_x, t_y) \\ &= \exp\left(it^* \mu - \frac{1}{2} t^* C t\right) \\ &= \exp\left(it_x^* \mu_x + it_y^* \mu_y - \frac{1}{2} t_x^* C_{xx} t_x - \frac{1}{2} t_x^* C_{xy} t_y - \frac{1}{2} t_y^* C_{yx} t_x - \frac{1}{2} t_y^* C_{yy} t_y\right) \\ &= \varphi_{\lambda_x}(t_x) \varphi_{\lambda_y}(t_y) \exp(-t_x^* C_{xy} t_y) \end{aligned}$$

and using Kac's theorem (theorem A.2.),  $\lambda_x \perp \lambda_y \Leftrightarrow \varphi_{(\lambda_x, \lambda_y)} = \varphi_{\lambda_x} \varphi_{\lambda_y} \Leftrightarrow C_{xy} = 0_{xy}$ .  $\square$

**Definition A.9.** Let  $C_{xx.y} \equiv C_{xx} - C_{xy} C_{yy}^{-1} C_{yx}$ , the so-called generalized Schur-complement of  $C_{yy}$  in  $C$ .

**Lemma A.10.**

$$\begin{pmatrix} \lambda_x - C_{xy} C_{yy}^{-1} \lambda_y \\ \lambda_y \end{pmatrix} \sim \mathcal{N}_n \left[ \begin{pmatrix} \mu_x - C_{xy} C_{yy}^{-1} \mu_y \\ \mu_y \end{pmatrix}, \begin{pmatrix} C_{xx.y} & 0_{xy} \\ 0_{yx} & C_{yy} \end{pmatrix} \right]. \quad (\text{A.5})$$

*Proof.* Consider  $A = \begin{pmatrix} 1_{xx} & -C_{xy} C_{yy}^{-1} \\ 0_{yx} & 1_{yy} \end{pmatrix}$ . The lemma follows by considering  $A\lambda$  and using proposition A.5.  $\square$

**Proposition A.11.** The conditional distribution of  $\lambda_x$  given  $\lambda_y$  is the Gaussian distribution given by

$$\mathcal{N}_m[\mu_x + C_{xy} C_{yy}^{-1}(\lambda_y - \mu_y), C_{xx.y}].$$

*Proof.* Since  $\lambda_x - C_{xy} C_{yy}^{-1} \lambda_y$  and  $\lambda_y$  have zero covariance matrix (lemma A.10.), they are independently distributed according to lemma A.8. Therefore, using also the result obtained for the marginals (proposition A.7.), we get

$$\begin{aligned} (\lambda_x - C_{xy} C_{yy}^{-1} \lambda_y) | \lambda_y &\sim \lambda_x - C_{xy} C_{yy}^{-1} \lambda_y \\ &\sim \mathcal{N}_m[\mu_x - C_{xy} C_{yy}^{-1} \mu_y, C_{xx.y}] \end{aligned}$$

and hence

$$\begin{aligned} \lambda_x | \lambda_y &\sim (\lambda_x - C_{xy} C_{yy}^{-1} \lambda_y + C_{xy} C_{yy}^{-1} \lambda_y) | \lambda_y \\ &\sim \mathcal{N}_m[\mu_x + C_{xy} C_{yy}^{-1}(\lambda_y - \mu_y), C_{xx.y}] \end{aligned}$$

by just translating the above normal density by the constant vector  $C_{xy} C_{yy}^{-1} \lambda_y$ .  $\square$





# Simulating collisionless dark matter fluids

## Contents

<b>B.1 Model equations</b>	<b>166</b>
B.1.1 Model equations in the standard PM code	166
B.1.2 Model equations with COLA	166
<b>B.2 Steps and data structures</b>	<b>167</b>
B.2.1 Main PM steps	167
B.2.2 Definitions and data structures	167
<b>B.3 Mesh assignments and interpolations</b>	<b>168</b>
B.3.1 The mesh assignment function	169
B.3.2 Low-pass filtering	169
B.3.3 Common mesh assignment schemes	170
B.3.4 Interpolation	173
<b>B.4 Poisson equation and accelerations</b>	<b>173</b>
B.4.1 Solving the Poisson equation	173
B.4.2 Computation of the accelerations	174
<b>B.5 Update of positions and momenta</b>	<b>175</b>
B.5.1 Time integrators	175
B.5.2 Kick and Drift operators	176
<b>B.6 Setting up initial conditions</b>	<b>177</b>
B.6.1 The initial Gaussian random field	177
B.6.2 The high-redshift particle realization	178

“Simulation:

1. **a.** The action or practice of simulating, with intent to deceive; false pretence, deceitful profession. (...)

2. A false assumption or display, a surface resemblance or imitation, of something. (...)

— The Oxford English Dictionary

Quoted by Peter Coles (2014)

## Abstract

This technical appendix describes the implementation of the simulation codes used in this thesis. It reviews the particle-mesh approach for simulating a collisionless cold dark matter fluid, as well as the COLA modification. The generation of initial conditions using Lagrangian perturbation theory is also discussed.

Many of the projects described in this thesis rely on the particle-mesh (PM) simulation technique. It has originally been introduced and applied in many different areas of physics, such as electromagnetism, hydrodynamics, magnetohydrodynamics, plasma physics and self-gravitating systems (see e.g. the books by [Hockney & Eastwood, 1981](#) and [Birdsall & Langdon, 1985](#)). In a cosmological context, the reference papers include [Klypin & Shandarin \(1983\)](#); [Efstathiou \*et al.\* \(1985\)](#).

This appendix reviews the PM technique, the COLA modification, and the numerical implementation of Lagrangian perturbation theory. More details on cosmological PM codes can be found in the review by [Bertschinger \(1998\)](#) or the lectures notes by [Kravtsov \(2002\)](#); [Springel \(2014\)](#); [Teyssier \(2014\)](#). The reader is also referred

to the COLA papers, Tassev, Zaldarriaga & Eisenstein (2013); Tassev *et al.* (2015); and to Scoccimarro (1998, appendix D), for the implementation of LPT.

This appendix is organized as follows. In section B.1, we write down the equations actually solved by PM/COLA codes. We describe the main PM steps and the required data structures in section B.2. Section B.3 reviews mesh assignments and interpolation schemes; section B.4 discusses the resolution of the Poisson equation and the computation of forces; and section B.5 examines how to update the positions and momenta of particles. Finally, B.6 describes the generation of cosmological initial conditions using Lagrangian perturbation theory.

## B.1 Model equations

### B.1.1 Model equations in the standard PM code

A PM codes solves the equation of motion for dark matter particles in comoving coordinates (see equation (1.74); below the mass of particles  $m$  is absorbed in the definition of the momentum  $\mathbf{p}$ ):

$$\mathbf{p} = a \frac{d\mathbf{x}}{d\tau}, \quad (\text{B.1})$$

$$\frac{d\mathbf{p}}{d\tau} = -a\nabla\Phi, \quad (\text{B.2})$$

coupled with the Poisson equation for the gravitational potential (equation (1.72)),

$$\Delta\Phi = 4\pi G a^2 \bar{\rho}(\tau) \delta = \frac{3}{2} \Omega_m(\tau) \mathcal{H}^2(\tau) \delta. \quad (\text{B.3})$$

It is convenient to choose the scale factor as time variable. Using  $\partial_\tau = a' \partial_a = \dot{a} a \partial_a$  and  $\bar{\rho}(\tau) = \rho^{(0)} a^{-3}$ , the equations to solve are rewritten:

$$\frac{d\mathbf{x}}{da} = \frac{\mathbf{p}}{a'a} = \frac{\mathbf{p}}{\dot{a}a^2}, \quad (\text{B.4})$$

$$\frac{d\mathbf{p}}{da} = -\frac{a\nabla\Phi}{a'} = -\frac{\nabla\Phi}{\dot{a}}, \quad (\text{B.5})$$

$$\Delta\Phi = 4\pi G \rho^{(0)} a^{-1} \delta = \frac{3}{2} \Omega_m^{(0)} a^{-1} \delta. \quad (\text{B.6})$$

We will use the equivalent formulation

$$\frac{d\mathbf{x}}{da} = \mathcal{D}(a)\mathbf{p}, \quad (\text{B.7})$$

$$\frac{d\mathbf{p}}{da} = \mathcal{K}(a)\nabla(\Delta^{-1}\delta), \quad (\text{B.8})$$

where we have combined equations (B.5) and (B.6), and defined  $f(a) \equiv \dot{a}^{-1} = a/a' = \mathcal{H}^{-1}(a)$ ;  $\mathcal{D}(a) \equiv f(a)/a^2$  (the “drift prefactor”) and  $\mathcal{K}(a) \equiv -(3/2)\Omega_m^{(0)} f(a)/a$  (the “kick prefactor”).

### B.1.2 Model equations with COLA

If one desires to include the COLA scheme (see Tassev, Zaldarriaga & Eisenstein, 2013, and section 7.3.1), then one works in a frame comoving with the Lagrangian displacements. Recall the LPT position of a particle is given by (see section 1.5),

$$\mathbf{x}_{\text{LPT}}(a) = \mathbf{q} - D_1(a)\Psi_1 + D_2(a)\Psi_2. \quad (\text{B.9})$$

Noting  $\mathbf{x}(a) = \mathbf{x}_{\text{LPT}}(a) + \mathbf{x}_{\text{MC}}(a)$  the real position of the same particle, including the mode-coupling residual  $\mathbf{x}_{\text{MC}}(a)$ , one has (see equation (B.9)):

$$\frac{d\mathbf{x}}{da} = \frac{d\mathbf{x}_{\text{LPT}}}{da} + \frac{d\mathbf{x}_{\text{MC}}}{da}; \quad \text{with} \quad \frac{d\mathbf{x}_{\text{LPT}}}{da} = -\frac{dD_1}{da}\Psi_1 + \frac{dD_2}{da}\Psi_2 \equiv \mathcal{D}(a)\mathbf{p}_{\text{LPT}}. \quad (\text{B.10})$$

We also define  $\mathbf{p}_{\text{MC}}$  such that  $d\mathbf{x}_{\text{MC}}/da \equiv \mathcal{D}(a)\mathbf{p}_{\text{MC}}$ . Then  $\mathbf{p} = \mathbf{p}_{\text{LPT}} + \mathbf{p}_{\text{MC}}$  (see equation (B.7)). Furthermore,

$$\frac{d\mathbf{p}_{\text{LPT}}}{da} = \frac{d}{da} \left( \frac{1}{\mathcal{D}(a)} \frac{d\mathbf{x}_{\text{LPT}}}{da} \right) \equiv -\mathcal{K}(a)\mathcal{V}[\mathbf{x}_{\text{LPT}}](a), \quad (\text{B.11})$$

where the differential operator  $\mathcal{V}[\cdot](a)$  is defined by

$$\mathcal{V}[\cdot](a) \equiv -\frac{1}{\mathcal{K}(a)} \frac{d}{da} \left( \frac{1}{\mathcal{D}(a)} \frac{d\cdot}{da} \right). \quad (\text{B.12})$$

With these notations, equation (B.8) reads

$$\frac{d\mathbf{p}}{da} = \frac{d\mathbf{p}_{\text{LPT}}}{da} + \frac{d\mathbf{p}_{\text{MC}}}{da} = -\mathcal{K}(a) \mathcal{V}[\mathbf{x}_{\text{LPT}}](a) + \frac{d\mathbf{p}_{\text{MC}}}{da} = \mathcal{K}(a) \nabla (\Delta^{-1} \delta). \quad (\text{B.13})$$

It is straightforward to check from equation (B.9) that  $\mathcal{V}[\mathbf{x}_{\text{LPT}}](a) = -\mathcal{V}[D_1](a) \Psi_1 + \mathcal{V}[D_2](a) \Psi_2$ . Using the differential equation verified by  $D_1$  (equation (1.96)) and the second Friedmann equation (equation (1.7)), we get

$$\mathcal{V}[D_1](a) = D_1(a). \quad (\text{B.14})$$

Similarly for the second-order growth factor, using equation (1.118),

$$\mathcal{V}[D_2](a) = D_2(a) - D_1^2(a). \quad (\text{B.15})$$

In the COLA framework, the natural variables are therefore  $\mathbf{x}$  and  $\mathbf{p}_{\text{MC}}$ , and the equations of motion to solve (equivalents of equations (B.7) and (B.8)) are

$$\frac{d\mathbf{x}}{da} = \mathcal{D}(a) \mathbf{p}_{\text{MC}} - \frac{dD_1}{da} \Psi_1 + \frac{dD_2}{da} \Psi_2, \quad (\text{B.16})$$

$$\frac{d\mathbf{p}_{\text{MC}}}{da} = \mathcal{K}(a) [\nabla (\Delta^{-1} \delta) - \mathcal{V}[D_1](a) \Psi_1 + \mathcal{V}[D_2](a) \Psi_2]. \quad (\text{B.17})$$

In the initial conditions, generated with LPT (see section B.6), we have  $\mathbf{p} = \mathbf{p}_{\text{LPT}}$ ; therefore the mode-coupling momentum residual in the rest frame of LPT observers,  $\mathbf{p}_{\text{MC}}$ , should be initialized to zero (this corresponds to the  $L_-$  operator in Tassev, Zaldarriaga & Eisenstein, 2013, appendix A). At the end, the LPT momentum  $\mathbf{p}_{\text{LPT}}$  has to be added to  $\mathbf{p}_{\text{MC}}$  to recover the full momentum of particles,  $\mathbf{p}$  (this corresponds to the  $L_+$  operator in Tassev, Zaldarriaga & Eisenstein, 2013, appendix A). In the following, wherever we do not make the explicit distinction between the standard PM and the COLA approaches, we will drop the subscript “MC” for COLA momenta and simply note  $\mathbf{p}$ ; however, one should keep in mind these two transformations at the beginning and at the end.

## B.2 Steps and data structures

### B.2.1 Main PM steps

Equations (B.7) and (B.8) are solved iteratively in a PM code, which consists of three main steps:

1. estimate the density field on the grid from current particle positions; solve the Poisson equation on the grid to get the potential; take the gradient of the potential to get the accelerations on the grid; and interpolate back to particles (see sections B.3 and B.4),
2. advance particle momenta using the new accelerations (equation (B.8); see section B.5)
3. update particle positions using their new momenta (equation (B.7); see section B.5).

In the COLA scheme, steps 2 and 3 are replaced with the equivalents that come from equations (B.17) and (B.16), respectively.

### B.2.2 Definitions and data structures

**Grids and box size.** A PM cosmological simulation is characterized by

- the number of particles,  $N_p$  (if particles start from a regular Lagrangian grid – see section B.6 –, we note  $N_{p0}, N_{p1}, N_{p2}$  the number of particles along each direction, such that  $N_p \equiv N_{p0} N_{p1} N_{p2}$ );

- the size of the periodic box along each direction,  $L_0, L_1, L_2$  (the total volume simulated is therefore  $V \equiv L_0 L_1 L_2$ );
- and the number of cells of the PM grid (i.e. the grid on which density and potential are defined) along each direction,  $N_{g0}, N_{g1}, N_{g2}$ , with  $N_g \equiv N_{g0} N_{g1} N_{g2}$ .

In many cases we will assume that the box is cubic, and that the particle grid and the PM grid are isotropic:  $L_0 = L_1 = L_2 \equiv L$ ;  $N_{p0} = N_{p1} = N_{p2}$ ;  $N_{g0} = N_{g1} = N_{g2}$ . In the following, we denote the side lengths of cells by  $\Delta x \equiv L_0/N_{g0}$ ,  $\Delta y \equiv L_1/N_{g1}$ ,  $\Delta z \equiv L_2/N_{g2}$  and their volume by  $V_c \equiv \Delta x \Delta y \Delta z$ . We have  $V = N_g V_c$ .

**Particle variables.** Assuming that particles all have the same mass,<sup>1</sup> a PM code needs a minimum of six real numbers (`float` or `double`) for each particle: three coordinates and three momenta. If the COLA modification is included (see section 7.3.1), a minimum of nine (for LPT at order one) or twelve (for LPT at order two) real numbers per particle is required (three additional real numbers per particle to store the LPT displacements at each order).

We call these arrays `x[mp]`, `y[mp]`, `z[mp]` (particles' positions); `px[mp]`, `py[mp]`, `pz[mp]` (particles' momenta); and if COLA is enabled, `psix_1[mp]`, `psiy_1[mp]`, `psiz_1[mp]` (for the ZA displacements,  $\Psi_1$ ), `psix_2[mp]`, `psiy_2[mp]`, `psiz_2[mp]` (for the 2LPT displacements,  $\Psi_2$ ). Here `mp` indexes a particle. It is interesting to note that the arrays containing the Lagrangian displacements are constants, i.e. that they are never updated within the code (their time-independence can be checked in equations (B.16) and (B.17)). Convenient data structures are 1D arrays of size  $N_p$  for particles' variables.

**Grid variables.** In addition, the code needs real numbers (`float` or `double`) for the density contrast  $\delta$  and the potential  $\Phi$  at each grid cell. An array of size  $N_g$  is needed to store such grid variables. This array can be shared between density and potential: we first use it to store the density contrast  $\delta$ , then replace its values with the potential when the Poisson equation is solved.<sup>2</sup>

We call this array `density_or_Phi`. A convenient data structure is a 3D array, such that the grid quantity at position  $(i, j, k)$  is `density_or_Phi[i, j, k]` (with  $0 \leq i < N_{g0}$ ,  $0 \leq j < N_{g1}$ ,  $0 \leq k < N_{g2}$ ). Equivalently, we decided to implement `density_or_Phi` as a 1D array of size  $N_g$ , such that the grid quantity at position  $(i, j, k)$  is given by `density_or_Phi[mc]` where the current cell is indexed by  $mc = k + N_{g2} \times (j + N_{g1} \times i)$ .

**Accelerations.** It is also convenient to have three additional arrays of size  $N_g$  to store the components of the acceleration on the grid, and three arrays of size  $N_p$  to store the components of particles' acceleration.<sup>3</sup> In the following, we note these arrays `gx[mc]`, `gy[mc]`, `gz[mc]`, `gpx[mp]`, `gpy[mp]`, `gpz[mp]`, where  $0 \leq mc < N_g$  indexes a grid cell and  $0 \leq mp < N_p$  indexes a particle.<sup>4</sup>

### B.3 Mesh assignments and interpolations

This section describes how to assign to the grid a quantity carried by particles (the “mesh assignment” operation, from particles to the grid), and how to distribute to particles a quantity that is known on the grid (the “interpolation” operation, from the grid to particles).

In a PM code, the first operation is used to compute the density on the grid from particle positions; and the second operation is used to assign an acceleration to each particle from grid values. Both are used in step 1 of the main PM steps (see section B.2.1).

<sup>1</sup> From the definition of  $\Omega_m^{(0)}$ , it is easy to see that the mass carried by each particle is  $m = \frac{3\Omega_m^{(0)} H_0^2}{8\pi G} \frac{V}{N_p}$  (this number is called the *mass resolution*).

<sup>2</sup> The quantity stored is actually the reduced gravitational potential,  $\tilde{\Phi} \equiv \Delta^{-1}\delta$ , as the overall time-dependent coefficients needed to go from  $\tilde{\Phi}$  to  $\Phi$  are factored out in  $\mathcal{K}(a)$  (see equations (B.8) and (B.17)).

<sup>3</sup> Actually the reduced acceleration  $\tilde{g} \equiv \nabla(\Delta^{-1}\delta)$  instead of the physical acceleration, see footnote 2.

<sup>4</sup> These arrays are not absolutely required. Indeed, it is possible to get rid of them and to make the code more memory-efficient, if one performs in one step the finite difference (to go from  $\Delta^{-1}\delta$  to  $\nabla(\Delta^{-1}\delta)$ ), the interpolation (from the grid quantities to particles, see section B.3) and the kick operation (see section B.5).

### B.3.1 The mesh assignment function

The general idea to assign particles to the grid is to assume that they have a “shape”  $S$  that intersects the grid. Let us first describe the one-dimensional case, where  $S(x)$  is the 1D particle shape. The fraction of the particle at  $x_p$  assigned to the cell at  $x_c$  is the shape function averaged over this cell:

$$W(x_p - x_c) \equiv \int_{x_c - \Delta x/2}^{x_c + \Delta x/2} S(x' - x_p) dx' = \int \Pi\left(\frac{x' - x_c}{\Delta x}\right) S(x' - x_p) dx' \quad (\text{B.18})$$

The assignment function is hence the convolution:

$$W(x) = \Pi\left(\frac{x}{\Delta x}\right) * S(x) \quad \text{where} \quad \Pi(s) = \begin{cases} 1 & \text{if } |s| \leq \frac{1}{2} \\ 0 & \text{otherwise.} \end{cases} \quad (\text{B.19})$$

In 3D,

$$W(\mathbf{x}_p - \mathbf{x}_c) \equiv W(x_p - x_c)W(y_p - y_c)W(z_p - z_c). \quad (\text{B.20})$$

For some quantity  $A$ , if  $A_p$  are the values carried by the particles at positions  $\mathbf{x}_p$ , the quantity  $A$  at position  $\mathbf{x}_c$  on the grid is

$$A(\mathbf{x}_c) = \sum_{\{\mathbf{x}_p\}} A_p W(\mathbf{x}_p - \mathbf{x}_c). \quad (\text{B.21})$$

In particular, for gravitational PM codes, the quantity carried by particles is their mass  $m$ . The density on the mesh is then a sum over the contributions of each particle as given by the assignment function,

$$\rho(\mathbf{x}_c) = \frac{1}{V_c} \sum_{\{\mathbf{x}_p\}} m W(\mathbf{x}_p - \mathbf{x}_c). \quad (\text{B.22})$$

The mean density is  $\bar{\rho} = mN_p/V$ , from which we deduce the density contrast  $\delta \equiv \rho/\bar{\rho} - 1$  on the mesh,

$$\delta(\mathbf{x}_c) = \left( \frac{N_g}{N_p} \sum_{\{\mathbf{x}_p\}} W(\mathbf{x}_p - \mathbf{x}_c) \right) - 1. \quad (\text{B.23})$$

### B.3.2 Low-pass filtering

The Nyquist-Shannon sampling theorem (Nyquist, 1928; Shannon, 1948, 1949) states that the information content of a sampled signal can be correctly recovered if two conditions hold: the signal must be band-limited, and the sampling frequency must be greater than twice the maximum frequency present in the signal. If this is not the case, replicated spectra cannot be separated of the signal we seek to recover, a phenomenon known as aliasing (e.g. Manolakis, Ingle & Kogon, 2000). Natural signals, however, are generally not band-limited, so must be low-pass filtered before they are sampled. Equivalently, the sampling operation must include some form of local averaging, reflecting the finite spatial resolution.

The Fourier representation<sup>5</sup> of the ideal low-pass filter that one should use as assignment function is given as

$$W(k) = \frac{1}{\sqrt{2\pi}} \Pi\left(\frac{k}{k_{\text{Nyq},x}}\right) = \frac{1}{\sqrt{2\pi}} \times \begin{cases} 1 & \text{if } |k| < k_{\text{max}} \\ 0 & \text{if } |k| \geq k_{\text{max}}, \end{cases} \quad (\text{B.24})$$

where  $k_{\text{max}} \equiv k_{\text{Nyq},x}/2$ , and  $k_{\text{Nyq},x} \equiv 2\pi/\Delta x$  is the Nyquist wavenumber. This filter is ideal in the sense that it has unity gain in the pass-band region and it perfectly suppresses all the power in the stop-band regions. The configuration space representation is

$$W(x) = \frac{1}{\Delta x} \text{sinc}\left(\frac{x}{\Delta x}\right), \quad (\text{B.25})$$

where  $s \mapsto \text{sinc}(s) \equiv \frac{\sin(\pi s)}{\pi s}$  is the cardinal sine function (using the signal processing convention). It is interesting to note that  $W(x)$  is not always positive. Therefore, the physical property of a continuous density field to be positive will not be reflected in its discretized representation, using ideal low-pass filtering. The loss of physicality is an expression of a fundamental problem of any data processing procedure: the loss of information due to discretizing the continuous signal.

<sup>5</sup> Here, we use the conventions for forward and inverse Fourier transforms as introduced in section 1.2.4.1.

Furthermore, due to the infinite support of the cardinal sine function in configuration space, the ideal sampling method is generally not tractable, because computationally too expensive. For this reason, practical approaches often rely on approximating the ideal cardinal sine operator by less accurate, but faster calculable functions (often with compact support in configuration space). In Fourier space, this will generally introduce artificial attenuation of the pass-band modes and leakage of stop-band modes into the signal (i.e. incomplete suppression of the aliasing power). The optimal choice of a low-pass filter approximation is therefore always a choice between accuracy and computational speed (see e.g. [Manolakis, Ingle & Kogon, 2000](#), for detailed studies). In the following section we discuss common approaches used in particle simulations.

### B.3.3 Common mesh assignment schemes

Commonly used particle shape functions and assignment schemes are often presented as a hierarchy ([Hockney & Eastwood, 1981](#)). The simplest scheme is to consider that particles are punctual and to assign each of them to the nearest grid point:  $W(x_p - x_c) = 1$  if  $x_c - \frac{\Delta x}{2} \leq x_p \leq x_c + \frac{\Delta x}{2}$ , 0 otherwise. The shape function is therefore

$$S_{\text{NGP}}(x) \equiv \delta_D(x) \quad \text{and} \quad S_{\text{NGP}}(\mathbf{x}) \equiv \delta_D(x)\delta_D(y)\delta_D(z). \quad (\text{B.26})$$

This is the Nearest Grid Point (NGP) assignment scheme.

The second particle shape function in the hierarchy is a rectangular parallelepiped (a “cloud”) of side length  $\Delta x$ ,  $\Delta y$ ,  $\Delta z$ . This scheme involves the 8 nearest cells for each particle and is called the Cloud-in-Cell (CiC) scheme. The shape function is

$$S_{\text{CiC}}(x) \equiv \frac{1}{\Delta x} \Pi\left(\frac{x}{\Delta x}\right) \quad \text{and} \quad S_{\text{CiC}}(\mathbf{x}) \equiv \frac{1}{\Delta x \Delta y \Delta z} \Pi\left(\frac{x}{\Delta x}\right) \Pi\left(\frac{y}{\Delta y}\right) \Pi\left(\frac{z}{\Delta z}\right). \quad (\text{B.27})$$

This shape function can be seen as the convolution  $\frac{1}{\Delta x} \Pi\left(\frac{x}{\Delta x}\right) * \delta_D(x)$ . Higher-order assignment schemes are obtained by successively convolving with  $\frac{1}{\Delta x} \Pi\left(\frac{x}{\Delta x}\right)$  along each direction. For example, the third-order scheme is called the Triangular Shaped Cloud (TSC) and involves the 27 neighboring cells for each particle. In one-dimension, the shape function is

$$S_{\text{TSC}}(x) \equiv \frac{1}{\Delta x} \Pi\left(\frac{x}{\Delta x}\right) * \frac{1}{\Delta x} \Pi\left(\frac{x}{\Delta x}\right). \quad (\text{B.28})$$

The Fourier transform of  $x \mapsto \frac{1}{\Delta x} \Pi\left(\frac{x}{\Delta x}\right)$  is  $k \mapsto \frac{1}{\sqrt{2\pi}} \text{sinc}\left(\frac{k}{k_{\text{Nyq},x}}\right)$ . Therefore, in Fourier space, building the hierarchy is taking successive powers of  $\frac{1}{\sqrt{2\pi}} \text{sinc}\left(\frac{k}{k_{\text{Nyq},x}}\right)$ . The assignment function  $W$  is found by an additional convolution of  $S$  with  $x \mapsto \Pi\left(\frac{x}{\Delta x}\right)$ , which means, in Fourier space, an additional multiplication by  $\frac{\Delta x}{\sqrt{2\pi}} \times \text{sinc}\left(\frac{k}{k_{\text{Nyq},x}}\right)$ . In figure [B.1](#), we show the shape functions  $S$  for the NGP, CiC and TSC schemes (first row), the corresponding assignment functions  $W$  (second row) and their normalized Fourier transforms,  $\hat{W}/\Delta x$  (rescaled such that  $\hat{W}(k=0)/\Delta x = 1$ ; third row).

High order schemes are obviously more expensive numerically, but they also give more precise results: from equation [\(B.21\)](#) and the shape functions, we see that resulting quantities on the grid (density, forces) are piecewise constant in cells (NGP);  $C^0$  and piecewise linear (CiC);  $C^1$  with piecewise linear first derivative (TSC), etc. (see figure [B.1](#)). The choice is a tradeoff between accuracy and computational expense.

We summarize the results of this section in table [B.1](#). In the following, we further comment on the well-known CiC scheme, which is the prescription used to assign particles to the grid throughout this thesis, including in PM and COLA implementations.

Let us consider the CiC density assignment for a particle with coordinates  $(x_p, y_p, z_p)$ . The cell containing the particle has indexes given by

$$i = \left\lfloor \frac{x_p}{\Delta x} \right\rfloor; \quad j = \left\lfloor \frac{y_p}{\Delta y} \right\rfloor; \quad k = \left\lfloor \frac{z_p}{\Delta z} \right\rfloor, \quad (\text{B.29})$$

where  $\lfloor \cdot \rfloor$  is the integer floor function. We consider that the cell center is at  $(x_c, y_c, z_c) = (i \times \Delta x, j \times \Delta y, k \times \Delta z)$ .<sup>6</sup>

<sup>6</sup> The other common convention is to displace the cell center by half a voxel with respect to  $(i \times \Delta x, j \times \Delta y, k \times \Delta z)$ , i.e.  $(x_c, y_c, z_c) = (i \times \Delta x + \frac{\Delta x}{2}, j \times \Delta y + \frac{\Delta y}{2}, k \times \Delta z + \frac{\Delta z}{2})$ .



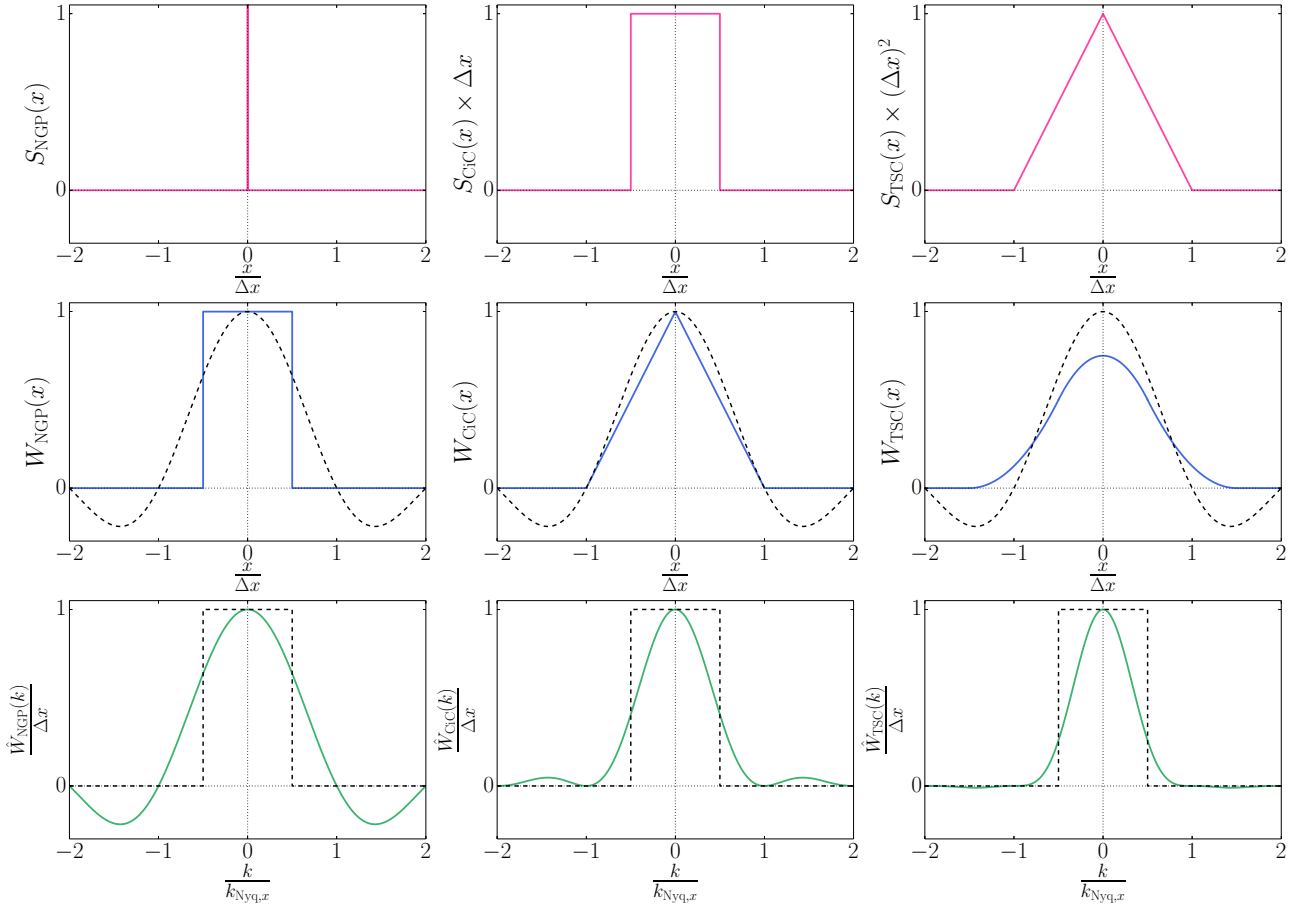


Figure B.1: Shape functions in configuration space for the first three schemes of the natural hierarchy of mesh assignments ( $S$ , first row); the corresponding assignment functions ( $W$ , second row) and their normalized Fourier transform ( $\hat{W}$ , third row). From left to right, the schemes are: Nearest Grid Point (NGP), Cloud-in-Cell (CiC), Triangular Shaped Cloud (TSC). The Nyquist wavenumber is defined by  $k_{\text{Nyq},x} \equiv 2\pi/\Delta x$ . For comparison, the dashed black lines show the configuration and Fourier space representations of the ideal low-pass filter kernel.

Name	Shape function $S(x)$	Number of cells involved	Properties of grid-wise quantities
NGP	$\delta(x)$	$1^3 = 1$	Piecewise constant in cells
CiC	$\frac{1}{\Delta x} \Pi\left(\frac{x}{\Delta x}\right)$	$2^3 = 8$	$C^0$ , piecewise linear
TSC	$\frac{1}{\Delta x} \Pi\left(\frac{x}{\Delta x}\right) * \frac{1}{\Delta x} \Pi\left(\frac{x}{\Delta x}\right)$	$3^3 = 27$	$C^1$ , differentiable with piecewise linear derivative

Table B.1: Summary of the properties of commonly used particle shape functions.

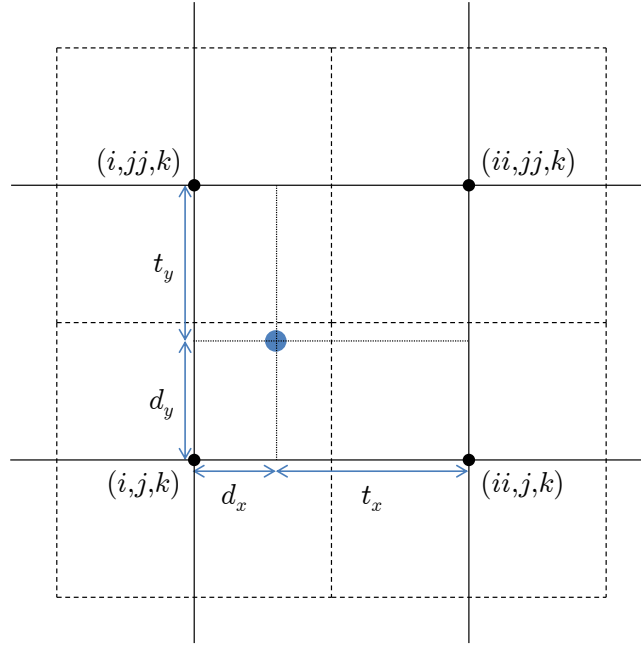


Figure B.2: Two-dimensional illustration of the Cloud-in-Cell assignment scheme. Everything is expressed in units of the cell size,  $\Delta x$  along the  $x$  direction and  $\Delta y$  along the  $y$  direction. In three dimensions, the particle is assigned to the eight neighboring cells with different weights given by equations (B.33)–(B.40).

As noted before the particle may contribute to densities in the parent cell  $(x_c, y_c, z_c)$  and the seven neighboring cells. Let us define

$$ii = \text{mod}(i + 1, N_{g0}); \quad jj = \text{mod}(j + 1, N_{g1}); \quad kk = \text{mod}(k + 1, N_{g2}). \quad (\text{B.30})$$

The modulo function enforces periodic boundary conditions. The particle contributes to the eight cells indexed by  $(i, j, k)$ ,  $(ii, j, k)$ ,  $(i, jj, k)$ ,  $(i, j, kk)$ ,  $(ii, jj, k)$ ,  $(ii, j, kk)$ ,  $(i, jj, kk)$  and  $(ii, jj, kk)$ . Let us define

$$d_x = \frac{x_p - x_c}{\Delta x} = \frac{x_p}{\Delta x} - i; \quad d_y = \frac{y_p - y_c}{\Delta y} = \frac{y_p}{\Delta y} - j; \quad d_z = \frac{z_p - z_c}{\Delta z} = \frac{z_p}{\Delta z} - k; \quad (\text{B.31})$$

$$t_x = 1 - d_x; \quad t_y = 1 - d_y; \quad t_z = 1 - d_z. \quad (\text{B.32})$$

Contributions to the eight cells are given by the formulae below, which also correspond to linear interpolations in 3D:

$$W(\mathbf{x}_p - \mathbf{x}_{(i,j,k)}) = t_x t_y t_z, \quad (\text{B.33})$$

$$W(\mathbf{x}_p - \mathbf{x}_{(ii,j,k)}) = d_x t_y t_z, \quad (\text{B.34})$$

$$W(\mathbf{x}_p - \mathbf{x}_{(i,jj,k)}) = t_x d_y t_z, \quad (\text{B.35})$$

$$W(\mathbf{x}_p - \mathbf{x}_{(i,j,kk)}) = t_x t_y d_z, \quad (\text{B.36})$$

$$W(\mathbf{x}_p - \mathbf{x}_{(ii,jj,k)}) = d_x d_y t_z, \quad (\text{B.37})$$

$$W(\mathbf{x}_p - \mathbf{x}_{(ii,j,kk)}) = d_x t_y d_z, \quad (\text{B.38})$$

$$W(\mathbf{x}_p - \mathbf{x}_{(i,jj,kk)}) = t_x d_y d_z, \quad (\text{B.39})$$

$$W(\mathbf{x}_p - \mathbf{x}_{(ii,jj,kk)}) = d_x d_y d_z. \quad (\text{B.40})$$

Summing over all particles will result in the calculation of any quantity  $A$  on the grid (equation (B.21)), in particular the density contrast (equation (B.23)).

In figure B.2, we illustrate the CiC scheme in two dimensions. The first step is to identify the cell indexes  $i, ii, j, jj, k, kk$ . Then, one computes the weight coefficients  $d_x, t_x, d_y, t_y, d_z, t_z$  as shown on the figure, and assigns the particle to the neighboring cells using the formulae above.

### B.3.4 Interpolation

Interpolation is used to distribute a grid-wise quantity to particles. For example, for PM codes, accelerations are computed on the grid (see section B.4), then interpolated back to each particle's position.

Using the same notations as before, for some quantity  $A$ , the problem is to compute  $A_p$  given the values of  $A(\mathbf{x}_c)$  in all the cells. This can be written in a similar fashion as equation (B.21), but summing on grid cells instead of particles:

$$A_p = A(\mathbf{x}_p) = \sum_{\{\mathbf{x}_c\}} A(\mathbf{x}_c) W(\mathbf{x}_p - \mathbf{x}_c). \quad (\text{B.41})$$

$W$  is the assignment function defined in section B.3.1, which involves a shape function  $S$  as previously (NGP, CiC, TSC, etc.). It is generally important to be consistent between the mesh assignment scheme and the interpolation scheme. In particular, for PM codes, the same prescription should be used for density assignment and for interpolating accelerations at particles' positions. This ensures the absence of artificial self-forces (forces exerted by a particle on itself) and momentum conservation (Hockney & Eastwood, 1981).

For the NGP scheme, the value of  $A_p$  for a particle is just the value of  $A(\mathbf{x}_c)$  in its parent cell  $(i, j, k)$ . For the CiC scheme, using equations (B.41) and (B.33)–(B.40), we find:

$$\begin{aligned} A_p = & A_{(i,j,k)} t_x t_y t_z + A_{(ii,j,k)} d_x t_y t_z + A_{(i,jj,k)} t_x d_y t_z + A_{(i,j,kk)} t_x t_y d_z \\ & + A_{(ii,jj,k)} d_x d_y t_z + A_{(ii,j,kk)} d_x t_y d_z + A_{(i,jj,kk)} t_x d_y d_z + A_{(ii,jj,kk)} d_x d_y d_z. \end{aligned} \quad (\text{B.42})$$

This is identical to trilinear interpolation.

## B.4 Poisson equation and accelerations

After density assignment, several steps are done on the mesh in PM codes: solving the Poisson equation to get the reduced gravitational potential  $\tilde{\Phi} \equiv \Delta^{-1} \delta$  (section B.4.1), and then differentiating to get the reduced accelerations  $\tilde{g} \equiv \nabla (\Delta^{-1} \delta)$  (section B.4.2).

### B.4.1 Solving the Poisson equation

It is customary to solve the Poisson equation in Fourier space:

1. the configuration-space density contrast  $\delta(\mathbf{x})$  is Fourier-transformed to get  $\delta(\mathbf{k})$ ;
2. the reduced gravitational potential is estimated by solving the Poisson equation in Fourier space,  $\tilde{\Phi}(\mathbf{k}) = G(\mathbf{k})\delta(\mathbf{k})$ , where  $G(\mathbf{k})$  is a Green's function for the Laplacian, discussed below;
3. the reduced gravitational potential  $\tilde{\Phi}(\mathbf{k})$  is transformed back to real space to get  $\tilde{\Phi}(\mathbf{x})$ .

As noted in section B.2.2, the same array can be used to store  $\delta$  and  $\tilde{\Phi}$ , by doing in-place Fourier transforms.

**Fourier transforms.** Steps 1 and 3 involve forward and backward discrete Fourier transforms. In the codes implemented for this thesis, we use the Fast Fourier Transform approach for discrete data, provided by the FFTW software library,<sup>7</sup> defined and normalized as follows, for the forward and backward operations respectively:

$$\begin{aligned} \hat{f}_{\ell,m,n} &= \Delta x \Delta y \Delta z \sum_{i=0}^{N_{g0}-1} \sum_{j=0}^{N_{g1}-1} \sum_{k=0}^{N_{g2}-1} f_{i,j,k} e^{-2i\pi(i\ell+jm+kn)/N_g}, \\ f_{i,j,k} &= \frac{1}{L_0 L_1 L_2} \sum_{i=0}^{N_{g0}-1} \sum_{j=0}^{N_{g1}-1} \sum_{k=0}^{N_{g2}-1} \hat{f}_{\ell,m,n} e^{2i\pi(i\ell+jm+kn)/N_g}. \end{aligned}$$

In the following, we note the components of a Fourier mode  $\mathbf{k}$  as  $k_x = \frac{2\pi}{L_0} \ell$ ,  $k_y = \frac{2\pi}{L_1} m$ ,  $k_z = \frac{2\pi}{L_2} n$ .

<sup>7</sup> <http://www.fftw.org/>

**Green's function.** The choice for the Green's function  $G(\mathbf{k})$  depends on how one wants to represent the Laplacian in configuration space. In Fourier space, the reduced potential obeys  $-k^2 \tilde{\Phi}(\mathbf{k}) \equiv \delta(\mathbf{k})$  where  $k^2 \equiv |\mathbf{k}|^2 = k_x^2 + k_y^2 + k_z^2$ . It is therefore natural to simply use as Green's function for the Laplacian  $G(\mathbf{k}) = -1/k^2$ . This is the choice adopted in GADGET-2 (Springel, Yoshida & White, 2001; Springel, 2005) and in the codes used in this thesis. Care should be taken however, as this choice corresponds to a highly non-local function in configuration space (see e.g. the discussion in Birdsall & Langdon, 1985, appendix E). Alternatively, we can discretize the Laplacian operator using the so-called 7-point template,

$$(\Delta\Phi)_{i,j,k} = \Phi_{i-1,j,k} + \Phi_{i+1,j,k} + \Phi_{i,j-1,k} + \Phi_{i,j+1,k} + \Phi_{i,j,k-1} + \Phi_{i,j,k+1} - 6\Phi_{i,j,k}, \quad (\text{B.43})$$

for which the Green's function is given by

$$G(\mathbf{k}) = -\frac{1}{4} \left[ \sin^2 \left( \frac{k_x \Delta x}{2} \right) + \sin^2 \left( \frac{k_y \Delta y}{2} \right) + \sin^2 \left( \frac{k_z \Delta z}{2} \right) \right]^{-1}. \quad (\text{B.44})$$

**Force smoothing.** Due to the finite resolution of the PM grid, short-range forces cannot be accurately resolved, which can cause spurious effects in simulations (Hockney & Eastwood, 1981). For this reason, we smooth the short-range forces by multiplying by a Gaussian kernel in Fourier space,

$$K_{k_s}(k) = \exp \left( -\frac{1}{2} \frac{k^2}{k_s^2} \right), \quad \text{where} \quad k_s \equiv \frac{2\pi}{L} A_s. \quad (\text{B.45})$$

$A_s$  is a free parameter that defines the split between long-range and short-range forces, in units of mesh cells. In our codes, we adopted  $A_s = 1.25$ , the default value used in GADGET-2.

**Deconvolution of the CiC kernel.** We also correct for the convolution with the CiC kernel, by dividing twice by (see section B.3.3)

$$K_{\text{CiC}}(\mathbf{k}) = \text{sinc}^2 \left( \frac{k_x}{k_{\text{Nyq},x}} \right) \text{sinc}^2 \left( \frac{k_y}{k_{\text{Nyq},y}} \right) \text{sinc}^2 \left( \frac{k_z}{k_{\text{Nyq},z}} \right). \quad (\text{B.46})$$

One deconvolution corrects for the smoothing effect of the CiC in the density assignment, the other for the force interpolation (Springel, 2005).

**Overall factor in Fourier space.** Summing up our discussions in this section, the overall factor that we apply to  $\delta$  in Fourier space (that we still note  $G(\mathbf{k})$  for convenience) is

$$G(\mathbf{k}) = -\frac{1}{k^2} \times \frac{K_{k_s}(k)}{K_{\text{CiC}}(\mathbf{k})^2}. \quad (\text{B.47})$$

After performing an inverse Fourier transform, we obtain the reduced gravitational potential on the mesh.

## B.4.2 Computation of the accelerations

We get the reduced accelerations on the mesh by finite differencing the reduced potential. It would also be possible to take the gradient in Fourier space, by multiplying the potential by a factor  $-i\mathbf{k}$  and obtaining directly the accelerations. However, this would require an inverse Fourier transform for each coordinate (i.e. three instead of one), with little gain in accuracy compared to finite differences (Springel, 2005).

We adopt central finite differences. Several schemes are possible depending on the desired accuracy. The two-point finite difference approximation (FDA2) is

$$\tilde{g}_{x(i,j,k)} \equiv \frac{\partial \tilde{\Phi}}{\partial x} \bigg|_{(i,j,k)} \approx \frac{1}{\Delta x} \left[ \frac{1}{2} \tilde{\Phi}_{(i+1,j,k)} - \frac{1}{2} \tilde{\Phi}_{(i-1,j,k)} \right] \quad (\text{B.48})$$

and similar formulae for the other coordinates  $\tilde{g}_y$  and  $\tilde{g}_z$ . The accuracy is of order  $\mathcal{O}(\Delta x^2)$ .

In the codes implemented for this thesis, we adopted the four-point finite difference approximation (FDA4), as in GADGET-2,

$$\tilde{g}_{x(i,j,k)} \equiv \frac{\partial \tilde{\Phi}}{\partial x} \bigg|_{(i,j,k)} \approx \frac{1}{\Delta x} \left[ \frac{2}{3} \left( \tilde{\Phi}_{(i+1,j,k)} - \tilde{\Phi}_{(i-1,j,k)} \right) - \frac{1}{12} \left( \tilde{\Phi}_{(i+2,j,k)} - \tilde{\Phi}_{(i-2,j,k)} \right) \right] \quad (\text{B.49})$$

which offers order  $\mathcal{O}(\Delta x^4)$  accuracy. In the two equations above, periodic boundary conditions should always be enforced:  $i + 1$  is actually  $\text{mod}(i + 1, N_{g0})$ , etc.

After having computed the three components of the accelerations on the grid,  $\tilde{g}x(\mathbf{x}_c)$ ,  $\tilde{g}y(\mathbf{x}_c)$ ,  $\tilde{g}z(\mathbf{x}_c)$ , we interpolate with the CiC scheme (see section B.3.4) to get the accelerations at particles' positions,  $\tilde{g}x(\mathbf{x}_p)$ ,  $\tilde{g}y(\mathbf{x}_p)$ ,  $\tilde{g}z(\mathbf{x}_p)$ .

## B.5 Update of positions and momenta

Now that we have the accelerations for each particle from the grid-based Poisson solver (step 1 in section B.2.1), we are able to update their momenta (“kick”) and their positions (“drift”). This corresponds to steps 2 and 3 in section B.2.1. At this point, we have to adopt a time integration scheme to update positions and momenta from  $a_i$  to  $a_f$ , and to define Kick and Drift operators. This is the object of sections B.5.1 and B.5.2, respectively.

### B.5.1 Time integrators

Let us consider a Hamiltonian system, described in phase space by the canonical coordinates  $\mathbf{z} = (q, p)$  and the Hamiltonian  $\mathcal{H}(p, q) \equiv p^2/2 + \Phi(q)$ . If we call  $f(\mathbf{z}) = (p, -\partial\Phi/\partial q)$ , then Hamilton's equations simply read  $\dot{\mathbf{z}} = f(\mathbf{z})$ . Hamilton's equations are a symplectic map, which means that the energy and the volume in phase space are time-invariants:

$$\frac{d\mathcal{H}}{dt} = 0 \quad \text{and} \quad \nabla \cdot f = 0. \quad (\text{B.50})$$

It is generally important to adopt a numerical integrator that respects these two conditions, at least approximately (see also the discussion in section 3.4.3). For a map  $\mathbf{z}(t) = \mathcal{F}(\mathbf{z}_0)$ , the volume in phase space is conserved if  $\det \frac{\partial \mathcal{F}}{\partial \mathbf{z}} = 1$ . Classical first order time integrators use Euler's method. In particular, the explicit Euler method,

$$\mathbf{z}_{n+1} = \mathbf{z}_n + f(\mathbf{z}_n)\Delta t; \quad \text{for which} \quad \det \frac{\partial \mathcal{F}}{\partial \mathbf{z}} = 1 + \Delta t^2 \frac{\partial^2 \Phi}{\partial q^2}, \quad (\text{B.51})$$

and the implicit Euler method,

$$\mathbf{z}_{n+1} = \mathbf{z}_n + f(\mathbf{z}_{n+1})\Delta t; \quad \text{for which} \quad \det \frac{\partial \mathcal{F}}{\partial \mathbf{z}} = \frac{1}{1 + \Delta t^2 \frac{\partial^2 \Phi}{\partial q^2}}, \quad (\text{B.52})$$

are only approximately symplectic. Using the particles' positions at time  $t_n$  and momenta at time  $t_{n+1}$  makes the Euler integrator symplectic:

$$\mathbf{z}_{n+1} = \mathbf{z}_n + f(q_n, p_{n+1})\Delta t; \quad \det \frac{\partial \mathcal{F}}{\partial \mathbf{z}} = 1. \quad (\text{B.53})$$

For this thesis, we adopted the second-order symplectic “kick-drift-kick” algorithm, also known as the leapfrog scheme (e.g. [Birdsall & Langdon, 1985](#), see also section 4.3.4):

$$p_{n+1/2} = p_n - \left. \frac{\partial \Phi}{\partial q} \right|_n \frac{\Delta t}{2}, \quad (\text{B.54})$$

$$q_{n+1} = q_n + p_{n+1/2} \Delta t, \quad (\text{B.55})$$

$$p_{n+1} = p_{n+1/2} - \left. \frac{\partial \Phi}{\partial q} \right|_{n+1} \frac{\Delta t}{2}. \quad (\text{B.56})$$

It is a straightforward exercise to check that this scheme exactly preserves volume in phase space.

For PM and COLA codes, we assume a constant integration step  $\Delta a \equiv \frac{a_f - a_i}{n}$ , in such a way that the initial scale factor is  $a_i = a_0$  and the final scale factor is  $a_f = a_{n+1} = a_i + n\Delta a$ . A schematic view of the leapfrog integration scheme is show in figure B.3. Note that during the evolution, positions and momenta are not synchronized but displaced by half a timestep. For this reason during the first timestep, we give the particles only “half a kick” using the accelerations computed at  $a_i$ ; and during the last timestep, we give the particles an additional “half a kick”, to synchronize momenta with positions at  $a_f$ .

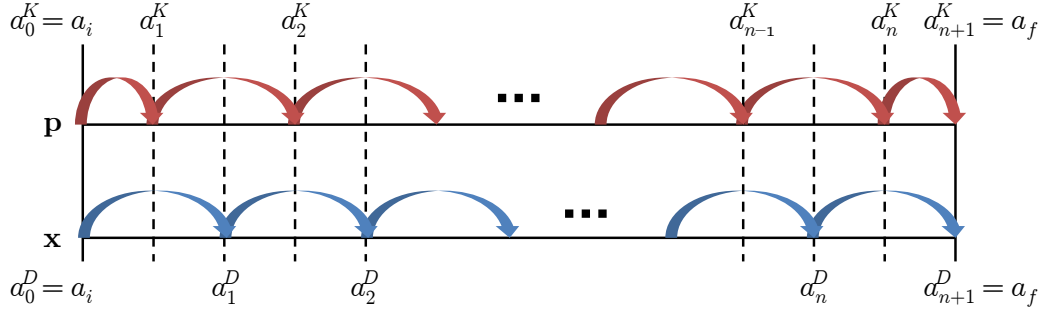


Figure B.3: Schematic illustration of the leapfrog integrator. Particles' momenta and positions are updated in turn, given the value of the other variable within the time interval.

### B.5.2 Kick and Drift operators

In equations (B.7) and (B.8), all the explicit dependence on the scale factor is in the prefactors  $\mathcal{D}(a)$  and  $\mathcal{K}(a)$ . The leapfrog scheme algorithm relies on integrating the equations on a small timestep and approximating the momenta or accelerations in the integrands by their value at some time within the interval. More precisely, for the “drift equation”:

$$\mathbf{x}(a_f^D) - \mathbf{x}(a_i^D) = \int_{a_i^D}^{a_f^D} \mathcal{D}(\tilde{a}) \mathbf{p}(\tilde{a}) d\tilde{a} \approx \left( \int_{a_i^D}^{a_f^D} \mathcal{D}(\tilde{a}) d\tilde{a} \right) \mathbf{p}(a^K) \quad (\text{B.57})$$

and similarly for the “kick equation”:

$$\mathbf{p}(a_f^K) - \mathbf{p}(a_i^K) = \int_{a_i^K}^{a_f^K} \mathcal{K}(\tilde{a}) [\nabla (\Delta^{-1} \delta)](\tilde{a}) d\tilde{a} \approx \left( \int_{a_i^K}^{a_f^K} \mathcal{K}(\tilde{a}) d\tilde{a} \right) [\nabla (\Delta^{-1} \delta)](a^D) \quad (\text{B.58})$$

This defines the Drift (D) and Kick (K) operators:

$$D(a_i^D, a_f^D, a^K) : \quad \mathbf{x}(a_i^D) \mapsto \mathbf{x}(a_f^D) = \mathbf{x}(a_i^D) + \left( \int_{a_i^D}^{a_f^D} \mathcal{D}(\tilde{a}) d\tilde{a} \right) \mathbf{p}(a^K) \quad (\text{B.59})$$

$$K(a_i^K, a_f^K, a^D) : \quad \mathbf{p}(a_i^K) \mapsto \mathbf{p}(a_f^K) = \mathbf{p}(a_i^K) + \left( \int_{a_i^K}^{a_f^K} \mathcal{K}(\tilde{a}) d\tilde{a} \right) [\nabla (\Delta^{-1} \delta)](a^D) \quad (\text{B.60})$$

Consistently with the scheme described in section B.5.1, the time evolution between  $a_0$  and  $a_{n+1}$  is then achieved by applying the following operator,  $E(a_{n+1}, a_0)$ , to the initial state  $(\mathbf{x}(a_0), \mathbf{p}(a_0))$ :

$$K(a_{n+1/2}, a_{n+1}, a_{n+1}) D(a_n, a_{n+1}, a_{n+1/2}) \left[ \prod_{i=0}^n K(a_{i+1/2}, a_{i+3/2}, a_{i+1}) D(a_i, a_{i+1}, a_{i+1/2}) \right] K(a_0, a_{1/2}, a_0). \quad (\text{B.61})$$

If the COLA scheme is adopted, we obtain in a similar manner, from equations (B.16) and (B.17):

$$\begin{aligned} \mathbf{x}(a_f^D) - \mathbf{x}(a_i^D) &\approx \left( \int_{a_i^D}^{a_f^D} \mathcal{D}(\tilde{a}) d\tilde{a} \right) \mathbf{p}_{\text{MC}}(a^K) - \left( \int_{a_i^D}^{a_f^D} \frac{dD_1(\tilde{a})}{d\tilde{a}} d\tilde{a} \right) \Psi_1 + \left( \int_{a_i^D}^{a_f^D} \frac{dD_2(\tilde{a})}{d\tilde{a}} d\tilde{a} \right) \Psi_2, \\ &= \left( \int_{a_i^D}^{a_f^D} \mathcal{D}(\tilde{a}) d\tilde{a} \right) \mathbf{p}_{\text{MC}}(a^K) - [D_1]_{a_i^D}^{a_f^D} \Psi_1 + [D_2]_{a_i^D}^{a_f^D} \Psi_2, \end{aligned} \quad (\text{B.62})$$

$$\begin{aligned} \mathbf{p}_{\text{MC}}(a_f^K) - \mathbf{p}_{\text{MC}}(a_i^K) &\approx \left( \int_{a_i^K}^{a_f^K} \mathcal{K}(\tilde{a}) d\tilde{a} \right) ([\nabla (\Delta^{-1} \delta)](a^D) - \mathcal{V}[D_1](a^D) \Psi_1 - \mathcal{V}[D_2](a^D) \Psi_2) \\ &= \left( \int_{a_i^K}^{a_f^K} \mathcal{K}(\tilde{a}) d\tilde{a} \right) ([\nabla (\Delta^{-1} \delta)](a^D) - D_1(a^D) \Psi_1 + (D_2(a^D) - D_1^2(a^D)) \Psi_2). \end{aligned} \quad (\text{B.63})$$



In the last line we used equations (B.14) and (B.15). This defines new Drift ( $\tilde{D}$ ) and Kick ( $\tilde{K}$ ) operators:

$$\tilde{D}(a_i^D, a_f^D, a^K) : \quad \mathbf{x}(a_i^D) \mapsto \mathbf{x}(a_f^D) = \mathbf{x}(a_i^D) + \left( \int_{a_i^D}^{a_f^D} \mathcal{D}(\tilde{a}) d\tilde{a} \right) \mathbf{p}_{MC}(a^K) - [D_1]_{a_i^D}^{a_f^D} \Psi_1 + [D_2]_{a_i^D}^{a_f^D} \Psi_2 \quad (\text{B.64})$$

$$\begin{aligned} \tilde{K}(a_i^K, a_f^K, a^D) : \quad \mathbf{p}_{MC}(a_i^D) \mapsto \mathbf{p}_{MC}(a_f^D) = \mathbf{p}_{MC}(a_i^D) + \left( \int_{a_i^K}^{a_f^K} \mathcal{K}(\tilde{a}) d\tilde{a} \right) \times \\ ([\nabla (\Delta^{-1} \delta)](a^D) - D_1(a^D) \Psi_1 + (D_2(a^D) - D_1^2(a^D)) \Psi_2). \end{aligned} \quad (\text{B.65})$$

With COLA, the time evolution between  $a_0$  and  $a_{n+1}$  is achieved by applying the following operator to the initial state  $(\mathbf{x}(a_0), \mathbf{p}(a_0))$ :

$$L_+(a_{n+1}) \tilde{E}(a_{n+1}, a_0) L_-(a_0), \quad (\text{B.66})$$

where  $\tilde{E}(a_{n+1}, a_0)$  is the operator given by equation (B.61), replacing  $D$  by  $\tilde{D}$  and  $K$  by  $\tilde{K}$ , and we where we use (see Tassev, Zaldarriaga & Eisenstein, 2013, appendix A):

$$L_{\pm}(a) : \quad \mathbf{p}(a) \mapsto \mathbf{p}(a) \pm \mathbf{p}_{LPT}(a) = \mathbf{p}(a) \pm \frac{1}{\mathcal{D}(a)} \left( -\frac{dD_1}{da} \Psi_1 + \frac{dD_2}{da} \Psi_2 \right). \quad (\text{B.67})$$

$L_-$  transforms the initial conditions to the rest frame of LPT observers (this is the same as initializing  $\mathbf{p}_{MC}$  to zero), and  $L_+$  adds back the LPT momenta to  $\mathbf{p}_{MC}$  at the end.

In the codes implemented for this thesis, the integrals appearing in the Kick and Drift operators (equations (B.59), (B.60), (B.64), (B.65)) are explicitly computed numerically. Another approach for the discretization of time operators is proposed by Tassev, Zaldarriaga & Eisenstein (2013, section A.3.2.). When needed, the first order growth factor  $D_1$  and its logarithmic derivative  $f_1$  are also computed numerically by explicit integration. For the second-order growth factor and its logarithmic derivative, we use the fitting functions given by equations (1.119) and (1.138) (Bouchet *et al.*, 1995),

$$D_2(\tau) \approx -\frac{3}{7} D_1(\tau) \Omega_m^{-1/143} \quad \text{and} \quad f_2(\tau) \approx 2f_1(\tau)^{54/55}. \quad (\text{B.68})$$

## B.6 Setting up initial conditions

The last missing part for a full cosmological pipeline including the PM/COLA codes described in previous sections is a way to set up initial conditions at  $a = a_i$ . The first step (section B.6.1) is to generate a realization of the random density field describing the early Universe. As argued in chapter 1, it is physically relevant to describe this field as a Gaussian random field.

The second step (section B.6.2) is to produce a high-redshift particle realization from this initial density field, to be given to the PM code. The common approach is to use Lagrangian perturbation theory (the ZA or 2LPT). Several existing codes perform this task: among others, GRAFIC (Bertschinger, 2001), N-GenIC (Springel, Yoshida & White, 2001; Springel, 2005, using the ZA) and its 2LPT extension, 2LPTIC (Crocce, Pueblas & Scoccimarro, 2006b; Pueblas & Scoccimarro, 2009), MPGRAFIC (Prunet *et al.*, 2008), MUSIC (Hahn & Abel, 2011). However, for the purpose of this thesis, we implemented an independent ZA/2LPT initial conditions generator. It is especially designed for full consistency with the BORG algorithm (see chapter 4); in particular, it uses the same routine as BORG for the generation of LPT displacement fields.

### B.6.1 The initial Gaussian random field

There exists many software packages that allow generating normal random variates (i.e. single Gaussian random variates with mean 0 and variance 1), for example using the well-known Box-Müller method. We choose the routines provided by the GNU scientific library (Galassi *et al.*, 2003). We generate one such normal random variate in each cell of the initial grid, and call the resulting vector the “initial white noise field”  $\xi$ . It is a random signal with constant power spectrum ( $\langle \xi \xi^T = \mathbf{1} \rangle$ ). Alternatively, we can choose to import “constrained white noise” that comes, for example, of large-scale structure inferences performed with BORG.

Generally, using a vector of normal variates  $\xi$ , one can generate a realization of a grf with mean  $\mu$  and covariance matrix  $C$  by simply taking any matrix  $\sqrt{C}$  that satisfies  $\sqrt{C} \sqrt{C}^T = C$  and computing  $x = \sqrt{C} \xi + \mu$ .

One general way to generate  $\sqrt{C}$  under the condition that  $C$  has only positive definite eigenvalues is to use the so-called Cholesky decomposition, implemented in many numerical packages.

For cosmological initial conditions, however, the problem is generally much simpler. As we are generating a random realization of the density contrast  $\delta$ , the mean is  $\mu = 0$  and, from statistical homogeneity and isotropy, the covariance matrix  $C$  should be diagonal in Fourier space and contain the power spectrum coefficients  $P(k)/(2\pi)^{3/2}$  (see section 1.2.4.1). Hence, an obvious choice for the matrix  $\sqrt{C}$  is the diagonal matrix containing the coefficients  $\sqrt{P(k)/(2\pi)^{3/2}}$ . Therefore, the procedure is to Fourier-transform  $\xi$ , to multiply each of its Fourier modes of norm  $k$  by  $\sqrt{P(k)/(2\pi)^{3/2}}$ , and to perform an inverse Fourier transform to get  $\delta$  in configuration space.

Physical assumptions are needed for the power spectrum coefficients  $P(k)$ . One possible approach is to use the outputs of Boltzmann codes that describe the early Universe (e.g. CMBFAST – Seljak & Zaldarriaga, 1996, CAMB – Lewis & Challinor, 2002, or CLASS – Lesgourgues, 2011; Blas, Lesgourgues & Tram, 2011). However, in our implementation, we choose (as in BORG) to use the analytical power spectrum from Eisenstein & Hu (1998, 1999) for the baryon-CDM fluid (including baryonic wiggles). It depends on the following cosmological parameters, which have to be specified:  $\Omega_\Lambda$ ,  $\Omega_m$ ,  $\Omega_b$ ,  $n_s$  and  $\sigma_8$ .

When performing constrained simulations (see section 7.1.3), all the steps described in this section are bypassed, and we directly make use of the initial density contrast field inferred with BORG.

### B.6.2 The high-redshift particle realization

We start from “grid-like” initial conditions, i.e. a realization of  $N_p$  dark matter particles, placed on a regular lattice. More precisely, for  $0 \leq i < N_{p0}$ ,  $0 \leq j < N_{p1}$ ,  $0 \leq k < N_{p2}$ , we place a particle at Lagrangian coordinates  $\mathbf{q} = (iL_0/N_{p0}, jL_1/N_{p1}, kL_2/N_{p2})$ . All the masses are set to the constant value given in footnote 1, and at this point all the velocities are zero. Finally, each particle’s id is set to  $\mathbf{mp} = k + N_{p2} \times (j + N_{p1} \times i)$ . This allows to keep a memory of the initial position of particles at any later time, even in the PM code.

The following step is to compute the ZA and 2LPT displacements for each particle, given the initial density contrast field  $\delta(\mathbf{q})$  generated in section B.6.1. We proceed as follows. The first-order potential field,  $\phi^{(1)}(\mathbf{q})$ , is evaluated on the Lagrangian grid by solving equation (1.134) in Fourier space,<sup>8</sup>

$$\phi^{(1)}(\mathbf{\kappa}) = -\delta(\mathbf{\kappa})/\kappa^2. \quad (\text{B.69})$$

Each of its second order derivatives are also evaluated in Fourier space, using

$$\phi_{,ab}^{(1)}(\mathbf{\kappa}) = -\phi^{(1)}(\mathbf{\kappa})\kappa_a \cdot \kappa_b. \quad (\text{B.70})$$

and inverse Fourier-transformed. From the configuration-space quantity

$$\phi(\mathbf{q}) \equiv \phi_{,xx}^{(1)}(\mathbf{q})\phi_{,yy}^{(1)}(\mathbf{q}) + \phi_{,xx}^{(1)}(\mathbf{q})\phi_{,zz}^{(1)}(\mathbf{q}) + \phi_{,yy}^{(1)}(\mathbf{q})\phi_{,zz}^{(1)}(\mathbf{q}) - \phi_{,xy}^{(1)}(\mathbf{q})^2 - \phi_{,xz}^{(1)}(\mathbf{q})^2 - \phi_{,yz}^{(1)}(\mathbf{q})^2, \quad (\text{B.71})$$

we compute the second-order potential field,  $\phi^{(2)}(\mathbf{q})$ , again in Fourier space, using (see equation (1.135))

$$\phi^{(2)}(\mathbf{\kappa}) = -\phi(\mathbf{\kappa})/\kappa^2. \quad (\text{B.72})$$

Once  $\phi^{(1)}(\mathbf{q})$  and  $\phi^{(2)}(\mathbf{q})$  are known, we evaluate the first and second order displacements  $\Psi^{(1)}(\mathbf{q}) \equiv \nabla_{\mathbf{q}}\phi^{(1)}(\mathbf{q})$  and  $\Psi^{(2)}(\mathbf{q}) \equiv \nabla_{\mathbf{q}}\phi^{(2)}(\mathbf{q})$  on the initial grid in configuration space, by using a finite difference approximation scheme at order 2 (see section B.4.2). Then, we interpolate from the grid to particles’ Lagrangian positions using a CiC scheme (see section B.3.4).

Finally, particles are displaced from their Lagrangian positions and their velocities are modified as prescribed by LPT (equations (1.136) and (1.137)). More precisely, particles are given a zeroth “kick”,

$$\mathbf{K}_0(a_i) : \quad \mathbf{u} = 0 \mapsto \mathbf{u}(a_i) = -f_1(a_i)D_1(a_i)\mathcal{H}(a_i)\Psi_1(\mathbf{q}) + f_2(a_i)D_2(a_i)\mathcal{H}(a_i)\Psi_2(\mathbf{q}), \quad (\text{B.73})$$

where  $\mathbf{u} \equiv d\mathbf{x}/d\tau = a\mathcal{H}d\mathbf{x}/da$ . From this we deduce the initial momenta in code units,

$$\mathbf{p}(a_i) = \frac{1}{a_i\mathcal{H}(a_i)\mathcal{D}(a_i)}\mathbf{u}(a_i). \quad (\text{B.74})$$

They also follow a zeroth “drift”:

$$\mathbf{D}_0(a_i) : \quad \mathbf{q} \mapsto \mathbf{x}(a_i) = \mathbf{q} - D_1(a_i)\Psi_1(\mathbf{q}) + D_2(a_i)\Psi_2(\mathbf{q}). \quad (\text{B.75})$$

The required numerical prefactors are computed as described at the end of section B.5.2.

<sup>8</sup> We denote by  $\mathbf{\kappa}$  a Fourier mode on the Lagrangian grid,  $\kappa$  its norm.

# Cosmic structures identification and classification algorithms

## Contents

<b>C.1 VIDE: the Void IDentification and Examination toolkit</b>	<b>179</b>
C.1.1 Voronoi Tessellation Density Estimation	179
C.1.2 The watershed algorithm	180
C.1.3 Processing and analysis of void catalogs	180
C.1.4 Radial density profiles	181
<b>C.2 The T-web</b>	<b>181</b>
C.2.1 The tidal tensor	181
C.2.2 Analogy with the Zel'dovich formalism	182
C.2.3 The T-web: original procedure	182
C.2.4 Extensions of the T-web	183
C.2.5 Implementation	184
C.2.6 Example	185

---

“Whenever a theory appears to you as the only possible one, take this as a sign that you have neither understood the theory nor the problem which it was intended to solve.”

— [Karl Popper \(1972\)](#), *Objective Knowledge: An Evolutionary Approach*

---

## Abstract

This appendix discusses methods for identifying and classifying structures in the cosmic web. As many approaches exist (see the introduction of chapter 9), in the following we only focus on the algorithms used in this thesis: the VIDE toolkit for the identification of static voids (section C.1), and the T-web approach for dissecting the dynamic cosmic web into clusters, filaments, sheets, and voids (section C.2).

## C.1 VIDE: the Void IDentification and Examination toolkit

This section describes VIDE, the Void IDentification and Examination toolkit. It is a static void finder operating on density fields, used in chapter 8 of this thesis. The details behind VIDE are described in its accompanying paper, [Sutter \*et al.\* \(2015b\)](#), and its website <http://www.cosmicvoids.net/>. VIDE is based on ZOBOV (ZOnes Bordering On Voidness, [Neyrinck, 2008](#)) for the void finding part (sections C.1.1 and C.1.2), and includes a set of additional features for pre- and post-processing void catalogs (section C.1.3).

### C.1.1 Voronoi Tessellation Density Estimation

The algorithm begins by building a Voronoi tessellation of the tracer particle population ([Schaap & van de Weygaert, 2000](#); [Schaap, 2007](#)). This provides a density field estimator (the Voronoi Tessellation Field Estimator, VTFE) based on the underlying particle positions. The VTFE (along with its dual, the Delaunay

Tessellation Field Estimator, DTFE) is a local density estimate that is especially suitable for astronomical data (van de Weygaert & Schaap, 2009; Cautun & van de Weygaert, 2011).

The Voronoi tessellation is a partitioning of space into cells around each particle. For each particle  $i$ , the corresponding Voronoi cell is the region consisting of all points closer to that particle than to any other. The density estimate at particle  $i$  is  $1/V(i)$ , where  $V(i)$  is the volume of the Voronoi cell around particle  $i$ . It is further assumed constant density across the volume of each Voronoi cell, which effectively sets a smoothing scale for the continuous density field.

Finally, the Voronoi tessellation also provides the adjacency measurement for each particle  $i$  (i.e. the set of particles whose Voronoi cells have a common boundary with  $i$ 's cell), which ZOBOV uses in the next step.

### C.1.2 The watershed algorithm

ZOBOV then uses the watershed transform (Platen, van de Weygaert & Jones, 2007) to group Voronoi cells into zones and subsequently voids. Minima (also called cores or basins) are first identified as particles with lower density than any of their Voronoi neighbors. Then, the algorithm merges nearby Voronoi cells into zones (the set of cells for which density flows downward into the zone's core). Finally, the watershed transform groups adjacent zones into voids by finding minimum-density barriers between them and joining zones together. This can be thought of, for each zone  $z$ , as setting the “water level” to its minimum density and raising it gradually. Water may flow along lines joining adjacent Voronoi zones, adding them to the void defined around zone  $z$ . The process is stopped when water flows into a deeper zone (one with a lower core than  $z$ ) or if  $z$  is the deepest “parent” void, when water floods the whole field. The void corresponding to zone  $z$  is defined as the set of zones filled with water just before this happens, and its boundary is the ridgeline which retains the flow of water. As can be understood from this description, the watershed transform naturally builds a nested hierarchy of voids (Lavaux & Wandelt, 2012; Bos *et al.*, 2012).

ZOBOV imposes a density-based criterion within the void finding operation: adjacent zones are only added to a void if the density of the wall between them is less than 0.2 times the mean particle density (Platen, van de Weygaert & Jones, 2007; see Blumenthal *et al.*, 1992; Sheth & van de Weygaert, 2004 for the role of the corresponding  $\delta = -0.8$  underdensity). This density threshold prevents voids from expanding deeply into overdense structures and limits the depth of the void hierarchy (Neyrinck, 2008). By default, VIDE reports every identified basin as a void (regardless of the density of the initial zone), but facilities exist for filtering the void catalogs based on various criteria (Sutter *et al.*, 2015b).

### C.1.3 Processing and analysis of void catalogs

The VIDE toolkit provides routines for performing many analysis tasks, such as manipulating, filtering, and comparing void catalogs, plotting void properties, stacking, computing clustering statistics and fitting density profiles (Sutter *et al.*, 2015b). In this section, we briefly describe the details behind the three void statistics used in chapter 8: number functions, ellipticity distributions, and density profiles.

#### C.1.3.1 Number functions

The effective radius of a void is defined as

$$R_v \equiv \left( \frac{3}{4\pi} V \right)^{1/3}, \quad (\text{C.1})$$

where  $V$  is the total volume of the Voronoi cells that make up the void. From this definition, voids with effective radius smaller than  $\bar{n}^{-1/3}$ , where  $\bar{n}$  is the mean number density of tracers, are excluded to prevent the effects of shot noise.

Based on this definition, VIDE includes a built-in plotting routine for the cumulative number functions of multiple void catalogs on a logarithmic scale (see figure 8.3).

#### C.1.3.2 Ellipticity distributions

For each void in the catalog, VIDE also reports the volume-weighted center of all Voronoi cells in the void, or macrocenter:

$$\mathbf{x}_v \equiv \frac{1}{\sum_i V_i} \sum_i \mathbf{x}_i V_i, \quad (\text{C.2})$$

where  $\mathbf{x}_i$  and  $V_i$  are the positions and Voronoi volumes of each tracer particle  $i$ , respectively.

Void shapes are computed from void member particles by constructing the inertia tensor:

$$M_{xx} = \sum_{i=1}^{N_p} (y_i^2 + z_i^2), \quad (\text{C.3})$$

$$M_{xy} = -\sum_{i=1}^{N_p} x_i y_i, \quad (\text{C.4})$$

where  $N_p$  is the number of particles in the void, and  $(x_i, y_i, z_i)$  is the set of coordinates of particle  $i$  relative to the void macrocenter. The other components of the inertia tensor are obtained by cyclic permutation of coordinates. The eigenstructure of the inertia tensor gives the ellipticity of the void:

$$\varepsilon = 1 - \left( \frac{J_1}{J_3} \right)^{1/4}, \quad (\text{C.5})$$

where  $J_1$  and  $J_3$  are the smallest and the largest eigenvalues of the inertia tensor, respectively. The ellipticity distribution of voids as a function of their effective radius follows from this definition (see figure 8.4).

### C.1.4 Radial density profiles

VIDE contains a routine to construct three-dimensional stacks of voids, where void macrocenters are superposed and particle positions are shifted to be expressed as relative to the stack center. This routine builds stacks of voids whose effective radius is in some given range. From each of these three-dimensional stacks, VIDE builds a spherically-averaged one-dimensional profile.

This is used in particular for building radial density profiles of voids at a given size (see figure 8.5).

## C.2 The T-web

This section describes the “T-web”, a dynamic web classifier which dissects the entire large-scale structure into different structure types: voids, sheets, filaments, and clusters. It is used in section 2.3, chapters 9 and 10 of this thesis.

### C.2.1 The tidal tensor

We start here from the Vlasov-Poisson system in Eulerian coordinates, equations (1.72) and (1.75). It is always possible to rescale the cosmological gravitational potential by defining  $\tilde{\Phi} \equiv \Phi / (4\pi G a^2 \bar{\rho})$  in such a way that  $\tilde{\Phi}$  obeys a reduced Poisson equation,

$$\Delta \tilde{\Phi}(\mathbf{x}) = \delta(\mathbf{x}). \quad (\text{C.6})$$

In this context, we define the *tidal tensor*  $\mathcal{T}$  as the Hessian  $H(\tilde{\Phi})$  of the rescaled gravitational potential  $\tilde{\Phi}$ ,

$$\mathcal{T}_{ij} \equiv H(\tilde{\Phi})_{ij} = \frac{\partial^2 \tilde{\Phi}}{\partial \mathbf{x}_i \partial \mathbf{x}_j}. \quad (\text{C.7})$$

With this definition, the left-hand side of equation (C.6) can be seen as the application of the Laplace-Beltrami operator  $\mathcal{LB}$  (or tensor Laplacian), trace of the Hessian, to  $\tilde{\Phi}$ :

$$\mathcal{LB}(\tilde{\Phi}) \equiv \text{tr}(H(\tilde{\Phi})) = \Delta \tilde{\Phi}. \quad (\text{C.8})$$

Let us denote by  $\mu_1(\mathbf{x}) \leq \mu_2(\mathbf{x}) \leq \mu_3(\mathbf{x})$  the three local eigenvalues of the tidal tensor.<sup>1</sup> They are dimensionless and real (since  $\mathcal{T}$  is symmetric). We have  $\text{tr}(\mathcal{T})(\mathbf{x}) = \mu_1(\mathbf{x}) + \mu_2(\mathbf{x}) + \mu_3(\mathbf{x})$ , and the reduced Poisson equation can therefore be seen as a decomposition of the Eulerian density contrast field, in the sense that it reads

$$\mu_1(\mathbf{x}) + \mu_2(\mathbf{x}) + \mu_3(\mathbf{x}) = \delta(\mathbf{x}). \quad (\text{C.9})$$

<sup>1</sup> These eigenvalues are often noted  $\lambda_i$  in the literature. We changed the notation in this thesis to avoid the confusion with the Zel'dovich formalism (see sections 1.5.2 and C.2.2).

At this point, it is useful to introduce some notations commonly found in the literature to characterize the tidal field. Given equation (C.9), the eigenvalues of the tidal tensor define an ellipsoid with semi-axes (e.g. Peacock & Heavens, 1985)

$$a_i(\mathbf{x}) \equiv \sqrt{\frac{\delta(\mathbf{x})}{\mu_i(\mathbf{x})}}. \quad (\text{C.10})$$

The triaxiality parameters are defined by Bardeen *et al.* (1986) in terms of the eigenvalues as

$$\varepsilon(\mathbf{x}) = \frac{\mu_1(\mathbf{x}) - \mu_3(\mathbf{x})}{2\delta(\mathbf{x})} \quad \text{and} \quad p(\mathbf{x}) = \frac{\mu_1(\mathbf{x}) - 2\mu_2(\mathbf{x}) + \mu_3(\mathbf{x})}{2\delta(\mathbf{x})}. \quad (\text{C.11})$$

$\varepsilon$  is called the ellipticity (in the  $\mu_1 - \mu_3$  plane) and  $p$  the prolateness (or oblateness). If  $-\varepsilon \leq p \leq 0$  then the ellipsoid is prolate-like, and if  $0 \leq p \leq \varepsilon$  it is oblate-like. The limiting cases are  $p = -\varepsilon$  for prolate spheroids and  $p = \varepsilon$  for oblate spheroids.

### C.2.2 Analogy with the Zel’dovich formalism

The above equations have a strong similarity with that of the Zel’dovich formalism. Indeed, we have seen that the first Lagrangian potential  $\phi^{(1)}$ , defined by  $\Psi^{(1)}(\mathbf{q}, \tau) = -D_1(\tau)\nabla_{\mathbf{q}}\phi^{(1)}(\mathbf{q})$ , satisfies a reduced Poisson equation (equation (1.134)),

$$\Delta_{\mathbf{q}}\phi^{(1)}(\mathbf{q}) = \delta(\mathbf{q}). \quad (\text{C.12})$$

As discussed in section 1.5.2, the shear of the displacement  $\mathcal{R} \equiv \partial\Psi/\partial\mathbf{q}$  verifies

$$\mathcal{R}_{ij} = -D_1(\tau)H(\phi^{(1)})_{ij} = -D_1(\tau)\frac{\partial^2\phi^{(1)}}{\partial\mathbf{q}_i\partial\mathbf{q}_j}. \quad (\text{C.13})$$

The local eigenvalues of Hessian of the first Lagrangian potential,  $\lambda_1(\mathbf{q}) \leq \lambda_2(\mathbf{q}) \leq \lambda_3(\mathbf{q})$ , permit to rewrite the reduced Poisson equation as a decomposition of the initial density contrast,

$$\lambda_1(\mathbf{q}) + \lambda_2(\mathbf{q}) + \lambda_3(\mathbf{q}) = \delta(\mathbf{q}). \quad (\text{C.14})$$

### C.2.3 The T-web: original procedure

In analogy with the Zel’dovich “pancake” theory, where the sign of the  $\lambda_i$  permit an interpretation of what happens at shell-crossing in the ZA in terms of structure types (see section 1.5.2), Hahn *et al.* (2007a) proposed to classify structures using the sign of the  $\mu_i$ . Namely, a void point corresponds to no positive eigenvalue, a sheet to one, a filament to two, and a cluster to three positive eigenvalues (see table C.1).

Structure type	Rule
Void	$\mu_1, \mu_2, \mu_3 < 0$
Sheet	$\mu_1, \mu_2 < 0$ and $\mu_3 > 0$
Filament	$\mu_1 < 0$ and $\mu_2, \mu_3 > 0$
Cluster	$\mu_1, \mu_2, \mu_3 > 0$

Table C.1: Rules for classification of structure types according to the T-web procedure (Hahn *et al.*, 2007a).

The interpretation of this rule is straightforward, as the sign of an eigenvalue at a given position defines whether the gravitational force in the direction of the corresponding eigenvector is contracting (positive eigenvalues) or expanding (negative eigenvalues). Thus, the signature of the tidal tensor characterizes the number of axes along which there is gravitational expansion or collapse. This procedure is sometimes called the “T-web”, in reference to the tidal tensor.

In Hahn *et al.* (2007a), an interpretation of the above rule in terms of the orbit stability of test particles is also discussed. The equation of motion in comoving coordinates and in conformal time reads (see equation (1.74))

$$\frac{d\mathbf{p}}{d\tau} = -ma\nabla\Phi \quad \text{with} \quad \mathbf{p} = ma\frac{d\mathbf{x}}{d\tau} \quad (\text{C.15})$$

The local extrema of the gravitational potential (i.e. points  $\bar{\mathbf{x}}$  such that  $\nabla\Phi(\bar{\mathbf{x}}) = 0$ ) are fixed points of the test particle equation of motion. These can be, for example, the center of mass of halos. In their neighborhood, we can linearize the equation of motion at the points  $\bar{\mathbf{x}}$ , which yields the linear system

$$\frac{d}{d\tau} \left( ma \frac{d\mathbf{x}}{d\tau} \right) \approx -ma \nabla^2 \Phi(\bar{\mathbf{x}}) \cdot (\mathbf{x} - \bar{\mathbf{x}}), \quad (\text{C.16})$$

or, in terms of coordinates,

$$\frac{d}{d\tau} \left( ma \frac{d\mathbf{x}_i}{d\tau} \right) \approx -ma \sum_j \frac{\partial^2 \Phi}{\partial \mathbf{x}_i \partial \mathbf{x}_j}(\bar{\mathbf{x}}) (\mathbf{x}_j - \bar{\mathbf{x}}_j) \propto -ma \sum_j \mathcal{T}_{ij}(\bar{\mathbf{x}}) (\mathbf{x}_j - \bar{\mathbf{x}}_j). \quad (\text{C.17})$$

This equation means that the linear dynamics near local extrema of the gravitational potential is fully governed by the tidal field. The number of positive eigenvalues is equivalent to the dimension of the stable manifold at the fixed points:

- voids are regions of space where the orbits of test particles are unstable (no positive eigenvalue);
- sheets correspond to one-dimensional stable manifolds (one positive, two negative eigenvalues);
- filaments correspond to two-dimensional stable manifolds (two positive, one negative eigenvalues);
- clusters are attractive fixed points (three positive eigenvalues).

Dropping the assumption of local extrema of the gravitational potential introduces a constant acceleration term to the linearized equation of motion. This zeroth-order effect can be ignored by changing to free-falling coordinates. The behavior introduced by the first-order term, representing the tidal deformation of orbits, and thus the web-type classification, remain unchanged.

## C.2.4 Extensions of the T-web

### C.2.4.1 Varying threshold

Several extensions of this classification procedure exist. [Forero-Romero \*et al.\* \(2009\)](#) pointed out that rather than using a threshold value  $\mu_{\text{th}}$  of zero, different positive values can be used. The corresponding set of rules is given by table C.2.

Structure type	Rule
Void	$\mu_1, \mu_2, \mu_3 < \mu_{\text{th}}$
Sheet	$\mu_1, \mu_2 < \mu_{\text{th}}$ and $\mu_3 > \mu_{\text{th}}$
Filament	$\mu_1 < \mu_{\text{th}}$ and $\mu_2, \mu_3 > \mu_{\text{th}}$
Cluster	$\mu_1, \mu_2, \mu_3 > \mu_{\text{th}}$

Table C.2: Rules for classification of structure types according to the extended T-web procedure with varying threshold ([Forero-Romero \*et al.\*, 2009](#)).

This introduces a new free parameter, which *a priori* can take any value. However, [Forero-Romero \*et al.\* \(2009\)](#) argued that a natural threshold can be roughly estimated by equating the collapse time (determined by the eigenvalues) to the age of the Universe. For an isotropic collapse, they calculated explicitly  $\mu_{\text{th}} = 3.21$  (appendix A in [Forero-Romero \*et al.\*, 2009](#)). As gravitational collapse is often highly anisotropic, they used an empirical approach to determine the threshold and argued that  $\mu_{\text{th}} \approx 1$  can yield better web classifications than the original T-web, down to the megaparsec scale.

The T-web procedure and/or this extension have been used, for example, by [Jasche \*et al.\* \(2010b\)](#); [Wang \*et al.\* \(2012\)](#); [Forero-Romero, Contreras & Padilla \(2014\)](#); [Nuza \*et al.\* \(2014\)](#); [Alonso, Eardley & Peacock \(2015\)](#); [Eardley \*et al.\* \(2015\)](#); [Forero-Romero & González \(2015\)](#); [Leclercq, Jasche & Wandelt \(2015c\)](#); [Zhao \*et al.\* \(2015\)](#); [Aung & Cohn \(2015\)](#).



### C.2.4.2 The V-web

Hoffman *et al.* (2012) reformulated the extended T-web procedure using the velocity shear tensor instead of the gravitational tidal tensor. More precisely, they use the eigenvalues  $\mu_i^V(\mathbf{x})$  of the rescaled shear tensor defined by

$$\Sigma_{ij} \equiv -\frac{1}{2H(z)} \left( \frac{\partial \mathbf{v}_i}{\partial \mathbf{r}_j} + \frac{\partial \mathbf{v}_j}{\partial \mathbf{r}_i} \right). \quad (\text{C.18})$$

This new scheme is generally referred to as the “V-web” and the rules are given in table C.3. Hoffman *et al.* (2012) showed that the two classifications coincide at large scales (where the gravitational and velocity fields are proportional) and that the velocity field resolves finer structure than the gravitational field at the smallest scales (sub-megaparsec). They empirically determined the threshold value  $\mu_{\text{th}}^V = 0.44$  to yield the best visualization of the geometrical characteristics of the four environments at  $z = 0$ .

Structure type	Rule
Void	$\mu_1^V, \mu_2^V, \mu_3^V < \mu_{\text{th}}^V$
Sheet	$\mu_1^V, \mu_2^V < \mu_{\text{th}}^V$ and $\mu_3^V > \mu_{\text{th}}^V$
Filament	$\mu_1^V < \mu_{\text{th}}^V$ and $\mu_2^V, \mu_3^V > \mu_{\text{th}}^V$
Cluster	$\mu_1^V, \mu_2^V, \mu_3^V > \mu_{\text{th}}^V$

Table C.3: Rules for classification of structure types according to the V-web procedure (Hoffman *et al.*, 2012).

The V-web has been used, for example, by Libeskind *et al.* (2013); Carlesi *et al.* (2014); Nuza *et al.* (2014); Lee, Rey & Kim (2014); Libeskind, Hoffman & Gottlöber (2014). In this thesis, we probe scales down to a few Mpc/h (the voxel size in our reconstructions or simulations). Therefore, we will be content with the original T-web procedure as formulated by Hahn *et al.* (2007a).

### C.2.5 Implementation

This section gives details on how the T-web procedure is implemented when used in this thesis. First, the density contrast field is computed by assigning particles to the grid with a CiC scheme (see section B.3). It is transformed to Fourier space using a Fourier transform on the grid. At this point, if desired, the density field can be smoothed using a Gaussian kernel  $K_{k_s}(k) \equiv \exp\left(-\frac{1}{2} \frac{k^2}{k_s^2}\right)$  (usually this step is bypassed in the projects described in this thesis). This corresponds to a mass scale  $M_s$  which is linked to the smoothing length  $R_s \equiv \frac{2\pi}{k_s}$  by

$$R_s = \frac{1}{\sqrt{2\pi}} \left( \frac{M_s}{\bar{\rho}} \right)^{1/3}. \quad (\text{C.19})$$

The reduced gravitational potential is estimated by solving the Poisson equation in Fourier space,  $\tilde{\Phi}(\mathbf{k}) = G(\mathbf{k})\delta(\mathbf{k})$ , where  $G(\mathbf{k})$  is the Green function corresponding to the discretization adopted for the Laplacian. For the projects described in this thesis, we adopted the simple form  $G(\mathbf{k}) = -1/k^2$  (with also a smoothing of short-range forces and two deconvolutions of the CiC kernel, see section B.4.1). Hence, the gravitational potential is given by the convolution

$$\tilde{\Phi}(\mathbf{x}) = (G * \delta)(\mathbf{x}), \quad (\text{C.20})$$

or, if the density field had been smoothed, by

$$\tilde{\Phi}_{R_s}(\mathbf{x}) = (G * K_{k_s} * \delta)(\mathbf{x}). \quad (\text{C.21})$$

We compute the components of the tidal tensor in Fourier space using  $\mathcal{T}_{ab} = -\tilde{\Phi}(\mathbf{k})\mathbf{k}_a\mathbf{k}_b$ , and transform them back to configuration space by inverse Fourier transform. In practice, only one Fourier transform is required to go from  $\delta$  to  $\mathcal{T}_{ab} \propto -\delta(\mathbf{k})\mathbf{k}_a\mathbf{k}_b/k^2$  (or  $\mathcal{T}_{ab} \propto -\delta(\mathbf{k})\mathbf{k}_a\mathbf{k}_b K_{k_s}(k)/k^2$ ). Finally, we compute the eigenvalues of the tidal tensor at each voxel of the grid and classify structures using the rules given in table C.1. In this fashion, every voxel of the density field gets assigned a flag corresponding to the structure type:  $T_0$  for voids,  $T_1$  for sheets,  $T_2$  for filaments,  $T_3$  for clusters.

The T-web classification takes a few seconds on 8 cores, for a typical density field used in this thesis ( $L = 750$  Mpc/h,  $N_v = 256^3$ ).

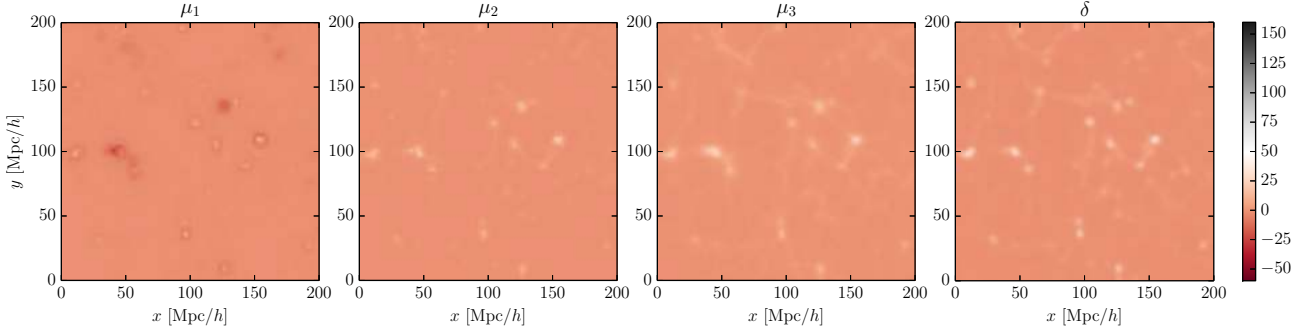


Figure C.1: Slices through the voxel-wise eigenvalues  $\mu_1 \leq \mu_2 \leq \mu_3$  of the tidal field tensor in the final conditions of a dark matter simulation. The rightmost panel shows the corresponding slice through the final density contrast  $\delta = \mu_1 + \mu_2 + \mu_3$  (equation (C.9)). See also figure 9.2 for comparison.

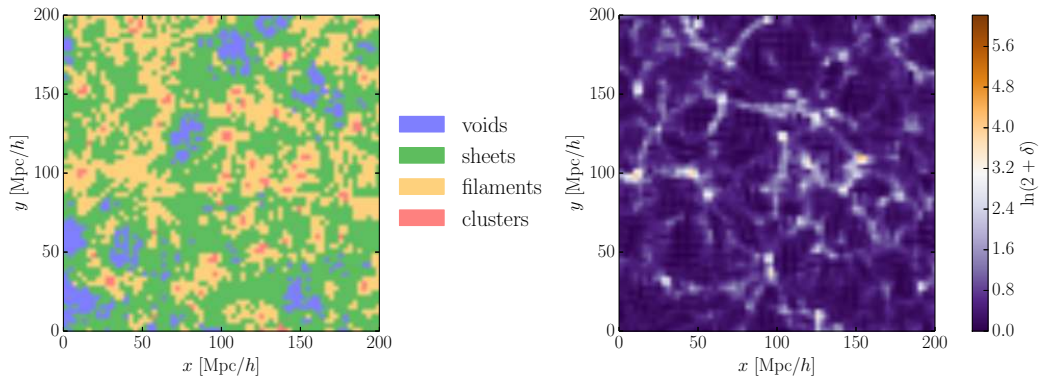


Figure C.2: *Left panel.* Classification of structures with the T-web procedure in the final conditions of a dark matter simulation. The color coding is blue for voids, green for sheets, yellow for filaments and red for clusters. *Right panel.* Dark matter density in the corresponding slice (for convenience, the quantity shown in  $\ln(2 + \delta)$ ).

### C.2.6 Example

As an example, in this section, we show the results of the T-web classification for a simulated density field.

The simulation contains  $512^3$  dark matter particles in a comoving box of  $750 \text{ Mpc}/h$  with periodic boundary conditions. The initial conditions have been generated at  $z = 69$  using second-order Lagrangian perturbation theory. They obey Gaussian statistics with an [Eisenstein & Hu \(1998, 1999\)](#) power spectrum. The  $N$ -body simulation has been run to  $z = 0$  with GADGET-2 ([Springel, Yoshida & White, 2001](#); [Springel, 2005](#)). Particles are assigned to the grid using a CiC method. The cosmological parameters used are

$$\Omega_\Lambda = 0.728, \Omega_m = 0.272, \Omega_b = 0.045, \sigma_8 = 0.807, h = 0.702, n_s = 0.961, \quad (\text{C.22})$$

which gives a mass resolution of  $2.37 \times 10^{11} M_\odot/h$ .

For clarity, we show slices through a  $200 \text{ Mpc}/h$  region of the simulation. Figure C.1 shows the eigenvalues of the tidal tensor and the density contrast. A slice through the corresponding voxel-wise classification of structures is shown in the left panel of figure C.2.



---

# Bibliography

- (Abazajian *et al.*, 2009) K. N. Abazajian, J. K. Adelman-McCarthy, M. A. Agüeros, S. S. Allam, C. Allende Prieto, D. An, K. S. J. Anderson, S. F. Anderson, J. Annis, N. A. Bahcall, et al., *The Seventh Data Release of the Sloan Digital Sky Survey*, *Astrophysical Journal Supplement* **182**, 543 (2009), [arXiv:0812.0649](#).
- (Abdalla *et al.*, 2012) F. Abdalla, J. Annis, D. Bacon, S. Bridle, F. Castander, M. Colless, D. DePoy, H. T. Diehl, M. Eriksen, B. Flaugher, J. Frieman, E. Gaztanaga, C. Hogan, S. Jouvel, S. Kent, D. Kirk, R. Kron, S. Kuhlmann, O. Lahav, J. Lawrence, H. Lin, J. Marriner, J. Marshall, J. Mohr, R. C. Nichol, M. Sako, W. Saunders, M. Soares-Santos, D. Thomas, R. Wechsler, A. West, H. Wu, *The Dark Energy Spectrometer (DESPEC): A Multi-Fiber Spectroscopic Upgrade of the Dark Energy Camera and Survey for the Blanco Telescope*, *ArXiv e-prints* (2012), [arXiv:1209.2451 \[astro-ph.CO\]](#).
- (Abel, Hahn & Kaehler, 2012) T. Abel, O. Hahn, R. Kaehler, *Tracing the dark matter sheet in phase space*, *Monthly Notices of the Royal Astronomical Society* **427**, 61 (2012), [arXiv:1111.3944 \[astro-ph.CO\]](#).
- (Albrecht & Steinhardt, 1982) A. Albrecht, P. J. Steinhardt, *Cosmology for grand unified theories with radiatively induced symmetry breaking*, *Physical Review Letters* **48**, 1220 (1982).
- (Alcock & Paczynski, 1979) C. Alcock, B. Paczynski, *An evolution free test for non-zero cosmological constant*, *Nature* **281**, 358 (1979).
- (Alonso, Eardley & Peacock, 2015) D. Alonso, E. Eardley, J. A. Peacock, *Halo abundances within the cosmic web*, *Monthly Notices of the Royal Astronomical Society* **447**, 2683 (2015), [arXiv:1406.4159](#).
- (Alpher, Bethe & Gamow, 1948) R. A. Alpher, H. Bethe, G. Gamow, *The Origin of Chemical Elements*, *Physical Review* **73**, 803 (1948).
- (Altay, Colberg & Croft, 2006) G. Altay, J. M. Colberg, R. A. C. Croft, *The influence of large-scale structures on halo shapes and alignments*, *Monthly Notices of the Royal Astronomical Society* **370**, 1422 (2006), [astro-ph/0605296](#).
- (Amendola *et al.*, 2013) L. Amendola, S. Appleby, D. Bacon, T. Baker, M. Baldi, N. Bartolo, A. Blanchard, C. Bonvin, S. Borgani, E. Branchini, C. Burrage, S. Camera, C. Carbone, L. Casarini, M. Cropper, C. de Rham, C. Di Porto, A. Ealet, P. G. Ferreira, F. Finelli, J. García-Bellido, T. Giannantonio, L. Guzzo, A. Heavens, L. Heisenberg, C. Heymans, H. Hoekstra, L. Hollenstein, R. Holmes, O. Horst, K. Jahnke, T. D. Kitchoing, T. Koivisto, M. Kunz, G. La Vacca, M. March, E. Majerotto, K. Markovic, D. Marsh, F. Marulli, R. Massey, Y. Mellier, D. F. Mota, N. Nunes, W. Percival, V. Pettorino, C. Porciani, C. Quercellini, J. Read, M. Rinaldi, D. Sapone, R. Scaramella, C. Skordis, F. Simpson, A. Taylor, S. Thomas, R. Trotta, L. Verde, F. Vernizzi, A. Vollmer, Y. Wang, J. Weller, T. Zlosnik, *Cosmology and Fundamental Physics with the Euclid Satellite*, *Living Reviews in Relativity* **16**, 6 (2013), [arXiv:1206.1225](#).
- (Anderes, Wandelt & Lavaux, 2015) E. Anderes, B. D. Wandelt, G. Lavaux, *Bayesian Inference of CMB Gravitational Lensing*, *Astrophysical Journal* **808**, 152 (2015), [arXiv:1412.4079](#).
- (Aragon-Calvo & Szalay, 2013) M. A. Aragon-Calvo, A. S. Szalay, *The hierarchical structure and dynamics of voids*, *Monthly Notices of the Royal Astronomical Society* **428**, 3409 (2013), [arXiv:1203.0248 \[astro-ph.CO\]](#).
- (Aragon-Calvo & Yang, 2014) M. A. Aragon-Calvo, L. F. Yang, *The hierarchical nature of the spin alignment of dark matter haloes in filaments*, *Monthly Notices of the Royal Astronomical Society* **440**, L46 (2014), [arXiv:1303.1590 \[astro-ph.CO\]](#).
- (Aragón-Calvo, van de Weygaert & Jones, 2010) M. A. Aragón-Calvo, R. van de Weygaert, B. J. T. Jones, *Multiscale phenomenology of the cosmic web*, *Monthly Notices of the Royal Astronomical Society* **408**, 2163 (2010), [arXiv:1007.0742 \[astro-ph.CO\]](#).
- (Aragón-Calvo *et al.*, 2007) M. A. Aragón-Calvo, B. J. T. Jones, R. van de Weygaert, J. M. van der Hulst, *The multiscale morphology filter: identifying and extracting spatial patterns in the galaxy distribution*, *Astronomy and Astrophysics* **474**, 315 (2007), [arXiv:0705.2072](#).

- (Arber, 1954) A. R. Arber, *The Mind and the Eye* (Cambridge University Press, 1954).
- (Ata, Kitaura & Müller, 2015) M. Ata, F.-S. Kitaura, V. Müller, *Bayesian inference of cosmic density fields from non-linear, scale-dependent, and stochastic biased tracers*, *Monthly Notices of the Royal Astronomical Society* **446**, 4250 (2015), [arXiv:1408.2566](#).
- (Aung & Cohn, 2015) H. Aung, J. D. Cohn, *Mean maps for cosmic web structures in cosmological initial conditions*, *ArXiv e-prints* (2015), [arXiv:1505.07887](#).
- (Babul & Starkman, 1992) A. Babul, G. D. Starkman, *A quantitative measure of structure in the three-dimensional galaxy distribution - Sheets and filaments*, *Astrophysical Journal* **401**, 28 (1992).
- (Bardeen, 1980) J. M. Bardeen, *Gauge-invariant cosmological perturbations*, *Physical Review D* **22**, 1882 (1980).
- (Bardeen, Steinhardt & Turner, 1983) J. M. Bardeen, P. J. Steinhardt, M. S. Turner, *Spontaneous creation of almost scale-free density perturbations in an inflationary universe*, *Physical Review D* **28**, 679 (1983).
- (Bardeen *et al.*, 1986) J. M. Bardeen, J. R. Bond, N. Kaiser, A. S. Szalay, *The statistics of peaks of Gaussian random fields*, *Astrophysical Journal* **304**, 15 (1986).
- (Barrow, Bhavsar & Sonoda, 1985) J. D. Barrow, S. P. Bhavsar, D. H. Sonoda, *Minimal spanning trees, filaments and galaxy clustering*, *Monthly Notices of the Royal Astronomical Society* **216**, 17 (1985).
- (Baumann, 2011) D. Baumann, *The Physics of Inflation* (2011).
- (Baumann *et al.*, 2012) D. Baumann, A. Nicolis, L. Senatore, M. Zaldarriaga, *Cosmological non-linearities as an effective fluid*, *Journal of Cosmology and Astroparticle Physics* **7**, 051 (2012), [arXiv:1004.2488 \[astro-ph.CO\]](#).
- (Bellman, 1961) R. E. Bellman, *Adaptive Control Processes: A Guided Tour* (Princeton University Press, 1961).
- (Benítez *et al.*, 2015) N. Benítez, R. Dupke, M. Moles, L. Sodré, A. J. Cenarro, A. Marín Franch, K. Taylor, D. Cristóbal, A. Fernández-Soto, C. Mendes de Oliveira, J. Cepa-Nogué, L. R. Abramo, J. S. Alcaniz, R. Overzier, C. Hernández-Monteagudo, E. J. Alfaro, A. Kanaan, M. Carvano, R. R. R. Reis, J-PAS collaboration, *J-PAS: The Javalambre-Physics of the Accelerated Universe Astrophysical Survey*, in *Highlights of Spanish Astrophysics VIII*, edited by A. J. Cenarro, F. Figueras, C. Hernández-Monteagudo, J. Trujillo Bueno, L. Valdivielso (2015) pp. 148–153, [arXiv:1403.5237 \[astro-ph.CO\]](#).
- (Benson *et al.*, 2003) A. J. Benson, F. Hoyle, F. Torres, M. S. Vogeley, *Galaxy voids in cold dark matter universes*, *Monthly Notices of the Royal Astronomical Society* **340**, 160 (2003), [astro-ph/0208257](#).
- (Berger, 1985) J. O. Berger, *Statistical decision theory and Bayesian analysis* (Springer, 1985).
- (Bernardeau, 1994) F. Bernardeau, *The nonlinear evolution of rare events*, *Astrophysical Journal* **427**, 51 (1994), [astro-ph/9311066](#).
- (Bernardeau *et al.*, 2002) F. Bernardeau, S. Colombi, E. Gaztañaga, R. Scoccimarro, *Large-scale structure of the Universe and cosmological perturbation theory*, *Physics Reports* **367**, 1 (2002), [astro-ph/0112551](#).
- (Bertschinger, 1998) E. Bertschinger, *Simulations of Structure Formation in the Universe*, *Annual review of astronomy and astrophysics* **36**, 599 (1998).
- (Bertschinger, 2001) E. Bertschinger, *Multiscale Gaussian Random Fields and Their Application to Cosmological Simulations*, *Astrophysical Journal Supplement* **137**, 1 (2001), [astro-ph/0103301](#).
- (Bertschinger, 1987) E. Bertschinger, *Path integral methods for primordial density perturbations - Sampling of constrained Gaussian random fields*, *Astrophysical Journal Letters* **323**, L103 (1987).
- (Bertschinger & Jain, 1994) E. Bertschinger, B. Jain, *Gravitational instability of cold matter*, *Astrophysical Journal* **431**, 486 (1994), [arXiv:astro-ph/9307033](#).
- (Betancort-Rijo *et al.*, 2009) J. Betancort-Rijo, S. G. Patiri, F. Prada, A. E. Romano, *The statistics of voids as a tool to constrain cosmological parameters:  $\sigma_8$  and  $\Omega_m h$* , *Monthly Notices of the Royal Astronomical Society* **400**, 1835 (2009), [arXiv:0901.1609](#).

- (Birdsall & Langdon, 1985) C. K. Birdsall, A. B. Langdon, *Plasma Physics via Computer Simulation* (CRC Press, 1985).
- (Biswas, Alizadeh & Wandelt, 2010) R. Biswas, E. Alizadeh, B. D. Wandelt, *Voids as a precision probe of dark energy*, *Physical Review D* **82**, 023002 (2010), arXiv:1002.0014 [astro-ph.CO].
- (Blanton & Roweis, 2007) M. R. Blanton, S. Roweis, *K-Corrections and Filter Transformations in the Ultraviolet, Optical, and Near-Infrared*, *Astronomical Journal* **133**, 734 (2007), astro-ph/0606170.
- (Blanton *et al.*, 2003a) M. R. Blanton, H. Lin, R. H. Lupton, F. M. Maley, N. Young, I. Zehavi, J. Loveday, *An Efficient Targeting Strategy for Multiobject Spectrograph Surveys: the Sloan Digital Sky Survey “Tiling” Algorithm*, *Astronomical Journal* **125**, 2276 (2003a), astro-ph/0105535.
- (Blanton *et al.*, 2003b) M. R. Blanton, J. Brinkmann, I. Csabai, M. Doi, D. Eisenstein, M. Fukugita, J. E. Gunn, D. W. Hogg, D. J. Schlegel, *Estimating Fixed-Frame Galaxy Magnitudes in the Sloan Digital Sky Survey*, *Astronomical Journal* **125**, 2348 (2003b), astro-ph/0205243.
- (Blanton *et al.*, 2005) M. R. Blanton, D. J. Schlegel, M. A. Strauss, J. Brinkmann, D. Finkbeiner, M. Fukugita, J. E. Gunn, D. W. Hogg, Ž. Ivezić, G. R. Knapp, R. H. Lupton, J. A. Munn, D. P. Schneider, M. Tegmark, I. Zehavi, *New York University Value-Added Galaxy Catalog: A Galaxy Catalog Based on New Public Surveys*, *Astronomical Journal* **129**, 2562 (2005), astro-ph/0410166.
- (Blanton *et al.*, 2003c) M. R. Blanton, D. W. Hogg, N. A. Bahcall, J. Brinkmann, M. Britton, A. J. Connolly, I. Csabai, M. Fukugita, J. Loveday, A. Meiksin, J. A. Munn, R. C. Nichol, S. Okamura, T. Quinn, D. P. Schneider, K. Shimasaku, M. A. Strauss, M. Tegmark, M. S. Vogeley, D. H. Weinberg, *The Galaxy Luminosity Function and Luminosity Density at Redshift  $z = 0.1$* , *Astrophysical Journal* **592**, 819 (2003c), astro-ph/0210215.
- (Blas, Lesgourgues & Tram, 2011) D. Blas, J. Lesgourgues, T. Tram, *The Cosmic Linear Anisotropy Solving System (CLASS). Part II: Approximation schemes*, *Journal of Cosmology and Astroparticle Physics* **7**, 034 (2011), arXiv:1104.2933.
- (Blumenthal *et al.*, 1984) G. R. Blumenthal, S. M. Faber, J. R. Primack, M. J. Rees, *Formation of galaxies and large-scale structure with cold dark matter*, *Nature* **311**, 517 (1984).
- (Blumenthal *et al.*, 1992) G. R. Blumenthal, L. N. da Costa, D. S. Goldwirth, M. Lecar, T. Piran, *The largest possible voids*, *Astrophysical Journal* **388**, 234 (1992).
- (Bond & Szalay, 1983) J. R. Bond, A. S. Szalay, *The collisionless damping of density fluctuations in an expanding universe*, *Astrophysical Journal* **274**, 443 (1983).
- (Bond, Kofman & Pogosyan, 1996) J. R. Bond, L. Kofman, D. Pogosyan, *How filaments of galaxies are woven into the cosmic web*, *Nature* **380**, 603 (1996), astro-ph/9512141.
- (Bond, Szalay & Turner, 1982) J. R. Bond, A. S. Szalay, M. S. Turner, *Formation of galaxies in a gravitino-dominated universe*, *Physical Review Letters* **48**, 1636 (1982).
- (Bond, Strauss & Cen, 2010) N. A. Bond, M. A. Strauss, R. Cen, *Crawling the cosmic network: identifying and quantifying filamentary structure*, *Monthly Notices of the Royal Astronomical Society* **409**, 156 (2010), arXiv:1003.3237 [astro-ph.CO].
- (Bos *et al.*, 2012) E. G. P. Bos, R. van de Weygaert, K. Dolag, V. Pettorino, *The darkness that shaped the void: dark energy and cosmic voids*, *Monthly Notices of the Royal Astronomical Society* **426**, 440 (2012), arXiv:1205.4238 [astro-ph.CO].
- (Bouchet *et al.*, 1995) F. R. Bouchet, S. Colombi, E. Hivon, R. Juszkiewicz, *Perturbative Lagrangian approach to gravitational instability*, *Astronomy and Astrophysics* **296**, 575 (1995), astro-ph/9406013.
- (Bryan, Cameron & Allen, 1999) M. Bryan, J. Cameron, C. A. Allen, *The Artist’s Way at Work: Riding the Dragon* (William Morrow, 1999).



- (Buchert, 1989) T. Buchert, *A class of solutions in Newtonian cosmology and the pancake theory*, *Astronomy and Astrophysics* **223**, 9 (1989).
- (Buchert, Melott & Weiß, 1994) T. Buchert, A. L. Melott, A. G. Weiß, *Testing higher-order Lagrangian perturbation theory against numerical simulations I. Pancake models*, *Astronomy and Astrophysics* **288**, 349 (1994), [astro-ph/9309056](#).
- (Cai *et al.*, 2010) Y.-C. Cai, S. Cole, A. Jenkins, C. S. Frenk, *Full-sky map of the ISW and Rees-Sciama effect from Gpc simulations*, *Monthly Notices of the Royal Astronomical Society* **407**, 201 (2010), [arXiv:1003.0974 \[astro-ph.CO\]](#).
- (Cai *et al.*, 2014) Y.-C. Cai, M. C. Neyrinck, I. Szapudi, S. Cole, C. S. Frenk, *A Possible Cold Imprint of Voids on the Microwave Background Radiation*, *Astrophysical Journal* **786**, 110 (2014), [arXiv:1301.6136 \[astro-ph.CO\]](#).
- (Cameron & Pettitt, 2012) E. Cameron, A. N. Pettitt, *Approximate Bayesian Computation for astronomical model analysis: a case study in galaxy demographics and morphological transformation at high redshift*, *Monthly Notices of the Royal Astronomical Society* **425**, 44 (2012), [arXiv:1202.1426 \[astro-ph.IM\]](#).
- (Carlesi *et al.*, 2014) E. Carlesi, A. Knebe, G. F. Lewis, S. Wales, G. Yepes, *Hydrodynamical simulations of coupled and uncoupled quintessence models - I. Halo properties and the cosmic web*, *Monthly Notices of the Royal Astronomical Society* **439**, 2943 (2014), [arXiv:1401.5005 \[astro-ph.CO\]](#).
- (Carrasco, Hertzberg & Senatore, 2012) J. J. M. Carrasco, M. P. Hertzberg, L. Senatore, *The effective field theory of cosmological large scale structures*, *Journal of High Energy Physics* **9**, 82 (2012), [arXiv:1206.2926 \[astro-ph.CO\]](#).
- (Carroll, Press & Turner, 1992) S. M. Carroll, W. H. Press, E. L. Turner, *The cosmological constant*, *Annual review of astronomy and astrophysics* **30**, 499 (1992).
- (Carron, 2012) J. Carron, *Information Escaping the Correlation Hierarchy of the Convergence Field in the Study of Cosmological Parameters*, *Physical Review Letters* **108**, 071301 (2012), [arXiv:1201.1000 \[astro-ph.IM\]](#).
- (Carron & Neyrinck, 2012) J. Carron, M. C. Neyrinck, *On the Inadequacy of N-point Correlation Functions to Describe Nonlinear Cosmological Fields: Explicit Examples and Connection to Simulations*, *Astrophysical Journal* **750**, 28 (2012), [arXiv:1201.1444 \[astro-ph.CO\]](#).
- (Casas-Miranda *et al.*, 2002) R. Casas-Miranda, H. J. Mo, R. K. Sheth, G. Boerner, *On the distribution of haloes, galaxies and mass*, *Monthly Notices of the Royal Astronomical Society* **333**, 730 (2002), [astro-ph/0105008](#).
- (Cautun & van de Weygaert, 2011) M. C. Cautun, R. van de Weygaert, *The DTFE public software - The Delaunay Tessellation Field Estimator code*, *ArXiv e-prints* (2011), [arXiv:1105.0370 \[astro-ph.IM\]](#).
- (Cautun, van de Weygaert & Jones, 2013) M. Cautun, R. van de Weygaert, B. J. T. Jones, *NEXUS: tracing the cosmic web connection*, *Monthly Notices of the Royal Astronomical Society* **429**, 1286 (2013), [arXiv:1209.2043 \[astro-ph.CO\]](#).
- (Cautun *et al.*, 2014) M. Cautun, R. van de Weygaert, B. J. T. Jones, C. S. Frenk, *Evolution of the cosmic web*, *Monthly Notices of the Royal Astronomical Society* **441**, 2923 (2014), [arXiv:1401.7866](#).
- (Ceccarelli *et al.*, 2013) L. Ceccarelli, D. Paz, M. Lares, N. Padilla, D. G. Lambas, *Clues on void evolution - I. Large-scale galaxy distributions around voids*, *Monthly Notices of the Royal Astronomical Society* **434**, 1435 (2013), [arXiv:1306.5798 \[astro-ph.CO\]](#).
- (Chan, 2014) K. C. Chan, *Helmholtz decomposition of the Lagrangian displacement*, *Physical Review D* **89**, 083515 (2014), [arXiv:1309.2243](#).
- (Clampitt & Jain, 2014) J. Clampitt, B. Jain, *Lensing Measurements of the Mass Distribution in SDSS Voids*, *ArXiv e-prints* (2014), [arXiv:1404.1834](#).
- (Clampitt, Cai & Li, 2013) J. Clampitt, Y.-C. Cai, B. Li, *Voids in modified gravity: excursion set predictions*, *Monthly Notices of the Royal Astronomical Society* **431**, 749 (2013), [arXiv:1212.2216 \[astro-ph.CO\]](#).



- (Codis *et al.*, 2012) S. Codis, C. Pichon, J. Devriendt, A. Slyz, D. Pogosyan, Y. Dubois, T. Sousbie, *Connecting the cosmic web to the spin of dark haloes: implications for galaxy formation*, *Monthly Notices of the Royal Astronomical Society* **427**, 3320 (2012), arXiv:1201.5794 [astro-ph.CO].
- (Codis *et al.*, 2015) S. Codis, R. Gavazzi, Y. Dubois, C. Pichon, K. Benabed, V. Desjacques, D. Pogosyan, J. Devriendt, A. Slyz, *Intrinsic alignment of simulated galaxies in the cosmic web: implications for weak lensing surveys*, *Monthly Notices of the Royal Astronomical Society* **448**, 3391 (2015), arXiv:1406.4668.
- (Coelho, 1988) P. Coelho, *The Alchemist* (HarperTorch, 1988).
- (Colberg *et al.*, 2005) J. M. Colberg, R. K. Sheth, A. Diaferio, L. Gao, N. Yoshida, *Voids in a  $\Lambda$ CDM universe*, *Monthly Notices of the Royal Astronomical Society* **360**, 216 (2005), astro-ph/0409162.
- (Colberg *et al.*, 2008) J. M. Colberg, F. Pearce, C. Foster, E. Platen, R. Brunino, M. Neyrinck, S. Basilakos, A. Fairall, H. Feldman, S. Gottlöber, O. Hahn, F. Hoyle, V. Müller, L. Nelson, M. Plionis, C. Porciani, S. Shandarin, M. S. Vogeley, R. van de Weygaert, *The Aspen-Amsterdam void finder comparison project*, *Monthly Notices of the Royal Astronomical Society* **387**, 933 (2008), arXiv:0803.0918.
- (Cole & Kaiser, 1989) S. Cole, N. Kaiser, *Biased clustering in the cold dark matter cosmogony*, *Monthly Notices of the Royal Astronomical Society* **237**, 1127 (1989).
- (Cole *et al.*, 2005) S. Cole, W. J. Percival, J. A. Peacock, P. Norberg, C. M. Baugh, C. S. Frenk, I. Baldry, J. Bland-Hawthorn, T. Bridges, R. Cannon, M. Colless, C. Collins, W. Couch, N. J. G. Cross, G. Dalton, V. R. Eke, R. De Propris, S. P. Driver, G. Efstathiou, R. S. Ellis, K. Glazebrook, C. Jackson, A. Jenkins, O. Lahav, I. Lewis, S. Lumsden, S. Maddox, D. Madgwick, B. A. Peterson, W. Sutherland, K. Taylor, *The 2dF Galaxy Redshift Survey: power-spectrum analysis of the final data set and cosmological implications*, *Monthly Notices of the Royal Astronomical Society* **362**, 505 (2005), astro-ph/0501174.
- (Coles & Jones, 1991) P. Coles, B. Jones, *A lognormal model for the cosmological mass distribution*, *Monthly Notices of the Royal Astronomical Society* **248**, 1 (1991).
- (Coles, Melott & Shandarin, 1993) P. Coles, A. L. Melott, S. F. Shandarin, *Testing approximations for non-linear gravitational clustering*, *Monthly Notices of the Royal Astronomical Society* **260**, 765 (1993).
- (Colless *et al.*, 2003) M. Colless, B. A. Peterson, C. Jackson, J. A. Peacock, S. Cole, P. Norberg, I. K. Baldry, C. M. Baugh, J. Bland-Hawthorn, T. Bridges, R. Cannon, C. Collins, W. Couch, N. Cross, G. Dalton, R. De Propris, S. P. Driver, G. Efstathiou, R. S. Ellis, C. S. Frenk, K. Glazebrook, O. Lahav, I. Lewis, S. Lumsden, S. Maddox, D. Madgwick, W. Sutherland, K. Taylor, *The 2dF Galaxy Redshift Survey: Final Data Release*, *ArXiv Astrophysics e-prints* (2003), astro-ph/0306581.
- (Colombi, 1994) S. Colombi, *A 'skewed' lognormal approximation to the probability distribution function of the large-scale density field*, *Astrophysical Journal* **435**, 536 (1994), astro-ph/9402071.
- (Cooray & Sheth, 2002) A. Cooray, R. Sheth, *Halo models of large scale structure*, *Physics Reports* **372**, 1 (2002), arXiv:astro-ph/0206508.
- (Cox, 1946) R. T. Cox, *Probability, Frequency and Reasonable Expectation*, *American Journal of Physics* **14**, 1 (1946).
- (Crocce & Scoccimarro, 2006) M. Crocce, R. Scoccimarro, *Renormalized cosmological perturbation theory*, *Physical Review D* **73**, 063519 (2006), astro-ph/0509418.
- (Crocce, Pueblas & Scoccimarro, 2006a) M. Crocce, S. Pueblas, R. Scoccimarro, *Transients from initial conditions in cosmological simulations*, *Monthly Notices of the Royal Astronomical Society* **373**, 369 (2006a), astro-ph/0606505.
- (Crocce, Pueblas & Scoccimarro, 2006b) M. Crocce, S. Pueblas, R. Scoccimarro, *Transients from initial conditions in cosmological simulations*, *Monthly Notices of the Royal Astronomical Society* **373**, 369 (2006b), astro-ph/0606505.

- (Croft *et al.*, 1998) R. A. C. Croft, D. H. Weinberg, N. Katz, L. Hernquist, *Recovery of the Power Spectrum of Mass Fluctuations from Observations of the Ly  $\alpha$  Forest*, *Astrophysical Journal* **495**, 44 (1998), [arXiv:astro-ph/9708018](#).
- (Croft *et al.*, 1999) R. A. C. Croft, D. H. Weinberg, M. Pettini, L. Hernquist, N. Katz, *The Power Spectrum of Mass Fluctuations Measured from the LY $\alpha$  Forest at Redshift  $Z=2.5$* , *Astrophysical Journal* **520**, 1 (1999), [arXiv:astro-ph/9809401](#).
- (Dark Energy Survey Collaboration, 2005) Dark Energy Survey Collaboration, *The Dark Energy Survey*, *ArXiv Astrophysics e-prints* (2005), [astro-ph/0510346](#).
- (Davis *et al.*, 1985) M. Davis, G. Efstathiou, C. S. Frenk, S. D. M. White, *The evolution of large-scale structure in a universe dominated by cold dark matter*, *Astrophysical Journal* **292**, 371 (1985).
- (Davis *et al.*, 2003) M. Davis, S. M. Faber, J. Newman, A. C. Phillips, R. S. Ellis, C. C. Steidel, C. Conselice, A. L. Coil, D. P. Finkbeiner, D. C. Koo, P. Guhathakurta, B. Weiner, R. Schiavon, C. Willmer, N. Kaiser, G. A. Luppino, G. Wirth, A. Connolly, P. Eisenhardt, M. Cooper, B. Gerke, *Science Objectives and Early Results of the DEEP2 Redshift Survey*, in *Discoveries and Research Prospects from 6- to 10-Meter-Class Telescopes II*, Society of Photo-Optical Instrumentation Engineers (SPIE) Conference Series, Vol. 4834, edited by P. Guhathakurta (2003) pp. 161–172, [astro-ph/0209419](#).
- (Davis *et al.*, 2007) M. Davis, P. Guhathakurta, N. P. Konidakis, J. A. Newman, M. L. N. Ashby, A. D. Biggs, P. Barmby, K. Bundy, S. C. Chapman, A. L. Coil, C. J. Conselice, M. C. Cooper, D. J. Croton, P. R. M. Eisenhardt, R. S. Ellis, S. M. Faber, T. Fang, G. G. Fazio, A. Georgakakis, B. F. Gerke, W. M. Goss, S. Gwyn, J. Harker, A. M. Hopkins, J.-S. Huang, R. J. Ivison, S. A. Kassin, E. N. Kirby, A. M. Koekemoer, D. C. Koo, E. S. Laird, E. Le Floch, L. Lin, J. M. Lotz, P. J. Marshall, D. C. Martin, A. J. Metevier, L. A. Moustakas, K. Nandra, K. G. Noeske, C. Papovich, A. C. Phillips, R. M. Rich, G. H. Rieke, D. Rigopoulou, S. Salim, D. Schiminovich, L. Simard, I. Smail, T. A. Small, B. J. Weiner, C. N. A. Willmer, S. P. Willner, G. Wilson, E. L. Wright, R. Yan, *The All-Wavelength Extended Groth Strip International Survey (AEGIS) Data Sets*, *Astrophysical Journal Letters* **660**, L1 (2007), [astro-ph/0607355](#).
- (de Lapparent, Geller & Huchra, 1986) V. de Lapparent, M. J. Geller, J. P. Huchra, *A slice of the universe*, *Astrophysical Journal Letters* **302**, L1 (1986).
- (Dickey, 1971) J. M. Dickey, *The weighted likelihood ratio, linear hypotheses on normal location parameters*, *The Annals of Mathematical Statistics* **42**, 204 (1971).
- (Doroshkevich, 1970a) A. G. Doroshkevich, *The space structure of perturbations and the origin of rotation of galaxies in the theory of fluctuation.*, *Astrofizika* **6**, 581 (1970a).
- (Doroshkevich, 1970b) A. G. Doroshkevich, *Spatial structure of perturbations and origin of galactic rotation in fluctuation theory*, *Astrophysics* **6**, 320 (1970b).
- (Drinkwater *et al.*, 2010) M. J. Drinkwater, R. J. Jurek, C. Blake, D. Woods, K. A. Pimbblet, K. Glazebrook, R. Sharp, M. B. Pracy, S. Brough, M. Colless, W. J. Couch, S. M. Croom, T. M. Davis, D. Forbes, K. Forster, D. G. Gilbank, M. Gladders, B. Jelliffe, N. Jones, I.-H. Li, B. Madore, D. C. Martin, G. B. Poole, T. Small, E. Wisnioski, T. Wyder, H. K. C. Yee, *The WiggleZ Dark Energy Survey: survey design and first data release*, *Monthly Notices of the Royal Astronomical Society* **401**, 1429 (2010), [arXiv:0911.4246](#).
- (Driver *et al.*, 2009) S. P. Driver, P. Norberg, I. K. Baldry, S. P. Bamford, A. M. Hopkins, J. Liske, J. Loveday, J. A. Peacock, D. T. Hill, L. S. Kelvin, A. S. G. Robotham, N. J. G. Cross, H. R. Parkinson, M. Prescott, C. J. Conselice, L. Dunne, S. Brough, H. Jones, R. G. Sharp, E. van Kampen, S. Oliver, I. G. Roseboom, J. Bland-Hawthorn, S. M. Croom, S. Ellis, E. Cameron, S. Cole, C. S. Frenk, W. J. Couch, A. W. Graham, R. Proctor, R. De Propriis, I. F. Doyle, E. M. Edmondson, R. C. Nichol, D. Thomas, S. A. Eales, M. J. Jarvis, K. Kuijken, O. Lahav, B. F. Madore, M. Seibert, M. J. Meyer, L. Staveley-Smith, S. Phillipps, C. C. Popescu, A. E. Sansom, W. J. Sutherland, R. J. Tuffs, S. J. Warren, *GAMA: towards a physical understanding of galaxy formation*, *Astronomy and Geophysics* **50**, 12 (2009), [arXiv:0910.5123 \[astro-ph.CO\]](#).
- (Duane *et al.*, 1987) S. Duane, A. D. Kennedy, B. J. Pendleton, D. Roweth, *Hybrid Monte Carlo*, *Physics Letters B* **195**, 216 (1987).

- (Dubinski *et al.*, 1993) J. Dubinski, L. N. da Costa, D. S. Goldwirth, M. Lecar, T. Piran, *Void evolution and the large-scale structure*, *Astrophysical Journal* **410**, 458 (1993).
- (Dubois *et al.*, 2014) Y. Dubois, C. Pichon, C. Welker, D. Le Borgne, J. Devriendt, C. Laigle, S. Codis, D. Pogosyan, S. Arnouts, K. Benabed, E. Bertin, J. Blaizot, F. Bouchet, J.-F. Cardoso, S. Colombi, V. de Lapparent, V. Desjacques, R. Gavazzi, S. Kassin, T. Kimm, H. McCracken, B. Milliard, S. Peirani, S. Prunet, S. Rouberol, J. Silk, A. Slyz, T. Sousbie, R. Teyssier, L. Tresse, M. Treyer, D. Vibert, M. Volonteri, *Dancing in the dark: galactic properties trace spin swings along the cosmic web*, *Monthly Notices of the Royal Astronomical Society* **444**, 1453 (2014), arXiv:1402.1165.
- (Eardley *et al.*, 2015) E. Eardley, J. A. Peacock, T. McNaught-Roberts, C. Heymans, P. Norberg, M. Alpaslan, I. Baldry, J. Bland-Hawthorn, S. Brough, M. E. Cluver, S. P. Driver, D. J. Farrow, J. Liske, J. Loveday, A. S. G. Robotham, *Galaxy And Mass Assembly (GAMA): the galaxy luminosity function within the cosmic web*, *Monthly Notices of the Royal Astronomical Society* **448**, 3665 (2015), arXiv:1412.2141.
- (Efstathiou *et al.*, 1985) G. Efstathiou, M. Davis, S. D. M. White, C. S. Frenk, *Numerical techniques for large cosmological N-body simulations*, *Astrophysical Journal Supplement* **57**, 241 (1985).
- (Einstein & de Sitter, 1932) A. Einstein, W. de Sitter, *On the Relation between the Expansion and the Mean Density of the Universe*, *Proceedings of the National Academy of Science* **18**, 213 (1932).
- (Eisenstein & Hu, 1999) D. J. Eisenstein, W. Hu, *Power Spectra for Cold Dark Matter and Its Variants*, *Astrophysical Journal* **511**, 5 (1999), astro-ph/9710252.
- (Eisenstein & Hu, 1998) D. J. Eisenstein, W. Hu, *Baryonic Features in the Matter Transfer Function*, *Astrophysical Journal* **496**, 605 (1998), astro-ph/9709112.
- (Eisenstein *et al.*, 2007) D. J. Eisenstein, H.-J. Seo, E. Sirko, D. N. Spergel, *Improving Cosmological Distance Measurements by Reconstruction of the Baryon Acoustic Peak*, *Astrophysical Journal* **664**, 675 (2007), astro-ph/0604362.
- (Eisenstein *et al.*, 2005) D. J. Eisenstein, I. Zehavi, D. W. Hogg, R. Scoccimarro, M. R. Blanton, R. C. Nichol, R. Scranton, H.-J. Seo, M. Tegmark, Z. Zheng, S. F. Anderson, J. Annis, N. Bahcall, J. Brinkmann, S. Burles, F. J. Castander, A. Connolly, I. Csabai, M. Doi, M. Fukugita, J. A. Frieman, K. Glazebrook, J. E. Gunn, J. S. Hendry, G. Hennessy, Z. Ivezić, S. Kent, G. R. Knapp, H. Lin, Y.-S. Loh, R. H. Lupton, B. Margon, T. A. McKay, A. Meiksin, J. A. Munn, A. Pope, M. W. Richmond, D. Schlegel, D. P. Schneider, K. Shimasaku, C. Stoughton, M. A. Strauss, M. SubbaRao, A. S. Szalay, I. Szapudi, D. L. Tucker, B. Yanny, D. G. York, *Detection of the Baryon Acoustic Peak in the Large-Scale Correlation Function of SDSS Luminous Red Galaxies*, *Astrophysical Journal* **633**, 560 (2005), astro-ph/0501171.
- (Elsner & Wandelt, 2013) F. Elsner, B. D. Wandelt, *Efficient Wiener filtering without preconditioning*, *Astronomy and Astrophysics* **549**, A111 (2013), arXiv:1210.4931 [astro-ph.CO].
- (Elsner & Wandelt, 2010) F. Elsner, B. D. Wandelt, *Local Non-Gaussianity in the Cosmic Microwave Background the Bayesian Way*, *Astrophysical Journal* **724**, 1262 (2010), arXiv:1010.1254 [astro-ph.CO].
- (Elyiv *et al.*, 2015) A. Elyiv, F. Marulli, G. Pollina, M. Baldi, E. Branchini, A. Cimatti, L. Moscardini, *Cosmic voids detection without density measurements*, *Monthly Notices of the Royal Astronomical Society* **448**, 642 (2015), arXiv:1410.4559.
- (Erdoğdu *et al.*, 2004) P. Erdoğdu, O. Lahav, S. Zaroubi, G. Efstathiou, S. Moody, J. A. Peacock, M. Colless, I. K. Baldry, C. M. Baugh, J. Bland-Hawthorn, T. Bridges, R. Cannon, S. Cole, C. Collins, W. Couch, G. Dalton, R. De Propriis, S. P. Driver, R. S. Ellis, C. S. Frenk, K. Glazebrook, C. Jackson, I. Lewis, S. Lumsden, S. Maddox, D. Madgwick, P. Norberg, B. A. Peterson, W. Sutherland, K. Taylor, *The 2dF Galaxy Redshift Survey: Wiener reconstruction of the cosmic web*, *Monthly Notices of the Royal Astronomical Society* **352**, 939 (2004), astro-ph/0312546.
- (Eriksen *et al.*, 2004) H. K. Eriksen, I. J. O'Dwyer, J. B. Jewell, B. D. Wandelt, D. L. Larson, K. M. Górski, S. Levin, A. J. Banday, P. B. Lilje, *Power Spectrum Estimation from High-Resolution Maps by Gibbs Sampling*, *Astrophysical Journal Supplement* **155**, 227 (2004), astro-ph/0407028.

- (Falck, Neyrinck & Szalay, 2012) B. L. Falck, M. C. Neyrinck, A. S. Szalay, *ORIGAMI: Delineating Halos Using Phase-space Folds*, *Astrophysical Journal* **754**, 126 (2012), arXiv:1201.2353 [astro-ph.CO].
- (Falck, Koyama & Zhao, 2015) B. Falck, K. Koyama, G.-B. Zhao, *Cosmic web and environmental dependence of screening: Vainshtein vs. chameleon*, *Journal of Cosmology and Astroparticle Physics* **7**, 049 (2015), arXiv:1503.06673.
- (Fendt & Wandelt, 2007) W. A. Fendt, B. D. Wandelt, *Pico: Parameters for the Impatient Cosmologist*, *Astrophysical Journal* **654**, 2 (2007), astro-ph/0606709.
- (Feng & Fang, 2000) L.-L. Feng, L.-Z. Fang, *Non-Gaussianity and the Recovery of the Mass Power Spectrum from the Ly $\alpha$  Forest*, *Astrophysical Journal* **535**, 519 (2000), arXiv:astro-ph/0001348.
- (Fitzgerald, 1925) F. S. Fitzgerald, *The Great Gatsby* (Charles Scribner's Sons, 1925).
- (Forero-Romero & González, 2015) J. E. Forero-Romero, R. González, *The Local Group in the Cosmic Web*, *Astrophysical Journal* **799**, 45 (2015), arXiv:1408.3166.
- (Forero-Romero, Contreras & Padilla, 2014) J. E. Forero-Romero, S. Contreras, N. Padilla, *Cosmic web alignments with the shape, angular momentum and peculiar velocities of dark matter haloes*, *Monthly Notices of the Royal Astronomical Society* **443**, 1090 (2014), arXiv:1406.0508.
- (Forero-Romero *et al.*, 2009) J. E. Forero-Romero, Y. Hoffman, S. Gottlöber, A. Klypin, G. Yepes, *A dynamical classification of the cosmic web*, *Monthly Notices of the Royal Astronomical Society* **396**, 1815 (2009), arXiv:0809.4135.
- (Furlanetto & Piran, 2006) S. R. Furlanetto, T. Piran, *The evidence of absence: galaxy voids in the excursion set formalism*, *Monthly Notices of the Royal Astronomical Society* **366**, 467 (2006), astro-ph/0509148.
- (Galassi *et al.*, 2003) M. Galassi, J. Davies, J. Theiler, B. Gough, G. Jungman, M. Booth, F. Rossi, *Gnu Scientific Library: Reference Manual* (Network Theory Ltd., 2003).
- (Gaztañaga & Yokoyama, 1993) E. Gaztañaga, J. Yokoyama, *Probing the statistics of primordial fluctuations and their evolution*, *Astrophysical Journal* **403**, 450 (1993).
- (Geller & Huchra, 1989) M. J. Geller, J. P. Huchra, *Mapping the universe*, *Science* **246**, 897 (1989).
- (Gelman & Rubin, 1992) A. Gelman, D. B. Rubin, *Inference from Iterative Simulation Using Multiple Sequences*, *Statistical Science* **7**, 457 (1992).
- (Gelman *et al.*, 2013) A. Gelman, J. B. Carlin, H. S. Stern, D. B. Dunson, A. Vehtari, D. B. Rubin, *Bayesian Data Analysis, Third Edition* (Taylor & Francis, 2013).
- (Gil-Marín *et al.*, 2012) H. Gil-Marín, C. Wagner, F. Fraga Koudi, R. Jimenez, L. Verde, *An improved fitting formula for the dark matter bispectrum*, *Journal of Cosmology and Astroparticle Physics* **2**, 047 (2012), arXiv:1111.4477 [astro-ph.CO].
- (Gil-Marín *et al.*, 2011) H. Gil-Marín, F. Schmidt, W. Hu, R. Jimenez, L. Verde, *The bispectrum of  $f(R)$  cosmologies*, *Journal of Cosmology and Astroparticle Physics* **11**, 019 (2011), arXiv:1109.2115 [astro-ph.CO].
- (Goldberg & Vogeley, 2004) D. M. Goldberg, M. S. Vogeley, *Simulating Voids*, *Astrophysical Journal* **605**, 1 (2004), astro-ph/0307191.
- (Gott, Dickinson & Melott, 1986) J. R. Gott, III, M. Dickinson, A. L. Melott, *The sponge-like topology of large-scale structure in the universe*, *Astrophysical Journal* **306**, 341 (1986).
- (Gott *et al.*, 2005) J. R. Gott, III, M. Jurić, D. Schlegel, F. Hoyle, M. Vogeley, M. Tegmark, N. Bahcall, J. Brinkmann, *A Map of the Universe*, *Astrophysical Journal* **624**, 463 (2005), astro-ph/0310571.



- (Green *et al.*, 2012) J. Green, P. Schechter, C. Baltay, R. Bean, D. Bennett, R. Brown, C. Conselice, M. Donahue, X. Fan, B. S. Gaudi, C. Hirata, J. Kalirai, T. Lauer, B. Nichol, N. Padmanabhan, S. Perlmutter, B. Rauscher, J. Rhodes, T. Roellig, D. Stern, T. Sumi, A. Tanner, Y. Wang, D. Weinberg, E. Wright, N. Gehrels, R. Sambruna, W. Traub, J. Anderson, K. Cook, P. Garnavich, L. Hillenbrand, Z. Ivezic, E. Kerins, J. Lunine, P. McDonald, M. Penny, M. Phillips, G. Rieke, A. Riess, R. van der Marel, R. K. Barry, E. Cheng, D. Content, R. Cutri, R. Goullioud, K. Grady, G. Helou, C. Jackson, J. Kruk, M. Melton, C. Peddie, N. Rioux, M. Seifert, *Wide-Field InfraRed Survey Telescope (WFIRST) Final Report*, ArXiv e-prints (2012), [arXiv:1208.4012 \[astro-ph.IM\]](#).
- (Gregory & Thompson, 1978) S. A. Gregory, L. A. Thompson, *The Coma/A1367 supercluster and its environs*, *Astrophysical Journal* **222**, 784 (1978).
- (Gregory, Thompson & Tift, 1981) S. A. Gregory, L. A. Thompson, W. G. Tift, *The Perseus supercluster*, *Astrophysical Journal* **243**, 411 (1981).
- (Groth & Peebles, 1975) E. J. Groth, P. J. E. Peebles, *Closed-form solutions for the evolution of density perturbations in some cosmological models*, *Astronomy and Astrophysics* **41**, 143 (1975).
- (Gunn & Gott, 1972) J. E. Gunn, J. R. Gott, III, *On the Infall of Matter Into Clusters of Galaxies and Some Effects on Their Evolution*, *Astrophysical Journal* **176**, 1 (1972).
- (Gurbatov, Saichev & Shandarin, 1989) S. N. Gurbatov, A. I. Saichev, S. F. Shandarin, *The large-scale structure of the universe in the frame of the model equation of non-linear diffusion*, *Monthly Notices of the Royal Astronomical Society* **236**, 385 (1989).
- (Guth, 1981) A. H. Guth, *Inflationary universe: A possible solution to the horizon and flatness problems*, *Physical Review D* **23**, 347 (1981).
- (Guth & Pi, 1982) A. H. Guth, S.-Y. Pi, *Fluctuations in the new inflationary universe*, *Physical Review Letters* **49**, 1110 (1982).
- (Guzzo *et al.*, 2014) L. Guzzo, M. Scodreggio, B. Garilli, B. R. Granett, A. Fritz, U. Abbas, C. Adami, S. Arnouts, J. Bel, M. Bolzonella, D. Bottini, E. Branchini, A. Cappi, J. Coupon, O. Cucciati, I. Davidzon, G. De Lucia, S. de la Torre, P. Franzetti, M. Fumana, P. Hudelot, O. Ilbert, A. Iovino, J. Krywult, V. Le Brun, O. Le Fèvre, D. Maccagni, K. Malek, F. Marulli, H. J. McCracken, L. Paioro, J. A. Peacock, M. Polletta, A. Pollo, H. Schlagenhauser, L. A. M. Tasca, R. Tojeiro, D. Vergani, G. Zamorani, A. Zanichelli, A. Burden, C. Di Porto, A. Marchetti, C. Marinoni, Y. Mellier, L. Moscardini, R. C. Nichol, W. J. Percival, S. Phleps, M. Wolk, *The VIMOS Public Extragalactic Redshift Survey (VIPERS). An unprecedented view of galaxies and large-scale structure at  $0.5 < z < 1.2$* , *Astronomy and Astrophysics* **566**, A108 (2014), [arXiv:1303.2623](#).
- (Guzzo *et al.*, 2008) L. Guzzo, M. Pierleoni, B. Meneux, E. Branchini, O. Le Fèvre, C. Marinoni, B. Garilli, J. Blaizot, G. De Lucia, A. Pollo, H. J. McCracken, D. Bottini, V. Le Brun, D. Maccagni, J. P. Picat, R. Scaramella, M. Scodreggio, L. Tresse, G. Vettolani, A. Zanichelli, C. Adami, S. Arnouts, S. Bardelli, M. Bolzonella, A. Bongiorno, A. Cappi, S. Charlot, P. Ciliegi, T. Contini, O. Cucciati, S. de la Torre, K. Dolag, S. Foucaud, P. Franzetti, I. Gavignaud, O. Ilbert, A. Iovino, F. Lamareille, B. Marano, A. Mazure, P. Memeo, R. Merighi, L. Moscardini, S. Paltani, R. Pellò, E. Perez-Montero, L. Pozzetti, M. Radovich, D. Vergani, G. Zamorani, E. Zucca, *A test of the nature of cosmic acceleration using galaxy redshift distortions*, *Nature* **451**, 541 (2008), [arXiv:0802.1944](#).
- (Hahn & Abel, 2011) O. Hahn, T. Abel, *Multi-scale initial conditions for cosmological simulations*, *Monthly Notices of the Royal Astronomical Society* **415**, 2101 (2011), [arXiv:1103.6031](#).
- (Hahn, Angulo & Abel, 2014) O. Hahn, R. E. Angulo, T. Abel, *The Properties of Cosmic Velocity Fields*, ArXiv e-prints (2014), [arXiv:1404.2280](#).
- (Hahn *et al.*, 2007a) O. Hahn, C. Porciani, C. M. Carollo, A. Dekel, *Properties of dark matter haloes in clusters, filaments, sheets and voids*, *Monthly Notices of the Royal Astronomical Society* **375**, 489 (2007a), [astro-ph/0610280](#).

- (Hahn *et al.*, 2007b) O. Hahn, C. M. Carollo, C. Porciani, A. Dekel, *The evolution of dark matter halo properties in clusters, filaments, sheets and voids*, *Monthly Notices of the Royal Astronomical Society* **381**, 41 (2007b), arXiv:0704.2595.
- (Hahn *et al.*, 2009) O. Hahn, C. Porciani, A. Dekel, C. M. Carollo, *Tidal effects and the environment dependence of halo assembly*, *Monthly Notices of the Royal Astronomical Society* **398**, 1742 (2009), arXiv:0803.4211.
- (Hajian, 2007) A. Hajian, *Efficient cosmological parameter estimation with Hamiltonian MonteCarlo technique*, *Physical Review D* **75**, 083525 (2007), arXiv:astro-ph/0608679.
- (Hamaus, Sutter & Wandelt, 2014) N. Hamaus, P. M. Sutter, B. D. Wandelt, *Universal Density Profile for Cosmic Voids*, *Physical Review Letters* **112**, 251302 (2014), arXiv:1403.5499.
- (Hamaus *et al.*, 2014a) N. Hamaus, P. M. Sutter, G. Lavaux, B. D. Wandelt, *Testing cosmic geometry without dynamic distortions using voids*, *Journal of Cosmology and Astroparticle Physics* **12**, 013 (2014a), arXiv:1409.3580.
- (Hamaus *et al.*, 2014b) N. Hamaus, B. D. Wandelt, P. M. Sutter, G. Lavaux, M. S. Warren, *Cosmology with Void-Galaxy Correlations*, *Physical Review Letters* **112**, 041304 (2014b), arXiv:1307.2571 [astro-ph.CO].
- (Hawking, 1982) S. W. Hawking, *The development of irregularities in a single bubble inflationary universe*, *Physics Letters B* **115**, 295 (1982).
- (Hawkins *et al.*, 2003) E. Hawkins, S. Maddox, S. Cole, O. Lahav, D. S. Madgwick, P. Norberg, J. A. Peacock, I. K. Baldry, C. M. Baugh, J. Bland-Hawthorn, T. Bridges, R. Cannon, M. Colless, C. Collins, W. Couch, G. Dalton, R. De Propris, S. P. Driver, G. Efstathiou, R. S. Ellis, C. S. Frenk, K. Glazebrook, C. Jackson, B. Jones, I. Lewis, S. Lumsden, W. Percival, B. A. Peterson, W. Sutherland, K. Taylor, *The 2dF Galaxy Redshift Survey: correlation functions, peculiar velocities and the matter density of the Universe*, *Monthly Notices of the Royal Astronomical Society* **346**, 78 (2003), astro-ph/0212375.
- (Heath, 1977) D. J. Heath, *The growth of density perturbations in zero pressure Friedmann-Lemaître universes*, *Monthly Notices of the Royal Astronomical Society* **179**, 351 (1977).
- (Heavens, 2009) A. F. Heavens, *Statistical techniques in cosmology*, ArXiv e-prints (2009), arXiv:0906.0664 [astro-ph.CO].
- (Heavens & Taylor, 1995) A. F. Heavens, A. N. Taylor, *A spherical harmonic analysis of redshift space*, *Monthly Notices of the Royal Astronomical Society* **275**, 483 (1995), astro-ph/9409027.
- (Heavens, Kitching & Verde, 2007) A. F. Heavens, T. D. Kitching, L. Verde, *On model selection forecasting, dark energy and modified gravity*, *Monthly Notices of the Royal Astronomical Society* **380**, 1029 (2007), astro-ph/0703191.
- (Heisenberg, Schäfer & Bartelmann, 2011) L. Heisenberg, B. M. Schäfer, M. Bartelmann, *A study of relative velocity statistics in Lagrangian perturbation theory with PINOCCHIO*, *Monthly Notices of the Royal Astronomical Society* **416**, 3057 (2011), arXiv:1011.1559 [astro-ph.CO].
- (Heitmann *et al.*, 2010) K. Heitmann, M. White, C. Wagner, S. Habib, D. Higdon, *The Coyote Universe. I. Precision Determination of the Nonlinear Matter Power Spectrum*, *Astrophysical Journal* **715**, 104 (2010), arXiv:0812.1052.
- (Heitmann *et al.*, 2009) K. Heitmann, D. Higdon, M. White, S. Habib, B. J. Williams, E. Lawrence, C. Wagner, *The Coyote Universe. II. Cosmological Models and Precision Emulation of the Nonlinear Matter Power Spectrum*, *Astrophysical Journal* **705**, 156 (2009), arXiv:0902.0429 [astro-ph.CO].
- (Hemans, 1826) F. Hemans, *Casabianca*, in *The New Monthly Magazine* (1826).
- (Heß, Kitaura & Gottlöber, 2013) S. Heß, F.-S. Kitaura, S. Gottlöber, *Simulating structure formation of the Local Universe*, *Monthly Notices of the Royal Astronomical Society* **435**, 2065 (2013), arXiv:1304.6565 [astro-ph.CO].



- (Hidding *et al.*, 2012) J. Hidding, R. van de Weygaert, G. Vegter, B. J. T. Jones, *Adhesion and the Geometry of the Cosmic Web*, ArXiv e-prints (2012), [arXiv:1211.5385 \[astro-ph.CO\]](#).
- (Hill *et al.*, 2008) G. J. Hill, K. Gebhardt, E. Komatsu, N. Drory, P. J. MacQueen, J. Adams, G. A. Blanc, R. Koehler, M. Rafal, M. M. Roth, A. Kelz, C. Gronwall, R. Ciardullo, D. P. Schneider, *The Hobby-Eberly Telescope Dark Energy Experiment (HETDEX): Description and Early Pilot Survey Results*, in *Panoramic Views of Galaxy Formation and Evolution*, Astronomical Society of the Pacific Conference Series, Vol. 399, edited by T. Kodama, T. Yamada, K. Aoki (2008) p. 115, [arXiv:0806.0183](#).
- (Ho & Pepyne, 2002) Y. C. Ho, D. L. Pepyne, *Simple Explanation of the No-Free-Lunch Theorem and Its Implications*, *Journal of Optimization Theory and Applications* **115**, 549 (2002).
- (Hobson, 2010) M. P. Hobson, *Bayesian Methods in Cosmology*, edited by M. P. Hobson, A. H. Jaffe, A. R. Liddle, P. Mukherjee, D. Parkinson (Cambridge University Press, 2010).
- (Hockney & Eastwood, 1981) R. W. Hockney, J. W. Eastwood, *Computer Simulation Using Particles* (McGraw-Hill, 1981).
- (Hoffman & Ribak, 1991) Y. Hoffman, E. Ribak, *Constrained realizations of Gaussian fields - A simple algorithm*, *Astrophysical Journal Letters* **380**, L5 (1991).
- (Hoffman *et al.*, 2012) Y. Hoffman, O. Metuki, G. Yepes, S. Gottlöber, J. E. Forero-Romero, N. I. Libeskind, A. Knebe, *A kinematic classification of the cosmic web*, *Monthly Notices of the Royal Astronomical Society* **425**, 2049 (2012), [arXiv:1201.3367 \[astro-ph.CO\]](#).
- (Hubble, 1934) E. Hubble, *The Distribution of Extra-Galactic Nebulae*, *Astrophysical Journal* **79**, 8 (1934).
- (Huchra *et al.*, 2012) J. P. Huchra, L. M. Macri, K. L. Masters, T. H. Jarrett, P. Berlind, M. Calkins, A. C. Crook, R. Cutri, P. Erdoğdu, E. Falco, T. George, C. M. Hutcheson, O. Lahav, J. Mader, J. D. Mink, N. Martimbeau, S. Schneider, M. Skrutskie, S. Tokarz, M. Westover, *The 2MASS Redshift Survey – Description and Data Release*, *Astrophysical Journal Supplement* **199**, 26 (2012), [arXiv:1108.0669 \[astro-ph.CO\]](#).
- (Hugo, 1856) V. Hugo, *Les Contemplations* (1856).
- (Hui & Bertschinger, 1996) L. Hui, E. Bertschinger, *Local Approximations to the Gravitational Collapse of Cold Matter*, *Astrophysical Journal* **471**, 1 (1996), [arXiv:astro-ph/9508114](#).
- (Icke, 1984) V. Icke, *Voids and filaments*, *Monthly Notices of the Royal Astronomical Society* **206**, 1P (1984).
- (Ilić, Langer & Douspis, 2013) S. Ilić, M. Langer, M. Douspis, *Detecting the integrated Sachs-Wolfe effect with stacked voids*, *Astronomy and Astrophysics* **556**, A51 (2013), [arXiv:1301.5849 \[astro-ph.CO\]](#).
- (Jasche & Lavaux, 2015) J. Jasche, G. Lavaux, *Matrix-free large-scale Bayesian inference in cosmology*, *Monthly Notices of the Royal Astronomical Society* **447**, 1204 (2015), [arXiv:1402.1763](#).
- (Jasche & Wandelt, 2013a) J. Jasche, B. D. Wandelt, *Bayesian physical reconstruction of initial conditions from large-scale structure surveys*, *Monthly Notices of the Royal Astronomical Society* **432**, 894 (2013a), [arXiv:1203.3639 \[astro-ph.CO\]](#).
- (Jasche & Kitaura, 2010) J. Jasche, F. S. Kitaura, *Fast Hamiltonian sampling for large-scale structure inference*, *Monthly Notices of the Royal Astronomical Society* **407**, 29 (2010), [arXiv:0911.2496 \[astro-ph.CO\]](#).
- (Jasche & Wandelt, 2012) J. Jasche, B. D. Wandelt, *Bayesian inference from photometric redshift surveys*, *Monthly Notices of the Royal Astronomical Society* **425**, 1042 (2012), [arXiv:1106.2757 \[astro-ph.CO\]](#).
- (Jasche & Wandelt, 2013b) J. Jasche, B. D. Wandelt, *Methods for Bayesian Power Spectrum Inference with Galaxy Surveys*, *Astrophysical Journal* **779**, 15 (2013b), [arXiv:1306.1821 \[astro-ph.CO\]](#).
- (Jasche, Leclercq & Wandelt, 2015) J. Jasche, F. Leclercq, B. D. Wandelt, *Past and present cosmic structure in the SDSS DR7 main sample*, *Journal of Cosmology and Astroparticle Physics* **1**, 036 (2015), [arXiv:1409.6308](#).

- (Jasche *et al.*, 2010a) J. Jasche, F. S. Kitaura, B. D. Wandelt, T. A. Enßlin, *Bayesian power-spectrum inference for large-scale structure data*, *Monthly Notices of the Royal Astronomical Society* **406**, 60 (2010a), arXiv:0911.2493 [astro-ph.CO].
- (Jasche *et al.*, 2010b) J. Jasche, F. S. Kitaura, C. Li, T. A. Enßlin, *Bayesian non-linear large-scale structure inference of the Sloan Digital Sky Survey Data Release 7*, *Monthly Notices of the Royal Astronomical Society* **409**, 355 (2010b), arXiv:0911.2498 [astro-ph.CO].
- (Jaynes, 2003) E. T. Jaynes, *Probability Theory: The Logic of Science*, edited by G. L. Bretthorst (Cambridge University Press, 2003).
- (Jennings, Li & Hu, 2013) E. Jennings, Y. Li, W. Hu, *The abundance of voids and the excursion set formalism*, *Monthly Notices of the Royal Astronomical Society* **434**, 2167 (2013), arXiv:1304.6087.
- (Jeong & Komatsu, 2009) D. Jeong, E. Komatsu, *Primordial Non-Gaussianity, Scale-dependent Bias, and the Bispectrum of Galaxies*, *Astrophysical Journal* **703**, 1230 (2009), arXiv:0904.0497 [astro-ph.CO].
- (Jewell *et al.*, 2009) J. B. Jewell, H. K. Eriksen, B. D. Wandelt, I. J. O'Dwyer, G. Huey, K. M. Górski, *A Markov Chain Monte Carlo Algorithm for Analysis of Low Signal-To-Noise Cosmic Microwave Background Data*, *Astrophysical Journal* **697**, 258 (2009), arXiv:0807.0624.
- (Jewell, Levin & Anderson, 2004) J. Jewell, S. Levin, C. H. Anderson, *Application of Monte Carlo Algorithms to the Bayesian Analysis of the Cosmic Microwave Background*, *Astrophysical Journal* **609**, 1 (2004), astro-ph/0209560.
- (Jing, 2005) Y. P. Jing, *Correcting for the Alias Effect When Measuring the Power Spectrum Using a Fast Fourier Transform*, *Astrophysical Journal* **620**, 559 (2005), astro-ph/0409240.
- (Jones, van de Weygaert & Aragón-Calvo, 2010) B. J. T. Jones, R. van de Weygaert, M. A. Aragón-Calvo, *Fossil evidence for spin alignment of Sloan Digital Sky Survey galaxies in filaments*, *Monthly Notices of the Royal Astronomical Society* **408**, 897 (2010), arXiv:1001.4479 [astro-ph.CO].
- (Kaiser, 1987) N. Kaiser, *Clustering in real space and in redshift space*, *Monthly Notices of the Royal Astronomical Society* **227**, 1 (1987).
- (Kayo, Taruya & Suto, 2001) I. Kayo, A. Taruya, Y. Suto, *Probability Distribution Function of Cosmological Density Fluctuations from a Gaussian Initial Condition: Comparison of One-Point and Two-Point Lognormal Model Predictions with N-Body Simulations*, *Astrophysical Journal* **561**, 22 (2001), arXiv:astro-ph/0105218.
- (Kendall & Stuart, 1968) M. G. Kendall, A. Stuart, *The advanced theory of statistics* (Griffin, 1968).
- (Kirshner *et al.*, 1981) R. P. Kirshner, A. Oemler, Jr., P. L. Schechter, S. A. Shectman, *A million cubic megaparsec void in Bootes*, *Astrophysical Journal Letters* **248**, L57 (1981).
- (Kitaura, 2012) F.-S. Kitaura, *Bayesian Analysis of Cosmic Structures*, in *Astrostatistics and Data Mining*, edited by L. M. Sarro, L. Eyer, W. O'Mullane, J. De Ridder (2012) p. 143.
- (Kitaura, 2013) F.-S. Kitaura, *The initial conditions of the Universe from constrained simulations*, *Monthly Notices of the Royal Astronomical Society* **429**, L84 (2013), arXiv:1203.4184 [astro-ph.CO].
- (Kitaura & Heß, 2013) F.-S. Kitaura, S. Heß, *Cosmological structure formation with augmented Lagrangian perturbation theory*, *Monthly Notices of the Royal Astronomical Society* **435**, L78 (2013), arXiv:1212.3514 [astro-ph.CO].
- (Kitaura & Enßlin, 2008) F. S. Kitaura, T. A. Enßlin, *Bayesian reconstruction of the cosmological large-scale structure: methodology, inverse algorithms and numerical optimization*, *Monthly Notices of the Royal Astronomical Society* **389**, 497 (2008), arXiv:0705.0429.
- (Kitaura, Gallerani & Ferrara, 2012) F.-S. Kitaura, S. Gallerani, A. Ferrara, *Multiscale inference of matter fields and baryon acoustic oscillations from the Ly $\alpha$  forest*, *Monthly Notices of the Royal Astronomical Society* **420**, 61 (2012), arXiv:1011.6233 [astro-ph.CO].

- (Kitaura, Jasche & Metcalf, 2010) F.-S. Kitaura, J. Jasche, R. B. Metcalf, *Recovering the non-linear density field from the galaxy distribution with a Poisson-lognormal filter*, *Monthly Notices of the Royal Astronomical Society* **403**, 589 (2010), [arXiv:0911.1407 \[astro-ph.CO\]](#).
- (Kitaura *et al.*, 2009) F. S. Kitaura, J. Jasche, C. Li, T. A. Enßlin, R. B. Metcalf, B. D. Wandelt, G. Lemson, S. D. M. White, *Cosmic cartography of the large-scale structure with Sloan Digital Sky Survey data release 6*, *Monthly Notices of the Royal Astronomical Society* **400**, 183 (2009), [arXiv:0906.3978 \[astro-ph.CO\]](#).
- (Klypin & Shandarin, 1983) A. A. Klypin, S. F. Shandarin, *Three-dimensional numerical model of the formation of large-scale structure in the Universe*, *Monthly Notices of the Royal Astronomical Society* **204**, 891 (1983).
- (Kofman & Shandarin, 1988) L. A. Kofman, S. F. Shandarin, *Theory of adhesion for the large-scale structure of the universe*, *Nature* **334**, 129 (1988).
- (Kofman *et al.*, 1992) L. Kofman, D. Pogosyan, S. F. Shandarin, A. L. Melott, *Coherent structures in the universe and the adhesion model*, *Astrophysical Journal* **393**, 437 (1992).
- (Kolb & Turner, 1990) E. W. Kolb, M. S. Turner, *Front. Phys., Vol. 69*, (Westview Press, 1990).
- (Komatsu *et al.*, 2011) E. Komatsu, K. M. Smith, J. Dunkley, C. L. Bennett, B. Gold, G. Hinshaw, N. Jarosik, D. Larson, M. R. Nolta, L. Page, D. N. Spergel, M. Halpern, R. S. Hill, A. Kogut, M. Limon, S. S. Meyer, N. Odegard, G. S. Tucker, J. L. Weiland, E. Wollack, E. L. Wright, *Seven-year Wilkinson Microwave Anisotropy Probe (WMAP) Observations: Cosmological Interpretation*, *Astrophysical Journal Supplement* **192**, 18 (2011), [arXiv:1001.4538 \[astro-ph.CO\]](#).
- (Kovač *et al.*, 2014) K. Kovač, S. J. Lilly, C. Knobel, T. J. Bschorr, Y. Peng, C. M. Carollo, T. Contini, J.-P. Kneib, O. Le Fèvre, V. Mainieri, A. Renzini, M. Scodeggio, G. Zamorani, S. Bardelli, M. Bolzonella, A. Bongiorno, K. Caputi, O. Cucciati, S. de la Torre, L. de Ravel, P. Franzetti, B. Garilli, A. Iovino, P. Kampczyk, F. Lamareille, J.-F. Le Borgne, V. Le Brun, C. Maier, M. Mignoli, P. Oesch, R. Pello, E. P. Montero, V. Presotto, J. Silverman, M. Tanaka, L. Tasca, L. Tresse, D. Vergani, E. Zucca, H. Aussel, A. M. Koekemoer, E. Le Floch, M. Moresco, L. Pozzetti, *zCOSMOS 20k: satellite galaxies are the main drivers of environmental effects in the galaxy population at least to  $z \sim 0.7$* , *Monthly Notices of the Royal Astronomical Society* **438**, 717 (2014), [arXiv:1307.4402 \[astro-ph.CO\]](#).
- (Kravtsov, 2002) A. Kravtsov, *Writing a PM code* (2002).
- (Kullback & Leibler, 1951) S. Kullback, R. A. Leibler, *On Information and Sufficiency*, *The Annals of Mathematical Statistics* **22**, 79 (1951).
- (Lahav & Suto, 2004) O. Lahav, Y. Suto, *Measuring our Universe from Galaxy Redshift Surveys*, *Living Reviews in Relativity* **7**, 8 (2004), [arXiv:astro-ph/0310642](#).
- (Lahav *et al.*, 1991) O. Lahav, P. B. Lilje, J. R. Primack, M. J. Rees, *Dynamical effects of the cosmological constant*, *Monthly Notices of the Royal Astronomical Society* **251**, 128 (1991).
- (Lahav *et al.*, 1994) O. Lahav, K. B. Fisher, Y. Hoffman, C. A. Scharf, S. Zaroubi, *Wiener Reconstruction of All-Sky Galaxy Surveys in Spherical Harmonics*, *Astrophysical Journal Letters* **423**, L93 (1994), [astro-ph/9311059](#).
- (Laigle *et al.*, 2015) C. Laigle, C. Pichon, S. Codis, Y. Dubois, D. Le Borgne, D. Pogosyan, J. Devriendt, S. Peirani, S. Prunet, S. Rouberol, A. Slyz, T. Sousbie, *Swirling around filaments: are large-scale structure vortices spinning up dark haloes?*, *Monthly Notices of the Royal Astronomical Society* **446**, 2744 (2015), [arXiv:1310.3801](#).
- (Langlois, 2005) D. Langlois, *Inflation, Quantum Fluctuations and Cosmological Perturbations*, in *NATO ASIB Proc. 188: Particle Physics and Cosmology: the Interface*, edited by D. Kazakov, G. Smadja (2005) p. 235, [arXiv:hep-th/0405053](#).
- (Langlois, 2010) D. Langlois, *Inflation and Cosmological Perturbations*, in *Lectures on Cosmology Accelerated Expansion of the Universe by Georg Wolschin, Lecture Notes in Physics vol. 800, Springer Berlin / Heidelberg, ISSN 1616-6361; ISBN 978-3-642-10597-5, pp.1-57*, Vol. 800, edited by G. Wolschin (2010) pp. 1–57, [arXiv:1001.5259 \[astro-ph.CO\]](#).

- (Laureijs *et al.*, 2011) R. Laureijs, J. Amiaux, S. Arduini, J. . Augères, J. Brinchmann, R. Cole, M. Cropper, C. Dabin, L. Duvet, A. Ealet, et al., *Euclid Definition Study Report*, ArXiv e-prints (2011), [arXiv:1110.3193 \[astro-ph.CO\]](#).
- (Lavaux, 2008) G. Lavaux, *Reconstruction of peculiar velocities of galaxies: methods and applications to observations*, Ph.D. thesis, Institut d’Astrophysique de Paris, UMR 7095 CNRS – Université Pierre et Marie Curie – Paris 6 (2008).
- (Lavaux, 2010) G. Lavaux, *Precision constrained simulation of the local Universe*, *Monthly Notices of the Royal Astronomical Society* **406**, 1007 (2010), [arXiv:0912.3525](#).
- (Lavaux & Jasche, 2016) G. Lavaux, J. Jasche, *Unmasking the masked Universe: the 2M++ catalogue through Bayesian eyes*, *Monthly Notices of the Royal Astronomical Society* **455**, 3169 (2016), [arXiv:1509.05040](#).
- (Lavaux & Wandelt, 2010) G. Lavaux, B. D. Wandelt, *Precision cosmology with voids: definition, methods, dynamics*, *Monthly Notices of the Royal Astronomical Society* **403**, 1392 (2010), [arXiv:0906.4101 \[astro-ph.CO\]](#).
- (Lavaux & Wandelt, 2012) G. Lavaux, B. D. Wandelt, *Precision Cosmography with Stacked Voids*, *Astrophysical Journal* **754**, 109 (2012), [arXiv:1110.0345 \[astro-ph.CO\]](#).
- (Lavaux & Hudson, 2011) G. Lavaux, M. J. Hudson, *The 2M++ galaxy redshift catalogue*, *Monthly Notices of the Royal Astronomical Society* **416**, 2840 (2011), [arXiv:1105.6107](#).
- (Lawrence *et al.*, 2010) E. Lawrence, K. Heitmann, M. White, D. Higdon, C. Wagner, S. Habib, B. Williams, *The Coyote Universe. III. Simulation Suite and Precision Emulator for the Nonlinear Matter Power Spectrum*, *Astrophysical Journal* **713**, 1322 (2010), [arXiv:0912.4490 \[astro-ph.CO\]](#).
- (Layzer, 1956) D. Layzer, *A new model for the distribution of galaxies in space*, *Astronomical Journal* **61**, 383 (1956).
- (Le Fèvre *et al.*, 2005) O. Le Fèvre, G. Vettolani, B. Garilli, L. Tresse, D. Bottini, V. Le Brun, D. Maccagni, J. P. Picat, R. Scaramella, M. Scodeggio, A. Zanichelli, C. Adami, M. Arnaboldi, S. Arnouts, S. Bardelli, M. Bolzonella, A. Cappi, S. Charlot, P. Cilieggi, T. Contini, S. Foucaud, P. Franzetti, I. Gavignaud, L. Guzzo, O. Ilbert, A. Iovino, H. J. McCracken, B. Marano, C. Marinoni, G. Mathez, A. Mazure, B. Meneux, R. Merighi, S. Paltani, R. Pellò, A. Pollo, L. Pozzetti, M. Radovich, G. Zamorani, E. Zucca, M. Bondi, A. Bongiorno, G. Busarello, F. Lamareille, Y. Mellier, P. Merluzzi, V. Ripepi, D. Rizzo, *The VIMOS VLT deep survey. First epoch VVDS-deep survey: 11 564 spectra with  $17.5 \leq i_{AB} \leq 24$ , and the redshift distribution over  $0 \leq z \leq 5$* , *Astronomy and Astrophysics* **439**, 845 (2005), [astro-ph/0409133](#).
- (Le Fèvre *et al.*, 2013) O. Le Fèvre, P. Cassata, O. Cucciati, B. Garilli, O. Ilbert, V. Le Brun, D. Maccagni, C. Moreau, M. Scodeggio, L. Tresse, G. Zamorani, C. Adami, S. Arnouts, S. Bardelli, M. Bolzonella, M. Bondi, A. Bongiorno, D. Bottini, A. Cappi, S. Charlot, P. Cilieggi, T. Contini, S. de la Torre, S. Foucaud, P. Franzetti, I. Gavignaud, L. Guzzo, A. Iovino, B. Lemaux, C. López-Sanjuan, H. J. McCracken, B. Marano, C. Marinoni, A. Mazure, Y. Mellier, R. Merighi, P. Merluzzi, S. Paltani, R. Pellò, A. Pollo, L. Pozzetti, R. Scaramella, L. Tasca, D. Vergani, G. Vettolani, A. Zanichelli, E. Zucca, *The VIMOS VLT Deep Survey final data release: a spectroscopic sample of 35 016 galaxies and AGN out to  $z \sim 6.7$  selected with  $17.5 \leq i_{AB} \leq 24.75$* , *Astronomy and Astrophysics* **559**, A14 (2013), [arXiv:1307.0545](#).
- (Leclercq, Pisani & Wandelt, 2014) F. Leclercq, A. Pisani, B. D. Wandelt, *Cosmology: from theory to data, from data to theory*, in *New horizons for observational cosmology*, Proceedings of the International School of Physics “Enrico Fermi”, Vol. 186, edited by A. Cooray, A. Melchiorri, E. Komatsu, L. Lamagna (2014) pp. 189–233, [arXiv:1403.1260 \[astro-ph.CO\]](#).
- (Leclercq, Jasche & Wandelt, 2015a) F. Leclercq, J. Jasche, B. Wandelt, *Cosmic web-type classification using decision theory*, *Astronomy and Astrophysics* **576**, L17 (2015a), [arXiv:1503.00730](#).
- (Leclercq, Jasche & Wandelt, 2015b) F. Leclercq, J. Jasche, B. Wandelt, *One-point statistics of the Lagrangian displacement field*, *Journal of Cosmology and Astroparticle Physics* **4**, 026 (2015b), [arXiv:1507.08664](#).



- (Leclercq, Jasche & Wandelt, 2015c) F. Leclercq, J. Jasche, B. Wandelt, *Bayesian analysis of the dynamic cosmic web in the SDSS galaxy survey*, *Journal of Cosmology and Astroparticle Physics* **6**, 015 (2015c), arXiv:1502.02690.
- (Leclercq *et al.*, 2013) F. Leclercq, J. Jasche, H. Gil-Marín, B. Wandelt, *One-point remapping of Lagrangian perturbation theory in the mildly non-linear regime of cosmic structure formation*, *Journal of Cosmology and Astroparticle Physics* **11**, 048 (2013), arXiv:1305.4642 [astro-ph.CO].
- (Leclercq *et al.*, 2015) F. Leclercq, J. Jasche, P. M. Sutter, N. Hamaus, B. Wandelt, *Dark matter voids in the SDSS galaxy survey*, *Journal of Cosmology and Astroparticle Physics* **3**, 047 (2015), arXiv:1410.0355.
- (Lee & Li, 2008) J. Lee, C. Li, *Connecting the Physical Properties of Galaxies with the Overdensity and Tidal Shear of the Large-Scale Environment*, ArXiv e-prints (2008), arXiv:0803.1759.
- (Lee & Park, 2006) J. Lee, D. Park, *Rotation of Cosmic Voids and Void Spin Statistics*, *Astrophysical Journal* **652**, 1 (2006), astro-ph/0606477.
- (Lee & Lee, 2008) J. Lee, B. Lee, *The Variation of Galaxy Morphological Type with Environmental Shear*, *Astrophysical Journal* **688**, 78 (2008), arXiv:0801.1558.
- (Lee, Rey & Kim, 2014) J. Lee, S. C. Rey, S. Kim, *Alignments of the Galaxies in and around the Virgo Cluster with the Local Velocity Shear*, *Astrophysical Journal* **791**, 15 (2014), arXiv:1406.5250.
- (Lesgourgues, 2011) J. Lesgourgues, *The Cosmic Linear Anisotropy Solving System (CLASS) I: Overview*, ArXiv e-prints (2011), arXiv:1104.2932 [astro-ph.IM].
- (Lesgourgues, 2004) J. Lesgourgues, *An overview of Cosmology*, ArXiv Astrophysics e-prints (2004), astro-ph/0409426.
- (Levi *et al.*, 2013) M. Levi, C. Bebek, T. Beers, R. Blum, R. Cahn, D. Eisenstein, B. Flaugher, K. Honscheid, R. Kron, O. Lahav, P. McDonald, N. Roe, D. Schlegel, representing the DESI collaboration, *The DESI Experiment, a whitepaper for Snowmass 2013*, ArXiv e-prints (2013), arXiv:1308.0847 [astro-ph.CO].
- (Lewis & Challinor, 2002) A. Lewis, A. Challinor, *Evolution of cosmological dark matter perturbations*, *Physical Review D* **66**, 023531 (2002), astro-ph/0203507.
- (Lewis & Bridle, 2002) A. Lewis, S. Bridle, *Cosmological parameters from CMB and other data: A Monte Carlo approach*, *Physical Review D* **66**, 103511 (2002), arXiv:astro-ph/0205436.
- (Lewis, 1955) C. S. Lewis, *The Chronicles of Narnia, The Magician's Nephew* (The Bodley Head, 1955).
- (Li & Zhao, 2009) B. Li, H. Zhao, *Structure formation by a fifth force: N-body versus linear simulations*, *Physical Review D* **80**, 044027 (2009), arXiv:0906.3880 [astro-ph.CO].
- (Li, Zhao & Koyama, 2012) B. Li, G.-B. Zhao, K. Koyama, *Haloes and voids in  $f(R)$  gravity*, *Monthly Notices of the Royal Astronomical Society* **421**, 3481 (2012), arXiv:1111.2602 [astro-ph.CO].
- (Li *et al.*, 2014) M. Li, R. E. Angulo, S. D. M. White, J. Jasche, *Matched filter optimization of  $kSZ$  measurements with a reconstructed cosmological flow field*, *Monthly Notices of the Royal Astronomical Society* **443**, 2311 (2014), arXiv:1404.0007.
- (Libeskind, Hoffman & Gottlöber, 2014) N. I. Libeskind, Y. Hoffman, S. Gottlöber, *The velocity shear and vorticity across redshifts and non-linear scales*, *Monthly Notices of the Royal Astronomical Society* **441**, 1974 (2014), arXiv:1310.5706.
- (Libeskind *et al.*, 2013) N. I. Libeskind, Y. Hoffman, J. Forero-Romero, S. Gottlöber, A. Knebe, M. Steinmetz, A. Klypin, *The velocity shear tensor: tracer of halo alignment*, *Monthly Notices of the Royal Astronomical Society* **428**, 2489 (2013), arXiv:1210.4559 [astro-ph.CO].
- (Liddle & Lyth, 2000) A. R. Liddle, D. H. Lyth, *Cosmological Inflation and Large-Scale Structure*, by Andrew R. Liddle and David H. Lyth, pp. 414. ISBN 052166022X. Cambridge, UK: Cambridge University Press, April 2000. (Cambridge University Press, 2000).

- (Lidz *et al.*, 2007) A. Lidz, O. Zahn, M. McQuinn, M. Zaldarriaga, S. Dutta, L. Hernquist, *Higher Order Contributions to the 21 cm Power Spectrum*, *Astrophysical Journal* **659**, 865 (2007), [astro-ph/0610054](#).
- (Lightman & Schechter, 1990) A. P. Lightman, P. L. Schechter, *The Omega dependence of peculiar velocities induced by spherical density perturbations*, *Astrophysical Journal Supplement* **74**, 831 (1990).
- (Lilly *et al.*, 2007) S. J. Lilly, O. Le Fèvre, A. Renzini, G. Zamorani, M. Scodeggio, T. Contini, C. M. Carollo, G. Hasinger, J.-P. Kneib, A. Iovino, V. Le Brun, C. Maier, V. Mainieri, M. Mignoli, J. Silverman, L. A. M. Tasca, M. Bolzonella, A. Bongiorno, D. Bottini, P. Capak, K. Caputi, A. Cimatti, O. Cucciati, E. Daddi, R. Feldmann, P. Franzetti, B. Garilli, L. Guzzo, O. Ilbert, P. Kampczyk, K. Kovac, F. Lamareille, A. Leauthaud, J.-F. L. Borgne, H. J. McCracken, C. Marinoni, R. Pello, E. Ricciardelli, C. Scarlata, D. Vergani, D. B. Sanders, E. Schinnerer, N. Scoville, Y. Taniguchi, S. Arnouts, H. Aussel, S. Bardelli, M. Brusa, A. Cappi, P. Ciliegi, A. Finoguenov, S. Foucaud, A. Franceschini, C. Halliday, C. Impey, C. Knobel, A. Koekemoer, J. Kurk, D. Maccagni, S. Maddox, B. Marano, G. Marconi, B. Meneux, B. Mobasher, C. Moreau, J. A. Peacock, C. Porciani, L. Pozzetti, R. Scaramella, D. Schiminovich, P. Shopbell, I. Smail, D. Thompson, L. Tresse, G. Vettolani, A. Zanichelli, E. Zucca, *zCOSMOS: A Large VLT/VIMOS Redshift Survey Covering  $0 < z < 3$  in the COSMOS Field*, *Astrophysical Journal Supplement* **172**, 70 (2007), [astro-ph/0612291](#).
- (Lin & Kilbinger, 2015) C.-A. Lin, M. Kilbinger, *A new model to predict weak-lensing peak counts II. Parameter constraint strategies*, ArXiv e-prints (2015), [arXiv:1506.01076](#).
- (Linde, 1995) A. Linde, *Lectures on inflationary cosmology.*, in *Particle Physics and Cosmology*, edited by A. Astbury, B. A. Campbell, W. Israel, F. C. Khanna, D. Page, J. L. Pinfold (1995) p. 72, [arXiv:hep-th/9410082](#).
- (Linde, 1982) A. D. Linde, *A new inflationary universe scenario: A possible solution of the horizon, flatness, homogeneity, isotropy and primordial monopole problems*, *Physics Letters B* **108**, 389 (1982).
- (Little & Weinberg, 1994) B. Little, D. H. Weinberg, *Cosmic Voids and Biased Galaxy Formation*, *Monthly Notices of the Royal Astronomical Society* **267**, 605 (1994), [astro-ph/9306006](#).
- (London, 1903) J. London, *The Call of the Wild* (Macmillan, 1903).
- (LSST Science Collaboration, 2012) LSST Science Collaboration, *Large Synoptic Survey Telescope: Dark Energy Science Collaboration*, ArXiv e-prints (2012), [arXiv:1211.0310 \[astro-ph.CO\]](#).
- (LSST Science Collaboration, 2009) LSST Science Collaboration, *LSST Science Book, Version 2.0*, ArXiv e-prints (2009), [arXiv:0912.0201 \[astro-ph.IM\]](#).
- (Lucretius, c. 55 BC) Lucretius, *De Rerum Natura (On the Nature of Things)* (c. 55 BC) Trad. R. E. Latham, J. Godwin, 1951.
- (Manera *et al.*, 2013) M. Manera, R. Scoccimarro, W. J. Percival, L. Samushia, C. K. McBride, A. J. Ross, R. K. Sheth, M. White, B. A. Reid, A. G. Sánchez, R. de Putter, X. Xu, A. A. Berlind, J. Brinkmann, C. Maraston, B. Nichol, F. Montesano, N. Padmanabhan, R. A. Skibba, R. Tojeiro, B. A. Weaver, *The clustering of galaxies in the SDSS-III Baryon Oscillation Spectroscopic Survey: a large sample of mock galaxy catalogues*, *Monthly Notices of the Royal Astronomical Society* **428**, 1036 (2013), [arXiv:1203.6609 \[astro-ph.CO\]](#).
- (Manolakis, Ingle & Kogon, 2000) D. G. Manolakis, V. K. Ingle, S. M. Kogon, *Statistical and Adaptive Signal Processing: Spectral Estimation, Signal Modeling, Adaptive Filtering, and Array Processing* (McGraw-Hill, 2000).
- (March *et al.*, 2011) M. C. March, G. D. Starkman, R. Trotta, P. M. Vaudrevange, *Should we doubt the cosmological constant?*, *Monthly Notices of the Royal Astronomical Society* **410**, 2488 (2011), [arXiv:1005.3655 \[astro-ph.CO\]](#).
- (Marin *et al.*, 2011) J.-M. Marin, P. Pudlo, C. P. Robert, R. Ryder, *Approximate Bayesian Computational methods*, ArXiv e-prints (2011), [arXiv:1101.0955 \[stat.CO\]](#).
- (Martel & Wasserman, 1990) H. Martel, I. Wasserman, *Simulation of cosmological voids in Lambda greater than 0 Friedmann models*, *Astrophysical Journal* **348**, 1 (1990).



- (Martínez & Saar, 2002) V. J. Martínez, E. Saar, *Statistics of the Galaxy Distribution* (Chapman & Hall, 2002).
- (Matarrese, Verde & Heavens, 1997) S. Matarrese, L. Verde, A. F. Heavens, *Large-scale bias in the Universe: bispectrum method*, *Monthly Notices of the Royal Astronomical Society* **290**, 651 (1997), [astro-ph/9706059](#).
- (Mecke, Buchert & Wagner, 1994) K. R. Mecke, T. Buchert, H. Wagner, *Robust Morphological Measures for Large-Scale Structure in the Universe*, *Astronomy and Astrophysics* **288**, 697 (1994), [astro-ph/9312028](#).
- (Melchior *et al.*, 2014) P. Melchior, P. M. Sutter, E. S. Sheldon, E. Krause, B. D. Wandelt, *First measurement of gravitational lensing by cosmic voids in SDSS*, *Monthly Notices of the Royal Astronomical Society* **440**, 2922 (2014), [arXiv:1309.2045](#).
- (Melott, 1993) A. L. Melott, *Improving the reconstruction of the velocity potential and primordial density fluctuations by choice of smoothing windows*, *Astrophysical Journal* **414**, L73 (1993).
- (Melott, Buchert & Weiß, 1995) A. L. Melott, T. Buchert, A. G. Weiß, *Testing higher-order Lagrangian perturbation theory against numerical simulations. 2: Hierarchical models*, *Astronomy and Astrophysics* **294**, 345 (1995), [astro-ph/9404018](#).
- (Melott, Pellman & Shandarin, 1994) A. L. Melott, T. F. Pellman, S. F. Shandarin, *Optimizing the Zeldovich Approximation*, *Monthly Notices of the Royal Astronomical Society* **269**, 626 (1994), [astro-ph/9312044](#).
- (Melott *et al.*, 1983) A. L. Melott, J. Einasto, E. Saar, I. Suisalu, A. A. Klypin, S. F. Shandarin, *Cluster analysis of the nonlinear evolution of large-scale structure in an axion/gravitino/photino-dominated universe*, *Physical Review Letters* **51**, 935 (1983).
- (Mesinger & Furlanetto, 2007) A. Mesinger, S. Furlanetto, *Efficient Simulations of Early Structure Formation and Reionization*, *Astrophysical Journal* **669**, 663 (2007), [arXiv:0704.0946](#).
- (Microsoft Research, 2009) Microsoft Research, *The Fourth Paradigm: Data-intensive Scientific Discovery*, edited by T. Hey, S. Tansley, K. Tolle (Microsoft Research, 2009).
- (Miyazaki *et al.*, 2012) S. Miyazaki, Y. Komiyama, H. Nakaya, Y. Kamata, Y. Doi, T. Hamana, H. Karoji, H. Furusawa, S. Kawanomoto, T. Morokuma, Y. Ishizuka, K. Nariai, Y. Tanaka, F. Uruguchi, Y. Utsumi, Y. Obuchi, Y. Okura, M. Oguri, T. Takata, D. Tomono, T. Kurakami, K. Namikawa, T. Usuda, H. Yamanoi, T. Terai, H. Uekiyo, Y. Yamada, M. Koike, H. Aihara, Y. Fujimori, S. Mineo, H. Miyatake, N. Yasuda, J. Nishizawa, T. Saito, M. Tanaka, T. Uchida, N. Katayama, S.-Y. Wang, H.-Y. Chen, R. Lupton, C. Loomis, S. Bickerton, P. Price, J. Gunn, H. Suzuki, Y. Miyazaki, M. Muramatsu, K. Yamamoto, M. Endo, Y. Ezaki, N. Itoh, Y. Miwa, H. Yokota, T. Matsuda, R. Ebinuma, K. Takeshi, *Hyper Suprime-Cam*, in *Society of Photo-Optical Instrumentation Engineers (SPIE) Conference Series*, Society of Photo-Optical Instrumentation Engineers (SPIE) Conference Series, Vol. 8446 (2012) p. 0.
- (Mo & White, 1996) H. J. Mo, S. D. M. White, *An analytic model for the spatial clustering of dark matter haloes*, *Monthly Notices of the Royal Astronomical Society* **282**, 347 (1996), [astro-ph/9512127](#).
- (Mohayaee *et al.*, 2006) R. Mohayaee, H. Mathis, S. Colombi, J. Silk, *Reconstruction of primordial density fields*, *Monthly Notices of the Royal Astronomical Society* **365**, 939 (2006), [astro-ph/0501217](#).
- (Monaco, Theuns & Taffoni, 2002) P. Monaco, T. Theuns, G. Taffoni, *The pinocchio algorithm: pinpointing orbit-crossing collapsed hierarchical objects in a linear density field*, *Monthly Notices of the Royal Astronomical Society* **331**, 587 (2002), [astro-ph/0109323](#).
- (Monaco *et al.*, 2002) P. Monaco, T. Theuns, G. Taffoni, F. Governato, T. Quinn, J. Stadel, *Predicting the Number, Spatial Distribution, and Merging History of Dark Matter Halos*, *Astrophysical Journal* **564**, 8 (2002), [astro-ph/0109322](#).
- (Monaco *et al.*, 2013) P. Monaco, E. Sefusatti, S. Borgani, M. Crocce, P. Fosalba, R. K. Sheth, T. Theuns, *An accurate tool for the fast generation of dark matter halo catalogues*, *Monthly Notices of the Royal Astronomical Society* **433**, 2389 (2013), [arXiv:1305.1505](#) [[astro-ph.CO](#)].

- (Moutarde *et al.*, 1991) F. Moutarde, J.-M. Alimi, F. R. Bouchet, R. Pellat, A. Ramani, *Precollapse scale invariance in gravitational instability*, *Astrophysical Journal* **382**, 377 (1991).
- (Mukhanov, Feldman & Brandenberger, 1992) V. F. Mukhanov, H. A. Feldman, R. H. Brandenberger, *Theory of cosmological perturbations*, *Physics Reports* **215**, 203 (1992).
- (Müller *et al.*, 2000) V. Müller, S. Arbabi-Bidgoli, J. Einasto, D. Tucker, *Voids in the Las Campanas Redshift Survey versus cold dark matter models*, *Monthly Notices of the Royal Astronomical Society* **318**, 280 (2000), astro-ph/0005063.
- (Munshi & Starobinsky, 1994) D. Munshi, A. A. Starobinsky, *Nonlinear approximations to gravitational instability: A comparison in second-order perturbation theory*, *Astrophysical Journal* **428**, 433 (1994), astro-ph/9311056.
- (Nadathur & Hotchkiss, 2014) S. Nadathur, S. Hotchkiss, *A robust public catalogue of voids and superclusters in the SDSS Data Release 7 galaxy surveys*, *Monthly Notices of the Royal Astronomical Society* **440**, 1248 (2014), arXiv:1310.2791.
- (Nadathur *et al.*, 2014) S. Nadathur, S. Hotchkiss, J. M. Diego, I. T. Iliev, S. Gottlöber, W. A. Watson, G. Yepes, *Self-similarity and universality of void density profiles in simulation and SDSS data*, ArXiv e-prints (2014), arXiv:1407.1295.
- (Narayanan & Weinberg, 1998) V. K. Narayanan, D. H. Weinberg, *Reconstruction Analysis of Galaxy Redshift Surveys: A Hybrid Reconstruction Method*, *Astrophysical Journal* **508**, 440 (1998), arXiv:astro-ph/9806238.
- (Neal, 2011) R. Neal, *Handbook of Markov Chain Monte Carlo* (Chapman & Hall/CRC, 2011) Chap. MCMC Using Hamiltonian Dynamics, pp. 113–162.
- (Neyrinck, 2013) M. C. Neyrinck, *Quantifying distortions of the Lagrangian dark-matter mesh in cosmology*, *Monthly Notices of the Royal Astronomical Society* **428**, 141 (2013), arXiv:1204.1326 [astro-ph.CO].
- (Neyrinck, 2015a) M. C. Neyrinck, *Truthing the stretch: Non-perturbative cosmological realizations with multi-scale spherical collapse*, ArXiv e-prints (2015a), arXiv:1503.07534.
- (Neyrinck, 2008) M. C. Neyrinck, *ZOBOV: a parameter-free void-finding algorithm*, *Monthly Notices of the Royal Astronomical Society* **386**, 2101 (2008), arXiv:0712.3049.
- (Neyrinck, 2015b) M. C. Neyrinck, *Kolmogorov complexity in the Milky Way and its reduction with warm dark matter*, *Monthly Notices of the Royal Astronomical Society* **452**, L26 (2015b), arXiv:1409.0057.
- (Neyrinck, 2012) M. C. Neyrinck, *Origami constraints on the initial-conditions arrangement of dark-matter caustics and streams*, *Monthly Notices of the Royal Astronomical Society* **427**, 494 (2012), arXiv:1202.3364 [astro-ph.CO].
- (Neyrinck & Yang, 2013) M. C. Neyrinck, L. F. Yang, *Ring the initial Universe: the response of overdensity and transformed-density power spectra to initial spikes*, *Monthly Notices of the Royal Astronomical Society* **433**, 1628 (2013), arXiv:1305.1629 [astro-ph.CO].
- (Neyrinck, Szapudi & Szalay, 2011) M. C. Neyrinck, I. Szapudi, A. S. Szalay, *Rejuvenating Power Spectra. II. The Gaussianized Galaxy Density Field*, *Astrophysical Journal* **731**, 116 (2011), arXiv:1009.5680 [astro-ph.CO].
- (Neyrinck, Szapudi & Szalay, 2009) M. C. Neyrinck, I. Szapudi, A. S. Szalay, *Rejuvenating the Matter Power Spectrum: Restoring Information with a Logarithmic Density Mapping*, *Astrophysical Journal Letters* **698**, L90 (2009), arXiv:0903.4693 [astro-ph.CO].
- (Norberg *et al.*, 2001) P. Norberg, C. M. Baugh, E. Hawkins, S. Maddox, J. A. Peacock, S. Cole, C. S. Frenk, J. Bland-Hawthorn, T. Bridges, R. Cannon, M. Colless, C. Collins, W. Couch, G. Dalton, R. De Propris, S. P. Driver, G. Efsthathiou, R. S. Ellis, K. Glazebrook, C. Jackson, O. Lahav, I. Lewis, S. Lumsden, D. Madgwick, B. A. Peterson, W. Sutherland, K. Taylor, *The 2dF Galaxy Redshift Survey: luminosity dependence of galaxy clustering*, *Monthly Notices of the Royal Astronomical Society* **328**, 64 (2001), astro-ph/0105500.

- (Novikov, Colombi & Doré, 2006) D. Novikov, S. Colombi, O. Doré, *Skeleton as a probe of the cosmic web: the two-dimensional case*, *Monthly Notices of the Royal Astronomical Society* **366**, 1201 (2006), [astro-ph/0307003](#).
- (Nuza *et al.*, 2014) S. E. Nuza, F.-S. Kitaura, S. Heß, N. I. Libeskind, V. Müller, *The cosmic web of the Local Universe: cosmic variance, matter content and its relation to galaxy morphology*, *Monthly Notices of the Royal Astronomical Society* **445**, 988 (2014), [arXiv:1406.1004](#).
- (Nyquist, 1928) H. Nyquist, *Certain Topics in Telegraph Transmission Theory*, *Transactions of the American Institute of Electrical Engineers* **47**, 617 (1928).
- (Obreschkow *et al.*, 2013) D. Obreschkow, C. Power, M. Bruderer, C. Bonvin, *A Robust Measure of Cosmic Structure beyond the Power Spectrum: Cosmic Filaments and the Temperature of Dark Matter*, *Astrophysical Journal* **762**, 115 (2013), [arXiv:1211.5213 \[astro-ph.CO\]](#).
- (Padilla, Ceccarelli & Lambas, 2005) N. D. Padilla, L. Ceccarelli, D. G. Lambas, *Spatial and dynamical properties of voids in a  $\Lambda$  cold dark matter universe*, *Monthly Notices of the Royal Astronomical Society* **363**, 977 (2005), [astro-ph/0508297](#).
- (Padmanabhan *et al.*, 2012) N. Padmanabhan, X. Xu, D. J. Eisenstein, R. Scalzo, A. J. Cuesta, K. T. Mehta, E. Kazin, *A 2 per cent distance to  $z = 0.35$  by reconstructing baryon acoustic oscillations - I. Methods and application to the Sloan Digital Sky Survey*, *Monthly Notices of the Royal Astronomical Society* **427**, 2132 (2012), [arXiv:1202.0090](#).
- (Pan *et al.*, 2012) D. C. Pan, M. S. Vogeley, F. Hoyle, Y.-Y. Choi, C. Park, *Cosmic voids in Sloan Digital Sky Survey Data Release 7*, *Monthly Notices of the Royal Astronomical Society* **421**, 926 (2012), [arXiv:1103.4156 \[astro-ph.CO\]](#).
- (Park & Lee, 2007) D. Park, J. Lee, *Void Ellipticity Distribution as a Probe of Cosmology*, *Physical Review Letters* **98**, 081301 (2007), [astro-ph/0610520](#).
- (Park, Kim & Park, 2010) H. Park, J. Kim, C. Park, *Gravitational Potential Environment of Galaxies. I. Simulation*, *Astrophysical Journal* **714**, 207 (2010), [arXiv:1004.0280 \[astro-ph.CO\]](#).
- (Paz, Stasyszyn & Padilla, 2008) D. J. Paz, F. Stasyszyn, N. D. Padilla, *Angular momentum-large-scale structure alignments in  $\Lambda$ CDM models and the SDSS*, *Monthly Notices of the Royal Astronomical Society* **389**, 1127 (2008), [arXiv:0804.4477](#).
- (Paz *et al.*, 2013) D. Paz, M. Lares, L. Ceccarelli, N. Padilla, D. G. Lambas, *Clues on void evolution-II. Measuring density and velocity profiles on SDSS galaxy redshift space distortions*, *Monthly Notices of the Royal Astronomical Society* **436**, 3480 (2013), [arXiv:1306.5799 \[astro-ph.CO\]](#).
- (Peacock, 1999) J. A. Peacock, *Cosmological Physics* (Cambridge University Press, 1999).
- (Peacock & Smith, 2000) J. A. Peacock, R. E. Smith, *Halo occupation numbers and galaxy bias*, *Monthly Notices of the Royal Astronomical Society* **318**, 1144 (2000), [astro-ph/0005010](#).
- (Peacock & Heavens, 1985) J. A. Peacock, A. F. Heavens, *The statistics of maxima in primordial density perturbations*, *Monthly Notices of the Royal Astronomical Society* **217**, 805 (1985).
- (Peacock *et al.*, 2001) J. A. Peacock, S. Cole, P. Norberg, C. M. Baugh, J. Bland-Hawthorn, T. Bridges, R. D. Cannon, M. Colless, C. Collins, W. Couch, G. Dalton, K. Deeley, R. De Propris, S. P. Driver, G. Efstathiou, R. S. Ellis, C. S. Frenk, K. Glazebrook, C. Jackson, O. Lahav, I. Lewis, S. Lumsden, S. Maddox, W. J. Percival, B. A. Peterson, I. Price, W. Sutherland, K. Taylor, *A measurement of the cosmological mass density from clustering in the 2dF Galaxy Redshift Survey*, *Nature* **410**, 169 (2001), [astro-ph/0103143](#).
- (Peebles, 1980) P. J. E. Peebles, *The large-scale structure of the universe* (Princeton University Press, 1980).
- (Peebles, 1984) P. J. E. Peebles, *Dark matter and the origin of galaxies and globular star clusters*, *Astrophysical Journal* **277**, 470 (1984).
- (Peebles, 1976) P. J. E. Peebles, *The Peculiar Velocity Field in the Local Supercluster*, *Astrophysical Journal* **205**, 318 (1976).

- (Peebles, 1982a) P. J. E. Peebles, *Primeval adiabatic perturbations - Effect of massive neutrinos*, *Astrophysical Journal* **258**, 415 (1982a).
- (Peebles, 1982b) P. J. E. Peebles, *Large-scale background temperature and mass fluctuations due to scale-invariant primeval perturbations*, *Astrophysical Journal Letters* **263**, L1 (1982b).
- (Percival, 2005a) W. J. Percival, *Markov chain reconstruction of the 2dF Galaxy Redshift Survey real-space power spectrum*, *Monthly Notices of the Royal Astronomical Society* **356**, 1168 (2005a), [astro-ph/0410631](#).
- (Percival, 2005b) W. J. Percival, *Cosmological structure formation in a homogeneous dark energy background*, *Astronomy and Astrophysics* **443**, 819 (2005b), [astro-ph/0508156](#).
- (Percival, 2014) W. J. Percival, *Large Scale Structure Observations*, in *Lecture Notes of the Les Houches Summer School "Post-Planck Cosmology": Volume 100, July 2013*, edited by C. Deffayet, P. Peter, B. Wandelt, M. Zaldarriaga, L. F. Cugliandolo (2014) [arXiv:1312.5490 \[astro-ph.CO\]](#).
- (Percival & White, 2009) W. J. Percival, M. White, *Testing cosmological structure formation using redshift-space distortions*, *Monthly Notices of the Royal Astronomical Society* **393**, 297 (2009), [arXiv:0808.0003](#).
- (Percival, Verde & Peacock, 2004) W. J. Percival, L. Verde, J. A. Peacock, *Fourier analysis of luminosity-dependent galaxy clustering*, *Monthly Notices of the Royal Astronomical Society* **347**, 645 (2004), [astro-ph/0306511](#).
- (Percival *et al.*, 2001) W. J. Percival, C. M. Baugh, J. Bland-Hawthorn, T. Bridges, R. Cannon, S. Cole, M. Colless, C. Collins, W. Couch, G. Dalton, R. De Propris, S. P. Driver, G. Efstathiou, R. S. Ellis, C. S. Frenk, K. Glazebrook, C. Jackson, O. Lahav, I. Lewis, S. Lumsden, S. Maddox, S. Moody, P. Norberg, J. A. Peacock, B. A. Peterson, W. Sutherland, K. Taylor, *The 2dF Galaxy Redshift Survey: the power spectrum and the matter content of the Universe*, *Monthly Notices of the Royal Astronomical Society* **327**, 1297 (2001), [astro-ph/0105252](#).
- (Percival *et al.*, 2010) W. J. Percival, B. A. Reid, D. J. Eisenstein, N. A. Bahcall, T. Budavari, J. A. Frieman, M. Fukugita, J. E. Gunn, Ž. Ivezić, G. R. Knapp, R. G. Kron, J. Loveday, R. H. Lupton, T. A. McKay, A. Meiksin, R. C. Nichol, A. C. Pope, D. J. Schlegel, D. P. Schneider, D. N. Spergel, C. Stoughton, M. A. Strauss, A. S. Szalay, M. Tegmark, M. S. Vogeley, D. H. Weinberg, D. G. York, I. Zehavi, *Baryon acoustic oscillations in the Sloan Digital Sky Survey Data Release 7 galaxy sample*, *Monthly Notices of the Royal Astronomical Society* **401**, 2148 (2010), [arXiv:0907.1660 \[astro-ph.CO\]](#).
- (Pichon & Bernardeau, 1999) C. Pichon, F. Bernardeau, *Vorticity generation in large-scale structure caustics*, *Astronomy and Astrophysics* **343**, 663 (1999), [astro-ph/9902142](#).
- (Pirates of the Caribbean: At World's End, 2007) Pirates of the Caribbean: At World's End, (2007).
- (Pisani *et al.*, 2014) A. Pisani, G. Lavaux, P. M. Sutter, B. D. Wandelt, *Real-space density profile reconstruction of stacked voids*, *Monthly Notices of the Royal Astronomical Society* **443**, 3238 (2014), [arXiv:1306.3052 \[astro-ph.CO\]](#).
- (Pisani *et al.*, 2015) A. Pisani, P. M. Sutter, N. Hamaus, E. Alizadeh, R. Biswas, B. D. Wandelt, C. M. Hirata, *Counting voids to probe dark energy*, *ArXiv e-prints* (2015), [arXiv:1503.07690](#).
- (Planck Collaboration, 2015) Planck Collaboration, *Planck 2015 results. XVII. Constraints on primordial non-Gaussianity*, *ArXiv e-prints* (2015), [arXiv:1502.01592](#).
- (Planck Collaboration, 2014a) Planck Collaboration, *Planck 2013 results. XIX. The integrated Sachs-Wolfe effect*, *Astronomy and Astrophysics* **571**, A19 (2014a), [arXiv:1303.5079 \[astro-ph.CO\]](#).
- (Planck Collaboration, 2014b) Planck Collaboration, *Planck 2013 results. XXIV. Constraints on primordial non-Gaussianity*, *Astronomy and Astrophysics* **571**, A24 (2014b), [arXiv:1303.5084](#).
- (Platen, van de Weygaert & Jones, 2008) E. Platen, R. van de Weygaert, B. J. T. Jones, *Alignment of voids in the cosmic web*, *Monthly Notices of the Royal Astronomical Society* **387**, 128 (2008), [arXiv:0711.2480](#).



- (Platen, van de Weygaert & Jones, 2007) E. Platen, R. van de Weygaert, B. J. T. Jones, *A cosmic watershed: the WVF void detection technique*, *Monthly Notices of the Royal Astronomical Society* **380**, 551 (2007), [arXiv:0706.2788](#).
- (Plionis & Basilakos, 2002) M. Plionis, S. Basilakos, *The size and shape of local voids*, *Monthly Notices of the Royal Astronomical Society* **330**, 399 (2002), [astro-ph/0106491](#).
- (Poincaré, 1900) H. Poincaré, Letter in *Le Temps* (1900).
- (Pólya, 1954a) G. Pólya, *Mathematics and Plausible Reasoning, Volume 1: Induction and Analogy in Mathematics* (Princeton University Press, 1954).
- (Pólya, 1954b) G. Pólya, *Mathematics and Plausible Reasoning, Volume 2: Patterns of Plausible Inference* (Princeton University Press, 1954).
- (Popper, 1972) K. R. Popper, *Objective Knowledge: An Evolutionary Approach* (Oxford University Press, 1972).
- (Pratchett, 1990) T. Pratchett, *Moving Pictures* (Victor Gollancz, 1990).
- (Protogeros & Scherrer, 1997) Z. A. M. Protogeros, R. J. Scherrer, *Local Lagrangian approximations for the evolution of the density distribution function in large-scale structure*, *Monthly Notices of the Royal Astronomical Society* **284**, 425 (1997), [astro-ph/9603155](#).
- (Prunet *et al.*, 2008) S. Prunet, C. Pichon, D. Aubert, D. Pogosyan, R. Teyssier, S. Gottloeber, *Initial Conditions For Large Cosmological Simulations*, *Astrophysical Journal Supplement* **178**, 179 (2008), [arXiv:0804.3536](#).
- (Pueblas & Scoccimarro, 2009) S. Pueblas, R. Scoccimarro, *Generation of vorticity and velocity dispersion by orbit crossing*, *Physical Review D* **80**, 043504 (2009), [arXiv:0809.4606](#).
- (Rees & Ostriker, 1977) M. J. Rees, J. P. Ostriker, *Cooling, dynamics and fragmentation of massive gas clouds - Clues to the masses and radii of galaxies and clusters*, *Monthly Notices of the Royal Astronomical Society* **179**, 541 (1977).
- (Reeve, 1995) F. D. Reeve, *Coasting*, in *The American Poetry Review*, Vol. 24 (1995) p. 38.
- (Ricciardelli, Quilis & Varela, 2014) E. Ricciardelli, V. Quilis, J. Varela, *On the universality of void density profiles*, *Monthly Notices of the Royal Astronomical Society* **440**, 601 (2014), [arXiv:1402.2976](#) [[astro-ph.CO](#)].
- (Ryden, 1995) B. S. Ryden, *Measuring  $Q_0$  from the Distortion of Voids in Redshift Space*, *Astrophysical Journal* **452**, 25 (1995), [astro-ph/9506028](#).
- (Sahni & Shandarin, 1996) V. Sahni, S. Shandarin, *Accuracy of Lagrangian approximations in voids*, *Monthly Notices of the Royal Astronomical Society* **282**, 641 (1996), [astro-ph/9510142](#).
- (Sahni, Sathyaprakash & Shandarin, 1998) V. Sahni, B. S. Sathyaprakash, S. F. Shandarin, *Shapefinders: A New Shape Diagnostic for Large-Scale Structure*, *Astrophysical Journal Letters* **495**, L5 (1998), [astro-ph/9801053](#).
- (Sahni, Sathyaprakah & Shandarin, 1994) V. Sahni, B. S. Sathyaprakah, S. F. Shandarin, *The evolution of voids in the adhesion approximation*, *Astrophysical Journal* **431**, 20 (1994), [astro-ph/9403044](#).
- (Schaap, 2007) W. E. Schaap, *DTFE: the Delaunay Tessellation Field Estimator*, Ph.D. thesis, University of Groningen (2007).
- (Schaap & van de Weygaert, 2000) W. E. Schaap, R. van de Weygaert, *Continuous fields and discrete samples: reconstruction through Delaunay tessellations*, *Astronomy and Astrophysics* **363**, L29 (2000), [astro-ph/0011007](#).
- (Schechter, 1976) P. Schechter, *An analytic expression for the luminosity function for galaxies.*, *Astrophysical Journal* **203**, 297 (1976).

- (Schlegel *et al.*, 2011) D. Schlegel, F. Abdalla, T. Abraham, C. Ahn, C. Allende Prieto, J. Annis, E. Aubourg, M. Azzaro, S. B. C. Baltay, C. Baugh, C. Bebek, S. Becerril, M. Blanton, A. Bolton, B. Bromley, R. Cahn, P. . Carton, J. L. Cervantes-Cota, Y. Chu, M. Cortes, K. Dawson, A. Dey, M. Dickinson, H. T. Diehl, P. Doel, A. Ealet, J. Edelstein, D. Eppelle, S. Escoffier, A. Evrard, L. Faccioli, C. Frenk, M. Geha, D. Gerdes, P. Gondolo, A. Gonzalez-Arroyo, B. Grossan, T. Heckman, H. Heetderks, S. Ho, K. Honscheid, D. Huterer, O. Ilbert, I. Ivans, P. Jelinsky, Y. Jing, D. Joyce, R. Kennedy, S. Kent, D. Kieda, A. Kim, C. Kim, J. . Kneib, X. Kong, A. Kosowsky, K. Krishnan, O. Lahav, M. Lampton, S. LeBohec, V. Le Brun, M. Levi, C. Li, M. Liang, H. Lim, W. Lin, E. Linder, W. Lorenzon, A. de la Macorra, C. Magneville, R. Malina, C. Marinoni, V. Martinez, S. Majewski, T. Matheson, R. McCloskey, P. McDonald, T. McKay, J. McMahon, B. Menard, J. Miralda-Escude, M. Modjaz, A. Montero-Dorta, I. Morales, N. Mostek, J. Newman, R. Nichol, P. Nugent, K. Olsen, N. Padmanabhan, N. Palanque-Delabrouille, I. Park, J. Peacock, W. Percival, S. Perlmutter, C. Peroux, P. Petitjean, F. Prada, E. Prieto, J. Prochaska, K. Reil, C. Rockosi, N. Roe, E. Rollinde, A. Roodman, N. Ross, G. Rudnick, V. Ruhlmann-Kleider, J. Sanchez, D. Sawyer, C. Schmid, M. Schubnell, R. Scoccimarro, U. Seljak, H. Seo, E. Sheldon, M. Sholl, R. Shulte-Ladbeck, A. Slosar, D. S. Smith, G. Smoot, W. Springer, A. Stril, A. S. Szalay, C. Tao, G. Tarle, E. Taylor, A. Tilquin, J. Tinker, F. Valdes, J. Wang, T. Wang, B. A. Weaver, D. Weinberg, M. White, M. Wood-Vasey, J. Yang, X. Y. C. Yeche, N. Zakamska, A. Zentner, C. Zhai, P. Zhang, *The BigBOSS Experiment*, ArXiv e-prints (2011), [arXiv:1106.1706 \[astro-ph.IM\]](#).
- (Schmittfull, Baldauf & Seljak, 2015) M. Schmittfull, T. Baldauf, U. Seljak, *Near optimal bispectrum estimators for large-scale structure*, *Physical Review D* **91**, 043530 (2015), [arXiv:1411.6595](#).
- (Schuecker & Ott, 1991) P. Schuecker, H.-A. Ott, *Scales of structures and homogeneity in the universe*, *Astrophysical Journal Letters* **378**, L1 (1991).
- (Scoccimarro, 1997) R. Scoccimarro, *Cosmological Perturbations: Entering the Nonlinear Regime*, *Astrophysical Journal* **487**, 1 (1997), [astro-ph/9612207](#).
- (Scoccimarro, 1998) R. Scoccimarro, *Transients from initial conditions: a perturbative analysis*, *Monthly Notices of the Royal Astronomical Society* **299**, 1097 (1998), [astro-ph/9711187](#).
- (Scoccimarro, 2000) R. Scoccimarro, *The Bispectrum: From Theory to Observations*, *Astrophysical Journal* **544**, 597 (2000), [astro-ph/0004086](#).
- (Scoccimarro & Sheth, 2002) R. Scoccimarro, R. K. Sheth, *PTHALOS: a fast method for generating mock galaxy distributions*, *Monthly Notices of the Royal Astronomical Society* **329**, 629 (2002), [astro-ph/0106120](#).
- (Scoccimarro *et al.*, 2001) R. Scoccimarro, H. A. Feldman, J. N. Fry, J. A. Frieman, *The Bispectrum of IRAS Redshift Catalogs*, *Astrophysical Journal* **546**, 652 (2001), [astro-ph/0004087](#).
- (Sefusatti & Komatsu, 2007) E. Sefusatti, E. Komatsu, *Bispectrum of galaxies from high-redshift galaxy surveys: Primordial non-Gaussianity and nonlinear galaxy bias*, *Physical Review D* **76**, 083004 (2007), [arXiv:0705.0343](#).
- (Seljak, 2000) U. Seljak, *Analytic model for galaxy and dark matter clustering*, *Monthly Notices of the Royal Astronomical Society* **318**, 203 (2000), [astro-ph/0001493](#).
- (Seljak & Zaldarriaga, 1996) U. Seljak, M. Zaldarriaga, *A Line-of-Sight Integration Approach to Cosmic Microwave Background Anisotropies*, *Astrophysical Journal* **469**, 437 (1996), [astro-ph/9603033](#).
- (Senatore & Zaldarriaga, 2014) L. Senatore, M. Zaldarriaga, *The IR-resummed Effective Field Theory of Large Scale Structures*, ArXiv e-prints (2014), [arXiv:1404.5954](#).
- (Service, 1907) R. W. Service, *The Spell of the Yukon*, in *Songs of a Sourdough* (1907).
- (Shandarin & Zel'dovich, 1989) S. F. Shandarin, Y. B. Zel'dovich, *The large-scale structure of the universe: Turbulence, intermittency, structures in a self-gravitating medium*, *Reviews of Modern Physics* **61**, 185 (1989).
- (Shandarin, Habib & Heitmann, 2012) S. Shandarin, S. Habib, K. Heitmann, *Cosmic web, multistream flows, and tessellations*, *Physical Review D* **85**, 083005 (2012), [arXiv:1111.2366 \[astro-ph.CO\]](#).



- (Shandarin *et al.*, 2006) S. Shandarin, H. A. Feldman, K. Heitmann, S. Habib, *Shapes and sizes of voids in the Lambda cold dark matter universe: excursion set approach*, *Monthly Notices of the Royal Astronomical Society* **367**, 1629 (2006), [astro-ph/0509858](#).
- (Shannon, 1948) C. E. Shannon, *A Mathematical Theory of Communication*, *Bell System Technical Journal* **27**, 379 (1948).
- (Shannon, 1949) C. E. Shannon, *Communication in the Presence of Noise*, *Proc. Institute of Radio Engineers* **37**, 10 (1949).
- (Shectman *et al.*, 1996) S. A. Shectman, S. D. Landy, A. Oemler, D. L. Tucker, H. Lin, R. P. Kirshner, P. L. Schechter, *The Las Campanas Redshift Survey*, *Astrophysical Journal* **470**, 172 (1996), [astro-ph/9604167](#).
- (Shen *et al.*, 2006) J. Shen, T. Abel, H. J. Mo, R. K. Sheth, *An Excursion Set Model of the Cosmic Web: The Abundance of Sheets, Filaments, and Halos*, *Astrophysical Journal* **645**, 783 (2006), [astro-ph/0511365](#).
- (Sheth & van de Weygaert, 2004) R. K. Sheth, R. van de Weygaert, *A hierarchy of voids: much ado about nothing*, *Monthly Notices of the Royal Astronomical Society* **350**, 517 (2004), [astro-ph/0311260](#).
- (Shi, Wang & Mo, 2015) J. Shi, H. Wang, H. Mo, *Flow Patterns around Dark Matter Halos: the Link between Halo Dynamical Properties and Large Scale Tidal Field*, *ArXiv e-prints* (2015), [arXiv:1501.07764](#).
- (Shirata *et al.*, 2007) A. Shirata, Y. Suto, C. Hikage, T. Shiromizu, N. Yoshida, *Galaxy clustering constraints on deviations from Newtonian gravity at cosmological scales. II. Perturbative and numerical analyses of power spectrum and bispectrum*, *Physical Review D* **76**, 044026 (2007), [arXiv:0705.1311](#).
- (Shoji & Lee, 2012) M. Shoji, J. Lee, *Voids in Redshift Space*, *ArXiv e-prints* (2012), [arXiv:1203.0869 \[astro-ph.CO\]](#).
- (Short & Coles, 2006a) C. J. Short, P. Coles, *Gravitational instability via the Schrödinger equation*, *Journal of Cosmology and Astroparticle Physics* **12**, 12 (2006a), [arXiv:astro-ph/0605012](#).
- (Short & Coles, 2006b) C. J. Short, P. Coles, *Wave mechanics and the adhesion approximation*, *Journal of Cosmology and Astroparticle Physics* **12**, 16 (2006b), [arXiv:astro-ph/0605013](#).
- (Silk, 1968) J. Silk, *Cosmic Black-Body Radiation and Galaxy Formation*, *Astrophysical Journal* **151**, 459 (1968).
- (Silk, 1977) J. Silk, *On the fragmentation of cosmic gas clouds. I - The formation of galaxies and the first generation of stars*, *Astrophysical Journal* **211**, 638 (1977).
- (Somerville *et al.*, 2001) R. S. Somerville, G. Lemson, Y. Sigad, A. Dekel, G. Kauffmann, S. D. M. White, *Non-linear stochastic galaxy biasing in cosmological simulations*, *Monthly Notices of the Royal Astronomical Society* **320**, 289 (2001), [astro-ph/9912073](#).
- (Sousbie, 2011) T. Sousbie, *The persistent cosmic web and its filamentary structure - I. Theory and implementation*, *Monthly Notices of the Royal Astronomical Society* **414**, 350 (2011), [arXiv:1009.4015 \[astro-ph.CO\]](#).
- (Sousbie, Pichon & Kawahara, 2011) T. Sousbie, C. Pichon, H. Kawahara, *The persistent cosmic web and its filamentary structure - II. Illustrations*, *Monthly Notices of the Royal Astronomical Society* **414**, 384 (2011), [arXiv:1009.4014 \[astro-ph.CO\]](#).
- (Sousbie *et al.*, 2008) T. Sousbie, C. Pichon, S. Colombi, D. Novikov, D. Pogosyan, *The 3D skeleton: tracing the filamentary structure of the Universe*, *Monthly Notices of the Royal Astronomical Society* **383**, 1655 (2008), [arXiv:0707.3123](#).
- (Spergel *et al.*, 2013) D. Spergel, N. Gehrels, J. Breckinridge, M. Donahue, A. Dressler, B. S. Gaudi, T. Greene, O. Guyon, C. Hirata, J. Kalirai, N. J. Kasdin, W. Moos, S. Perlmutter, M. Postman, B. Rauscher, J. Rhodes, Y. Wang, D. Weinberg, J. Centrella, W. Traub, C. Baltay, J. Colbert, D. Bennett, A. Kiessling, B. Macintosh, J. Merten, M. Mortonson, M. Penny, E. Rozo, D. Savransky, K. Stapelfeldt, Y. Zu, C. Baker, E. Cheng, D. Content, J. Dooley, M. Foote, R. Goullioud, K. Grady, C. Jackson, J. Kruk, M. Levine, M. Melton, C. Peddie, J. Ruffa, S. Shaklan, *Wide-Field InfraRed Survey Telescope-Astrophysics Focused Telescope Assets WFIRST-AFTA Final Report*, *ArXiv e-prints* (2013), [arXiv:1305.5422 \[astro-ph.IM\]](#).

- (Spolyar, Sahlén & Silk, 2013) D. Spolyar, M. Sahlén, J. Silk, *Topology and Dark Energy: Testing Gravity in Voids*, *Physical Review Letters* **111**, 241103 (2013), arXiv:1304.5239 [astro-ph.CO].
- (Springel, 2005) V. Springel, *The cosmological simulation code GADGET-2*, *Monthly Notices of the Royal Astronomical Society* **364**, 1105 (2005), astro-ph/0505010.
- (Springel, 2014) V. Springel, *High performance computing and numerical modelling*, in *Lecture notes given at the 43rd Saas Fee Advanced School, March 11-16, 2013, Villars-sur-Ollon, Switzerland* (2014) arXiv:1412.5187.
- (Springel, Yoshida & White, 2001) V. Springel, N. Yoshida, S. D. M. White, *GADGET: a code for collisionless and gasdynamical cosmological simulations*, *New Astronomy* **6**, 79 (2001), astro-ph/0003162.
- (Star Trek: First Contact, 1996) Star Trek: First Contact, (1996).
- (Starkman, Trotta & Vaudrevange, 2008) G. D. Starkman, R. Trotta, P. M. Vaudrevange, *Introducing doubt in Bayesian model comparison*, *ArXiv e-prints* (2008), 0811.2415.
- (Starobinsky, 1982) A. A. Starobinsky, *Dynamics of phase transition in the new inflationary universe scenario and generation of perturbations*, *Physics Letters B* **117**, 175 (1982).
- (Stoica, Martínez & Saar, 2010) R. S. Stoica, V. J. Martínez, E. Saar, *Filaments in observed and mock galaxy catalogues*, *Astronomy and Astrophysics* **510**, A38 (2010), arXiv:0912.2021 [astro-ph.CO].
- (Stoica, Martínez & Saar, 2007) R. S. Stoica, V. J. Martínez, E. Saar, *A three-dimensional object point process for detection of cosmic filaments.*, *Journal of the Royal Statistical Society: Series C (Applied Statistics)* **56** (4), 459-477 **56**, 1 (2007).
- (Stoica et al., 2005) R. S. Stoica, V. J. Martínez, J. Mateu, E. Saar, *Detection of cosmic filaments using the Candy model*, *Astronomy and Astrophysics* **434**, 423 (2005), astro-ph/0405370.
- (Stover, 2003) M. Stover, *Star Wars: Shatterpoint* (Del Rey, 2003).
- (Strauss et al., 2002) M. A. Strauss, D. H. Weinberg, R. H. Lupton, V. K. Narayanan, J. Annis, M. Bernardi, M. Blanton, S. Burles, A. J. Connolly, J. Dalcanton, M. Doi, D. Eisenstein, J. A. Frieman, M. Fukugita, J. E. Gunn, Ž. Ivezić, S. Kent, R. S. J. Kim, G. R. Knapp, R. G. Kron, J. A. Munn, H. J. Newberg, R. C. Nichol, S. Okamura, T. R. Quinn, M. W. Richmond, D. J. Schlegel, K. Shimasaku, M. SubbaRao, A. S. Szalay, D. Vanden Berk, M. S. Vogeley, B. Yanny, N. Yasuda, D. G. York, I. Zehavi, *Spectroscopic Target Selection in the Sloan Digital Sky Survey: The Main Galaxy Sample*, *Astronomical Journal* **124**, 1810 (2002), astro-ph/0206225.
- (Sutter et al., 2015a) P. M. Sutter, E. Carlesi, B. D. Wandelt, A. Knebe, *On the observability of coupled dark energy with cosmic voids*, *Monthly Notices of the Royal Astronomical Society* **446**, L1 (2015a), arXiv:1406.0511.
- (Sutter et al., 2014a) P. M. Sutter, A. Pisani, B. D. Wandelt, D. H. Weinberg, *A measurement of the Alcock-Paczynski effect using cosmic voids in the SDSS*, *Monthly Notices of the Royal Astronomical Society* **443**, 2983 (2014a), arXiv:1404.5618.
- (Sutter et al., 2012a) P. M. Sutter, G. Lavaux, B. D. Wandelt, D. H. Weinberg, *A First Application of the Alcock-Paczynski Test to Stacked Cosmic Voids*, *Astrophysical Journal* **761**, 187 (2012a), arXiv:1208.1058 [astro-ph.CO].
- (Sutter et al., 2012b) P. M. Sutter, G. Lavaux, B. D. Wandelt, D. H. Weinberg, *A Public Void Catalog from the SDSS DR7 Galaxy Redshift Surveys Based on the Watershed Transform*, *Astrophysical Journal* **761**, 44 (2012b), arXiv:1207.2524 [astro-ph.CO].
- (Sutter et al., 2014b) P. M. Sutter, G. Lavaux, B. D. Wandelt, D. H. Weinberg, M. S. Warren, *The dark matter of galaxy voids*, *Monthly Notices of the Royal Astronomical Society* **438**, 3177 (2014b), arXiv:1311.3301 [astro-ph.CO].
- (Sutter et al., 2014c) P. M. Sutter, G. Lavaux, N. Hamaus, B. D. Wandelt, D. H. Weinberg, M. S. Warren, *Sparse sampling, galaxy bias, and voids*, *Monthly Notices of the Royal Astronomical Society* **442**, 462 (2014c), arXiv:1309.5087.

- (Sutter *et al.*, 2014d) P. M. Sutter, G. Lavaux, B. D. Wandelt, D. H. Weinberg, M. S. Warren, A. Pisani, *Voids in the SDSS DR9: observations, simulations, and the impact of the survey mask*, *Monthly Notices of the Royal Astronomical Society* **442**, 3127 (2014d), arXiv:1310.7155.
- (Sutter *et al.*, 2015b) P. M. Sutter, G. Lavaux, N. Hamaus, A. Pisani, B. D. Wandelt, M. Warren, F. Villaescusa-Navarro, P. Zivick, Q. Mao, B. B. Thompson, *VIDE: The Void IDentification and Examination toolkit*, *Astronomy and Computing* **9**, 1 (2015b), arXiv:1406.1191.
- (Szalay, 2014) A. Szalay, *From Genes to Stars: the Fourth Paradigm of Science* (Public conference given at the Academia das Ciências de Lisboa on May 27th, 2014).
- (Tadros *et al.*, 1999) H. Tadros, W. E. Ballinger, A. N. Taylor, A. F. Heavens, G. Efstathiou, W. Saunders, C. S. Frenk, O. Keeble, R. McMahon, S. J. Maddox, S. Oliver, M. Rowan-Robinson, W. J. Sutherland, S. D. M. White, *Spherical harmonic analysis of the PSCz galaxy catalogue: redshift distortions and the real-space power spectrum*, *Monthly Notices of the Royal Astronomical Society* **305**, 527 (1999), astro-ph/9901351.
- (Taffoni, Monaco & Theuns, 2002) G. Taffoni, P. Monaco, T. Theuns, *PINOCCHIO and the hierarchical build-up of dark matter haloes*, *Monthly Notices of the Royal Astronomical Society* **333**, 623 (2002), astro-ph/0109324.
- (Takada *et al.*, 2014) M. Takada, R. S. Ellis, M. Chiba, J. E. Greene, H. Aihara, N. Arimoto, K. Bundy, J. Cohen, O. Doré, G. Graves, J. E. Gunn, T. Heckman, C. M. Hirata, P. Ho, J.-P. Kneib, O. L. Fèvre, L. Lin, S. More, H. Murayama, T. Nagao, M. Ouchi, M. Seiffert, J. D. Silverman, L. Sodré, D. N. Spergel, M. A. Strauss, H. Sugai, Y. Suto, H. Takami, R. Wyse, *Extragalactic science, cosmology, and Galactic archaeology with the Subaru Prime Focus Spectrograph*, *Publications of the Astronomical Society of Japan* **66**, R1 (2014), arXiv:1206.0737.
- (Taoso, Bertone & Masiero, 2008) M. Taoso, G. Bertone, A. Masiero, *Dark matter candidates: a ten-point test*, *Journal of Cosmology and Astroparticle Physics* **3**, 022 (2008), arXiv:0711.4996.
- (Tassev & Zaldarriaga, 2012a) S. Tassev, M. Zaldarriaga, *The mildly non-linear regime of structure formation*, *Journal of Cosmology and Astroparticle Physics* **4**, 013 (2012a), arXiv:1109.4939 [astro-ph.CO].
- (Tassev & Zaldarriaga, 2012b) S. Tassev, M. Zaldarriaga, *Towards an optimal reconstruction of baryon oscillations*, *Journal of Cosmology and Astroparticle Physics* **10**, 006 (2012b), arXiv:1203.6066 [astro-ph.CO].
- (Tassev & Zaldarriaga, 2012c) S. Tassev, M. Zaldarriaga, *Estimating CDM particle trajectories in the mildly non-linear regime of structure formation. Implications for the density field in real and redshift space*, *Journal of Cosmology and Astroparticle Physics* **12**, 011 (2012c), arXiv:1203.5785 [astro-ph.CO].
- (Tassev, Zaldarriaga & Eisenstein, 2013) S. Tassev, M. Zaldarriaga, D. J. Eisenstein, *Solving large scale structure in ten easy steps with COLA*, *Journal of Cosmology and Astroparticle Physics* **6**, 036 (2013), arXiv:1301.0322 [astro-ph.CO].
- (Tassev *et al.*, 2015) S. Tassev, D. J. Eisenstein, B. D. Wandelt, M. Zaldarriaga, *sCOLA: The N-body COLA Method Extended to the Spatial Domain*, ArXiv e-prints (2015), arXiv:1502.07751.
- (Taylor, Ashdown & Hobson, 2008) J. F. Taylor, M. A. J. Ashdown, M. P. Hobson, *Fast optimal CMB power spectrum estimation with Hamiltonian sampling*, *Monthly Notices of the Royal Astronomical Society* **389**, 1284 (2008), arXiv:0708.2989.
- (Tegmark *et al.*, 2004) M. Tegmark, M. R. Blanton, M. A. Strauss, F. Hoyle, D. Schlegel, R. Scoccimarro, M. S. Vogeley, D. H. Weinberg, I. Zehavi, A. Berlind, T. Budavari, A. Connolly, D. J. Eisenstein, D. Finkbeiner, J. A. Frieman, J. E. Gunn, A. J. S. Hamilton, L. Hui, B. Jain, D. Johnston, S. Kent, H. Lin, R. Nakajima, R. C. Nichol, J. P. Ostriker, A. Pope, R. Scranton, U. Seljak, R. K. Sheth, A. Stebbins, A. S. Szalay, I. Szapudi, L. Verde, Y. Xu, J. Annis, N. A. Bahcall, J. Brinkmann, S. Burles, F. J. Castander, I. Csabai, J. Loveday, M. Doi, M. Fukugita, J. R. Gott, III, G. Hennessy, D. W. Hogg, Ž. Ivezić, G. R. Knapp, D. Q. Lamb, B. C. Lee, R. H. Lupton, T. A. McKay, P. Kunszt, J. A. Munn, L. O’Connell, J. Peoples, J. R. Pier, M. Richmond, C. Rockosi, D. P. Schneider, C. Stoughton, D. L. Tucker, D. E. Vanden Berk, B. Yanny, D. G. York, SDSS Collaboration, *The Three-Dimensional Power Spectrum of Galaxies from the Sloan Digital Sky Survey*, *Astrophysical Journal* **606**, 702 (2004), astro-ph/0310725.

- (Tempel, Stoica & Saar, 2013) E. Tempel, R. S. Stoica, E. Saar, *Evidence for spin alignment of spiral and elliptical/S0 galaxies in filaments*, *Monthly Notices of the Royal Astronomical Society* **428**, 1827 (2013), arXiv:1207.0068 [astro-ph.CO].
- (Tempel *et al.*, 2014) E. Tempel, R. S. Stoica, V. J. Martínez, L. J. Liivamägi, G. Castellan, E. Saar, *Detecting filamentary pattern in the cosmic web: a catalogue of filaments for the SDSS*, *Monthly Notices of the Royal Astronomical Society* **438**, 3465 (2014), arXiv:1308.2533 [astro-ph.CO].
- (Teyssier, 2014) R. Teyssier, *Computational cosmology*, in *Lecture Notes of the Les Houches Summer School “Post-Planck Cosmology”: Volume 100, July 2013*, edited by C. Deffayet, P. Peter, B. Wandelt, M. Zaldarriaga, L. F. Cugliandolo (2014).
- (Tinker & Conroy, 2009) J. L. Tinker, C. Conroy, *The Void Phenomenon Explained*, *Astrophysical Journal* **691**, 633 (2009), arXiv:0804.2475.
- (Tolkien, 1954) J. R. R. Tolkien, *The Lord of the Rings – The Fellowship of the Ring* (George Allen & Unwin, 1954).
- (Trodden & Carroll, 2004) M. Trodden, S. M. Carroll, *TASI Lectures: Introduction to Cosmology*, *Astronomy* (2004), arXiv:astro-ph/0401547.
- (Trotta, 2008) R. Trotta, *Bayes in the sky: Bayesian inference and model selection in cosmology*, *Contemporary Physics* **49**, 71 (2008), arXiv:0803.4089.
- (Valageas, 2007) P. Valageas, *Large-N expansions applied to gravitational clustering*, *Astronomy and Astrophysics* **465**, 725 (2007), astro-ph/0611849.
- (Valageas & Bernardeau, 2011) P. Valageas, F. Bernardeau, *Density fields and halo mass functions in the geometrical adhesion toy model*, *Physical Review D* **83**, 043508 (2011), arXiv:1009.1974 [astro-ph.CO].
- (van de Weygaert & Schaap, 2009) R. van de Weygaert, W. Schaap, *The Cosmic Web: Geometric Analysis*, in *Data Analysis in Cosmology*, *Lecture Notes in Physics*, Berlin Springer Verlag, Vol. 665, edited by V. J. Martínez, E. Saar, E. Martínez-González, M.-J. Pons-Bordería (2009) pp. 291–413.
- (van de Weygaert & Platen, 2011) R. van de Weygaert, E. Platen, *Cosmic Voids: Structure, Dynamics and Galaxies*, *International Journal of Modern Physics Conference Series* **1**, 41 (2011), arXiv:0912.2997 [astro-ph.CO].
- (van de Weygaert & van Kampen, 1993) R. van de Weygaert, E. van Kampen, *Voids in Gravitational Instability Scenarios - Part One - Global Density and Velocity Fields in an Einstein - De-Sitter Universe*, *Monthly Notices of the Royal Astronomical Society* **263**, 481 (1993).
- (van de Weygaert & Bertschinger, 1996) R. van de Weygaert, E. Bertschinger, *Peak and gravity constraints in Gaussian primordial density fields: An application of the Hoffman-Ribak method*, *Monthly Notices of the Royal Astronomical Society* **281**, 84 (1996), astro-ph/9507024.
- (Verde, 2010) L. Verde, *Statistical Methods in Cosmology*, in *Lecture Notes in Physics, Berlin Springer Verlag*, *Lecture Notes in Physics*, Berlin Springer Verlag, Vol. 800, edited by G. Wolschin (2010) pp. 147–177, arXiv:0911.3105.
- (Verde *et al.*, 1998) L. Verde, A. F. Heavens, S. Matarrese, L. Moscardini, *Large-scale bias in the Universe - II. Redshift-space bispectrum*, *Monthly Notices of the Royal Astronomical Society* **300**, 747 (1998), astro-ph/9806028.
- (Verde *et al.*, 2002) L. Verde, A. F. Heavens, W. J. Percival, S. Matarrese, C. M. Baugh, J. Bland-Hawthorn, T. Bridges, R. Cannon, S. Cole, M. Colless, C. Collins, W. Couch, G. Dalton, R. De Propris, S. P. Driver, G. Efstathiou, R. S. Ellis, C. S. Frenk, K. Glazebrook, C. Jackson, O. Lahav, I. Lewis, S. Lumsden, S. Maddox, D. Madgwick, P. Norberg, J. A. Peacock, B. A. Peterson, W. Sutherland, K. Taylor, *The 2dF Galaxy Redshift Survey: the bias of galaxies and the density of the Universe*, *Monthly Notices of the Royal Astronomical Society* **335**, 432 (2002), arXiv:astro-ph/0112161.



- (Verdinelli & Wasserman, 1995) I. Verdinelli, L. Wasserman, *Computing Bayes Factors Using a Generalization of the Savage-Dickey Density Ratio*, *Journal of the American Statistical Association* **90**, 614 (1995).
- (Verleysen & François, 2005) M. Verleysen, D. François, *The curse of dimensionality in data mining and time series prediction*, in *Computational Intelligence and Bioinspired Systems* (Springer, 2005) pp. 758–770.
- (Vettolani *et al.*, 1997) G. Vettolani, E. Zucca, G. Zamorani, A. Cappi, R. Merighi, M. Mignoli, G. M. Stirpe, H. MacGillivray, C. Collins, C. Balkowski, V. Cayatte, S. Maurogordato, D. Proust, G. Chincarini, L. Guzzo, D. Maccagni, R. Scaramella, A. Blanchard, M. Ramella, *The ESO Slice Project (ESP) galaxy redshift survey. I. Description and first results.*, *Astronomy and Astrophysics* **325**, 954 (1997), [astro-ph/9704097](#).
- (Viel, Colberg & Kim, 2008) M. Viel, J. M. Colberg, T.-S. Kim, *On the importance of high-redshift intergalactic voids*, *Monthly Notices of the Royal Astronomical Society* **386**, 1285 (2008), [arXiv:0801.1105](#).
- (Vogelsberger *et al.*, 2014) M. Vogelsberger, S. Genel, V. Springel, P. Torrey, D. Sijacki, D. Xu, G. Snyder, S. Bird, D. Nelson, L. Hernquist, *Properties of galaxies reproduced by a hydrodynamic simulation*, *Nature* **509**, 177 (2014), [arXiv:1405.1418](#).
- (Wandelt, 2013) B. D. Wandelt, *Astrostatistical Challenges for the New Astronomy* (Springer, 2013) Chap. Gaussian Random Fields in Cosmostatistics, pp. 87–105.
- (Wandelt, Larson & Lakshminarayanan, 2004) B. D. Wandelt, D. L. Larson, A. Lakshminarayanan, *Global, exact cosmic microwave background data analysis using Gibbs sampling*, *Physical Review D* **70**, 083511 (2004), [astro-ph/0310080](#).
- (Wang *et al.*, 2012) H. Wang, H. J. Mo, X. Yang, F. C. van den Bosch, *Reconstructing the cosmic velocity and tidal fields with galaxy groups selected from the Sloan Digital Sky Survey*, *Monthly Notices of the Royal Astronomical Society* **420**, 1809 (2012), [arXiv:1108.1008 \[astro-ph.CO\]](#).
- (Wang *et al.*, 2013) H. Wang, H. J. Mo, X. Yang, F. C. van den Bosch, *Reconstructing the Initial Density Field of the Local Universe: Methods and Tests with Mock Catalogs*, *Astrophysical Journal* **772**, 63 (2013), [arXiv:1301.1348 \[astro-ph.CO\]](#).
- (Weinberg, 1992) D. H. Weinberg, *Reconstructing primordial density fluctuations. I - Method*, *Monthly Notices of the Royal Astronomical Society* **254**, 315 (1992).
- (Weinberg & Gunn, 1990) D. H. Weinberg, J. E. Gunn, *Large-scale Structure and the Adhesion Approximation*, *Monthly Notices of the Royal Astronomical Society* **247**, 260 (1990).
- (Welker *et al.*, 2014) C. Welker, J. Devriendt, Y. Dubois, C. Pichon, S. Peirani, *Mergers drive spin swings along the cosmic web*, *Monthly Notices of the Royal Astronomical Society* **445**, L46 (2014), [arXiv:1403.2728 \[astro-ph.CO\]](#).
- (Weyant, Schafer & Wood-Vasey, 2013) A. Weyant, C. Schafer, W. M. Wood-Vasey, *Likelihood-free Cosmological Inference with Type Ia Supernovae: Approximate Bayesian Computation for a Complete Treatment of Uncertainty*, *Astrophysical Journal* **764**, 116 (2013), [arXiv:1206.2563 \[astro-ph.CO\]](#).
- (White & Rees, 1978) S. D. M. White, M. J. Rees, *Core condensation in heavy halos - A two-stage theory for galaxy formation and clustering*, *Monthly Notices of the Royal Astronomical Society* **183**, 341 (1978).
- (Wolpert & Macready, 1997) D. H. Wolpert, W. G. Macready, *No free lunch theorems for optimization*, *IEEE Transactions on Evolutionary Computation* **1**, 67 (1997).
- (Wolstenhulme, Bonvin & Obreschkow, 2014) R. Wolstenhulme, C. Bonvin, D. Obreschkow, *Three-point phase correlations: A new measure of non-linear large-scale structure*, *ArXiv e-prints* (2014), [arXiv:1409.3007](#).
- (Yan, Fan & White, 2012) H. Yan, Z. Fan, S. D. M. White, *On the Tidal Dependence of Galaxy Properties*, *ArXiv e-prints* (2012), [arXiv:1203.1225 \[astro-ph.GA\]](#).
- (York *et al.*, 2000) D. G. York, J. Adelman, J. E. Anderson, Jr., et al., *The Sloan Digital Sky Survey: Technical Summary*, *Astronomical Journal* **120**, 1579 (2000), [astro-ph/0006396](#).

- (Yoshisato *et al.*, 2006) A. Yoshisato, M. Morikawa, N. Gouda, H. Mouri, *Why is the Zel'dovich Approximation So Accurate?*, *Astrophysical Journal* **637**, 555 (2006), [astro-ph/0510107](#).
- (Yu *et al.*, 2011) Y. Yu, P. Zhang, W. Lin, W. Cui, J. N. Fry, *Gaussianizing the non-Gaussian lensing convergence field: The performance of the Gaussianization*, *Physical Review D* **84**, 023523 (2011), [arXiv:1103.2858 \[astro-ph.CO\]](#).
- (Yu *et al.*, 2012) Y. Yu, P. Zhang, W. Lin, W. Cui, J. N. Fry, *Gaussianizing the non-Gaussian lensing convergence field II. The applicability to noisy data*, *Physical Review D* **86**, 023515 (2012), [arXiv:1201.4527 \[astro-ph.CO\]](#).
- (Zaroubi, 2002) S. Zaroubi, *Unbiased reconstruction of the large-scale structure*, *Monthly Notices of the Royal Astronomical Society* **331**, 901 (2002), [astro-ph/0010561](#).
- (Zel'dovich & Novikov, 1983) I. B. Zel'dovich, I. D. Novikov, *Chicago, IL, University of Chicago Press, 1983, 751 p. Translation.* (University of Chicago Press, 1983).
- (Zel'dovich, Einasto & Shandarin, 1982) I. B. Zel'dovich, J. Einasto, S. F. Shandarin, *Giant voids in the universe*, *Nature* **300**, 407 (1982).
- (Zel'dovich, 1970) Y. B. Zel'dovich, *Gravitational instability: An approximate theory for large density perturbations.*, *Astronomy and Astrophysics* **5**, 84 (1970).
- (Zhang *et al.*, 2009) Y. Zhang, X. Yang, A. Faltenbacher, V. Springel, W. Lin, H. Wang, *The Spin and Orientation of Dark Matter Halos Within Cosmic Filaments*, *Astrophysical Journal* **706**, 747 (2009), [arXiv:0906.1654 \[astro-ph.GA\]](#).
- (Zhang *et al.*, 2013) Y. Zhang, X. Yang, H. Wang, L. Wang, H. J. Mo, F. C. van den Bosch, *Alignments of Galaxies within Cosmic Filaments from SDSS DR7*, *Astrophysical Journal* **779**, 160 (2013), [arXiv:1309.3847 \[astro-ph.CO\]](#).
- (Zhao *et al.*, 2015) C. Zhao, F.-S. Kitaura, C.-H. Chuang, F. Prada, G. Yepes, C. Tao, *Halo mass distribution reconstruction across the cosmic web*, *ArXiv e-prints* (2015), [arXiv:1501.05520](#).



---

# Index

- N*-body simulation** 4, 12, 25, 29–41, 44, 45, 74, 95–103, 105, 106, 112, 114, 117, 120, 125, 132, 135, 141, 149, 155, 161, 165, 167, 170, 174, 184, 185
- $\Gamma$ -distribution** 71, 72
- $\Lambda$ CDM** lambda cold dark matter 8, 20, 22, 24, 53, 80, 117, 119, 126, 129, 150, 157
- 21 cm surveys** 106
- 2LPT** second-order Lagrangian perturbation theory 24, 29–32, 34, 35, 37–44, 68, 69, 73–75, 80, 81, 83, 86, 87, 89, 91, 96, 98, 99, 101–105, 109–114, 121, 122, 125, 126, 133, 135, 138, 141, 148, 154, 155, 168, 177, 178, 185
- 2LPTRM** second-order Lagrangian perturbation theory remapped 30–32, 34, 35, 103, 104
- 2LPTic** 29, 177
- 3LPT** third-order Lagrangian perturbation theory 41
- ABC** Approximate Bayesian Computation 56
- acceptance rate** 59, 60, 62, 66, 74, 81, 82, 91
- adhesion approximation** 26, 27, 96
- Alcock-Paczynski effect** 2, 9, 126
- aliasing** 31, 169, 170
- ALPT** Augmented Lagrangian perturbation theory 43, 44
- ARES** Algorithm for REconstruction and Sampling 66, 70, 75, 77
- assignment function** 169–171, 173
- auto-correlation function (Markov chain)** 60
- BAO** baryon acoustic oscillations 2, 3, 67, 74, 96, 97, 157, 178
- Bayes factor** 57
- Bayes’ theorem** 51–54, 57, 71
- Bayesian statistics** 4, 49–53, 56, 62, 71, 111, 118, 129, 138, 149, 155
- BBN** Big Bang nucleosynthesis 2
- Bernstein-von Mises theorem** 53
- bias** 2, 34, 52, 62, 66, 68–70, 74, 75, 77, 79–83, 89, 91, 117–119, 121, 125–129, 134, 135, 137, 148, 155, 157
- bispectrum** 15, 34–37, 95, 105, 106, 156
- Blackwell-Rao estimator** 119, 120, 122, 124–127, 129
- Boltzmann constant** 61
- BORG** Bayesian Origin Reconstruction from Galaxies 4, 49, 56, 60, 63, 66–72, 74–77, 79, 80, 82, 86, 89, 91, 92, 109–114, 117, 119–123, 125–129, 131, 133–136, 138, 143, 148, 149, 151, 154–157, 177, 178
- Box-Müller method** 177
- Burgers’ equation** 26, 27
- burn-in** 58, 60, 73–75, 81–83, 91
- canonical distribution** 61, 62
- cdf** cumulative distribution function 97, 100, 101
- CDM** cold dark matter 2, 8, 15, 18, 20, 22, 95, 165
- characteristic function** 161–163
- Cholesky decomposition** 178
- chrono-cosmography** 79, 80, 89, 92, 131, 133, 143, 148, 155, 158
- CiC** cloud-in-cell 29, 31, 34, 68, 73, 74, 101, 113, 138, 170–175, 178, 184, 185
- classical mechanics** 60, 113
- cluster** 4, 29, 37, 38, 40, 44, 45, 75, 91, 92, 96, 99, 100, 103, 111, 118, 126, 131–137, 140–142, 145, 147–152, 154, 156, 179, 181–185
- CMB** cosmic microwave background 10, 52, 62, 75, 118, 129, 133, 156, 157
- CMB lensing** 62, 157
- COLA** COmoving Lagrangian Acceleration 109, 111–114, 133–136, 138, 148, 155, 165–168, 170, 175–177
- comoving coordinates** 10, 16, 22, 23, 25, 37, 40, 68, 74, 75, 86, 89, 90, 92, 106, 147, 166, 182, 185
- compensation** 118, 128, 132, 137
- conditional density contrast** 14
- conditional independence** 11, 71, 75, 121, 124, 161–163

- conditional pdf** 11, 14, 51, 58, 60, 67, 71, 72, 77, 136, 140, 150, 163
- conformal expansion rate** 8
- conformal time** 8, 16, 22, 23, 182
- conservative map** 151, 152, 154
- constrained likelihood** 53
- constrained simulation** 109, 110, 117, 119, 121, 122, 128, 131, 133, 134, 140, 148, 155, 178
- continuity equation** 17, 19, 25
- Cosmic Emulator** 30, 31
- cosmic time** 8
- cosmic variance** 32, 34, 118
- cosmic web** 1, 4, 29, 40, 75, 91, 110, 118, 121, 123, 131–135, 140, 147–149, 154–156, 158, 179
- cosmic web classification** 4, 24, 44, 56, 131, 133–136, 138, 140, 142, 147–150, 154, 156, 179, 181–185
- cosmological constant** 8, 20
- cosmological parameters** 8, 15, 19, 20, 22, 30, 37, 42, 62, 67, 74, 75, 80, 101, 103, 106, 125, 138, 157, 178, 185
- CosmoMC** 58
- cosmostatistics** 3, 10, 49
- Cox’s desiderata** 51, 53
- Cox-Jaynes theorem** 51
- Cromwell’s rule** 53
- cross-correlation** 32, 33, 42, 43, 75, 105, 113, 114, 129, 148, 154, 156
- curse of dimensionality** 63–66
- dark energy** 2, 8, 19, 54, 56, 118, 125–127, 157, 158
- dark matter** 2, 15, 17, 18, 40, 117–119, 125, 129, 135, 155, 156
- dark matter particles** 15, 29, 31, 32, 34, 41, 42, 68, 74, 80, 86, 87, 89, 90, 92, 95, 107, 111–113, 119, 122, 123, 125–128, 138, 166–170, 172, 173, 175, 178, 185
- dark matter void** 4, 110, 111, 117–120, 122–129, 155
- dark-energy domination** 2, 8
- data** 52, 53, 66, 68, 71, 72, 74, 75, 79, 80, 83, 85, 86, 89, 92, 110, 117, 119, 122–124, 127–129, 133–140, 142–144, 147–152, 154–158
- data assimilation** 4, 63, 155, 157, 158
- data model** 4, 54, 63, 66, 67, 69, 70, 155, 157
- decaying mode** 19–21, 23
- decision theory** 4, 149–152, 154, 156
- declination** 68, 86
- decoupling** 2
- density contrast** 9–13, 16–19, 22, 23, 30, 34, 37–41, 43, 67–69, 73, 75, 95, 97–99, 101, 103, 104, 106, 121, 122, 136, 137, 141, 142, 168, 169, 172, 173, 178, 180–182, 184, 185
- density field** 2, 4, 10, 12, 17, 19, 21–26, 29–34, 37, 41–45, 66–69, 72, 74–77, 79–86, 88, 89, 91, 92, 95–107, 109–114, 118–122, 124–126, 129, 131–136, 138, 141, 143, 147, 148, 154–156, 167–170, 177, 179, 180, 184, 185
- density profile** 117–119, 122, 125, 127–129, 180, 181
- detailed balance** 58–60
- diffusion equation** 27
- Dirac delta distribution** 13, 15, 52, 55, 67
- displacement field** 22, 23, 25, 29, 31, 37, 40, 41, 44, 112, 132, 155, 156, 166, 168, 177, 178
- DIVA** DynamIcal Void Analysis 40, 132
- divergence of the Lagrangian displacement field** 23, 29, 37–42
- drift** 74, 166, 175–178
- eigenvalue** 23, 24, 44, 132, 134, 136, 137, 141, 142, 178, 181–185
- Einstein’s equations** 8, 132
- Einstein-de Sitter universe** 20, 21
- ellipticity distribution** 117, 119, 122, 125–127, 129, 180, 181
- ensemble average** 9, 12–14
- entropy** 134, 138, 139, 142–144, 147, 148
- EPT** Eulerian perturbation theory 7, 18, 21, 25, 96, 101, 107, 132

- equation of motion** 15–17, 19, 22, 73, 74, 112, 166, 182, 183
- equation of state** 1, 8, 18, 54, 56, 126, 157
- ergodicity** 9, 58
- estimator** 37, 44, 50, 52, 99, 179
- Euler’s equation** 17, 19, 25, 26, 96
- Euler’s method** 175
- evidence** 52, 54, 56, 57
- exascale computers** 3
- excess kurtosis** 38, 40
- expansion** 1, 2, 15–17, 19, 23, 118, 147, 157
- exploration of the posterior** 54, 55, 62
- extended logic** 49, 51
- fair game** 151
- FDA** finite difference approximation 168, 174, 178
- filament** 4, 24, 26, 29, 44, 45, 75, 79, 83, 86, 91, 96, 99, 111, 121, 131–137, 140, 142, 145, 147–150, 152, 154, 156, 179, 181–185
- final conditions** 40, 41, 67, 68, 71, 72, 74, 75, 77, 80–86, 88, 89, 91, 92, 97, 98, 100, 106, 109–111, 113, 114, 117, 119, 122, 128, 132–139, 141–143, 147, 151, 152, 154, 155, 157, 158, 175, 185
- flat prior** 53
- fluid** 2, 15, 17, 18, 22, 23, 25, 27, 96, 155, 165, 178
- formation history** 2, 4, 63, 71, 79, 80, 86, 88, 89, 91, 92, 96, 126, 131, 133, 134, 143, 148, 155, 156
- forward modeling** 51, 68, 74, 110, 135
- Fourier transform** 3, 41, 161, 162, 169–171, 173, 174, 178, 184
- free-particle approximation** 27
- frequentist statistics** 49–53, 57, 124
- Friedmann’s equations** 8, 16, 17, 19, 20, 167
- frozen flow approximation** 26
- full gravity** 29, 32, 37, 39–43, 68, 69, 95–101, 103–106, 109–111, 114, 117, 119, 121, 128, 131, 135, 148, 155
- Gadget-2** 29, 109–114, 121, 125, 155, 174, 185
- gain function** 150, 151, 154
- galaxy formation** 2, 69, 118, 121, 156
- galaxy survey** 1, 2, 4, 9, 12, 15, 29, 40, 62, 64, 66, 80, 86, 89, 95, 97, 106, 107, 117, 118, 120, 128, 129, 132, 134, 149, 155
- galaxy void** 117, 118, 120, 122, 124–129
- Gaussian kernel** 43, 174, 184
- Gaussianization** 96, 97, 106
- general relativity** 2, 7, 8, 15, 54, 56, 127, 133
- Gibbs sampling** 60, 75
- gravitational constant** 8
- gravitational evolution** 1, 2, 7, 9–11, 15, 16, 18, 24, 25, 97, 110, 126, 133, 155, 156, 182
- gravitational field** 25, 184
- gravitational potential** 9, 16–18, 23, 25, 26, 44, 136, 157, 166–168, 173, 174, 181, 183, 184
- Green function** 173, 174, 184
- grf** Gaussian random field 2, 4, 10–12, 14, 41, 55, 66, 67, 74, 75, 77, 83, 86, 91, 118, 121, 122, 125, 129, 132, 134, 135, 138, 142, 143, 155, 161, 162, 177, 185
- growing mode** 19, 21, 23, 24
- HADES** HAmiltonian Density Estimation and Sampling 12, 66
- halo** 2, 24, 26, 31, 38, 40, 45, 113, 119, 132, 133, 135, 141, 148, 183
- Hamilton’s equations** 61, 62, 66, 73, 175
- Hastings ratio** 59, 60
- HDM** hot dark matter 2
- Helmholtz decomposition** 43
- high-dimensional function** 65, 89
- high-dimensional parameter space** 53, 55, 56, 59, 60, 64, 65, 72, 73, 75, 80, 82, 89, 91, 121, 133–135, 155
- high-order correlation function** 2, 10, 11, 14, 40, 79, 83, 86, 89, 91, 95, 96, 99, 101, 106, 119, 121, 132, 134, 135, 148
- HMC** Hamiltonian Monte Carlo 60–63, 66, 72–74, 77, 80, 89, 121, 135, 155, 157
- homogeneous Universe** 8, 16, 19, 64, 96, 158

- Hot Big Bang** 1, 2  
**Hubble flow** 16, 112  
**Hubble parameter** 8, 19, 20  
**Hubble radius** 15  
**hypothesis testing** 50, 54  
**inference** 49, 50, 52, 54, 62, 79, 80, 85, 89, 91, 92, 133–135, 143, 148, 154, 156, 157  
**inflation** 1, 2, 9, 10, 132, 156  
**inflaton** 1  
**information content** 2, 4, 86, 92, 95, 97, 106, 107, 135, 138, 139, 142–144, 147, 148, 156–158, 169  
**information theory** 51, 131, 134, 138, 148, 156  
**initial conditions** 1–4, 10, 15, 24, 29, 31, 32, 37, 40, 41, 43, 62, 66–69, 71–75, 77, 79–86, 88, 89, 91, 92, 97–101, 104–106, 109–111, 113, 117, 119–122, 124, 125, 128, 129, 131–135, 138, 141–144, 148, 151, 154–158, 161, 165–167, 175–178, 182, 185  
**integrated Sachs-Wolfe effect** 118, 129, 133, 157  
**interpolation** 166–168, 172–175, 178  
**invariant distribution** 58  
**inverse problem** 51, 91  
**isocurvature perturbations** 56, 157  
**Jeffreys’ priors** 53  
**Jeffreys’ scale** 57  
**Kac’s theorem** 161, 163  
**KDK** kick drift kick 74, 175  
**kick** 62, 74, 166, 168, 175–178  
**Kronecker symbol** 18, 73, 136  
**Kullback-Leibler divergence** 134, 138–140, 143, 144, 148  
**Lagrangian potential** 24, 42, 44, 178, 182  
**Lagrangian transport** 85, 89, 90, 92, 110, 122, 135, 147, 148, 158  
**large-scale structure inference** 4, 63, 66, 69, 74, 75, 79, 82, 86, 89, 90, 107, 109, 112, 117–120, 129, 131, 133–135, 148, 149, 154–157, 177  
**large-scale structure likelihood** 68, 69, 71, 75, 109, 119, 129, 135  
**leapfrog** 73, 74, 175, 176  
**lightcone** 9, 69, 157  
**likelihood** 52–54, 56, 57, 60, 68, 73, 134  
**likelihood-free methods** 56  
**linear evolution** 2, 96  
**linear growth factor** 19–21, 23, 25, 40, 73, 113, 167, 177  
**linear potential approximation** 26  
**linear regime** 19, 23, 26, 30, 32, 63, 89, 109, 111, 119, 120, 132, 135, 157  
**Liouville’s theorem** 17, 61  
**local** 23–26, 37, 41, 69, 99, 107, 133, 169, 180  
**local Lagrangian approximations** 42  
**local tidal approximation** 26  
**log-normal distribution** 10, 12, 31, 62, 83, 91, 118, 134  
**low-pass filter** 169–171  
**LPT** Lagrangian perturbation theory 4, 7, 22, 23, 25, 29–35, 37–45, 95–103, 105–107, 110, 112, 113, 132, 135, 141, 155, 165–168, 177, 178  
**LSS** large-scale structure. 1–4, 9, 15, 29, 37, 45, 64, 66, 71, 79, 80, 82, 83, 86, 88, 89, 91, 92, 95–97, 99, 101, 106, 109, 110, 117–119, 121, 122, 126–128, 131–135, 137, 138, 141–143, 147–153, 155–157, 181  
**luminosity** 66, 68–71, 74, 79–81, 83, 86, 88, 89, 91, 121, 122, 129, 133–135, 156  
**machine epsilon** 65  
**machine learning** 51  
**marginal pdf** 11, 54–58, 62, 68, 163  
**mask** 52, 66, 70, 74, 80, 86, 118, 134, 154  
**mass matrix** 61, 73, 74  
**mass resolution** 30, 106, 168, 185  
**matter domination** 2, 8, 15, 67  
**maximum-entropy** 51  
**MCMC** Markov Chain Monte Carlo 49, 56, 58–60, 65, 82, 91, 119

- mesh assignment** 34, 68, 101, 147, 166, 168, 170–174, 184
- Metropolis ratio** 59
- Metropolis update** 59, 62
- MFF** mass filling fraction 131, 133, 140, 141, 143, 146–148
- MH** Metropolis-Hastings 59, 60, 62, 65
- mildly non-linear regime** 4, 30–32, 34, 37, 63, 89, 95–97, 100, 105, 106, 109–111, 119, 120, 132, 134, 135, 155, 157
- mock catalog** 63, 74–76, 95–97, 101, 106, 118
- mode coupling** 96, 97, 112, 134, 166, 167
- model comparison** 15, 49, 50, 53, 54, 56, 57, 119
- moment** 10, 11, 15, 17, 18, 40, 96
- momentum** 17, 18, 61, 62, 96, 166–168, 173, 175–178
- MUSCLE** Multiscale spherical collapse 42, 43
- N-GenIC** 29, 177
- nested model** 57
- neutrino** 2
- Newtonian gravity** 15, 27
- NGP** nearest grid point 68, 170, 171, 173
- no-free lunch theorem** 49, 53, 58
- noise** 52, 54, 66, 69, 79, 83, 85, 89, 91, 118, 119, 121, 127–129, 135, 148, 155
- noise parameter** 66, 70–72, 75, 77, 80, 81, 83, 89, 129
- non-committal prior** 57
- non-Gaussianity** 4, 10, 30, 34, 40, 41, 56, 62, 67, 119, 121, 124, 135, 156
- non-linear approximation** 7, 25, 96
- non-linear evolution** 2, 4, 10, 23, 25, 40, 43, 66, 95–97, 101, 106, 107, 110, 119, 121, 134, 141, 155, 157
- non-linear filtering** 4, 109–113, 119, 121, 127–129, 134–136, 141, 147, 155
- non-linear regime** 12, 19, 25, 26, 32, 44, 97, 106, 107, 111, 114, 128, 131–135, 148, 149
- non-local** 21, 24, 25, 31, 34, 40–42, 69, 85, 86, 89, 90, 92, 122, 134, 174
- non-magnetic approximation** 26
- nuisance parameters** 54, 61
- number function** 68, 71, 84, 103, 117, 119, 122, 125, 126, 129, 180
- Nyquist wavenumber** 31, 111, 169, 171
- Nyquist-Shannon sampling theorem** 169
- Occam’s razor** 56, 57
- OCDM** open cold dark matter 20
- one-point distribution** 10, 12, 30, 31, 37, 40–42, 75, 95–101, 103, 106, 121, 134, 135, 155
- ORIGAMI** Order-ReversIng Gravity, Apprehended Mangling Indices 40, 132
- pancake** 24, 26, 182
- paradigms of science** 3
- parameter inference** 49, 50, 54, 56, 58
- particle realization** 29, 41, 44, 45, 68, 72, 74, 75, 86, 98, 99, 101, 103, 104, 109–114, 155, 177, 178
- partition function** 61
- path integral formalism** 96
- pdf** probability distribution function 2, 9–13, 30, 31, 37, 40, 52–54, 56–58, 60, 61, 65, 66, 75, 97–99, 101, 103, 119, 129, 134, 136–145, 147, 155, 161, 162
- peculiar velocity** 16–18, 66
- peculiar velocity flow** 17, 25
- periodic boundary conditions** 29, 74, 98, 104, 113, 122, 168, 172, 175, 185
- phase** 32, 44, 105, 126, 134, 156
- phase space** 17, 18, 40, 61, 62, 74, 119, 132, 156, 175
- photometric redshift** 52, 62, 66, 157
- physical density prior** 67, 68
- plausibility** 51
- plausible reasoning** 49, 51
- PM** particle-mesh 4, 112, 113, 165–170, 173–175, 177, 178

- Poisson equation** 17, 19, 23–27, 42, 166–168, 173, 181, 182, 184
- Poisson intensity field** 69, 70
- Poisson likelihood** 69, 71, 85, 121
- Poisson process** 69, 74, 85, 91, 138
- posterior** 4, 52–58, 63, 66, 71, 72, 74, 75, 77, 82, 86, 119, 121, 122, 124, 129, 134–136, 138–145, 147, 148, 150–152, 154–156
- posterior mean** 54, 75, 81, 83–85, 91, 92, 136, 137, 140–142
- posterior odds** 57
- posterior standard deviation** 54, 75, 81, 83, 85, 89, 91, 92, 137
- potential well** 2, 21, 95
- power spectrum** 2, 13–15, 29–34, 41, 42, 44, 62, 66, 67, 74, 75, 77, 80–83, 91, 95, 99, 100, 105, 106, 111, 112, 118, 119, 122, 125, 126, 134, 138, 177, 178, 185
- principal component analysis** 66
- prior** 12, 49, 52–54, 56, 57, 66–69, 71, 73, 75, 77, 117, 119, 121–123, 126–129, 134, 135, 137–145, 147, 148, 150, 151, 154, 156
- prior choice** 52, 53
- prior volume** 53, 57
- probability (definition)** 50
- probability theory** 4, 49–53, 149, 155
- proper prior** 53
- proposal distribution** 59, 60, 62, 65
- quantum field theory** 2, 96
- quantum fluctuation** 1, 10
- radiation domination** 2
- recombination** 2
- reconstruction** 3, 32, 62, 69, 75, 79, 92, 96, 99, 111, 114, 118, 119, 121, 123–129, 133–136, 155, 184
- redshift** 8, 29–38, 40, 41, 52, 68, 75, 80, 86, 95, 97, 98, 101–106, 110–114, 119, 134, 140, 147, 151, 154, 157, 177
- redshift-space distortions** 2, 9, 66, 69, 127, 135, 157
- reduced bispectrum** 15
- Rees-Sciama effect** 133, 157
- reionization** 106
- remapping** 4, 30–35, 95–107, 110
- remapping function** 97, 100–103
- renormalization group flow** 96
- renormalized perturbation theory** 96
- reversibility** 58, 61, 62, 74
- right ascension** 68, 86
- risk aversion** 151, 152, 154
- sample** 4, 50, 55–59, 63–65, 68–72, 74, 75, 77, 80–91, 109–113, 121–124, 129, 134–138, 140–142, 147, 148, 151, 154, 155
- sample average** 9, 13
- sampling** 55, 56, 58–61, 63–67, 71, 72, 74, 75, 77, 89, 118, 119, 121, 122, 126, 128, 129, 135, 155, 157, 169, 170
- Savage-Dickey ratio** 57
- SC** spherical collapse 24, 26, 42, 43, 96, 183
- scalar field** 1, 9, 10, 12, 136, 161, 162
- scalar part** 43, 44
- scale factor** 1, 8, 19, 20, 42, 67, 82, 85, 86, 88, 89, 91, 114, 121, 138, 147, 166, 175, 176
- SCDM** standard cold dark matter 20
- Schechter luminosity functions** 74, 80
- Schrödinger equation** 27
- Schur-complement** 163
- SDSS** Sloan Digital Sky Survey 4, 53, 56, 70, 74, 79, 80, 82, 84, 86, 89, 91, 92, 117–126, 128, 129, 131–135, 137, 139, 140, 142–144, 147–149, 151, 154, 155
- second-order growth factor** 21, 24, 73, 167, 177
- selection effects** 2, 52, 66, 68–70, 74, 79, 80, 83, 86, 89, 91, 118, 119, 121, 122, 125, 126, 129, 134–136, 140, 148, 154, 155, 157
- shape function** 169–171, 173
- sheet** 4, 24, 29, 44, 45, 79, 96, 99, 117, 131–137, 140, 142, 145, 147–150, 152, 154, 156, 179, 181–185



- shell-crossing** 18, 22, 24, 26, 42, 44, 96, 97, 106, 155, 182  
**shot noise** 37, 85, 129, 180  
**single-stream approximation** 18, 26  
**skewness** 30, 38, 40  
**sparsity** 53, 64, 117–119, 121, 125–129  
**spectroscopic redshift** 80  
**speculative map** 151, 152  
**statistical homogeneity** 1, 2, 4, 9, 12–15, 67, 69, 135, 178  
**statistical isotropy** 1, 2, 4, 9, 12, 13, 15, 69, 135, 178  
**statistical mechanics** 61, 96  
**statistical uncertainty** 4, 55, 69, 79, 89, 91, 92, 105, 119, 124, 126, 127, 129, 156  
**stress tensor** 17–19  
**structure formation** 2, 4, 7, 10, 15, 18, 24, 40, 44, 54, 66–68, 71, 74, 75, 79, 86, 89, 91, 95, 96, 101, 105, 106, 109–112, 119, 121, 122, 131–134, 136, 141, 148, 149, 154, 155, 157  
**structure type** 44, 45, 75, 96, 99, 100, 131–145, 147–152, 154, 155, 179, 181–184  
**Sunyaev-Zel’dovich effect** 133, 157  
**survey geometry** 52, 70, 74, 75, 79, 83, 86, 89–92, 110, 119, 121, 122, 125, 126, 129, 135, 137, 140, 148, 151, 154, 155  
**survey response operator** 66, 70, 74, 83, 122, 123, 140, 143, 147  
**symplecticity** 61, 62, 74, 175  
**systematic uncertainty** 55, 79, 82, 86, 89, 119, 126  
**T-web** 132–138, 142, 143, 148, 150, 154, 179, 181–185  
**three-point correlation function** 34, 35, 37, 86, 95, 100, 103, 105, 106, 121, 135, 155  
**tidal effects** 24, 34, 126, 135, 183  
**tidal field** 126, 131–133, 137, 154, 156, 182, 183  
**tidal tensor** 22, 132, 134, 136, 137, 141, 142, 147, 148, 181, 182, 184, 185  
**transfer function** 98, 100, 101, 103, 104, 106, 112  
**transition probability** 58–60  
**trispectrum** 15  
**TSC** triangular shaped cloud 170, 171, 173  
**two-point correlation function** 2, 12–14, 31, 32, 34, 44, 83, 95, 100, 103, 105, 106, 111, 118, 121, 122, 134, 135, 155  
**uncertainty quantification** 50, 52, 53, 55, 63, 75, 76, 79, 80, 82, 85, 89, 91, 92, 110, 112, 117, 119, 121, 122, 124, 129, 131, 133–136, 138, 148, 155  
**utility function** 150, 151  
**V-web** 132, 150, 184  
**vector part** 41, 43, 44  
**velocity dispersion** 17, 18  
**velocity field** 9, 16, 18, 19, 21, 22, 24–26, 75, 80, 86, 87, 91, 120, 128, 133, 134, 155, 157, 184  
**velocity potential** 25, 26, 96  
**velocity profile** 128  
**velocity shear field** 132, 184  
**VFF** volume filling fraction 44, 45, 99, 131, 133, 135, 140, 141, 143, 145, 147, 148, 150  
**VIDE** Void IDentification and Examination toolkit 119, 121–124, 126, 127, 129, 155, 179–181  
**viscosity** 18, 26, 27, 96  
**Vlasov equation** 17, 18  
**Vlasov-Poisson system** 17, 18, 32, 96, 110, 181  
**void** 4, 24, 29, 38–41, 44, 45, 86, 91, 92, 96, 99, 100, 111, 117–129, 131–137, 140, 142, 145, 147–152, 154–156, 179–185  
**void hierarchy** 1, 117, 118, 121, 128, 129, 132, 134, 180  
**void-in-cloud** 43, 128  
**void-in-void** 128  
**Voronoi tessellation** 121, 122, 179–181  
**vorticity** 19, 23–25  
**watershed transform** 121, 180  
**WDM** warm dark matter 157  
**weak gravitational lensing** 118, 129, 133, 157  
**white noise** 177

**Wick's theorem** 11, 14

**Wiener filter** 11, 75, 77

**WMAP-7** 30, 101

**ZA** Zel'dovich approximation 23–27, 29–32, 34, 35, 37, 38, 40, 41, 43, 44, 96, 98, 99, 101–105, 112,

155, 168, 177, 178, 182

**ZARM** Zel'dovich approximation remapped 30–32, 34, 35, 103, 104

**ZOBOV** 119, 121, 122, 179, 180

---

## Bayesian large-scale structure inference and cosmic web analysis

Surveys of the cosmic large-scale structure carry opportunities for building and testing cosmological theories about the origin and evolution of the Universe. This endeavor requires appropriate data assimilation tools, for establishing the contact between survey catalogs and models of structure formation.

In this thesis, we present an innovative statistical approach for the *ab initio* simultaneous analysis of the formation history and morphology of the cosmic web: the BORG algorithm infers the primordial density fluctuations and produces physical reconstructions of the dark matter distribution that underlies observed galaxies, by assimilating the survey data into a cosmological structure formation model. The method, based on Bayesian probability theory, provides accurate means of uncertainty quantification.

We demonstrate the application of BORG to the Sloan Digital Sky Survey data and describe the primordial and late-time large-scale structure in the observed volume. We show how the approach has led to the first quantitative inference of the cosmological initial conditions and of the formation history of the observed structures. We then use these results for several cosmographic projects aiming at analyzing and classifying the large-scale structure. In particular, we build an enhanced catalog of cosmic voids probed at the level of the dark matter distribution, deeper than with the galaxies. We present detailed probabilistic maps of the dynamic cosmic web, and offer a general solution to the problem of classifying structures in the presence of uncertainty.

The results described in this thesis constitute accurate chrono-cosmography of the inhomogeneous cosmic structure.

---

## Inférence bayésienne et analyse des grandes structures de l'Univers

Les observations de la structure à grande échelle de l'Univers sont précieuses pour établir et tester des théories cosmologiques sur son origine et son évolution. Cette démarche requiert des outils appropriés d'assimilation des données, afin d'établir le contact entre les catalogues de galaxies et les modèles de formation des structures.

Dans cette thèse, une nouvelle approche pour l'analyse *ab initio* et simultanée de la formation et de la morphologie de la toile cosmique est présentée : l'algorithme BORG infère les fluctuations de densité primordiales et produit des reconstructions physiques de la distribution de matière noire, en assimilant les relevés de galaxies dans un modèle cosmologique de formation des structures. La méthode, basée sur la théorie bayésienne des probabilités, fournit un moyen de quantifier précisément les incertitudes.

On présente l'application de BORG aux données du Sloan Digital Sky Survey et on décrit la structure de l'Univers dans le volume considéré. On démontre que cette approche a mené à la première inférence quantitative des conditions initiales et du scénario de formation des structures observées. On utilise ces résultats pour plusieurs projets cosmographiques visant à analyser et classifier la toile cosmique. En particulier, on construit un catalogue de vides, décrits au niveau de la matière noire et non des galaxies. On présente des cartes probabilistes détaillées de la dynamique de la toile cosmique et on propose une solution générale pour la classification des structures en présence d'incertitude.

Les résultats de cette thèse constituent une précise description chrono-cosmographique des inhomogénéités de la structure cosmique.

---